

THE INITIAL STAGES OF ATOMIC LAYER DEPOSITION ON  
SUBSTRATES MODIFIED BY ORGANIC THIN FILMS

A Dissertation

Presented to the Faculty of the Graduate School  
of Cornell University

in Partial Fulfillment of the Requirements for the Degree of  
Doctor of Philosophy

by

Kevin James Hughes

August 2011

© Kevin J. Hughes 2011

# THE INITIAL STAGES OF ATOMIC LAYER DEPOSITION ON SUBSTRATES MODIFIED BY ORGANIC THIN FILMS

Kevin J. Hughes

Cornell University 2011

Atomic layer deposition (ALD) provides the ability to deposit highly conformal thin films with essentially molecular level control over film thickness. These characteristics have made it an active area of research for a number of applications, notably in the field of semiconductor devices. The focus of the work presented here is on the initial stages of film growth, including the first interaction of gas phase ALD precursors with the substrate, and the period in which the growing surface transitions from the starting substrate to the steady-state growing film. Of particular interest are substrates modified using thin organic films. These organic films are used to alter the identity, density and spatial extent of functional groups on the surface.

We begin with a review of the prior work in this area, focusing on the ALD of  $\text{TiN}_x$  on a variety of organic films, including self-assembled monolayers with various endgroup chemistries, and branched films with a more 3-d distribution of functional groups. Here connections are observed between the initial interactions of the gas phase precursors with the organic film, and the subsequent stages of ALD growth. A relationship between the initial rate of ALD growth and the resulting film morphology is also observed, and can be explained by a variation in nucleation site density due to the structure of the organic film.

The next section involves the ALD of a range of materials ( $\text{Al}_2\text{O}_3$ ,  $\text{HfO}_2$ ,  $\text{Ta}_2\text{O}_5$ , and  $\text{TaN}_x$ ), on a single organic layer, branched poly(ethylene imine) (PEI).

Here, the presence of the organic layer causes an attenuation in the amount of material deposited per ALD cycle in the initial stages of growth. A strong correlation was found between the thermodynamic driving force of the ALD reaction and the degree of attenuation, suggesting that ALD processes in which there is a strong driving force (or low activation energy) for the formation of the final products can more easily overcome the obstacles presented by the organic layer.

The ALD of one material,  $\text{TaN}_x$ , was examined in more detail using *in situ* XPS. Substrates in this study included nonporous  $\text{SiO}_2$ , a porous low dielectric constant or ‘low- $\kappa$ ’ material, and both substrates modified by PEI films. PEI was used here in part because of the tendency of smaller molecules to infiltrate and deposit within the pore network of the low- $\kappa$ . The chemical structure of the chemisorbed tantalum precursor,  $\text{Ta}[\text{N}(\text{CH}_3)_2]_5$ , after the first cycle of ALD, as well as the oxidation state and chemical composition of the  $\text{TaN}_x$  film in the first 10 cycles ( $\sim 6$ - $10$  Å) were strongly affected by the starting substrate. Substrates with a high density of oxygen containing groups led to a more oxidized  $\text{TaN}_x$  film, and less efficient incorporation of N in a nitride binding state. Furthermore, the presence of a PEI film enhanced the growth of  $\text{TaN}_x$  at the surface of the porous low- $\kappa$ , and limited infiltration of the pore network by the gas phase ALD precursors.

A final set of experiments involved the early stages of cobalt film formation on tantalum substrates using chemical vapor deposition with the metalorganic precursor dicobalt hexacarbonyl tert-butylacetylene (CCTBA). Here it was found that growth proceeded in two phases. The first involved the formation of an intermixed cobalt/tantalum layer, while the second took place after the intermixed layer was covered and was characterized by the formation of a mixed carbon/cobalt film.



## **BIOGRAPHICAL SKETCH**

Kevin J. Hughes was born and raised in northeast Ohio, the oldest of three children. He was interested in science and technology from an early age, and was particularly fascinated by the scale and complexity of chemical plants; a trip to the Bellefield boiler plant in Pittsburgh, PA being a particularly formative experience. He attended Carnegie Mellon University, pursuing a degree in chemical engineering, with a minor in colloids, polymers, and surfaces. As an undergraduate, he interned twice at Intel, working in semiconductor fabrication facilities in Portland, OR (2001), and Rio Rancho, NM (2002). After graduating with university honors in 2003, he began work at Lubrizol Corp. in Wickliffe, OH, as a research engineer in the Applied Sciences Department. Here he focused on applications related to colloids and surface science, and had the opportunity to work on a wide range of products, including engine oil additives, personal care products, and emulsion explosives. Leaving industry, he returned to school in 2005 to enter the PhD program at Cornell University, in the research group of Prof. James Engstrom,. He was awarded an SRC/Novellus graduate fellowship in 2006, which supported his PhD through 2011. After graduation he went on to work at Intel, at the technology development site in Hillsboro, OR.

Outside of the lab, Kevin found time to attend 104 Cornell hockey games, in Ithaca and away, at which the team compiled a record of 66-31-7.

*Dedicated to my parents,  
for their love, generosity, and support.*

## ACKNOWLEDGEMENTS

There are many people who have been instrumental in guiding and assisting me through the work presented here, and who have shaped my experience at Cornell. First I would like to take the opportunity to thank my academic advisor Prof. Jim Engstrom. The thorough, critical, and analytical approach to research that I learned from him is invaluable, and is something that I will continue to use throughout my career. I've become the engineer I am in large part through Jim's example and guidance.

I would also like to acknowledge the other members of my PhD committee. Prof. Abraham Stroock has provided advice at a number of key points, and in particular his suggestion of looking into the use of polyamines as surface modifiers has made a significant impact on my work. Prof. David Muller, and his students Dr. Peter Ercius and Huolin Xin, have provided valuable insights through the use of transmission electron microscopy, which would not have been possible with any other technique. I was glad to have the opportunity to work with them on a publication; the Muller group also shares a passion for thorough, high quality research work.

Within the Engstrom group, I would first like to thank Dr. Abhishek Dube and Dr. Manish Sharma, who 'showed me the ropes' of the Engstrom group lab equipment early on. I learned a lot from them in the years we worked together. Their work, along with that of Dr. Paul Ma and Dr. Aravind Killampalli, laid the groundwork for much of the work described here. I'd also like to thank my other colleagues along the way, Dr. Sukwon Hong, Tushar Desai, Ed Kish, Wenyu Zhang, and Rambert Nahm. Teamwork is an integral component of working in our group, and it was great to work as a team with these guys. We shared some difficult times, and more than a few laughs also. Wen and Rambert took over the day to day operations in 312 with a great

amount of motivation and skill. I feel great about leaving the system in their hands, which has helped me a lot in the final stages of my time at Cornell.

Along the way I have also had the opportunity to work with a number of talented and highly motivated undergraduate students through REU programs provided by CNF and CCMR, and I feel great gratitude for the long hours they put in the lab in support of a number of projects described here. These students included Luke Zhu, Krista Cosert (Summer 2007), Scott I. Isaacson (Summer 2009), Deirdre Mannion-Fischer (Summer 2009), and John Davis (Summer 2010).

Within the Chemical Engineering department there were many professors and staff members who provided assistance along the way. I would like to particularly recognize Glenn Swan, whose support in the Olin Hall machine shop was a great help on several occasions, and Brian Ford, who helped us through a number of issues with utilities in the building. I would also like to acknowledge the Cornell Nanofabrication Facility and Nanobiotechnology Center. Much of the work described here would not have been possible without the use of these facilities.

For financial support, I would like to acknowledge the Semiconductor Research Corporation and Novellus Systems, Inc., who provided funding for my PhD from Fall 2006 through Spring 2011. SRC also provided support to travel to the yearly TechConnect conference, where I was able to interact and share my research with a number of other graduate students and researchers from the semiconductor industry.

On a personal note, I'd like to thank all the great friends I've made here in Ithaca. This experience would not have been the same without all of them. And finally to my parents, my sisters Colleen and Kara, and to Laura. Their support and encouragement has meant more than I can say. In one way or another, they've been with me through it all.

## TABLE OF CONTENTS

<b>1. Introduction.....</b>	<b>1</b>
1.1 Overview .....	1
1.2 Atomic layer deposition .....	1
1.3 Thin film deposition on surfaces modified by organic layers .....	7
1.4 Copper/low- $\kappa$ integration and diffusion barriers.....	8
1.5 Overview of dissertation .....	12
1.6 References.....	14
<b>2. Experimental techniques .....</b>	<b>17</b>
2.1 Overview .....	17
2.2 Materials .....	17
2.3 Substrate preparation .....	21
2.4 Formation of organic thin films .....	22
2.5 Description of vacuum systems .....	24
2.6 X-ray photoelectron spectroscopy (XPS) .....	30
2.7 Angle-resolved XPS (ARXPS).....	33
2.8 Spectroscopic ellipsometry .....	43
2.9 Atomic Force Microscopy.....	47
2.10 Ellipsometric porosimetry .....	48
2.11 References.....	49
<b>3. Review of the use of organic thin films to alter the nucleation and growth in atomic layer deposition .....</b>	<b>52</b>
3.1 Overview.....	52
3.2 Introduction .....	53
3.3 The formation of inorganic-organic interfaces.....	63
3.3.1. Formation and characterization of interfacial organic layers.....	64
3.3.1.1. Experimental approach.....	64
3.3.1.2. Straight-chain self-assembled monolayers.....	67
3.3.1.3. Interfacial organic layers with branched microstructure.....	69

3.3.2. Reaction of transition metal coordination complexes with interfacial organic layers.....	79
3.3.2.1. Experimental approach .....	80
3.3.2.2. The kinetics of adsorption .....	81
3.3.2.2.1. Coverage-exposure relationships .....	81
3.3.2.2.2. Effects of microstructure of the organic layer on reactivity .....	85
3.3.2.3. Spatial extent of reaction .....	87
3.3.2.4. Structure and composition of the chemisorbed species in the saturated adlayers .....	95
3.3.2.4.1. Correlation between M and OFG densities .....	96
3.3.2.4.2. Stoichiometry of the chemisorbed species in the saturated adlayers .....	103
3.3.3. Atomic layer deposition on organic layers .....	111
3.3.3.1. Experimental approach .....	112
3.3.3.2. Effects of interfacial organic layers on thin film growth via ALD .....	114
3.3.3.2.1. Kinetics of nucleation and growth .....	114
3.3.3.2.2. Morphological evolution of thin film topology ....	126
3.3.3.3. Correlations between chemisorption and ALD growth .....	132
3.4. Conclusions and Outlook .....	138
3.5 References .....	146
<b>4. Nucleation delay in atomic layer deposition on a thin organic layer and the role of reaction thermochemistry .....</b>	<b>155</b>
4.1 Overview .....	155
4.2 Introduction .....	156
4.3 Experimental Procedures .....	159
4.4 Results .....	163
4.4.1. Poly(ethylene imine) thin film characterization .....	163
4.4.2. ALD of Al <sub>2</sub> O <sub>3</sub> on SiO <sub>2</sub> and PEI SiO <sub>2</sub> .....	168

4.4.3 ALD of HfO <sub>2</sub> on SiO <sub>2</sub> and PEI SiO <sub>2</sub> .....	180
4.4.4 ALD of Ta <sub>2</sub> O <sub>5</sub> and TaN <sub>x</sub> on SiO <sub>2</sub> and PEI SiO <sub>2</sub> .....	185
4.5 Discussion .....	193
4.6 Conclusions and future directions .....	205
4.7 Appendix: ALD of Al <sub>2</sub> O <sub>3</sub> on FOTS SiO <sub>2</sub> .....	208
4.8 References .....	213
<b>5. Atomic layer deposition of titanium and tantalum nitrides on substrates</b>	
<b>modified by branched polymer layers .....</b>	<b>217</b>
5.1 Overview .....	217
5.2 Introduction .....	218
5.3 Experimental Procedures .....	222
5.3.1. Substrate preparation .....	223
5.3.2. ALD of TiN <sub>x</sub> and TaN <sub>x</sub> films .....	225
5.3.3. Characterization techniques .....	228
5.4 Results and discussion .....	231
5.4.1. Initial chemisorption of Ta[N(CH <sub>3</sub> ) <sub>2</sub> ] <sub>5</sub> on unmodified substrates .....	231
5.4.2. PEI and poly-G film characterization .....	237
5.4.3. Effect of PEI and poly-G on initial chemisorption of Ta[N(CH <sub>3</sub> ) <sub>2</sub> ] <sub>5</sub> ..	245
5.4.4. Effect of poly-G and PEI on TaN <sub>x</sub> and TiN <sub>x</sub> ALD conducted in UHV .....	261
5.4.5. Effect of PEI on TaN <sub>x</sub> ALD conducted in a conventional ALD reactor .....	277
5.4.6. Effect of poly-G on TiN <sub>x</sub> ALD conducted in UHV .....	282
5.4.7. Effect of poly-G and PEI on TaN <sub>x</sub> and TiN <sub>x</sub> thin film morphology ...	285
5.5 Conclusions .....	291
5.6 References .....	296
<b>6. Infiltration of organic film precursors into porous low-κ material.....</b>	<b>302</b>
6.1 Overview .....	302
6.2 Introduction .....	303
6.3 Experimental Procedures .....	306

6.3.1. Materials, substrate preparation, and formation of organic films .....	306
6.3.2. Characterization techniques .....	307
6.4 Results and Discussion .....	309
6.4.1. Deposition of FOTS on low- $\kappa$ .....	309
6.4.2. Effect of surface modifier structure and deposition parameters on infiltration .....	326
6.5. Determination of pore size distribution from EP isotherms .....	333
6.6. Conclusions .....	337
6.7. References .....	339
<b>7. <i>In situ</i> XPS study of the initial stages of cobalt CVD on tantalum using dicobalt hexacarbonyl tert-butylacetylene (CCTBA) .....</b>	<b>344</b>
7.1 Overview .....	344
7.2 Introduction .....	344
7.3 Experimental Procedures .....	345
7.4 Results and discussion .....	348
7.4.1 Characterization of the tantalum substrate .....	348
7.4.2 Characterization of the CCTBA beam and formation of terraces .....	350
7.4.4. Evolution of Co and Ta .....	356
7.4.5. Film Morphology .....	361
7.4.6. Evolution of carbon .....	364
7.4.7. Evolution of oxygen .....	357
7.5 Future experiments .....	374
7.6 Conclusions .....	374
7.7 References .....	376
<b>8. Summary .....</b>	<b>377</b>
<b>9. Appendix: Addition of x-ray photoelectron spectroscopy components to the Olin Hall 312 system .....</b>	<b>381</b>
9.1 References .....	398



## LIST OF FIGURES

<b>Figure 1-1</b>	Schematic of an ALD process to form $\text{TiO}_2$ using $\text{TiCl}_4$ and $\text{H}_2\text{O}$ .....	3
<b>Figure 1-2</b>	Number of research publications and patents related to ALD by year...	5
<b>Figure 1-3</b>	SEM image of the cross section of a modern Cu/low- $\kappa$ interconnect....	9
<b>Figure 1-4</b>	Schematic demonstrating the use of a branched organic layer to enhance ALD growth on a porous substrate .....	11
<b>Figure 2-1</b>	Structures of molecules used to form organic thin films.....	19-20
<b>Figure 2-2</b>	Schematic of the UHV system used for deposition and analysis.....	25
<b>Figure 2-3</b>	XPS analysis of a material of interest ( $i = 1$ ) buried by two materials ( $i = 2,3$ ), with a photoelectron takeoff angle of $\theta$ .....	34
<b>Figure 2-4</b>	Schematic of the ARXPS procedure used in this work.....	37
<b>Figure 2-5</b>	Summary of the assumed concentration profiles used for analyzing ARXPS results.....	39-40
<b>Figure 2-6</b>	Integrated photoelectron intensity from of the $\text{O}(1s)$ , $\text{Si}^0(2p)$ , and $\text{Si}^{4+}(2p)$ peaks as a function of takeoff angle, from a sample consisting of a thin film of $\text{SiO}_2$ on $\text{Si}(100)$ .....	42
<b>Figure 3-1</b>	Parameter space accessed by interfacial organic layers using the factors of density and dimensionality .....	65
<b>Figure 3-2</b>	Models of two $-\text{NH}_2$ terminated first generation PAMAM dendrons ..	71
<b>Figure 3-3</b>	XP spectra of the (a) $\text{C}(1s)$ and (b) $\text{N}(1s)$ features for the Gen-1 PAMAM dendrons with 3 carbon (3C) and 12 carbon (12C) anchors.	73
<b>Figure 3-4</b>	Ball and stick models of polyglycidol at two stages of growth .....	75
<b>Figure 3-5</b>	Attenuation length for photoelectrons from the $\text{C}(1s)$ core level as a function of the density of valence electrons in the organic film .....	78

<b>Figure 3-6</b>	Coverage-exposure relationship, deduced from XPS, for the adsorption of $\text{Ti}[\text{N}(\text{CH}_3)_2]_4$ on chemical oxide, -OH and -CH <sub>3</sub> terminated SAMs, at a substrate temperature of -50 °C .....82-83
<b>Figure 3-7</b>	Coverage-exposure relationship, deduced from XPS, for the adsorption of $\text{Ta}[\text{N}(\text{CH}_3)_2]_5$ at 25 °C on (a) a Gen-0 and Gen-1 PAMAM dendron, and (b) two different thicknesses of poly-G .....86
<b>Figure 3-8</b>	The predicted form for the photoemission intensity, $I(\theta)$ , from a 2-d layer of photoemitters as a function of takeoff angle, $\theta$ , for a series of values of $d_{\text{ML}}/\lambda$ , where $d_{\text{ML}}$ is the depth of a 2-d layer .....89
<b>Figure 3-9</b>	Integrated area of the Ti(2p) feature as a function of takeoff angle for saturated layers of $\text{Ti}[\text{N}(\text{CH}_3)_2]_4$ on straight-chain -NH <sub>2</sub> and -CH <sub>3</sub> terminated SAMs .....91
<b>Figure 3-10</b>	Integrated peak area of the Ta(4f) region for saturated layers of $\text{Ta}[\text{N}(\text{CH}_3)_2]_5$ on (a) -NH <sub>2</sub> terminated PAMAM dendrons, and (b) an 84 Å thick polyglycidol layer .....92
<b>Figure 3-11</b>	The density of Ti atoms produced by saturation exposures to $\text{Ti}[\text{N}(\text{CH}_3)_2]_4$ ( $T_s = 25$ °C) as a function of the SAM density, as deduced from XPS, for mostly unreactive SAMs .....97
<b>Figure 3-12</b>	The density of Ti atoms produced by saturation exposures to $\text{Ti}[\text{N}(\text{CH}_3)_2]_4$ ( $T_s = 25$ °C) as a function of OFG density, as deduced from XPS, for IOLs with reactive endgroups and backbones .....99
<b>Figure 3-13</b>	(a) The density of Ta atoms produced by saturation exposures to $\text{Ta}[\text{N}(\text{CH}_3)_2]_5$ ( $T_s = 25$ °C) as a function of OFG density, as deduced from XPS, for two generations of PAMAM dendrons .....100
<b>Figure 3-13</b>	(b) Density of Ta atoms produced by saturation exposures to $\text{Ta}[\text{N}(\text{CH}_3)_2]_5$ ( $T_s = 25$ °C) as a function of OFG density, for three thicknesses of poly-G, and one layer of poly-G that has been modified by a -NH <sub>2</sub> terminated SAM .....101

<b>Figure 3-14</b>	Number of $-\text{N}(\text{CH}_3)_2$ ligands retained by $\text{Ti}[\text{N}(\text{CH}_3)_2]_4$ after chemisorption on three straight-chain SAMs ( $-\text{CH}_3$ , $-\text{OH}$ , and $-\text{NH}_2$ terminated) and bare $\text{SiO}_2$ , as a function of substrate temperature ...	105
<b>Figure 3-15</b>	XP spectra of saturated layers of $\text{Ta}[\text{N}(\text{CH}_3)_2]_5$ for the $\text{N}(1s)$ and $\text{Ta}(4p_{3/2})$ regions. The substrates include, bare chemical oxide, two thicknesses (30 and 84 Å) of poly-G, and an 84 Å poly-G film modified by a $-\text{NH}_2$ terminated SAM .....	108
<b>Figure 3-16</b>	$\text{TiN}_x$ film thickness as a function of the number of ALD cycles at $T_s = 167^\circ\text{C}$ and $207^\circ\text{C}$ , on (a) on chemical oxide and two unreactive SAMs (ODTS and TTS); and (b) on chemical oxide and three reactive $-\text{NH}_2$ terminated, straight-chain and branched IOLs .....	118
<b>Figure 3-17</b>	$\text{TiN}_x$ film thickness as a function of the number of ALD cycles at $T_s = 167^\circ\text{C}$ and $207^\circ\text{C}$ , on chemical oxide, a straight chain $-\text{OH}$ SAM, and three thicknesses (30, 47 and 84 Å) of poly-G .....	121
<b>Figure 3-18</b>	Growth attenuation factor $\alpha$ as a function of IOL thickness .....	124
<b>Figure 3-19</b>	Atomic force micrographs of representative $\text{TiN}_x$ films grown by ALD on bare chemical oxide, and a variety of IOLs, including a $-\text{NH}_2$ terminated dendron (Gen-1-3C), two unreactive SAMs (HMDS and TTS), and two thicknesses of poly-G .....	127
<b>Figure 3-20</b>	RMS surface roughness, measured by AFM, vs. ellipsometric film thickness for $\text{TiN}_x$ ALD films grown on (a) Gen-1-3C and an $-\text{OH}$ SAM), and two unreactive SAMs (HMDS and TTS); and (b) on three IOLs with reactive endgroups (an $-\text{OH}$ SAM, and two thicknesses of poly-G), and an unreactive SAM (TTS) .....	129
<b>Figure 3-21</b>	(a) Annular dark field transmission electron micrograph of a $\text{TiN}_x$ film grown on a $-\text{NH}_2$ terminated IOL (Gen-1-3C) at $167^\circ\text{C}$ , and (b) Elemental profiles for Ti, Si and C obtained from corresponding high-resolution electron energy loss spectra .....	131

<b>Figure 3-22</b>	Growth attenuation factor $\alpha$ vs. the saturation density of $\text{Ti}[\text{N}(\text{CH}_3)_2]_4$ (at $T_s = 25^\circ\text{C}$ ) measured from beam reflectivity .....	134
<b>Figure 3-23</b>	RMS roughness for the early stages of growth vs. $1/\alpha$ for $\text{TiN}_x$ ALD .....	137
<b>Figure 4-1</b>	AF micrographs of the (a) bare $\text{SiO}_2$ substrate, (b) as-deposited PEI thin film on $\text{SiO}_2$ , and (c) as-deposited PEI thin film after annealing at $T_s = 210^\circ\text{C}$ for 3 min in 200 mTorr of Ar; and integrated areas of the (d) N(1s) and (e) C(1s) XPS features as a function of photoelectron takeoff angle for as deposited PEI .....	162
<b>Figure 4-2</b>	Reflected x-ray intensity as a function of the out-of-plane scattering vector, $q_z$ , for a PEI thin film on a thermally oxidized Si(100) substrate .....	165
<b>Figure 4-3</b>	(a) $\text{Al}_2\text{O}_3$ film thickness as a function of ALD cycles on an unmodified $\text{SiO}_2$ substrate and on $\text{PEI} \text{SiO}_2$ . (b) X-ray photoelectron spectra of the Al(2p) region for 20 cycles of $\text{Al}_2\text{O}_3$ ALD on $\text{SiO}_2$ and $\text{PEI} \text{SiO}_2$ ...	179
<b>Figure 4-4</b>	Atomic force micrographs of $\text{Al}_2\text{O}_3$ films deposited on unmodified $\text{SiO}_2$ and $\text{PEI} \text{SiO}_2$ .....	171
<b>Figure 4-5</b>	RMS roughness of $\text{Al}_2\text{O}_3$ films deposited on unmodified $\text{SiO}_2$ and $\text{PEI} \text{SiO}_2$ .....	172
<b>Figure 4-6</b>	X-ray photoelectron spectra of the N(1s) region for as-deposited PEI on $\text{SiO}_2$ and for 20 cycles of $\text{Al}_2\text{O}_3$ ALD on $\text{PEI} \text{SiO}_2$ .....	173
<b>Figure 4-7</b>	Four possible final structures of the thin film stack resulting from 20 cycles of $\text{Al}_2\text{O}_3$ ALD on $\text{PEI} \text{SiO}_2$ shown in cross-section .....	175
<b>Figure 4-8</b>	Integrated areas of the (a) Al(2p), (b) N(1s), and (c) $\text{Si}^{4+}(2p)$ XPS features as a function of takeoff angle for 20 cycles $\text{Al}_2\text{O}_3$ ALD on $\text{PEI} \text{SiO}_2$ .....	176

<b>Figure 4-9</b>	(a) HfO <sub>2</sub> film thickness as a function of ALD cycles on an unmodified SiO <sub>2</sub> substrate and on PEI SiO <sub>2</sub> . (b) X-ray photoelectron spectra of the Hf(4d) region for 10 cycles of HfO <sub>2</sub> ALD on SiO <sub>2</sub> and PEI SiO <sub>2</sub> ....	181
<b>Figure 4-10</b>	X-ray photoelectron spectra of the (a) N(1s) and (b) Hf(4d) regions for 1 and 10 cycles of HfO <sub>2</sub> ALD on PEI SiO <sub>2</sub> .....	183
<b>Figure 4-11</b>	(a) Ta <sub>2</sub> O <sub>5</sub> and (b) TaN <sub>x</sub> film thickness as a function of ALD cycles on an unmodified SiO <sub>2</sub> substrate and on PEI SiO <sub>2</sub> . X-ray photoelectron spectra of the Ta(4d) region for (c) 20 cycles of Ta <sub>2</sub> O <sub>5</sub> and (d) 50 cycles TaN <sub>x</sub> ALD on SiO <sub>2</sub> and PEI SiO <sub>2</sub> .....	186
<b>Figure 4-12</b>	TaN <sub>x</sub> film thickness as a function of ALD cycles on unmodified SiO <sub>2</sub> (open symbols) and on PEI SiO <sub>2</sub> (filled), at T <sub>s</sub> = 255 °C .....	188
<b>Figure 4-13</b>	AF micrographs of TaN <sub>x</sub> thin films formed by (a) 10 ALD cycles on an unmodified SiO <sub>2</sub> substrate and (b) 40 ALD cycles on PEI SiO <sub>2</sub> .....	189
<b>Figure 4-14</b>	X-ray photoelectron spectra of the Ta(4d) region for (a) one cycle of Ta <sub>2</sub> O <sub>5</sub> ALD on unmodified SiO <sub>2</sub> and PEI SiO <sub>2</sub> , and (b) one cycle of TaN <sub>x</sub> ALD on unmodified SiO <sub>2</sub> .....	191
<b>Figure 4-15</b>	X-ray photoelectron spectra of the N(1s)/Ta(4p <sub>3/2</sub> ) region for zero, one, and 20 cycles of Ta <sub>2</sub> O <sub>5</sub> ALD on PEI SiO <sub>2</sub> .....	192
<b>Figure 4-16</b>	Inverse of the attenuation coefficient, 1/ <i>m</i> , for all the processes examined in Chapter 4 for ALD on PEI SiO <sub>2</sub> vs. the thermochemical driving force for these reactions .....	203
<b>Figure 4-17</b>	Al <sub>2</sub> O <sub>3</sub> film thickness as a function of ALD cycles on an unmodified SiO <sub>2</sub> substrate and on FOTS SiO <sub>2</sub> .....	210
<b>Figure 4-18</b>	Integrated areas of the (a) Al(2p), (b) F(1s), and (c) Si <sup>4+</sup> (2p) XPS features as a function of takeoff angle for 40 cycles Al <sub>2</sub> O <sub>3</sub> ALD on FOTS SiO <sub>2</sub> .....	211

<b>Figure 4-19</b>	X-ray photoelectron spectra in the F(1s) region for 40 cycles of Al <sub>2</sub> O <sub>3</sub> ALD on FOTS SiO <sub>2</sub> after ~ 7 minutes and ~ 35 minutes of exposure the x-ray source .....	212
<b>Figure 5-1</b>	Peak binding energy of the Ta(4p <sub>3/2</sub> ) XPS feature versus N:Ta atomic ratio for adlayers of Ta[N(CH <sub>3</sub> ) <sub>2</sub> ] <sub>5</sub> on a number of substrates .....	233
<b>Figure 5-2</b>	(a) Summary of N(1s) peak binding energy and surface atomic N concentration for PEI films deposited on SiO <sub>2</sub> and low-κ and subjected to various treatments .....	240
<b>Figure 5-2</b>	(b) Detailed XP spectra in the N(1s) region and (c) integrated area under the N(1s) peak as a function of photoelectron takeoff angle for PEI films on SiO <sub>2</sub> and low-κ .....	241
<b>Figure 5-3</b>	X-ray photoelectron spectra of the Si(2p) region for polyglycidol films deposited on low-κ substrates .....	243
<b>Figure 5-4</b>	X-ray photoelectron spectra of the combined Ta(4p <sub>3/2</sub> ) and N(1s) regions for adlayers of Ta[N(CH <sub>3</sub> ) <sub>2</sub> ] <sub>5</sub> on (a) SiO <sub>2</sub> , (b) a thin film of PEI on SiO <sub>2</sub> , (c) low-κ, and (d) a thin film of PEI on low-κ .....	248
<b>Figure 5-5</b>	Binding energy of the Ta(4p <sub>3/2</sub> ) XPS feature vs. the density of Ta for adlayers formed on a variety on surfaces, each after a constant dose of Ta[N(CH <sub>3</sub> ) <sub>2</sub> ] <sub>5</sub> delivered in UHV via a molecular beam.....	249
<b>Figure 5-6</b>	Area of the Ta(4d <sub>5/2</sub> ) peak as a function of photoelectron takeoff angle for unmodified low-κ and PEI low-κ substrates after exposure to Ta[N(CH <sub>3</sub> ) <sub>2</sub> ] <sub>5</sub> . Ta[N(CH <sub>3</sub> ) <sub>2</sub> ] <sub>5</sub> was delivered using (a) a supersonic molecular beam under UHV conditions and (b) using a conventional ALD system (Oxford FlexAL) .....	253
<b>Figure 5-7</b>	Concentration of Ta vs. depth below the substrate vacuum interface for unmodified low-κ and PEI low-κ exposed to Ta[N(CH <sub>3</sub> ) <sub>2</sub> ] <sub>5</sub> via a molecular beam, or via conventional ALD methods.....	254

<b>Figure 5-8</b>	XP spectra of the combined Ta(4p <sub>3/2</sub> ) and N(1s) regions for adlayers of Ta[N(CH <sub>3</sub> ) <sub>2</sub> ] <sub>5</sub> on (a) SiO <sub>2</sub> , (b) a thin film of polyglycidol on SiO <sub>2</sub> , (c) low-κ, and (d) a thin film of polyglycidol on low-κ .....256
<b>Figure 5-9</b>	XP spectra in the Ta(4p <sub>3/2</sub> ) and N(1s) region for Ta[N(CH <sub>3</sub> ) <sub>2</sub> ] <sub>5</sub> adlayers on unmodified SiO <sub>2</sub> at room temperature. Ta[N(CH <sub>3</sub> ) <sub>2</sub> ] <sub>5</sub> was delivered via: (a) an effusive doser, and (b) a hyperthermal molecular beam ..258
<b>Figure 5-10</b>	Integrated area under the Ta(4f <sub>7/2</sub> ) peak [after correction to remove the O(1s) contribution] for thin films of polyglycidol on SiO <sub>2</sub> and low-κ after exposure to Ta[N(CH <sub>3</sub> ) <sub>2</sub> ] <sub>5</sub> .....260
<b>Figure 5-11</b>	Calculated atomic density of Ta, deduced from XPS, as a function of number of ALD cycles for TaN <sub>x</sub> ALD on (a) SiO <sub>2</sub> , SiO <sub>2</sub> pre-annealed at 550 °C, SiO <sub>2</sub> modified with a thin layer of PEI, and (b) unmodified low-κ, and low-κ with a thin layer of PEI .....262
<b>Figure 5-12</b>	The binding energies of the <b>(a)</b> Ta(4d <sub>5/2</sub> ) and <b>(b)</b> Ta(4p <sub>3/2</sub> ) core levels as a function of the density of Ta for TaN <sub>x</sub> ALD conducted in UHV on several substrates. The binding energy scales were corrected for charging effects using the Si(2p) signal from the underlying substrates.....265
<b>Figure 5-13</b>	Binding energies of the <b>(a)</b> Ta(4d <sub>5/2</sub> ) and <b>(b)</b> Ta(4p <sub>3/2</sub> ) XPS features as a function of the density of Ta for TaN <sub>x</sub> ALD conducted in UHV on several substrates, using the C(1s) peak from amine type carbon to correct the binding energy scale for sample charging effects.....268
<b>Figure 5-14</b>	X-ray photoelectron spectra in the N(1s) region for 0.5, 7, and 15 cycles of TaN <sub>x</sub> ALD on unmodified SiO <sub>2</sub> .....269
<b>Figure 5-15</b>	Calculated atomic ratio of N (of nitride, i.e. TaN <sub>x</sub> type only) to Ta as a function of deposited Ta density .....271

<b>Figure 5-16</b>	Calculated atomic ratio of N (of nitride, i.e. TaN <sub>x</sub> type only) to Ta as a function of deposited Ta density, corrected by removing the low binding energy N contribution measured after 0.5 cycles of ALD ...	274
<b>Figure 5-17</b>	Results highlighting the effect of the pause in ALD to collect XPS data on TaN <sub>x</sub> film properties .....	275
<b>Figure 5-18</b>	Film thickness as a function of ALD cycles for TaN <sub>x</sub> films deposited on unmodified SiO <sub>2</sub> and PEI/SiO <sub>2</sub> using either UHV techniques or a conventional ALD reactor (Oxford FlexAL) .....	278
<b>Figure 5-19</b>	Ta density as a function of ALD cycles for TaN <sub>x</sub> films deposited on unmodified low-κ and PEI/low-κ in a conventional ALD reactor ....	279
<b>Figure 5-20</b>	Integrated area under the Ta(4d <sub>5/2</sub> ) peak for unmodified low-κ and PEI/low-κ substrates after 20 cycles of TaN <sub>x</sub> ALD using a conventional ALD reactor. (Oxford FlexAL).....	281
<b>Figure 5-21</b>	TiN <sub>x</sub> film thickness as a function of ALD cycles for deposition on unmodified SiO <sub>2</sub> , unmodified low-κ, and poly-G/low-κ .....	283
<b>Figure 5-22</b>	AF micrographs of unmodified low-κ and PEI/low-κ after 0 and 5 cycles of TaN <sub>x</sub> ALD, conducted in a conventional ALD reactor .....	287
<b>Figure 5-23</b>	Power spectral density (PSD) plots extracted from the AFM images shown in Fig. 5-22 .....	288
<b>Figure 5-24</b>	AF micrographs of unmodified low-κ, low-κ modified with a thin film of poly-G (as deposited), and both substrates after 100 cycles of TiN <sub>x</sub> ALD conducted under UHV conditions .....	289
<b>Figure 5-25</b>	RMS roughness as a function of film thickness for TiN <sub>x</sub> ALD films deposited in UHV on unmodified SiO <sub>2</sub> , unmodified low-κ, and both substrates modified with a thin layer of polyglycidol .....	290
<b>Figure 6-1</b>	Measured Ψ and Δ values as a function of photon energy for low-κ exposed to 0 s and 1200 s exposure to FOTS vapor .....	311



<b>Figure 6-2</b>	Direct calculation of $n$ and $k$ for as a function of photon energy for low- $\kappa$ exposed to 0 s and 1200 s exposure to FOTS vapor .....	313
<b>Figure 6-3</b>	(a) Thickness and (b) refractive index $n$ at 589 nm ( $\sim 2.1$ eV photon energy) of FOTS low- $\kappa$ as a function of FOTS vapor exposure time.	315
<b>Figure 6-4</b>	Volume fraction of FOTS in low- $\kappa$ as a function of FOTS vapor exposure time .....	319
<b>Figure 6-5</b>	Volume fraction of 2-propanol condensed within low- $\kappa$ or FOTS low- $\kappa$ as a function of the pressure of 2-propanol .....	321
<b>Figure 6-6</b>	XP spectra of the (a) Si(2p) / Si(2s) and (b) F(1s) regions for low- $\kappa$ substrates exposed to FOTS vapor for 20 s and 1200 s .....	324
<b>Figure 6-7</b>	Volume fraction of infiltrated organic material as a function of molecular volume of the organic, for two low- $\kappa$ pretreatments .....	327
<b>Figure 6-8</b>	Measured $\Psi$ and $\Delta$ values as a function of photon energy for 4 low- $\kappa$ samples before and after exposure to APTMS vapor .....	333
<b>Figure 6-9</b>	Pore size distribution for UV/Ozone treated low- $\kappa$ from the SOPRA EP-12 automatic calculation routine, the Kelvin equation (Eq. 6-6), and the Dubinin-Radushkevich equation (Eq. 6-7) .....	336
<b>Figure 7-1</b>	Schematic of the setup within the UHV chamber used for experiments .....	347
<b>Figure 7-2</b>	XP Spectra of sputtered Ta surface before and after annealing .....	349
<b>Figure 7-3</b>	Mass spectra of the direct beam of CCTBA in He .....	351
<b>Figure 7-4</b>	QMS intensity at $m/z = 118$ as a function of time, during modulation of the molecular beam shutter .....	354
<b>Figure 7-5</b>	(a) Photograph of the visible beam spot observed on Ta substrate after 3 hour exposure to CCTBA molecular beam. (b) XPS survey scans taken before and after 3 hours of CCTBA exposure .....	352

<b>Figure 7-6</b>	Schematic of terraced films, and XPS Co(2p <sub>3/2</sub> ) integrated intensity as a function of vertical position on a terraced film .....	355
<b>Figure 7-7</b>	X-ray photoelectron spectra taken in the (a) Ta(4d) and (b) Co(2p) regions for the bare Ta substrate and after 30s of exposure to the CCTBA beam .....	357
<b>Figure 7-8</b>	Integrated intensities of the (a,b) Ta(4d <sub>5/2</sub> ) and (c,d) Co(2p <sub>3/2</sub> ) peaks as a function of beam exposure time .....	358
<b>Figure 7-9</b>	Angle-resolved XPS measurements (ratio of Co to Ta intensity) for three representative CCTBA exposures .....	360
<b>Figure 7-10</b>	Co(2p <sub>3/2</sub> ) and Ta(4d <sub>5/2</sub> ) peak binding energies as a function of CCTBA beam exposure time .....	362
<b>Figure 7-11</b>	AF micrographs of (a) the bare Ta substrate, post annealing, and (b) the film formed after 60 s exposure to the CCTBA beam .....	363
<b>Figure 7-12</b>	(a) XP spectrum in the C(1s) region for a 60 s exposure to the CCTBA beam. (b) Angle-resolved XPS of the feature shown in 7-13(a) .....	365
<b>Figure 7-13</b>	Integrated intensity of the (a) carbide-type and (b) non-carbide type C peaks as a function of CCTBA beam exposure time .....	367
<b>Figure 7-14</b>	ARXPS measurement of the C(1s) intensity of the non-carbide carbon for a number of representative CCTBA beam exposure times .....	368
<b>Figure 7-15</b>	Integrated O(1s) intensity vs. CCTBA beam exposure time .....	369
<b>Figure 7-16</b>	ARXPS of the O(1s) feature for CCTBA beam exposures from 0 s to 1800 s .....	371
<b>Figure 7-17</b>	Proposed film structures during the main stages of film growth .....	372
<b>Figure 7-18</b>	XP spectra in the (a) O(1s) and (b) Co(2p) regions of the film resulting from 3 hours of exposure to the CCTBA beam before and after 20 minutes exposure to ambient air .....	373

<b>Figure 9-1</b>	AutoCAD drawing of the OH 312 system with new XPS components .....	382
<b>Figure 9-2</b>	Schematics of the translation stage built for the Sphera U5 electron energy analyzer .....	383
<b>Figure 9-3</b>	Drawing of the Mo sample platen used for angle-resolved XPS .....	385
<b>Figure 9-4</b>	XPS survey scans of three films of known composition .....	387
<b>Figure 9-5</b>	Schematic of the sample position during XPS analysis .....	390
<b>Figure 9-6</b>	XPS intensity as a function of y axis position (see Fig. 8-5), for positions close to the sample/sample platen edge .....	391
<b>Figure 9-7</b>	Ta(4d <sub>5/2</sub> ) intensity as a function of photoelectron takeoff angle, normalized by the intensity at 0° takeoff, for a thick Ta film after annealing at 375 °C for 1 hour .....	393
<b>Figure 9-8</b>	(a) Au(4f <sub>7/2</sub> ) and (b) C(1s) peak intensity as a function of photoelectron takeoff angle for a thick Au film with no sputter cleaning .....	395
<b>Figure 9-9</b>	XP spectra in the (a) C(1s) and (b) Au(4f <sub>7/2</sub> ) regions, and (c) ARXPS of the Au(4f <sub>7/2</sub> ) feature before and after sputter cleaning with 3 keV Ar <sup>+</sup> .....	397

## LIST OF ABBREVIATIONS

AFM	atomic force microscopy
ALD	atomic layer deposition
ALE	atomic layer epitaxy
APDMES	3-aminopropyldimethylethoxysilane
APTMS	3-aminopropyltrimethoxysilane
ARXPS	angle-resolved XPS
AUTES	11-aminoundecyltriethoxysilane
BEOL	back end of line
BOE	buffered oxide etch
CCTBA	dicobalt hexacarbonyl tert-butylacetylene
CMOS	complementary metal oxide semiconductor
CVD	chemical vapor deposition
DFT	density functional theory
EELS	electron energy loss spectroscopy
EMA	effective medium approximation
EP	ellipsometric porosimetry
eV	electron volt
FOTS	tridecafluoro-1,1,2,2-tetrahydrooctyltrichlorosilane
FWHM	full width at half maximum
HMDS	hexamethyldisilazane
IOL	interfacial organic layer
IR	infrared (or infrared spectroscopy)
ITRS	international technology roadmap for semiconductors
IUPAC	international union of pure and applied chemistry
OFG	organic functional group
ODTS	octadecyltrichlorosilane
PAMAM	polyamidoamine
PECVD	plasma enhanced CVD

PEI	poly(ethylene imine)
PSD	power spectral density
PVD	physical vapor deposition
QMS	quadrupole mass spectrometry
RBS	Rutherford backscattering spectrometry
RC	resistance-capacitance
RGA	residual gas analysis
RMS	root-mean-squared (roughness)
SAM	self-assembled monolayer
SEM	scanning electron microscopy
STEM	scanning transmission electron microscopy
TEM	transmission electron microscopy
TOF	time of flight
TTS	triacontyltrichlorosilane
UHV	ultra-high vacuum
XPS	x-ray photoelectron spectroscopy

## LIST OF SYMBOLS

$\alpha$	Initial attenuation of growth rate factor
$c$	atomic concentration
$D$	deposited film thickness
$\Delta$	ellipsometric parameter representing phase change
$\Delta E$	internal energy change on reaction
	Full width at half maximum
$\Delta H$	enthalpy change on reaction
$\tilde{\epsilon}$	complex dielectric function
$\epsilon$	exposure
$\gamma$	surface tension
$\lambda$	photoelectron attenuation length
$\Lambda$	light wavelength
$n$	refractive index
	number of ALD cycles
$\kappa$	dielectric constant
$k$	extinction coefficient
$\varphi$	contact angle
$\phi$	angle between x-ray source and electron energy analyzer lens axis
$\Psi$	ellipsometric parameter representing amplitude change
$P_n$	nozzle pressure or stagnation pressure
$R$	universal gas constant
$\theta$	photoelectron takeoff angle
$\Theta$	fractional coverage of a surface species
$T_n$	nozzle temperature
$T_s$	substrate temperature
$\xi$	correlation length

## **1. Introduction**

### **1.1 Overview**

The primary theme of this dissertation is an investigation of the initial stages of inorganic thin film growth using mainly atomic layer deposition (ALD), and to a lesser degree chemical vapor deposition (CVD), on a variety of substrates, with an emphasis on substrates which are modified using thin organic films. A set of *in situ* and *ex situ* experimental techniques are used to study these initial stages, which include the first interactions of gas phase film precursors with a substrate, as well as the transition of the surface from the starting substrate to the steady-state growing film. In the following chapters we will discuss and explore the connections between the chemical functionality and microstructure of the starting substrate, and these early processes. The main body of the dissertation is organized as a set of independent chapters, where the appropriate introductory material (including a survey of relevant literature and summary of experiments) is given in each individual introduction section. The purpose of this chapter is to introduce relevant ideas and place each chapter in context.

### **1.2. Atomic layer deposition**

Inorganic thin film deposition using gas phase precursors can be divided into two broad categories: physical vapor deposition or PVD, which includes techniques

such as evaporation and sputtering, where the film is built up by exposure to atoms or clusters of the film material, and chemical vapor deposition or CVD. In CVD, growth is mediated by chemical reactions which take place between gas-phase precursors, between precursors and the substrate, or between adsorbed precursors. Atomic layer deposition (ALD) can be considered a sub-type of CVD, as it involves chemical reactions which take place on the substrate surface. ALD relies on the sequential exposure of a substrate to two vapor phase precursors in an A-purge-B-purge-A... sequence [1,2], where each single sequence is termed an “ALD cycle”. During each cycle, vapor phase precursors chemisorb or otherwise react on the substrate surface to form a monolayer or less of the desired film material (generally less, due to limitations on the saturation density of the gas phase precursors [3,4]). At the end of each cycle, sites have been regenerated on the surface which are chemically reactive towards the first precursor, and the process is repeated. The purge step prevents mixing of the gas phase precursors, ensuring that the only reactions which take place are on the substrate surface. One key aspect to the ALD process is that precursor adsorption takes place only at chemically active sites on the surface, and as a consequence is *self-limiting*. The ALD process is shown schematically in Fig. 1-1 for the deposition of  $\text{TiO}_2$  from  $\text{TiCl}_4$  and  $\text{H}_2\text{O}$ . This simplified schematic depicts a full monolayer of  $\text{TiO}_2$  formation after one cycle.

There are two notable advantages to ALD over other thin film deposition techniques. The first is the potential for digital molecular level control over the thickness of the deposited film, simply by controlling the number of cycles.



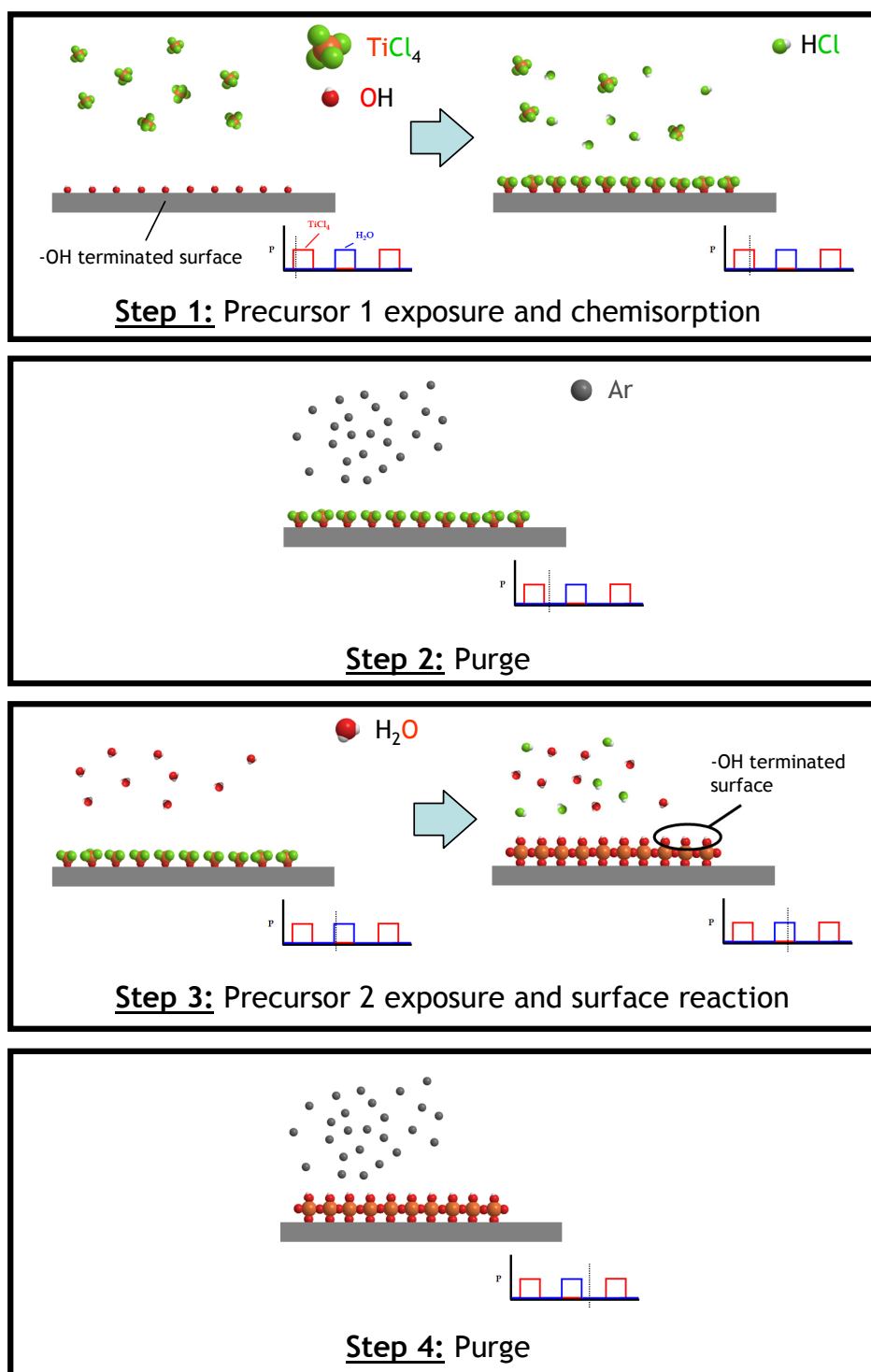


**Figure 1-1:** Simplified schematic of an ALD process to form  $\text{TiO}_2$  using  $\text{TiCl}_4$  and  $\text{H}_2\text{O}$ .

Second is the high degree of conformality provided by ALD, meaning that all surfaces are covered with the same film thickness regardless of location (trench sidewalls, flat areas, inner pore surfaces, etc). This is because, given a sufficiently long precursor exposure time, all surfaces will become saturated with the precursor, due to the self-limiting nature of the surface reactions.

ALD was invented independently by groups working in Finland and the USSR in the 1960s and 1970s [2], with the first US patent for an ALD process issued in 1977 [5]. In the early development of ALD, the films deposited were mainly epitaxial, and therefore the technique was known as “atomic layer epitaxy” (ALE) [6]. Fig. 1-2 summarizes the number of research publications and patents related to ALD (and ALE) published by year from 1980 through 2010 [7,8]. This summary shows that the area saw limited research activity from its invention through 1990. However, since that time, particularly since 2000, the amount of research regarding ALD has steadily increased from year to year. This increase is mainly due to the adoption of ALD in conventional microelectronics manufacturing, for a number of applications.

One such application is the deposition of the gate oxide in a Si-based transistor. Here, an extremely thin film must be deposited with very good thickness precision, making ALD an ideal technique. As such, adoption of ALD has already taken place in high volume manufacturing, with Intel beginning to use ALD to deposit the  $\text{HfO}_2$  gate oxide starting at the 45 nm technology node [9]. Other areas in microelectronics fabrication in which ALD could be used include any step requiring the deposition of thin films within very high aspect ratio structures where near perfect conformality is required.

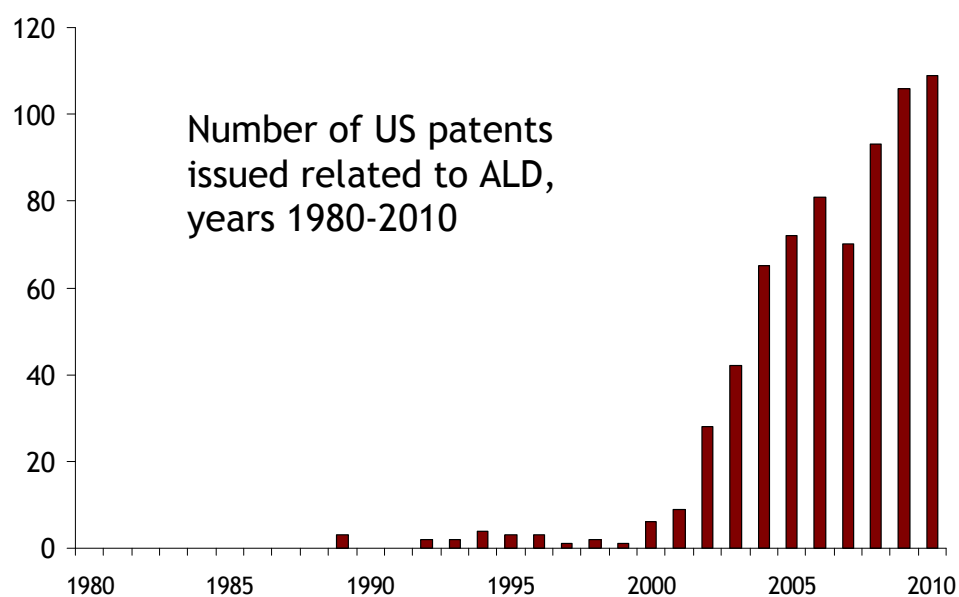
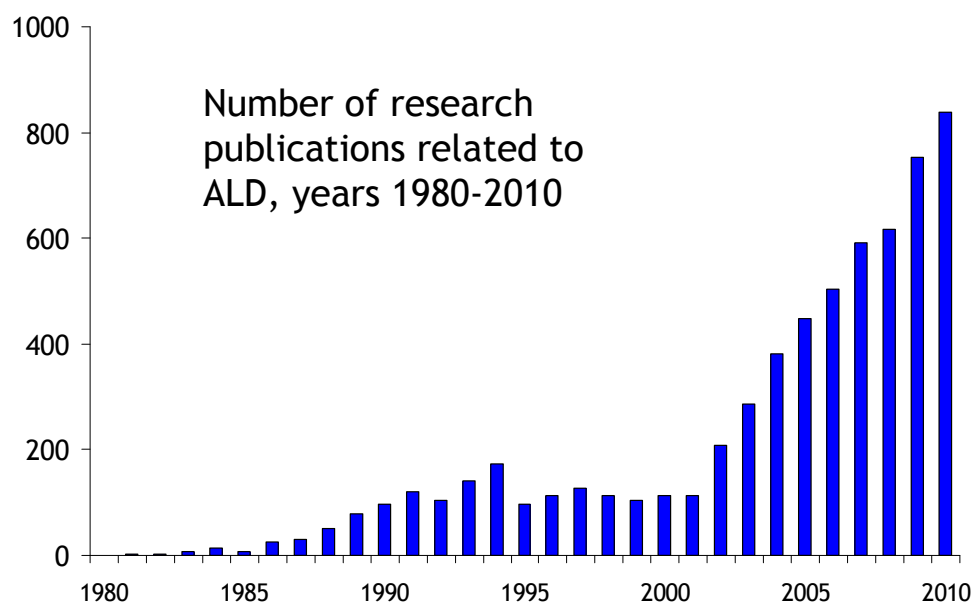


**Figure 1-2:** Number of research publications and patents (US patents issued) related to ALD by year [7,8].

This situation is encountered in the formation of thin diffusion barrier layers on an insulating material prior to the deposition of a metal, commonly copper [10], in the back end of line (BEOL) steps of integrated circuit manufacturing. This application is addressed by a number of experiments in this dissertation, and as such it will be discussed in detail in Sec. 1.3, as well as in Chapters 4-6.

ALD is also envisioned to have applications in fields outside of microelectronics manufacturing, including catalysis [11], biology [12], textiles [13], and photovoltaics [14]. The large amount of research and potential applications of ALD has led to the development of many new ALD processes. A recent review [2] has shown that recipes now exist for the deposition of films incorporating more than half the elements in the periodic table, with the most common materials being oxides, nitrides, sulfides, and pure metals. Furthermore, the same techniques used to form inorganic materials using ALD can be used to make organic thin films, and organic/inorganic hybrid materials and superlattices [15-19].

Despite the significant amount of research into ALD, there are a number of fundamental aspects that have not been fully explored. One of these aspects is the initial interaction of the vapor phase precursors with the starting substrate (first half cycle), and the transition of the surface from the starting substrate to the steady state growing film (subsequent cycles, up to the point where steady state growth is achieved). This is of particular importance when the chemical identity of the ALD film and the substrate are very different. During this transition region, the amount of material added per cycle, as well as the chemical composition of the deposited film, can be very different from the steady-state growth observed after many ALD cycles

[20-29]. These initial stages of growth make up a substantial focus of this dissertation-specifically, as they relate to the ALD of inorganic materials on substrates which have been modified by organic layers. These substrates include SiO<sub>2</sub>, which is a relatively well studied and well characterized material, and porous low-dielectric constant materials (described more fully below), which are not. We will see that the chemical functionality, as well as the morphology, of the starting substrate can play an influential role in the early stages of film growth. In general, changing the surface chemistry of the starting substrate using an organic layer, by adding or blocking reactive sites, or by changing the chemical identity of active sites, can have an effect on film growth for any deposition technique (reviewed in Sec. 3.2). The effect of the starting substrate on ALD, however, is expected to be stronger compared to other techniques (i.e. PVD) since the key processes in ALD are chemical reactions taking place at the growing interface. A separate consideration in the process of ALD growth on organic films is the final fate of the organic, a topic is discussed in detail in Chapters 3 and 4.

### **1.3. Thin film deposition on surfaces modified by organic layers**

As stated above, much of the work presented here relates to the deposition of inorganic thin films, mainly through ALD, on substrates modified with organic layers. Chapter 3 is devoted to a review of this topic, so it will only be not be discussed fully here. Of particular importance to the results presented in subsequent chapters is work previously conducted in the Engstrom group, which helped to inspire and guide the

experiments described in subsequent chapters. This previous work includes examinations of the initial interactions between organic thin films and gas-phase  $\text{TiN}_x$  precursors [30-34], as well as the effects of organic thin films on the initial stages of  $\text{TiN}_x$  ALD [23-25].

#### **1.4. Copper/low- $\kappa$ integration and diffusion barriers**

In the interconnect structures of modern integrated circuits, Damascene processing techniques are used to inlay copper wiring lines into trenches etched into an insulating material. Copper has replaced aluminum as the primary metal in the interconnect due to its lower resistivity. Likewise,  $\text{SiO}_2$  is being replaced as the insulator by alternative low dielectric constant or “low- $\kappa$ ” materials [35,36]. This was driven by the goal of decreasing delays caused by capacitance between adjacent copper lines. In combination, the adoption of copper and low- $\kappa$  dielectrics has reduced the resistance-capacitance (RC) delay of the interconnect structure and increased the overall speed of microprocessors. An SEM image of a cross-section of a modern Cu/low- $\kappa$  based interconnect with 8 wiring levels (45 nm technology node) is shown in Fig. 1-3 [37].

In order to prevent copper from diffusing out of the lines, a barrier material is deposited on the insulating material prior to the addition of copper. This barrier must be thin ( $< 5$  nm in future technology nodes [38]), conformal, and essentially free of defects such as pinholes. As stated in the previous section, this combination of requirements makes ALD an ideal technique to deposit the diffusion barrier film [38].

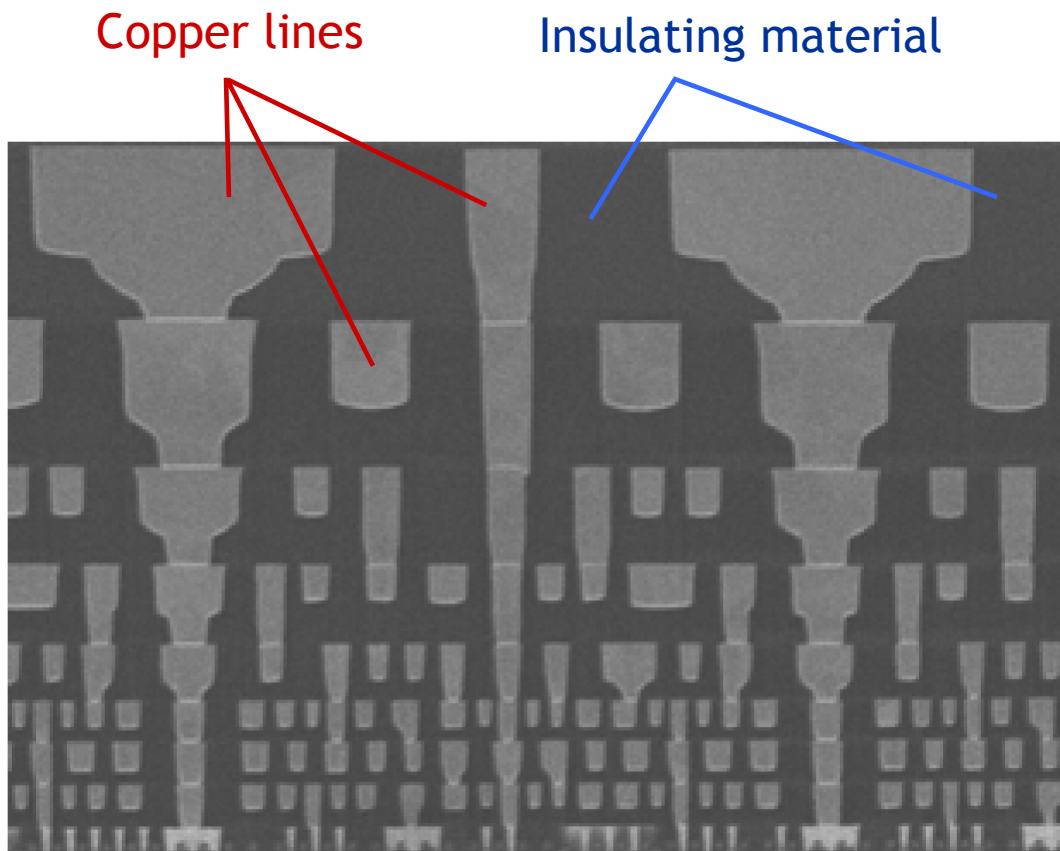


**Figure 1-3:** SEM image of the cross section of a modern Cu/low- $\kappa$  interconnect (45 nm technology node) with 8 wiring levels. Image source: Intel [9], [developer.intel.com/technology/itj/index.htm](http://developer.intel.com/technology/itj/index.htm).

Low- $\kappa$  materials, however, present a number of issues regarding the use of ALD. First, to decrease the bulk dielectric constant, low- $\kappa$  materials can incorporate pores, which in some cases form an interconnected network [35,36]. Because ALD leads to the deposition of highly conformal films, the film material can deposit within the pore structure, which is undesirable [39-41]. Furthermore, low- $\kappa$  materials have a much lower density of surface active sites for thin film nucleation as compared to SiO<sub>2</sub>. These sites, typically in the form of Si-OH groups, are intentionally removed from low- $\kappa$  materials to limit the adsorption of water within the pore structure, which causes an increase in the bulk dielectric constant. This decreased density in nucleation sites can lead to low initial growth rate, rough, islanded or defective, barrier films, as well as decreased density of the barrier [42-46]. These issues, as well as a number of possible solutions proposed by other researchers, are described in detail in Sec. 6.2.

One solution to both issues considered here is the deposition of a branched organic layer on the porous low- $\kappa$  substrate prior to ALD, shown schematically in Fig. 1-4. Because the organic molecule is branched, it would have the potential to ‘multiply’ nucleation sites on the surface by binding to a single site, while presenting many reactive terminations to incoming vapor phase precursors [31,32]. Also, if the size of the organic molecule is significant compared to pore openings in the low- $\kappa$ , it can block diffusion of precursors into the low- $\kappa$ , effectively sealing it. This prospect is investigated in Chapter 5, in which a set of *in situ* and *ex situ* techniques are used to study the ALD of tantalum nitride, a candidate barrier material [10,38], on dielectric substrates modified with a branched organic layer.



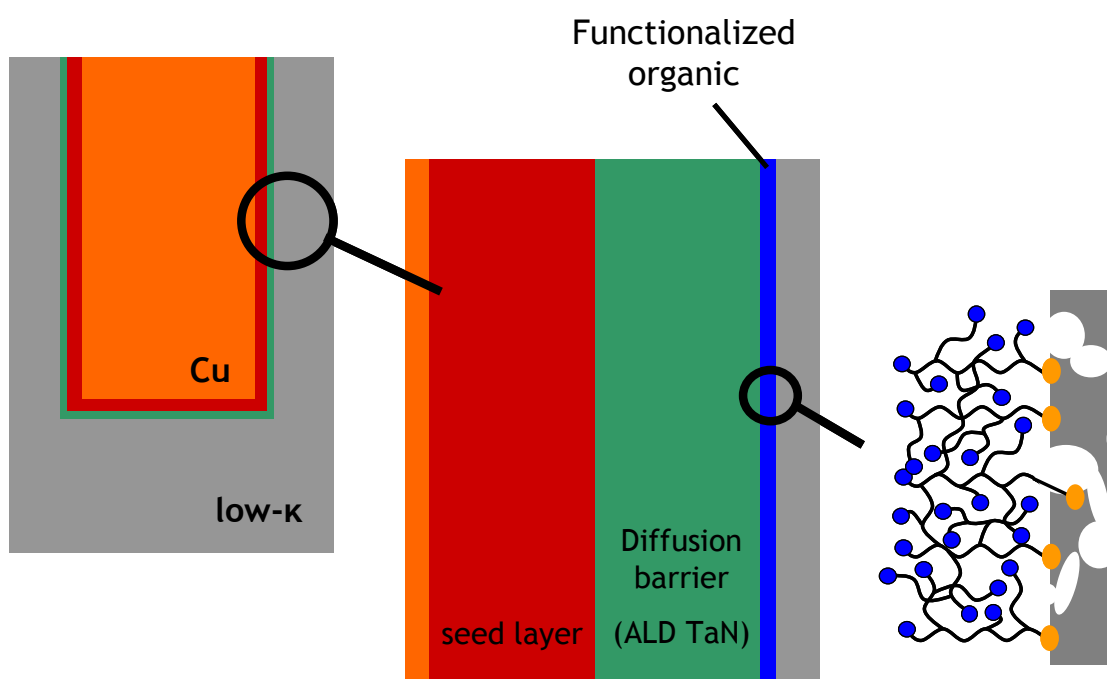


**Figure 1-4:** Schematic demonstrating the use of a branched organic layer to enhance ALD growth on a porous low- $\kappa$  dielectric material with a scarcity of nucleation sites.

Modifying a material which has interconnected pores with organic molecules can be somewhat complicated by the possible infiltration of the organic molecules into the pore structure. Methods for measuring and controlling the level of infiltration are discussed in detail in Chapter 6.

In addition to the diffusion barrier, various other thin films are added during fabrication of the interconnect. One such class of films includes “wetting” or “seed” layers, which are deposited on top of the diffusion barrier to optimize the surface for subsequent copper deposition. Cobalt is currently being investigated as a possible wetting/seed enhancement layer [47]. An investigation of the early stages of Co deposition by CVD using *in situ* XPS, representing the initial part of an ongoing project, is discussed in Chapter 7.

## **1.5. Overview of dissertation**

The following chapter contains a focused description of the experimental techniques used throughout the dissertation. Subsequent individual chapters describe additional experimental methods in detail where appropriate. Chapter 3 contains a review of inorganic thin film deposition on substrates modified by interfacial organic layers, or IOLs, with an emphasis on experiments conducted in the Engstrom research group [25]. Chapter 4 describes a series of experiments undertaken to study the ALD of several materials ( $\text{Al}_2\text{O}_3$ ,  $\text{HfO}_2$ ,  $\text{Ta}_2\text{O}_5$ , and  $\text{TaN}_x$ ) on thin layers of a polyamine, poly(ethylene imine), deposited on  $\text{SiO}_2/\text{Si}(100)$ . This study is continued in Chapter 5, where we will further examine the ALD of  $\text{TaN}_x$  on  $\text{SiO}_2/\text{Si}(100)$  and a porous low- $\kappa$

material modified using poly(ethylene imine). The focus of Chapter 6 is the infiltration of organic surface modifiers into porous low- $\kappa$  materials. Chapter 7 contains a description of an *in situ* XPS study of the initial stages of cobalt film formation by CVD on tantalum.

## 1.6 References

1. M. Ritala and M. Leskelä, in *Handbook of Thin Film Materials*, edited by H. S. Nalwa, Academic, San Diego, CA, 2001, Vol. 1.
2. R.L. Puurunen, J. Appl. Phys. **97**, 121301 (2005)
3. M. Ylilammi, Thin Solid Films **279**, 124 (1996).
4. R. L. Puurunen, Chem. Vap. Desposition **9**, 327 (2003).
5. T. Suntola and J. Antson, U.S. Patent No. 4,058,430 (1977).
6. T. Suntola, Thin Solid Films **216**, 84 (1992).
7. Number of citations obtained using Scifinder Scholar 2007 edition, accessed April 2011. Search terms included “atomic layer deposition” and “atomic layer epitaxy”.
8. Number of US patents issued obtained using Micropatent, accessed April 2011. Search terms included “atomic layer deposition” and “atomic layer epitaxy”, anywhere in the patent title or abstract.
9. K. Mistry et al., IEDM Tech. Dig. 2007, 247.
10. A. E. Kaloyeros and E. Eisenbraun, Annu. Rev. Mater. Sci. **30**, 363 (2000).
11. J.W. Elam, G. Xiong, C.Y. Han, H.Hau Wang, J.P. Birrell, U. Welp, J.N. Hryn, M.J. Pellin, T.F. Baumann, J.F. Poco, and J.H. Satcher, J. Nanomaterials **2006**, 1 (2006).
12. M. Knez, K. Nielsch, and L. Niinisto, Adv. Mater. **19**, 3425 (2007).
13. G. K. Hyde, K.-J. Park, S. M. Stewart, J. P. Hinstroza, G. N. Parsons, Langmuir **23**, 9844 (2007).
14. M. Godlewski, E. Guziejewicz, G. Luka, T. Krajewski, M. Lukasiewicz, L. Wachnicki, A. Wachnicka, K. Kopalko, A. Sarem, and B. Dalati, Thin Solid Films **518**, 1145 (2009).
15. T. Yoshimura, S. Tatsuura, and W. Sotoyama, Appl. Phys. Lett. **59**, 482 (1991).
16. A. A. Dameron, D. Seghete, B. B. Burton, S. D. Davidson, A. S. Cavanagh, J. A. Bertrand, and S. M. George, Chem. Mater. **20**, 3315 (2008).
17. S. M. George, B. Yoon, and A. A. Dameron, Acc. Chem. Res. **42**, 498 (2009).

18. B. H. Lee, M. K. Ryu, S.-Y. Choi, K.-H. Lee, S. Im, and M. M. Sung, *J. Am. Chem. Soc.* **129**, 16034 (2007).
19. B. H. Lee, K. H. Lee, S. Im, and M. M. Sung, *Org. Electron.* **9**, 1146 (2008).
20. E. Langereis, S. B. S. Heil, M. C. M. van de Sanden, and W. M. M. Kessels, *Phys. Status Solidi C* **2**, 3958 (2005).
21. E. Langereis, S. B. S. Heil, M. C. M. van de Sanden, and W. M. M. Kessels, *J. Appl. Phys.* **100**, 023534 (2006).
22. A. Martin Hoyas, C. M. Whelan, J. Schuhmacher, J. P. Celis, and K. Maex, *Electrochem. Solid-State Lett.* **9**, F64-F68 (2006).
23. A. Dube, M. Sharma, P. F. Ma, and J. R. Engstrom, *Appl. Phys. Lett.* **2006**, 89, 164108.
24. A. Dube, M. Sharma, P. F. Ma, P. A. Ercius, D. A. Muller, and J. R. Engstrom, *J. Phys. Chem. C* **111**, 11045 (2007).
25. K. J. Hughes and J. R. Engstrom, *J. Vac. Sci. Technol. A* **28**, 1033 (2010).
26. A. M. Lemonds, T. Bolom, J. W. Ahearn, D. C. Gay, J. M. White, and J. G. Ekerdt, *Thin Solid Films* **488**, 9 (2005).
27. M. Tallarida, K. Karavaev, and D. Schmeisser, *J. Appl. Phys.* **104**, 064116 (2008).
28. M. Tallarida, K. Karavaev, and D. Schmeisser, *J. Vac. Sci. Technol. B* **27**, 300 (2009).
29. R. Methaapanon and S. F. Bent, *J. Phys Chem. C* **114**, 10498 (2010).
30. A. S. Killampalli, P. F. Ma, and J. R. Engstrom, *J. Am. Chem Soc.* **127**, 6300 (2005).
31. M. Sharma, A. Dube, K. J. Hughes, and J. R. Engstrom, *Langmuir* **24**, 8610 (2008).
32. M. Sharma, A. Dube, and J. R. Engstrom, *J. Am. Chem. Soc.* **129**, 15022 (2007).
33. A. Dube, A. R. Chadeayne, M. Sharma, P. T. Wolczanski, and J. R. Engstrom, *J. Am. Chem. Soc.* **127**, 14299 (2005).
34. P. F. Ma, A. Dube, A. S. Killampalli, and J. R. Engstrom, *J. Chem. Phys.* **125**, 034706 (2006).

35. K. Maex, M. R. Baklanov, D. Shamiryan, F. Iacopi, S. H. Brongersma, and Z. S. Yanovitskaya, *J. Appl. Phys.* **93**, 8793 (2003).
36. R. J. O. M. Hoofman, G. J. A. M. Verheijden, J. Michelon, F. Iacopi, Y. Travaly, M. R. Baklanov, Zs. Tőkei, and G. P. Beyer, *Microelectron. Eng.* **80**, 337 (2005).
37. P. Moon, V. Chikarmene, K. Fischer, R. Grover, T. A. Ibrahim, D. Ingerly, K. J. Lee, C. Litteken, T. Mule, and S. Williams, *Intel Technology Journal* **12**, 87 (2008), [developer.intel.com/technology/itj/index.htm](http://developer.intel.com/technology/itj/index.htm)
38. International Technology Roadmap for Semiconductors, <http://www.itrs.net>, 2009.
39. A. Furuya, N. Ohtsuka, K. Misawa, M. Shimada, and S. Ogawa, *J. Appl. Phys.* **98**, 094902-1-6 (2005).
40. W. Besling, A. Satta, J. Schuhmacher, T. Abell, V. Sutcliffe, A.-M. Hoyas, G. Beyer, D. Gravesteijn, and K. Maex, *International Interconnect Technology Conference June 6–8 2002, IEEE 2002*, pp. 288–291.
41. Y. Travaly, J. Schuhmacher, M. R. Baklanov, S. Giangrandi, O. Richard, B. Brijs, M. Van Hove, K. Maex, T. Abell, K. R. F. Somers, M. F. A. Hendrickx, L. G. Vanquickenborne, A. Ceulemans, and A. M. Jonas, *J. Appl. Phys.* **98**, 083515 (2005).
42. A. Martin Hoyas, J. Schuhmacher, D. Shamiryan, J. Waeterloos, W. Besling, J. P. Celis, and K. Maex, *J. Appl. Phys.* **95**, 381 (2004).
43. O. Van der Straten, Y. Zhu, J. Rullan, K. Topol, K. Dunn, and A. Kaloyeros, *Mater. Res. Soc. Symp. Proc.* **812**, F3.13.1 (2004).
44. J. Liu, J. Bao, M. Scharnberg, W. C. Kim, P. S. Ho, and R. Laxman, *J. Vac. Sci. Technol. A* **23**, 1107 (2005).
45. S. M. Rossnagel and T. S. Kuan, *J. Vac. Sci. Technol. B* **22**, 240 (2004).
46. Y. Travaly, J. Schuhmacher, A. M. Hoyas, M. Van Hove, K. Maex, T. Abell, V. Sutcliffe, and A. M. Jonas, *J. Appl. Phys.* **97**, 084316 (2005).
47. Carbonell, L., et al, *IEEE International Interconnect Technology Conference 2009*, pp 200-202.

## **2. Experimental Techniques**

### **2.1 Overview**

This chapter provides an accounting, description, and short background of the materials and experimental techniques which are utilized in subsequent chapters. As these techniques are discussed fully in various texts and other publications, here the focus will be on aspects which are of most interest to the work described in this dissertation. Where techniques are used in only a single chapter, the reader is referred to more detailed discussions provided in the relevant chapter.

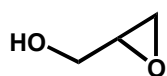
### **2.2 Materials**

The following solvents were used as received: chloroform (HPLC grade, Fisher Scientific, Pittsburgh, PA), anhydrous toluene (Sigma-Aldrich Corp., St. Louis, MO), acetone (CMOS grade, Mallinckrodt Baker Inc., Phillipsburg, NJ), methanol (99.9%, Alfa-Aesar, Ward Hill, MA), and anhydrous methanol (Sigma-Aldrich Corp.). Filtered, deionized water (resistivity  $\sim 18.2 \text{ M}\Omega$ ) was obtained from a Milli-Q Biocel system (Millipore, Billerica, MA). These materials were used in the course of substrate preparation, and were used as received: buffered oxide etch or BOE (6:1 aqueous solution of hydrofluoric acid and ammonium fluoride, CMOS grade, Mallinckrodt Baker), Nanostrip (mixture of sulfuric acid and hydrogen peroxide, Cyantec, Fremont, CA). These materials were used to form organic thin

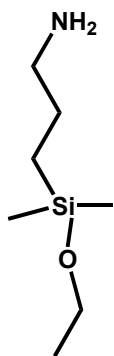
films, in methods described in detail below, and were used as received: glycidol (Acros Organics USA, Morris Plains, NJ), sodium methoxide (Sigma-Aldrich Corp.), 3-aminopropyldimethylethoxysilane [APDMES,  $(\text{CH}_3)_2(\text{CH}_3\text{CH}_2\text{O})\text{Si}(\text{CH}_2)_3\text{NH}_2$ ] (Gelest, Inc., Morrisville, PA), 11-aminoundecyltriethoxysilane [AUTES,  $(\text{CH}_3\text{CH}_2\text{O})_3\text{Si}(\text{CH}_2)_{11}\text{NH}_2$ ] (Gelest), octadecyltrichlorosilane [ODTS,  $\text{Cl}_3\text{Si}(\text{CH}_2)_{17}\text{CH}_3$ ] (Gelest), triacontyltrichlorosilane [TTS,  $\text{Cl}_3\text{Si}(\text{CH}_2)_{29}\text{CH}_3$ ] (Gelest). Branched poly(ethylene imine) or PEI (Sigma-Aldrich Corp.) with  $M_n \sim 60,000$  and  $M_w \sim 750,000$  was supplied as a 50 wt% solution in water and further diluted in deionized water before use. The following were used as precursors in the deposition of inorganic films: tetrakis(dimethylamido) titanium,  $\text{Ti}[\text{N}(\text{CH}_3)_2]_4$ , (Schumacher, Carlsbad, CA), hydrogen (Airgas East, Salem, NH, ultra high purity grade),  $\text{NH}_3$  (Airgas, semiconductor product grade), pentakis(dimethylamido) tantalum  $\text{Ta}[\text{N}(\text{CH}_3)_2]_5$  (99.9%, Sigma-Aldrich Corp.), and dicobalt hexacarbonyl tert-butylacetylene (CCTBA). Structures of key molecules used in forming organic and inorganic films are given in Fig. 2-1.

For experiments involving nonporous  $\text{SiO}_2$ , substrates were cleaved from single-side polished, 100 mm Si(100) wafers (B doped, resistivity 38-63  $\Omega$  cm). The low- $\kappa$  substrate used here is a “SiOCH type” film ( $\sim 1500\text{-}4500$  Å) provided by an industrial collaborator on 300 mm Si wafers. From XPS, the low- $\kappa$  material consists of approximately, by atomic fraction, 34% Si, 52% O, and 14% C. Heating to the temperature used for  $\text{TaN}_x$  ALD (230 °C for  $\sim 20$  min) results in a decrease in the atomic content of C to approximately 10%, due presumably to decomposition and desorption of carbon containing groups at elevated temperature in vacuum.

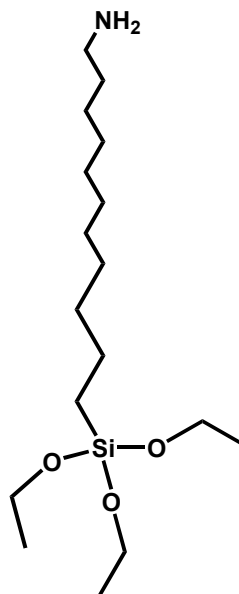




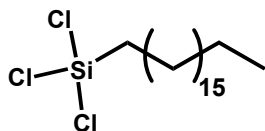
glycidol



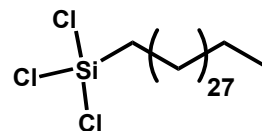
3-aminopropyl-  
dimethylethoxysilane  
(APDMES)



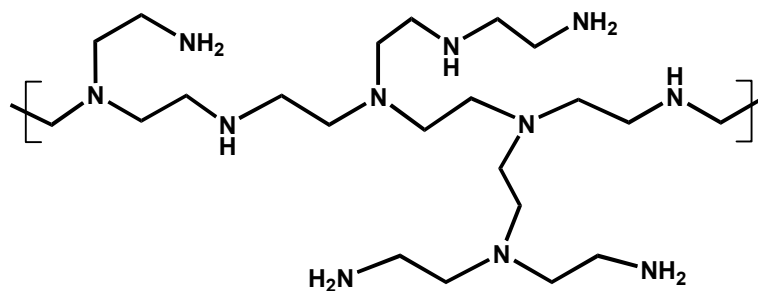
11-aminoundecyl-  
triethoxysilane  
(AUTES)



octadecyltrichlorosilane  
(ODTS)

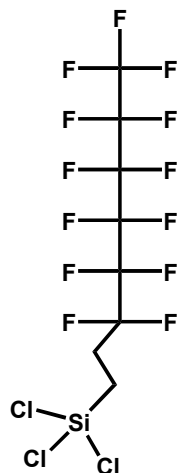


triacontyltrichlorosilane  
(TTS)

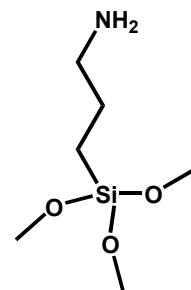


Poly(ethylene imine) (PEI) - representative unit

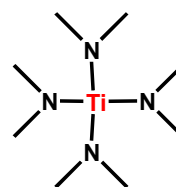
**Figure 2-1:** Structures of molecules used to form thin films in Chapters 4-7.



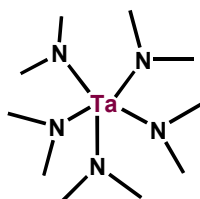
(1H,1H,2H,2H-perfluorooctyl)-trichlorosilane (FOTS)



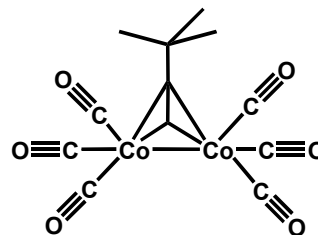
3-aminopropyl-trimethoxysilane (APTMS)



tetrakis(dimethylamido) titanium (TDMAT)



pentakis(dimethylamido) tantalum (PDMAT)



dicobalt hexacarbonyl *tert*-butylacetylene (CCTBA)

**Figure 2-1, continued:** Structures of molecules used to form thin films in Chapters 4-7.

As received, the dielectric constant ( $\kappa$ ) of the material is 2.5. The internal structure of the material has also been elucidated in detail by TEM tomography and ellipsometric porosimetry [1]. EP indicates that the void fraction the low- $\kappa$  is  $\sim 18.4\%$ , and that 90 % of the pores (by volume) have a diameter of less than 5 nm (full pore size distribution is given in Chapter 6). Complementary EP and TEM results suggest that the structure of this low- $\kappa$  includes large ellipsoidal pores connected through smaller necks or micropores in the skeleton material.

### 2.3 Substrate preparation

The procedure used for preparation of the SiO<sub>2</sub> substrates is identical to procedures described earlier [2]. To summarize,  $17 \times 17 \text{ mm}^2$  Si substrates were cleaved from Si(100) wafers, and sonicated in chloroform to remove organic contaminants. The native SiO<sub>2</sub> layer was removed from the substrates by dipping in BOE for 2 minutes. The substrates were then re-oxidized by dipping in Nanostrip for 15 min at a temperature of  $\sim 75^\circ\text{C}$ . The BOE/Nanostrip treatment was then repeated. This procedure produces a flat,  $\sim 15\text{-}20 \text{ \AA}$  thick layer of nonporous SiO<sub>2</sub> with a surface Si-OH density of  $\sim 5 \times 10^{14} \text{ cm}^{-2}$  [2-4]. This SiO<sub>2</sub> layer is referred to as “chemical oxide” in later section. The substrates consisting of a low- $\kappa$  thin film deposited on Si were also cleaved into  $17 \times 17 \text{ mm}^2$  samples. The low- $\kappa$  was either used as-received (water contact angle of  $93^\circ/71^\circ$  advancing/receding), or exposed to one of two pre-treatments: a 2 second exposure to an air plasma (Harrick Plasma PDC-001, plasma power of 7.16 W), which reduced the water contact angle to

30°/19°, or a simultaneous exposure to ozone gas and UV irradiation for 2 minutes (Samco model UV-1, 5 L/min O<sub>2</sub> flowrate into O<sub>3</sub> generator), reducing the contact angle to 67°/46°. Both pre-treatments enhance the reactivity of the low- $\kappa$ , and the air plasma in particular can be used as a simulation for plasma damage due to processing steps used to pattern low- $\kappa$  in practice.

For the experiments described in Chapter 5, prior to deposition of polyglycidol (poly-G), low- $\kappa$  substrates were exposed to air plasma or UV/Ozone treatment, while poly(ethylene imine) films were deposited on the low- $\kappa$  with no pretreatment. For the experiments involving infiltration of organic materials (Chapter 6), the low- $\kappa$  was either used as received, after exposure to plasma, or after exposure to UV/Ozone pretreatment. The specific pretreatment used is noted where relevant.

For experiments involving growth on tantalum (Chapter 7), substrates were prepared by depositing 500 Å-800 Å Ta on cleaned native SiO<sub>2</sub>/Si(100) using sputtering in the Cornell Nanofabrication Facility (CNF).

## **2.4 Formation of organic thin films**

Poly(ethylene imine) thin films (Chapters 4-5) were deposited by submerging substrates in a 0.1 weight % solution of PEI in deionized H<sub>2</sub>O for 15 min. The pH of this solution was measured to be ~ 11. At this pH, the PEI molecules in solution are not highly charged [5], such that electrostatic repulsion, which could have the effect of decreasing the density and uniformity of the PEI thin film, is minimized. After removal from the deposition solution, substrates were rinsed with deionized H<sub>2</sub>O and

dried using a stream of dry N<sub>2</sub>, and were used within 24 hr of preparation. PEI was deposited on SiO<sub>2</sub> and low- $\kappa$  substrates using identical methods. Unlike the other methods of attachment, where a covalent bond is formed between the molecule and the surface, in this case the binding is mediated by interactions between amine groups on the PEI and Si-OH or similar oxygen containing sites on the low- $\kappa$  surface (See Sec. 4.4.1 and 5.4.2).

Procedures for the formation of thin films of poly-G on nonporous SiO<sub>2</sub> using glycidol has been described in detail previously [6,7]. With the exception of the plasma pretreatment described above, poly-G was deposited on the low- $\kappa$  substrates using identical methods. The thickness (and degree of branching) of the poly-G layer can be controlled by varying the amount of time the substrate is submerged in neat glycidol. On SiO<sub>2</sub>, the growth rate of poly-G was measured to be  $\sim 1.1 \text{ \AA min}^{-1}$ .

APDMES, AUTES, ODTS, and TTS (Chapter 6) were deposited from liquid solutions in toluene in a nitrogen environment (M. Braun Inc. glovebox, Stratham, NH). Methods for depositing these materials on nonporous SiO<sub>2</sub> have been described in detail previously [8-10], and were used without modification here to treat low- $\kappa$  substrates. (1H,1H,2H,2H-perfluorooctyl) trichlorosilane (FOTS) and 3-aminopropyltrimethoxysilane (APTMS) were deposited from the gas phase using a MVD 100 (Applied Microstructures Inc., San Jose, CA). In this tool, the substrates were placed in a vacuum chamber which was first evacuated to  $< 0.04$  Torr. For FOTS, the samples were first exposed to water vapor, then FOTS vapor for periods of 20 s to 1200 s. For APTMS, samples were exposed to pure APTMS vapor for 900 s.

## 2.5 Description of vacuum systems

Experiments involving film deposition and/or analysis under ultra high vacuum (UHV) were carried out in the Engstrom group chamber in Olin Hall 312. The results of these experiments are described in Chapters 4, 5, and 7. A schematic of this system is shown in Fig. 2-2. Full details of the design and capabilities of this chamber are given elsewhere [11-13], so the focus here will be the aspects of the chamber which are of most relevant to the results presented in subsequent chapters.

The UHV system can be divided into 5 sub-chambers: the source chamber, antechamber, main chamber, analysis chamber, and loadlock. The source and antechambers are used in the generation, differential pumping, and collimation of hyperthermal molecular beams [14], and are pumped by turbomolecular pumps (source: BOC Edwards STP-301CB1 , installed January 2010, antechamber: Pfeiffer TPU 261 PC, installed January 2010). Exposure of the sample to the molecular beam, as well as XPS analysis, takes place in the main chamber. A full description of the XPS components is given in Chapter 9. The main chamber, which is pumped by a turbomolecular pump (Osaka TG 403M), typically reaches a base pressure of  $\sim 1 \times 10^{-9}$  Torr after 24 hr bakeout. The main chamber is equipped with a quadrupole mass spectrometer (QMS, Hiden 3F/EPIC, Hiden Analytical, Warrington, UK), which is mounted perpendicular to the molecular beam axis, with the ionizer region aligned with the molecular beam. This allows the QMS to be used to directly analyze the molecular beam, to measure the background due to scattered components of a beam, or to analyze the residual gases in the chamber (RGA).

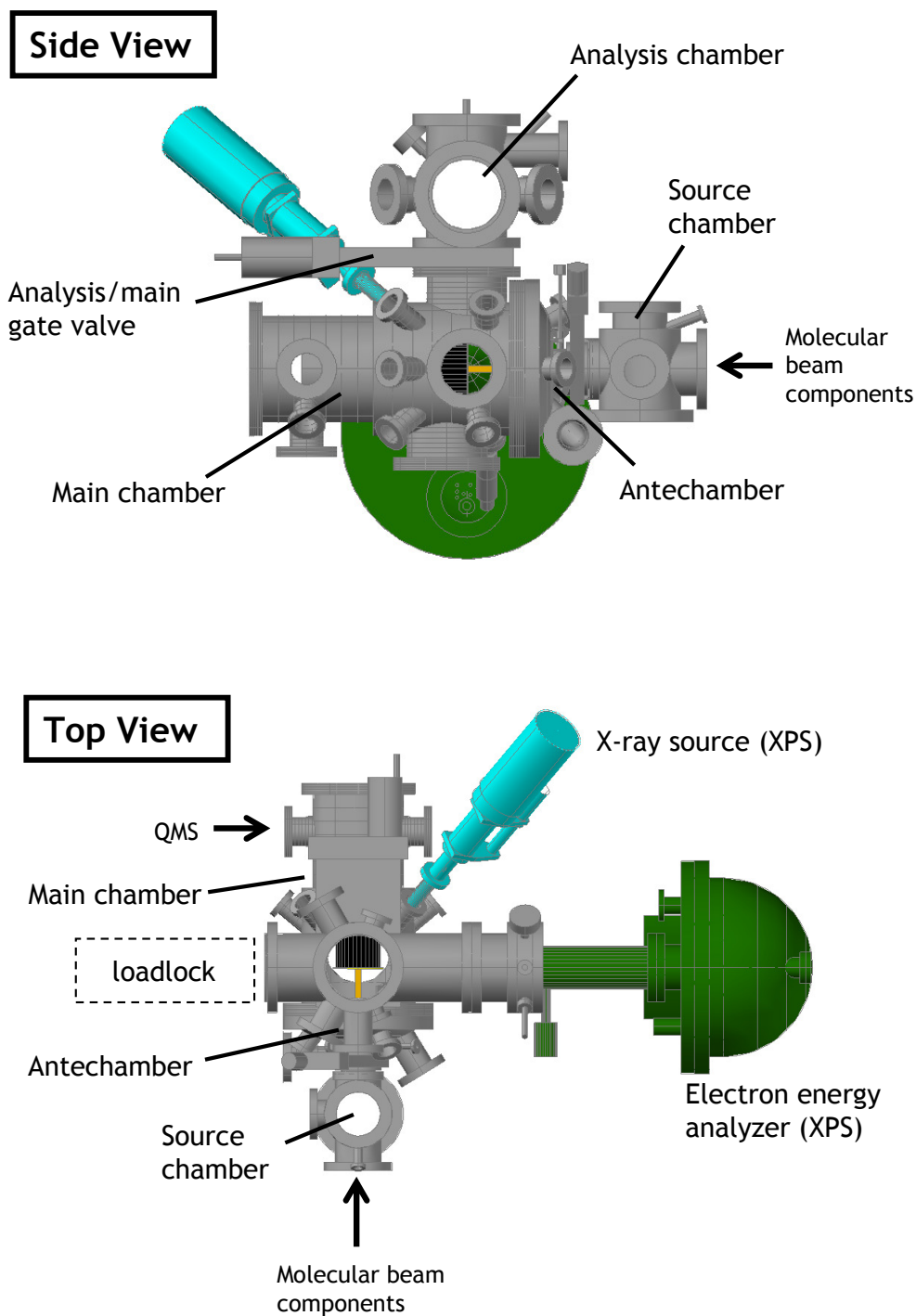


**Figure 2-2:** AutoCAD drawing of the UHV system used for deposition and analysis in Chapters 4, 5 and 7 [15]. Note that the feed lines and other components for molecular beam generation, the QMS, and loadlock chamber are not shown.

Above the main chamber, and separated from it by a gate valve, is the analysis chamber, which contains optics for performing LEED measurements. This chamber is pumped either through the main chamber, or the loadlock, depending on the gate valve configuration. The loadlock is also separated from the analysis chamber by a gate valve, and is used for sample introduction. It is pumped by a Pfeiffer TMU 071 P turbomolecular pump (installed August 2007). The controllers for the source, antechamber, and main turbomolecular pumps are connected via an interlock which controls initial pumpdown and venting of the system, including emergency venting in the event of a power failure or other malfunction [11].

The sample manipulator (Thermionics SMR-3, Thermionics Northwest, Port Townsend, WA) allows for controlled motion of the sample along three linear axes, as well as polar rotation (out of the sample plane, with a vertical axis of rotation), and azimuthal rotation (rotation within the sample plane). Positioning of the sample in the  $x$ ,  $z$ , polar, and azimuth coordinates was achieved using computer controlled stepper motors. Positioning in the  $y$  direction was controlled by a manual micrometer. The range of motion in the  $x$  and  $y$  directions was 1 inch, in the  $z$  direction was  $\sim 16$  inches. In principle, the range of motion of the azimuth and polar angles is a full  $360^\circ$ , though in practice polar motion is limited by other hardware in the UHV system. Samples were radiatively heated by a pyrolytic boron nitride heating element incorporated in the manipulator. Due to experimental constraints, the temperature of the sample surface could not be measured directly during experiment. Instead, a reference temperature was measured near the sample heater; a linear correlation was then established between this temperature and the actual sample surface temperature.



To develop this correlation, the sample temperature was measured using a thermocouple which was brought into direct contact with the sample, for a range of reference temperatures.

The bakeout procedure performed when pumping down the system from atmospheric pressure required removing motors and micrometers from the system, which can potentially cause misalignment between the beam axis and sample manipulator. Realignment was performed after reinstalling motors and micrometers by depositing a thick spot on a sample to visually determine the position of the beam axis (an example of such a spot is shown in Fig. 7-5). The sample position was then adjusted as needed to center the molecular beam on the sample. Alignment of the sample relative to the XPS analyzer was also required, and involved translating the sample in the  $y$  and  $z$  directions while collecting spectra relevant to the sample material and sample holder. Detailed information on the initial alignment of the sample with the XPS hardware is given in the Chapter 9.

One of two molybdenum platens (Thermionics Northwest) was used to hold samples during deposition and analysis. In these platens, the sample is held within a shallow well by a retaining plate secured by clips. With the exception of a narrow lip to prevent the sample from falling through, the well is open, so that the back of the sample is directly exposed to the sample heater, allowing efficient radiative heat transfer from the heated element in the manipulator and the back of the sample. The sample holder used for most experiments incorporated three wells designed to hold  $17 \times 17 \text{ mm}^2$  samples (shown in **Fig. 9-3**) along the axis of rotation of the manipulator. A second sample holder could accommodate up to four samples, two  $17 \times 17 \text{ mm}^2$ , and

two 1 x 1 mm<sup>2</sup>. The retaining plate is reversible, allowing either ~ 500 µm or ~ 760 µm thick samples to be used. Two holes were tapped on either side of the center sample well, which allowed the use of clips to secure samples of irregular thickness or shape using a backing plate of standard size.

To introduce samples, the analysis/loadlock gate valve is closed, then the loadlock is vented with high purity N<sub>2</sub>, using the pump controller's automated vent routine. The sample is then placed on the end of a transfer arm, and the loadlock is pumped down, again using an automated routine (Pfeiffer DCU controller). When the loadlock reaches a satisfactory pressure (typically  $< 1 \times 10^{-6}$  Torr), the loadlock/analysis gate valve is opened and the sample is transferred to the manipulator (Thermionics STLC Series II transfer system), which is positioned in the analysis chamber for transfer.

Transition metal coordination complexes used as precursors for film growth were delivered to the surface via a collimated molecular beam (for a full description of the principles underlying molecular beam formation, see Ref. **14**). The beam was generated by first passing an ultra high purity carrier gas through a stainless steel vessel, the 'bubbler', containing the complex. The resulting gas mixture is expanded through a heated 150 µm aperture, or nozzle, into the source chamber. Collisions in the nozzle region accelerate the heavier transition metal coordination complexes in the beam to a hyperthermal energy, which can be measured using time-of-flight techniques [16]. The beam passes through a conical skimmer with a 1.5 mm circular opening at its apex (Precision Instrument Services, Inc.), then into an antechamber containing a shutter, which allows the passage of the beam into the deposition

chamber to be modulated. Finally, an aperture defines the beam into an approximately  $12 \times 12 \text{ mm}^2$  square area on the substrate surface at normal incidence.  $\text{NH}_3$ , used as a coreactant for  $\text{TiN}_x$  and  $\text{TaN}_x$  ALD, was delivered via a doser utilizing a glass microcapillary array [17,18] (Burle Technologies, Lancaster, PA), which is located in the main chamber. The method used to deposit films by ALD in this system was similar to the method described previously [19,20]. Details regarding the formation of the specific inorganic films are given in Chapter 5 ( $\text{TiN}_x$  and  $\text{TaN}_x$ ), and Chapter 7 (Co).

The advantages of using a collimated molecular beam for precursor delivery are twofold. First, it allows for relatively high flux of the precursor to the substrate while allowing the chamber to return to UHV conditions quickly for XPS analysis. Second, it allows terraces of different thicknesses to be grown by ALD, which would not be possible using a conventional ALD reactor. This is achieved by translating the substrate perpendicular to the beam axis after certain cycle intervals. If the distance the substrate is translated is less than the width of the beam spot, multiple terraces are formed, where each represents a different number of ALD cycles. This technique is valuable for *ex situ* analysis, because it allows multiple thickness points to be studied on a single substrate, increasing throughput and decreasing possible substrate-to-substrate variations.

In addition to the ALD conducted in the UHV system described here, additional films ( $\text{Al}_2\text{O}_3$ ,  $\text{HfO}_2$ ,  $\text{Ta}_2\text{O}_5$ , and  $\text{TaN}_x$ ) were deposited using conventional techniques in an Oxford FlexAL system (Oxford Instruments, Oxfordshire, UK) in the

Cornell Nanofabrication Facility (CNF). Details regarding this system and its use are given in Chapters 4 and 5.

## **2.6 X-ray photoelectron spectroscopy (XPS)**

XPS is a surface-sensitive analytical technique which is described in detail in numerous sources, examples of which are given in Refs. **21** and **22**. The technique involves measuring the kinetic energy of electrons emitted by a sample from atomic core levels upon x-ray irradiation. Knowing the x-ray photon energy (as well as various correction factors including the work function of the spectrometer and static charge on the sample), the binding energy of the electron to its atom prior to ejection can be calculated. The binding energies of core level electrons are characteristic for each element, so that a wide range survey scan of a sample can be used to identify which elements are present (see Fig. 9-4 for an example of such scans). Small shifts in the binding energy, known as ‘chemical shifts’, can be used to characterize the chemical binding environment of an element, or to aid in the identification of chemical structures [23]. The surface sensitivity of XPS is due to the very short length that a photoelectron travels through a solid material - typically 1-5 nm- before experiencing an inelastic collision event. This has the effect of severely attenuating the signal from buried atoms, so that in most cases almost all of the signal in XPS comes from within  $\sim 10$  nm from the vacuum interface. The intensity of the binding energy peak for a given element is proportional to the density of that element in the near surface region. The relationship between atomic density and XPS intensity also depends on

instrumental factors, photoionization cross-sections (which are tabulated for each element [24]), and attenuation effects related to the depth of a given atom below the vacuum interface. Methods for calculating absolute atomic densities from XPS data, using a reference standard, are described in detail in Chapters 3, 4, and 5.

*In situ* and *ex situ* XPS measurements, including angle-resolved XPS, were carried out in the vacuum chamber described above, using an Omicron Sphera U5 concentric hemispherical electron energy, and an Omicron DAR 400 twin anode source (Omicron Nanotechnology USA, Eden Prairie, MN). The analysis spot size and the acceptance angle of the spectrometer lens are independently variable, though a combination a computer and mechanical control. Details of the installation of these components (2008) are given in Chapter 9. To collect XPS data, typically a wide range survey scan was first taken ( $\sim 0 - 1000$  eV binding energy range), then detailed scans were performed to more closely examine specific core levels (carbon 1s, tantalum 4d, gold 4f, for example). All XPS components were computer controlled using Omicron software. After collection, data were exported and analyzed using CasaXPS software, version 2.3.13. A complex photoelectron background is present in XPS, due to photoelectrons undergoing inelastic collisions or other energy loss events. This background was subtracted using a method proposed by Shirley [25]. Peak areas and positions were extracted by fitting peaks using a Gaussian/Lorentzian product formula with a mixing ratio of 0.7 [26]. An additional correction was applied as needed to account for the slight asymmetry observed in metals [27,28], due to the presence of closely spaced electron energy levels near the vacuum level. Where doublets are observed [Ta(4d<sub>5/2</sub>) and Ta(4d<sub>3/2</sub>), Au(4f<sub>7/2</sub>) and Au(4f<sub>5/2</sub>) were commonly

encountered], the ratio of peak areas was constrained using theoretical values [21]. Additional information regarding peak fitting is provided in individual chapters.

During XPS, thick, insulating films can build up a static charge due to the small amount of photoemission current. For conducting films, or very thin dielectric films, this effect is avoided because the sample is electrically grounded during analysis. If the sample is electrically charged, the binding energy scale is shifted by an amount equal to the charge, because photoelectrons leaving the sample surface must overcome an additional electrical field. This effect causes a constant shift over the entire range of the binding energy scale. Therefore, one way to correct for charging effects is to measure the binding energy of a core level peak from a component in the sample of known binding energy. The shift between the measured and known peak position is then applied to all data collected for that sample. Note that this correction must be carried out individually for each sample and experimental configuration. One commonly used method is to measure the position of so-called “adventitious carbon” or carbon contamination which builds up on the sample under ambient conditions in air or in the vacuum chamber. The position of the C(1s) peak for such carbon is generally set to 284.6-285.0 eV. For example, if the position of this peak is measured to be 286.0 eV, then a correction factor of -1.4 to -1.0 eV is applied to the entire binding energy scale. If adventitious carbon cannot be used, because other types of carbon with a similar C(1s) binding energy are present, or because the sample is cleaned *in situ* (i.e. by sputter cleaning or annealing), situations encountered in the experiments described later, then alternately the underlying substrate may be used. In many cases, the position of the underlying substrate will be more reliable than

adventitious carbon, because its composition can be known with certainty, for example with a single crystal Si substrate, and it is not affected by chemical reactions taking place within overlayer films, which can also cause shifts in binding energy. In subsequent chapters, for thin films on SiO<sub>2</sub>/Si(100), the Si(2p) signal from the underlying Si substrate (binding energy of  $99.5 \pm 0.2$  eV [21,23]) is used for charging correction. For comparing thin film growth on very different substrates, the charging correction can often be a significant factor in the interpretation of XPS data. This is encountered in Chapter 5, in which the growth of thin TaN<sub>x</sub> films on both SiO<sub>2</sub>/Si(100) and porous low- $\kappa$  is examined. In this case, we observe little charging on SiO<sub>2</sub>/Si(100), and significant charging on low- $\kappa$  ( $\sim 2$  V). Charging correction for these two substrates is therefore discussed in detail in (Sec. 5.3.3).

## 2.7 Angle-resolved XPS (ARXPS)

As discussed above, attenuation of photoelectrons as they pass through solid material is a significant factor in XPS, and is the effect which provides a high degree of surface sensitivity. The distance that an emitted photoelectron must travel through solid material to reach vacuum is generally a function of its depth below the vacuum interface, and the takeoff angle, defined here as the angle between the direction of photoelectron travel and the surface normal. By collecting XPS data over a range of takeoff angles (*angle resolved* XPS or ARXPS), we can use this fact to gain insight on the spatial distribution of various elements, particularly in the direction normal to the substrate surface [21,29]. This technique is illustrated in Fig. 2-3.

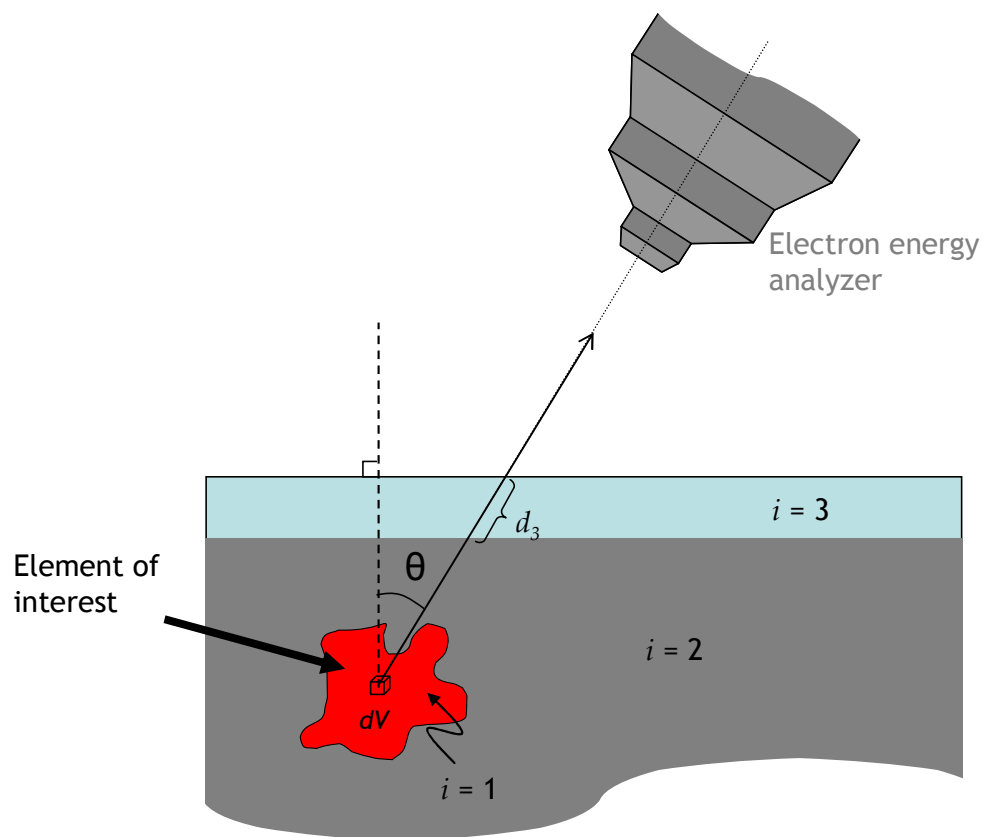


**Figure 2-3:** Diagram illustrating the terms in Eq. 2-1. Shown is the XPS analysis of a material of interest ( $i = 1$ ) buried by two materials ( $i = 2,3$ ), with a photoelectron takeoff angle of  $\theta$ .



For an arbitrary distribution of a single element buried in a substrate of any composition (uniform or nonuniform), as shown in Fig. 2-3 we can write the photoelectron intensity as a function of takeoff angle [21,30]:

$$I(\theta) = I_0 \iiint \frac{c(x,y,z)}{c_0} \exp\left(\sum_i \frac{-d_i(x,y,z,\theta)}{\lambda_i}\right) dV \quad (2-1)$$

where  $I_0$  is the unattenuated photoelectron intensity from a given element at an atomic concentration of  $c_0$ ,  $c(x,y,z)$  is the position-dependent atomic concentration,  $d_i$  is the distance the photoelectron must travel through material  $i$  to reach the vacuum interface as a function of position and takeoff angle, and  $\lambda_i$  is the attenuation length of the photoelectron in material  $i$ . Quantification of XPS, in other words relating  $c_0$  to  $I_0$ , requires the use of a suitable standard and is discussed in detail in Chapters 3-5. Use of Eq. 2-1 to directly extract concentration profiles [or relative concentration profiles  $I_0 c(x,y,z)/c_0$ ] is not practical given the data sets that are collected in ARXPS. Therefore, ARXPS data analysis strategies rely on making simplifying assumptions regarding concentration profiles. If we assume that: (i) the only compositional variation is in the direction normal to the substrate surface ( $z$ ), (ii) that the material through which the photoelectron travels is uniform and has  $\lambda_i$  which does not vary with position, and (iii) that all interfaces are abrupt and flat [29], a common set of assumptions used in analysis of ARXPS data, we can write:

$$I(\theta) = I_0 \int_0^\infty \frac{c(z)}{c_0} \exp\left(-\frac{z}{\lambda \cos \theta}\right) dz \quad (2-2)$$

Included in Eq. 2-2 is the  $1/\cos \theta$  proportionality between the takeoff angle and the path a photoelectron must travel through solid material to reach the vacuum interface. Because of this, XPS taken at more glancing takeoff angles is considered to be more surface sensitive, since photoelectrons from buried atoms are more strongly attenuated. Eq. 2-2 is further simplified by making assumptions about the concentration profiles (i.e. buried 2-d film, buried substrate, exponentially decaying concentration profile, etc.). This is discussed in further detail for our measurement geometry below (Fig. 2-5).

In our system, XPS data was collected as a function of takeoff angle by turning the sample relative to the electron energy analyzer lens axis, as shown in Fig. 2-4. Note that, as shown in the figure, this causes the analysis spot to be stretched at higher takeoff angle, so a prefactor of  $1/\cos \theta$  must be added to Eq. 2-1 or 2-2.

Even with the use of Eq. 2-2, it is generally not possible to directly calculate concentration profiles given the experimental limitations present in ARXPS. In practice, a commonly employed strategy is to further simplify Eq. 2-2 by modeling the concentration profile as one of a number of simple cases [31], where the profile can be expressed with a small number of parameters (typically these parameters are a characteristic depth and unattenuated intensity).

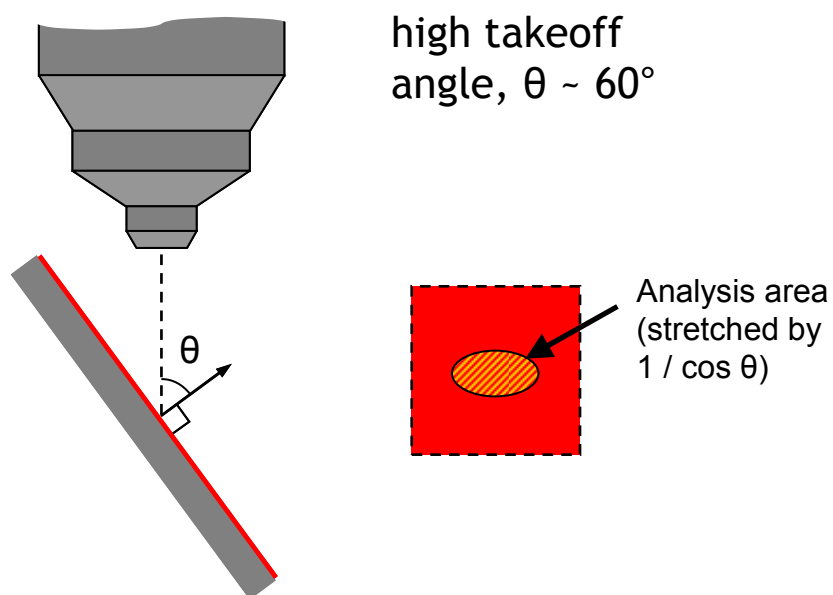
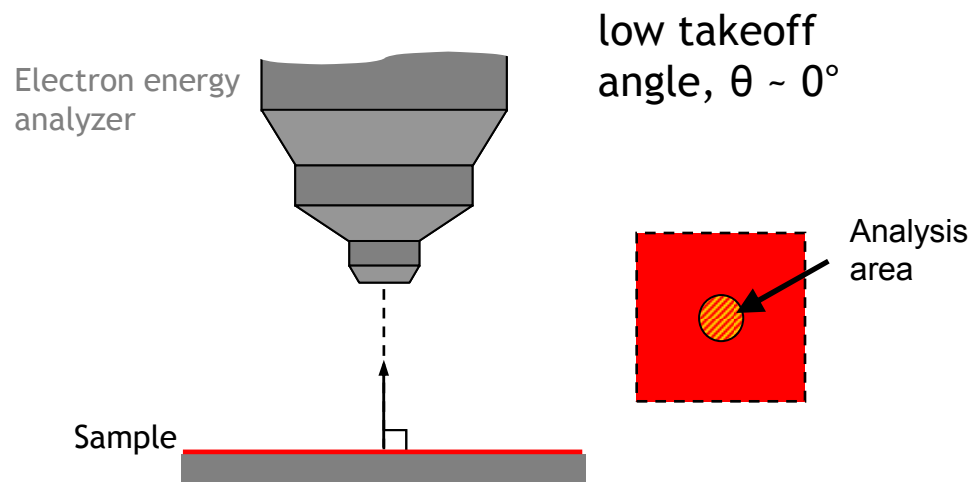


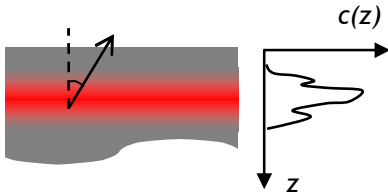
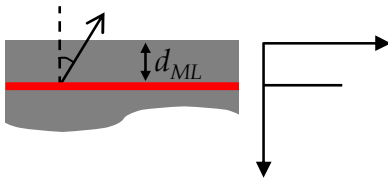
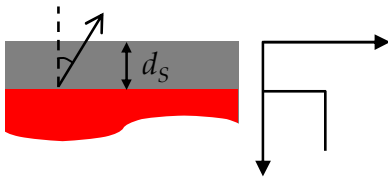
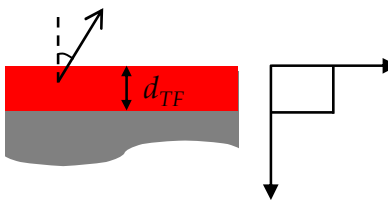
**Figure 2-4:** Schematic of the ARXPS procedure used in this work, in which the photoelectron takeoff angle is varied by turning the sample relative to the electron energy analyzer lens. Note that this has the effect of enlarging the analysis spot.

For example, for a 2-d monolayer of atoms buried by a uniform thin film of thickness  $d_{ML}$ , Eq. 2-1 or 2-2 can be simplified to give:

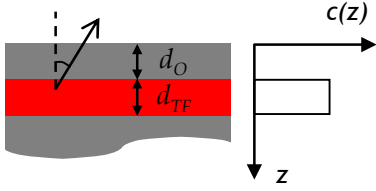
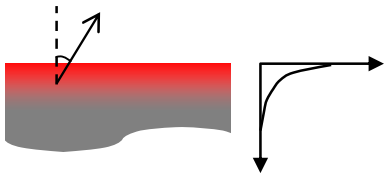
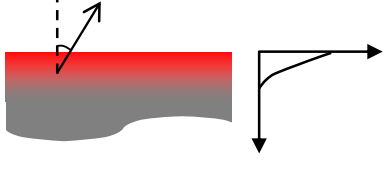
$$I(\theta) = \frac{I_0}{\cos \theta} \exp\left(-\frac{d_{ML}}{\lambda \cos \theta}\right) \quad (2-3)$$

where  $I_0$  is the unattenuated intensity from the 2-d layer, and  $\lambda$  is the characteristic attenuation length of the overlying film. The  $1/\cos \theta$  prefactor accounts for the increase in analysis area at higher takeoff angle, and the exponential term accounts for attenuation of the photoelectron as it travels through the overlayer film. Solutions for Eq. 2-1 and 2-2 for other film structures encountered later in this dissertation are shown in Fig. 2-5. One should note that the interpretation of ARXPS is highly model dependent, so selection of an appropriate model is an important aspect to data analysis.

The strategy employed here (Chapters 3, 4, 5, and 7) is to collect XPS intensity as a function of takeoff angle from 0-60° for an element of interest, determine the best model to employ, and then use an optimization routine to obtain  $I_0$  and  $\lambda$ . A complete list of the assumptions required to analyze ARXPS data have been described [29], and have been judged to be reasonable given the systems studied here. Generally 6 takeoff angles were used, at values of  $\cos \theta = 0, 0.1, 0.2, 0.3, 0.4$ , and  $0.5$ . Due to space limitations and other practical considerations we have not collected data above 60°. At high takeoff angles, effects including surface roughness, x-ray flux nonuniformity, and finite sample size (i.e., at high takeoff angle the analysis spot can become large relative to the sample size), can come into play.

Concentration profile	Intensity as a function of takeoff angle
Arbitrary distribution	 $I(\theta) = \frac{I_0}{\cos \theta} \int_0^{\infty} \frac{c(z)}{c_0} \exp\left(-\frac{z}{\lambda \cos \theta}\right) dz$
Buried 2-d film	 $I(\theta) = \frac{I_0}{\cos \theta} \exp\left(-\frac{d_{ML}}{\lambda \cos \theta}\right)$
Buried substrate	 $I(\theta) = I_0 \exp\left(-\frac{d_S}{\lambda \cos \theta}\right)$
Thin film (not buried)	 $I(\theta) = I_0 \left[ 1 - \exp\left(-\frac{d_{TF}}{\lambda \cos \theta}\right) \right]$

**Figure 2-5:** Summary of the assumed concentration profiles used here for analyzing ARXPS results (left and center columns), and the corresponding functional dependence of photoelectron intensity on takeoff angle (right column).

Concentration profile	Intensity as a function of takeoff angle
Thin film (buried)	 $I(\theta) = I_0 \exp\left(-\frac{d_O}{\lambda_o \cos \theta}\right) \left[1 - \exp\left(-\frac{d_{FF}}{\lambda_{FF} \cos \theta}\right)\right]$
Smoothly decreasing, $c = c_0 \exp(-z/d)$	 $I(\theta) = \frac{I_0}{d / (\lambda \cos \theta) + 1}$
Smoothly decreasing, $c = c_0 \operatorname{erfc}(z/d)$	 $I(\theta) = I_0 \left\{1 - \exp\left[\left(\frac{d}{2\lambda \cos \theta}\right)^2\right] \operatorname{erfc}\left(\frac{d}{2\lambda \cos \theta}\right)\right\}$

**Figure 2-5, continued:** Summary of the assumed concentration profiles used here for analyzing ARXPS results (left and center columns), and the corresponding functional dependence of photoelectron intensity on takeoff angle (right column).

Furthermore, for takeoff angles greater than  $60^\circ$ , elastic scattering begins to become a significant phenomenon [29,32]. Elastic scattering, a complex process which is material and structure dependent, should be minimized in ARXPS as it can not be easily incorporated into existing analysis techniques. Further details regarding the ARXPS measurement in the Olin Hall 312 UHV system are given in the Chapter 9, and where appropriate in individual chapters. In all cases, ARXPS data was collected in the low magnification mode of the spectrometer ( $\pm 2^\circ$  acceptance angle), with an analysis spot size of  $\sim 2.5$  mm diameter at normal incidence.

One key assumption is that analyzed films and overlayers leading are isotropic and free of any long-range order [29]. This is violated by the Si(100) substrate used commonly here, where a crystalline structure leads to photoelectron diffraction effects [33,34]. This is demonstrated in Fig. 2-6, which shows angle-resolved XPS data for a film of SiO<sub>2</sub> on Si(100), with O(1s) (from SiO<sub>2</sub>), Si<sup>0</sup>(2p) [from Si(100)], and Si<sup>4+</sup>(2p) (from SiO<sub>2</sub>). Because of the large diffraction effect, generally the Si<sup>4+</sup> peak was used instead of the Si<sup>0</sup> peak to characterize the behavior of the underlying substrate [note, for example, Fig. 4-8(c)].

We have chosen to use ARXPS as the main technique to characterize the depth distribution for a number of reasons. First, it can be performed *in situ*, which is a requirement given the sensitivity of many of the deposited layers to air. Second, unlike TEM and sputter depth profiling it is non-destructive, and well suited for fragile organic films or organic/inorganic hybrids, which may undergo significant structural changes as a result of sputtering or the sample preparation required for TEM.

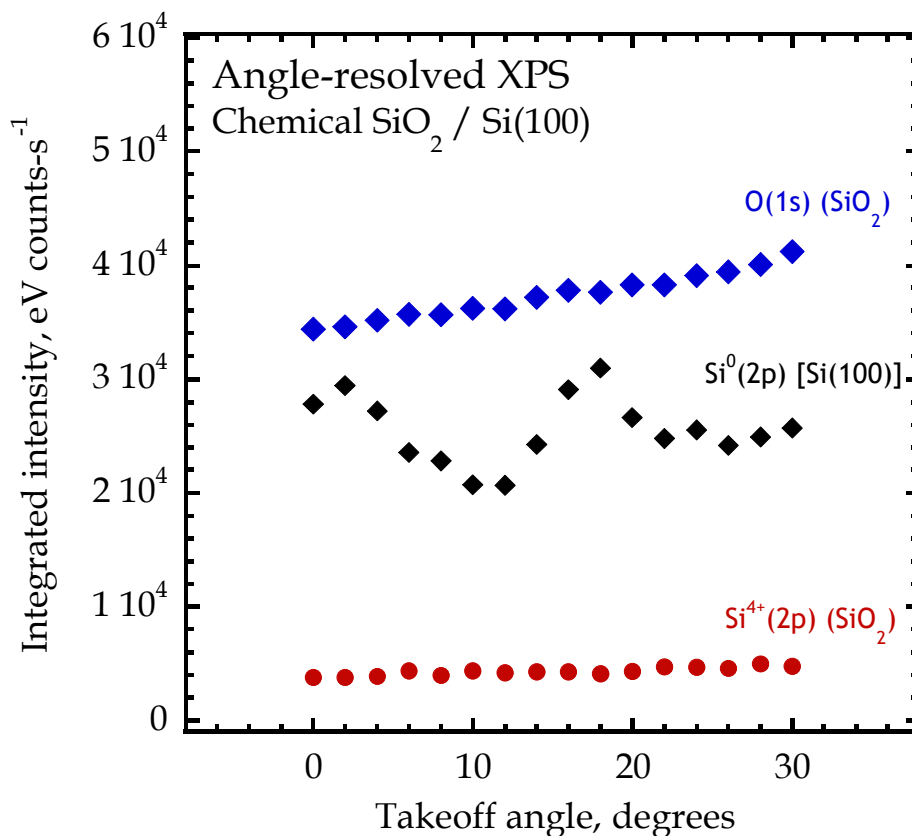


**Figure 2-6:** Integrated photoelectron intensity from of the O(1s), Si<sup>0</sup>(2p), and Si<sup>4+</sup>(2p) peaks, as a function of takeoff angle, from a sample consisting of a thin film of SiO<sub>2</sub> (chemical oxide) on Si(100). The behavior of the Si<sup>0</sup>(2p) intensity with angle compared to the other two demonstrates the effect of photoelectron diffraction from single crystal Si [33,34].



Finally, ARXPS is sensitive across depths of  $\sim 0\text{-}10$  nm, which makes it a good match for the thicknesses of the films deposited here.

## 2.8 Spectroscopic ellipsometry

Spectroscopic ellipsometry (SE) was used to measure film thickness and, in some cases, to extract information on the volume fraction of various components in a composite film (Chapter 6). In this technique, the change in polarization state of light is measured after reflection off of a substrate, which may be covered by a stack of thin films. Here we will focus on the aspects of this technique that are most relevant to the experiments performed here, for a more detailed description of SE in general the reader is referred to Refs. **35-38**. The change in polarization state is expressed as two independent parameters,  $\Psi$  and  $\Delta$ . In SE, these parameters are measured as a function of light wavelength, or, equivalently, photon energy (as opposed to non-spectroscopic or single wavelength ellipsometry). The advantages of spectroscopic ellipsometry over single wavelength ellipsometry include the ability to probe sample properties, in particular optical properties, over a range of wavelengths, the ability to collect additional data, allowing more accurate determination of physical properties including film thickness, and the potential to use parameterized optical models to fit and extract optical properties. This final point will be discussed in further detail below. The measured parameters  $\Psi$  and  $\Delta$  are a function of the number of films in the stack, the thickness of the films, and their optical properties (refractive index  $n$  and extinction coefficient  $k$ ). The optical properties may also be expressed as the complex dielectric

function,  $\tilde{\varepsilon} = (n - ik)^2$ . Each film in the stack has its own  $n$  and  $k$ , which are both a function of wavelength.

Analysis of  $\Psi$  and  $\Delta$  data from SE will often require some elements of modeling and optimization, and so a consistent, fixed procedure for analysis is helpful in producing accurate and repeatable results. The procedure we have used is given in detail elsewhere [39]. The first step is to assume a film structure (the number of films on the substrate), and to make initial guesses for the optical properties of each film. From these initial guesses, the analysis software can compute theoretical  $\Psi$  and  $\Delta$  values. An optimization routine is then used to adjust the film thicknesses and optical properties to obtain the best fit for the measured  $\Psi$  and  $\Delta$ . The figure of merit used here in the optimization was a mean squared error in which the contribution to the overall error of each  $\Psi$  and  $\Delta$  value was weighted by the uncertainty on the measured value [40]. In principle, using this technique, one can calculate the optical properties and the thickness of every film in a stack. However, this is often not practical due to the presence of extremely thin films ( $< 10$  nm), for which the optical properties and thickness are highly cross-correlated in the data analysis, or adjacent films with very similar optical properties (for example an  $\text{Al}_2\text{O}_3$  /  $\text{SiO}_2$  film stack). For these reasons, independent fitting of many parameters results in very high uncertainty values, high levels of cross-correlation, and at times unphysical results.

In practice, the number of fit parameters is reduced to obtain accurate and physically meaningful results. Optical properties are specified in one of two ways. If the identity of the film is known (for example, in the case of  $\text{Al}_2\text{O}_3$  films deposited by ALD), previously measured and tabulated  $n$  and  $k$  values as a function of wavelength

can be used if available. If the optical properties of all films in the measured stack can be fixed, then the result of the analysis will be the thicknesses of all films. If the optical properties of a film are unknown (for example, a low- $\kappa$  film of unknown porosity),  $n$  and  $k$  values may be parameterized using one of a number of established approximations. For transparent, dielectric materials ( $k = 0$ ), for example, the Sellmeier approximation may be used [35]:

$$n(\lambda) = \sqrt{1 + \sum_j \frac{A_j \Lambda^2}{\Lambda^2 - \Lambda_{0,j}^2}} \quad (2-4)$$

where  $\Lambda$  is the wavelength of light, and  $\Lambda_{0,j}$  and  $A_j$  are parameters. For the accuracy required for typical spectroscopic ellipsometry methods, a single term in the expansion (i.e.  $j = 1$ ) is sufficient. If this approximation were used, rather than fitting  $n$  at each measured wavelength, the optimization routine would produce values of  $\Lambda_{0,j}$  and  $A_j$  that gave the best result for  $n$  across the entire measurement range. This greatly reduces the number of fit variables and ensures that  $n$  follows the behavior described by Eq. 2-4. For more optically complex films, metals or composites for example, other parameterizations exist which describe  $n$  and  $k$  simultaneously in a physically consistent manner [36]. For some optical models, the potential exists to extract material properties of the film, for example the electrical resistivity [41].

As stated above, if two optically similar films ( $\text{SiO}_2$  and  $\text{Al}_2\text{O}_3$ , for example) are adjacent in the film stack, it is often not possible to independently calculate their thickness, even if their optical properties are well known. This difficulty is

compounded if the films are very thin ( $< 10$  nm). This problem frequently arises when measuring the thickness of organic thin films, or inorganic ALD films on  $\text{SiO}_2/\text{Si}$ . For this reason we have attempted to measure the thickness of the bare  $\text{SiO}_2$  (chemical oxide) layer before subsequent film growth, in order to be able to fix this thickness in subsequent analysis. For organic films measurement of the unmodified  $\text{SiO}_2$  layer thickness was straightforward. For ALD films, the pre-deposition thickness measurement should take into account any potential changes in the thickness of the  $\text{SiO}_2$  film (or combined organic/ $\text{SiO}_2$  film) thickness due to the ALD process. The pre-measurement used in this case involved loading the substrate into the ALD chamber and performing the preheating routine, and is discussed in detail in Chapter 4.

For very thick ( $>> 10$  nm) dielectric films, such as the low- $\kappa$  materials discussed in Chapter 6, the optical properties and thickness of the film are sufficiently decoupled in the fit and can be measured independently. In these cases a function describing  $n$  as a function of wavelength is normally used (for the analysis in Chapter 6 we have chosen to use the Sellmeier approximation, Eq. 2-4). In order to check the calculated optical constants, a thickness can be assumed, and  $n$  and  $k$  values directly calculated for each wavelength. Because two parameters are measured at each wavelength ( $\Psi$  and  $\Delta$ ), the two optical parameters can be calculated unambiguously if there are no other variables in the optimization.

The instrument used for SE measurements is a Woollam VASE (J. A. Woollam Co., Inc. Lincoln, NE). Data was analyzed using WVASE32 software. In all cases, test measurements were taken to determine the optimal wavelength range to use for the measurement, with the goal of obtaining precise and independent values, while

minimizing analysis time. Typically, the substrate was strongly absorbing in the wavelength of the measurement, so any light passing into the substrate is absorbed and does not contribute to the measurement. Si is appreciably transparent in the IR region, so for samples with a smooth back side this must be accounted for if photon energies less than  $\sim 1.5$  eV are used. For Si substrates with a rough back side, the light reflected from the back of the sample is diffuse and does not affect the measurement. A satisfactory fit was defined as one in which the reduced mean squared error (MSE) was less than 30 (in most cases less than 10), with all cross-correlation matrix elements less than 0.97 [40]. This final criteria ensures that all values (i.e. thickness and optical properties) could be calculated independently.

## **2.9 Atomic Force Microscopy (AFM)**

AFM was carried out using a Digital Instruments Dimension 3100 atomic force microscope (Veeco Instruments, Woodbury, NY) in tapping mode, located either in the Cornell Nanofabrication Facility (CNF) or the Cornell Nanobiotechnology Center (NBTC). AFM data were exported and analyzed using Gwyddion software, version 2.19. Image processing involved leveling by mean plane subtraction, and removal of scan lines by matching the height median between lines. In-plane correlation length was determined using previously developed methods [20]. Examples of data used to extract correlation length are given in Fig. 5-23.

## **2.10 Ellipsometric porosimetry**

Ellipsometric porosimetry (EP) was carried out on a Sopra EP-12 instrument, using 2-propanol as the adsorbate. Full details regarding this technique are given in Chapter 6.

## 2.11 References

1. H. L. Xin, P. Ercius, K. J. Hughes, J. R. Engstrom, and D. A. Muller, Appl. Phys. Lett. **96**, 223108 (2010).
2. A. S. Killampalli, P. F. Ma, and J. R. Engstrom, J. Am. Chem Soc. **127**, 6300 (2005).
3. L. T. Zhuravlev, Langmuir **316**, 3 (1987).
4. S. R. Wasserman, Y. T. Tao, and G. M. Whitesides, Langmuir **5**, 1074 (1989).
5. H. Wang, Y. Wang, H. Yan, J. Zhang, and R. K. Thomas, Langmuir **22**, 1526 (2006).
6. M. Khan and W. T. S. Huck, Macromolecules **36**, 5088 (2003).
7. M. Sharma, A. Dube, K. J. Hughes, and J. R. Engstrom, Langmuir **24**, 8610 (2008).
8. M. Sharma, A. Dube, and J. R. Engstrom, J. Am. Chem. Soc. **129**, 15022 (2007).
9. R. Chen, H. Kim, P. C. McIntyre, and S. F. Bent, Chem. Mater. **17**, 536 (2005).
10. J. H. Moon, J. W. Shin, S. Y. Kim, and J. W. Park, Langmuir **12**, 4621 (1996).
11. N. Maity, Ph. D. dissertation, Cornell University, 1996.
12. S. E. Roadman, N. Maity, J. N. Carter, and J. R. Engstrom, J. Vac. Sci. Technol. A **16**, 3423 (1998).
13. A. Dube, PhD dissertation, Cornell University, 2007.
14. G. Scoles, *Atomic and Molecular Beam Methods, Vol. 1* (New York, Oxford University Press, 1988).
15. P. F. Ma, PhD dissertation, Cornell University, 2004.
16. T. W. Schroeder, PhD dissertation, Cornell University, 2004.
17. C. T. Campbell and S. M. Valone, J. Vac. Sci. Technol. A **3**, 408 (1985).
18. Yates, J. T. *Experimental Innovations in Surface Science* (1998, Springer-Verlag, New York), pp. 604-607, and references therein.
19. A. Dube, M. Sharma, P. F. Ma, and J. R. Engstrom, Appl. Phys. Lett. **89**, 164108 (2006).

20. A. Dube, M. Sharma, P. F. Ma, P. A. Ercius, D. A. Muller, and J. R. Engstrom, *J. Phys. Chem. C* **111**, 11045 (2007).
21. M. P. Seah and D. Briggs, *Auger and X-Ray Photoelectron Spectroscopy*, Practical Surface Analysis, 2nd ed. Wiley, Chichester, England, 1990, Vol. 1.
22. A.-S. Duwez, *J. Electron Spectrosc. Relat. Phenom.* **134**, 97 (2004).
23. National Institute of Standards and Technology X-ray Photoelectron Spectroscopy Database, <http://srdata.nist.gov/xps/>
24. J. H. Scofield, *J. Electron. Spectrosc. Relat. Phen.* **8**, 129 (1976).
25. D. A. Shirley, *Phys. Rev. B* **5**, 4709 (1972).
26. *Practical Surface Analysis: Volume I, Auger and X-ray Photoelectron Spectroscopy*, 2nd ed., edited by M. P. Seah and D. Briggs (John Wiley and Sons, Chichester, England, 1990).
27. G. K. Wertheim, *J. Electron Spectrosc. Relat. Phen.* **6**, 239 (1975).
28. CasaXPS software, version 2.3.13 help file.
29. P. J. Cumpson, *J. Electron Spectrosc. Relat. Phen.* **73**, 25 (1995).
30. An example of the use of this general equation to analyze ARXPS data is given in: J. Čechal, T. Matlocha, J. Polčák, M. Kolíbal, O. Tomanec, R. Kalousek, P. Dub, and T. Šíkola, *Thin Solid Films* **517**, 1928 (2009).
31. P. J. Cumpson, *Appl. Surf. Sci.* **144-145**, 16 (1999).
32. A. Jablonski and C. J. Powell, *J. Electron Spectrosc. Relat. Phen.* **100**, 137 (1999).
33. J. M. Hill, D. G. Royce, C. S. Fadley, L. F. Wagner and F. J. Grunthaner, *Chem. Phys. Lett.* **44**, 225 (1976)
34. T. Katayama, H. Yamamoto, M. Ikeno, Y. Mashiko, S. Kawazu, and M. Umeno, *Jpn. J. Appl. Phys.* **38**, L770 (1999).
35. H. G. Tompkins and E. A. Irene, *Handbook of Ellipsometry* (William Andrew Publishing, Norwich, NY, 2005).
36. H. G. Tompkins and W. A. McGahan, *Spectroscopic Ellipsometry and Reflectometry: a User's Guide* (John Wiley and Sons, New York, 1999).



37. R. M. A. Azzam and N. M. Bashara, *Ellipsometry and Polarized Light* (North-Holland, Amsterdam, 1977).
38. J. A. Woollam online ellipsometry tutorial, [www.jawoollam.com/tutorial\\_1.html](http://www.jawoollam.com/tutorial_1.html)
39. G. E. Jellison, *Thin Solid Films* **313-314**, 33 (1998).
40. J. A. Woollam Co., Inc. Standard short course on data analysis for spectroscopic ellipsometry, Cornell University, July 30 - August 2, 2007.
41. See, for example: P. Patsalas and S. Logothetidis, *J. Appl. Phys.* **93**, 989 (2003).

### **3. Review of the use of organic thin films to alter nucleation and growth in atomic layer deposition<sup>\*</sup>**

#### **3.1. Overview**

The interfaces between inorganic and organic materials are important to a wide variety of technologies. A significant challenge concerns the formation of these interfaces when the inorganic layer must be grown on a pre-existing organic layer. The focus of this chapter is a review of the on fundamental aspects of inorganic-organic interface formation using transition metal coordination complexes and atomic layer deposition. First, the aspects of the synthesis and characterization of ultrathin interfacial organic layers, formed mostly on SiO<sub>2</sub> and possessing a variety of functional groups, including layers with a branched microstructure will be discussed. Further discussion will relate to the reactions of transition metal coordination complexes with these layers. A number of factors control the uptake of the transition metal complex and the composition of the adsorbed species that are formed, including identity, density, and dimensionality or spatial distribution of the functional groups. At room temperature, adsorption on layers that lack functional groups results in penetration of the organic layer by the transition metal complex, and reaction with residual -OH at the organic|SiO<sub>2</sub> interface. Adsorption on layers with a mostly two-dimensional arrangement of reactive functional groups results in the formation of molecular “bipods,” where the surface bound functional groups react with the complex

---

<sup>\*</sup> K. J. Hughes and J. R. Engstrom, *J. Vac. Sci. Technol. A* **28**, 1033 (2010).

via two ligand exchange reactions. In contrast, for layers that possess a high density of functional groups arranged three-dimensionally, the transition metal complex can be virtually stripped of its ligands. Atomic layer deposition on interfacial organic layers also depends strongly on the density and accessibility of reactive functional groups. On surfaces that possess a high density of functional groups, in a 2-d arrangement, growth via atomic layer deposition is initially weakly attenuated, mostly uniform and smooth, and eventually evolves to growth characteristic of unmodified SiO<sub>2</sub>. Growth on layers that lack sufficient densities of functional groups is initially strongly attenuated, in contrast, and the resulting films are rough, severely islanded and three-dimensional. As a consequence, there is a correlation between the strength of the initial attenuation in the rate of growth, and the thin film morphology. Correlations between the initial uptake of the transition metal complex by the organic layer and the initial rate of thin film growth are less direct, however, as the composition and structure of the chemisorbed species must also be considered.

### **3.2. Introduction**

The wide palette of chemical functionality available in organic chemistry, combined with the tunability of the physical, optical and electrical properties of organic molecules, allows a high degree of customization for individual applications. In certain cases, chemical reactions, as well as inter- and intramolecular forces, can be used to assemble organic molecules into nm-scale structures, a useful property in modern semiconductor devices, which often require the patterning and deposition of

extremely thin films. The integration of organic molecules into a device almost always involves the formation of an interface between the organic and the other (inorganic) components. As such, the interfaces between inorganic materials such as metals, oxides, and semiconductor crystals, and organic matter such as polymers, small molecules and self-assembled monolayers play a key role in a number of existing and emerging technologies.

Developing an understanding of how to build robust interfaces between these two classes of materials is an important and challenging problem. One aspect of the problem is associated with the processing/fabrication gap between these two sets of materials. Inorganic materials are often subjected to harsh processing environments, such as plasmas and high temperature furnaces, while organic materials are commonly synthesized and processed at or near room temperature, often in solution. Formation of inorganic-organic interfaces will in many cases require effectively integrating the two processing environments, or developing new ones. The differences in material properties between inorganic and organic materials can present a number of additional complications. In terms of their molecular-level structure, inorganic materials are characterized by simple building blocks held together by strong metallic, covalent and ionic bonds, and often exist in only one stable crystal structure. Organics are comprised of larger, more complex building blocks, held together by weak van der Waals forces and possibly hydrogen bonding interactions. Organic materials are often amorphous at processing and ambient conditions, and can also possess a number of crystalline phases that are very close in energy. In most situations, one class of material will be present and the task will be to deposit a thin film or otherwise make

contact with the other. Perhaps due to greater stability of inorganic materials, the formation of “organic-on-inorganic” interfaces is more developed than its inverse. The most well-defined and perhaps best examples of these are self-assembled monolayers (SAMs) [1-3]. While the formation of organic layers on inorganic substrates is a relatively well-studied area, where SAMs represent the prototype, the process of inorganic film growth on organic surfaces and/or substrates is less so.

In any device in which an organic molecule plays an active role, the quality of the interface between the organic and other (inorganic) components often makes a large contribution to the overall performance of the device, for example, in organic thin film transistors (OTFTs) [4-8], organic light emitting diodes (OLEDs) [9,10], photovoltaic cells, and in molecular electronics [11-14]. Engineering electrode-organic interfaces using a third interfacial material can allow better control over band/orbital offsets across the interface, perhaps affecting the injection/extraction of carriers. Such a strategy has been shown to be effective in OTFTs, using thin interfacial layers of metal oxides, [15,16], copper phthalocyanine [17], and the organic electron acceptor tetracyanoquinodimethane [18]. Beyond their use as active electrical components, thin organic films can also be used to improve the mechanical properties of interfaces between two inorganic materials. For example, functionalized organic films have been used to enhance the adhesion of gold to glass [19] and SiO<sub>2</sub> [20].

Organic films may also be useful in controlling the subsequent nucleation and growth of inorganic films. In such cases, partial or complete degradation of the organic layer may be acceptable, perhaps even desired. A minimum requirement could be that the layer does not adversely affect either the properties of the underlying

substrate, or the inorganic thin film that is deposited. Concerning the promotion of nucleation and growth, there are several reasons as to why this may be necessary. First, a substrate of interest may lack a sufficient density of nucleation sites for the growth of the inorganic thin film—this is particularly true for materials grown using reactive processes such as chemical vapor deposition (CVD) or atomic layer deposition (ALD). If the density of sites is low, e.g., due to the chemical makeup of the substrate, the film that is deposited may first consist of discrete 3-d islands, which only merge after longer growth times, leading to a rough film. To address this issue, it is possible that an organic layer with an appropriate structure could be used as a *nucleation site amplifier/multiplier*. Such an organic layer could be made by binding or growing an organic molecule with branched microstructure and reactive terminal functionalities. A related example is provided by substrates that are porous—by definition empty space does not provide sites for nucleation. On a substrate with interconnected pores, branched or “space-filling” molecules could be used to seal the pores against infiltration of an inorganic precursor while simultaneously enhancing the reactivity of the surface. Here the deposited or grown organic layer would both provide nucleation sites, and fill the empty spaces at the surface of the porous substrate. In this application, the infiltration of the organic material *itself* into the pores is an additional factor to consider when selecting the building blocks of the organic layer. A final example of what an organic layer might produce is a *surface normalization coating*, where the deposition/growth of the organic molecule on a surface with dissimilar materials exposed would act to “normalize” the nucleation and subsequent growth of inorganic films over the entire surface.

Most early work on the formation of inorganic-on-organic interfaces involved the evaporation of elemental metals in vacuum onto thin polymeric films [21-23], straight chain alkanethiol SAMs on gold, as well as on oligophenylene and oligo(phenylene-ethynylene) SAMs, which are of interest in molecular electronics. Evaporation in vacuum is simple and accessible to many investigators, and therefore is an obvious first method to examine. A range of metal/terminal organic functional group (OFG) combinations have been studied [24-40]. Combinations likely to lead to chemical reaction gave results consistent with reaction of the metal primarily at the OFG—for example Cu/-COOH, Au/-SH, and Al/-OH. Metal/OFG combinations with weak interactions led to penetration of the SAM by the metal species, with significant metal deposition at the SAM/substrate interface. Intermediate strength interactions gave results consistent with a mixture of reaction with the OFG and at the SAM/substrate interface, e.g., Au, Al, Cu, and Ag with -OCH<sub>3</sub>. Very reactive transition metals, such as Ti and Ca, can react with reactive endgroups and the SAM backbone [28], eventually leading to degradation of the SAM [36,38]. In addition to the effect of the terminal OFG, we may expect that infiltration of the SAM layer can also be controlled to a certain extent by making use of backbone chemistry. Indeed, crosslinking the backbones of thiol-terminated oligophenylene SAMs using electron irradiation has been shown to limit the deposition of evaporated Ni to the SAM/vacuum interface [41,42]. The evaporative deposition of Mg, Al and Ca with SAMs possessing -OCH<sub>3</sub>, -COOH, and -OH endgroups has also recently been examined using a combination of experiment and density functional theory (DFT) [43-45]. Research is continuing in the area of metal evaporation on SAMs, with recent

examples including the use of a condensed Xe buffer layer [46,47] and indirect evaporation techniques [48] to control penetration of the SAM by metal adatoms.

An attractive alternative to evaporative deposition is the use of *metal coordination complexes*, as control over the ligand groups attached to the metal center allows further tunability of the interactions between the inorganic precursor and organic layer, with the potential for *self-limiting* adsorption (saturation) under the proper conditions. Such properties may be useful for devices that require a robust electrical connection between the (metal) electrodes and the organic, without causing disruptions to the organic molecule or short circuits. For example, exposure of -OH and -COOH terminated SAMs to trimethylamine alane,  $\text{H}_3\text{AlN}(\text{CH}_3)_3$ , leads to the formation of a thin layer of  $\text{AlO}_x$ , leaving the backbone of the SAM intact [49]. On an -SH terminated SAM, sufficiently short exposures to cyclopentadienyl-allyl-palladium,  $(\text{C}_5\text{H}_5)\text{Pd}(\text{C}_3\text{H}_5)$  lead to a plateau in Pd coverage [50,51]. Several experiments demonstrate that these types of chemically specific interactions between coordination complexes and surfaces with organic functionality can be used to control film growth by CVD. Nucleation of palladium and gold films grown using  $(\text{C}_5\text{H}_5)\text{Pd}(\text{C}_3\text{H}_5)$  and trimethylphosphine-methylgold,  $[(\text{CH}_3)_3\text{P}]\text{AuCH}_3$ , was found to take place preferentially on -SH terminated SAMs over -CH<sub>3</sub> and -OH terminated SAMs [52]. Furthermore, the nucleation density of gold films was affected by changing the ratio of -SH to -CH<sub>3</sub> terminations on the surface. For Cu films deposited using Cu(II) bis-hexafluoroacetylacetonate,  $\text{Cu}^{\text{II}}(\text{hfac})_2$ , the presence of an -SH terminated SAM increased both the rate of growth and the Cu grain size [53]. Complete oxidation of the -SH termination to -SO<sub>3</sub>H prior to Cu deposition further



increased the continuity of the film. Spatial control of the CVD of inorganic thin films has been demonstrated using SAMs patterned by microcontact printing [54,55] or exposure of selected areas to UV light [56]. Comparing CVD to physical vapor deposition (PVD, which includes evaporation), it has been found that gold deposited by CVD using  $[(\text{CH}_3)_3\text{P}]\text{AuCH}_3$  grows at significantly different rates on -SH vs. -CH<sub>3</sub> terminated SAMs, while gold grown by evaporation does not show this sensitivity to the OFG present on the surface [57].

As with CVD, chemical functionality plays a role when inorganic materials are deposited on organic films from the liquid phase. It has been demonstrated that the chemical termination and structure of the organic film can be used to control the crystal phase [58], crystal orientation [59-61], and growth mode (i.e., 3-D island vs. 2-D layer by layer growth) [62] of inorganic films deposited from liquid solution. However, a significant difference between film deposition conducted in the liquid vs. the gas phase is that, in the liquid phase, charged species are much more likely to exist on the substrate and in solution. Long range electrostatic interactions between these species may then play a role in the initial stages of film growth. With the exception of plasma-based deposition, in gas phase deposition both the substrate and precursor are neutral, so influence over the initial structure of the film is controlled by much shorter range steric and chemical interactions. We may expect, therefore, that direct transfer of results observed in solution to the cases of growth from the gas phase is problematic at best due to the differences in the driving forces.

Clearly the work conducted to date, both concerning evaporative (PVD) and reactive (CVD) deposition, suggests that control of the surface chemistry of the

organic layer is essential concerning subsequent growth of the inorganic layer. The nature of the deposition process is also important. PVD approaches lack sufficient selectivity for many applications, and the interfaces that are formed may be highly defective. CVD, on the other hand, can result in uncontrolled, continuous growth and/or require temperatures too high for many organic layers. Atomic layer deposition (ALD) [63,64] is a technique that holds significant promise for deposition of inorganic thin films on organic surfaces. Thin film growth using ALD is determined exclusively by sequential self-limiting gas-surface reactions, thus, precise control of nucleation and growth may be enabled by judicious choice of the surface chemistry. In addition, in many cases the processing temperatures for ALD are lower compared to those for CVD, making them more compatible with surfaces possessing organic functionality.

Compared to other film growth techniques, relatively few studies have examined the ALD of inorganic thin films on the surfaces of organic materials. A large fraction of this work does not involve growth *on* the organic, but instead the use of a SAM to block growth of an inorganic thin film [65]. For example, SAMs have been shown to be effective masking agents for the ALD of HfO<sub>2</sub> [66], Pt [67], TiO<sub>2</sub> [68], ZrO<sub>2</sub> [69], ZnO [70], Ir [71], Co [72] and Ru [73], where in most cases a SAM with a -CH<sub>3</sub> termination was employed. Concerning growth *on* SAMs, the ALD of WC<sub>x</sub>N<sub>y</sub>, using B(C<sub>2</sub>H<sub>5</sub>)<sub>3</sub>, WF<sub>6</sub>, and NH<sub>3</sub> as the thin film precursors, has been examined on SAMs possessing -Br, -CH<sub>3</sub>, and -CN terminations [74]. On -Br and -CH<sub>3</sub> terminated SAMs, no measurable growth took place in the initial ~100 cycles of ALD. Growth on the -CN terminated SAM, in contrast, appeared similar to growth on SiO<sub>2</sub> with no organic functionality. In another study, investigators used a gold surface

patterned with -OH and -CH<sub>3</sub> terminated SAMs to spatially control the subsequent deposition of TiO<sub>2</sub> using Ti[OCH(CH<sub>3</sub>)<sub>2</sub>]<sub>4</sub> and H<sub>2</sub>O [75]. In a mixed layer of these same SAMs, it was found that the morphology of the subsequently deposited TiO<sub>2</sub> depended on the relative surface concentration of -OH vs. -CH<sub>3</sub> terminations [76]. In a different system, it was shown that ALD of Al<sub>2</sub>O<sub>3</sub> from H<sub>2</sub>O and Al(CH<sub>3</sub>)<sub>3</sub> on a -CH<sub>3</sub> terminated SAM results in a very rough 3-d film, while ALD on SiO<sub>2</sub> gives much smoother 2-d thin films [77]. The roughness of the Al<sub>2</sub>O<sub>3</sub> thin film grown on the -CH<sub>3</sub> terminated SAM could be significantly reduced by using isopropyl alcohol in place of water in the first ~20 cycles [78]. In this work it was argued that the isopropyl alcohol could better “wet” the surface of the -CH<sub>3</sub> SAM. In another study, Al<sub>2</sub>O<sub>3</sub> films were grown on -COOH terminated SAMs formed on H-terminated Si [79]. Here it was shown that the SAM prevented oxidation of the underlying Si, which takes place if no SAM is present. Furthermore, *in situ* IR showed that Al<sub>2</sub>O<sub>3</sub> films grown on the -COOH SAM were similar to those grown on SiO<sub>2</sub>. For a -COOH terminated SAM on a gold substrate, tunneling current measurements showed that a thin interfacial layer of Al<sub>2</sub>O<sub>3</sub> deposited on the SAM by ALD protected the SAM during subsequent evaporation of the Al top electrode [80].

ALD using copper(I) N,N'-di-*sec*-butylacetamidate, [Cu(<sup>s</sup>Bu-amd)]<sub>2</sub>, and H<sub>2</sub> has been used to form a thin Cu film on top of a -COOH terminated SAM [81]. Here IR and XPS analysis demonstrated no diffusion of Cu to the SAM/Si interface, or damage to the SAM layer. Furthermore, during ALD Cu forms a bidentate complex with the SAM endgroup, interacting with both the -OH and C=O oxygen atoms, a phenomenon not observed when Cu is evaporated on a -COOH SAM. ALD has also

been used to fabricate thin layers of a  $(\text{Ti,Al})\text{O}_x/\text{SiO}_y/(-\text{CH}_2)_8\text{O}_z$  inorganic-organic hybrid material, and nanolaminates of this hybrid and (pure)  $\text{TiO}_2$  or  $\text{Al}_2\text{O}_3$  ALD thin films [82,83]. The hybrid layers were formed by sequential pulses of a vinyl-terminated  $(-\text{CH}=\text{CH}_2)$  SAM precursor (7-octenyltrichlorosilane), “activation” of the layer by exposure to  $\text{O}_3$ , followed by a single titanium isopropoxide/ $\text{H}_2\text{O}$  or trimethylaluminum/ $\text{H}_2\text{O}$  ALD cycle. STEM images revealed clear differences in contrast between layers of pure  $\text{TiO}_2$ , next to layers of the inorganic-organic hybrid as thin as the length of the backbone of a single SAM molecule. Finally, in addition to these experimental studies, computational work has been undertaken concerning the initial stages of ALD on a number of thin organic layers [84,85].

The goal of this chapter is to provide a review of recent work, conducted mostly in the Engstrom research group, concerning the formation of inorganic-on-organic interfaces. First, the formation of tailored *interfacial organic layers* (IOLs), including SAMs, will be described. As discussed above, in many cases SAMs with relatively simple structures will be insufficient for some applications. Consequently, work concerning the formation of IOLs with both regular [86] and random [87] branched microstructures which are grown, i.e., not deposited whole, will also be discussed. This will afford us the opportunity to discuss methods that may be used to characterize the organic layers themselves, including XPS, contact angle, and ellipsometry. The next topic of discussion will be the initial steps of interface formation- the chemisorption of transition metal coordination complexes on surfaces terminated with these organic layers. Here the focus is on characterizing the reactions of  $\text{Ti}[\text{N}(\text{CH}_3)_2]_4$  and  $\text{Ta}[\text{N}(\text{CH}_3)_2]_5$  with a variety of IOLs using surface sensitive

techniques including *in situ* XPS [88] and supersonic molecular beam scattering [89]. These two precursors are used for ALD and CVD of  $\text{TiN}_x$  [90-93] and  $\text{TaN}_x$  [94,95], materials which have a number of applications, including use as barriers to prevent copper diffusion into dielectric materials in micro- and nanoelectronic devices [96]. In related work, the adsorption and decomposition pathways of  $\text{Ti}[\text{N}(\text{CH}_3)_2]_4$  and  $\text{Ta}[\text{N}(\text{CH}_3)_2]_5$  on  $\text{Si}(100)\text{-}2\times 1$  and  $\text{-NH}_x$  terminated surfaces, as well as the growth of thin  $\text{TiC}_x\text{N}_y$  films by CVD using  $\text{Ti}[\text{N}(\text{CH}_3)_2]_4$  have been examined [97-102].

The final topic to be discussed involves an examination of the growth of  $\text{TiN}_x$  thin films on organic layers using ALD [103,104], with emphasis on the evolution of the growth processes. Here there is an opportunity to make connections between phenomena occurring in the monolayer regime, to phenomena occurring in both the nucleation and the steady-state stages of growth. There are good correlations and connections in a number of cases, but there are also gaps in the understanding of inorganic-organic interface formation.

### 3.3. The formation of inorganic-organic interfaces

The following sections will highlight the surface-sensitive characterization carried out after various steps of the process of inorganic-organic interface formation. Afterwards, we may make connections between the chemistry, density and structure of the organic layers, the composition, density and spatial distribution of the chemisorbed transition metal layer, and the rate of growth and morphology of the subsequently grown/deposited inorganic thin film.

### 3.3.1. Formation and characterization of interfacial organic layers

#### 3.3.1.1. Experimental approach

Concerning the structure of organic layers to be used in this application, there are three factors that are important—these are the *type*, *density* and *dimensionality* of the organic functional groups. These factors are considered in schematic form in Fig. 3-1, where the parameter space that one may cover using density and dimensionality is displayed. Concerning the synthesis and/or assembly of the organic layers, there are a number of considerations, including the phase that is used for the synthesis (liquid or vapor), patterning where necessary, using methods such as microcontact printing [105] or “dip-pen” lithography [106], and the complexity of the formation process. Some SAMs can be formed in a single step, while others, due to functional group incompatibility, must undergo post assembly conversion. Likewise, surface initiated and grown oligomers and polymers can also be distinguished by the complexity of the synthesis, which can be a simple “single pot” process, or one involving multiple step, additive reactions. The latter could include processes such as molecular layer deposition [107-109], a molecular organic version of ALD.

The entire palette of surface analytical tools can be applied to the characterization of thin organic layers [1, 110], but this chapter will emphasize primarily the application of four techniques—contact angle, ellipsometry, XPS, and AFM.

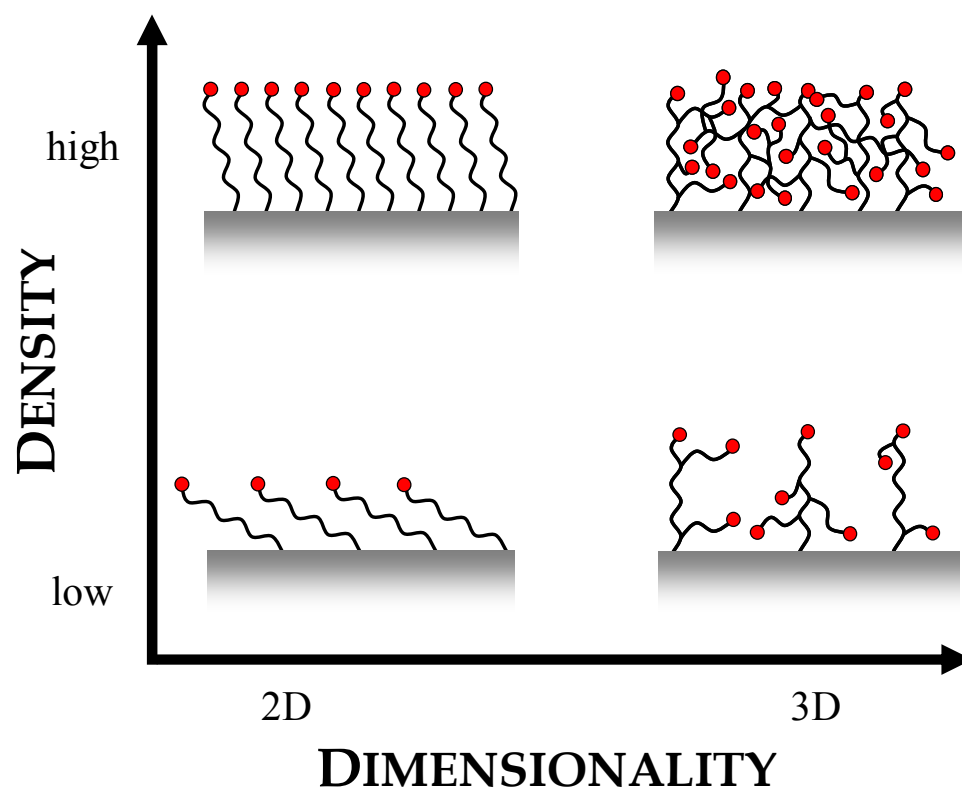


**Figure 3-1:** Parameter space accessed by interfacial organic layers using the factors of density and dimensionality. Here we show four versions of IOLs schematically and in cross-section.

*Contact angle* [111] can verify the presence of certain classes of functional groups at the surface, and contact angle hysteresis, the difference between values measured using an advancing and receding contact line, is a measure of the uniformity of the layer [112]. *Ellipsometry* (particularly multiple wavelength, or spectroscopic ellipsometry) [113-115] provides an excellent measure of the average thin film thickness, even for layers as thin as 1 nm. These techniques allow for quick evaluation of the layers, which can be an effective screen to verify the quality of the synthesis. In terms of quantifying the chemical composition of thin layers, XPS [116,117] is probably the most powerful, noninvasive, useful and accessible technique. It can give absolute densities/concentrations if appropriate calibration standards are used, and holds the potential for depth resolution using ARXPS. In many cases information concerning bonding in the surface layers can be achieved from binding energy shifts in the core levels. Vibrational spectroscopies such as *Fourier transform infrared (FTIR) spectroscopy* [118] can often be applied to great effect to reveal the presence of specific functional groups, but are problematic concerning quantifying their concentration or spatial location. Regarding the direct imaging of the organic layer, *atomic force microscopy* (AFM) is capable of providing information on the organic layer structure/morphology over relatively large areas of the surface, which is useful in assessing the uniformity of the organic layer, and identifying structures such as islands or defects in the organic [119-121].



### 3.3.1.2. Straight-chain self-assembled monolayers

Perhaps the most examined form of interfacial organic layers are straight-chain SAMs such as alkylthiols [2] and alkylsilanes [122]. These classic systems are represented by a simple structure—a headgroup that binds to the surface, an alkyl backbone, and finally a tailgroup defined by an organic functional group (OFG). The headgroup is chosen to effectively couple to the chemistry of the starting substrate—e.g., thiols on Au, or silanes on SiO<sub>2</sub>. Regarding the three factors referred to above, the type is determined primarily by the tailgroup OFG, the density can be controlled up to a saturation value by the duration of the self-assembly process, and the dimensionality is essentially 2-D (assuming the starting substrate is flat and smooth).

A variety of straight-chain SAMs has been employed as platforms to examine how the type of SAM affects chemical reactivity as judged by both XPS [88] and *supersonic molecular beam scattering* [89]. The SAMs consist of either  $\equiv\text{Si}-(\text{CH}_2)_{17}-\text{CH}_3$ ,  $\equiv\text{Si}-(\text{CH}_2)_{12}-\text{NH}_2$ , or  $\equiv\text{Si}-(\text{CH}_2)_{11}-\text{OH}$  covalently bound to a 20-25 Å layer of SiO<sub>2</sub> on Si(100). This SiO<sub>2</sub> layer, referred to as “chemical oxide”, was used throughout this work, and is reported to have a surface density of Si-OH groups of  $\sim 5 \times 10^{14} \text{ cm}^{-2}$  [122,123]. The SAMs were formed by first exposing a chemical oxide substrate to liquid solutions of Cl<sub>3</sub>-Si-(CH<sub>2</sub>)<sub>17</sub>-CH<sub>3</sub>, (octadecyltrichlorosilane, ODTS), Cl<sub>3</sub>-Si-(CH<sub>2</sub>)<sub>9</sub>-CH=CH<sub>2</sub> (10-undecenyltrichlorosilane), and Cl<sub>3</sub>-Si-(CH<sub>2</sub>)<sub>11</sub>-CN (11-cyanoundecyltrichlorosilane), respectively. The first of these produces, in one step, a hydrophobic -CH<sub>3</sub> terminated SAM. The second two can be converted, post-assembly, to -OH and -NH<sub>2</sub> terminated SAMs [88]. A larger set of SAMs, including these three,

have been examined for their effects on subsequent inorganic thin film growth using ALD [103,104].

Quantifying the absolute density of a SAM is a challenge. Unlike alkylthiolate SAMs on Au(111), essentially without exception alkylsilanes on SiO<sub>2</sub> do not form ordered, epitaxial-like structures, a feature that can often be exploited to quantify coverage. Provided a suitable reference standard exists, XPS can be quantitative, however. The values required to provide a quantitative analysis include: *x-ray photoelectron cross-sections* for the standard and the sample (both well known), *atomic density* of the standard (well known), *transmission function* of the analyzer (well known), and *inelastic mean free path/attenuation length*,  $\lambda$ , of photoelectrons in the standard (well known) and the sample of interest (in general, unknown). Thus, it is this last quantity that is most problematic concerning using peak intensities in XPS to compute absolute coverages and/or densities.

For a uniform thin film of thickness  $d$ , the correction factor to account for attenuation effects has the form  $\delta/[1 - \exp(-\delta/\cos \theta)]$ , where  $\delta = d/\lambda$ , and  $\theta$  is the take-off angle of the photoelectrons. In previous work [88], results obtained by others concerning attenuation lengths of alkanethiols on Au measured using x-ray synchrotron radiation [124] were used. Combined with measurements of the physical thickness of the SAM from ellipsometry, we could estimate  $\delta = d/\lambda = 27 \text{ \AA}/24.5 \text{ \AA} = 1.10$ , and make an appropriate correction for attenuation effects. Alternatively, results from ARXPS for photoemission from either the underlying substrate [e.g., from O(1s)] or the thin film itself [e.g., from C(1s)] could have been used to measure the quantity  $\delta$  directly [125]. For the case of ODTS on chemical oxide, such data was

collected was used to determine  $\delta = 0.85$  [88]. If this value had been employed vs. what we employed in previous work (1.10), densities of  $2.76\text{--}3.57 \times 10^{14}$  molec-cm<sup>-2</sup> would have been calculated vs. the previously reported  $3.09\text{--}3.99 \times 10^{14}$  molec-cm<sup>-2</sup>, for the two  $\equiv\text{Si}(\text{CH}_2)_{17}\text{--CH}_3$  SAMs examined there. These former values, using a  $\delta$  that is ~23% smaller, gave densities that are smaller by ~12% compared to that published previously. In fact, it is shown easily that in the limit of  $\delta \rightarrow 0$  that the correction becomes simply  $\cos \theta$ , i.e., independent of  $\delta$ , and the relative uncertainties in  $\delta$  are halved in the correction factor. Thus, it seems that for most SAMs of  $d < 30$  Å, and accounting for all experimental uncertainties, XPS can estimate the density of the layers to within  $\pm 20\%$  given knowledge of  $\delta$  to within  $\pm 40\%$ . This should be kept in mind when discussing results that make use of these densities, such as calculations of the adlayer stoichiometry.

### 3.3.1.3. Interfacial organic layers with branched microstructure

Straight chain SAMs have been investigated extensively, and provide a wide variety of chemistries useful for a number of applications. There are some applications, however, where more complicated structures are desired or necessary—layers with branched and/or interconnected microstructures, or layers that possess a 3-d distribution of active sites/functional groups. Such layers could be deposited from solution in a single step, or grown from a surface. One could argue that the latter method may be superior in terms of producing dense layers, as the packing of large

oligomers and macromolecules on surface could lead to defects on the order of the size of the molecule.

The growth of dendritic oligomers has been examined [86], borrowing directly from the chemistry used to make divergent-type polyamidoamine (PAMAM) dendrimers [126,127]. In solution, one begins this synthesis with a core amine. On a surface, SAMs terminated with primary amines were used. The amine termination of the SAM molecule, or *anchor*, provides a branch point, from which one expects to double the density of terminal -NH<sub>2</sub> groups for each “generation” of dendron. Two specific molecules were investigated for use as anchors: CH<sub>3</sub>CH<sub>2</sub>O-Si-(CH<sub>3</sub>)<sub>2</sub>(CH<sub>2</sub>)<sub>3</sub>-NH<sub>2</sub> [(3-aminopropyl)dimethylethoxysilane], and Cl<sub>3</sub>-Si-(CH<sub>2</sub>)<sub>11</sub>-CN (11-cyanoundecyltrichlorosilane), which after assembly and hydroboration forms ≡Si-(CH<sub>2</sub>)<sub>12</sub>-NH<sub>2</sub>. These will be referred to as Gen-0-*n*C, where *n* = 3 and 12, with *n* corresponding to the number of carbon atoms in the alkyl backbone. Subsequent reaction of the amine group with methyl acrylate [CH<sub>3</sub>O(C=O)CH=CH<sub>2</sub>] then ethylenediamine, H<sub>2</sub>N-(CH<sub>2</sub>)<sub>2</sub>-NH<sub>2</sub>, produces a layer with -NH<sub>2</sub> terminations, Gen-1-*n*C, ideally double in density of that of the starting anchor layer. The final products of these reactions are displayed in ball-and-stick form in Fig. 3-2. Decreases in both the static contact angle, as well as the contact angle hysteresis, indicate that the density and uniformity of the hydrophilic functional groups at the surface increase from Gen-0 to Gen-1. Thickness measurements from ellipsometry are also agreement with the expectations based on molecular models for the reactants, e.g., the layers increased in thickness by about 5-6 Å from Gen-0 to Gen-1.

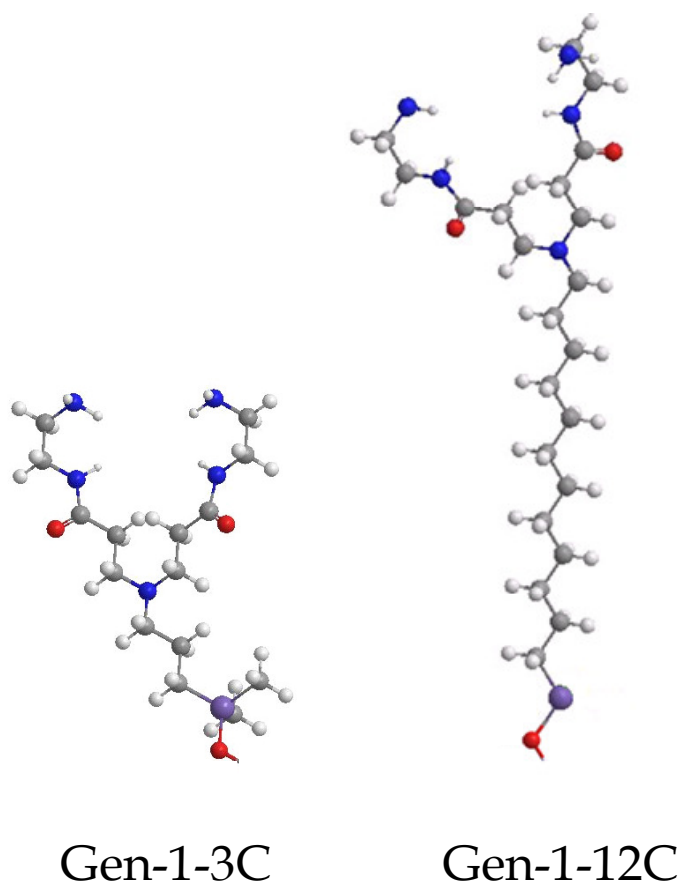


**Figure 3-2:** Ball and stick models of the two -NH<sub>2</sub> terminated first generation PAMAM dendrons, which differ in terms of the length (3 or 12) of their straight chain anchor: Gen-1-3C (left) and Gen-1-12C (right).

The use of XPS in this work provided a quantitative measure of both the density of the layers, and the efficiency of the conversion from Gen-0 to Gen-1. Unlike the straight chain SAMs described above, these PAMAM layers are “stuffed” with functional groups. At Gen-1, there are 2 primary amines, one tertiary amine and 2 amide groups per anchor. Thus, identification of the layer from chemical shifts in the C(1s) feature is quite plausible in this case. In addition, there should be 5 N atoms per anchor if the conversion is 100%. In Fig. 3-3(a), the C(1s) feature for both the Gen-1-3C and the Gen-1-12C layers has been plotted. The data is well described by a fit to three peaks, assuming contributions from 3 types of binding environments for C atoms: aliphatic,  $R-\underline{C}H_2-R$ , amino,  $R-\underline{C}H_2-NH_2$ , and amidic  $R-\underline{C}(=O)-NH-R$ . The stoichiometry measured by XPS (not accounting for attenuation effects) was in both cases close to the theoretical expectation. By modeling the overall intensities for the C(1s) peaks to estimate absolute densities, it was determined that the conversion from Gen-0 to Gen-1 was  $\sim 26\%$  for the 3C anchor, and  $\sim 90\%$  for the 12C anchor. The N(1s) signal could also be used to estimate the efficiency of the conversion. In Fig. 3-3(b) are plotted the N(1s) XP spectra for Gen-0 and Gen-1 for both anchors. For 100% conversion, ignoring effect of photoelectron attenuation, the intensity of the N(1s) feature should increase by a factor of 5 after conversion. However, the integrated N(1s) intensity increases by a factor of 1.5 for the 3C anchor and 3.42 for the 12C anchor. These results agree with that obtained from analysis of the C(1s) peaks, and are consistent with the more efficient conversion of the longer anchor, Gen-0-12C.

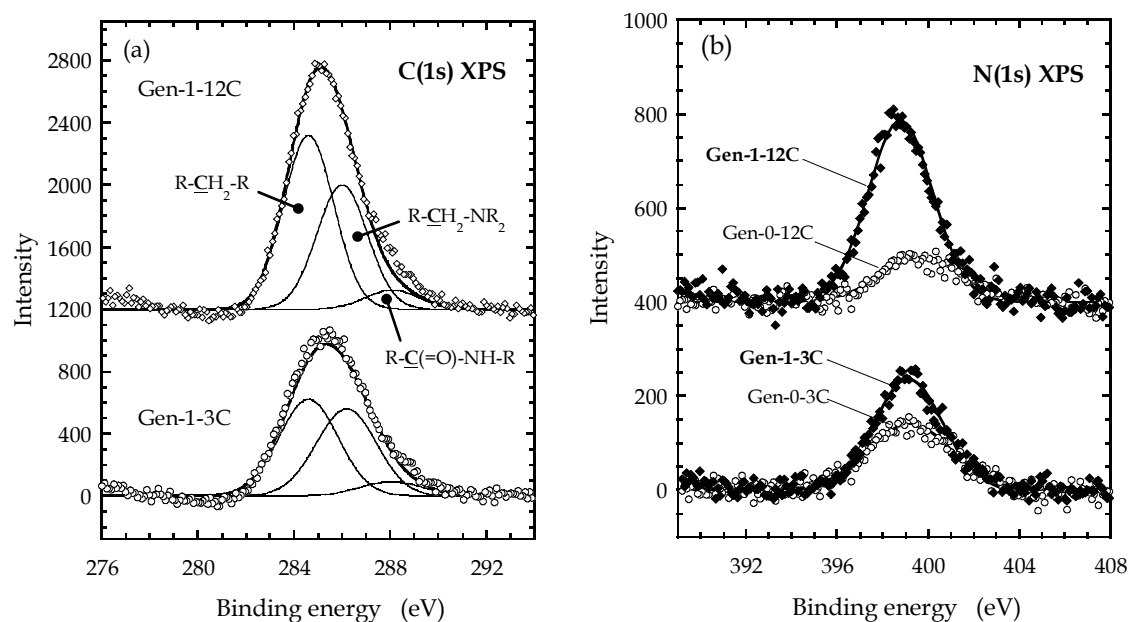


**Figure 3-3:** XP spectra of the (a) C(1s) and (b) N(1s) features for the Gen-1 PAMAM dendrons with 3 carbon (3C) and 12 carbon (12C) anchors displayed in Fig. 3-2. Gen-0 represents the  $\text{-NH}_2$  terminated straight-chain anchor, and Gen-1 the first-generation dendron. The C(1s) features were fit to three peaks corresponding to contributions from aliphatic (284.6 eV), amino (286 eV), and amidic (288.4 eV) carbons. Spectra have been shifted along the ordinate to facilitate presentation.

Potential causes for less than 100% conversion of the  $\text{-NH}_2$  branching sites are discussed in detail elsewhere [86], and include steric limitations arising from the density and flexibility of the anchors, as well as hydrogen bonding between the terminal  $\text{-NH}_2$  and  $\text{-OH(a)}$  species on the substrate (particularly in the case of the much shorter Gen-0-3C).

A potential disadvantage of the PAMAM dendron growth approach is that it involves multiple (deterministic) steps, which may be unacceptable for certain technological applications where speed and throughput are important. As an alternative, surface-initiated growth of polyglycidol (poly-G) from the base catalyzed reaction of glycidol [87] which takes place in a continuous and random fashion, was considered. The method adopted to form poly-G layers on  $\text{SiO}_2$  was first demonstrated by Khan and Huck [128], and is similar to bulk-phase methods used to make free-standing branched polyethers [129]. The stoichiometry of the layer is set by the monomer (excluding the anchor, O:C is 2:3), and as the film grows the ratio of  $\text{-OH}$  sites to C atoms quickly approaches the limiting value of 1:3, while the thickness is determined simply by the reaction time. Under the conditions used here the growth rate of the poly-G layer is  $\sim 1.1 \text{ \AA}\cdot\text{min}^{-1}$  [87]. Fig. 3-4 displays ball-and-stick models for poly-G<sub>2</sub> and poly-G<sub>6</sub>, where poly-G<sub>*n*</sub> is an oligomer consisting of *n* monomer units. XPS, AFM, and contact angle measurements on these films are consistent with the formation of a continuous hydrophilic thin film (all contact angles  $< 20^\circ$ ), where the RMS roughness increased from 6.8 to 11.7  $\text{\AA}$  as the film thickness increased from 30 to 84  $\text{\AA}$ .



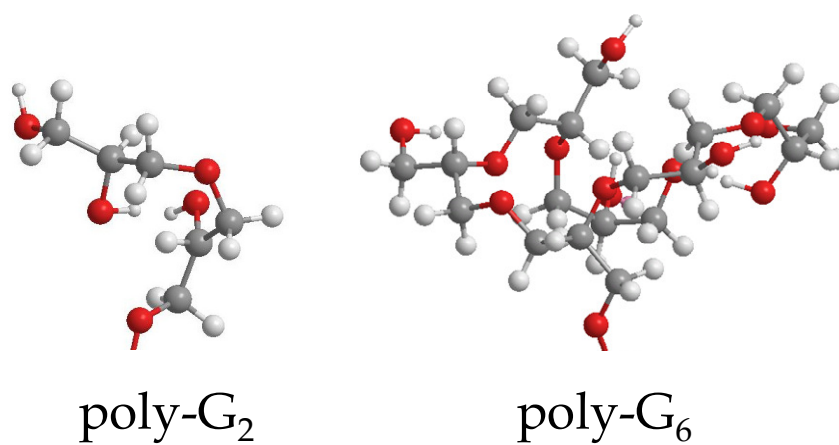


**Figure 3-4:** Ball and stick models of polyglycidol at two stages of growth: an oligomer of 2 monomeric units (poly-G<sub>2</sub>), and another with 6 (poly-G<sub>6</sub>). Each of these represents one of a number of possible configurations. For poly-G<sub>n</sub>, there are  $n!$  possible isomers.

Measurement of the Si(2p) substrate peak for a series of poly-G thin films gave a value for the attenuation length of 48.3 Å, a value that is somewhat larger than the values discussed above for the alkyl backbone SAMs (24.5 and 31.8 Å). This may indicate an overall lower electron density in poly-G, likely due to differences in molecular-level packing, porosity, and possibly molecular weight for this hyperbranched thin film.

XPS was used to make an estimate for the density of the -OH sites present in the poly-G layers, using the C(1s) feature to calculate the density of C in the layer, and the theoretical 1:3 C to -OH limiting ratio. This analysis assumes also that the poly-G is a continuous layer of constant density, in which functional groups are distributed uniformly. Making use of the attenuation length indicated above resulted in calculated densities of -OH of 3.1, 3.8, 4.6, and  $4.5 \times 10^{21}$  sites-cm<sup>-3</sup> for thin films of 30, 47, 66 and 84 Å in thickness (measured by ellipsometry). Making use of these thicknesses, effective 2-d densities of -OH for these 4 cases can be calculated, resulting in values of: 0.92, 1.8, 3.0 and  $3.8 \times 10^{15}$  sites-cm<sup>-2</sup>. All of these values are well above (factors of 2-8) what one could achieve from a well-packed alkyl backbone SAM with a single terminal functional group ( $\sim 0.46 \times 10^{15}$  sites-cm<sup>-2</sup>).

Because ALD processes are typically conducted at elevated temperatures, the thermal stability of the organic layer in vacuum is of interest in this application. In a study of the thermal stability of straight-chain -CH<sub>3</sub> terminated alkyl SAMs (C<sub>4</sub>, C<sub>8</sub> and C<sub>18</sub>) on SiO<sub>2</sub> [130], lack of changes to the HREELS spectra or contact angle upon annealing in UHV up to temperatures as high as 467 °C was cited as evidence for stability. In other work, AFM and contact angle measurements have indicated

degradation and/or disordering of a C<sub>18</sub> SAM annealed to 120-150 °C at pressures of 10<sup>-2</sup>-10<sup>-3</sup> Torr [131]. For a 84 Å poly-G film, a series of *in vacuo* anneals, followed by in situ XPS, have indicated modest changes up to a substrate temperature of ~ 200 °C, with more significant changes above this temperature, including decomposition and/or degradation between 250 and 350 °C. This is consistent with measurements of the stability of poly(ethylene oxide) in vacuum, a chemically similar molecule also containing C-O-C bonds in the backbone [132-136]. In poly(ethylene oxide), degradation takes place by random scission of the polymer chain, producing volatile oligomers, in the temperature range of 190–420 °C.

At this point we will return to the issue of the measurement of the attenuation length  $\lambda$  of thin organic films, as we are now in position to summarize results for a variety of IOLs. Fig. 3-5 shows  $\lambda$  for photoelectron emitted from the C(1s) core level (Mg K $\alpha$  excitation, ~ 968.6 eV kinetic energy) for ODTS, poly-G, and two conjugated oligo(phenylene-ethynylene) SAMs of different lengths deposited on Au [137]. The  $\lambda$  measured for an octadecanethiol SAM on gold by Lamont and Wilkes (interpolated value) [124] is also shown for reference. Values of  $\lambda$  are plotted against the density of valence electrons in the film, as the contribution to attenuation from scattering off valence electrons is known to dominate as compared to the contribution from core-level electrons. As expected, a decrease in  $\lambda$  with increasing valence electron density is observed. Fitting this data to a power law relationship results in an exponent of  $-0.77 \pm 0.29$ , using linear weighting. Including only our results gives values of -0.80 or -0.85 (linear vs. logarithmic weighting).

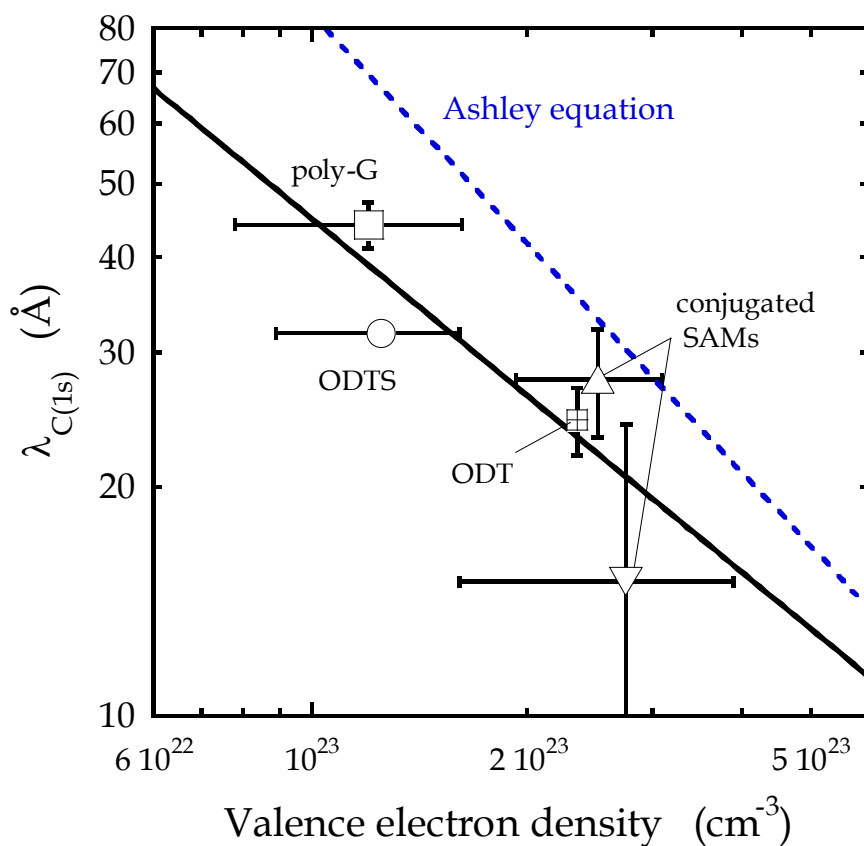


**Figure 3-5:** Attenuation length  $\lambda$  for electrons representing photoemission from the C(1s) core level as a function of the density of valence electrons in the organic film. Mg K $\alpha$  x-ray radiation gives an electron kinetic energy of  $\sim 970$  eV for the C(1s) level. The solid line represents a fit to a power law (exponent of  $-0.77 \pm 0.29$ ), whereas the dashed line is a prediction of the Ashley equation [Ref. 138].

Assuming an isotropic distribution of scattering sites, and considering inelastic scattering events only, an exponent of -1 would be expected.

For comparison, also plotted in Fig. 3-5 are the values expected from an empirical relationship between electron *inelastic mean free path* (IMFP) and valence electron density developed by Ashley [138], which is a power law with an exponent of -1. In all cases, the values predicted by the Ashley equation are higher than the measured values. A slight overestimation is expected by the Ashley equation, since it accounts only for scattering only off of valence electrons. Somewhat better agreement between predicted and measured values can be obtained using the TPP-2M relation [139], which includes additional material parameters. A possible source of deviation between the expected IMFP and the measured  $\lambda$  is elastic scattering, which can lead to complicated, potentially non-exponential attenuation functionality [140]. All in all, the values found for the attenuation lengths are within expectations, and lend weight to their use in the calculations that follow.

### **3.3.2. Reaction of transition metal coordination complexes with interfacial organic layers**

The first step in the formation of inorganic-on-organic interfaces involves the reaction of the inorganic containing species, e.g., a transition metal coordination complex, with a pre-existing organic layer, which could be considered the first half-cycle in an atomic layer deposition process. Key objectives in studying this reaction include quantifying the kinetics of adsorption, the spatial extent of reaction, and the

structure of the adlayer. All of these may have a role in determining the final properties of the inorganic-organic interface, including electrical, thermal, and mechanical properties.

### **3.3.2.1. Experimental approach**

Precise control of reactant exposures is essential to quantify the evolution of the adlayer with time, thus, focus has been on the use of ultrahigh vacuum (UHV) techniques, primarily XPS, to examine the chemisorption of transition metal compounds on interfacial organic layers. Examination under well-controlled UHV conditions ensures that the reaction products are not further modified by reaction with either residual gases or by exposure to the atmosphere. In this approach, the organic layer is first formed and characterized on an appropriate substrate using the techniques described above in Sec. 3.3.1. Next, the sample is transferred into one of two custom-designed UHV chambers [141,142], and exposed to controlled amounts of the transition metal coordination complex of interest. In one chamber, exposures are achieved using a glass capillary array doser [88,141], leading to fluxes at the sample surface of  $\sim 10^{12}$ - $10^{13}$  molec-cm<sup>-2</sup>-s<sup>-1</sup>. In the other, a collimated supersonic molecular beam [89,142] is used, giving fluxes at the sample surface of  $\sim 10^{15}$  molec-cm<sup>-2</sup>-s<sup>-1</sup>. Here the angle of incidence could also be varied, and interactions between the surface and metal coordination complexes could be probed using molecular beam reflectivity techniques [89]. After dosing, XP spectra could be collected immediately for regions representing the substrate [Si(2p), O(1s)], the organic layer [C(1s), O(1s)],

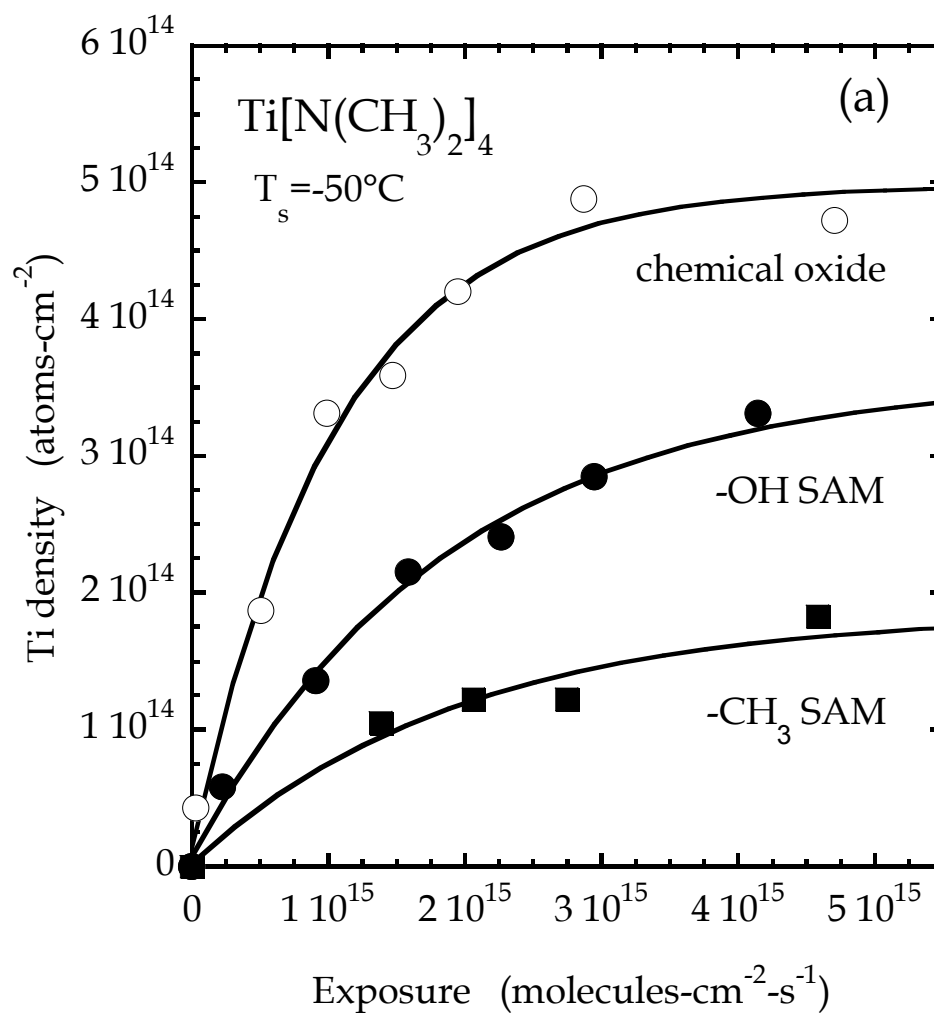
N(1s)], and the transition metal complex [Ti(2p), Ta(4p), Ta(4d), Ta(4f), C(1s), N(1s)]. Substrates could be subjected to a series of exposures, affording the opportunity to obtain a corresponding series of XP spectra, including ones taken at variable take-off angle (ARXPS).

### **3.3.2.2. The kinetics of adsorption**

#### **3.3.2.2.1. Coverage-exposure relationships**

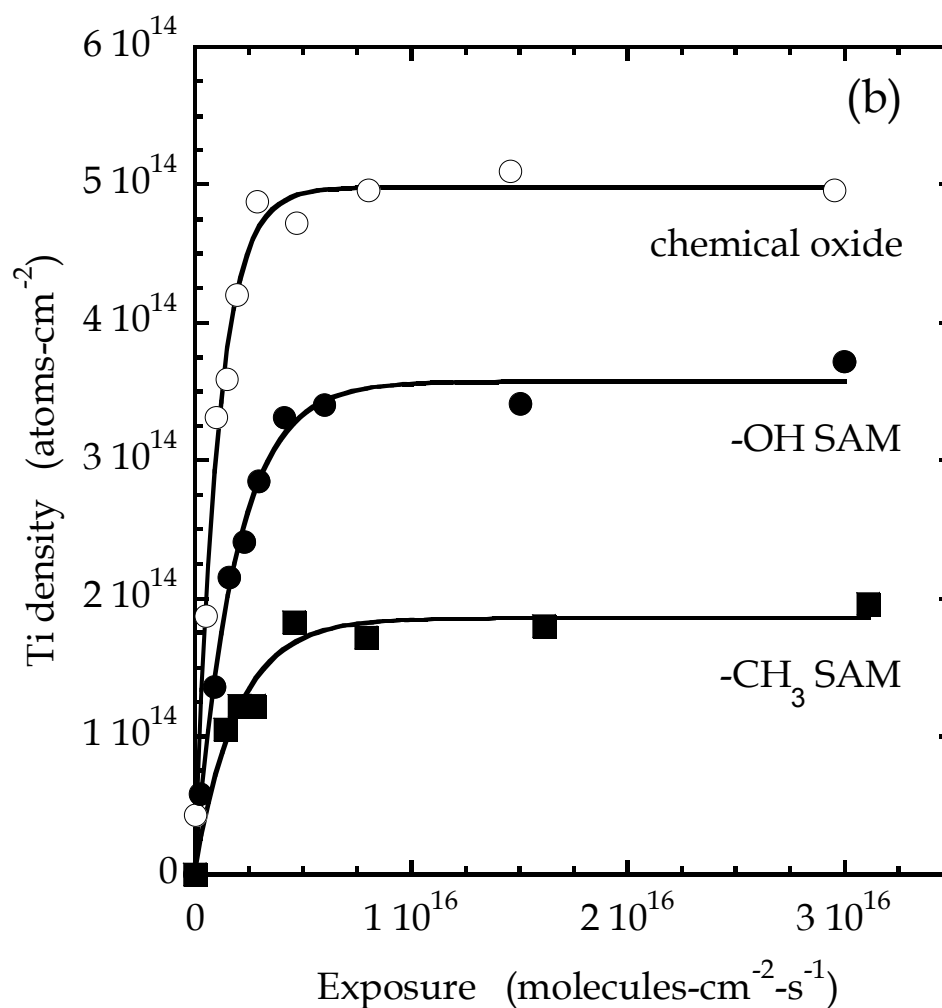
In cases where adsorption is dissociative and effectively irreversible, the kinetics of adsorption can be quantified by obtaining the *coverage-exposure relationship*. This can be achieved by employing XPS to monitor the absolute coverage of the transition metal. If the incident flux is also known, or can be calculated, the coverage-exposure relationship can be used to estimate the absolute value of the coverage-dependent probability of adsorption. Self-limiting, saturated adsorption of the thin film precursors is essential to ALD, and the coverage-exposure relationship is a direct indicator of the formation of a saturated adlayer.

Fig. 3-6 presents representative coverage-exposure relationships for  $\text{Ti}[\text{N}(\text{CH}_3)_2]_4$  adsorbed on chemical oxide, and two straight-chain (-OH and -CH<sub>3</sub> terminated) SAMs at a substrate temperature of  $T_s = -50\text{ }^\circ\text{C}$  (results were similar at  $T_s = 30$  and  $110\text{ }^\circ\text{C}$ ). In these experiments,  $\text{Ti}[\text{N}(\text{CH}_3)_2]_4$  was delivered to the substrate via a glass capillary array doser.



**Figure 3-6(a):** Coverage-exposure relationship, deduced from XPS, for the adsorption of  $\text{Ti}[\text{N}(\text{CH}_3)_2]_4$  on chemical oxide, -OH and -CH<sub>3</sub> terminated SAMs, at a substrate temperature of  $-50^\circ\text{C}$ . highlighting the low exposure regime, which illustrates the differing initial slopes. The fits to the data, shown as smooth curves, are for a first-order Langmuirian model of adsorption.





**Figure 3-6(b):** Coverage-exposure relationship, deduced from XPS, for the adsorption of  $\text{Ti}[\text{N}(\text{CH}_3)_2]_4$  on chemical oxide and an -OH and -CH<sub>3</sub> terminated SAMs, at a substrate temperature of -50 °C emphasizing the high exposure regime and the saturation coverage. The fits to the data, shown as smooth curves, are for a first-order Langmuirian model of adsorption.

The ordinate represents the density of Ti estimated from XPS [88], without making any corrections for attenuation effects (*vide infra*). Fig. 3-6(a) highlights the low exposure regime, which demonstrates most effectively differences in the initial probabilities of adsorption. The data for larger exposures, in Fig. 3-6(b), best indicate differences in the densities at saturation. All data could be fit well to a model assuming first-order Langmuirian kinetics,  $d\theta/dt = (S_{R,0}F/n_s)(1 - \theta)$ , where  $\theta$  is the fractional coverage of the chemisorbed species,  $S_{R,0}$  is the initial (zero-coverage) reaction probability,  $F$  is the incident flux, and  $n_s$  is the density of the chemisorbed species at saturation. From inspection, for these conditions chemical oxide is the most reactive surface ( $S_{R,0}$  largest), whereas the surface terminated with the  $-\text{CH}_3$  SAM is the least reactive. Using estimates for both the absolute coverage (not attenuation corrected), and the absolute exposure, results in initial probabilities of adsorption in this case of 0.48, 0.19 and 0.09 for the adsorption of  $\text{Ti}[\text{N}(\text{CH}_3)_2]_4$  on chemical oxide and the  $-\text{OH}$  and  $-\text{CH}_3$  terminated SAMs, respectively. The value on chemical oxide is close to unity, and given experimental uncertainties in the estimates for the absolute coverage and incident flux, it is plausible that the actual value is indeed unity. In this regard, a value close to unity was found using molecular beam techniques for  $\text{Ti}[\text{N}(\text{CH}_3)_2]_4$  reacting on chemical oxide [89]. The data shown in Fig. 3-6 also indicate that the capacity of the surface to adsorb the Ti complex depends on the surface termination. As may be seen the (apparent) saturation coverage follows in the same order as the initial probability of adsorption. Clearly, the identity or type of functional group has a large influence on the reactivity of the surface. What remains

concerning this data is to determine the spatial extent of reaction, and, if necessary, make corrections to the saturation densities due to attenuation of the Ti signal.

#### **3.3.2.2.2. Effects of microstructure of the organic layer on reactivity**

Sec. 3.3.1.3 described how both regular and irregular, randomly branched oligomers and polymers could be grown from a surface. These layers naturally introduce a way to increase the density of reactive functional groups, and to increase the dimensionality of the arrangement of groups in the organic layer. In Sec. 3.3.1.1 these two features were identified, along with the identity of the functional group, as the factors important in controlling inorganic-organic interface formation. Fig. 3-7(a) presents the coverage exposure relationship for  $\text{Ta}[\text{N}(\text{CH}_3)_2]_5$  reacting at room temperature with the straight chain anchor,  $\equiv\text{Si}-(\text{CH}_2)_{12}-\text{NH}_2$  (Gen-0-12C), and with the first generation dendron (Gen-1-12C, *cf.* Fig. 3-2). Here again, these densities, estimated from the Ta(4d) peak intensities, are uncorrected for attenuation effects. The initial probability of adsorption appears to be approximately the same for both layers,  $S_{\text{R},0} \sim 0.028$ . This could reflect the intrinsic reactivity of this Ta complex with the terminal  $-\text{NH}_2$  groups present in both layers. At higher exposures it can be seen that the two sets of data diverge, and the chemisorptive capacity of the Gen-1-12 layer exceeds that of the anchor by at least a factor of 2. This result is not surprising given the increase of the terminal  $-\text{NH}_2$  groups from Gen-0-12C to Gen-1-12C indicated by the data shown above in Fig. 3-3(b).

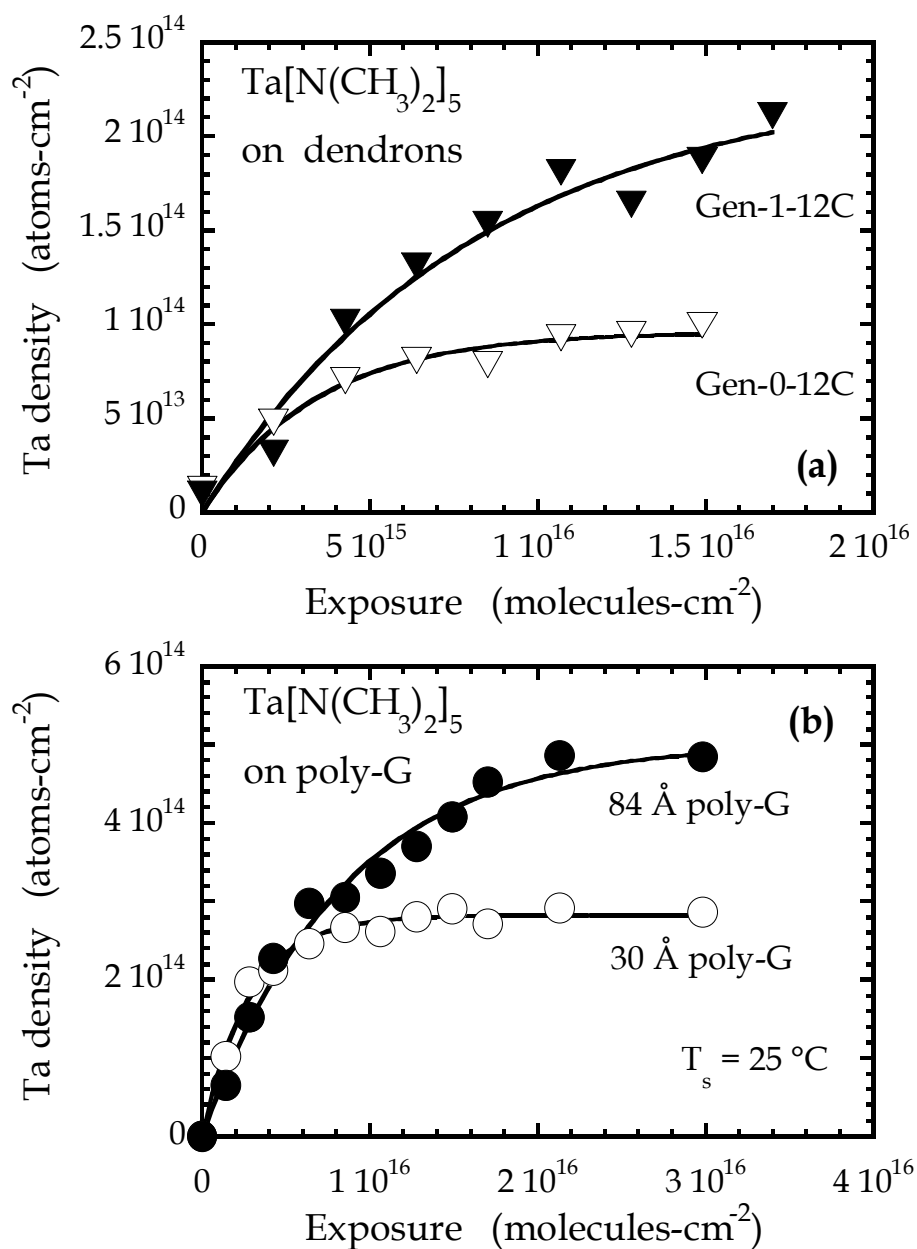


**Figure 3-7:** Coverage-exposure relationship, deduced from XPS, for the adsorption of  $\text{Ta}[\text{N}(\text{CH}_3)_2]_5$  at 25 °C on (a) a Gen-0 and Gen-1 PAMAM dendron, and (b) two different thicknesses of poly-G. Absolute densities were calculated from XPS.

A similar set of results is considered in Fig. 3-7(b) where the (uncorrected) coverage-exposure relationship for  $\text{Ta}[\text{N}(\text{CH}_3)_2]_5$  reacting with two different thicknesses of polyglycidol (poly-G, *cf.* Fig. 3-4) is presented. Similar to the results obtained on the regularly branched dendron, here we also find that the initial reactivity of the surface depends only weakly on the thickness of the organic layer, with  $S_{\text{R},0} \sim 0.10$  (0.06) on the 30 Å (84 Å) thick poly-G layer. The chemisorptive capacity of the surface is clearly higher for the thicker, more branched organic layer, however.

### 3.3.2.3. Spatial extent of reaction

Essential to developing an understanding of inorganic-organic interface formation is not only quantifying the amount of adsorption by the transition metal coordination complex, but also the details of the reaction—where does the complex react, and what is the extent of reaction? This subsection will concern the former, the spatial extent of reaction, and the next subsection (3.3.2.4) will concern the latter.

In order to quantify the location of the chemisorbed species with respect to the vacuum/organic and the organic/substrate (e.g.,  $\text{SiO}_2$ ) interfaces, ARXPS has been employed. ARXPS offers many advantages with respect to competing techniques. For example, direct imaging techniques such as transmission electron microscopy (TEM) and scanning TEM (STEM) are not only invasive, but are problematic concerning the imaging of organic materials and the air-sensitive near-monolayer adlayers that interest us here. Sputter depth profiling is also invasive and lacking concerning the analysis of the thin, relatively sensitive layers formed here. ARXPS can provide both

chemically specific and spatially resolved information assuming that the distribution of adsorbed species can be safely assumed to be one of a handful of simple cases. Even if the assumed model is over-simplified, ARXPS can nevertheless identify important trends concerning the spatial extent (i.e., depth from the IOL/vacuum interface) of adsorption in these systems.

Given the two-dimensional nature of the simpler IOLs, a reasonable assumption is that the transition metal complex forms a 2-d monolayer upon chemisorption, buried beneath the vacuum/organic interface by a distance  $d_{ML}$ . Neglecting photoelectron diffraction effects, and assuming that the organic overlayer is uniform, the predicted variation of the photoelectron intensity with take-off angle is given by  $I(\theta) = (I_0/\cos \theta)\exp[-d_{ML}/(\lambda \cos \theta)]$ , where  $I_0$  is the unattenuated intensity ( $d_{ML} = 0$ ) at the normal ( $0^\circ$ ) take-off angle,  $\theta$  is the take-off angle, and  $\lambda$  is the attenuation length of the photoelectrons. Fig. 3-8 displays the predicted form for  $I(\theta)$  as a function of take-off angle for a series of values of  $d_{ML}/\lambda$ . To highlight the change in functional form with changing values of  $d_{ML}/\lambda$ , all values are normalized to  $I$  at  $\theta = 0^\circ$ . For  $d_{ML}/\lambda \geq 1$ ,  $I(\theta)$  decreases continuously with increasing take-off angle. For intermediate values  $1 > d_{ML}/\lambda > 0$  the intensity passes through a maximum, and in the limit of  $d_{ML}/\lambda \rightarrow 0$  it approaches the functional form  $1/\cos \theta$ . This last form simply represents an increase in the area of the surface “seen” by the detector as the take-off angle is increased. Practically, due to the effects of finite sample sizes and surface roughness, it is difficult to collect meaningful data beyond a take-off angle of  $\theta \sim 75^\circ$ . In most cases, this range of take-off angles is sufficient to obtain useful information concerning the spatial extent of reaction.

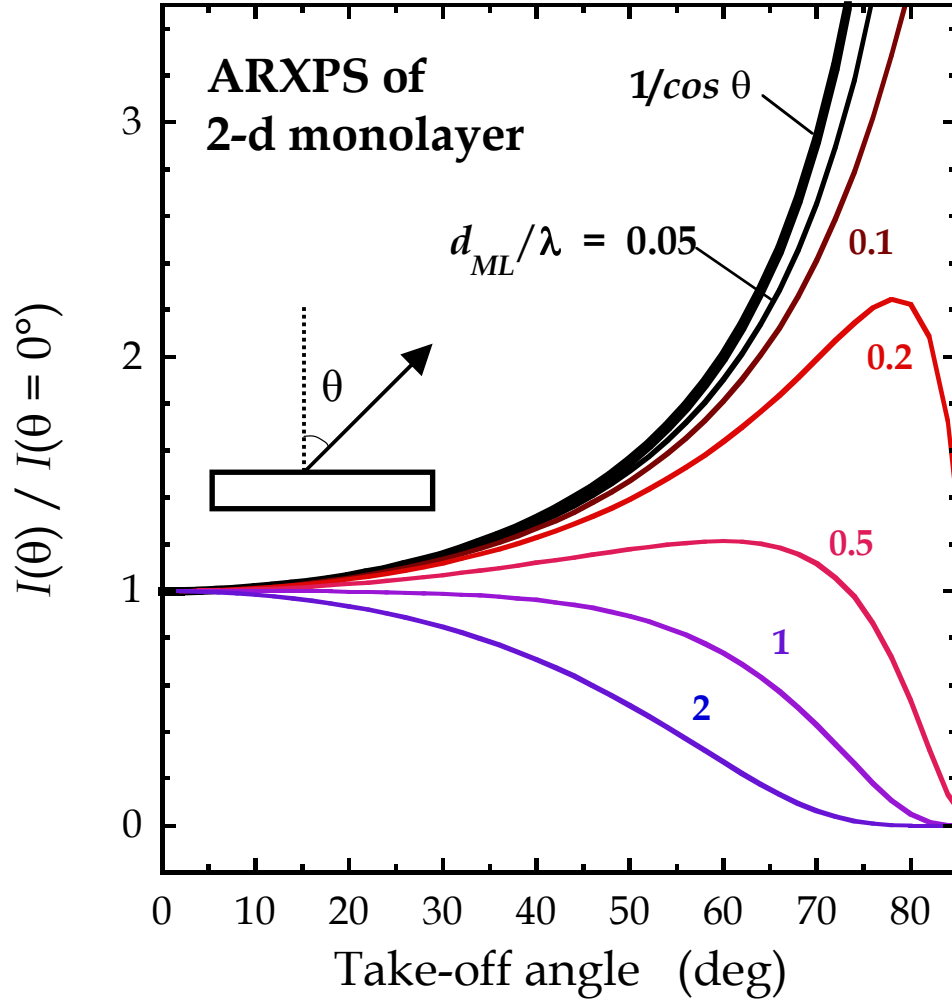


**Figure 3-8:** Predicted form for the photoemission intensity,  $I(\theta)$ , as a function of takeoff angle,  $\theta$ , for a series of values of  $d_{ML}/\lambda$ .  $d_{ML}$  is the depth of the 2-d monolayer of photo-emitters, and  $\lambda$  is the attenuation length. To highlight the change in functional form with changing values of  $d_{ML}/\lambda$ , all curves are normalized to  $I$  at  $\theta = 0^\circ$ .

Fig. 3-9 displays the results from ARXPS for take-off angles of  $\theta = 0^\circ$ - $65^\circ$  for the adsorption of  $\text{Ti}[\text{N}(\text{CH}_3)_2]_4$  on two straight chain SAMs: one with  $-\text{NH}_2$  termination, and one with  $-\text{CH}_3$  termination [88]. The trend of the Ti(2p) intensity with take-off angle is opposite for these two cases, indicating the Ti complex is near the SAM/vacuum interface and has reacted with the terminal  $-\text{NH}_2$  group in the first case, whereas the Ti complex has penetrated the  $-\text{CH}_3$  terminated SAM layer, and has reacted with residual  $-\text{OH}(a)$  present at the SAM/ $\text{SiO}_2$  interface in the second. A fit to these data, shown by the smooth curves, gave values for  $d_{\text{ML}}/\lambda = 0.12 \pm 0.09$  for the  $-\text{NH}_2$  SAM, and  $0.86 \pm 0.19$  for the  $-\text{CH}_3$  SAM. Making use of the attenuation length found using the methods described above in Sec. 3.3.1.2, and correcting for photoelectron energy,  $\lambda$  for the Ti(2p) photoelectrons was calculated to be  $28.8 \text{ \AA}$ . Using this value, the depth of the chemisorbed layer was found to be  $d_{\text{ML}} = 3.5 \pm 2.6 \text{ \AA}$  and  $24.8 \pm 5.5 \text{ \AA}$  for the  $-\text{NH}_2$  and  $-\text{CH}_3$  SAMs, respectively. These can be compared to measured thicknesses of  $\sim 14$  and  $27 \text{ \AA}$  for the  $-\text{NH}_2$  and  $-\text{CH}_3$  SAMs, respectively. These results are consistent with the reaction of  $\text{Ti}[\text{N}(\text{CH}_3)_2]_4$  with the terminal  $-\text{NH}_2$  group on the  $-\text{NH}_2$  SAM, and at the SAM/ $\text{SiO}_2$  interface with the  $-\text{CH}_3$  SAM.

A potentially more complex example is provided by the adsorption of  $\text{Ta}[\text{N}(\text{CH}_3)_2]_5$  on the Gen-1 PAMAM dendrons. These layers, as described in Sec. 3.3.1.3, possess functional groups on their (branched) backbones, in addition to the terminal  $-\text{NH}_2$  groups. Fig. 3-10(a) presents ARXPS results for  $\text{Ta}[\text{N}(\text{CH}_3)_2]_5$  adsorption on the Gen-1-3C and Gen-1-12C dendrons [86].



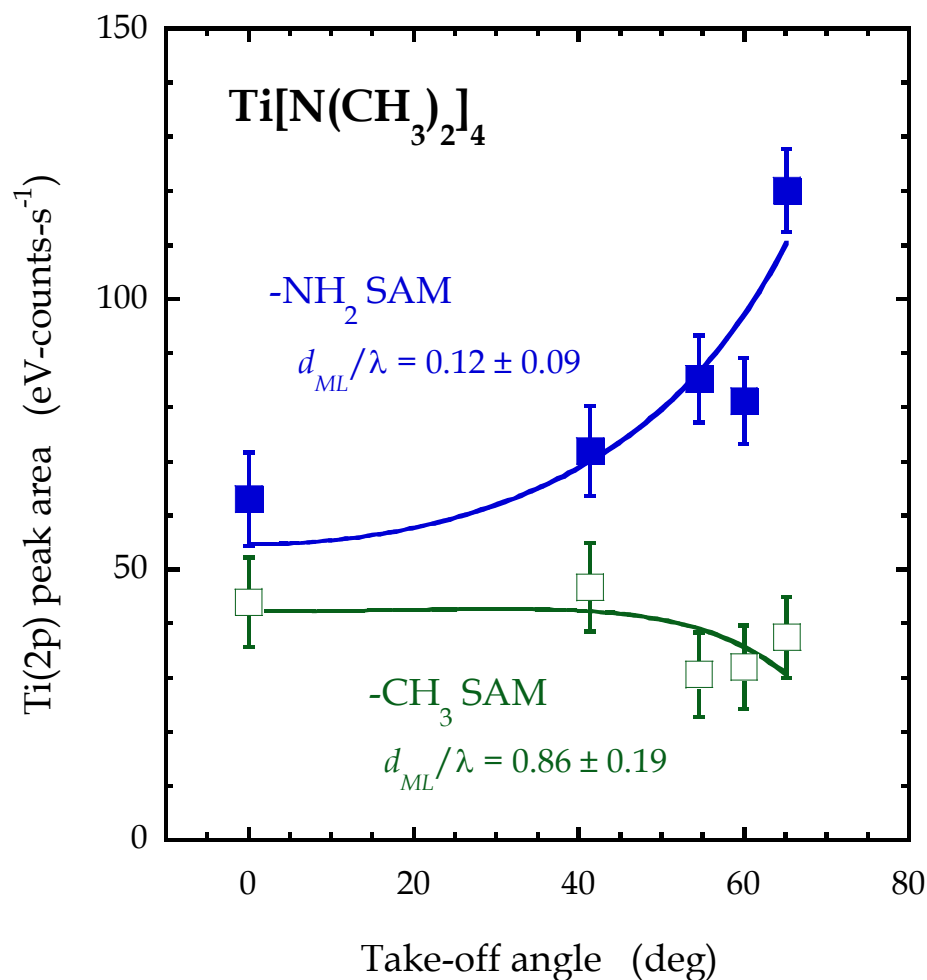


**Figure 3-9:** Integrated area of the Ti(2p) feature as a function of takeoff angle for saturated layers of Ti[N(CH<sub>3</sub>)<sub>2</sub>]<sub>4</sub> on straight-chain -NH<sub>2</sub> and -CH<sub>3</sub> terminated SAMs. The smooth curves are a fit to the model that assumes that the Ti is present in a 2-dimensional monolayer buried at a depth  $d_{ML}$  from the SAM/vacuum interface (*cf.* Fig. 3-8).

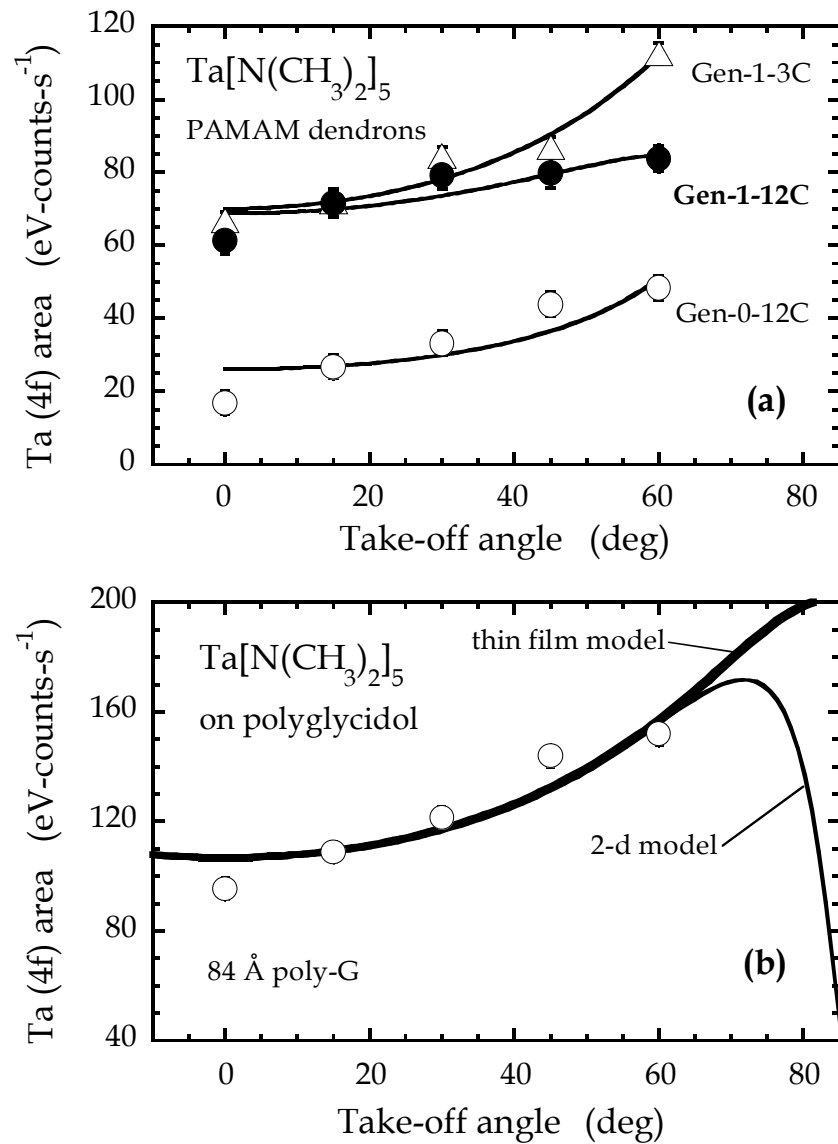


**Figure 3-10:** Integrated peak area of the Ta(4f) region for saturated layers of Ta[N(CH<sub>3</sub>)<sub>2</sub>]<sub>5</sub> on (a) -NH<sub>2</sub> terminated PAMAM dendrons, and (b) an 84 Å thick polyglycidol layer. In (a) the smooth curves are a fit to the model that assumes that the Ta is present in a 2-d monolayer buried at a depth  $d_{ML}$  from the SAM/vacuum interface. In (b) we display a fit to two models: the 2-d model as in (a) and Fig. 3-8, and a thin film model that assumes the Ta is uniformly distributed in a thin film which extends from the IOL/vacuum interface to a depth of  $d_{TF}$ .

For comparison, results are also shown for the anchor, Gen-0-12C, which is the straight-chain -NH<sub>2</sub> SAM considered in Fig. 3-9. First, taking note of the absolute intensity of the Ta signals, we see that these results verify those considered in Fig. 3-7(a), which showed that the branching step increases the chemisorptive capacity of the surface. We also see that the results for the two Gen-1 layers are similar at near normal take-off angles, but diverge at larger take-off angles, where the intensity from the Gen-1-3C layer is larger. This means that more of the Ta is near the surface on the Gen-1-3C layer, but, due to the higher degree of attenuation of the Ta signal in the Gen-1-12C case, there is actually more Ta adsorbed on the Gen-1-12C layer. Fits of these data to the 2-d monolayer model described above give these values:  $d_{ML}/\lambda = 0.02 \pm 0.22$  (Gen-0-12C),  $0.22 \pm 0.06$  (Gen-1-3C), and  $0.48 \pm 0.08$  (Gen-1-12C). Thus, penetration is least on the straight-chain anchor, and is the most on the branched dendrons formed from the longer anchor. This is consistent with the higher dimensionality of the arrangement of active sites in the Gen-1 dendrons. Again, making use of ARXPS of C(1s) for the bare dendrons,  $\lambda$  can be estimated and thus the absolute depth of penetration can be calculated. For the three cases we find  $d_{ML} = 0.3 \pm 3.1$  Å (Gen-0-12C),  $5.7 \pm 1.4$  Å (Gen-1-3C), and  $8.5 \pm 1.5$  Å (Gen-1-12C). From ellipsometry the thickness of the latter two layers is 11.2 and 19.5 Å, and thus it seems that adsorption involves reaction with the branched backbones on the Gen-1 dendrons.

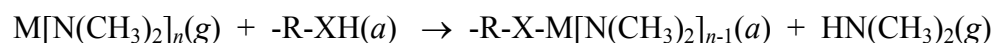
As a third example, we consider the adsorption of Ta[N(CH<sub>3</sub>)<sub>2</sub>]<sub>5</sub> on poly-G. As described above in Sec. 3.3.1.3, in poly-G films, potentially reactive -OH sites are distributed throughout the film, not confined to the top surface. Thus, one may

anticipate applying a different assumption concerning the distribution of chemisorbed Ta species in the adlayer. One simple model could be a uniform distribution of species throughout a thin film which extends from the vacuum interface to a depth of  $d_{TF}$ . The appropriate functional form in this case is  $I(\theta) = I_0[1 - \exp[-d_{TF}/(\lambda \cos \theta)]]$ , where  $I_0$  now represents the intensity from an infinitely thick film possessing this density of species. Fig. 3-10(b) displays a plot the results from ARXPS for a saturation exposure of Ta[N(CH<sub>3</sub>)<sub>2</sub>]<sub>5</sub> on a 84 Å thick poly-G thin film [87]. As may be seen, the 2-d model and the thin film model fit the data equally well, and are indistinguishable from each other for take-off angles  $\theta = 0^\circ$ -60°. Above angles of 65° the two models diverge. These observations indicate two things. First, there is motivation to collect data at very shallow ( $> 70^\circ$ ) take-off angles, provided sample size, electron optics, surface roughness, and elastic scattering effects can be dealt with. Second, given the results presented here, over take-off angles of 0°-60°, it is reasonable to expect only a single metric from the analysis—the average depth of penetration. For the results in Fig. 3-10(b),  $d_{ML}/\lambda = 0.31 \pm 0.09$  and  $d_{TF}/\lambda = 0.76 \pm 0.28$ . Again using results from ellipsometry and ARXPS of the substrate Si(2p) feature the attenuation length of Ta(4f) photoelectrons in these poly-G layers can be estimated to be  $\lambda = 50.1$  Å. Thus, the mean depth of penetration found from the two models is  $\langle d \rangle = 16 \pm 4$  Å (2-d model) and  $20 \pm 7$  Å (thin film model), values indistinguishable given the uncertainties. Given the nature of the exponentially damped weighting function it is expected that the thin film model will consistently predict a slightly larger value for the average depth of penetration. A final question involves how these values may depend upon the thickness of the poly-G layer. Analysis of ARXPS data using the 2-d

model from thinner layers gave values of  $\langle d \rangle = 15 \pm 4 \text{ \AA}$  (30 \AA thick poly-G) and  $19 \pm 4 \text{ \AA}$  (66 \AA thick poly-G). Thus, the average depth of penetration was confined to the range  $15\text{-}19 \pm 4 \text{ \AA}$  for all layers investigated.

#### **3.3.2.4. Structure and composition of the chemisorbed species in the saturated adlayers**

For the amido coordination complexes considered here, chemisorption involves a simple ligand exchange reaction:



where  $\text{M} = \text{Ti, Ta}$  (and  $n = 4, 5$ ), and  $\text{X} = \text{O}$  or  $\text{NH}$ . An important question is what happens after this initial reaction, and how might additional ligand exchange reactions depend on the identities of the functional groups, their density, and their arrangement in three-dimensional space. Considerable insight can be achieved if the stoichiometry of the adlayer can be deduced, so important values to measure are the density of functional groups present (*cf.* Sec. 3.3.1), the density of the metal center (previous parts of this Sec. 3.3.2.), and the number of ligands retained by the complex (this subsection). Identifying the nature of the chemisorbed species present at saturation coverage could have significant implications concerning additional reactions between this adlayer and, for example, co-reactants introduced in subsequent cycles of atomic layer deposition.

#### 3.3.2.4.1. Correlation between M and OFG densities

One expects a strong correlation between the density of the metal center at saturation and the density of organic functional groups. On one set of surfaces, based on results from ARXPS, reaction has occurred between  $\text{Ti}[\text{N}(\text{CH}_3)_2]_4$  and residual  $-\text{OH}(a)$  at the SAM/ $\text{SiO}_2$  interface. This was found to be the case for a straight-chain,  $-\text{CH}_3$  terminated SAM,  $\equiv\text{Si}-(\text{CH}_2)_{17}-\text{CH}_3$  (assembled at 2 different densities), and for two SAMs possessing reactive tail groups,  $\equiv\text{Si}-(\text{CH}_2)_{11}-\text{OH}$ , and  $-\text{Si}-(\text{CH}_3)_2(\text{CH}_2)_3-\text{NH}_2$ , i.e., Gen-0-3C. In the case of the  $-\text{OH}$  SAM, adsorption was modeled as being divided between reaction at the SAM/ $\text{SiO}_2$  interface, and at the reactive  $-\text{OH}$  tail group [88], while in the case of Gen-0-3C it is assumed that all species react at the SAM/ $\text{SiO}_2$  interface. Fig. 3-11 shows the Ti density at the  $\text{SiO}_2$ /SAM interface as a function of the SAM density. Also included on this plot is the bare chemical oxide surface. In this plot, the density of Ti has been corrected for attenuation effects. As may be seen, there is a negative correlation between the Ti density and the density of the SAM. This is of course consistent in this case as the SAMs, when formed, bind to the substrate via the  $-\text{OH}(a)$  groups, and thus they are not available to bind the Ti complex. For the SAMs with  $-\text{NH}_2$  and  $-\text{OH}$  terminations, lower Ti saturation densities are observed at a given SAM density as compared to the  $-\text{CH}_3$  terminated SAMs. This may be due to the presence of partially decomposed Ti complexes bound at the SAM/vacuum interface that could block the diffusion of other Ti complexes to the SAM/ $\text{SiO}_2$  interface.

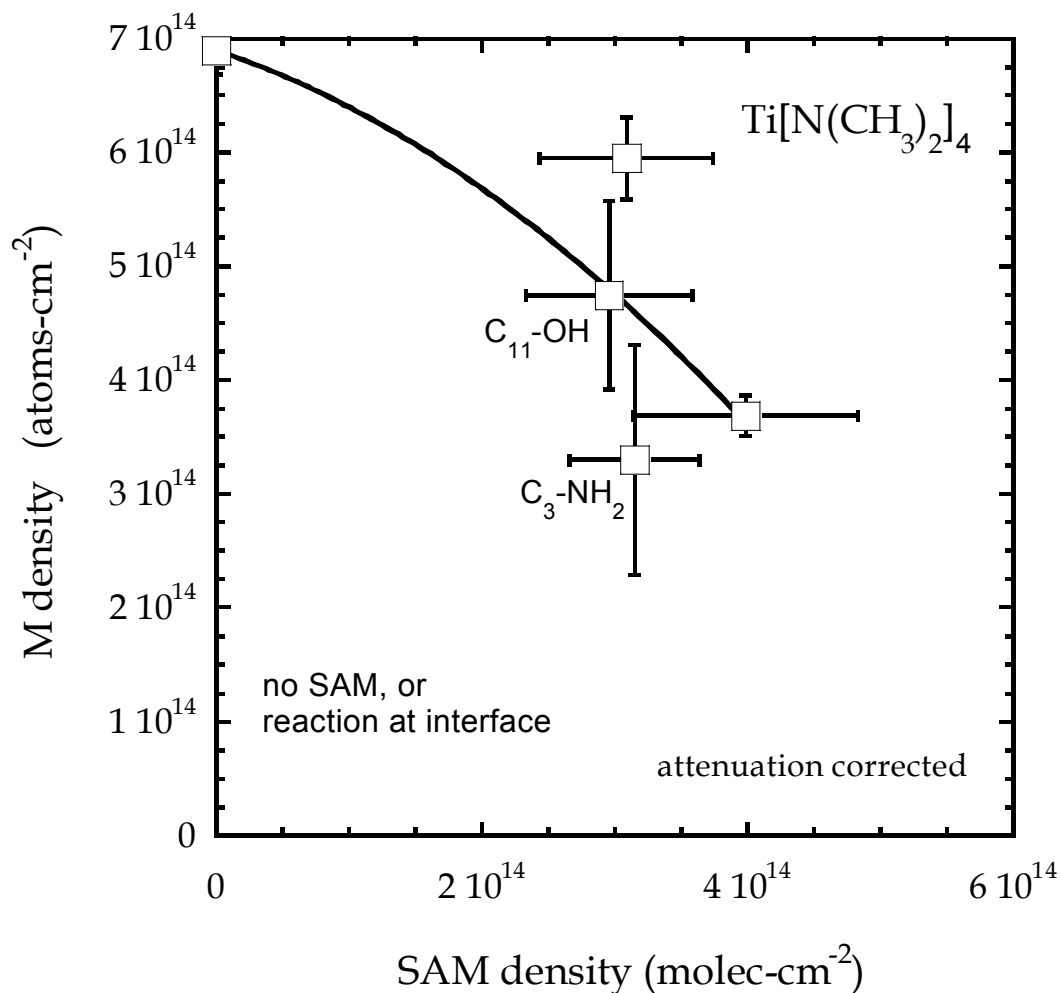


**Figure 3-11:** The density of Ti atoms produced by saturation exposures to  $\text{Ti}[\text{N}(\text{CH}_3)_2]_4$  ( $T_s = 25^\circ\text{C}$ ) as a function of the SAM density, as deduced from XPS, for mostly unreactive SAMs. The data point on the ordinate represents the starting surface, chemical oxide. In all cases, the Ti density has been corrected for attenuation effects and represents that attributed to adsorption at the SAM/ $\text{SiO}_2$  interface. For the -OH SAM, adsorption of Ti at the SAM/vacuum interface is also implicated [Ref. 88], and this value is considered in Fig. 3-12.

Of most interest here are the examples where the complex reacts with the functional group on the IOL. Fig. 3-12 contains a plot of a set of results for  $\text{Ti}[\text{N}(\text{CH}_3)_2]_4$  reacting with straight chain alkyl or aromatic [137] SAMs possessing either a terminal -OH or -NHR end group. Again the results for reaction on the -OH SAM were modeled as occurring both at the OFG and the SAM/ $\text{SiO}_2$  interface—here that due to the OFG is plotted. As may be seen, all of these results indicate a Ti:OFG ratio of approximately 1:2. Two scenarios are possible: first, half of the OFGs may react with each transition metal complex, while the other half do not, possibly due to steric effects. Second, two OFGs could react with each transition metal complex. In the former, a single  $-\text{N}(\text{CH}_3)_2$  ligand would be exchanged, while two would be exchanged in the latter case. This issue will be revisited below. Fig. 3-12 also plots the result for the adsorption of  $\text{Ti}[\text{N}(\text{CH}_3)_2]_4$  on the branched dendron, Gen-1-3C. For the plots shown here, the dendron OFG density was calculated assuming contributions from both the terminal primary amines,  $-\text{R}-\text{NH}_2$ , and the amides,  $-\text{C}(=\text{O})\text{NH}-$ . Given this assumption, the stoichiometry of Ti:OFG is also 1:2 for this case. Thus, there is a strong tendency towards this stoichiometry for the adsorption of  $\text{Ti}[\text{N}(\text{CH}_3)_2]_4$  on -OH, -NHR, and  $-\text{C}(=\text{O})\text{NH}-$  containing layers at room temperature.

In Fig. 3-13 the reaction of  $\text{Ta}[\text{N}(\text{CH}_3)_2]_5$  on a variety of IOLs is considered. First plotted in (a) are the results for the Ta:OFG ratio for the Ta complex reacting with the  $-\text{NH}_2$  terminated straight-chain anchors, and the first-generation dendrons [86]. Here, for comparison the results for the Ti complex displayed in Fig. 3-12 are re-plotted. We see that for the Ta complex the 1:2 ratio for Ta:OFG is also implicated by the data.



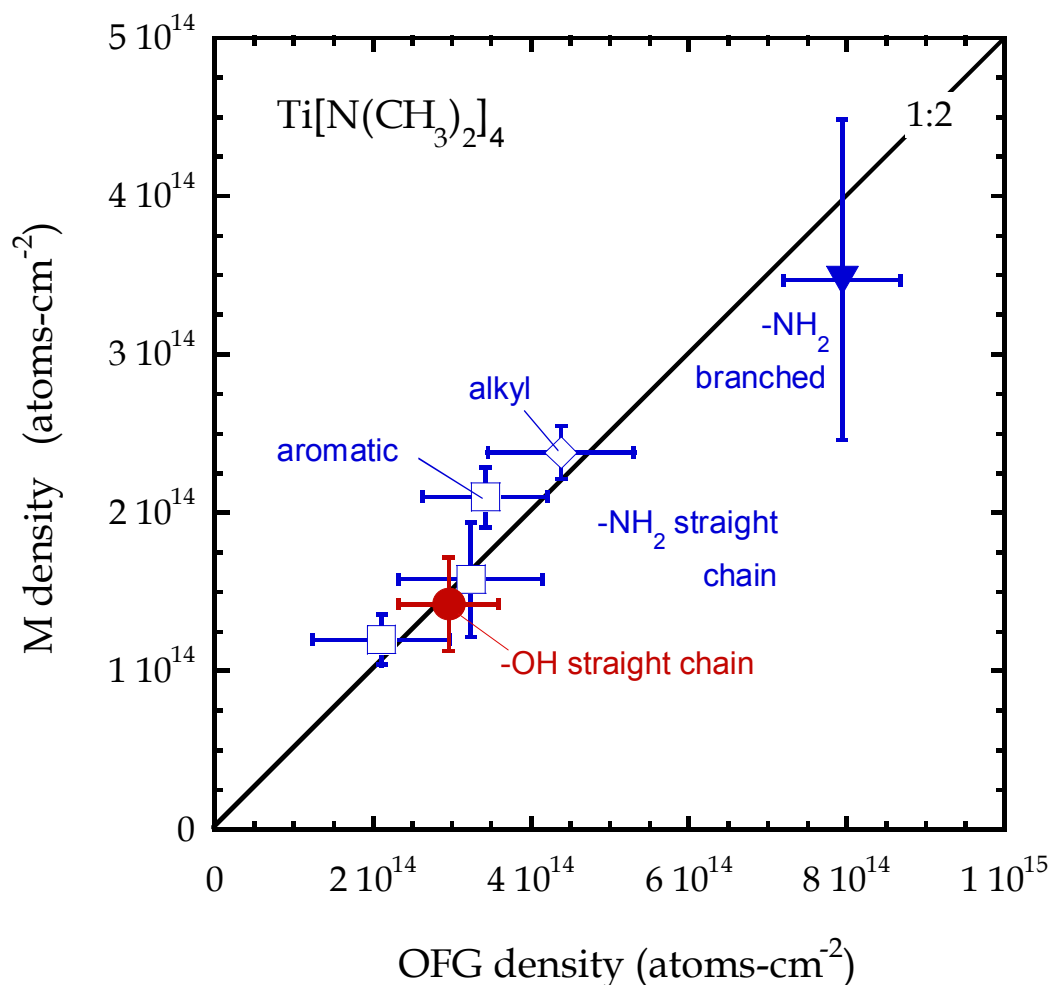


**Figure 3-12:** The density of Ti atoms produced by saturation exposures to  $\text{Ti}[\text{N}(\text{CH}_3)_2]_4$  ( $T_s = 25^\circ\text{C}$ ) as a function of OFG density, as deduced from XPS, for IOLs with reactive endgroups and backbones. For 5 of the cases, the SAMs possess either a straight chain alkyl or aromatic backbone and a single terminal  $-\text{OH}$  or  $-\text{NHR}$  endgroup. For the branched PAMAM dendron (Gen-1-3C), both terminal amine,  $-\text{NH}_2$ , and the backbone amide group,  $-\text{C}(=\text{O})\text{NH}-$ , contribute to the OFG density. In all cases, the Ti density has been corrected for attenuation effects.

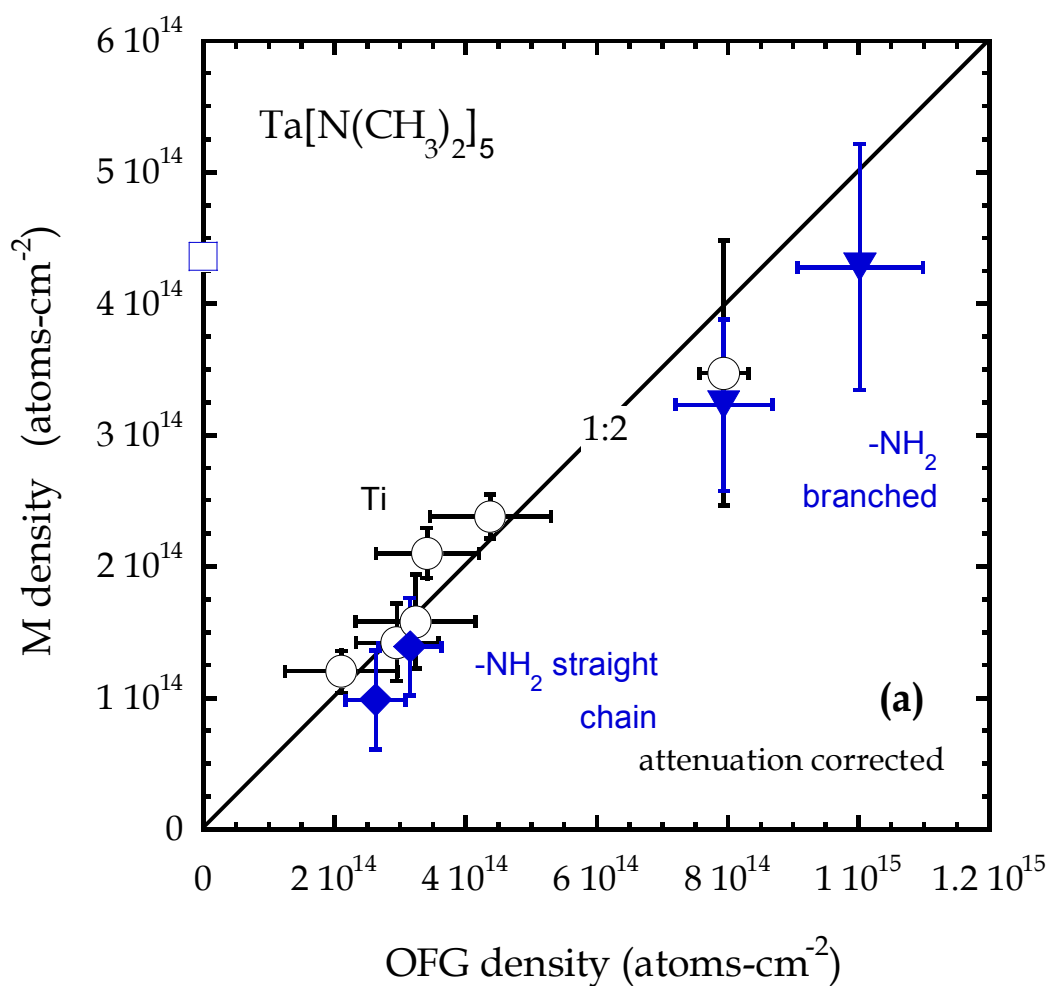


**Figure 3-13(a):** The density of Ta atoms produced by saturation exposures to Ta[N(CH<sub>3</sub>)<sub>2</sub>]<sub>5</sub> (T<sub>s</sub> = 25 °C) as a function of OFG density, as deduced from XPS, for two generations of PAMAM dendrons, and both the 3C and 12C anchors. For the Gen-1 dendrons both terminal amine, -NH<sub>2</sub>, and the backbone amide group, -C(=O)NH-, contribute to the OFG density. For comparison, the results shown in Fig. 3-12 for Ti[N(CH<sub>3</sub>)<sub>2</sub>]<sub>4</sub> on reactive IOLs are reproduced here also.

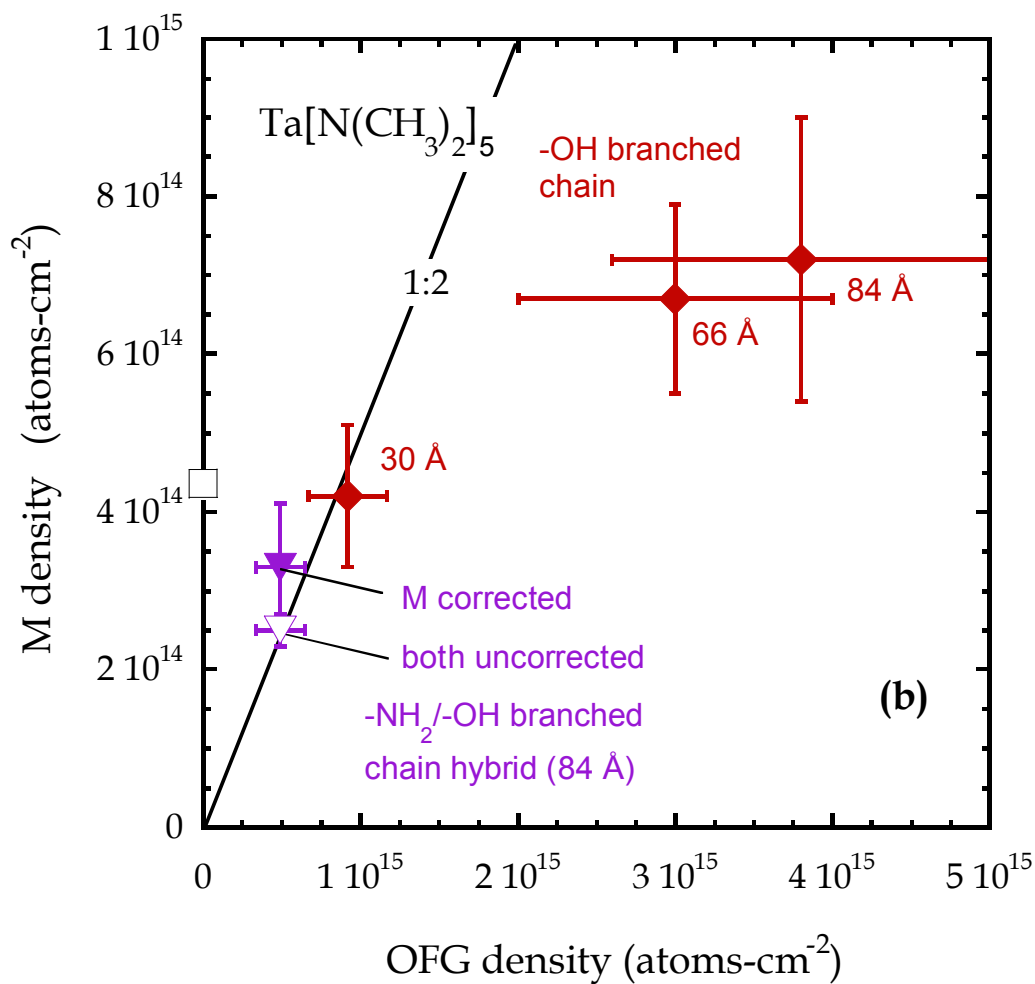


**Figure 3-13(b):** The density of Ta atoms produced by saturation exposures to Ta[N(CH<sub>3</sub>)<sub>2</sub>]<sub>5</sub> ( $T_s = 25\text{ }^{\circ}\text{C}$ ) as a function of OFG density. The IOLs here are three thicknesses of poly-G, and one layer of poly-G that has been modified by a -NH<sub>2</sub> terminated SAM. In all cases, the Ta or Ti density has been corrected for attenuation effects.

Thus, for both the Ti and Ta complexes, reactions on IOLs that are mostly two-dimensional in the configuration of their OFGs (only the Gen-1 dendrons have some 3-d character), the prevailing stoichiometry is a 1:2 M:OFG ratio for adsorption at room temperature. To further specify the nature of this interaction, the number of ligands lost upon chemisorption must be determined

Fig. 3-13(b) shows a plot the results for Ta[N(CH<sub>3</sub>)<sub>2</sub>]<sub>5</sub> reacting with poly-G, where there is a definitive 3-d character to the configuration of the -OH groups [87]. For the thinnest poly-G layer, we see that there are approximately 2 -OH groups (available to react) per chemisorbed Ta complex, consistent with the trend discussed above. For the thicker films, the implied Ta:OFG ratio is much smaller, and there are ~ 4.5 and 5.3 -OH groups (available to react) per Ta complex for poly-G films of 66 and 84 Å in thickness. These results suggest that ligand exchange could be extensive for adsorption on the thicker layers. Indeed, this inspired an additional set of experiments, to be discussed in the following subsection. Fig. 3-13(b) also displays the result from a “hybrid” organic layer. This layer was formed by first growing a 84 Å thick poly-G film, and then exposing it to the molecule used to form the Gen-0-3C layer, 3-aminopropyldimethylethoxysilane, CH<sub>3</sub>CH<sub>2</sub>O-Si-(CH<sub>3</sub>)<sub>2</sub>(CH<sub>2</sub>)<sub>3</sub>-NH<sub>2</sub>. Here one anticipates reaction between the ethoxy group and the -OH in the poly-G layer, forming new -NH<sub>2</sub> terminations. Fig. 3-13(b) shows the density of -NH<sub>2</sub> formed in this conversion, calculated from XPS, but uncorrected for attenuation effects. Ignored for the moment are unreacted -OH sites in the poly-G layer. Note that the density of -NH<sub>2</sub> formed in this case ( $\sim 4.9 \times 10^{14}$  molec-cm<sup>-2</sup>) was larger than that formed by reaction of this same molecule on chemical oxide ( $\sim 3.2 \times 10^{14}$  molec-cm<sup>-2</sup>). The uncorrected

density of Ta formed by a saturation exposure was found to be  $\sim 2.5 \times 10^{14}$  molec-cm<sup>-2</sup>. As ARXPS was performed on the reacted adlayer ( $d_{ML}/\lambda \sim 0.2$ ), a corrected value for the Ta density of  $3.3 \times 10^{14}$  molec-cm<sup>-2</sup> could be cited. However, concerning the Ta:OFG ratio it is probably better to consider the two uncorrected values, as they may be equally affected by attenuation effects. Doing so results in a Ta:OFG ratio of 1:2, again fitting into the trend identified for a number of the systems considered here.

#### **3.3.2.4.2 Stoichiometry of the chemisorbed species in the saturated adlayers**

A final issue to be considered in this subsection concerns the amount of ligand exchange that occurs when the Ti and Ta complexes react with these interfacial organic layers. The atomic N:metal ratio of the saturated adlayer can be calculated using the N(1s) and either the Ti(2p) or one of many Ta [Ta(4p), Ta(4d), Ta(4f)] photoelectron intensities, and applying corrections related to the photoemission cross-sections and analyzer transmission. One anticipates that attenuation effects may be quite similar for N and M (Ti or Ta), as N remaining in the film is still likely bound to the metal center. In the case of layers consisting of chemical oxide, and only C, H and O are in their backbones and terminal groups, the only N in the film comes from the metal complex. In these cases the N:metal ratio is a direct indicator of the number of ligands retained by the metal complex on chemisorption. In cases where N exists in the IOL, their presence must be accounted for to accurately estimate the amount of ligand exchange occurring.

We first consider results for the chemisorption of  $\text{Ti}[\text{N}(\text{CH}_3)_2]_4$  on simple straight chain alkyl SAMs, for a series of substrate temperatures. Fig. 3-14 shows a plot the number of ligands retained as a function of substrate temperature, for adsorption on chemical oxide and the SAMs with  $-\text{CH}_3$ ,  $-\text{OH}$  and  $-\text{NH}_2$  termination. Except for one case (chemical oxide,  $T_s = 30$  to  $110^\circ\text{C}$ ), in all cases the number of ligands retained is a decreasing function of  $T_s$ , indicating ligand loss is thermally activated. For either  $-\text{OH}$  or  $-\text{NH}_2$  termination, reaction of the Ti complex with 2 functional groups will release 2  $\text{HN}(\text{CH}_3)_2$  as products, and form 2 linkages with the alkyl SAM tail groups (scheme 1a). This seems to be the case for adsorption at  $T_s = -50^\circ\text{C}$ . The slightly higher value on the  $-\text{CH}_3$  SAM could reflect steric crowding at the SAM/ $\text{SiO}_2$  interface. At room temperature and above, on average  $\sim 1.2$ - $1.8$  ligands are retained on all surfaces, except the data point for the  $-\text{NH}_2$  SAM at  $T_s = 110^\circ\text{C}$  where on average only 0.4 are retained. For reaction with 2  $-\text{NH}_2$  groups, sufficient hydrogen exists to remove 3 or even 4 ligands via the formation of imine linkages (scheme 1b). The loss of 3 ligands via reaction with 2  $-\text{OH}$  groups is problematic, as sufficient hydrogen does not exist to produce 3  $\text{HN}(\text{CH}_3)_2$  molecules. In these cases, formation of a metallacycle, specifically an azametallacyclopropane (scheme 1c) is possible [143]. Finally, reaction between adjacent Ti complexes may also be in play, where a Ti center might react with a neighboring ligand, liberating an H atom and forming a  $\text{Ti}-(\text{CH}_2)\text{-N}$  linkage, similar to metallacycle formation.

Next to be considered is the adsorption of  $\text{Ta}[\text{N}(\text{CH}_3)_2]_5$  on the  $-\text{NH}_2$  terminated anchor and Gen-1 layers. First, on the short Gen-0-3C anchor that each Ta center retains an estimated  $\sim 3.1$  ligands.

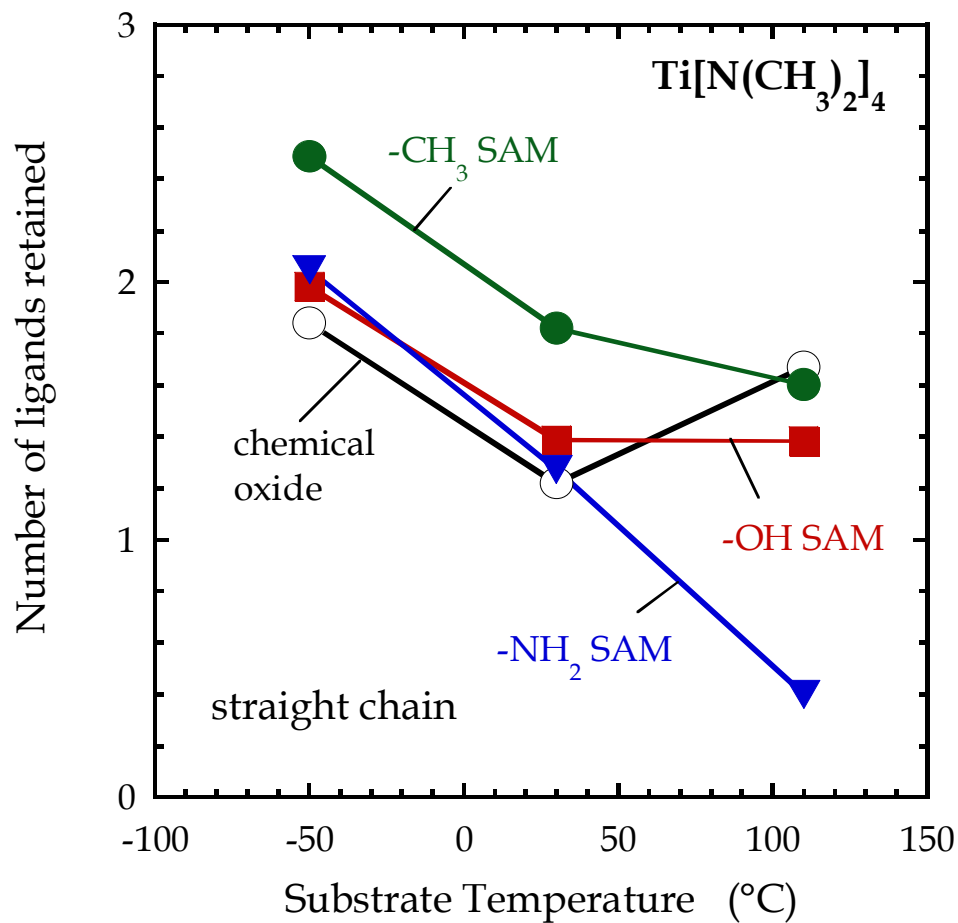
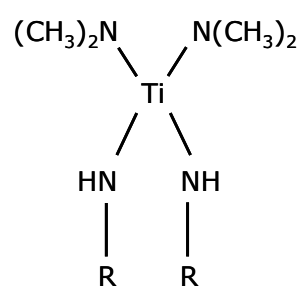
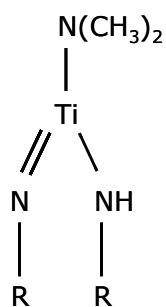


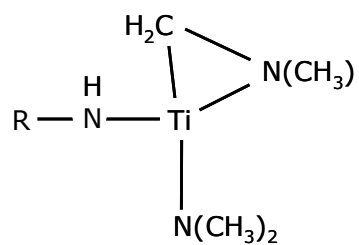
**Figure 3-14:** Number of  $-\text{N}(\text{CH}_3)_2$  ligands retained by  $\text{Ti}[\text{N}(\text{CH}_3)_2]_4$  after chemisorption on three straight-chain SAMs (terminated by  $-\text{CH}_3$ ,  $-\text{OH}$ , and  $-\text{NH}_2$ ) and bare chemical oxide, as a function of substrate temperature.



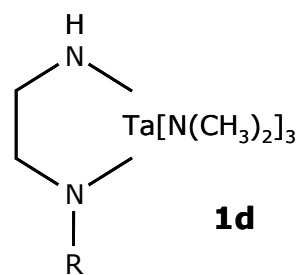
**1a**



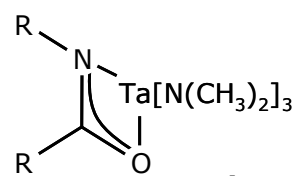
**1b**



**1c**



**1d**



**1e**

**Scheme 3-1:** Possible structures formed by the reaction of transition metal coordination complexes  $\text{Ti}[\text{N}(\text{CH}_3)_2]_4$  and  $\text{Ta}[\text{N}(\text{CH}_3)_2]_5$  with amine-functional organic layers.



Reaction in this case could be equivalent to that shown for Ti in scheme 1a, where the Ta complex would form 2 Ta-NH-R linkages. On this short anchor reaction with interfacial -OH might also occur, forming Ta-O-Si linkages. On the longer anchor, Gen-0-12C, ligand loss is more significant and on average 1.1 ligands are retained, suggesting imine formation (2 linkages), and retaining a single  $\text{N}(\text{CH}_3)_2$  ligand. On the Gen-1 layers significant loss of ligand is implicated: on average only 0.3 (Gen-1-3C) and 1.4 (Gen-1-12C) ligands are retained by the Ta center. For the Gen-1 layers, about 1 branch (comprising one amine and one amide group) is available per Ta complex to react. In terms of moieties that may form with a single branch, two examples are given in scheme 1d and 1e, and both of these lead to the loss of 2 ligands. In order to lose additional ligands the terminal  $-\text{NH}_2$  groups could form imine linkages, or schemes 1d and 1e may combine with -OH groups at the SAM/ $\text{SiO}_2$  interface (more likely for the short anchor, Gen-1-3C), or with functional groups on other branches to produce additional loss of ligand. It is also conceivable that metallacycles could form. The situation is certainly complex, and a number of additional reactions may occur under the actual growth conditions of ALD (*vide infra*) that are not considered in Scheme 1.

The reaction of  $\text{Ta}[\text{N}(\text{CH}_3)_2]_5$  with poly-G, and poly-G modified with the aminoalkoxysilane presents an interesting example of the effect of the IOL on the adlayer stoichiometry. For pure poly-G films, the number of  $-\text{N}(\text{CH}_3)_2$  ligands retained by  $\text{Ta}[\text{N}(\text{CH}_3)_2]_5$  can be calculated unambiguously from the measured N:Ta ratio. Spectra from the N(1s) and Ta(4p<sub>3/2</sub>) regions for saturated layers of  $\text{Ta}[\text{N}(\text{CH}_3)_2]_5$  on chemical oxide, 30 Å poly-G, 84 Å poly-G, and 84 Å poly-G modified by the Gen-0-3C -NH<sub>2</sub> terminated SAM are shown in Fig. 3-15.

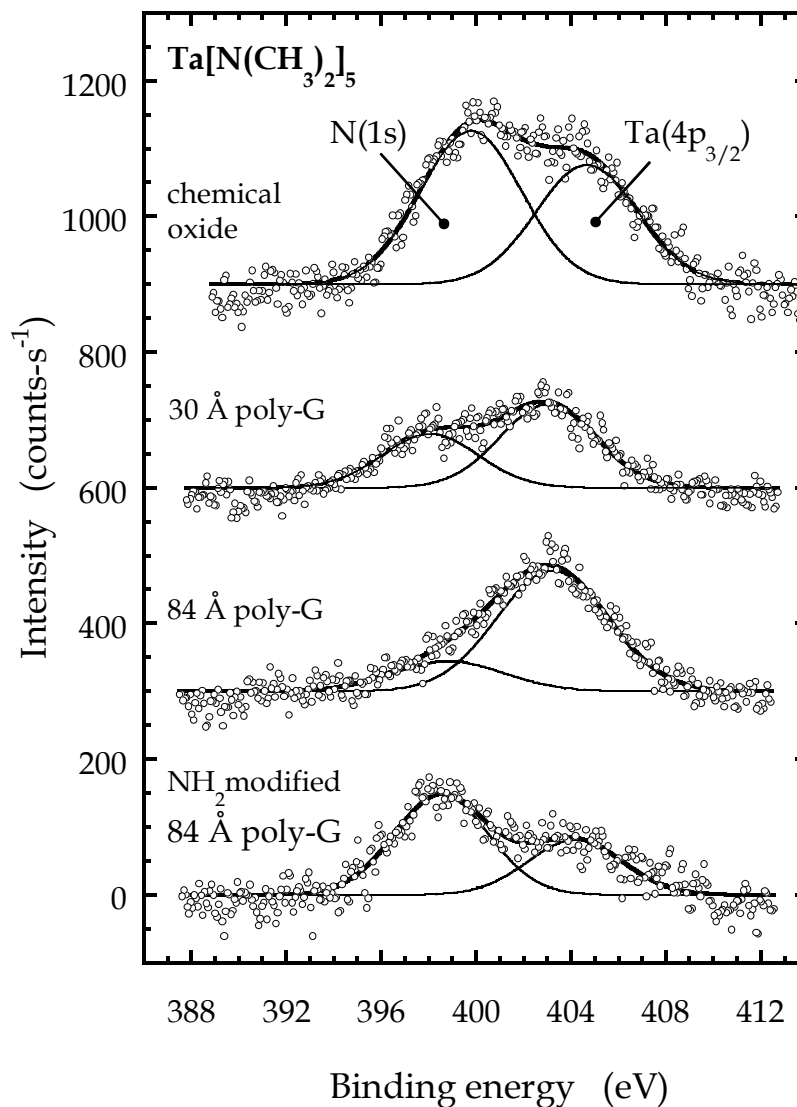


**Figure 3-15:** XP spectra of saturated layers of  $\text{Ta}[\text{N}(\text{CH}_3)_2]_5$  for the N(1s) and Ta(4p<sub>3/2</sub>) regions. The substrates include, top to bottom, bare chemical oxide, two thicknesses (30 and 84 Å) of poly-G, and an 84 Å poly-G film modified by a -NH<sub>2</sub> terminated SAM prior to exposure to  $\text{Ta}[\text{N}(\text{CH}_3)_2]_5$ . The spectra have been shifted along the ordinate to facilitate the presentation.

Focusing on the first 3 of these, we see by inspection that the Ta complex retains the most number of ligands on chemical oxide, followed by the thinner poly-G layer, and finally the thicker poly-G layer. Making appropriate accounting for the photoelectron cross-sections for the N(1s) and Ta(4p<sub>3/2</sub>) peaks, on average  $2.9 \pm 0.3$ ,  $1.4 \pm 0.3$ , and  $0.6 \pm 0.2$  N(CH<sub>3</sub>)<sub>2</sub> ligands are retained by Ta[N(CH<sub>3</sub>)<sub>2</sub>]<sub>5</sub> on these 3 surfaces. In regard to the result on chemical oxide, although the density of -OH sites is high on this surface, the sites are confined to a 2-d plane, which is nearly atomically flat. Thus, there may be steric limitations in terms of ligand exchange reactions, and at room temperature they appear to be limited to 2. What may lead to higher loss of ligand on poly-G films? One obvious factor is the distributed 3-d nature of the -OH sites in poly-G, as well as the fact that they are attached to a relatively flexible backbone. Thus, on the thicker poly-G film, the terminal -OH can probably virtually surround the Ta complex, stripping it almost entirely of ligands. Referring back to the estimates for the Ta:OFG ratio [*cf.* Fig. 3-13(b)] values of 1:2.2 (30 Å) and 1:5.3 (84 Å) were found. Thus, there is sufficient density of -OH on the thicker layer to facilitate almost complete ligand removal.

Moving on to the result for Ta[N(CH<sub>3</sub>)<sub>2</sub>]<sub>5</sub> on the poly-G layer modified by the -NH<sub>2</sub> terminated SAM, its effect is quite spectacular. The N:Ta ratio on this layer is 4.0. Using the densities uncorrected for attenuation, a Ta:OFG ratio of 1:1.96 is calculated for this case. Thus, it appears the Ta complex retains on average 2 ligands, and loses 3, upon reacting with this modified layer. If the reaction in this case were limited to the -NH<sub>2</sub> groups, this implies either imine or metallacycle formation. Perhaps equally as likely, however, is participation of -OH that has not reacted with

the aminoalkoxysilane. In any event, the modification of the poly-G has made the layer much less aggressive in terms of ligand removal, and  $\sim 1.4$  more ligands are retained. The fact that the modification reduces the total amount of  $\text{Ta}[\text{N}(\text{CH}_3)_2]_5$  chemisorbed and its depth of penetration ( $d_{\text{ML}}/\lambda \sim 0.2$  with  $-\text{NH}_2$  modification,  $d_{\text{ML}}/\lambda \sim 0.31$  without), while decreasing the number of ligands lost, suggests that modification may not only change the chemistry of the topmost layers, but also increases the density, retarding diffusion to lower layers where additional  $-\text{OH}$  sites are present.

Examining the reactions of  $\text{Ti}[\text{N}(\text{CH}_3)_2]_4$  for the 9 chemically distinct systems reviewed here, no obvious trends of ligands retained/lost with OFG identity, density or dimensionality could be established. In 8 of the 9 systems, the Ti center retained an average of 1.47 ligands for adsorption at room temperature, spanning a range of 1.19-1.95. The most noticeable effect of OFG identity concerning the Ti complex is probably the results for  $T_s = 110^\circ\text{C}$  (*cf.* Fig. 3-14), where the  $-\text{NH}_2$  terminated SAM is the outlier, retaining one less ligand on average vs. chemical oxide, and the  $-\text{OH}$  and  $-\text{CH}_3$  terminated SAMs. These differences are not seen at room temperature, where the number of ligands retained is  $\sim 1.5$  for both  $-\text{NH}_2$  and  $-\text{OH}$  terminated layers.

For the reaction of  $\text{Ta}[\text{N}(\text{CH}_3)_2]_5$  the results for the number of ligands retained is also not particularly clear for the 8 chemically distinct systems reviewed here. On the straight-chain and branched  $-\text{NH}_2$  terminated layers, the number of ligands retained spans a large range, from 0.3-3.1. Note, however, that this upper limit value of 3.1 is for reaction on Gen-0-3C, where for the Ti complex, reaction with the underlying chemical oxide at the SAM/ $\text{SiO}_2$  interface was implicated. Participation of the underlying substrate is also suggested here for Ta, as the number of ligands

retained on chemical oxide is  $\sim 2.9$ . The value for the poly-G layer modified with the aminoalkoxysilane, namely 2.0, also lies within the aforementioned range, but is above the range of 0.3-1.4, which one obtains if the Gen-0-3C results are excluded. One could conclude from these results that ligand loss is minimized on surfaces possessing a mostly 2-d configuration of -OH sites. This idea is supported when considering the reaction of the Ta complex on the unmodified poly-G layers. Here the thickest, most 3-d in character poly-G layer retained the least number of ligands (0.6), chemical oxide the most (2.9), with the thinner poly-G layer retaining an intermediate amount (1.4). This observation highlights the importance of both density and dimensionality, as the thick poly-G layer could almost entirely strip the Ta complex of its ligands.

### **3.3.3. Atomic layer deposition on organic layers**

As discussed in Chapter 1, much still remains to be learned concerning the initial stage of nucleation in ALD. As ALD involves sequential, self-limiting chemical reactions, one can expect that the chemistry and microstructure of the surface will have a strong effect on the early stages of film growth. Thus, the observations made in Sec. 3.3.2 will hopefully prove to be useful in building an understanding of the first few cycles of ALD. An important concern here is the effect of substrate temperature. Although ALD is typically a lower temperature process than CVD, the IOLs utilized here may be affected by thermal degradation, prior to deposition and/or during growth, as reviewed above in Sec. 3.3.1.3. The importance of the survival of the organic layer

is dependent upon the application. Where the organic layer is present only to promote nucleation and growth, degradation prior to growth, e.g., due to substrate heating, would likely not be desired as it could affect the density and/or configuration of OFGs present in the IOL. These issues should be kept in mind when drawing comparisons between growth via ALD and the observations made concerning the initial chemisorption regime discussed above in Sec. 3.3.2.

### 3.3.3.1. Experimental approach

ALD is conventionally carried out in low-pressure systems, where the flow is typically viscous and laminar and the operating total pressure is on the order of 1 Torr. The experiments to be described below take an alternative approach, making use of the custom-designed UHV system discussed in Sec. 2.5 [142], which is better suited to an examination of the ALD process, as opposed to the high throughput formation of “device quality” thin films. In this approach, although there is no upper limit on *exposure* (product of pressure  $\times$  time), there is a *pressure* limit (the highest pressure used in these experiments is  $\sim 10^{-4}$  Torr). For the systems examined, this might prove to be an issue for the  $\text{NH}_3$  exposure step, as there is evidence for a catalytic effect of  $\text{NH}_3$  on transamination ligand exchange reactions [85]. If this does occur, then the extent of the completion of ligand exchange reactions occurring in the  $\text{NH}_3$  exposure cycle may be reduced at the reduced pressure employed in this process. One may expect this to mostly effect the composition of the growing thin film.

Besides enabling the use of a variety of *in situ* analytical probes, working in UHV offers a number of additional benefits. First, the IOLs are brought to reaction temperature in UHV, minimizing potential degradation associated with background gases present in more conventional ALD systems. Second, in our system the transition metal complex is introduced via a well-collimated supersonic molecular beam, which permits one to use stepwise substrate translation (perpendicular to the supersonic beam) to vary exposures spatially on a *single* substrate [142]. A typical experiment produces a terraced thin film where each terrace represents a different experiment, e.g., differing by total number of ALD cycles, or exposure per cycle to the transition metal complex [104]. Given sufficient spatial resolution, each terrace can be analyzed *ex situ* separately, which provides a series of “snapshots” of the ALD process, improving experimental throughput and run-to-run reproducibility.

As shown in Sec. 3.3.2, the chemical functionality and molecular structure of the IOL has strong effects on the chemisorption of the transition metal complex. As this is in essence the first half cycle of ALD (possibly conducted at a lower temperature than actual ALD) one expects that the IOL will affect the nucleation and early stages of growth of ALD. To examine these effects, the focus will be on the use of characterization techniques that can provide information on the *kinetics of growth* and the *morphological evolution* of the inorganic film. Concerning the kinetics of growth, one key measure will be the thickness of the film as a function of the number of cycles of ALD. A variety of techniques are available for measuring film thickness, including direct imaging (SEM, TEM, STEM), and quicker, though more indirect techniques which may be used *in situ* or *ex situ*. The latter set includes ellipsometry,

interferometry, x-ray photoelectron attenuation, mass change measured by quartz crystal microbalance, and several others. The results reviewed here will rely on thickness measurements using ellipsometry, with a subset of these measured also using Rutherford backscattering spectroscopy (RBS) and cross-sectional STEM. Concerning film morphology, AFM provides quick, direct, and quantifiable information, and therefore will be central to the results presented here. With regard to the chemical composition of the thin films, EELS spectra taken in combination with STEM have been used to calculate relative atomic abundances. XPS has also been conducted on selected films. Both techniques were conducted *ex situ*, so caution must be used in interpreting these results as the films may have reacted with air and therefore may be significantly oxidized, and/or possibly contaminated by volatile organic carbon-containing species.

### **3.3.3.2. Effects of interfacial organic layers on thin film growth via ALD**

#### **3.3.3.2.1. Kinetics of nucleation and growth**

The kinetics of nucleation and growth in ALD is a bit of a misnomer, as the technique involves repetitive gas-surface reactions that reach saturation. Thus, although the kinetics embodied in coverage-exposure relationships, considered above in Sec. 3.3.2.2, establish the self-limiting nature of the half-reactions, the “kinetics” of the thickness ( $D$ ) vs. number of cycles ( $n$ ) relationship is mostly connected to the density of active sites present at the beginning of each cycle, steric interactions



between adsorbed species, and ligand stability. At saturation, for example, the density of accessible active sites is zero. Concerning nucleation, on surfaces where the density of active sites is less than the number of active sites achieved for steady state film growth, there is a transition region, often called an “incubation period.” In this region, the film thickness deposited per cycle ( $dD/dn$ ) increases from each cycle to the next as the original surface is transformed into one representing the steady-state growing film [144,145]. Interfacial organic layers can obviously be used to modify the density of active sites, and perhaps the tendency of the surface to engage in a variable number of reactions with the transition metal complex. Therefore, one expects the IOLs will have a large effect on  $dD/dn|_{n \rightarrow 0}$ . We will see that, in addition to the saturation density of precursor on the surface, the initial rate of growth is also sensitive to the spatial extent of chemisorption and the structure of the chemisorbed precursor.

To provide a baseline, the growth of  $\text{TiN}_x$  on chemical oxide using  $\text{Ti}[\text{N}(\text{CH}_3)_2]_4$  and  $\text{NH}_3$  as co-reactants is considered first. As discussed above,  $\text{Ti}[\text{N}(\text{CH}_3)_2]_4$  is delivered via a supersonic molecular beam, while  $\text{NH}_3$  is introduced via a glass capillary array effusive doser. Note that, for a number of ALD chemistries, the chemical oxide surface provides a substrate on which growth is initiated immediately and there is no detectable incubation period due to a high density of  $-\text{OH}(a)$ . The deposited thickness ( $D$ ) as a function of the exposure ( $\varepsilon$ ) to the Ti complex for growth on chemical oxide displays the signature of a saturated half cycle, where growth saturates at  $\sim 2 \text{ \AA-cycle}^{-1}$  [103]. In comparison, using a viscous flow reactor, and depending on dose times, values of  $\sim 0.9\text{-}3.0 \text{ \AA-cycle}^{-1}$  have been reported for this same process at  $180^\circ\text{C}$  [91]. The variation in  $dD/dn$  with substrate temperature has

also been measured, and used to define the so-called ALD “window,” where the deposited thickness per cycle shows only a weak or no dependence on substrate temperature. For the  $\text{TiN}_x$  ALD process reported here, the window appears at  $\sim 167$ - $207^\circ\text{C}$  [104].

Before moving on to results for ALD on the IOLs, note that  $dD/dn$  vs.  $\epsilon$  data can be used to estimate an *incorporation coefficient* for the transition metal complexes reacting with the growing surface at the beginning of the metal half cycle. For  $\text{TiN}_x$  it is  $\sim 0.07$  at  $T_s = 167$  and  $207^\circ\text{C}$  for growth initiated on chemical oxide. In comparison, the densities found from RBS are used, the implied coefficient is  $\sim 0.036$ . Perhaps the best comparison to make to these data is not the data discussed above in Sec. 3.3.2., as these were for reaction on pristine chemical oxide at  $T_s \leq 110^\circ\text{C}$ , but results from molecular beam scattering measurements at temperatures where steady-state decomposition is observed. At  $T_s = 271^\circ\text{C}$  the steady-state incorporation probability was  $\sim 0.1$  for  $\text{Ti}[\text{N}(\text{CH}_3)_2]_4$  reacting on the surface formed from its decomposition [89]. This value is close to that estimated here within the ALD window, but somewhat larger. A larger value could represent the fact that outside the ALD window at higher temperature the coverage of ligands is reduced, and more sites are active to react with the Ti complex.

We now move to a discussion of the results concerning ALD growth on IOLs, one of the core topics of this review. First, as shown elsewhere [104], saturation behavior for growth on IOLs is similar to the behavior on chemical oxide. One of the most interesting sets of data to consider when comparing growth on different surfaces is the  $D$  vs.  $n$  relationship. Fig. 3-16(a) shows ellipsometric thicknesses for the ALD of

TiN<sub>x</sub> on chemical oxide and two unreactive -CH<sub>3</sub> terminated IOLs (a C<sub>18</sub>, and a C<sub>30</sub> straight chain SAM). Results for two substrate temperatures are displayed, representing the lower (167 °C) and upper (207 °C) bounds of the ALD window observed on chemical oxide. The *D* vs. *n* relationship on chemical oxide is linear, as would be expected for ideal ALD growth. As can be seen, for these unreactive SAMs, film growth is significantly attenuated. This is expected, since ARXPS indicated that this type of chemical termination leads to chemisorption only at the SAM/SiO<sub>2</sub> interface. With the SAM present, accessibility to -OH groups will be limited, and there will be fewer of them, as many make linkages to the SAM Si headgroup. The ability of unreactive straight-chain SAMs to suppress ALD growth has also been observed in work by others using flow type ALD systems [65-73]. Take note of the fact that the longer SAM (TTS) suppresses growth more significantly.

Regarding the effect of substrate temperature, we see that, although the *D* vs. *n* on SiO<sub>2</sub> is very similar at both 167 and 207 °C, this is not the case for at least one of the SAMs. For the C<sub>18</sub> SAM, there is a sharp increase in the slope of the relationship at *n* ~ 200 cycles. Note that similar behavior (an abrupt change in the slope, *dD/dn*) is observed for a much shorter IOL, hexamethyldisilazane (HMDS), which produces a monolayer of -Si(CH<sub>3</sub>)<sub>3</sub> species [104]. The approximate slope between 200 and 300 cycles on the C<sub>18</sub> SAM is close to that observed on bare chemical oxide. This behavior seems to indicate a sudden change in the composition/structure of the topmost layers that result in an increase in the number of available reaction sites.

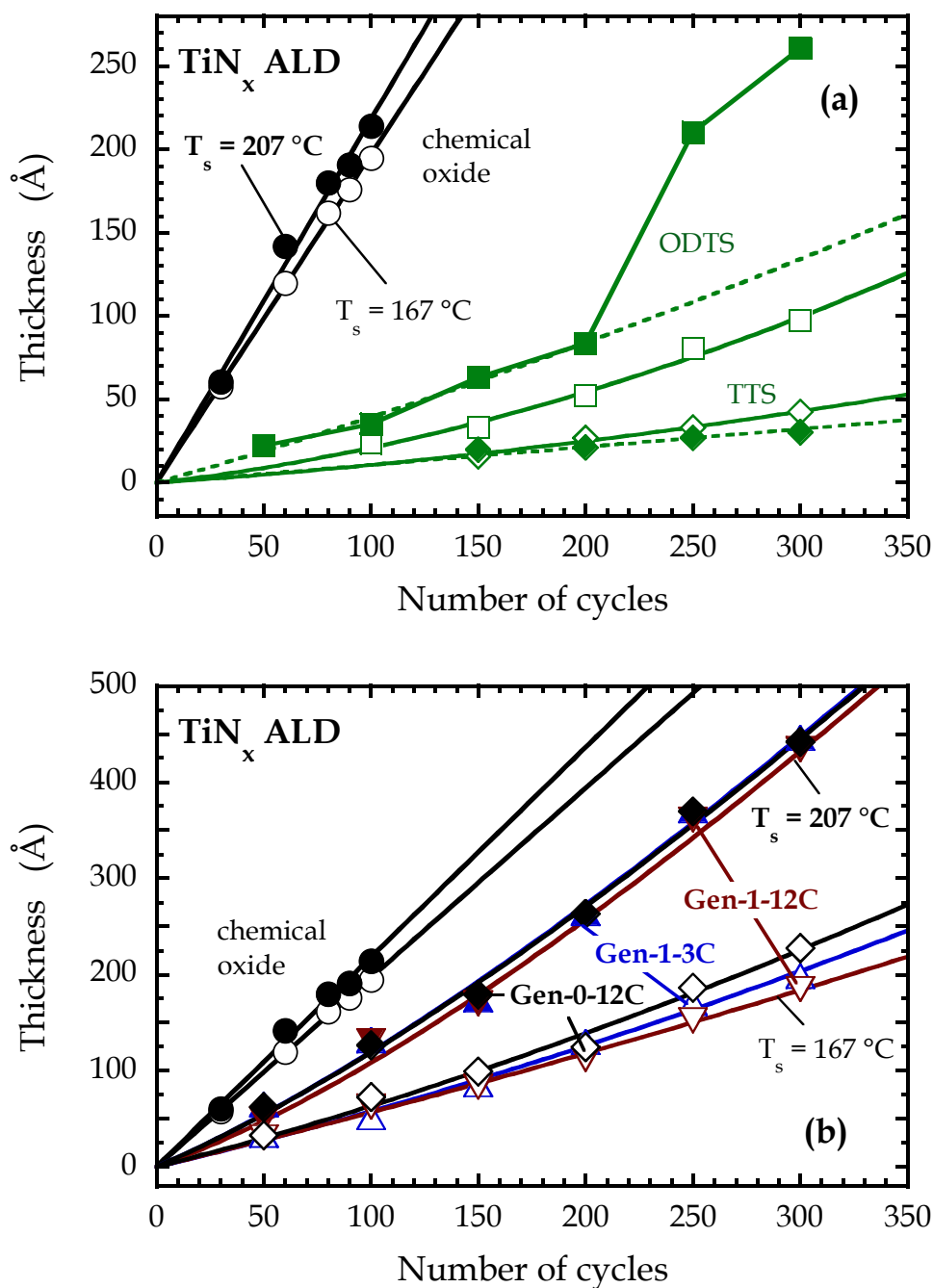


**Figure 3-16:**  $\text{TiN}_x$  film thickness (from ellipsometry) as a function of the number of ALD cycles at  $T_s = 167^\circ\text{C}$  (empty symbols) and  $207^\circ\text{C}$  (filled). The solid lines correspond to fits to the data using Eq. 3-1. Results are shown for growth (a) on chemical oxide and two unreactive SAMs (ODTS and TTS); and (b) on chemical oxide and three reactive  $-\text{NH}_2$  terminated, straight-chain and branched IOLs.

For the longer C<sub>30</sub> SAM, in contrast, there are negligible differences between growth at the two substrate temperatures, and the attenuation of growth is maintained over the entire temperature window. Taken in hand with the results on HMDS not reproduced here, it seems that for the unreactive SAMs the thickness of the layer plays an important role in attenuating growth.

In Fig. 3-16(b) sets of  $D$  vs.  $n$  data similar to those shown in (a) for growth on three IOLs possessing reactive endgroups are considered, namely the two first generation -NH<sub>2</sub> terminated dendrons considered above in Sec. 3.3.1.3, and one of the -NH<sub>2</sub> terminated anchors. Note the scale on the ordinate in (b) is about twice that in (a). A number of observations can be made from these results. First, there are minimal differences in growth between that on the Gen-1-3C vs. the Gen-1-12C layer, at both substrate temperatures. Recall that these two layers have the same functional endgroup(s), and only differ in the length of their -CH<sub>2</sub>- backbones (3 or 12). The fact that the growth is essentially identical for the two cases would indicate that the ALD film nucleates at the IOL/vacuum interface, thus it is insensitive to the length of the anchor backbone. In addition, the results for the C<sub>12</sub> straight chain anchor, Gen-0-12C, is essentially indistinguishable from the Gen-1 layers. This is somewhat unexpected, given the fact that the saturation density of Ta[N(CH<sub>3</sub>)<sub>2</sub>]<sub>5</sub>, representative of the first half cycle of ALD, is significantly higher for the branched layers for adsorption at room temperature as shown above in Sec. 3.3.2.2.2. However, all three IOLs possess reactive terminal groups, which would appear to be essential to explain this behavior.

As may be seen in Fig. 3-16(b), on these reactive IOLs the thickness deposited at 207 °C is approximately double that observed at 167 °C. All three IOLs exhibit

essentially identical behavior, and we see that the growth rate at 207 °C above ~ 200 cycles is approximately that observed on bare chemical oxide. This was not the case for growth at the lower substrate temperature where the attenuation of growth is still apparent at 300 cycles. From these observations it can be concluded that there is still some “memory” of the starting surface for growth at 167 °C. It has been speculated elsewhere [104] that this could involve partial degradation of the IOL, where fragments are bound to the growing surface, occupying sites and suppressing growth.

In Fig. 3-17, growth on four IOLs possessing -OH groups, including three poly-G films of different thickness is considered. First the results on the straight chain -OH terminated SAM are quite similar to those on the reactive -NH<sub>2</sub> terminated layers. Growth on this surface is also faster at the higher substrate temperature (207 °C), and approaches the  $dD/dn$  value on chemical oxide after about 200 cycles. Thus, it seems surfaces possessing reactive endgroups arranged mostly in a 2-d array give similar results. For poly-G, however, the thickness of the layer has a large effect. This is quite unlike the behavior of TiN<sub>x</sub> growth on the dendrons [*cf.* Fig. 3-16(b)], where growth was nearly indistinguishable on the 3 layers representing different thicknesses and degrees of branching. For the 2 thickest layers of poly-G (47 and 84 Å), growth is significantly attenuated. Indeed,  $D$  vs.  $n$  on these layers is similar growth on TTS, the unreactive -CH<sub>3</sub> terminated C<sub>30</sub> SAM (plotted in Fig. 3-17 for comparison). Recall that, for thicker poly-G layers, the saturation density of Ta[N(CH<sub>3</sub>)<sub>2</sub>]<sub>5</sub> increases [*cf.* Fig. 3-7(b)], but the depth of penetration does not [*cf.* Sec. 3.3.2.3]. We must conclude that, for poly-G, the larger saturation density observed in chemisorption does not result in higher  $dD/dn$  in ALD because of the *nature* of the adsorbed species.

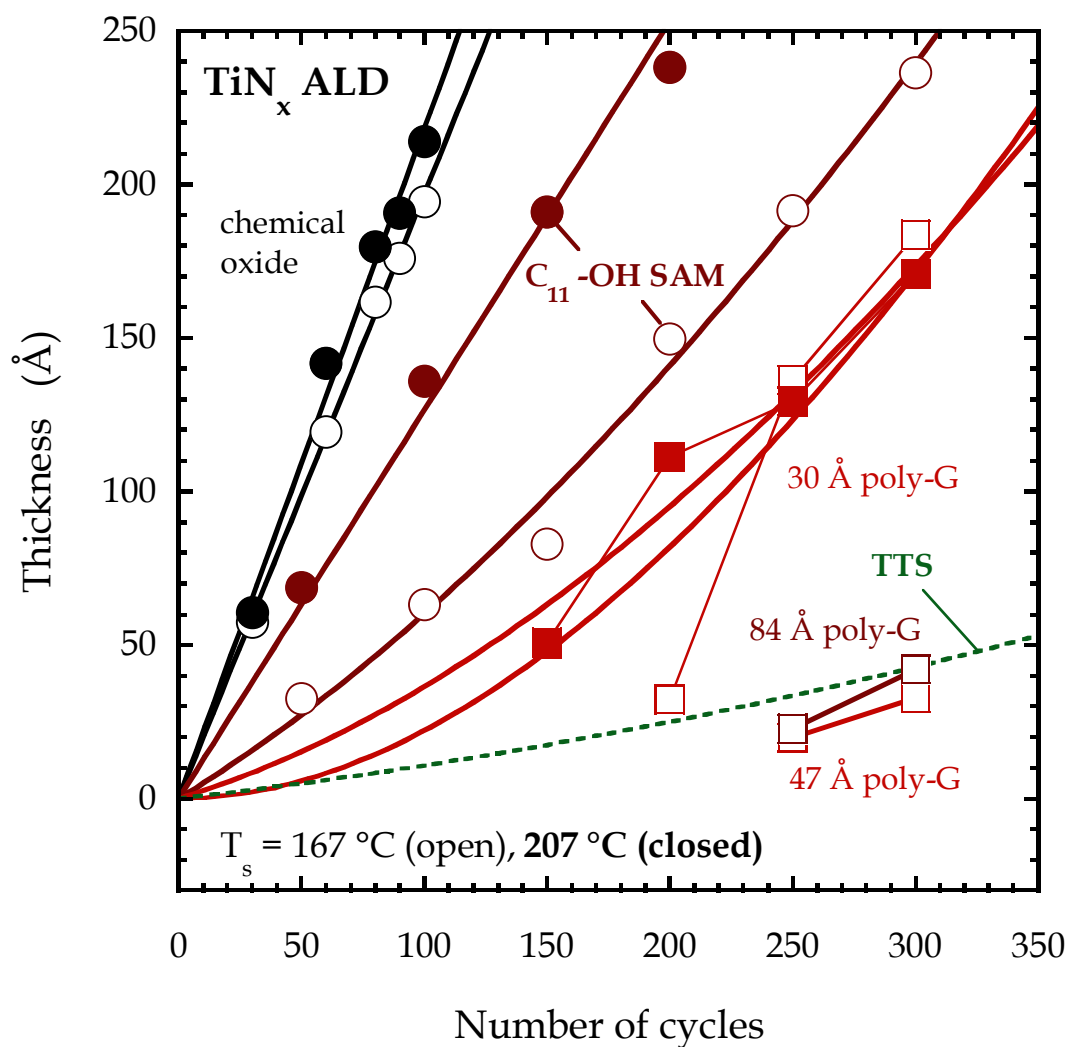


**Figure 3-17:** TiN<sub>x</sub> film thickness (from ellipsometry) as a function of the number of ALD cycles at T<sub>s</sub> = 167 °C (empty symbols) and 207 °C (filled). The solid lines correspond to fits to the data using Eq. 3-1. Results are shown for growth on chemical oxide, a straight chain -OH SAM, and three thicknesses (30, 47 and 84 Å) of poly-G, which also possesses -OH groups. The dashed line shows a fit to the data for TTS, taken from Fig. 3-16.

As described above in Sec. 3.3.2.4.2, for the thickest poly-G layer on average only  $\sim 0.6$  ligands were retained by the Ta center. The Ta-O-R linkages in these species will not react with/be displaced by  $\text{NH}_3$ , certainly for the partial pressures employed in this work. Thus, these Ta centers will essentially be “dead” concerning further growth. The thinnest poly-G layer, however, retains on average 1.4  $-\text{N}(\text{CH}_3)_2$  ligands, which may exchange with  $\text{NH}_3$ . Finally, although growth is faster on the thinnest poly-G layer, it is still significantly less than that achieved on the -OH terminated SAM, suggesting the “memory” of the starting substrate for growth on this poly-G layer may be associated with the spatial distribution of the reactive endgroups in this layer.

In order to quantify the discussion of  $D$  vs.  $n$  results, such as those shown in Fig. 3-16 and 3-17, the following phenomenological model equation can be used:

$$D = D'_{\infty} \{n + m(1 - \alpha)[\exp(-n/m) - 1]\} \quad (3-1)$$

where  $D$  is the film thickness,  $n$  is the number of ALD cycles,  $D'_{\infty}$  is the deposited thickness per cycle as  $n \rightarrow \infty$ , and  $\alpha$  and  $m$  are parameters. This form exhibits the following characteristics:  $D|_{n=0} = 0$ ;  $dD/dn|_{n=0} = \alpha D'_{\infty}$ , and  $dD/dn|_{n \rightarrow \infty} = D'_{\infty}$ , i.e., the initial deposited thickness per cycle is a fraction  $\alpha$  of the asymptotic value ( $D'_{\infty}$ ), but approaches it with an exponential decay constant of  $m$  cycles. In this model there is no “incubation” time, where the growth is identically zero, and the functional form is essentially that given previously [103,146]. In Figs. 3-16 and 3-17, the fits to the data given by the smooth solid lines made use of the functional form given by Eq. 3-1,



which in most cases describes the data well. Exceptions are growth on ODTS at  $T_s = 207\text{ }^{\circ}\text{C}$ , and, in general, growth on poly-G.

Fig. 3-18 contains a plot of the attenuation factor  $\alpha$ , where  $\alpha = 1$  represents no attenuation, as a function of the thickness of the IOL at two substrate temperatures: (a)  $167\text{ }^{\circ}\text{C}$ ; (b)  $207\text{ }^{\circ}\text{C}$ . Results are given for both reactive ( $\text{C}_{11}\text{-OH SAM}$ , Gen-0-12C, Gen-1-3C, and Gen-1-12C  $\text{-NH}_2$  terminated IOLs) and unreactive [HMDS, ODTS, TTS, and FOTS,  $\text{CF}_3(\text{CF}_2)_5(\text{CH}_2)_2\text{SiCl}_3$ ] layers. We see that  $\alpha$  depends on the chain length (thickness) of the unreactive IOLs. This observation further bolsters the idea that for these unreactive layers nucleation takes place at the  $\text{SiO}_2/\text{IOL}$  interface involving reaction with residual  $\text{-OH}(a)$ , where the thicker layers are more effective at limiting diffusion of the ALD precursors to this interface. Turning to the results for growth on the reactive layers, we see that there is essentially no dependence of  $\alpha$  on IOL thickness for these four IOLs, which is consistent with the data shown in Figs. 3-16(b) and 3-17 ( $\text{-OH SAM}$  data). This observation supports the conclusion that film nucleation takes place at the IOL/vacuum interface for these reactive layers. Compared to the other IOLs, the data for thin ( $30\text{ \AA}$ ) poly-G is not fit as well by the model, which may indicate more complex nucleation behavior on these surfaces. A fit to the data for the  $30\text{ \AA}$  poly-G layer at  $T_s = 207\text{ }^{\circ}\text{C}$  gives  $\alpha = 0.11 \pm 0.09$ , which, as may be seen, places it close to the line drawn for the *unreactive* IOLs in Fig. 3-18(b). One possible explanation for this could be the 3-d distribution of  $\text{-OH}$  groups in the poly-G layer which, as discussed above in Sec. 3.3.2.3, leads to penetration of the poly-G layers by the metal complex (in that case,  $\text{Ta}[\text{N}(\text{CH}_3)_2]_5$ ) by on average  $\sim 15 \pm 4\text{ \AA}$ .

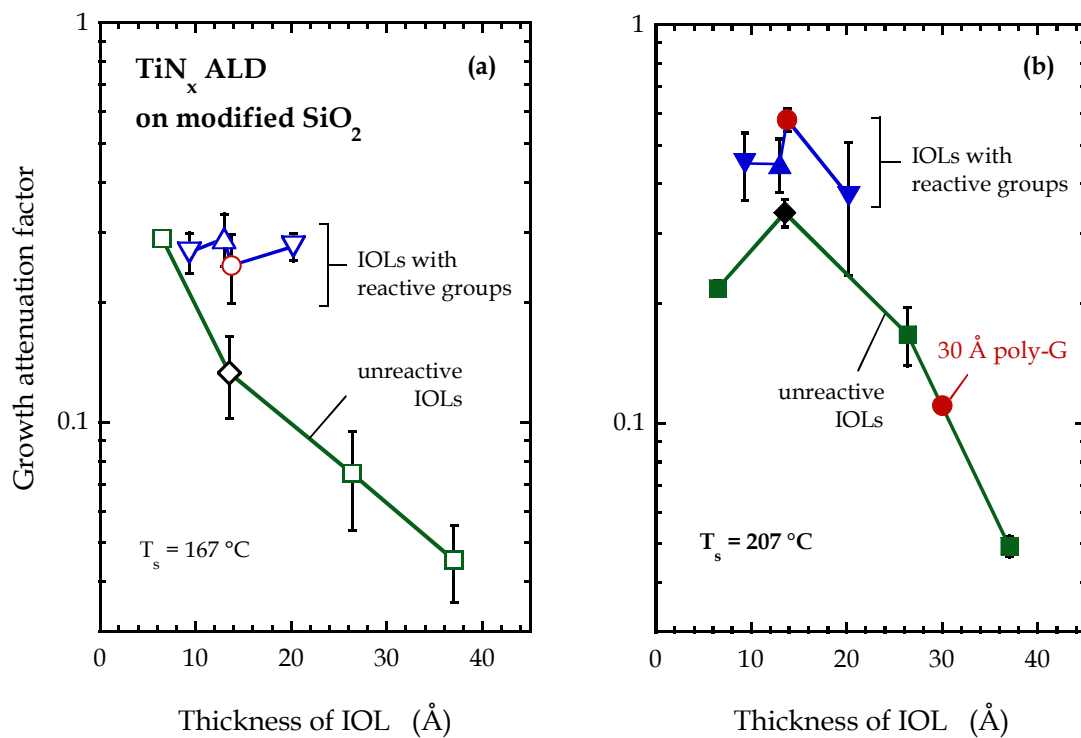


**Figure 3-18:** Growth attenuation factor  $\alpha$  from Eq. 3-1 as a function of IOL thickness. Data is separated into two groups, one for IOLs with reactive terminations (-OH and -NH<sub>2</sub>), and the other for those with both unreactive backbones (-CH<sub>2</sub>-, -CF<sub>2</sub>-) and terminations (-CH<sub>3</sub> and -CF<sub>3</sub>). Results are shown for **(a)** 167 °C and **(b)** 207 °C.

Thus, it seems that both the presence of reactive endgroups *and* their spatial distribution are important concerning the nucleation behavior.

The behavior of the decay constant,  $m$ , is somewhat more difficult to interpret as there is greater uncertainty in determining its value. For example, in many cases the best fit value for  $m$  exceeds (sometimes greatly) the total number of cycles examined (300 in most cases). The data set that gives the best fit to the model (Eq. 3-1) are the results on the -NH<sub>2</sub> terminated IOLs (Gen-0-12C, -1-3C, and -1-12C). At the lowest substrate temperature (167 °C) the values for  $m$  are all quite large, ranging from  $1040 \pm 560$  to  $2900 \pm 2080$ . At the higher substrate temperature (207 °C),  $m$  decreases in all cases, and ranges from  $217 \pm 107$  to  $247 \pm 77$ . As discussed elsewhere [104], such a change in  $m$  with substrate temperature could indicate a thermally activated reaction may be involved in the change of  $dD/dn$  towards its asymptotic value of  $D'_\infty$ . For example, if IOL degradation does occur as a consequence of ALD growth, these fragments may be bound to the growing surface, and their residence time on this surface could determine the time constant of attenuation. Using  $1/m$  as a reaction rate coefficient (and accounting for the total time per cycle) an Arrhenius analysis gives an apparent activation energy of 19 kcal-mol<sup>-1</sup>, with a preexponential factor of  $2 \times 10^4$  s<sup>-1</sup>. Using a more reasonable preexponential factor of  $10^{13}$  s<sup>-1</sup> results in an apparent activation energy of 39 kcal-mol<sup>-1</sup>. Both values are consistent with activation energies for bond breaking. If this analysis is correct, then  $m$  might be decreased by increasing the time per cycle, or the substrate temperature, although the latter might lead to non-self-limiting CVD-like growth.

### 3.3.3.2.2. Morphological evolution of thin film topology

In ideal atomic layer deposition, the film grown will have essentially the same topography as the underlying substrate, due to the high degree of conformality that characterizes ALD. However, not unlike the  $D$  vs.  $n$  relationship, the morphology of a film grown by ALD can be dependent on processes that take place early in growth of the thin film. If the substrate has a low density of nucleation sites, growth in the initial cycles will not occur uniformly across the surface, and may be limited to disconnected islands. Growth per cycle on these islands will be much higher than on the surrounding unreactive areas of the substrate (where it may be essentially zero), leading to the formation of mounds with significant 3-d character. Therefore, if an IOL has the effect of altering the nucleation characteristics of an ALD film, one would also expect it to have an effect on the thin film morphology.

Fig. 3-19 displays atomic force micrographs of  $\text{TiN}_x$  thin films formed after ALD growth ( $T_s = 167^\circ\text{C}$ ) on chemical oxide, and 5 different IOLs, two possessing no reactive functional groups (HMDS and TTS), one possessing OFGs confined primarily to a 2-d plane (Gen-1-3C), and two possessing a 3-d arrangement of OFGs (poly-G of 2 different thicknesses, 30 and 84 Å). The micrographs are in order of increasing value of the ratio RMS roughness ( $\sigma$ )/film thickness ( $D$ ). The differences in thin film morphology are readily apparent. The films grown on chemical oxide, the - $\text{NH}_2$  terminated dendron, and the short - $\text{CH}_3$  terminated IOL (HMDS) exhibit similar microstructure, are smoothest, and are characterized by small, closely spaced grain-like domains.

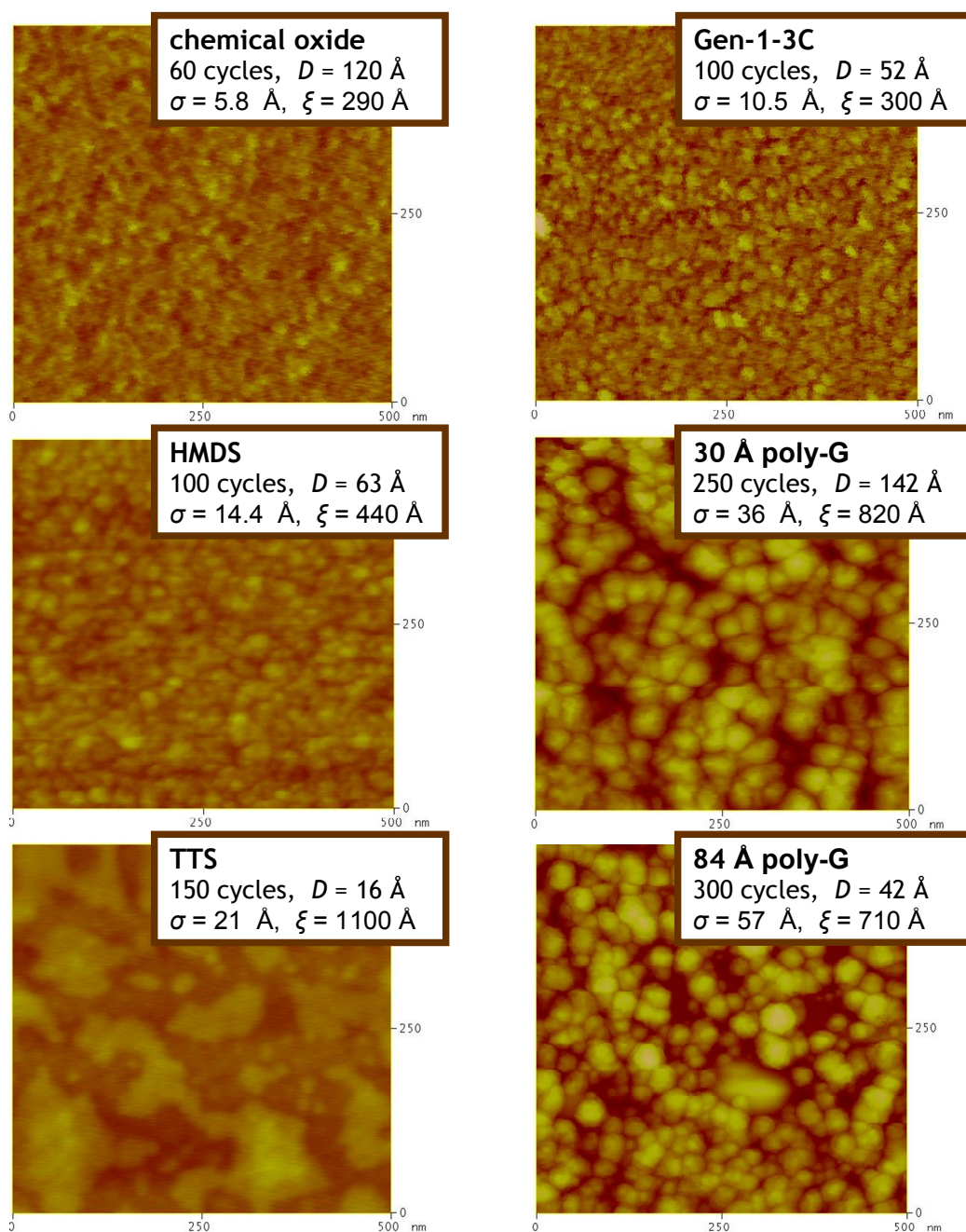


**Figure 3-19:** AF micrographs of representative  $\text{TiN}_x$  films grown by ALD on bare chemical oxide, and a variety of IOLs, including a  $-\text{NH}_2$  terminated dendron (Gen-1-3C), two unreactive SAMs (HMDS and TTS), and two thicknesses of poly-G. Here  $D$  is the ellipsometric film thickness,  $\sigma$  is the RMS roughness, and  $\xi$  is the in-plane correlation length. All images are  $500 \times 500 \text{ nm}^2$ .

The in-plane correlation lengths ( $\xi$ ) for these three films, determined from analysis of the power spectral densities, are also similar and span the range of 290-440 Å. It is of interest to note that for these two IOLs the values for initial attenuation factor are similar:  $\alpha = 0.27$  (Gen-1-3C) and 0.29 (HMDS). Moving on to the results on the 30 Å poly-G thin film we see that the relative roughness,  $\sigma/D$ , is similar to that observed on HMDS, albeit for a thicker  $\text{TiN}_x$  film, while the features are larger by about a factor of 2, with  $\xi \sim 820$  Å. A meaningful value for the attenuation factor on this surface at this substrate temperature could not be determined, but at the higher substrate temperature (207 °C) it was  $\alpha \sim 0.11$ , a value smaller than for growth on HMDS or Gen-1-3C. The film grown on TTS is much rougher, and consists of large patches ( $\xi \sim 1100$  Å), which appear to be only partially coalesced. Indeed, the measured value of the RMS roughness exceeds the thickness of the  $\text{TiN}_x$  film estimated from ellipsometry for this film (note of the value of  $\alpha \sim 0.05$  for TTS). Finally, the in-plane morphology of the  $\text{TiN}_x$  film formed on the thicker 84 Å poly-G film appears to be quite similar to that formed on the thinner poly-G thin film ( $\xi \sim 710$  Å), except that the  $\sigma/D$  of the film is larger and, similar to growth on TTS, the roughness exceeds the thickness of the  $\text{TiN}_x$  film. As indicated by the data shown in Fig. 3-17, the attenuation factor for growth on this thick poly-G layer is likely smaller than that observed on TTS.

One would expect the morphology to evolve with film thickness. The micrographs shown in Fig. 3-19 represent snapshots of specific points in this evolution. Fig. 3-20 shows a plot of the evolution of the RMS roughness with film thickness for the 6 cases considered in Fig. 3-19, and one additional case given by a straight chain SAM with -OH termination.

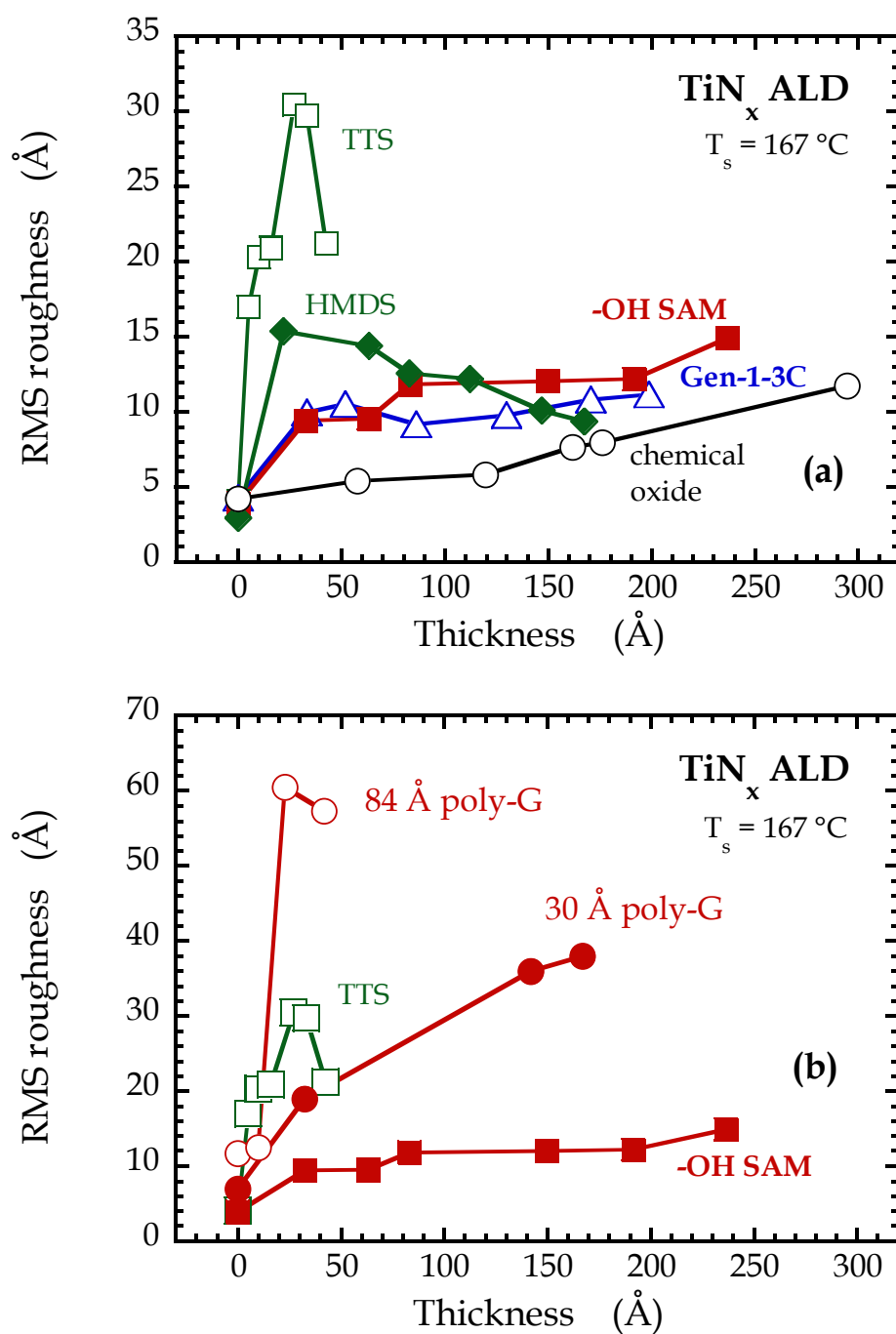


**Figure 3-20:** RMS surface roughness, measured by AFM, vs. ellipsometric film thickness for  $\text{TiN}_x$  ALD. **(a)** Results for growth on chemical oxide, two IOLs with reactive endgroups (Gen-1-3C and an -OH SAM), and two unreactive SAMs (HMDS and TTS). **(b)** Results for growth on three IOLs with reactive endgroups (an -OH SAM, and two thicknesses of poly-G), and an unreactive SAM (TTS).

As may be seen in (a), growth on chemical oxide leads to the smoothest film. Evolution of roughness for films grown on the reactive IOLs with 2-d character is similar to that on chemical oxide. Growth on the short unreactive IOL, HMDS, is initially rough, but the film smoothens with additional thickness and the roughness approaches that observed on chemical oxide at a thickness of  $D \sim 170 \text{ \AA}$ . Growth on TTS is quite different. Roughness increases almost linearly with thickness initially, then the film starts to smoothen, similar to the behavior observed on HMDS. As may be seen in (b), films formed on both poly-G layers are quite rough. On the thicker poly-G film, the roughness grows rapidly, faster than the thickness. This result is most likely due to rearrangement of the poly-G film itself, and possibly errors in the calculation of film thickness from ellipsometry. In any event growth on this thicker poly-G layer most closely resembles that on the thick, unreactive TTS layer. Growth on the thinner poly-G layer also results in rough films, but they are much smoother than those formed on the thicker poly-G layer. If they are compared to those grown on the -OH SAM, we see that the roughness exceeds that on the 2-d IOL by  $\sim 10\text{-}20 \text{ \AA}$ . Note that this distance is about the depth of penetration in the poly-G implicated by ARXPS for the Ta complex (*cf.* Sec. 3.3.2.3).

A final example concerning the effects of the IOL on thin film morphology considers a result from scanning transmission electron microscopy [104]. Fig. 3-21 displays a micrograph (annular dark field image) of a  $\text{TiN}_x$  thin film with a nominal thickness of  $\sim 120 \text{ \AA}$  grown on Gen-1-3C at  $T_s = 167 \text{ }^\circ\text{C}$ . Three distinct layers are observed: the  $\text{TiN}_x$  thin film; the chemical oxide/Gen-1-3C layer and the Si substrate.



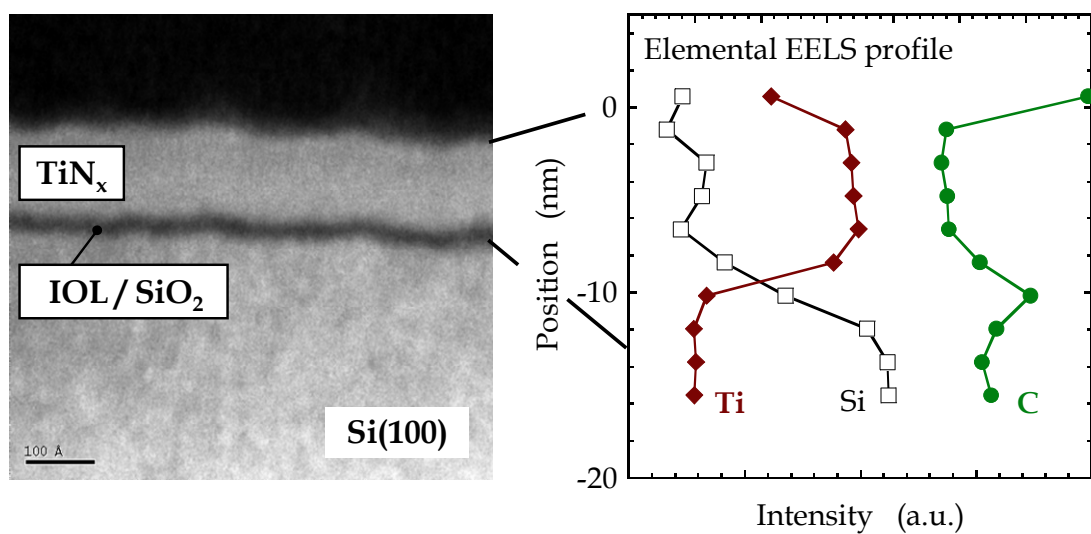


**Figure 3-21:** (a) Annular dark field transmission electron micrograph of a TiN<sub>x</sub> film grown on a -NH<sub>2</sub> terminated IOL (Gen-1-3C) at 167 °C. Nominal thickness of the film is ~120 Å. (b) Elemental profiles for Ti, Si and C obtained from corresponding high-resolution electron energy loss spectra. The absolute position of the surface is approximate.

The deposition is very conformal at the nm-scale, as seen from the similarity in the undulations of the  $\text{TiN}_x/\text{vacuum}$  and the  $\text{SiO}_2/\text{Si}$  interfaces. In this micrograph, however, the chemical oxide layer and the Gen-1-3C layer cannot be clearly resolved—has the IOL undergone some degradation due to the  $\text{TiN}_x$  ALD process? In order to make some statement as to the fate of the IOL, the STEM probe was used to acquire electron energy loss spectra (EELS), which can map the chemical composition of the thin film/IOL/ $\text{SiO}_2/\text{Si}$  stack. Also shown in Fig. 3-21 are the depth profiles for Ti, Si and C, as deduced from EELS (step size was 17.9 Å, similar to the expected thicknesses of the chemical oxide and the Gen-1-3C layer). We see that the Ti and Si signal behave as expected. Perhaps the most interesting observation is the peak in the C signal in the location where the Gen-1-3C layer is expected to be. These results support that, at minimum, some fragments of the original Gen-1-3C layer are at the  $\text{SiO}_2/\text{TiN}_x$  interface, and the layer has not been completely degraded or displaced. Clear resolution of the fate of the IOL from techniques such as STEM, however, remains a significant experimental challenge.

#### **3.3.3.3. Correlations between chemisorption and ALD growth**

In the work reviewed here one of the ultimate goals is to identify connections between phenomena occurring in the monolayer regime, which represents surface chemistry, to phenomena occurring in both the nucleation and the steady-state stages of growth, which represent thin film materials science. The first connection/correlation which can be identified involves the attenuation of the initial rate of inorganic film

growth by ALD, and the saturation density of the transition metal coordination complexes on the starting substrate (effectively the first  $\frac{1}{2}$  cycle of ALD). First, what is the expectation? If the initial rate of growth is attenuated via a mechanism that changes the *density* of chemisorbed precursors, but does not change their *character* (e.g., number of ligands retained) or their *accessibility* concerning subsequent growth, then one expects a strong correlation. Fig. 3-22 shows a plot of the attenuation factor  $\alpha$  from Eq. 3-1 (using thicknesses  $D$  determined both from ellipsometry and RBS) vs. the saturation density measured from beam reflectivity for four cases: chemical oxide, and 3 straight-chain SAMs terminated by  $-\text{NH}_2$ ,  $-\text{OH}$ , and  $-\text{CH}_3$  groups. The values for  $\alpha$  are from ALD of  $\text{TiN}_x$  at  $T_s = 167^\circ\text{C}$  (*cf.* Figs. 3-16 to 3-18), while the saturation densities for the  $\text{Ti}[\text{N}(\text{CH}_3)_2]_4$  precursor are determined from supersonic molecular beam scattering measurements at  $T_s = 25^\circ\text{C}$  [89], where the precursor is delivered to the surface in a way that is identical to that used in the ALD studies [103,104]. There is a good correlation between the attenuation factor and the saturation density for these four cases. A fit of these data to a power law gives an exponent of  $\sim 0.95$ , thus the attenuation factor scales essentially linearly with the density of available sites for the chemisorption of  $\text{Ti}[\text{N}(\text{CH}_3)_2]_4$  on these surfaces.

Which systems may not show such a good correlation?—ones where there is a fundamental change in the character of the chemisorbed species, such as adsorption on poly-G (*cf.* the results shown in Fig. 3-15). Although a direct comparison between the chemisorption of  $\text{Ta}[\text{N}(\text{CH}_3)_2]_5$  and the ALD growth of  $\text{TiN}_x$  cannot be made, large differences ( $>$  factor of 2) in the saturation density of the Ti and Ta amido compounds are not expected.

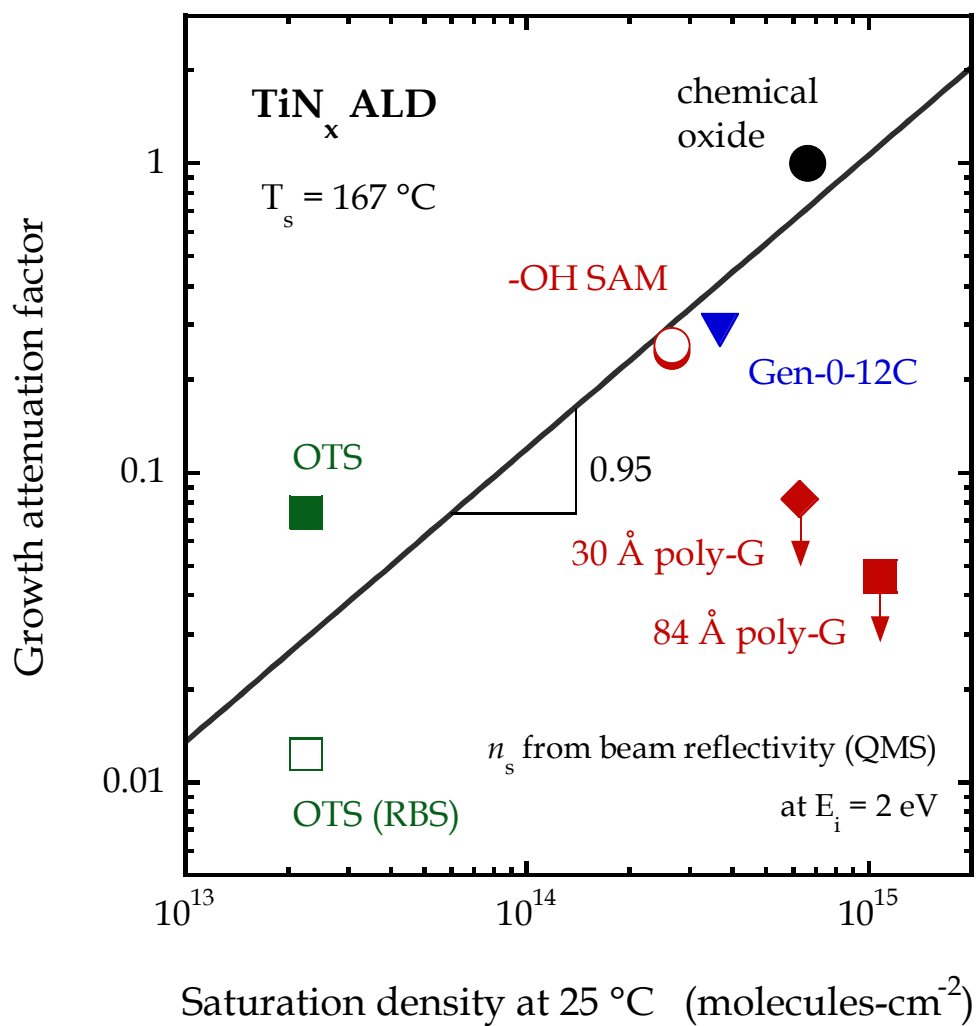


**Figure 3-22:** Growth attenuation factor [from ellipsometry and RBS (open symbols);  $\alpha$  in Eq. 3-1] vs. the saturation density of Ti[N(CH<sub>3</sub>)<sub>2</sub>]<sub>4</sub> (at T<sub>s</sub> = 25 °C) measured from beam reflectivity [89]. For the two data points on poly-G we have estimated the saturation density for exposure to Ti[N(CH<sub>3</sub>)<sub>2</sub>]<sub>4</sub> by using that found for thermal exposures to Ta[N(CH<sub>3</sub>)<sub>2</sub>]<sub>5</sub>, and estimated  $\alpha$  using the first measured thickness data point.

Indeed on chemical oxide at  $T_s = 25\text{ }^{\circ}\text{C}$  the saturation densities are  $\sim 6.9 \times 10^{14}$  and  $4.4 \times 10^{14}$  atoms-cm<sup>-2</sup> for the Ti and Ta complexes (thermal gas exposures), respectively, or a Ti/Ta ratio of  $\sim 1.6$ . For the three other cases where results exist for both complexes (Gen-0-3C, -0-12C, -1-3C) the average value for the ratios of saturation densities of Ti/Ta is  $\sim 1.5$ . Given a saturation density for Ta, this value can be used to estimate a corresponding one for the Ti complex. An estimate for the attenuation factor for TiN<sub>x</sub> ALD on poly-G at  $T_s = 25\text{ }^{\circ}\text{C}$  can be made making use of the first data point for which a thickness has been reliably measured, as shown in the  $D$  vs.  $n$  relationship in Fig. 3-17. This is likely an upper bound for  $\alpha$ . Using this approach, two additional points are plotted in Fig. 3-22 for TiN<sub>x</sub> ALD on 30 and 84 Å-thick poly-G. Again the saturation density has been corrected for the likely higher coverage of the Ti complex, and was measured for a thermal gas exposure (not a supersonic beam). We see that these two data points are displaced significantly from that for the other IOLs. Indeed, there seems to be a *negative* correlation considering only those data for the -OH SAM and the poly-G layers. The discrepancy between these two data points and the trend observed for the other IOLs is likely not explained by the different method of introduction of the metal complex (thermal vs. supersonic), but likely reflects true differences in the nature of the adlayer. A potential argument is that the additional uptake of the precursors by the thick poly-G layer does not aid subsequent growth as the metal complex has been virtually stripped of its -N(CH<sub>3</sub>)<sub>2</sub> ligands, forming an unreactive fully oxidized species as first discussed above in Sec. 3.3.2.4.2. The conclusion from this analysis is that both the density and the identity of the *chemisorbed precursors* are important concerning subsequent growth.

Poor nucleation as indicated by sluggish initial growth may lead to less-than ideal topology—e.g., islanded 3-D growth, which would lead to correlations between the kinetics of growth and the thin film morphology. In this case justifiable assumptions can be made concerning how these two phenomena are related. If growth involves first the formation of islands that are well separated, then these islands will grow until they “touch” and eventually coalesce into a uniform thin film. Before coalescence, one can expect the islands to grow both laterally and vertically and perhaps possess a shape similar to a truncated sphere. In this case the roughness should reach a maximum, or possibly exhibit a discontinuity at the point of coalescence. At this point, the height of the island should scale linearly with the spacing between islands, or equivalently the roughness should scale with  $N_s^{-1/2}$ , where  $N_s$  is the island density. Concerning the kinetics one can associate the attenuation factor with the density of the islands via  $\alpha = N_{s,IOL}/N_{s,max}$ , where  $N_{s,IOL}$  is the density of active sites and, hence, the islands on the surface with the IOL, while  $N_{s,max}$  is the density of active sites on the untreated chemical oxide. Thus, in this case a log-log plot of the roughness vs.  $1/\alpha$  should yield an exponent (slope) of  $1/2$ .

To examine this correlation we consider only those results for which good estimates for the attenuation factor and relevant results concerning the evolution of surface roughness with thickness exist. Fig. 3-23 is a plot of the RMS roughness vs.  $1/\alpha$  for 5 cases: growth of  $TiN_x$  on chemical oxide, 2 reactive IOLs (Gen-1-3C and the -OH terminated SAM) and 2 unreactive IOLs (HMDS and TTS).

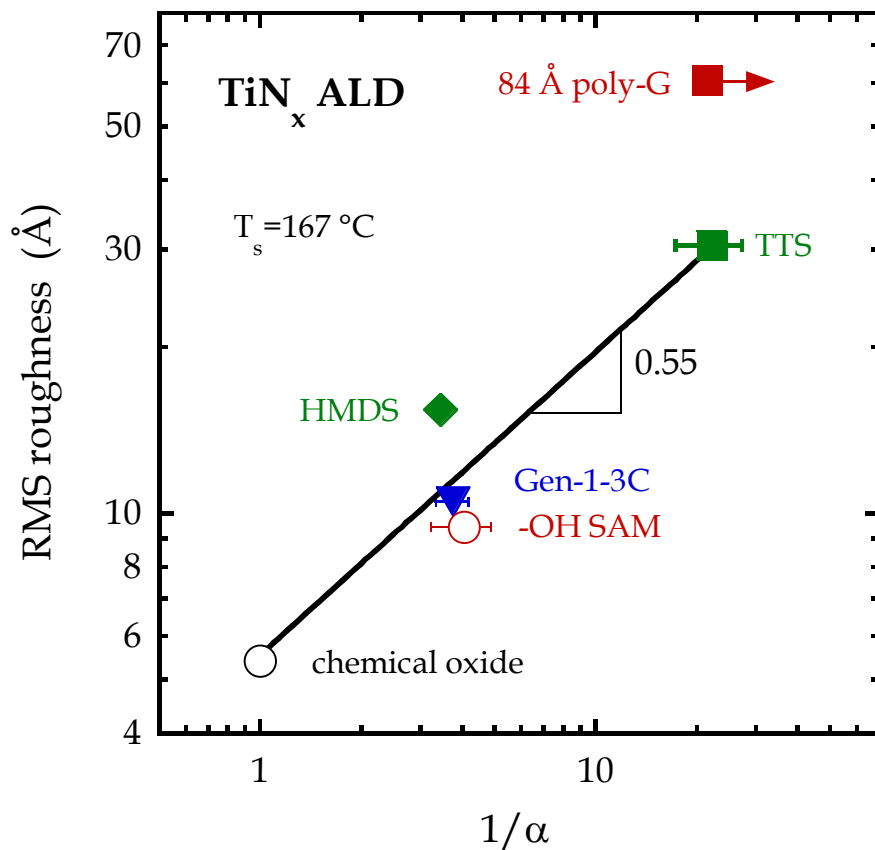


**Figure 3-23:** RMS roughness for the early stages of growth vs.  $1/\alpha$  for  $\text{TiN}_x$  ALD on six surfaces. The roughness plotted is either the maximum observed in the early stages of growth (valid for HMDS, TTS, Gen-1-3C and 84 Å-thick poly-G), or, if a maximum is not observed, it is the first value for which we have a thickness (chemical oxide and the -OH SAM) In all cases, *cf.* Fig. 3-20. The fit to a power law excludes the data point for poly-G, primarily due to the uncertainty in the value for  $\alpha$  (again estimated as in Fig. 3-22).

The roughness plotted in these cases was either the maximum observed vs. thickness, as shown in Fig. 3-20(a) for growth on TTS, HMDS, and Gen-1-3C, or if a maximum did not exist, the first value for which a thickness is reported (chemical oxide and the -OH SAM). These data are described well by a power law exponent of  $\sim 0.55$ , close to the value of  $1/2$  discussed above. In general, the degree of attenuation of the initial rate of growth correlates with a rougher film, which is clearly related to a scarcity of nucleation sites and leads to island-type growth in the initial cycles of ALD. Purely for comparison a data point for growth on the 84 Å-thick poly-G IOL is also plotted: here the upper bound for  $\alpha$  that was also used in the construction for Fig. 3-22 was used. Here it should be a lower bound for  $1/\alpha$ . We see that for this correlation of RMS roughness vs.  $1/\alpha$ , the data for growth on poly-G are in better agreement with the overall trend, unlike the case for the data shown in Fig. 3-22. Thus, it appears that the correlation between the attenuation of growth and the surface morphology is more universal than that between the attenuation of growth and the initial uptake of the chemisorbed transition metal complexes.

### 3.4. Conclusions and Outlook

Inorganic-organic interfaces play an important role in a wide variety of existing and emerging applications. Growth of an inorganic thin film on top of a pre-existing organic layer presents considerable challenges, particularly when the organic layer provides electronic, optical, or photonic functionality, as in these cases its properties can be changed dramatically by invasive chemistries. Most of the early



work concerning inorganic-on-organic interface formation involved the evaporative deposition of metallic thin films on polymers or surfaces terminated with self-assembled monolayers. However, more precise control of interface formation can be achieved by making use of transition metal coordination complexes, with suitable ligands, combined with an organic surface possessing an appropriately selected functional group(s).

As a first step to developing an understanding of inorganic-organic interface formation, x-ray photoelectron spectroscopy can be used effectively to determine both the absolute density of molecules present in a self-assembled monolayer and, in selected cases, the presence and concentration of certain functional groups. Evaluation of a dimensionless attenuation factor,  $d/\lambda$ , via either angle-resolved x-ray photoelectron spectroscopy, or direct estimates of the attenuation length ( $\lambda$ ) and film thickness ( $d$ ), enables these quantitative estimates. These techniques were used to characterize a series of interfacial organic layers possessing a variety of structures and functionalities, from simple straight chain self-assembled monolayers to organic layers with more complex, branched molecular structures. The latter set included both regular and randomly branched oligomers grown from the surface, which can increase the dimensionality of the functional groups present in the monolayer from essentially a 2-d to a 3-d spatial arrangement.

Having characterized one of the reactants in this case, the interfacial organic layers, the reaction of these with two amido compounds with Ti and Ta centers was considered next. *In situ* XPS was used as a primary technique to quantify the density of species that are formed, their composition, and using angle-resolved XPS, their

spatial distribution. Measurement of coverage-exposure relationships for the  $\text{Ti}[\text{N}(\text{CH}_3)_2]_4$  and  $\text{Ta}[\text{N}(\text{CH}_3)_2]_5$  complexes revealed that the initial probability of reaction is determined primarily by the chemical identity of the functional groups present at the surface. The adsorptive capacity/saturation coverage of the organic layer, on the other hand, is determined mostly by the density of the organic functional groups. These trends for the most part held true concerning reactions with organic layers with more complicated, branched structures, possessing functional groups distributed also along their backbones. Angle-resolved XPS revealed that, in the case of straight chain SAMs, for layers lacking a reactive endgroup, e.g., those terminated by  $-\text{CH}_3$ , the transition metal complexes penetrate the SAM and react at the SAM/ $\text{SiO}_2$  interface, whilst for layers possessing reactive terminal groups, e.g.,  $-\text{NH}_2$ , the reaction was confined to this endgroup. Adsorption and reaction on branched, multifunctional IOLs, in contrast, produced layers where penetration and reaction with functional groups on the backbone, in addition to the terminal functional groups, was implicated.

Concerning the stoichiometry of the adlayers formed at room temperature, for the IOLs where the OFGs were distributed mostly in a 2-d arrangement, there is a clear tendency towards the formation of species where the transition metal complex has undergone two ligand exchange reactions with these OFGs, producing a 1:2 M:OFG ratio. The reaction with the branched IOLs is more complex. With regular branched polyamidoamine dendrons, reactions between the complexes and functional groups both terminal and on the backbone of the molecule are suggested. In the case of the hyperbranched polyglycidol (poly-G) layers, the high density, 3-d arrangement

of the -OH groups in a sufficiently thick layer can exchange virtually all the ligands in the Ta complex forming a completely oxidized metal center.

ALD on the interfacial organic layers was examined using *ex situ* ellipsometry, AFM, and in selected cases, RBS and cross-sectional STEM. The deposited thickness ( $D$ ) vs. the number of ALD cycles ( $n$ ) relationship for growth on the IOLs was typically non-linear, exhibiting an attenuated rate of growth initially, which eventually evolved to the rate observed on unmodified chemical oxide. In most cases, the data could be fit to a two parameter model that included an initial attenuation factor, and a constant describing the exponential approach to the unattenuated steady-state rate of growth. Generally, initial growth on unreactive -CH<sub>3</sub> and -CF<sub>3</sub> terminated IOLs is significantly more attenuated than growth on those layers possessing reactive OFGs such as -NH<sub>2</sub> or -OH groups. In the case of growth on the unreactive straight-chain SAMs, the attenuation is greater as the chain length of the SAM increases, consistent with film nucleation at the SAM/SiO<sub>2</sub> interface. For IOLs with reactive endgroups, the initial attenuation of growth was approximately constant with IOL thickness, consistent with nucleation taking place at the endgroup. This was even the case for growth on the -NH<sub>2</sub> terminated first-generation dendrons, which, although branched, possess functional groups confined to essentially a 2-d layer of thickness  $\sim 6$  Å, thus the strong similarity. On poly-G, particularly 84 Å thick poly-G, growth is strongly attenuated, even though this surface has the largest adsorptive capacity of any IOL examined here. On this surface, nearly all ligands are lost by Ta[N(CH<sub>3</sub>)<sub>2</sub>]<sub>5</sub> on chemisorption via reaction with -OH groups, and ALD growth proceeds similarly to growth on an unreactive IOL.

The morphological evolution of films grown by ALD on a variety of IOLs was examined using atomic force microscopy. In general, ALD on IOLs with reactive endgroups confined mostly to a 2-d plane results in a relatively smooth film, similar to growth on unmodified chemical oxide. ALD on unreactive IOLs, on the other hand, is severely 3-d and islanded. Interestingly, growth on the *very reactive* IOLs—the poly-G layers—is also very 3-d and islanded. This is due to the formation of a highly oxidized Ta complex, which lacks suitable ligands for exchange, and leads to severely islanded 3-d growth. This result suggests that a better candidate for nucleation site amplification would be an organic thin film with a lower 3-d density of reactive sites, possibly leaving some ligands available for reaction in the second half of the ALD cycle. Alternately, an organic thin film with a different type of organic functionality, which do not bind as strongly to the metal center may be used. Bonds formed between the metal center and the organic layer, then, may be more susceptible to disruption in the second half cycle. Such a layer, with amine functionality, is considered in Chapters 4 and 5.

The type, density and dimensionality (spatial distribution) of the organic functional groups present in the organic layer will strongly influence the subsequent growth of the inorganic layer. An identifying feature of the work reviewed here is that results were presented which represent both phenomena occurring in the monolayer regime, and phenomena occurring in the nucleation and the steady-state regimes of thin film growth for the same chemical system. Concerning correlations between the initial rates of growth from the thickness/number-of-cycle relationship, there is good agreement with the saturation density observed at room temperature, particularly for

IOLs which possess an essentially 2-d configuration of active organic functional groups. The correlation is poor concerning those layers where the OFGs are high in density and distributed in 3-d. Another correlation involves that between morphology and the kinetics of growth, and an excellent correlation between the maximum roughness (or that representing the largest incremental increase) and the degree of attenuation of the initial rate of growth was found. In the cases where growth is strongly attenuated, nucleation sites are well separated and isolated, and this leads to 3-d islands and mounded growth with a corresponding increase in roughness.

Although a number of important correlations between phenomena in the monolayer regime and subsequent ALD growth of inorganics on a large variety of IOLs were established, a number of important questions remain. First, all of the results for ALD presented here were produced based on a process that used molecular beam dosing, not via the introduction of the reactants by conventional viscous flow. It was argued above that if there are differences, they are likely to be found in the non-metallic coreactant cycle, here involving  $\text{NH}_3$ . This might have an effect on the composition of the films that are deposited, e.g., ligand exchange might be reduced, leading to more incorporation of C in the thin films. It is not believed that these effects will greatly change the other conclusions and observations made in this review concerning connections between chemisorptive capacity and the initial rate of growth, as well as those between the thin film morphology and the growth attenuation factor.

Looking forward, additional issues remain however. Perhaps the most interesting fundamental question is: what is the fate of the IOL for the cases considered here? Clearly, there is no one single answer. In the case of the unreactive

IOLs, the layers are likely at least partially buried/incorporated into the growing ALD thin film. In the case of the reactive 2-d IOLs, these layers are also likely at least partially buried, but they also may be incorporated to some extent based on the arguments made concerning the length of the attenuation effects and their temperature dependencies. Further work is required to fully resolve this issue.

From the conclusions of the work presented here, a certain amount of guidance can be provided in selection of an organic layer based on the application of interest. First, if the purpose of the organic layer is to enhance the ALD growth rate, or to normalize the growth rate on a number of exposed surfaces, one should consider the connection between the location and chemical structure of the precursor adsorbed in the first half cycle of ALD, and the subsequent ALD growth rate. In the case of titanium and tantalum dimethylamido precursors, ALD growth rates are highest on organic films which lead to chemisorption of the precursor close to the vacuum interface, and the retention of a high number of ligands. This highlights the importance of maintaining a high level of accessibility and reactivity of the precursor towards the coreactant in the second half cycle. An approach which seeks to simply maximize the density of precursor taken up in the first half cycle (i.e. thick poly-G) may fail due to the reduced reactivity of the precursor. Second, in cases where a  $-CH_3$  terminated SAM is used to block or inhibit growth, we have observed that film growth nucleates at the  $SiO_2/SAM$  interface, as has been observed by other researchers [65]. This again suggests the use of a SAM layer which is as thick and well-packed as possible, providing a good barrier to diffusion of the precursor through the layer. Finally, the general correlation observed between the initial ALD growth rate and the roughness of

the deposited thin film suggests that a layer which normalizes the growth rate will also normalize the roughness of the deposited thin film. Likewise, strategies which enhance the ALD growth rate on unreactive substrates would also be expected to decrease the roughness of the deposited thin film.

### 3.5 References

1. A. Ulman, *An Introduction to Ultrathin Organic Films, From Langmuir-Blodgett to Self-Assembly* (Academic Press, Boston, MA 1991).
2. L. H. Dubois and R. G. Nuzzo, *Annu. Rev. Phys. Chem.* **43**, 437 (1992).
3. A. Ulman, *Chem. Rev.* **96**, 1533 (1996).
4. J. C. Scott, *J. Vac. Sci. Technol. A* **21**, 521 (2003).
5. L.-L. Chua, J. Zaumseil, J.-F. Chang, E. C.-W. Ou, P. K.-H. Ho, H. Sirringhaus, and R. H. Friend, *Nature* **434**, 194 (2005).
6. J. Hwang, A. Wan, and A. Khan, *Mater. Sci. Eng. R* **64**, 1 (2009).
7. H. Ma, M. S. Liu, and A. K.-Y. Jen, *Polym. Int.* **58**, 594 (2009).
8. N. Koch, *ChemPhysChem* **8**, 1438 (2007).
9. W. R. Salaneck, S. Stafström, and J.-L. Brédas, *Conjugated Polymer Surfaces and Interfaces, Electronic and Chemical Structure of Interfaces for Polymer Light Emitting Devices* (Cambridge University Press, Cambridge, 1996).
10. L. Yan and Y. Gao, *Thin Solid Films* **417**, 101 (2002).
11. A. Aviram and M. A. Ratner, *Molecular Electronics: Science and Technology* (NY Academy of Science, New York, 1998).
12. H. Haick and D. Cahen, *Prog. Surf. Sci.* **83**, 217 (2008).
13. R. L. McCreery, *Chem. Mater.* **16**, 4477 (2004).
14. H. B. Akkerman and B. de Boer, *J. Phys.: Condens. Matter* **20**, 013001 (2008).
15. C.-W. Chu, S.-H. Li, C.-W. Chen, V. Shrotriya, and Y. Yang, *Appl. Phys. Lett.* **87**, 193508 (2005).
16. K. Morii, M. Ishida, T. Takashima, T. Shimoda, Q. Wang, M. K. Nazeeruddin, and M. Grätzel, *Appl. Phys. Lett.* **89**, 183510 (2006).
17. F.-C. Chen, L.-J. Kung, T.-H. Chen, and Y.-S. Lin, *Appl. Phys. Lett.* **90**, 073594 (2007).
18. R. Hajlaoui, G. Horowitz, F. Garnier, A. Arce-Bouchet, L. Laigre, A. El Kassmi, F. Demanze, and F. Kouki, *Adv. Mater.* **9**, 389 (1997).



19. C. A. Goss, D. H. Charych, and M. Majda, *Anal. Chem.* **63**, 85 (1991).
20. S. R. Wasserman, H. Biebuyck, and G. M. Whitesides, *J. Mater. Res.* **4**, 886 (1989).
21. K. L. Mittal and J. R. Susko, *Metallized Plastics, 1-4*, (Plenum Press, New York, 1989, 1991, 1992, 1998).
22. E. Sacher, J.-J. Pireaux, and S. P. Kowalczyk, *Metallization of Polymers, ACS Symposium Series 440* (American Chemical Society, Washington, DC, 1990).
23. E. Sacher, *Metallization of Polymers 2* (Kluwer Academic/Plenum, New York, 2002).
24. A. W. Czanderna, D. E. King, and D. Spaulding, *J. Vac. Sci. Technol. A* **9**, 2607 (1991).
25. M. J. Tarlov, *Langmuir* **8**, 80 (1992).
26. D. R. Jung and A. W. Czanderna, *Crit. Rev. Solid State Mater. Sci.* **19**, 1 (1994).
27. G. C. Herdt, D. R. Jung, and A. W. Czanderna, *Prog. Surf. Sci.* **50**, 103 (1995).
28. K. Konstadinidis, P. Zhang, R. L. Opila, and D. L. Allara, *Surf. Sci.* **338**, 300 (1995).
29. D. R. Jung, A. W. Czanderna, and G. C. Herdt, *J. Vac. Sci. Technol. A* **14**, 1779 (1996).
30. D. Wacker, K. Weiss, U. Kizmaier, and C. Wöll, *Langmuir* **13**, 6689 (1997).
31. G. L. Fisher, A. Hooper, R. L. Opila, D. R. Jung, D. L. Allara, and N. Winograd, *J. Electron Spectrosc. Relat. Phenom.* **98-99**, 139 (1999).
32. A. Hooper, G. L. Fisher, K. Konstadinidis, D. Jung, H. Nguyen, R. Opila, R. W. Collins, N. Winograd, and D. L. Allara, *J. Am. Chem. Soc.* **121**, 8052 (1999).
33. G. L. Fisher, A. E. Hooper, R. L. Opila, D. L. Allara, and N. Winograd, *J. Phys. Chem. B* **104**, 3267 (2000).
34. G. L. Fisher, A. V. Walker, A. E. Hooper, T. B. Tighe, K. B. Bahnck, H. T. Skriba, M. D. Reinard, B. C. Haynie, R. L. Opila, N. Winograd, and D. L. Allara, *J. Am. Chem. Soc.* **124**, 5528 (2002).
35. H. Ahn and J. E. Whitten, *J. Phys. Chem. B* **107**, 6565 (2003).

36. B. C. Haynie, A. V. Walker, T. B. Tighe, D. L. Allara, and N. Winograd, *Appl. Surf. Sci.* **203-204**, 433 (2003).
37. A. V. Walker, T. B. Tighe, O. M. Cabarcos, M. D. Reinard, B. C. Haynie, S. Uppili, N. Winograd, and D. L. Allara, *J. Am. Chem. Soc.* **126**, 3954 (2004).
38. B. de Boer, M. M. Frank, Y. J. Chabal, W. Jiang, E. Garfunkel, and Z. Bao, *Langmuir* **20**, 1539 (2004).
39. Y. Tai, A. Shaporenko, W. Eck, M. Grunze, and M. Zharnikov, *Appl. Phys. Lett.* **85**, 6257 (2004).
40. M. M. Maitani, T. A. Daniel, O. M. Cabarcos, and D. L. Allara, *J. Am. Chem. Soc.* **131**, 8016 (2009).
41. Y. Tai, A. Shaporenko, H. Noda, M. Grunze, and M. Zharnikov, *Adv. Mater.* **17**, 1745 (2005).
42. H. Noda, Y. Tai, A. Shaporenko, M. Grunze, and M. Zharnikov, *J. Phys. Chem. B* **109**, 22371 (2005).
43. G. Nagy and A. V. Walker, *J. Phys. Chem. B* **110**, 12543 (2006).
44. A. V. Walker, T. B. Tighe, O. Cabarcos, B. C. Haynie, D. L. Allara, and N. Winograd, *J. Phys. Chem. C* **111**, 765 (2007).
45. G. Nagy and A. V. Walker, *J. Phys. Chem. C* **111**, 8543 (2007).
46. M. M. Maitani, D. A. A. Ohlberg, Z. Li, D. L. Allara, D. R. Stewart, and R. S. Williams, *J. Am. Chem. Soc.* **131**, 6310 (2009).
47. M. M. Maitani, D. L. Allara, D. A. A. Ohlberg, Z. Li, R. S. Williams, and D. R. Stewart, *Appl. Phys. Lett.* **96**, 173109 (2010).
48. H. Haick, O. Niitsoo, J. Ghabboun, and D. Cahen, *J. Phys. Chem. C* **111**, 2318 (2007).
49. P. Wohlfart, J. Weiß, J. Käshammer, M. Kreiter, C. Winter, R. Fischer, and S. Mittler-Neher, *Chem. Vap. Deposition* **5**, 165 (1999).
50. U. Weckenmann, S. Mittler, S. Krämer, A. K. A. Aliganga, and R. A. Fischer, *Chem. Mater.* **16**, 621 (2004).
51. K. Rajalingam, T. Strunskus, A. Terfort, R. A. Fischer, and C. Wöll, *Langmuir* **24**, 7986 (2008).

52. R. A. Fischer, U. Weckenmann, C. Winter, J. Kashammer, V. Scheumann, and S. Mittler, *J. Phys. IV: Proc.* **11**, Pr3/1183 (2001).
53. X. Liu, Q. Wang, S. Wu, and Z. Liu, *J. Electrochem. Soc.* **153**, C142 (2006).
54. J. Weiß, H.-J. Himmel, R. A. Fischer, and C. Wöll, *Chem. Vap. Deposition* **4**, 17 (1998).
55. N. L. Jeon and R. G. Nuzzo, *Langmuir* **11**, 3024 (1995).
56. P. Doppelt, N. Semaltianos, C. Deville Cavellin, J. L. Pastol, and D. Ballutaud, *Microelectron. Eng.* **76**, 113 (2004).
57. C. Winter, U. Weckenmann, R. A. Fischer, J. Kāshammer, V. Scheumann, and S. Mittler, *Chem. Vap. Deposition* **6**, 199 (2000).
58. J. Küther, R. Seshadri, W. Knoll, and W. Tremel, *J. Mater. Chem.* **8**, 641 (1998).
59. J. Aizenberg, A. J. Black, and G. M. Whitesides, *Nature* **398**, 495 (1999).
60. J. Aizenberg, A. J. Black, and G. M. Whitesides, *J. Am. Chem. Soc.* **121**, 4500 (1999).
61. D. D. Archibald, S. B. Qadri, and B. P. Gaber, *Langmuir* **12**, 538 (1996).
62. J. W. P. Hsu, W. M. Clift, and L. N. Brewer, *Langmuir* **24**, 5375 (2008).
63. M. Ritala and M. Leskelä, in *Handbook of Thin Film Materials*, edited by H. S. Nalwa (Academic, San Diego, CA, 2001), Vol.1.
64. R. L. Puurunen, *J. Appl. Phys.* **97**, 121301 (2005), and references therein.
65. X. Jiang and S. F. Bent, *J. Phys. Chem. C* **113**, 17613 (2009).
66. R. Chen, H. Kim, P. C. McIntyre, and S. F. Bent, *Chem. Mater.* **17**, 536 (2005).
67. R. Chen and S. F. Bent, *Adv. Mater.* **18**, 1086 (2006).
68. M. H. Park, Y. J. Jang, H. M. Sung-Suh, and M. M. Sung, *Langmuir* **20**, 2257 (2004).
69. R. Chen, H. Kim, P. C. McIntyre, and S. F. Bent, *Appl. Phys. Lett.* **84**, 4017 (2004).
70. M. Yan, Y. Koide, J. R. Babcock, P. R. Markworth, J. A. Belot, T. J. Marks, and R. P. H. Chang, *Appl. Phys. Lett.* **79**, 1709 (2001).

71. E. Färm, M. Kemell, M. Ritala, M. Leskelä, *Chem. Vap. Deposition* **12**, 415 (2006).
72. H.-B.-R. Lee, W.-H. Kim, J. W. Lee, J.-M. Kim, K. Heo, I. C. Hwang, Y. Park, S. Hong, and H. Kim, *J. Electrochem. Soc.* **157**, D10 (2010).
73. K. J. Park, J. M. Doub, T. Gougousi, G. N. Parsons, *Appl. Phys. Lett.* **86**, 051903 (2005).
74. C. M. Whelan, A.-C. Demas, J. Schuhmacher, L. Carbonell, and K. Maex, *Mater. Res. Soc. Symp. Proc.* **812**, F.2.2.1 (2004).
75. E. K. Seo, J. W. Lee, H. M. Sung-Suh, and M. M. Sung, *Chem. Mater.* **16**, 1878 (2004).
76. J. P. Lee, Y. J. Jang, and M. M. Sung, *Adv. Func. Mater.* **13**, 873 (2003).
77. N. P. Kobayashi, C. L. Donley, S.-Y. Wang, and R. S. Williams, *J. Cryst. Growth* **299**, 218 (2007).
78. N. P. Kobayashi and R. S. Williams, *Chem. Mater.* **20**, 5356 (2008).
79. M. Li, M. Dai, and Y. J. Chabal, *Langmuir* **25**, 1911 (2009).
80. M. J. Preiner and N. A. Melosh, *Appl. Phys. Lett.* **92**, 213301 (2008).
81. O. Seitz, M. Dai, F. S. Aguirre-Tostado, R. M. Wallace, and Y. J. Chabal, *J. Am. Chem. Soc.* **131**, 18159 (2009).
82. B. H. Lee, M. K. Ryu, S.-Y. Choi, K.-H. Lee, S. Im, and M. M. Sung, *J. Am. Chem. Soc.* **129**, 16034 (2007).
83. B. H. Lee, K. H. Lee, S. Im, and M. M. Sung, *Org. Electron.* **9**, 1146 (2008).
84. Y. Xu and C. B. Musgrave, *Chem. Mater.* **16**, 646 (2004).
85. M. Haran, J. R. Engstrom, and P. Clancy, *J. Am. Chem. Soc.* **128**, 836 (2006).
86. M. Sharma, A. Dube, and J. R. Engstrom, *J. Am. Chem. Soc.* **129**, 15022 (2007).
87. M. Sharma, A. Dube, K. J. Hughes, and J. R. Engstrom, *Langmuir* **24**, 8610 (2008).
88. A. S. Killampalli, P. F. Ma, and J. R. Engstrom, *J. Am. Chem. Soc.* **127**, 6300 (2005).

89. P. F. Ma, A. Dube, A. S. Killampalli, and J. R. Engstrom, *J. Chem. Phys.* **125**, 034706 (2006).
90. J.-W. Lim, H.-S. Park, and S.-W. Kang, *J. Electrochem. Soc.* **148**, C403 (2001).
91. J. W. Elam, M. Schuisky, J. D. Ferguson, and S. M. George, *Thin Solid Films* **436**, 145 (2003).
92. R. M. Fix, R. G. Gordon, and D. M. Hoffman, *Chem. Mater.* **2**, 235 (1990).
93. J. N. Musher and R. G. Gordon, *J. Mater. Res.* **11**, 989 (1996).
94. Y. Y. Wu, A. Kohn, and M. Eizenberg, *J. Appl. Phys.* **95**, 6167 (2004).
95. R. M. Fix, R. G. Gordon, and D. M. Hoffman, *Chem. Mater.* **5**, 614 (1993).
96. International Technology Roadmap for Semiconductors, <http://www.itrs.net>, 2009.
97. S. Bocharov, Z. Zhang, T. P. Beebe, and A. V. Teplyakov, *Thin Solid Films* **471**, 159 (2005).
98. J. C. F. Rodríguez-Reyes and A. V. Teplyakov, *J. Phys. Chem. C* **111**, 4800 (2007).
99. J. C. F. Rodríguez-Reyes and A. V. Teplyakov, *J. Phys. Chem. C* **111**, 16498 (2007).
100. J. C. F. Rodríguez-Reyes and A. V. Teplyakov, *J. Appl. Phys.* **104**, 084907 (2008).
101. J. C. F. Rodríguez-Reyes and A. V. Teplyakov, *J. Phys. Chem. C* **112**, 9695 (2008).
102. J. C. F. Rodríguez-Reyes, C. Ni, H. P. Bui, T. P. Beebe, and A. V. Teplyakov, *Chem. Mater.* **21**, 5163 (2009).
103. A. Dube, M. Sharma, P. F. Ma, and J. R. Engstrom, *Appl. Phys. Lett.* **89**, 164108 (2006).
104. A. Dube, M. Sharma, P. F. Ma, P. A. Ercius, D. A. Muller, and J. R. Engstrom, *J. Phys. Chem. C* **111**, 11045 (2007).
105. A. Kumar and G. M. Whitesides, *Appl. Phys. Lett.* **63**, 2002 (1993).
106. R. D. Piner, J. Zhu, F. Xu, S. H. Hong, and C. A. Mirkin, *Science* **283**, 661 (1999).

107. T. Yoshimura, S. Tatsuura, W. Sotoyama, Appl. Phys. Lett. **59**, 482 (1991).
108. A. A. Dameron, D. Seghete, B. B. Burton, S. D. Davidson, A. S. Cavanagh, J. A. Bertrand, and S. M. George, Chem. Mater. **20**, 3315 (2008).
109. S. M. George, B. Yoon, and A. A. Dameron, Acc. Chem. Res. **42**, 498 (2009).
110. F. Schreiber, Prog. Surf. Sci. **65**, 151 (2000), and references therein.
111. G. M. Whitesides and P. E. Laibinis, Langmuir **6**, 87 (1990).
112. J. F. Joanny and P. G. de Gennes, J. Chem. Phys. **81**, 552 (1984).
113. H. G. Tompkins, *A User's Guide to Ellipsometry* (Academic Press, New York, 1993).
114. H. G. Tompkins and W. A. McGahan, *Spectroscopic Ellipsometry and Reflectometry: A User's Guide* (John Wiley & Sons, New York, 1999).
115. R. M. A. Azzam and N. M. Bashara, *Ellipsometry and Polarized Light* (North-Holland, Amsterdam, 1977).
116. M. P. Seah and D. Briggs, *Practical Surface Analysis: Volume 1: Auger and X-ray Photoelectron Spectroscopy, 2nd Ed.* (John Wiley and Sons, Chichester, England, 1990).
117. A.-S. Duwez, J. Electron Spectrosc. Relat. Phenom. **134**, 97 (2004).
118. Y. J. Chabal, Surf. Sci. Rep. **8**, 211-357 (1988).
119. C. A. Alves, E. L. Smith and M. D. Porter, J. Am. Chem. Soc. **114**, 1222 (1992).
120. K. Tamada, M. Hara, H. Sasabe and W. Knoll, Langmuir **13**, 1558 (1997).
121. K. Bierbaum, M. Grunze, A. A. Baski, L. F. Chi, W. Schrepp, and H. Fuchs, Langmuir **11**, 2143 (1995).
122. S. R. Wasserman, Y. T. Tao, and G. M. Whitesides, Langmuir **5**, 1074 (1989).
123. L. T. Zhuravlev, Langmuir **3**, 316 (1987).
124. C. L. A. Lamont and J. Wilkes, Langmuir **15**, 2037 (1999).
125. Note that use of the Si(2p) peak is complicated by the presence of emission from the single crystalline Si substrate, which shows the difficult-to-predict effects of elastic (photoelectron diffraction) scattering. See, for example, J. M. Hill, D. G. Royce, C. S. Fadley, L. F. Wagner and F. J. Grunthaner, Chem. Phys. Lett. **44**,

- 225 (1976); T. Katayama, H. Yamamoto, M. Ikeno, Y. Mashiko, S. Kawazu, and M. Umeno, *Jpn. J. Appl. Phys.* **38**, L770 (1999).
126. D. A. Tomalia, H. Baker, J. Dewald, M. Hall, G. Kallos, S. Martin, J. Roeck, J. Ryder, and P. Smith, *Polym. J.* **17**, 117 (1985).
  127. D. A. Tomalia, H. Baker, J. Dewald, M. Hall, G. Kallos, S. Martin, J. Roeck, J. Ryder, and P. Smith, *Macromolecules* **19**, 2466 (1986).
  128. M. Khan and W. T. S. Huck, *Macromolecules* **36**, 5088 (2003).
  129. A. Sunder, R. Hanselmann, H. Frey, and R. Mülhaupt, *Macromolecules* **32**, 4240 (1999).
  130. G. J. Kluth, M. M. Sung, and R. Maboudian, *Langmuir* **13**, 3775 (1997).
  131. M. Calistri-Yeh, E. J. Kramer, R. Sharma, W. Zhao, M. H. Rafailovich, J. Sokolov, and J. D. Brock, *Langmuir* **12**, 2747 (1996).
  132. N. Grassie and G. A. Perdomo Mendoza, *Polym. Degrad. Stab.* **9**, 155 (1984).
  133. K. J. Voorhees, S. F. Baugh, and D. N. Stevenson, *J. Anal. Appl. Pyrolysis* **30**, 47 (1994).
  134. M. M. Fares, J. Hacaloglu, and S. Suzer, *Eur. Polym. J.* **30**, 845 (1994).
  135. S. Han, C. Kim, and D. Kwon, *Polymer* **38**, 317 (1997).
  136. A. Choukourov, A. Grinevich, O. Polonskyi, J. Hanus, J. Kousal, D. Slavinska, and H. Biederman, *J. Phys. Chem. B* **113**, 2984 (2009).
  137. A. Dube, A. R. Chadeayne, M. Sharma, P. T. Wolczanski, J. R. Engstrom, *J. Am. Chem. Soc.* **127**, 14299 (2005).
  138. J. C. Ashley, *J. Electron Spectrosc. Relat. Phenom.* **28**, 177 (1982).
  139. S. Tanuma, C. J. Powell, and D. R. Penn, *Surf. Interface Anal.* **21**, 165 (1994).
  140. A. Jablonski and C. J. Powell, *J. Electron Spectrosc. Relat. Phenom.* **100**, 137 (1999).
  141. L.-Q. Xia, M. E. Jones, N. Maity, and J. R. Engstrom, *J. Vac. Sci. Technol. A* **13**, 2651 (1995).
  142. S. E. Roadman, N. Maity, J. E. Carter, and J. R. Engstrom, *J. Vac. Sci. Technol. A* **16**, 3423 (1998).

143. M. Beaudoin and S. L. Scott, *Organometallics* **20**, 237 (2001).
144. E. Langereis, S. B. S. Heil, M. C. M. van de Sanden, and W. M. M. Kessels, *Phys. Status Solidi C* **2**, 3958 (2005).
145. E. Langereis, S. B. S. Heil, M. C. M. van de Sanden, and W. M. M. Kessels, *J. Appl. Phys.* **100**, 023534 (2006).
146. M. A. Alam and M. L. Green, *J. Appl. Phys.* **94**, 3403 (2003).



## 4. Nucleation delay in atomic layer deposition on a thin organic layer and the role of reaction thermochemistry<sup>\*</sup>

### 4.1 Overview

ALD of a set of inorganic thin films on an interfacial organic layer has been examined, focusing on the existence of a delay in thin film nucleation and its dependence on the chemistry of each ALD reaction. The inorganic thin films examined were  $\text{Al}_2\text{O}_3$ ,  $\text{HfO}_2$ ,  $\text{Ta}_2\text{O}_5$ , and  $\text{TaN}_x$ , while the organic layer was a thin ( $\sim 5$  Å thick) film of poly(ethylene imine), or PEI, on  $\text{SiO}_2$ . The early stages ( $< 50$  ALD cycles) of inorganic thin film growth in each case have been characterized using a combination of surface-sensitive techniques including ellipsometry, x-ray photoelectron spectroscopy, and atomic force microscopy. PEI has the effect of attenuating growth to different degrees depending on the subsequently grown ALD thin film, leading to no attenuation of growth for  $\text{Al}_2\text{O}_3$ , but significant incubation periods, in increasing order, for  $\text{Ta}_2\text{O}_5$ ,  $\text{HfO}_2$  and  $\text{TaN}_x$ . Angle-resolved x-ray photoelectron spectroscopy of an  $\text{Al}_2\text{O}_3$  thin film deposited on  $\text{PEI}|\text{SiO}_2$  demonstrates that, in this case, the PEI thin film is buried between the  $\text{Al}_2\text{O}_3$  thin film and the  $\text{SiO}_2$  substrate, with no significant decrease in the density of nitrogen from the as deposited PEI film. Results from the  $\text{HfO}_2$  and the Ta-containing thin films indicate that the processes that lead to the attenuation of growth are associated mostly with the second half-cycle of ALD ( $\text{H}_2\text{O}$  or  $\text{NH}_3$  exposure). The length of the incubation time is found

---

<sup>\*</sup> K. J. Hughes and J. R. Engstrom, *under review at the time of dissertation submission*.

to correlate with both the total enthalpy change of the overall ALD reaction, as well as the net internal energy change of a single ligand exchange reaction representative of the second half of the ALD reaction. These results suggest that the reaction thermochemistry, and activation barriers for the reactions involved the ALD process play a key role in determining the length of the incubation period caused by PEI.

## 4.2. Introduction

Recent work has demonstrated the feasibility of the use of thin organic layers to control the early stages of inorganic thin film growth via atomic layer deposition (ALD) [1,2]. A focus of much of the early work has concerned the effects of the structure and chemistry of the organic layer on the resulting ALD thin film; namely by examining the effect of a variety of organic layers on a single ALD chemistry. For example, it has been shown that the density, type, and spatial arrangement of reactive functional groups in an organic layer are important factors that influence the early stages of growth and resulting morphology of  $\text{TiN}_x$  thin films grown by ALD [1]. In other work it has been shown that the effectiveness of n-alkyl self-assembled monolayers (SAMs) in blocking ALD growth correlates strongly with the density and uniformity of the SAM [2]. In addition, it has been observed that the ability of a given SAM to block growth also depends on the ALD chemistry: a higher “quality” SAM is required to effectively block deposition of  $\text{HfO}_2$  {using either  $\text{Hf}[\text{N}(\text{CH}_3)_2]$  or  $\text{HfCl}_4$  as the Hf precursor}, while lesser quality SAMs are effective to block the ALD growth of metals such as Ru and Pt [2-4]. In these cases, it has been suggested that the

differences in blocking efficiency of the SAM layers could be related to intrinsic reactivity differences of the metal-containing precursor with the residual -OH groups at the SAM/SiO<sub>2</sub> interface.

Relatively few studies have been conducted, in contrast, to examine directly the effect of a single type of organic layer on a variety of ALD processes representing different chemistries. In two separate studies, the ALD growth of Ir, Ru, Pt, ZrO<sub>2</sub> (PVP only), and Al<sub>2</sub>O<sub>3</sub> thin films were examined on relatively thick (~ 100 nm) spin cast polymer films of poly(methyl methacrylate) (PMMA) [5] and poly(vinyl pyrrolidone) (PVP) [6]. Here it was found that both polymers were effective as blocking layers for the ALD growth of the metallic thin films, but not for the oxide layers. The ALD growth of TiO<sub>2</sub> on spin cast (32-420 nm thick) PMMA polymer films has also been examined, in this case using three Ti precursors: Ti(OCH<sub>3</sub>)<sub>4</sub> [5], TiCl<sub>4</sub>, and Ti[OCH(CH<sub>3</sub>)<sub>2</sub>]<sub>4</sub> [7]. The ALD process using TiCl<sub>4</sub> led to significant TiO<sub>2</sub> deposition on PMMA, while no deposition was observed using either of the Ti-alkoxide precursors. Here it was speculated that reactivity differences between the precursors and the C=O functional group in PMMA, or possibly differences in diffusivity of the Ti precursors within the polymer may have contributed to the observed behavior [7].

Here a series of experiments are described which were used to examine the ALD of a variety of inorganic thin films on the same thin organic layer. We will seek to make connections between the effect that the organic layer has on each process, particularly on the kinetics of nucleation, and the chemistry of the ALD reactions. The inorganic thin films examined include Al<sub>2</sub>O<sub>3</sub>, HfO<sub>2</sub>, Ta<sub>2</sub>O<sub>5</sub>, and TaN<sub>x</sub>. Concerning the

organic layer, here ALD growth will be examined on an ultrathin ( $\sim 0.5$  nm thick) layer of an amine-functional polymer on  $\text{SiO}_2$ , namely branched poly(ethylene imine) (PEI). This type of layer can be distinguished from previous work on either SAMs ( $\sim 1$ -3 nm thick) [1-4] or polymer films deposited using spin-on processes ( $\sim 10$ 's-100's nm thick) [5-8]. First, PEI is water-soluble and can be deposited rather simply from aqueous solutions, which is not the case with most SAMs. Second, the behavior of polyelectrolytes such as PEI can be sensitive to the solvent pH and ionic strength. Such sensitivity can be exploited to selectively remove, re-dissolve or “erase” layers previously deposited by adjusting the pH beyond some critical value [9,10]. Similarly, the functional groups on polyelectrolytes can be exploited to promote preferential adsorption on selected areas of a substrate, based on the active sites present on the surface [11]. Third, and perhaps of most importance, polyelectrolytes can form smooth, uniform ultrathin (nm-scale thickness) films, which are bound to the underlying substrate via van der Waals, hydrogen bonding, and/or covalent bonding type interactions, while still retaining functional groups that can react with the ALD thin film precursors. It will be determined whether the presence of these reactive functional groups has an equal effect on subsequent ALD thin film growth for a variety of ALD chemistries, or whether additional factors come into play causing each ALD process to be affected differently.

### 4.3 Experimental Procedures

The experiments described here involve a sequence of steps beginning with preparation of the substrate ( $\text{SiO}_2$ ), formation and characterization of the interfacial organic layer (PEI), and finally ALD film growth and characterization. In more detail, first thin layers of  $\text{SiO}_2$  were grown on  $\text{Si}(100)$  substrates using wet chemical methods, forming a so-called chemical oxide with surface Si-OH density of  $\sim 5 \times 10^{14} \text{ cm}^{-2}$  [12-14]. Next, thin layers of PEI were deposited on the substrates in aqueous solution, and characterized using a variety of methods (*vide infra*). Substrates, both PEI/ $\text{SiO}_2$ / $\text{Si}(100)$ , as well as bare  $\text{SiO}_2$ / $\text{Si}(100)$  with no PEI, were loaded into an ALD chamber. The substrates were then heated and exposed to a set number of cycles (0-50) of a single ALD process. Following thin film growth, the samples were removed from the ALD chamber, and the thicknesses of the deposited thin films were measured using ellipsometry (Woollam VASE). In selected cases, samples were loaded into the UHV system described in Sec. 2.5 for analysis using XPS, in order to characterize film thickness, chemical composition and, in some cases, the spatial distribution of relevant elements in the direction normal to the surface. Selected samples were imaged using AFM to characterize the morphology of the deposited thin film.

X-ray reflectivity (XRR) measurements were conducted at the Cornell High Energy Synchrotron Source (CHESS). These measurements are described in more detail elsewhere [15]. To facilitate this method, the underlying substrate must be sufficiently smooth. Thus for these experiments a thermally (furnace oxidation) grown  $\text{SiO}_2$ / $\text{Si}(100)$  sample was employed, rather than one with a chemical oxide layer.

Al<sub>2</sub>O<sub>3</sub>, HfO<sub>2</sub>, Ta<sub>2</sub>O<sub>5</sub>, and TaN<sub>x</sub> films were deposited using an Oxford FlexAL ALD tool (Oxford Instruments, Oxfordshire, UK) located in the Cornell NanoScale Science and Technology Facility (CNF). Prior to initiating ALD cycles, samples were pre-heated to the deposition temperature in 200 mTorr of Ar for 3 min to maximize temperature uniformity during growth. Al<sub>2</sub>O<sub>3</sub> thin films were deposited using trimethylaluminum, Al(CH<sub>3</sub>)<sub>3</sub>, and H<sub>2</sub>O as co-reactants, Ar for the purge gas, and a substrate temperature of  $T_s \sim 210$  °C. (It should be noted that the temperature of the substrate was not measured directly, and as such the substrate temperatures quoted here are estimated based on temperature measurements taken close to the sample heater. The absolute temperatures given here are estimated to be accurate within  $\pm 20$  °C.) Using an analogous method, HfO<sub>2</sub> was formed using tetrakis(ethylmethyamido) hafnium, Hf[N(CH<sub>3</sub>)(C<sub>2</sub>H<sub>5</sub>)]<sub>4</sub>, and H<sub>2</sub>O, at a substrate temperature of  $\sim 180$  °C. The Ta<sub>2</sub>O<sub>5</sub> and TaN<sub>x</sub> thin films were formed using pentakis(dimethylamido) tantalum, Ta[N(CH<sub>3</sub>)<sub>2</sub>]<sub>5</sub>, and either H<sub>2</sub>O (for Ta<sub>2</sub>O<sub>5</sub>) or NH<sub>3</sub> (for TaN<sub>x</sub>) as a co-reactant, both at  $T_s \sim 230$  °C. Total cycle times ranged from 5.77 s to 37 s, and were optimized to ensure saturation of the surface in each half-cycle at steady-state growth conditions, and adequate purging between cycles. The parameters used for ALD, including total chamber pressure during the metallic precursor and coreactant dosing steps, are given in Table 4-1. The carrier gas flowrate given in Table 4-1 refers to the flowrate of Argon through the precursor vessel or “bubbler” during the dosing step. Note that the total chamber pressure during the metallic precursor dosing step represents contributions from the partial pressure of the metallic precursor and carrier gas (if used).

Process	Sample temperature	Metallic precursor dosing step				Coreactant dosing step			
		precursor identity	precursor vessel temperature	Carrier gas flowrate, sccm	chamber pressure (mTorr)	dose time (ms)	coreactant identity	chamber pressure (mTorr)	dose time (ms)
Al <sub>2</sub> O <sub>3</sub>	210 °C	Al(CH <sub>3</sub> ) <sub>3</sub>	30 °C	0 (direct draw)	80	20	H <sub>2</sub> O	80	250
HfO <sub>2</sub>	180 °C	Hf[N(CH <sub>3</sub> )(C <sub>2</sub> H <sub>5</sub> )] <sub>4</sub>	85 °C	250	80	400	H <sub>2</sub> O	45	20
Ta <sub>2</sub> O <sub>5</sub>	230 °C	Ta[N(CH <sub>3</sub> ) <sub>2</sub> ] <sub>5</sub>	85 °C	150	80	2000	H <sub>2</sub> O	80	2000
TaN <sub>x</sub>	230 °C	Ta[N(CH <sub>3</sub> ) <sub>2</sub> ] <sub>5</sub>	85 °C	150	80	2000	NH <sub>3</sub>	80	5000

**Table 4-1:** Parameters used in the Oxford FlexAL tool for the ALD of Al<sub>2</sub>O<sub>3</sub>, HfO<sub>2</sub>, Ta<sub>2</sub>O<sub>5</sub>, and TaN<sub>x</sub>.

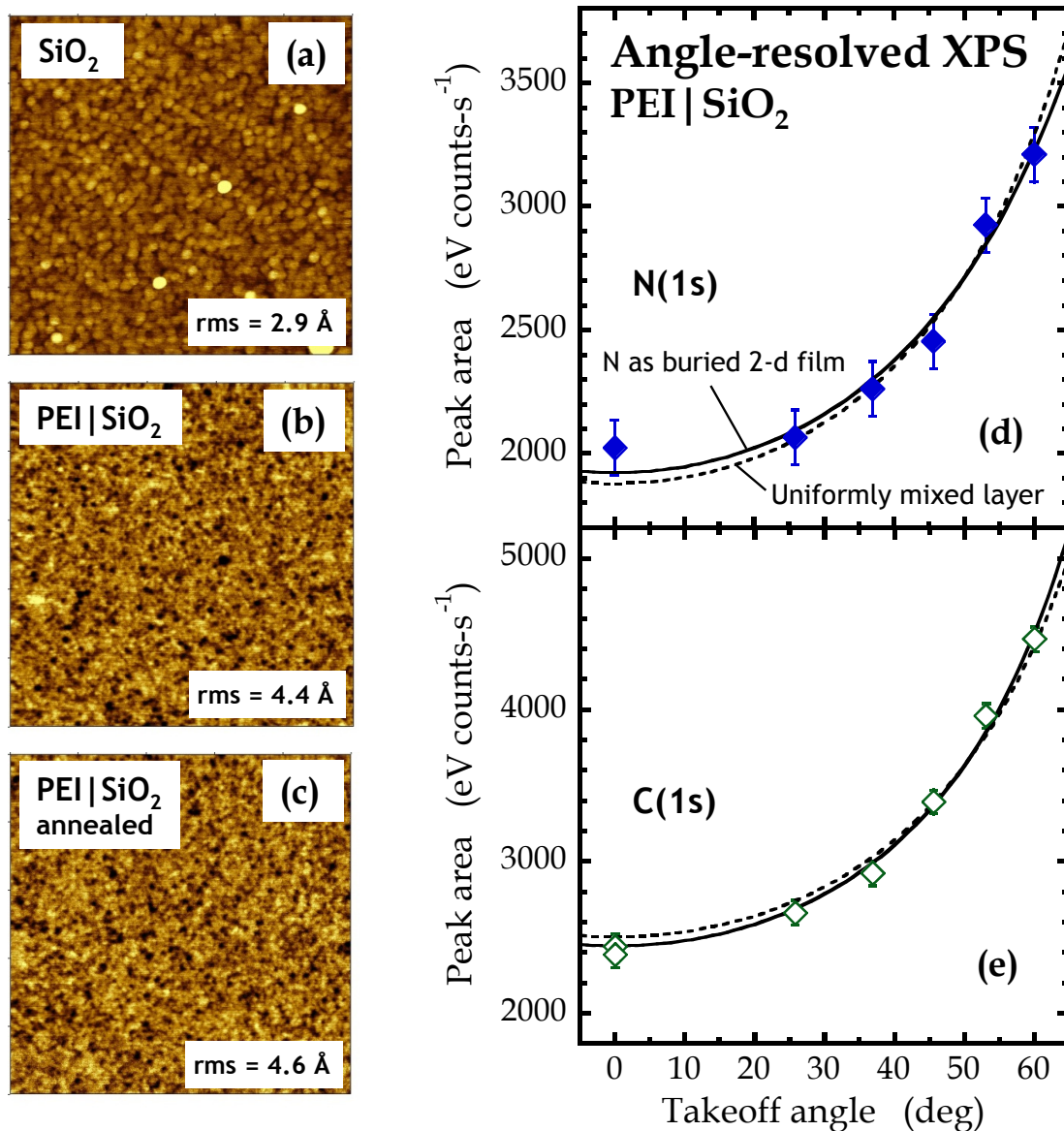


**Figure 4-1:** Atomic force micrographs of the (a) bare SiO<sub>2</sub> substrate, (b) as-deposited PEI thin film on SiO<sub>2</sub>, and (c) as-deposited PEI thin film after annealing at  $T_s = 210$  °C for 3 min in 200 mTorr of Ar. Area of the AFM images is  $1 \times 1 \mu\text{m}^2$ , with a height scale of 2.5 nm. Integrated areas of the (d) N(1s) and (e) C(1s) XPS features as a function of photoelectron takeoff angle for as-deposited PEI. The solid and dashed lines represent fits of the data to two models as described in the text.



## 4.4. Results

### 4.4.1. Poly(ethylene imine) thin film characterization

Subsequent to their formation from aqueous solution, the thin films of PEI were characterized using AFM, ellipsometry, XPS, and x-ray reflectivity. In Figs. 4-1(a-c) atomic force micrographs are displayed for (a) the bare SiO<sub>2</sub> substrate, (b) the as-deposited PEI thin film on SiO<sub>2</sub>, and (c) the as-deposited PEI thin film on SiO<sub>2</sub> after annealing at  $T_s = 210$  °C for 3 min in 200 mTorr of Ar in the ALD chamber. Concerning the latter, in all cases, prior to initiating ALD, samples were preheated at the deposition temperature for 3 min in 200 mTorr of Ar to maximize temperature uniformity during growth, so this case represents the state of the PEI/SiO<sub>2</sub> substrate at the start of the ALD process. The RMS roughness found from AFM is indicated in all cases. The SiO<sub>2</sub> substrate is smooth, with an RMS roughness of  $\sim 2.9$  Å. Adsorption of PEI results in modest changes in the morphology of the surface, with an increase in the RMS roughness (to 4.4 Å) that is comparable to the increases observed after the adsorption of SAMs and similar thin organic films on chemical SiO<sub>2</sub> [16-18]. It also appears that adsorption of PEI has modified the in-plane microstructure—the  $\sim 30$  nm dia. features on bare SiO<sub>2</sub> are absent and have been replaced by smaller and more grainy features, and features that may be pinholes are also apparent. Finally, from AFM no significant changes are observed in the surface morphology of the PEI/SiO<sub>2</sub> sample after annealing in the ALD chamber, suggesting that degradation or reorganization (e.g., creating patches of bare SiO<sub>2</sub>) has not occurred to a significant

extent. For example, the RMS surface roughness has changed from 4.4 to 4.6 Å, while spectral analysis reveals that the in-plane correlation length has changed from 42.7 to 46.4 nm, after annealing.

In Fig. 4-2 the reflected intensity as a function of the out-of-plane scattering vector,  $q_z$ , is plotted for a PEI thin film on a thermally oxidized Si(100) substrate. These data have been fit using a program based on Parratt formalism, and the surface is modeled as consisting of two uniform layers: the PEI and the bulk oxide. We see that the quality of the fit to the data is excellent, and from the fit we find that the thickness of this layer is  $d_{\text{PEI}} = 8.6 \pm 0.3 \text{ Å}$ , the electron density is  $n_{\text{el,PEI}} = 0.35 \pm 0.04 \text{ Å}^{-3}$ , and the root-mean-squared (RMS) roughness of the two interfaces is  $3.09 \pm 0.41 \text{ Å}$  (PEI|SiO<sub>2</sub>) and  $3.54 \pm 0.43 \text{ Å}$  (vacuum|PEI). Using of the number of electrons in the PEI monomer, the density of the N atoms in the PEI layer from XRR is  $n_{\text{N,PEI}} = 1.25 \pm 0.15 \times 10^{15} \text{ atoms-cm}^{-2}$ .

The thin film of PEI has also been characterized using XPS. For photoemission from the N(1s) core level a single symmetric peak characterized by a binding energy of  $400.8 \pm 0.3 \text{ eV}$  is observed. This value should be compared to those reported for neutral amines, including bulk PEI, which span the range of 398.6-399.1 eV [19-22], and the values reported for quaternary ammonium cations, in which the N atom carries a positive charge, of 401.3-402.5 eV [23-26]. The intermediate value measured for the nitrogen in the PEI thin film indicates that the N atoms likely carry a partial positive charge, due to hydrogen bonding or other type of interaction with the SiO<sub>2</sub> surface involving partial charging of the N atom.

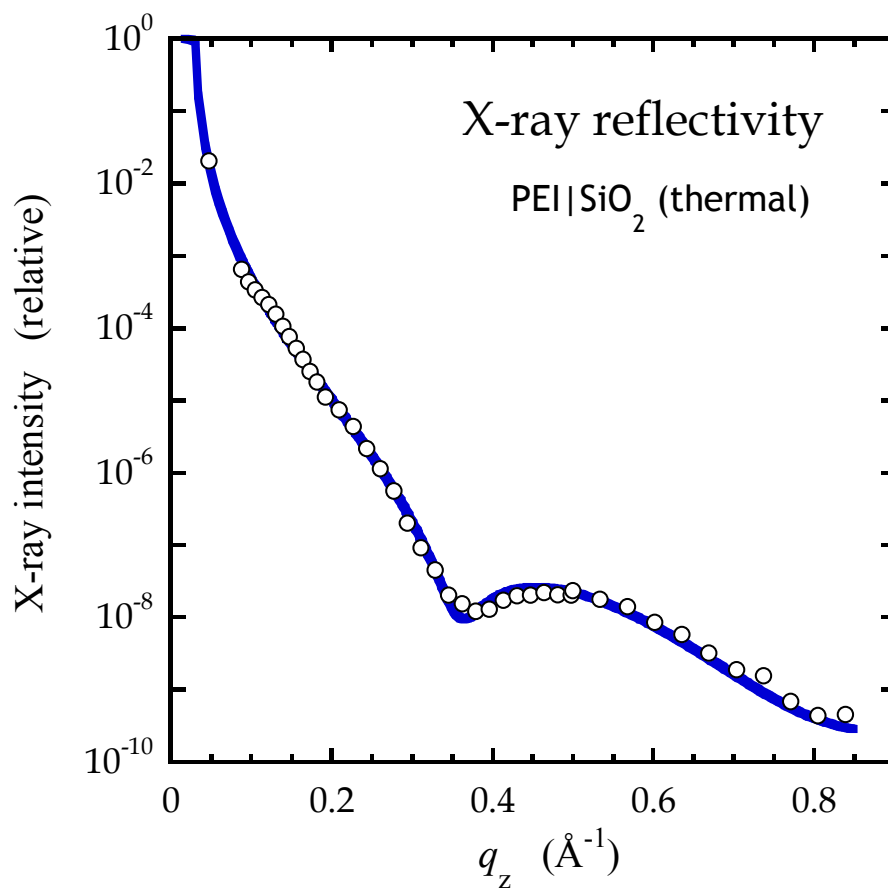


**Figure 4-2:** Reflected x-ray intensity as a function of the out-of-plane scattering vector,  $q_z$ , for a PEI thin film on a thermally oxidized Si(100) substrate. The solid line corresponds to a fit described in the text.

Spectroscopic ellipsometry indicates a thickness of  $4.3 \pm 0.7 \text{ \AA}$  for PEI on a SiO<sub>2</sub> (chemical oxide) thin film substrate. The thickness of the PEI thin film on SiO<sub>2</sub> (chemical oxide) was determined by measuring the difference in ellipsometric thickness between a bare SiO<sub>2</sub> thin film on Si(100) and the same substrate after PEI deposition (PEI/SiO<sub>2</sub>). Both the bare SiO<sub>2</sub> thin film and the combined PEI/SiO<sub>2</sub> layer were modeled using tabulated  $n$  and  $k$  values for native SiO<sub>2</sub>. Due to the ultrathin nature of the PEI layer, no attempt was made to directly measure its optical properties. However, by assuming a range of reasonable optical properties ( $n \sim 1.4$  to  $1.7$  at  $589 \text{ nm}$  with  $k = 0$ ), the calculated thickness of the PEI layer did not change by more than  $\sim 1 \text{ \AA}$ . To further probe the thickness of the PEI thin film, as well as the spatial distribution of the nitrogen and carbon atoms in the thin film, angle-resolved XPS (ARXPS) has been used. Figs. 4-1(d-e) show the intensity of the C(1s) and N(1s) XPS features as a function of takeoff angle for PEI/SiO<sub>2</sub>. Regarding the interpretation of this data, two simple cases are considered. In the first, the nitrogen atoms are bound to the SiO<sub>2</sub> surface, existing essentially in a 2-d arrangement, covered uniformly by the carbon containing portions of the PEI layer. Given this spatial arrangement, the intensity of the nitrogen peak  $I_N$  as a function of takeoff angle  $\theta$  would be  $I_N(\theta) = (I_0/\cos \theta)\exp[-d/(\lambda_{N(1s)} \cos \theta)]$ , where  $I_0$  is the unattenuated photoelectron intensity at normal takeoff,  $d$  is the thickness of the carbon containing overlayer, and  $\lambda_{N(1s)}$  is the attenuation length of N(1s) electrons through this carbon containing layer (See Figs. 2-3 through 2-5 for more detail on the fitting of ARXPS data). The intensity of the C(1s) peak as a function of takeoff angle in this case would be described by  $I_C(\theta) = I_0\{1 - \exp[-d/(\lambda_{C(1s)} \cos \theta)]\}$ . In a second possible spatial arrangement, the nitrogen and

carbon atoms are mixed uniformly throughout the thickness of the PEI thin film, and the function  $I(\theta) = I_0\{1-\exp[-d/(\lambda \cos \theta)]\}$  would describe both the N(1s) and C(1s) data sets, using an appropriate value for  $\lambda$  in each case. For the fits shown in Figs. 4-1(d-e), the N(1s) and C(1s) data have been fit simultaneously, using both methods. In order to reduce the number of variables in the fit, it was assumed that  $\lambda_{C(1s)}/\lambda_{N(1s)} = \{E[C(1s)]/E[N(1s)]\}^{1/2}$  [27], where  $E$  is the kinetic energy of the specified photoelectron. As can be seen in Figs. 4-1(d-e), both models fit the data well, however the model in which the N atoms are assumed to occupy a buried 2-d layer provides a slightly better fit, with a  $\sim 40\%$  lower squared error.

To extract a physical thickness  $d$  from both models, a value for  $\lambda$  is required. A reasonable value for  $\lambda$  can be obtained by using a correlation developed previously for thin organic films deposited on SiO<sub>2</sub> substrates [1], which is based on the density of valence electrons in the organic layer. A valence electron density of  $2.7 \times 10^{23} \text{ cm}^{-3}$  can be calculated based on the XRR measurements described above. Using this value and the correlation presented elsewhere [1] results in a value for  $\lambda_{N(1s)}$  of approximately 19.7 Å. The calculated physical thickness for the model assuming a buried 2-d layer of N is 3.6 Å, and 5.7 Å for the model which assumes both elements are mixed uniformly, with both values comparable to the thickness measured by ellipsometry of  $4.3 \pm 0.7$  Å. In any event, all methods point to the PEI polymer forming a thin, smooth and uniform layer.

The absolute density of N atoms in the layer can be calculated using data from XPS, provided an appropriate calibration standard is applied. These methods are described in detail elsewhere [1,12]. To calculate the atomic N density, the integrated

intensity for the N(1s) peak from PEI is compared to that for the Au(4f<sub>7/2</sub>) peak from an evaporated thin film of Au. Required to complete the calculation are the relative photoelectron cross-sections,  $\sigma_{Au}/\sigma_N = 5.53$  [28], analyzer transmission,  $T(E_{Au})/T(E_N) = (1170 \text{ eV}/853 \text{ eV})^{-1} = 0.73$ , the attenuation length of the Au(4f<sub>7/2</sub>) photoelectrons,  $\lambda_{Au} = 15.5 \text{ \AA}$  [29], and the atomic density of Au,  $N_{Au} = 5.90 \times 10^{22} \text{ cm}^{-3}$  [30]. The expected photoelectron attenuation effects given the location of the N atoms must also be accounted for, which can be done using the models described above. Using this method results in calculated surface densities for N of  $n_{N,PEI} = 6.0 \times 10^{14} \text{ atoms-cm}^{-2}$  and  $5.7 \times 10^{14} \text{ atoms-cm}^{-2}$ , assuming that the N atoms are buried as a 2-d monolayer, or mixed uniformly with C in the thin film respectively. Given the assumptions made in this analysis, an uncertainty of  $\pm 30\%$  in the absolute intensities calculated from XPS is estimated. XP spectra collected after annealing PEI films at 230 °C for 3 min at 200 mTorr Ar in the ALD chamber indicated a decrease in the total N atomic density of  $\sim 15\%$  due to thermal decomposition, with no change in the PEI thickness by ARXPS within statistical uncertainty.

#### 4.4.2. ALD of Al<sub>2</sub>O<sub>3</sub> on SiO<sub>2</sub> and PEI|SiO<sub>2</sub>

The first case considered is the ALD growth of Al<sub>2</sub>O<sub>3</sub> thin films using trimethylaluminum, Al(CH<sub>3</sub>)<sub>3</sub>, and H<sub>2</sub>O as co-reactants, and Ar for the purge gas, at a substrate temperature of  $T_s = 210 \text{ }^\circ\text{C}$ . Here the exposure sequence, Al(CH<sub>3</sub>)<sub>3</sub>|Ar|H<sub>2</sub>O|Ar was 20 ms|1.5 s|250 ms|4 s. Fig. 4-3(a) displays the thicknesses of Al<sub>2</sub>O<sub>3</sub> thin films deposited on unmodified SiO<sub>2</sub> and PEI|SiO<sub>2</sub> as a function of the

number of ALD cycles, determined from spectroscopic ellipsometry. As can be seen, the presence of PEI does not induce a measurable change in thickness at a given number of cycles. As a complement to ellipsometry, (*ex situ*) XPS data of the Al(2p) feature has been collected for 20 ALD cycles on both unmodified SiO<sub>2</sub> and PEI|SiO<sub>2</sub>, shown in Fig. 4-3(b). Here, and elsewhere in this chapter, the binding energy scale was corrected for substrate charging effects using the position of the Si<sup>(0)</sup>(2p) peak from the underlying Si(100) substrate, where its binding energy was set to  $99.5 \pm 0.2$  eV. The results from XPS are consistent with the ellipsometric measurements, with approximately the same signal intensity (within 13%) for 20 ALD cycles on unmodified SiO<sub>2</sub> and PEI|SiO<sub>2</sub>.

We have also examined the morphology of the Al<sub>2</sub>O<sub>3</sub> films deposited on SiO<sub>2</sub> and PEI|SiO<sub>2</sub> using atomic force microscopy, as shown in Fig. 4-4. The RMS roughness obtained from a series of micrographs on the two surfaces is shown as a function of film thickness (from ellipsometry) in Fig. 4-5. As can be seen, the vacuum|Al<sub>2</sub>O<sub>3</sub> interface is quite smooth for both substrates, with RMS roughness of  $\sim 3$  Å for all films analyzed (0 to  $\sim 40$  Å in thickness), which is consistent with ideal ALD growth. A close examination of the AF micrograph representing 10 cycles of Al<sub>2</sub>O<sub>3</sub> ALD on PEI|SiO<sub>2</sub> suggests the presence of pinholes or similar features in the film, which may indicate a regions with low nucleation site density. However, caution should be used in interpreting this result, as similar features were not observed in other micrographs in this series. XP spectra from the N(1s) region for as-deposited PEI|SiO<sub>2</sub>, and for 20 cycles Al<sub>2</sub>O<sub>3</sub> on PEI|SiO<sub>2</sub> are shown in Fig. 4-6.

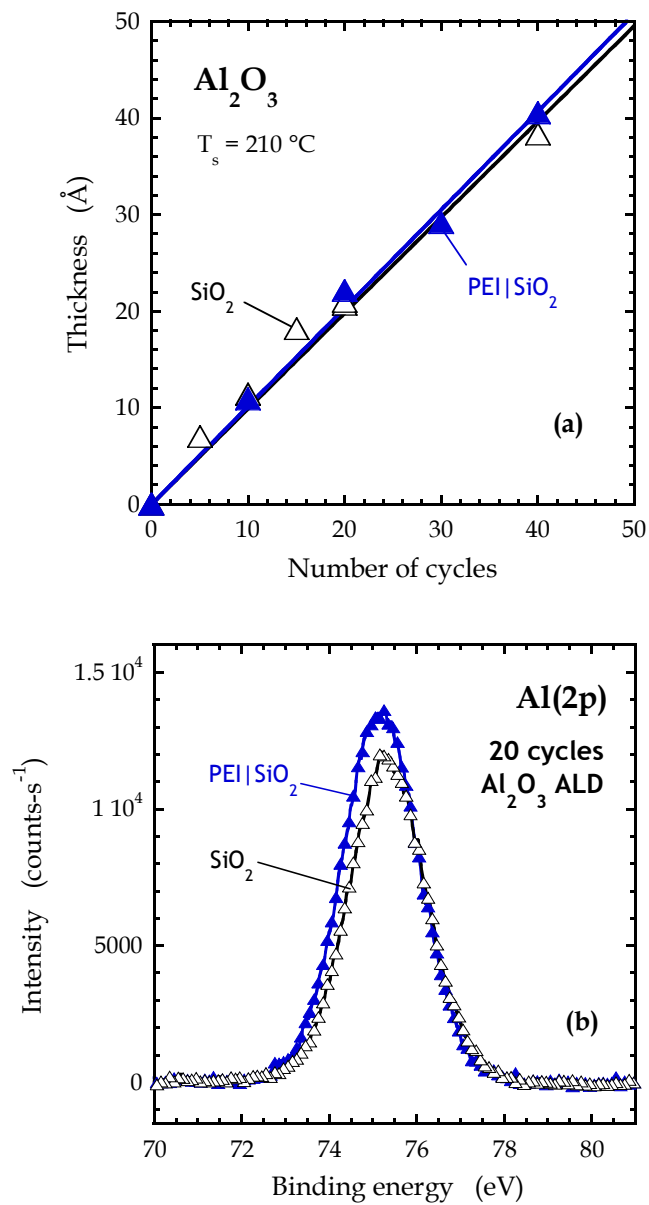


**Figure 4-3:** (a)  $\text{Al}_2\text{O}_3$  film thickness as a function of ALD cycles on an unmodified  $\text{SiO}_2$  substrate (open symbols) and on  $\text{PEI/SiO}_2$  (filled). (b) X-ray photoelectron spectra of the  $\text{Al}(2p)$  region for 20 cycles of  $\text{Al}_2\text{O}_3$  ALD on  $\text{SiO}_2$  and  $\text{PEI/SiO}_2$ .



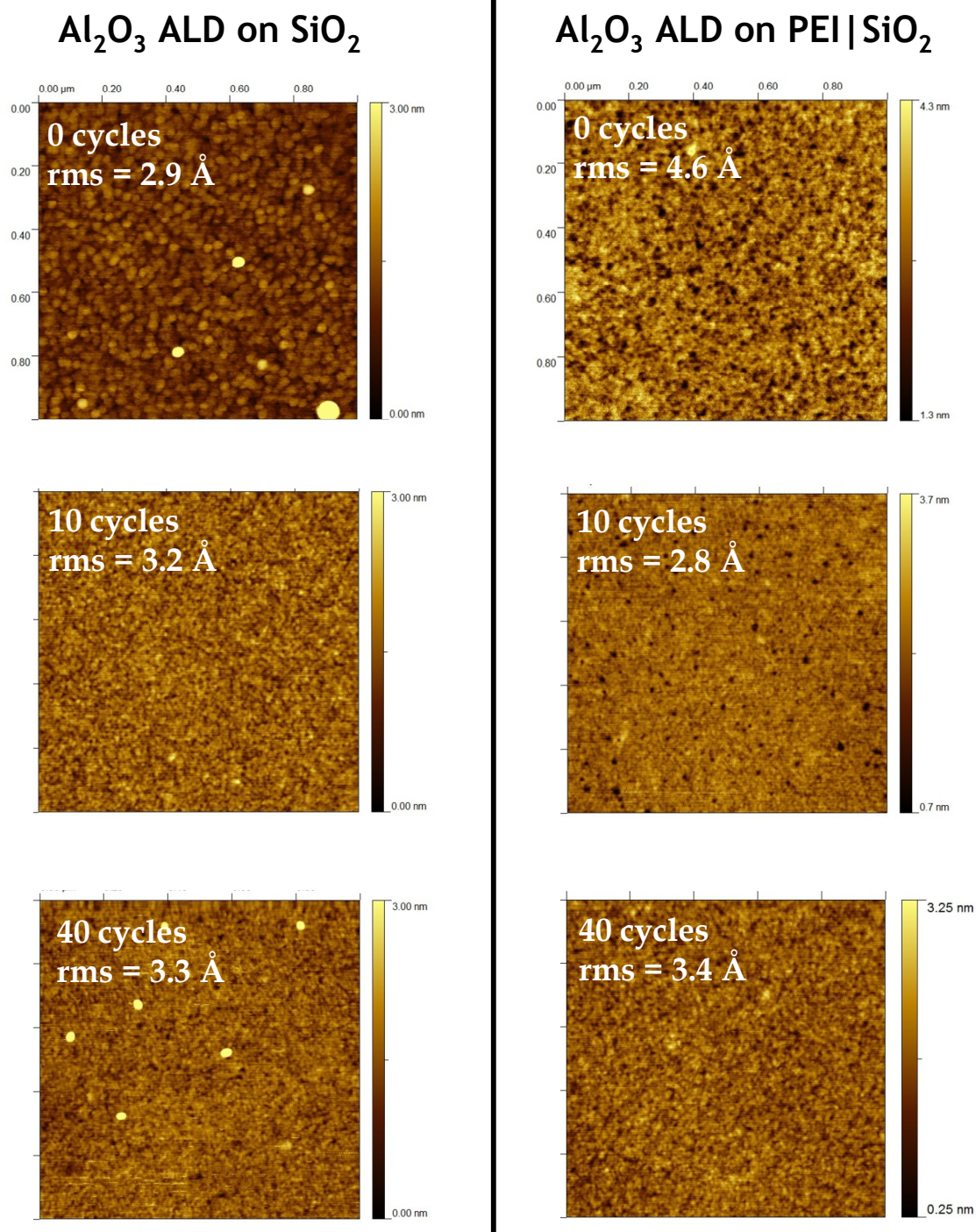


**Figure 4-4:** Atomic force micrographs of  $\text{Al}_2\text{O}_3$  films deposited on unmodified  $\text{SiO}_2$  and  $\text{PEI}|\text{SiO}_2$ . Images are  $1 \times 1 \mu\text{m}^2$ , with a vertical range of 3 nm. RMS roughness values obtained from analysis of the images is also shown.

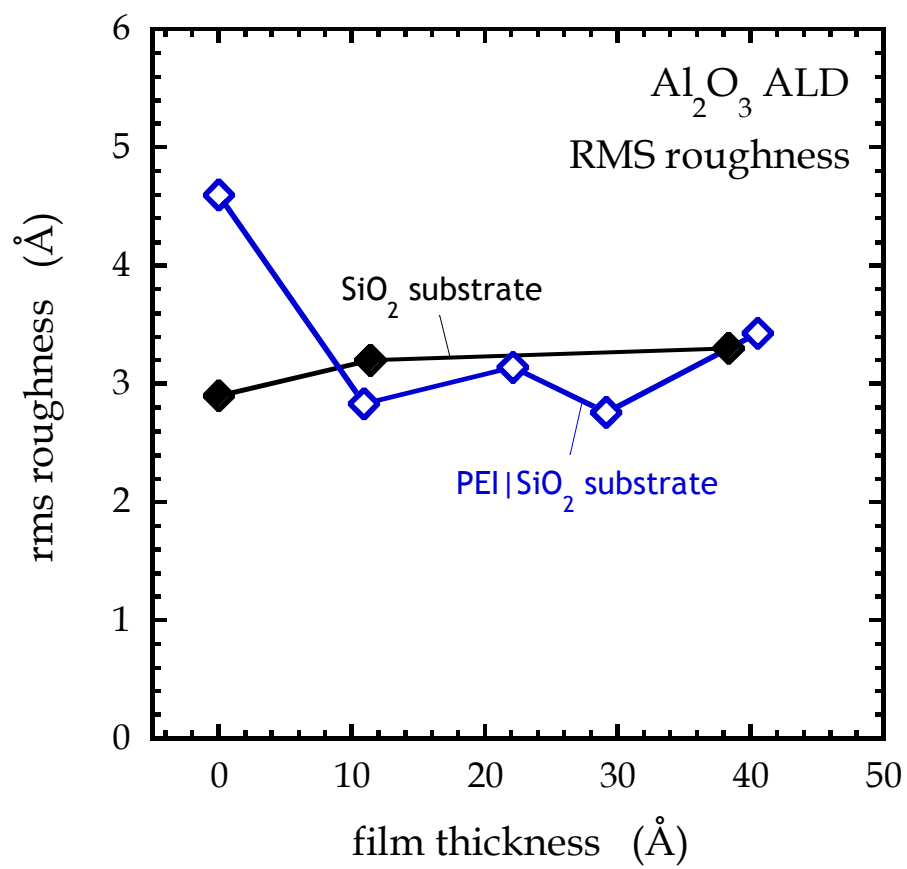


**Figure 4-5:** RMS roughness of  $\text{Al}_2\text{O}_3$  films deposited on unmodified  $\text{SiO}_2$  and PEI/ $\text{SiO}_2$ .

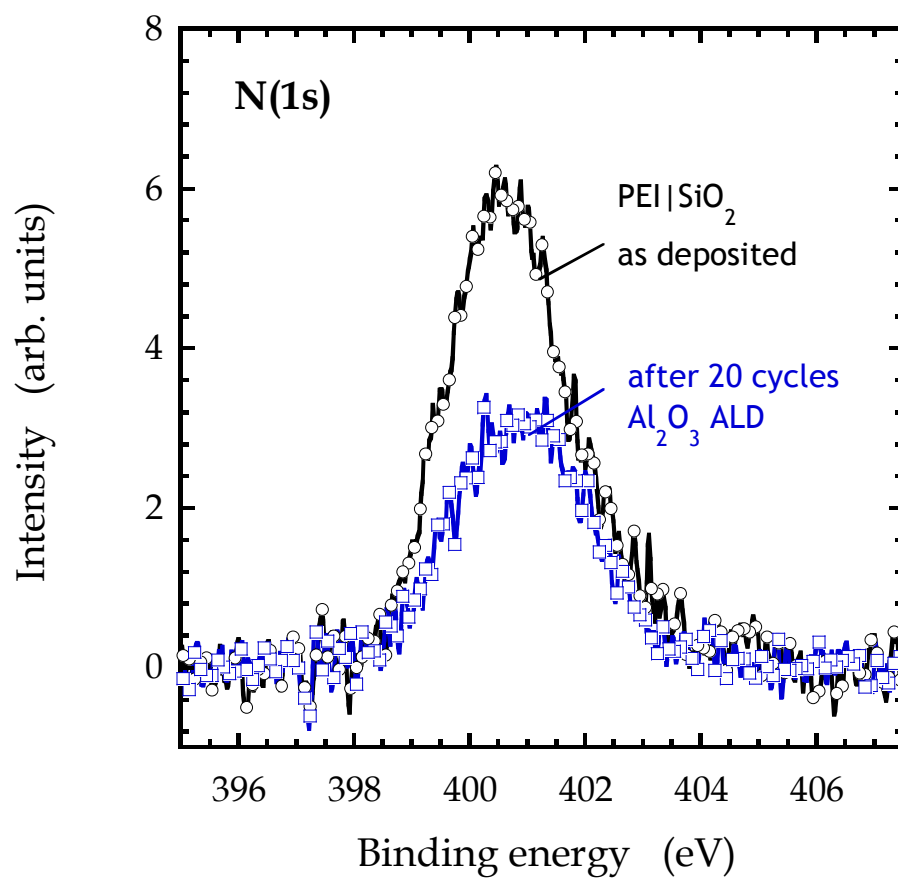


**Figure 4-6:** X-ray photoelectron spectra of the N(1s) region for as-deposited PEI on SiO<sub>2</sub> and for 20 cycles of Al<sub>2</sub>O<sub>3</sub> ALD on PEI|SiO<sub>2</sub>.

A significant N(1s) signal is measured for 20 cycles of Al<sub>2</sub>O<sub>3</sub> ALD on PEI/SiO<sub>2</sub>, which indicates that PEI, or a remnant of PEI, is still present in the near-surface region, as the only plausible source of N in the thin film structure is PEI. Furthermore, the peak binding energy measured for the N(1s) feature has changed only slightly, shifting from 400.7 eV to 400.9 eV, with no new peaks appearing in the spectrum, which indicates very little change in the chemical binding environment in the N atoms in PEI. Formation of a bulk-like, stoichiometric AlN, for example, would lead to the appearance of an N(1s) peak at a binding energy of 397.3 eV [31]), which is clearly not observed. The formation of species such as  $-(O)_2-Al-NR-$  remains a possibility, however.

To further quantify issues concerning the “fate” of the PEI, angle-resolved XPS (ARXPS) was conducted to determine the spatial location of the nitrogen atoms with respect to the top surface of the Al<sub>2</sub>O<sub>3</sub>. There are a handful of likely possibilities concerning the fate of the PEI: it could be (i) “buried” largely intact; (ii) incorporated in the Al<sub>2</sub>O<sub>3</sub> thin film (with likely decomposition of the PEI); (iii) completely decomposed and removed; or (iv) displaced to the surface, e.g., as a surfactant. These cases are presented schematically in Fig. 4-7. First the third possibility can be excluded as significant amounts of N are detected after Al<sub>2</sub>O<sub>3</sub> ALD. Possibilities (i) and (iv) can be easily distinguished in ARXPS [1], whereas possibility (ii) may be more difficult to quantify, but may be described in ARXPS as a weighted sum of (i) and (iv). Fig. 4-8 shows a plot of results from ARXPS for the (a) Al(2p), (b) N(1s), and (c) Si<sup>4+</sup>(2p) features for 20 cycles of Al<sub>2</sub>O<sub>3</sub> ALD on PEI/SiO<sub>2</sub>.

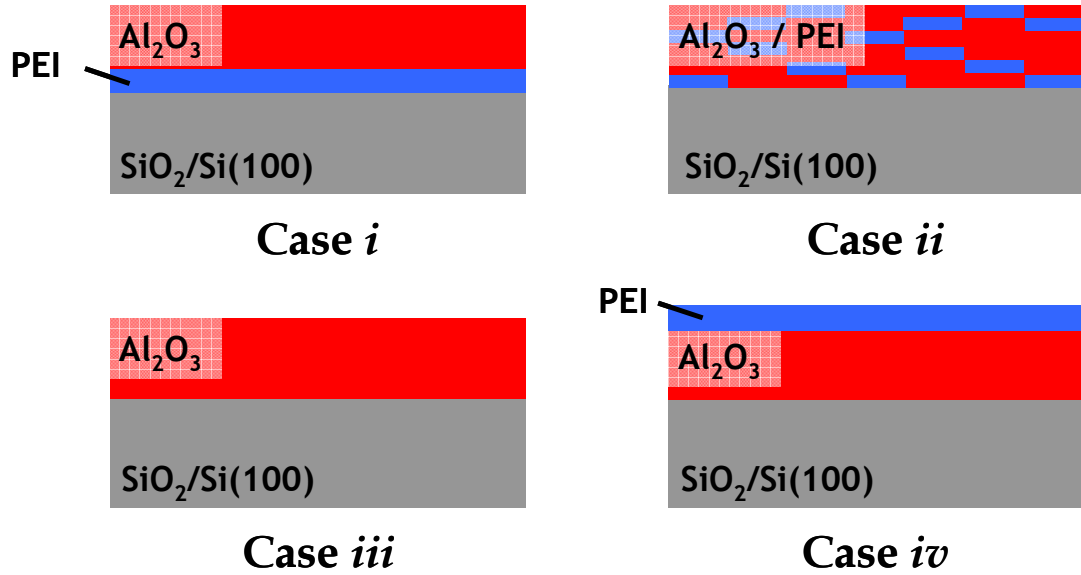


**Figure 4-7:** Four possible final structures of the thin film stack resulting from 20 cycles of  $\text{Al}_2\text{O}_3$  ALD on PEI/ $\text{SiO}_2$  shown in cross-section. In the four cases, the PEI thin film is (*i*) buried intact, (*ii*) incorporated uniformly in the  $\text{Al}_2\text{O}_3$  thin film, (*iii*) completely decomposed and removed, and (*iv*) displaced to the surface.

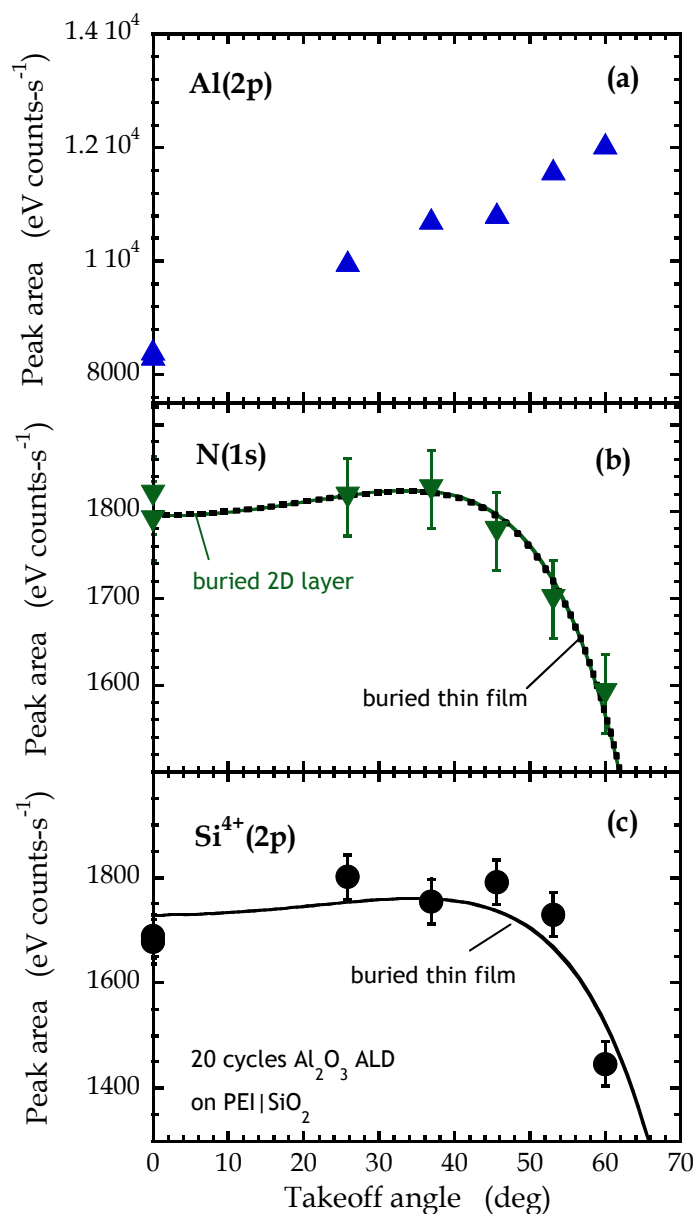


**Figure 4-8:** Integrated areas of the (a) Al(2p), (b) N(1s), and (c) Si<sup>4+</sup>(2p) XPS features as a function of takeoff angle for 20 cycles Al<sub>2</sub>O<sub>3</sub> ALD on PEI|SiO<sub>2</sub>. In (b), the (green) solid line corresponds to a model in which the N atoms exist in a 2-d layer buried at a uniform depth. The (black) dotted line represents a fit to a buried thin film model, in which N is assumed to exist in a layer of finite thickness buried by a thin film of Al<sub>2</sub>O<sub>3</sub>. The solid line shown in (c) corresponds to a model for a thin film of SiO<sub>2</sub> that is covered uniformly by a layer of Al<sub>2</sub>O<sub>3</sub> and PEI.

Concerning the latter, emission from the Si(100) single crystal substrate ( $\text{Si}^0$ ) is susceptible to photoelectron diffraction effects and has been excluded. Before describing the fits to the data some qualitative observations can be made. First, the Al(2p) intensity increases with increasing takeoff angle, consistent with the formation of a uniform thin film of  $\text{Al}_2\text{O}_3$ . In contrast, the intensities from the N(1s) and  $\text{Si}^{4+}$ (2p) features exhibit quite similar behavior, slightly increasing and then strongly decreasing with increasing takeoff angle. These results are consistent with layers being covered/buried uniformly by a deposited thin film, i.e., the  $\text{Al}_2\text{O}_3$ .

The results shown in Fig. 4-8 have been modeled using two approaches. First, the simplest model is to assume that the N atoms from PEI are present in an essentially 2-d layer, buried at a depth of  $d_{ML}$  from the vacuum interface. This is the 2-d model used above to fit the N(1s) data in Fig. 4-2(d) (solid line). A fit to this function is shown in Fig. 4-8(b) by the solid line, where a value of  $d_{ML}/\lambda_{\text{N}(1s)} = 0.83 \pm 0.01$  has been determined. By measuring the attenuation of the Si(2p) signal from the substrate as a function of thin film thickness from ellipsometry,  $\lambda_{\text{N}(1s)}$  was calculated to be  $20.6 \pm 0.3 \text{ \AA}$ , which compares well with the value of 18.7-19.2  $\text{\AA}$  obtained using direct calculations of inelastic mean free path based on optical data and empirical correlations published previously [32]. Fitting the ARXPS data for N(1s) to this simplest model, then, results in a value for the depth of the 2-d N layer of  $d_{ML} = 17.2 \pm 0.9 \text{ \AA}$ . This can be compared to the thickness of the  $\text{Al}_2\text{O}_3$  thin film measured using ellipsometry, which is  $22 \pm 1 \text{ \AA}$ . A thickness for the  $\text{Al}_2\text{O}_3$  layer can also be obtained using ARXPS of the  $\text{Si}^{4+}$ (2p) feature. Here the  $\text{SiO}_2$  film is modeled as a buried thin film with a finite thickness, where this thickness is measured for unmodified  $\text{SiO}_2$

prior to overlayer growth. Using ARXPS, we obtain a value of  $16.6 \pm 1.7 \text{ \AA}$  for the depth of the SiO<sub>2</sub> film below the vacuum|Al<sub>2</sub>O<sub>3</sub> interface. Using either this value, or the one obtained from ellipsometry, it can be concluded that after Al<sub>2</sub>O<sub>3</sub> deposition, the majority of the N from PEI resides near the SiO<sub>2</sub> surface.

The ARXPS result shown in Fig. 4-8(b) clearly rules out case (iv) above, and also rules out the mixing of the N atoms in PEI and Al<sub>2</sub>O<sub>3</sub> across the entire thickness of the Al<sub>2</sub>O<sub>3</sub> layer, case (ii), as the resulting structures in both cases would exhibit an increase in the N(1s) signal with takeoff angle [similar to Al(2p), *cf.* Fig. 4-8(a)]. So the remaining possibilities include case (i), and a case that is intermediate between (i) and (ii), in which there is some mixing of the PEI and the Al<sub>2</sub>O<sub>3</sub> layer close to the SiO<sub>2</sub> surface. The plausibility of this case can be determined by fitting the N(1s) data to a buried thin film model [1], where the film stack is given by Al<sub>2</sub>O<sub>3</sub>|mixed-PEI-Al<sub>2</sub>O<sub>3</sub>|SiO<sub>2</sub>. Actually, this is the same model used to fit the Si<sup>4+</sup>(2p) data shown in Fig. 4-8(c). Unlike a fit to those data, where the thickness of the SiO<sub>2</sub> layer was known, while the overlayer thickness was not, here the thickness of the mixed PEI-Al<sub>2</sub>O<sub>3</sub> layer will be used as a parameter in the fit, while the result from ellipsometry (22 Å) will be fixed as the thickness of the combined Al<sub>2</sub>O<sub>3</sub>|mixed PEI-Al<sub>2</sub>O<sub>3</sub> layers. The attenuation effects (values of  $\lambda_{N(1s)}$ ) will assumed to be identical in pure Al<sub>2</sub>O<sub>3</sub> and the mixed PEI-Al<sub>2</sub>O<sub>3</sub> layer. Using this method results in a thickness for the mixed PEI-Al<sub>2</sub>O<sub>3</sub> layer of  $9 \pm 0.4 \text{ \AA}$ . Thus, for this model the N from the PEI is distributed in a layer  $\sim 13\text{-}22 \text{ \AA}$  from the surface, or at a mean depth of  $\sim 17.5 \text{ \AA}$ . This value can be compared to the depth found from the model assuming a 2-d layer, namely  $17.2 \pm 0.9 \text{ \AA}$ . In both cases, the fits to the data argue for most of the PEI being near the SiO<sub>2</sub> surface.



The analysis conducted in association with Fig. 4-8 has established an important fact—the PEI is effectively buried by the Al<sub>2</sub>O<sub>3</sub> ALD thin film. Next, we seek to quantify how much of the N in PEI remains after Al<sub>2</sub>O<sub>3</sub> deposition. To answer this question the results from Figs. 4-4 and 4-8 can be used to calculate the density of N atoms between the Al<sub>2</sub>O<sub>3</sub> thin film and the SiO<sub>2</sub> substrate after ALD. Similar to the calculation described above for the bare PEI thin film, and making appropriate corrections for photoelectron cross-sections, analyzer transmission, and attenuation lengths results in a calculated density of N atoms of  $(6.2 \pm 1.4) \times 10^{14} \text{ cm}^{-2}$ . This range of values represents the application of both models for the N from the PEI just discussed: the 2-d layer buried at a depth of  $\sim 17.2 \text{ \AA}$ , or as a (mixed) thin film of thickness  $9 \text{ \AA}$ , buried under a  $\sim 13 \text{ \AA}$  layer of Al<sub>2</sub>O<sub>3</sub>. The most important observation is that this density is within the experimental error for the N atom density calculated from XPS for the bare PEI thin film prior to ALD ( $\sim 5.7\text{-}6.0 \times 10^{14} \text{ cm}^{-2}$ ). Thus, it is concluded that a significant amount, and possibly all, of the N present in the PEI is retained between the Al<sub>2</sub>O<sub>3</sub> thin film and the SiO<sub>2</sub> surface.

While significant loss of N can be excluded, disruption of the bonding in the PEI by the growth of the Al<sub>2</sub>O<sub>3</sub> thin film is possible, however, and probably likely. Some reactions could lead to the breakage of C-C and/or C-N bonds in the PEI. Other reactions, particularly in the H<sub>2</sub>O cycle, for example, could lead to loss of C from the PEI. ARXPS of the C(1s) feature, which might address this issue, was not successful, unfortunately, with these samples, due to the presence of adventitious carbon on the Al<sub>2</sub>O<sub>3</sub> surface. It is possible that other techniques such as dynamic SIMS or high resolution STEM could shed light on this issue. From a chemical viewpoint, the

selective loss of the entire C content from the PEI, while complete retention of the N content, seems very unlikely, however, as both species can form gas phase reaction products. In any event, an extremely detailed description of the remnant PEI layer awaits the application and/or development of an appropriate elementally specific atomic scale probe.

#### 4.4.3. ALD of HfO<sub>2</sub> on SiO<sub>2</sub> and PEI/SiO<sub>2</sub>

The next system considered is the ALD growth of HfO<sub>2</sub> thin films using tetrakis(ethylmethyamido) hafnium, Hf[N(CH<sub>3</sub>)(C<sub>2</sub>H<sub>5</sub>)]<sub>4</sub>, and H<sub>2</sub>O as co-reactants, Ar for the purge gas, and a substrate temperature of 180 °C. Here the exposure sequence, Hf(NRR')<sub>4</sub>|Ar|H<sub>2</sub>O|Ar was 400 ms|4 s|20 ms|11.5 s. Fig. 4-9(a) shows the thicknesses of HfO<sub>2</sub> thin films deposited on unmodified SiO<sub>2</sub> and PEI/SiO<sub>2</sub> as a function of the number of ALD cycles. Here the thicknesses were measured using spectroscopic ellipsometry. On bare SiO<sub>2</sub>, HfO<sub>2</sub> grows linearly with the number of ALD cycles at a rate of 1.25 Å-cycle<sup>-1</sup>, close to the upper end of the range of 0.71 - 1.2 Å-cycle<sup>-1</sup> from previous reports for growth under similar conditions [33-37]. As with the Al<sub>2</sub>O<sub>3</sub> thin film growth series, *ex situ* XPS of the Hf(4d) feature was conducted as a complement to ellipsometry, as shown in Fig. 4-9(b). After 10 ALD cycles, the Hf(4d) intensity measured for the HfO<sub>2</sub> thin film deposited on unmodified SiO<sub>2</sub> exceeds the Hf intensity of the HfO<sub>2</sub> thin film deposited on PEI/SiO<sub>2</sub> by a factor of ~8, consistent with the thin film thicknesses measured by ellipsometry. Of most interest here, in contrast to the ALD of Al<sub>2</sub>O<sub>3</sub>, the growth of HfO<sub>2</sub> is clearly attenuated by the presence of PEI.

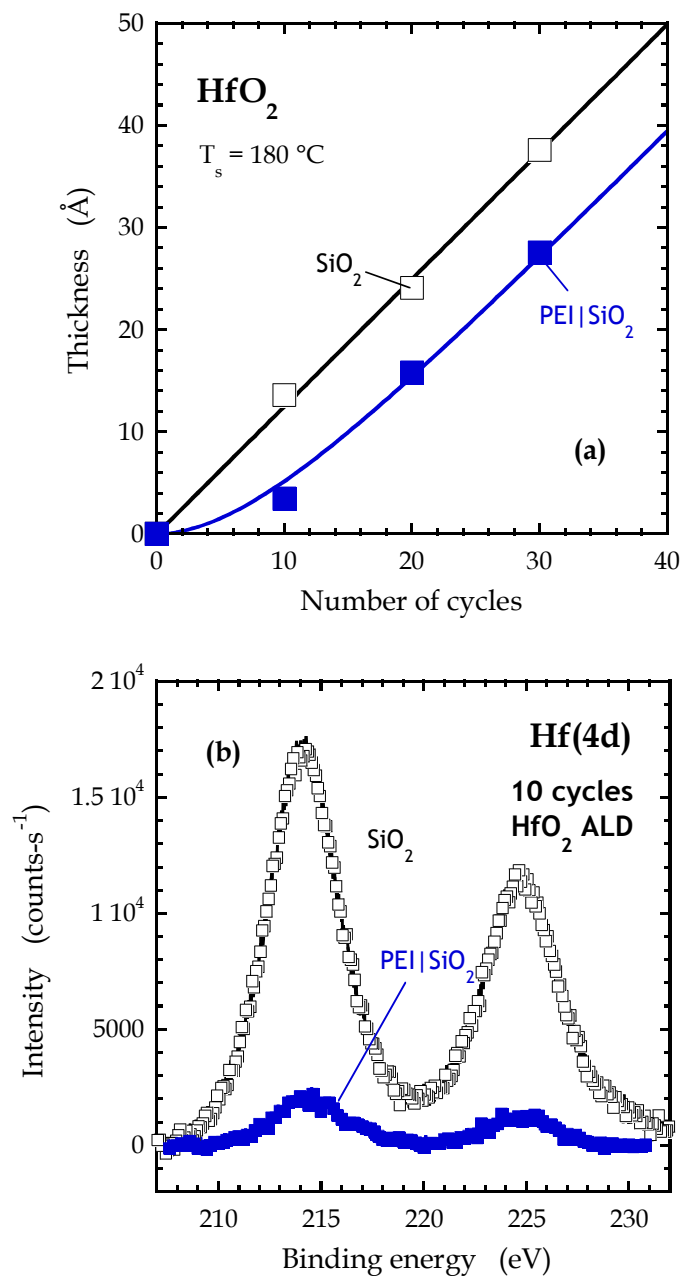


**Figure 4-9:** (a) HfO<sub>2</sub> film thickness as a function of ALD cycles on an unmodified SiO<sub>2</sub> substrate (open symbols) and on PEI/SiO<sub>2</sub> (filled). (b) X-ray photoelectron spectra of the Hf(4d) region for 10 cycles of HfO<sub>2</sub> ALD on SiO<sub>2</sub> and PEI/SiO<sub>2</sub>.

Specifically, growth per cycle is significantly reduced in the first  $\sim 10$  cycles, after which the growth rate approaches the steady-state rate of  $1.25 \text{ \AA-cycle}^{-1}$ . The data for ALD of  $\text{HfO}_2$  on  $\text{PEI/SiO}_2$  in Fig. 4-9(a) have been fit to the following form [16,17,38]:

$$D = D'_{\infty} \{n + m(1 - \alpha)[\exp(-n/m) - 1]\} \quad (4-1)$$

where  $D$  is the  $\text{HfO}_2$  film thickness,  $n$  is the number of ALD cycles,  $D'_{\infty}$  is the deposited thickness per cycle as  $n \rightarrow \infty$  (fixed to be the thickness deposited per cycle on bare  $\text{SiO}_2$ ), and  $\alpha$  and  $m$  are parameters. This form exhibits the following characteristics:  $D|_{n=0} = 0$ ;  $dD/dn|_{n=0} = \alpha D'_{\infty}$ , and  $dD/dn|_{n \rightarrow \infty} = D'_{\infty}$ . Regarding the physical interpretation of  $\alpha$  and  $m$ , the initial deposited thickness per cycle is a  $\alpha D'_{\infty}$ , while the growth rate approaches  $D'_{\infty}$  with an exponential decay constant of  $m$  cycles. Fitting the  $\text{HfO}_2$  on  $\text{PEI/SiO}_2$  results in  $\alpha \sim 10^{-5}$  and  $m = 8.4 \pm 4.3$ . Given the number of data points used in the fit, only the latter value ( $m$ ) is physically meaningful.

An important question to ask is what is occurring during the incubation period (also referred to as “incipient growth”) of  $m$  cycles of growth, i.e., up to  $\sim 10$  cycles. Fig. 4-10 presents results from (*ex situ*) XPS characterization of the early stages of ALD, namely after 1 and 10 cycles, focusing on the (a) N(1s) and (b) Hf(4d) features. In Fig. 4-10(a) we see that the N(1s) feature shows no major changes in the intensity or binding energy between 1 and 10 cycles, thus providing no evidence that the PEI has undergone any major chemical changes.

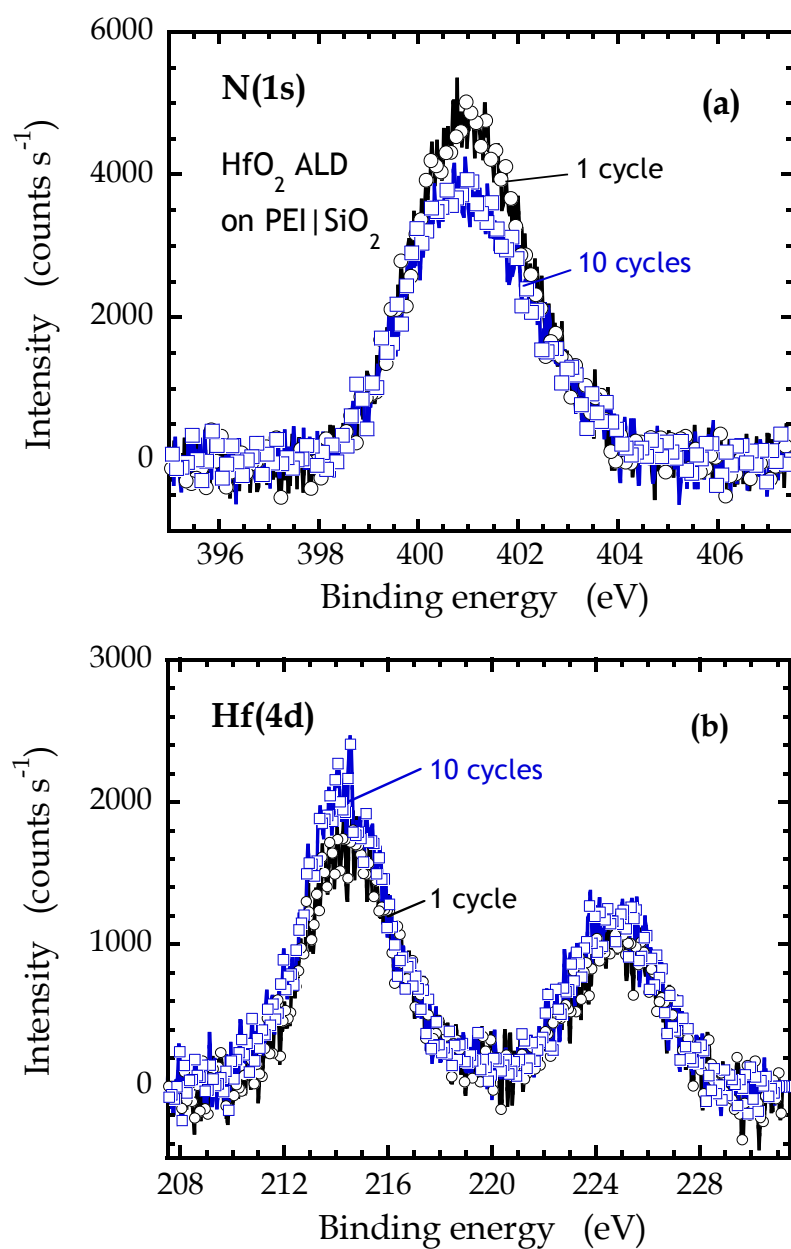


**Figure 4-10:** X-ray photoelectron spectra of the (a) N(1s) and (b) Hf(4d) regions for 1 and 10 cycles of HfO<sub>2</sub> ALD on PEI/SiO<sub>2</sub>.

Interestingly, as shown in Fig. 4-10(b), XPS of the Hf(4d) feature indicates that only a small amount of Hf has been added to the thin film from 1 to 10 cycles. For ALD of HfO<sub>2</sub> on SiO<sub>2</sub>, the integrated Hf(4d) intensity would be expected to increase by a factor of  $\sim 8$  from 1 to 10 cycles (taking photoelectron attenuation into account). Again using a Au calibration standard, and assuming that the Hf layer in the first cycle is well approximated by a 2-d thin film, results in a density of Hf atoms of  $1.6 \times 10^{14} \text{ cm}^{-2}$  after 1 cycle (with  $\pm 30\%$  uncertainty in the absolute density values from XPS, as discussed above). This value can be compared to values obtained by other investigators (same chemistry, but  $T_s = 250 \text{ }^\circ\text{C}$ ) where the density of Hf after 1 cycle on bare SiO<sub>2</sub> using Rutherford backscattering spectroscopy was reported to be  $\sim 1.75 \times 10^{14} \text{ cm}^{-2}$  [36]. These same investigators reported values of  $1.5\text{-}2.5 \times 10^{14} \text{ Hf atoms-cm}^{-2}$  added per cycle over the first 10 cycles. These latter values can be compared to what was calculated for the first 10 cycles of HfO<sub>2</sub> ALD on SiO<sub>2</sub>:  $(2.2 \pm 0.7) \times 10^{14} \text{ Hf atoms-cm}^{-2}\text{-cycle}^{-1}$ . Thus, it is evident that the PEI/SiO<sub>2</sub> surface takes up a significant fraction of the maximum or “ideal” amount of Hf in the first cycle, however, a much, much lower density is taken up in the subsequent 9 cycles. After this incubation period of  $\sim 10$  cycles, the HfO<sub>2</sub> thin film grows at the rate expected for the ideal process observed on SiO<sub>2</sub>. What remains curious at this point is the nature of the chemical transformations that occur between 1 and 10 cycles, and which seem to not be detected by *ex situ* XPS.

#### 4.4.4. ALD of Ta<sub>2</sub>O<sub>5</sub> and TaN<sub>x</sub> on SiO<sub>2</sub> and PEI|SiO<sub>2</sub>

In two final examples, we considered the ALD growth of Ta<sub>2</sub>O<sub>5</sub> and TaN<sub>x</sub> thin films using Ta[N(CH<sub>3</sub>)<sub>2</sub>]<sub>5</sub> either H<sub>2</sub>O (for Ta<sub>2</sub>O<sub>5</sub>) or NH<sub>3</sub> (for TaN<sub>x</sub>) as a co-reactant, Ar for the purge gas, and a  $T_s = 230$  °C. Here the exposure sequence for Ta(NR<sub>2</sub>)<sub>4</sub>|Ar|H<sub>2</sub>O|Ar was 2s|3s|2s|30s, and for Ta(NR<sub>2</sub>)<sub>4</sub>|Ar|NH<sub>3</sub>|Ar was 2s|3s|5s|5s. Fig. 4-11(a) displays the thicknesses of Ta<sub>2</sub>O<sub>5</sub> thin films deposited on unmodified SiO<sub>2</sub> and PEI|SiO<sub>2</sub> as a function of the number of ALD cycles. Here the thicknesses were measured using spectroscopic ellipsometry. As may be seen, the Ta<sub>2</sub>O<sub>5</sub> thin film grows on bare SiO<sub>2</sub> at a constant rate of 0.89 Å-cycle<sup>-1</sup>, a value near the upper end of the range of values reported previously of 0.65-0.85 Å-cycle<sup>-1</sup> [39,40]. Similar to the case of HfO<sub>2</sub>, the presence of PEI has the effect of attenuating the rate of growth in the early stages, although the effect is less pronounced. After this short incubation period, growth proceeds at a rate equal to that observed on bare SiO<sub>2</sub>. Here again the data have been fit to the model given in Eq. 4-1, resulting in values of  $\alpha = 0.41 \pm 0.26$  and  $m = 6.8 \pm 3.5$ . *Ex situ* XP spectra of the Ta(4d) region, shown in Fig. 4-11(c), also indicate a lower density of Ta deposited after 20 ALD cycles on PEI|SiO<sub>2</sub> as compared to unmodified SiO<sub>2</sub>, with the Ta(4d) intensity 22% lower for the Ta<sub>2</sub>O<sub>5</sub> thin film deposited on PEI|SiO<sub>2</sub>. Note here that the Ta(4d) feature was used, as opposed to the Ta(4f), because of possible overlap between the Ta(4f) and O(2s) peaks.

The ALD growth of TaN<sub>x</sub> on SiO<sub>2</sub> and PEI|SiO<sub>2</sub> is considered in Fig. 4-11(b). Similar to the other systems investigated here, on clean SiO<sub>2</sub> a linear thickness-number of ALD cycles relationship is observed, with no indication of an incubation period.

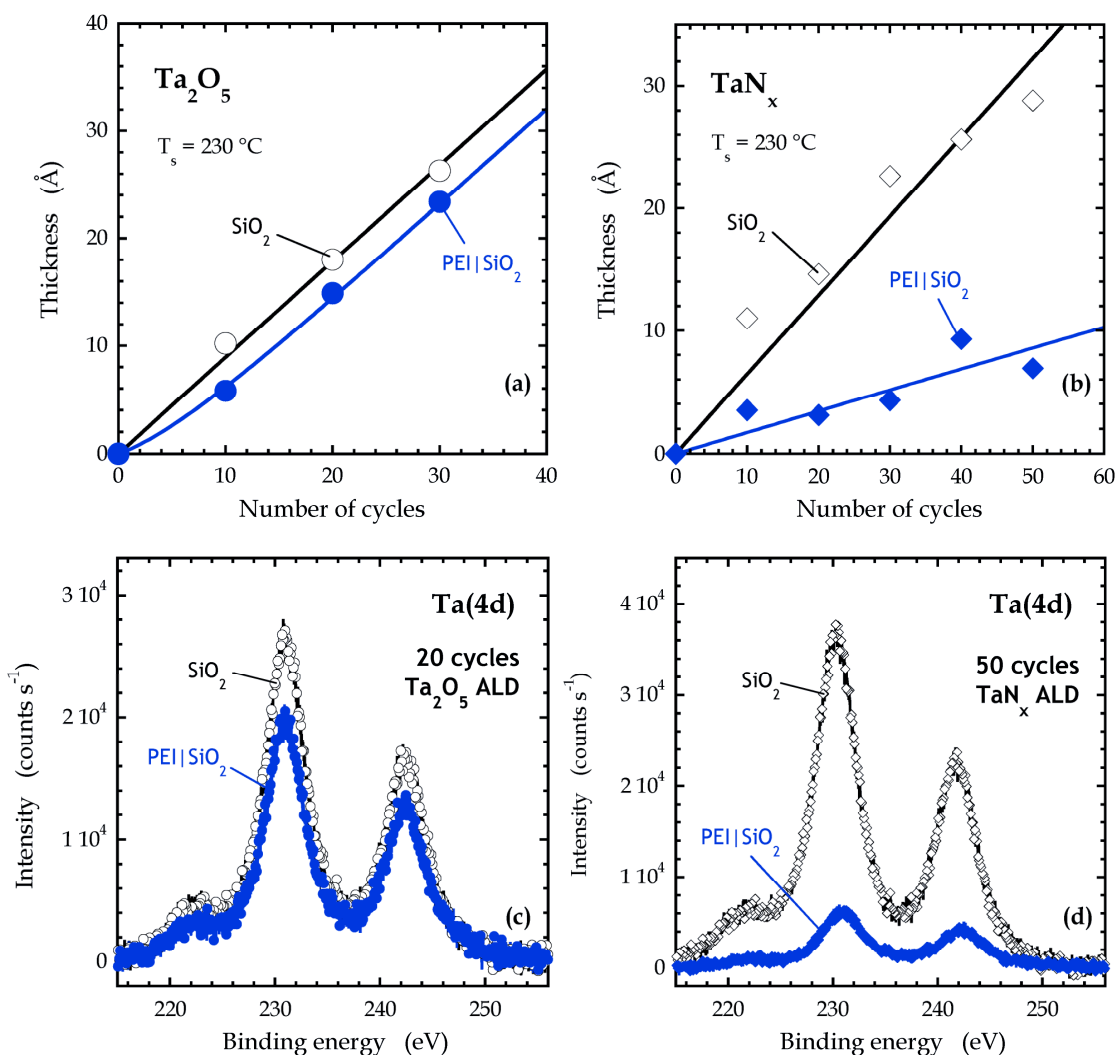


**Figure 4-11:** (a) Ta<sub>2</sub>O<sub>5</sub> and (b) TaN<sub>x</sub> film thickness as a function of ALD cycles on an unmodified SiO<sub>2</sub> substrate (open symbols) and on PEI|SiO<sub>2</sub> (filled), and XP spectra of the Ta(4d) region for (c) 20 cycles of Ta<sub>2</sub>O<sub>5</sub> and (d) 50 cycles TaN<sub>x</sub> ALD on SiO<sub>2</sub> and PEI|SiO<sub>2</sub>. All data corresponds to a substrate temperature of 230 °C.



A growth rate of  $0.64 \text{ \AA-cycle}^{-1}$  is observed on  $\text{SiO}_2$ , similar to the previously reported value of  $0.5 \text{ \AA-cycle}^{-1}$  using a substrate temperature of  $275 \text{ }^\circ\text{C}$  [41]. In contrast, the growth of  $\text{TaN}_x$  is strongly attenuated on the  $\text{PEI/SiO}_2$  surface, and even after 50 cycles of ALD there appears to be no strong evidence of achieving the “ideal” rate of growth observed on  $\text{SiO}_2$ . This conclusion is again supported by *ex situ* XP spectra, shown in Fig. 4-11(d), which indicates a much lower  $\text{Ta}(4d)$  intensity for the  $\text{TaN}_x$  thin film deposited on  $\text{PEI/SiO}_2$  after 50 cycles. Thickness vs. number of cycles was also measured using a temperature of  $255 \text{ }^\circ\text{C}$ , as shown in Fig. 4-12. Here the same trend is observed. Such an extended incubation period has been observed previously, for example work examining the growth of  $\text{TiN}_x$  thin films on  $-\text{CH}_3$  terminated SAMs [16,17]. Here, severely 3D growth was observed, as evidenced by *ex situ* AFM, where the  $\text{TiN}_x$  thin films did not appear to be continuous, but were 3D islands. In Fig. 4-13 presents two representative AF micrographs: in (a) for 10 cycles of  $\text{TaN}_x$  ALD on  $\text{SiO}_2$ ; and in (b) for 40 cycles of  $\text{TaN}_x$  ALD on  $\text{PEI/SiO}_2$ . The substrate temperature used during ALD of these films was  $255 \text{ }^\circ\text{C}$ . Based on ellipsometry these thin films should be of similar thickness, namely  $\sim 6 \text{ \AA}$ . As may be seen, the features are similar in both cases, and no indication of the formation of large 3D islands. The RMS surface roughness is similar in both cases:  $4.3 \text{ \AA}$  for 10 ALD cycles on  $\text{SiO}_2$ , and  $4.9 \text{ \AA}$  for 40 ALD cycles on  $\text{PEI/SiO}_2$ . The morphology for a much thicker ( $\sim 21 \text{ \AA}$ )  $\text{TaN}_x$  thin film on  $\text{SiO}_2$  is also similar to these two, with an RMS of  $4.6 \text{ \AA}$ . Similar behavior—significant attenuation of growth with only marginal increases in thin film roughness—has been observed for ALD  $\text{TiN}_x$  thin films grown on organic layers possessing  $-\text{NH}_2$  functionality [17].

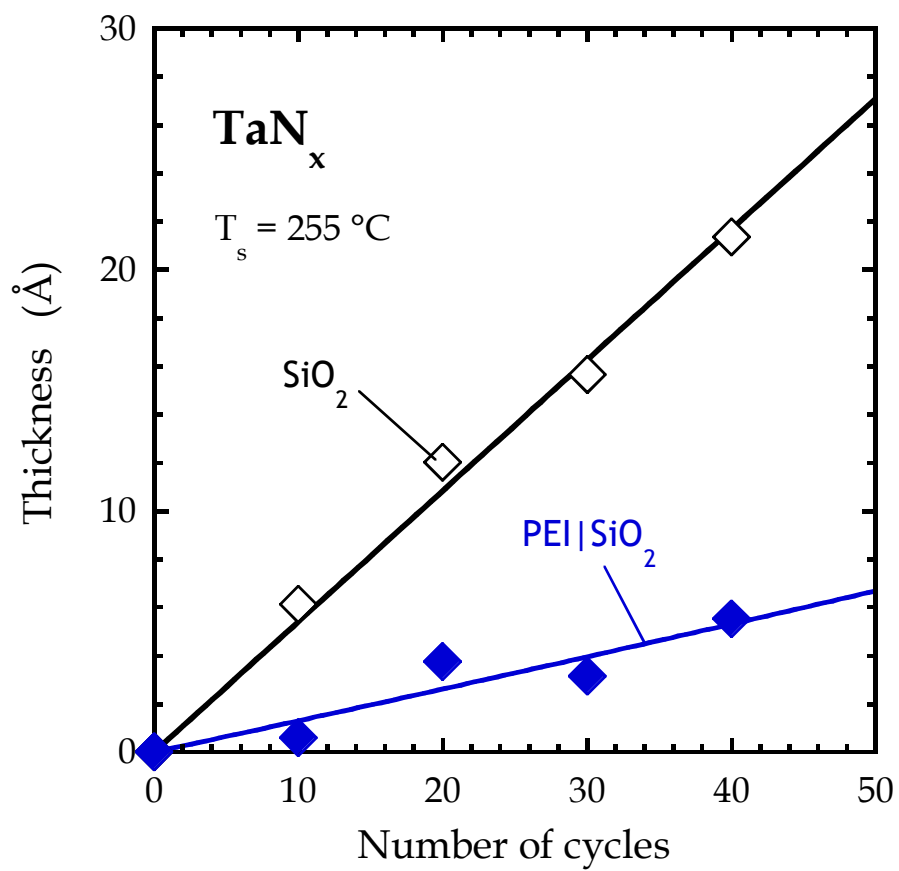


**Figure 4-12:**  $\text{TaN}_x$  film thickness as a function of ALD cycles on unmodified  $\text{SiO}_2$  (open symbols) and on  $\text{PEI/SiO}_2$  (filled), at a substrate temperature of  $255\text{ }^\circ\text{C}$ .

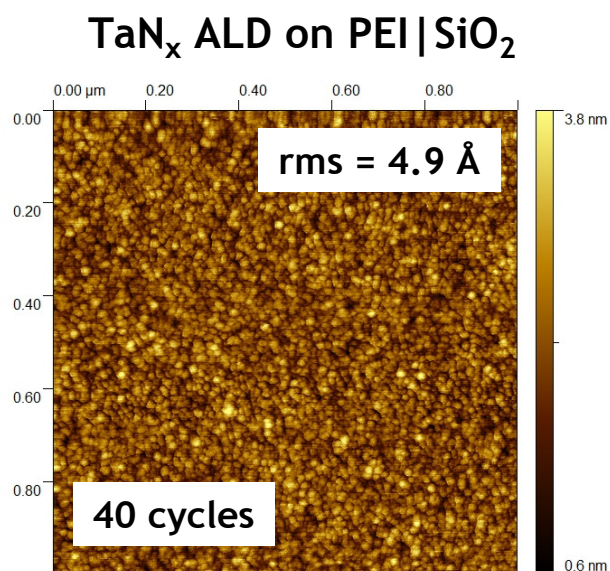
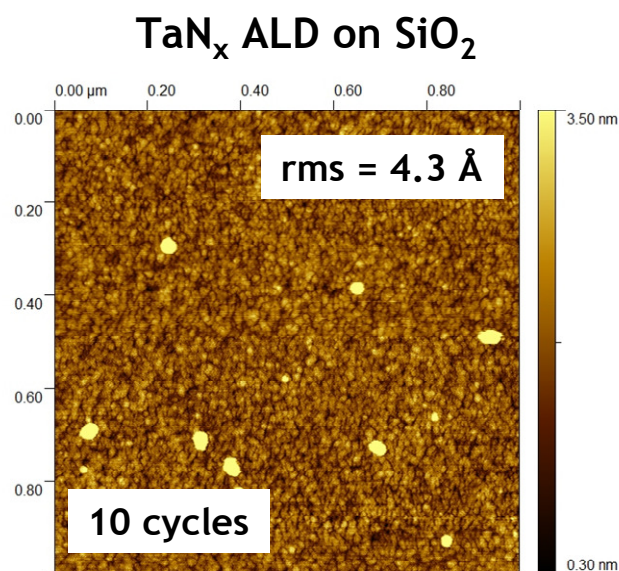


**Figure 4-13:** Atomic force micrographs of TaN<sub>x</sub> thin films formed by **(a)** 10 ALD cycles on an unmodified SiO<sub>2</sub> substrate and **(b)** 40 ALD cycles on PEI|SiO<sub>2</sub>. The thickness of the TaN<sub>x</sub> thin film is  $\sim 6$  Å in both cases.

Additional information concerning the behavior of the two Ta-based ALD processes can be obtained from XPS after a single cycle of ALD. XP spectra collected *ex situ* in the Ta(4d) region for 1 cycle of Ta<sub>2</sub>O<sub>5</sub> ALD on bare SiO<sub>2</sub> and PEI/SiO<sub>2</sub> are presented in Fig. 4-14(a). From the intensity of these Ta(4d) peaks, the density of Ta taken up in the first cycle on PEI/SiO<sub>2</sub> is calculated to be ~ 52% of that taken up on unmodified SiO<sub>2</sub>,  $(1.36 \pm 0.4) \times 10^{14} \text{ cm}^{-2}$  versus  $(2.61 \pm 0.8) \times 10^{14} \text{ cm}^{-2}$  (*cf.* value for  $\alpha = 0.41 \pm 0.26$ ). For the growth of TaN<sub>x</sub>, similar results are expected, and in Fig. 4-14(b) XP spectra collected *ex situ* in the Ta(4d) region for 1 cycle of TaN<sub>x</sub> ALD on bare SiO<sub>2</sub> are displayed. As may be seen the uptake of Ta is the same as is observed for Ta<sub>2</sub>O<sub>5</sub> ALD on SiO<sub>2</sub>, reflecting the fact that the first half-cycle is identical in both cases—exposure to Ta[N(CH<sub>3</sub>)]<sub>5</sub>.

Results from XPS in the N(1s) and Ta(4p<sub>3/2</sub>) regions for Ta<sub>2</sub>O<sub>5</sub> ALD on PEI/SiO<sub>2</sub> are considered in Fig. 4-15. A similar set of spectra for TaN<sub>x</sub> ALD are not considered due to the susceptibility of the TaN<sub>x</sub> thin films to oxidation during sample transfer in air for *ex situ* XPS. The 0 cycle thin film in this case represents approximately the surface just before ALD growth is initiated (i.e. The PEI/SiO<sub>2</sub> substrate was loaded into the ALD chamber, heated to the deposition temperature, then transferred in air for XPS). Two observations can be made from this data. First, the N(1s) binding energy, indicative of the chemical binding environment of the N atoms in the thin film, does not change significantly during ALD.

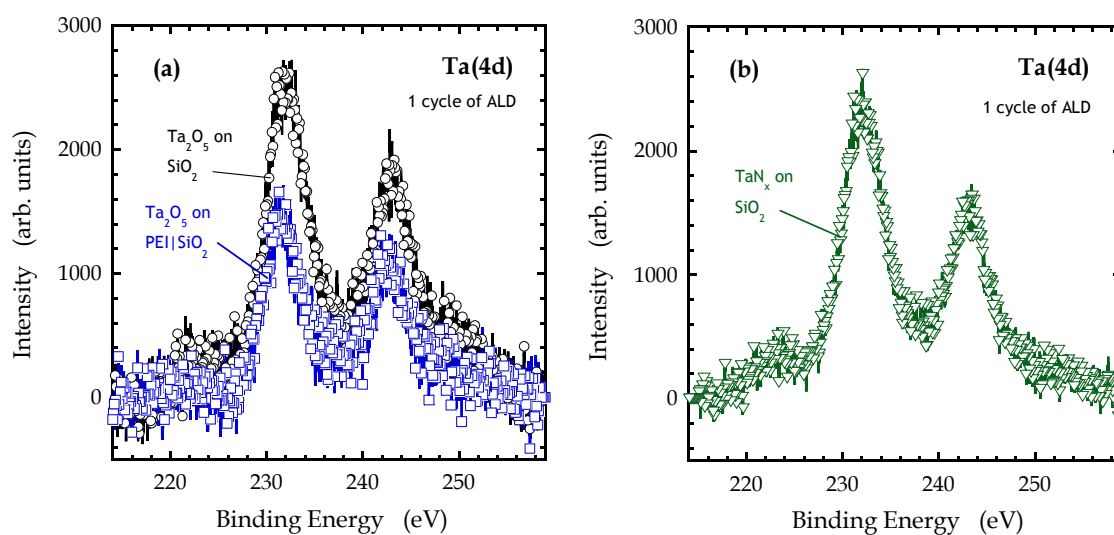


**Figure 4-14:** X-ray photoelectron spectra of the Ta(4d) region for **(a)** one cycle of Ta<sub>2</sub>O<sub>5</sub> ALD on unmodified SiO<sub>2</sub> and PEI/SiO<sub>2</sub>, and **(b)** one cycle of TaN<sub>x</sub> ALD on unmodified SiO<sub>2</sub>.

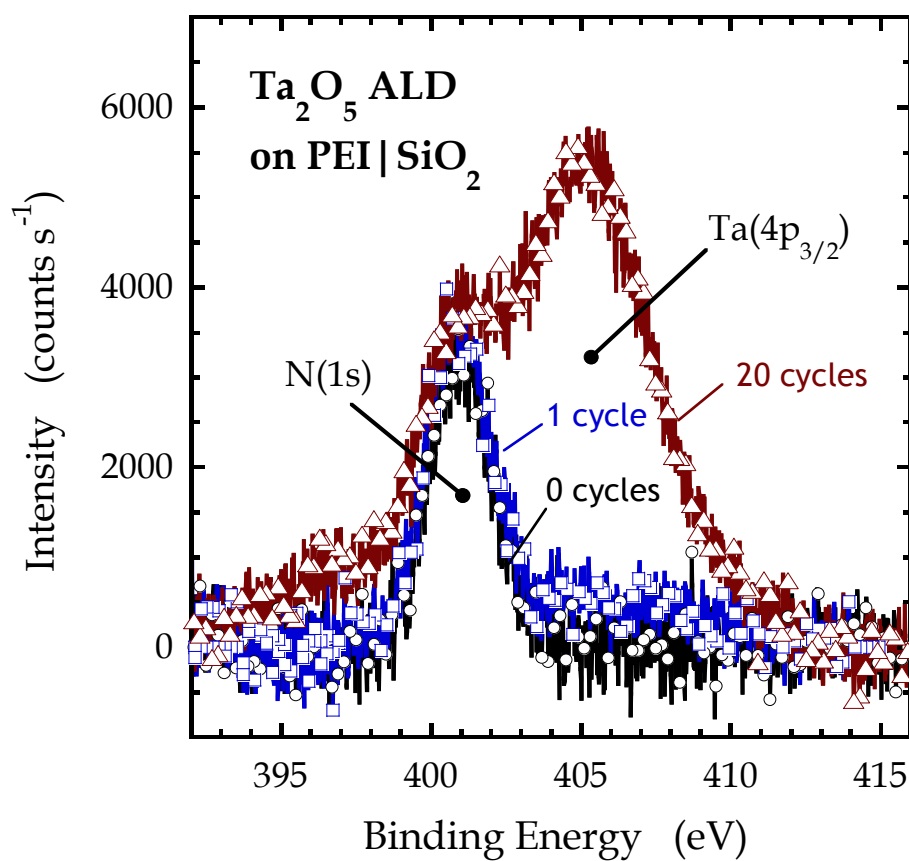


**Figure 4-15:** X-ray photoelectron spectra of the N(1s)/Ta(4p<sub>3/2</sub>) region for zero, one, and 20 cycles of Ta<sub>2</sub>O<sub>5</sub> ALD on PEI/SiO<sub>2</sub>.

What is the expectation? After the first half-cycle of ALD, one may expect that the Ta precursor is bound to the surface, probably forming Ta-N linkages via ligand exchange reactions with the  $\text{-NH}_{2-x}\text{R}_x$  groups in the PEI, or possibly Ta-O-Si bonds via ligand exchange reactions with Si-OH groups on the  $\text{SiO}_2$  surface. Following  $\text{H}_2\text{O}$  exposure, and/or air exposure before XPS, the chemisorbed Ta species is likely stripped of its  $\text{N}(\text{CH}_3)_2$  ligands, and these are replaced with -OH, or other oxygen containing ligands. Furthermore, some fraction of the N present in PEI that is interacting with the  $\text{SiO}_2$  surface, or has not reacted with  $\text{Ta}[\text{N}(\text{CH}_3)_2]_5$ , may remain unchanged. Thus the minimal change observed in the N(1s) feature is not surprising. A second observation is that the size of the N(1s) feature is largely unchanged for 0 and 1 cycles of ALD. This is consistent with the mechanism just described, where the Ta precursor chemisorbs in the first half-cycle, and loses all of its N-containing ligands in the  $\text{H}_2\text{O}$  cycle, or upon transfer in air for XPS.

#### **4.5. Discussion**

A focus of the work described above is to examine explicitly the effect of an interfacial organic layer (IOL) on the initial stages of ALD growth for a series of thin film chemical systems. In one case, the ALD of  $\text{Al}_2\text{O}_3$ , the layer seems to have no effect on growth vs. that on unmodified  $\text{SiO}_2$ . The results in this case are also consistent with the interfacial organic layer, PEI, being effectively buried essentially intact, certainly concerning its N content (no measurable change in the density or chemical binding environment of N by XPS), by the  $\text{Al}_2\text{O}_3$  thin film. In two cases,

ALD of  $\text{HfO}_2$  and  $\text{Ta}_2\text{O}_5$ , a modest delay in nucleation and growth is observed. Finally, in one case, the ALD of  $\text{Ta}_2\text{N}_x$ , the suppression of growth by the organic layer is significant. First note that the experiments were not conducted for these different chemical systems at identical substrate temperatures, rather they spanned a range of  $\sim 50$  °C. Despite this fact, it is unlikely that substrate temperature is a major factor in determining the degree of attenuation of the ALD growth. For example, the trend in deposition temperature is  $\text{HfO}_2 < \text{Al}_2\text{O}_3 < \text{Ta}_2\text{O}_5 = \text{Ta}_2\text{N}_x$ , the order of which has no apparent relationship with the trend in the degree of growth attenuation, which follows the order, least to most of  $\text{Al}_2\text{O}_3 < \text{HfO}_2 \sim \text{Ta}_2\text{O}_5 \ll \text{Ta}_2\text{N}_x$ . We are left to consider other explanations.

The best explanation for the effect of the interfacial organic layer on these ALD processes concerns differences in the chemical identities of the gas-phase co-reactants and the details of the chemical reactions occurring in each ALD cycle. At this point it is useful to review what is known about the attenuation of ALD growth by interfacial organic layers [1]. In situations where the functional groups are largely present in the form of a 2D array, the extent of attenuation correlates well with the density of these groups. Thus, SAMs such as  $-\text{CH}_3$  terminated alkyl trichlorosilanes, which bind to  $\text{SiO}_2$  via the  $-\text{OH}$  groups present on the surface but lack functional groups themselves, greatly diminish reactive sites and thus inhibit the chemisorption of transition metal complexes and greatly attenuate growth. Other SAMs or IOLs that possess reactive terminations in the form of  $-\text{NHR}$  or  $-\text{OH}$  groups, in general attenuate growth to a smaller degree and lead to thin films which are similar to those grown on unmodified  $\text{SiO}_2$ . In cases where functional groups are distributed in a more



3D way, the behavior can be more complex. Here, overly aggressive ligand exchange reactions can virtually strip a transition metal complex of all of its ligands, forming a species unlikely to react further with co-reactants such as  $\text{H}_2\text{O}$  or  $\text{NH}_3$ . In this case, the correlation between reactivity or first half-cycle uptake of the transition metal complex, and the initial attenuation of the rate of ALD growth is poor.

The most important observations to reconcile here involve the attenuation of the ALD growth of  $\text{HfO}_2$ , and perhaps most interestingly, the dramatic differences between the ALD of  $\text{Ta}_2\text{O}_5$  and  $\text{TaN}_x$  on  $\text{PEI}|\text{SiO}_2$ . Both sets of observations suggest that key mechanisms that cause growth attenuation act during the second half of the ALD cycle, i.e., the exposure to the co-reactants  $\text{H}_2\text{O}$  or  $\text{NH}_3$ . Concerning the first, as discussed above, exposure of the  $\text{PEI}|\text{SiO}_2$  surface to  $\text{Hf}[\text{N}(\text{CH}_3)(\text{C}_2\text{H}_5)]_4$  in the first half-cycle of ALD leads to significant chemisorption of this species, close to the uptake achieved in steady-state ALD of  $\text{HfO}_2$ . Despite this high density of Hf achieved after 1 cycle, growth is significantly attenuated in the subsequent 9 cycles, suggesting that accessible active sites are not effectively regenerated by the  $\text{H}_2\text{O}$  exposure step. Concerning the second, the ALD of  $\text{Ta}_2\text{O}_5$  and  $\text{TaN}_x$  obviously differ only in the second half-cycle, thus, it is in this half-cycle that one would seek to explain the observed differences between the growth of these two materials. These results suggest that, while the first half-cycle results in the deposition of an adequate density of metal atoms in all cases, PEI introduces variability in the efficiency of the second half-cycle to regenerate active sites for additional chemisorption of the metal precursor, a necessary step for ALD.

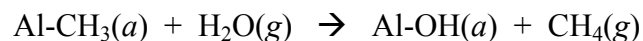
Concerning the attenuation of the ALD of  $\text{HfO}_2$  by  $\text{PEI/SiO}_2$ , and not  $\text{Al}_2\text{O}_3$ , one possible cause for the difference could be the relative size of the ligands in the metal containing precursors used in the two processes. The Al atom is surrounded by three  $-\text{CH}_3$  groups, while the Hf atom is surrounded by four much bulkier  $-\text{N}(\text{CH}_3)(\text{C}_2\text{H}_5)$  groups. The presence of PEI, then, may compound existing steric barriers to the reaction between  $\text{H}_2\text{O}$  and the Hf atom due to the large ligand groups. Such an explanation, when applied to the  $\text{Ta}_2\text{O}_5$  and  $\text{TaN}_x$  systems would seem to fail, as the two processes utilize identical Ta precursors, and the co-reactants  $\text{H}_2\text{O}$  and  $\text{NH}_3$  are of similar size.

The effect of potential interactions between the  $\text{H}_2\text{O}$  co-reactant and the PEI film can be evaluated by comparing the ALD of  $\text{Al}_2\text{O}_3$  and  $\text{Ta}_2\text{O}_5$ . Here measurable attenuation was observed in the case of  $\text{Ta}_2\text{O}_5$  on  $\text{PEI/SiO}_2$ , and no attenuation for  $\text{Al}_2\text{O}_3$  on  $\text{PEI/SiO}_2$ . However, both processes utilize water as the coreactant, and, in fact, the  $\text{H}_2\text{O}$  pulse time is much longer in the case of  $\text{Ta}_2\text{O}_5$  (2 vs. 0.25 s for  $\text{Al}_2\text{O}_3$ ). This result points to the reactions between the chemisorbed metal-containing fragment (which is likely bound to PEI) and  $\text{H}_2\text{O}$  being the key to attenuation, rather than reactions between  $\text{H}_2\text{O}$  and largely unreacted portions of the PEI film. If the determinative process was the reaction of  $\text{H}_2\text{O}$  with PEI in this way, one would expect the same degree of attenuation for both process, or in fact a shorter attenuation period in the case of  $\text{Ta}_2\text{O}_5$  due to the longer water pulse time used in that process.

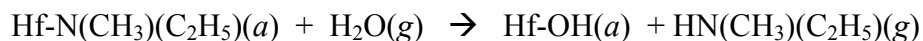
In the ideal case, atomic layer deposition is simply a sequence of chemical reactions that proceed to completion. In practice, the extent to which a reaction proceeds to completion during each half-cycle depends on geometric and energetic

factors. Geometry is a factor concerning frontier orbital overlap and interaction, and the ability to access the appropriate transition state. As discussed above, geometry (steric factors) may play a role in the differences between the ALD growth of Al<sub>2</sub>O<sub>3</sub> and HfO<sub>2</sub>. Chemical reaction thermochemistry, on the other hand, can have an effect on the existence and size of the activation barrier, and whether the reaction is effectively irreversible.

Given the *ex situ* nature of the analysis techniques used here, the structures formed by reactions between the various metal complexes and PEI cannot be determined with much certainty, as they are likely disrupted on exposure to air. Therefore, the analysis of possible thermochemical effects will be approached by determining whether the *overall* thermodynamic driving force (internal energy or enthalpy change) of the ALD reactions examined here exhibits any correlation to the degree of attenuation due to the presence of PEI. The first focus will be the thermochemistry associated with the second half-cycle reactions, since, as discussed above, the first half-cycle reactions and, namely, the density of chemisorbed metal precursors formed in these steps, cannot explain these results. The second half-cycle of Al<sub>2</sub>O<sub>3</sub> ALD involves the following reaction [42], which regenerates active -OH surface terminations:

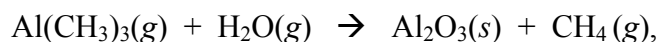


While the second half-cycle of HfO<sub>2</sub> ALD involves the following reaction:

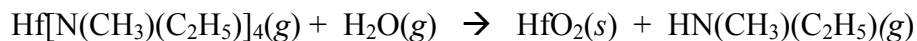


In each case only a single ligand exchange reaction was considered—in the overall ALD process there will be more than one. In the  $\text{HfO}_2$  case, two chemical bonds are broken (Hf-N and O-H), and two are formed (Hf-O and N-H). Similarly, two bonds are broken and two are formed in the second half-cycle reaction for  $\text{Al}_2\text{O}_3$  ALD. The relevant bond dissociation energies have been measured experimentally for some of the bonds shown above [43] (H-OH:  $118.7 \text{ kcal}\cdot\text{mol}^{-1}$ ; H-CH<sub>3</sub>:  $104.9 \text{ kcal}\cdot\text{mol}^{-1}$ ; Al-OH:  $130.7 \text{ kcal}\cdot\text{mol}^{-1}$ ; H-NR<sub>2</sub>:  $94.5 \text{ kcal}\cdot\text{mol}^{-1}$ ). For those that have not been measured experimentally, results from density functional theory (DFT) calculations (Al-CH<sub>3</sub>,  $75.2 \text{ kcal}\cdot\text{mol}^{-1}$  [44]; Hf-NR<sub>2</sub>,  $82.4 \text{ kcal}\cdot\text{mol}^{-1}$  [45]; Hf-OH,  $125.5 \text{ kcal}\cdot\text{mol}^{-1}$  [45]) will be used. With these values, the net energy change in the second half-cycle of ALD for these single ligand exchange reactions can be estimated to be  $-41.7 \text{ kcal}\cdot\text{mol}^{-1}$  for  $\text{Al}_2\text{O}_3$  and  $-18.9 \text{ kcal}\cdot\text{mol}^{-1}$  for  $\text{HfO}_2$ . Thus, in both cases there is a driving force for the reactions to proceed to completion, and the driving force is higher for the half-cycle reaction for  $\text{Al}_2\text{O}_3$ . Along with the steric factors indicated above, this would help explain the stronger attenuation of  $\text{HfO}_2$  ALD.

A second method for evaluating the thermodynamic driving force for the two reactions involves calculating the total enthalpy change for the complete ALD reaction, i.e., forming a thin film of  $\text{Al}_2\text{O}_3$ :

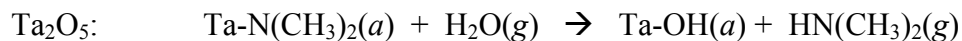


likewise for HfO<sub>2</sub>:

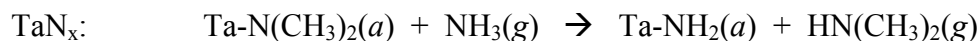


In the case of Al<sub>2</sub>O<sub>3</sub> ALD, measured values are available for all species [30,46]; for HfO<sub>2</sub> ALD, the required enthalpy of formation is not available for Hf[N(CH<sub>3</sub>)(C<sub>2</sub>H<sub>5</sub>)]<sub>4</sub>, so the analogous reaction using Hf[N(C<sub>2</sub>H<sub>5</sub>)<sub>2</sub>]<sub>4</sub> will be considered. The total enthalpy change on reaction is -149.3 kcal-mol<sup>-1</sup> for Al<sub>2</sub>O<sub>3</sub> and -90.3 kcal-mol<sup>-1</sup> for HfO<sub>2</sub>. This analysis also predicts a higher driving force in the case of Al<sub>2</sub>O<sub>3</sub>. Due to uncertainty regarding the heat capacity for some components, these enthalpy changes are calculated at a temperature of 25 °C. The difference between the enthalpy change for reaction at 25 °C vs. that at which ALD is conducted (180-230 °C) can be estimated to be no more than ± 10 kcal-mol<sup>-1</sup>.

Moving to the Ta-containing thin films, in the first half-cycle the two cases are identical, so as with the cases above, processes which occur in the second half-cycle of the ALD sequence are responsible for attenuation. The single ligand exchange reactions that occur in the second half-cycle for the Ta ALD processes are:



and



Here again the two methods employed above can be used to compare the thermodynamic driving force in the two cases. For these single ligand exchange reactions, a net energy change of  $-26.0 \text{ kcal}\cdot\text{mol}^{-1}$  for the second half-cycle reaction for the ALD of  $\text{Ta}_2\text{O}_5$  ALD, and  $-3.8 \text{ kcal}\cdot\text{mol}^{-1}$  for the second half-cycle reaction for the ALD of  $\text{TaN}_x$  is determined. This calculation utilized bond dissociation energies obtained from both experiment [43] and DFT calculations [45,47,48]. For the complete ALD reactions, total enthalpy changes of  $-65.6 \text{ kcal}\cdot\text{mol}^{-1}$  for  $\text{Ta}_2\text{O}_5$ , and either  $-38.2 \text{ kcal}\cdot\text{mol}^{-1}$  or  $-7.3 \text{ kcal}\cdot\text{mol}^{-1}$  for  $\text{TaN}_x$  are calculated, assuming the formation of predominantly the  $\text{Ta}_3\text{N}_5$  phase or the equimolar  $\text{TaN}$  phase respectively, again using a combination of experiment [30,46,49] and DFT calculations [50]. Under the conditions used here, the most likely phase to be formed is  $\text{Ta}_3\text{N}_5$  [51].

Summarizing these results, based on the single ligand exchange reactions for the second half-cycle reactions, the thermochemical driving forces follow this order, lowest to highest:  $\text{TaN}_x < \text{HfO}_2 < \text{Ta}_2\text{O}_5 < \text{Al}_2\text{O}_3$ . Concerning the overall complete ALD reactions, the order is slightly modified:  $\text{TaN}_x < \text{Ta}_2\text{O}_5 < \text{HfO}_2 < \text{Al}_2\text{O}_3$ . Based on these sequences, there does appear to be a correlation between the degree to which ALD growth is attenuated in the early stages by PEI, and the magnitude of the thermodynamic driving forces for the reactions. To quantify this relationship the following simple construction will be considered. The number of cycles associated with incipient growth is given by the parameter  $m$  given in Eq. 4-1, so the rate at which the surface is converted eventually to that representing what is achieved at steady-state is given by  $\sim 1/m$ . One may anticipate that this rate scales with  $\exp(-\Delta E/RT)$ , where  $\Delta E$  is the energetic ( $\sim$  enthalpic) driving force for reaction. In this case

a plot of  $\ln(1/m)$  vs.  $-\Delta E/RT$  would yield a straight line. Note that an additional factor not considered here is the total exposure of the surface to the reactant in the second half-cycle, which, in addition to the thermodynamic driving force effects discussed above, may also play a role in determining attenuation effects. In this case a more accurate accounting of the attenuation could be based on  $1/(m\varepsilon)$ , where  $\varepsilon$  is the exposure to the reactant in the second half-cycle ( $\text{molec}\cdot\text{cm}^{-2}$ ). Quantifying exposures in an ALD reactor, due to residence time effects/reactor wall adsorption, is not straightforward, in particular compared to experiments involving molecular beams [52]. Thus, the length of attenuation will be estimated simply by  $1/m$ .

Fig. 4-16 the quantity  $1/m$  ( $\log_{10}$  scale) vs.  $-\Delta E/RT$  is plotted, the latter calculated in the two ways described above: for the second half-cycle single ligand exchange reaction, and the overall enthalpy change of the ALD reaction. To plot the results for  $\text{Al}_2\text{O}_3$ ,  $m = 1$  was used, and indicated by the arrows that its value is likely less than 1. For the case of  $\text{TaN}_x$ , although the fit produced a value for  $m$ , the uncertainty was large, and this value is likely not physical as the steady-state rate was never achieved for the range of cycles of ALD considered here. In this case  $m \geq 50$  is used, i.e., the maximum number of cycles examined here, and indicated by arrows that the true value for  $m$  may be larger. From Fig. 4-16 we see that the correlation between attenuation and these energetic driving forces is quite good, somewhat better for that based on the single ligand exchange second half-cycle reactions.

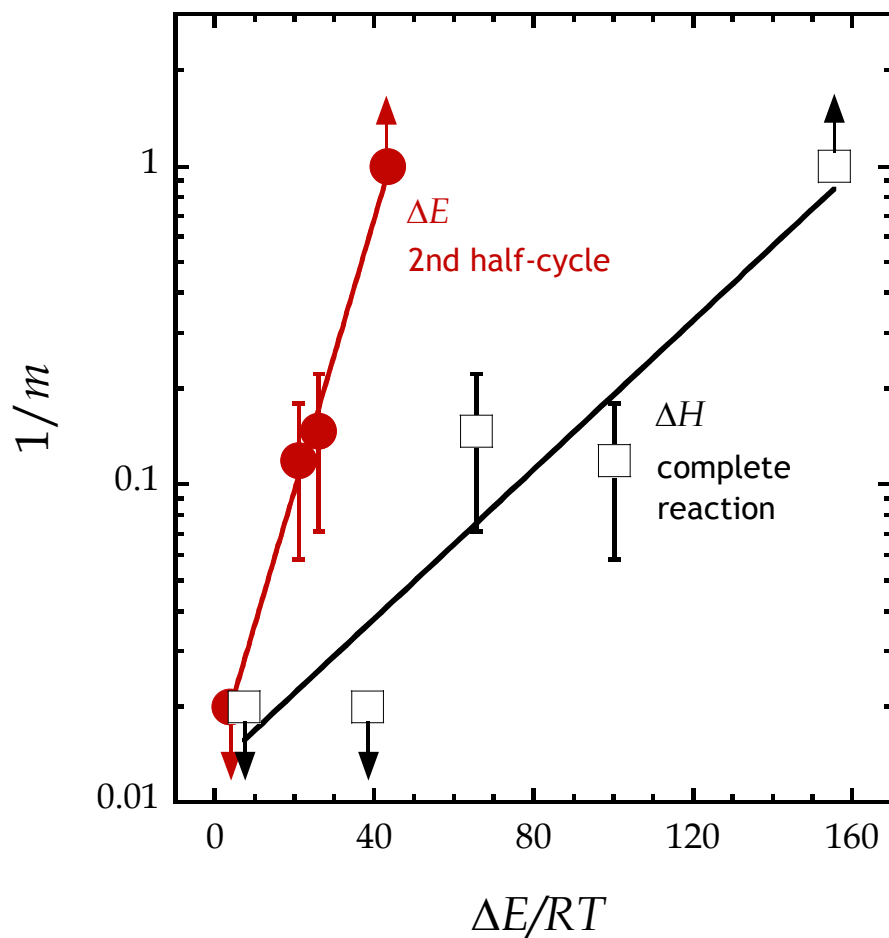


**Figure 4-16:** Inverse of the attenuation coefficient,  $1/m$ , for all the processes examined here for ALD on PEI/SiO<sub>2</sub> vs. the thermochemical driving force for these reactions. Two thermochemical driving forces are considered in the figure: one based on the internal energy change associated with a single ligand exchange reaction in the second half-cycle of ALD,  $\Delta E/RT$ , the other based on the total enthalpy change of the overall ALD reaction,  $\Delta H/RT$ .



Before considering any possible reaction mechanisms, note that the correlation demonstrated in Fig. 4-16 indicates that ALD reactions with an inherently high overall driving force (or, as discussed below, a low activation barrier) are not as susceptible to attenuation by PEI. In other words, effects of PEI which act to inhibit the ALD reactions, through steric hindrances or the formation of a stable metal-PEI complex, for example, can be overcome by a high thermodynamic driving force towards the formation of the final products. Should the attenuation in the initial rate of deposition scale with these energetic driving forces? Atomic layer deposition, as conventionally defined, involves consecutive self-limiting surface reactions. During each half-cycle, given the complexity of the co-reactants, particularly the transition metal complexes, multiple elementary reactions must occur to form ultimately the inorganic compounds in each case. A reactant such as  $\text{Ta}[\text{N}(\text{CH}_3)_2]_5$  likely loses 2-4 ligands in the first half-cycle [18]. Local stereochemistry may have an effect on how many ligands are lost by each individual molecule. On the other hand a co-reactant such as  $\text{H}_2\text{O}$  may displace multiple ligands attached to a metal center, forming perhaps multiple  $-\text{OH}$  species bound to single metal center. The ability of each of these elementary reactions to proceed to completion will depend on steric factors, as discussed above, but also on the activation barriers associated with each reaction. For some time, it has been recognized that for series of similar reactions the activation energy is linearly correlated with the enthalpy change of reaction [53,54], and to linear combinations of the energy required to break and form the necessary bonds to complete a reaction [55-57]. Thus, due to a strong driving force, reactions associated with the formation of  $\text{Al}_2\text{O}_3$  may mostly occur with little or no activation barrier, whereas more thermo-

neutral reactions associated with the formation of  $\text{TaN}_x$  may have sizable barriers. What must be kept in mind, however, is that in the absence of PEI, growth of these two materials under similar conditions ( $T_s$ ) is quite comparable. Indeed, the two processes differ in terms of thickness-per-cycle by about a factor of 1.5, and this difference probably reflects the effect of the size of the ligands, i.e.,  $-\text{CH}_3$  vs.  $\text{N}(\text{CH}_3)_2$ , in controlling the saturation coverage that can be achieved in each half-cycle, or the efficiency with which reactive sites are generated at completion of the second half-cycle by  $\text{H}_2\text{O}$  vs.  $\text{NH}_3$ .

PEI clearly has an effect on the initial stages of growth, and the difference between  $\text{Ta}_2\text{O}_5$  and  $\text{TaN}_x$  ALD is quite striking. Some discussion of what may be happening in these two cases is of interest. First, as the substrate temperature and the Ta precursor are identical in both cases, the adlayer formed at the end of the first half-cycle must be identical. The Ta complex, as indicated above, may have undergone multiple ligand exchange reactions, and each Ta fragment may be bound to the PEI layer via multiple linkages. The branched nature of the PEI, and its thickness of  $\sim 5 \text{ \AA}$  may facilitate chelation of the Ta complex. Exposure of this layer to  $\text{H}_2\text{O}$  likely breaks a number of these linkages with the PEI (e.g.,  $-\text{NH-Ta}$ ,  $-\text{N=Ta}$ ), forming new Ta-OH and other bonds with O. The linking groups on PEI are likely protonated, reforming  $-\text{NH}_{2-x}\text{R}_x$  groups. It has been observed that hydrogen bonds involving  $-\text{RNHR}'-$  groups in a  $\sim 30 \text{ nm}$  thick film of polyamide-6 are disrupted by exposure to  $\text{Al}(\text{CH}_3)_3$ , then reformed by subsequent exposure to  $\text{H}_2\text{O}$  [58], suggesting a similar process in the case of  $\text{Al}_2\text{O}_3$  ALD. In this case it should be noted that the majority of hydrogen bonds exist within the polymer, i.e. between  $-\text{RNHR}'-$  and  $\text{C=O}$  groups. Given the

thermochemistry in the case of Ta<sub>2</sub>O<sub>5</sub>, Al<sub>2</sub>O<sub>3</sub>, and HfO<sub>2</sub>, these conversions are irreversible, and may proceed quickly with little or no activation barrier. The situation with NH<sub>3</sub> could be quite different. In this case reaction of NH<sub>3</sub> with the linkages between the Ta complex and the PEI (e.g., -NH-Ta, -N=Ta) may be activated, and could possibly be reversible to some extent. An important difference between the initial layer formed on PEI/SiO<sub>2</sub> and that representing steady-state growth is that in the latter case NH<sub>3</sub> reacts with the -N(CH<sub>3</sub>)<sub>2</sub> ligands to form a gas phase reaction product, HN(CH<sub>3</sub>)<sub>2</sub>, while reaction in the presence of PEI may not lead to gas phase products, e.g., ligand exchange and protonation of the groups on PEI. For this reason, it is plausible that conversion of the layer bound to PEI to one representing the steady-state surface present during growth may be sluggish for the case where NH<sub>3</sub> is the co-reactant.

#### 4.6. Conclusions and future directions

The atomic layer deposition of a series of inorganic thin films, namely Al<sub>2</sub>O<sub>3</sub>, HfO<sub>2</sub>, Ta<sub>2</sub>O<sub>5</sub>, and TaN<sub>x</sub>, has been examined on an interfacial organic layer, poly(ethylene imine), focusing on the effects of this layer on the initial stages of growth. It was shown that PEI forms a smooth uniform thin film on SiO<sub>2</sub>, ~ 0.5 nm thick, with a high density ( $\sim 6 \times 10^{14} \text{ cm}^{-2}$ ) of -NH<sub>2-x</sub>R<sub>x</sub> groups. The ALD of Al<sub>2</sub>O<sub>3</sub> on PEI/SiO<sub>2</sub> is virtually identical to that observed on unmodified SiO<sub>2</sub>, i.e., a linear thickness vs. number of cycles relationship, with no incubation period. From angle-resolved XPS, it was shown that the deposition of Al<sub>2</sub>O<sub>3</sub> essentially buries the PEI,

with no significant loss of N density from the organic layer, although some disruption of the bonding in the PEI may have occurred. For the other three materials examined, an incubation period exists for growth on PEI/SiO<sub>2</sub>, which is short lived (~ 10 ALD cycles) for the ALD of Ta<sub>2</sub>O<sub>5</sub> and HfO<sub>2</sub>, but substantially long-lived (> 50 ALD cycles) for the ALD of TaN<sub>x</sub>. Concerning the ALD of HfO<sub>2</sub>, although the first half-cycle of exposure to the Hf co-reactant produces a coverage close to that at steady-state, growth is still strongly attenuated for ~ 10 cycles of ALD. This result highlights the effect of PEI/SiO<sub>2</sub> on the second half-cycle exposure to H<sub>2</sub>O. The effect of PEI/SiO<sub>2</sub> on the second half-cycle is further displayed when comparing the results for the ALD of Ta<sub>2</sub>O<sub>5</sub> and TaN<sub>x</sub>. The incubation period for TaN<sub>x</sub> ALD is much longer than for Ta<sub>2</sub>O<sub>5</sub>, however the two ALD processes differ only in the second half-cycle. Therefore, the effect of PEI/SiO<sub>2</sub> on the second half-cycle is implicated here also as being primarily responsible for the incubation period. Furthermore in this case the initial uptake of Ta is attenuated by about a factor of 2 by PEI, although this is not nearly enough to solely account for the attenuation of the initial thickness deposited per cycle. Viewing the results as a whole, a strong correlation between the thermodynamic driving force of the second half-cycle ligand exchange reaction and the length of the incubation period is observed. Chemical transformations in the ALD half-reactions that are more favorable thermodynamically exhibit shorter periods of incipient growth.

The work described in this chapter suggests a number of possible future directions. From an experimental point of view, the conclusions we can make from these results are somewhat limited due to the *ex situ* nature of the analysis. In other

work presented here, in Chapters 3 and 5, *in situ* XPS was used to determine the chemical state and molecular structure of adsorbed species. For a deeper understanding of the mechanisms underlying the results described here, similar *in situ* based techniques may prove very useful. Continuing work using the same *ex situ* techniques described here would also be of value. Suggested experimental plans would include changing the coreactant dose times and/or reaction temperatures. Studying the effect of these parameters using *ex situ* ellipsometry and XPS could provide further insight on the underlying mechanisms. For example, if the delay in nucleation is in fact due to inhibition of the second half cycle, we may expect the degree of nucleation delay ( $m$  parameter in Eq. 4-1) to decrease with increasing coreactant exposure.

The trend demonstrated in Fig. 4-16 suggests that the initial growth rate may be controlled by using alternate coreactants which result in different overall reaction thermochemistry. For oxide processes, for example, ozone could be used in place of water, or likewise for nitride processes hydrazine could be used in place of ammonia. In either case, a plasma process could be used to generate highly reactive O or N containing radicals for use as coreactants, however in this case any structural damage to the organic film due to the plasma should be closely monitored. Along this same line, alternate organic films to PEI could be used. One attractive possibility is the use of polyelectrolyte multilayers [11,59,60]. Extensive study of these organic multilayers has demonstrated the ability to deposit films with a high degree of thickness precision, while incorporating a variety of chemical functionalities, some of which may have purposes beyond simply controlling subsequent inorganic film growth.

Finally, the large difference in the initial growth attenuation suggests that, for applications where the formation of a film such as  $\text{TaN}_x$  is required on an organic modified substrate, that depositing a very thin inorganic film ( $\text{Ta}_2\text{O}_5$  for example) prior to initiating  $\text{TaN}_x$  ALD may allow the otherwise strong attenuation of growth to be overcome.

#### 4.6 Appendix: ALD of $\text{Al}_2\text{O}_3$ on FOTS| $\text{SiO}_2$

A short series of additional experiments was conducted to study the deposition of  $\text{Al}_2\text{O}_3$  on an organic layer which lacks any chemically reactive sites. To produce such a layer, a  $\text{SiO}_2$  surface was exposed to (1H,1H,2H,2H-perfluorooctyl) trichlorosilane (FOTS), which reacts with surface Si-OH groups to form a layer of covalently bound  $\equiv\text{Si}(\text{CH}_2)_2(\text{CF}_2)_5\text{CF}_3$  on the surface (see Fig. 2-1 for the structure of FOTS, and Sec. 2.4 for details regarding the formation of the layer). As this layer is not expected to have any reactivity towards the ALD precursors, its only role is to deactivate and block otherwise reactive Si-OH sites. As shown in Fig. 4-15, the presence of FOTS leads to the attenuation of  $\text{Al}_2\text{O}_3$  ALD. This is not unexpected, particularly in light of similar experiments which showed attenuation of  $\text{TiN}_x$ ,  $\text{HfO}_2$ , and Pt ALD on FOTS| $\text{SiO}_2$  [2,17]. Fitting the thickness vs. number of ALD cycles data Eq. 4-1, shown by a solid line in Fig. 4-15, results in a value of  $m$  of  $\sim 12$ . Similar to  $\text{Al}_2\text{O}_3$  films on PEI| $\text{SiO}_2$  (Fig. 4-8), ARXPS has also been performed to determine the distribution of the FOTS after  $\text{Al}_2\text{O}_3$  ALD. Fig. 4-16 displays the integrated XPS intensity as a function of photoelectron takeoff angle for 40 cycles of  $\text{Al}_2\text{O}_3$  ALD on

FOTS|SiO<sub>2</sub>. The thickness of the Al<sub>2</sub>O<sub>3</sub> film in this case was measured to be  $27 \pm 1$  Å. Here we observe similar behavior to that seen in Fig. 4-8, namely an increase in the Al(2p) intensity with takeoff angle, and a decrease in the Si(2p) and F(1s), where F(1s) is representative of the FOTS molecule. By fitting the F(1s) data to a model which assumes that F exists in a 2-d monolayer buried at a depth of  $d_{ML}$  from the vacuum interface [solid line in Fig. 4-16(b)], we obtain  $d_{ML} = 24.0 \pm 1.3$  Å. This value should be compared to the thickness of the Al<sub>2</sub>O<sub>3</sub> films obtained from ellipsometry (27 Å) and the value obtained using ARXPS of the Si<sup>4+</sup> feature of  $34.2 \pm 1.9$  Å. Therefore, the fluorine remaining after 40 cycles of ALD remains chiefly between the SiO<sub>2</sub> and Al<sub>2</sub>O<sub>3</sub> layers. A measurement of the F atomic density before and after ALD, conducted using identical methods as with PEI in Sec. 4.4.2 above, indicates that ~ 35% of the fluorine on the surface is lost during ALD. This may be due to a desorption process taking place in the early stages of ALD. However, caution must be used in interpreting this result, because of the difficulties involved with accurately measuring the F atomic density using XPS. This is due to the photoelectron induced desorption of fluorine when analyzing the 0 cycle FOTS|SiO<sub>2</sub> sample, or apparently photoelectron-induced reactions between F and Al atoms at the Al<sub>2</sub>O<sub>3</sub>|FOTS interface, as indicated by the appearance of a new peak in the F(1s) region of the XP spectrum, which can be assigned to F-Al species (Fig. 4-19). While efforts were made to correct for these effects (i.e. by taking multiple measurements of the F intensity and extrapolating back to zero x-ray exposure, or summing the contributions of the F-C and F-Al peaks in ARXPS), there may be nonlinear effects which affect the measurement.

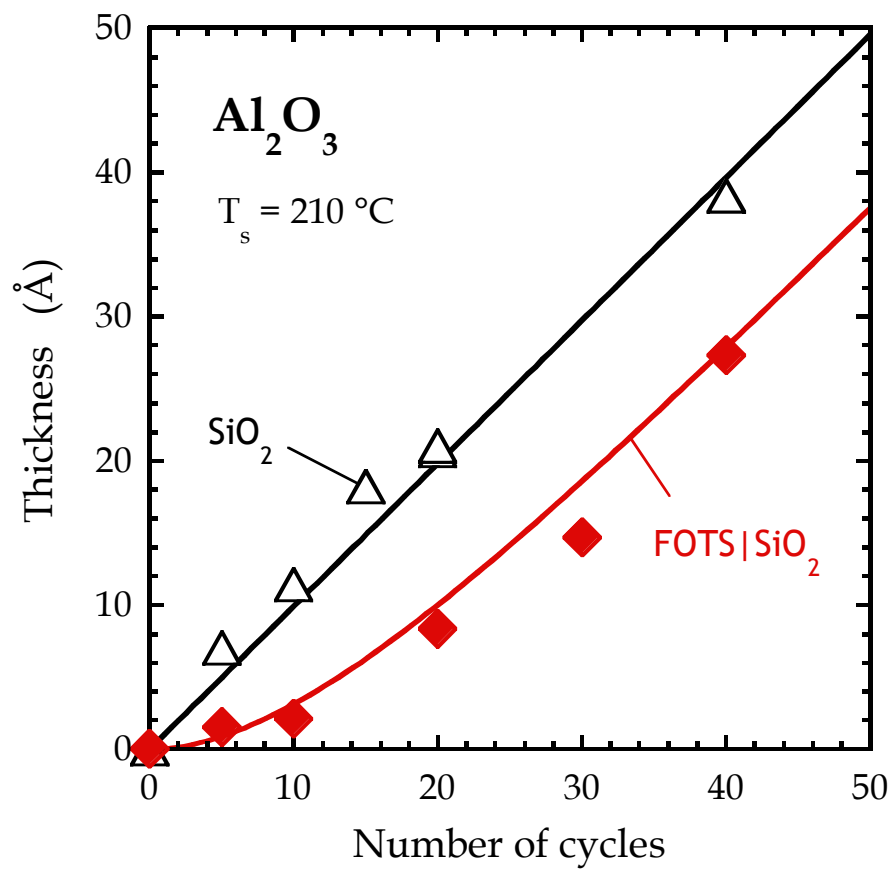


**Figure 4-17:** Al<sub>2</sub>O<sub>3</sub> film thickness as a function of ALD cycles on an unmodified SiO<sub>2</sub> substrate (open symbols) and on FOTS|SiO<sub>2</sub> (filled). Solid line through FOTS|SiO<sub>2</sub> series represents a fit to Eq. 4-1.



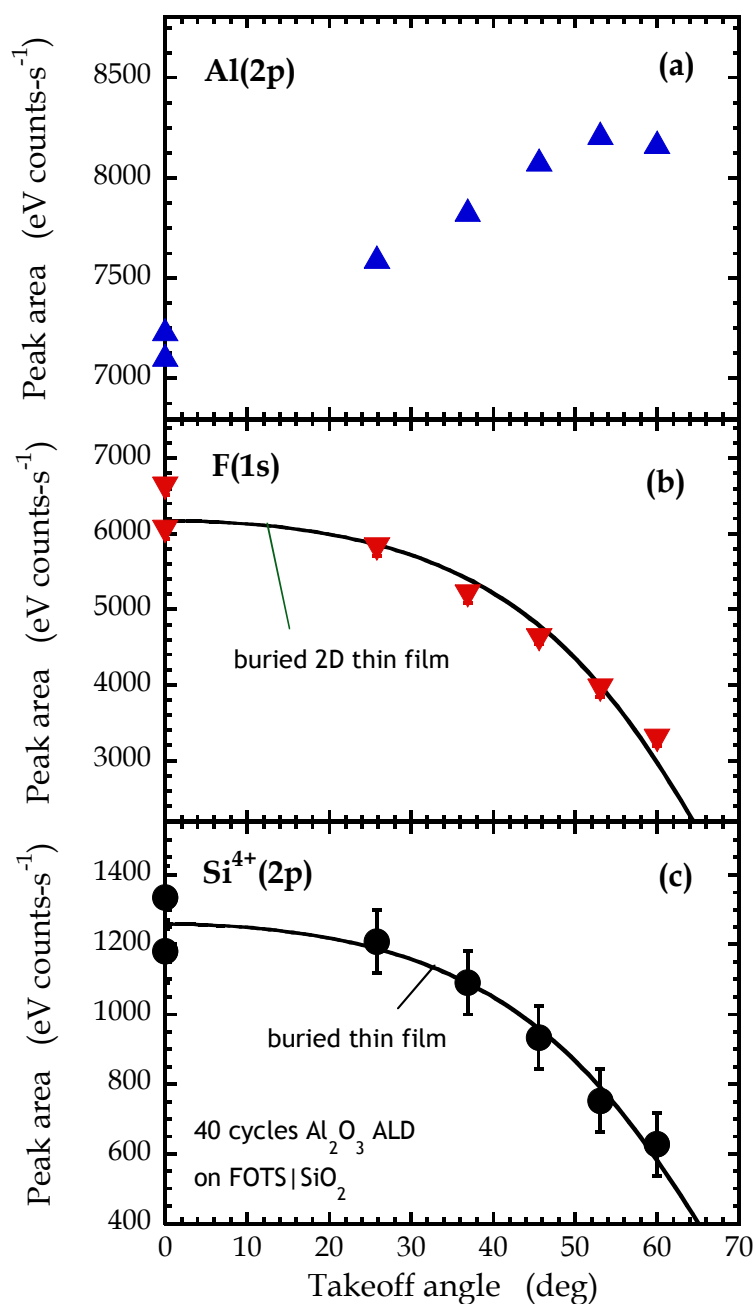


**Figure 4-18:** Integrated areas of the (a) Al(2p), (b) F(1s), and (c) Si<sup>4+</sup>(2p) XPS features as a function of takeoff angle for 40 cycles Al<sub>2</sub>O<sub>3</sub> ALD on FOTS|SiO<sub>2</sub>. In (b), the solid line corresponds to a model in which the F atoms exist in a 2-d layer buried at a uniform depth. The solid line shown in (c) corresponds to a model for a thin film of SiO<sub>2</sub> that is covered uniformly by a layer of Al<sub>2</sub>O<sub>3</sub> and FOTS.

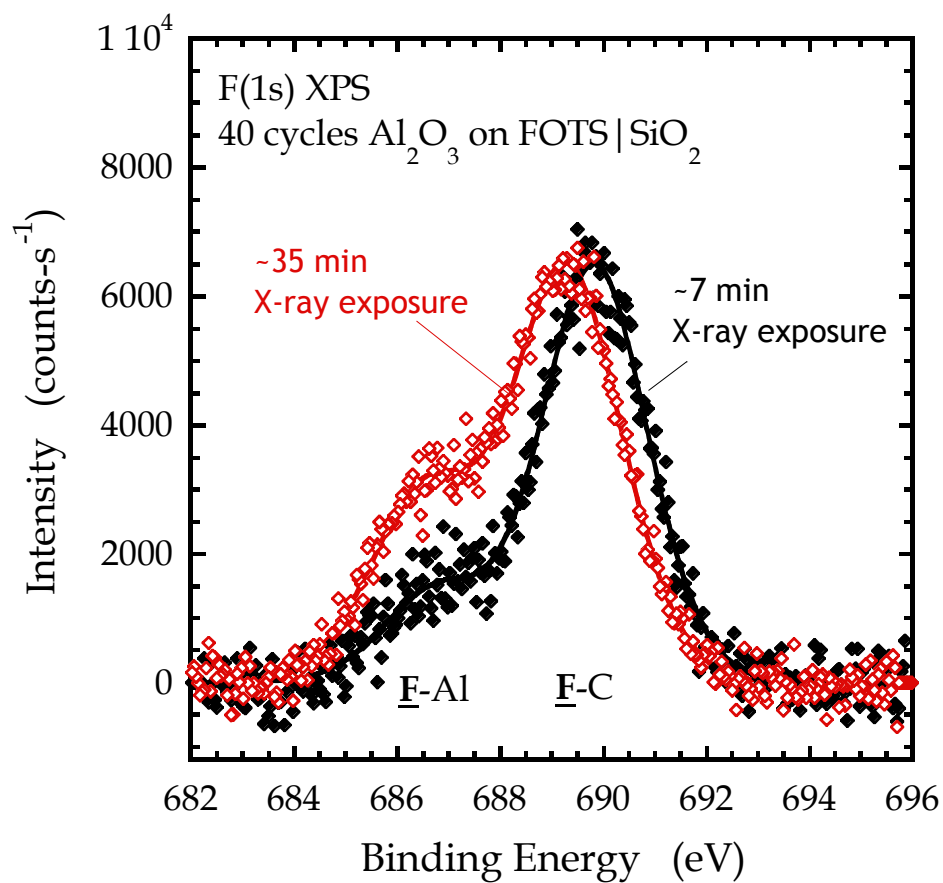


**Figure 4-19:** X-ray photoelectron spectra in the F(1s) region for 40 cycles of Al<sub>2</sub>O<sub>3</sub> ALD on FOTS|SiO<sub>2</sub> after ~ 7 minutes and ~ 35 minutes of exposure the x-ray source. Note the appearance, and increase in intensity, of the feature at ~686 eV binding energy, which indicates the formation of F-Al bonds.

## 4.8 References

1. K. J. Hughes and J. R. Engstrom, *J. Vac. Sci. Technol. A* **28**, 1033 (2010).
2. X. Jiang and S. F. Bent, *J. Phys. Chem. C* **113**, 17613 (2009).
3. R. Chen, H. Kim, P. C. McIntyre, and S. F. Bent, *Appl. Phys. Lett.* **84**, 4017 (2004).
4. K. J. Park, J. M. Doub, T. Gougousi, and G. N. Parsons, *Appl. Phys. Lett.* **86**, 051903 (2005).
5. E. Färm, M. Kemell, M. Ritala, and M. Leskelä, *J. Phys. Chem. C* **112**, 15791 (2008).
6. E. Färm, M. Kemell, E. Santala, M. Ritala, and M. Leskelä, *J. Electrochem. Soc.* **157**, K10 (2010).
7. A. Sinha, D. W. Hess, and C. L. Henderson, *J. Vac. Sci. Technol. B* **24**, 2523 (2006).
8. C. A. Wilson, R. K. Grubbs, and S. M. George, *Chem. Mater.* **17**, 5625 (2005).
9. S. A. Sukhishvili and S. Granick, *J. Am. Chem. Soc.* **122**, 9550 (2000).
10. R. Mészáros, I. Varga, and T. Gilányi, *Langmuir* **20**, 5026 (2004).
11. P. T. Hammond, *Adv. Mater.* **16**, 1271 (2004), and references therein.
12. A. S. Killampalli, P. F. Ma, and J. R. Engstrom, *J. Am. Chem Soc.* **127**, 6300 (2005).
13. L. T. Zhuravlev, *Langmuir* **3**, 316 (1987).
14. S. R. Wasserman, Y. T. Tao, and G. M. Whitesides, *Langmuir* **5**, 1074 (1989).
15. T. V. Desai, S. Hong, A. R. Woll, K. J. Hughes, P. Ananth, P. Clancy, and J. R. Engstrom, submitted for publication.
16. A. Dube, M. Sharma, P. F. Ma, and J. R. Engstrom, *Appl. Phys. Lett.* **89**, 164108 (2006).
17. A. Dube, M. Sharma, P. F. Ma, P. A. Ercius, D. A. Muller, and J. R. Engstrom, *J. Phys. Chem. C* **111**, 11045 (2007).
18. M. Sharma, A. Dube, K. J. Hughes, and J. R. Engstrom, *Langmuir* **24**, 8610 (2008).

19. M. Barber, J. A. Connor, M. F. Guest, I. H. Hiller, M. Schwarz, and M. Stacey, *J. Chem. Soc. Faraday Trans. 2* **69**, 551 (1973).
20. B. J. Lindberg and J. Hedman, *Chem. Scr.* **7**, 155 (1975).
21. B. Lindberg, R. Maripuu, K. Siegbahn, R. Larsson, C.-G. Gölander, and J. C. Eriksson, *J. Colloid Interface Sci.* **95**, 308 (1983).
22. G. Beamson and D. Briggs, *High Resolution XPS of Organic Polymers: the Scienta ESCA300 Database* (Wiley, New York, 1992).
23. J. T. Sampanthar, K. G. Neoh, S. W. Ng, E. T. Kang, and K. L Tan, *Adv. Mater.* **12**, 1536 (2000).
24. Z. J. Yu, E. T. Kang, and K. G. Neoh, *Polymer* **43**, 4137 (2002).
25. J. Thome, A. Holländer, W. Jaeger, I. Trick, and C. Oehr, *Surf. Coat. Technol.* **174-175**, 584 (2003).
26. E. H. Jeong, J. Yang, and J. H. Youk, *Mater. Lett.* **61**, 3991 (2007).
27. M. P. Seah and W. A. Dench, *Surf. Interface Anal.* **1**, 2 (1979).
28. J. H. Scofield, *J. Electron. Spectrosc. Relat. Phen.* **8**, 129 (1976).
29. C. J. Powell and A. Jablonski, *J. Vac. Sci. Technol. A* **17**, 1122 (1999).
30. *CRC handbook of Chemistry and Physics, 91st Ed.*, edited by D. R. Lide (CRC Press, Boca Raton, FL, 2011).
31. J. A. Taylor and J. W. Rabalais, *J. Chem. Phys.* **75**, 1735 (1981).
32. S. Tanuma, C. J. Powell, and D. R. Penn, *Surf. Interface Anal.* **17**, 927 (1991).
33. D. M. Hausmann, E. Kim, J. Becker, and R. G. Gordon, *Chem. Mater.* **14**, 4350 (2002).
34. K. Kukli, M. Ritala, J. Lu, A. Hårsta, and M. Leskelä, *J. Electrochem. Soc.* **151**, F189 (2004).
35. S. Dueñas, H. Castán, H. García, J. Barbolla, K. Kukli, M. Ritala, and M. Leskelä, *Thin Solid Films* **474**, 222 (2005).
36. J. C. Hackley, T. Gougousi, and J. D. Demaree, *J. Appl. Phys.* **102**, 034101 (2007).

37. D. W. McNeill, S. Bhattacharya, H. Wadsworth, F. H. Ruddell, S. J. N. Mitchell, B. M. Armstrong, and H. S. Gamble, *J. Mater. Sci.: Mater. Electron.* **19**, 119 (2008).
38. M. A. Alam and M. L. Green, *J. Appl. Phys.* **94**, 3403 (2003).
39. D. M. Hausmann, P. de Rouffignac, A. Smith, R. Gordon, and D. Monsma, *Thin Solid Films* **443**, 1 (2003).
40. W. J. Maeng and H. Kim, *Electrochem. Solid-State Lett.* **9**, G191 (2006).
41. A. Furuya, N. Ohtsuka, N. Ohashi, S. Kondo, and S. Ogawa, *J. Vac. Sci. Technol. A* **24**, 103 (2006).
42. Y. Widjaja and C. B. Musgrave, *Appl. Phys. Lett.* **80**, 3304 (2002).
43. Y. R. Luo, *Comprehensive Handbook of Chemical Bond Energies* (CRC Press, Boca Raton, FL, 2007).
44. Y. Xu and C. B. Musgrave, *Chem. Mater.* **16**, 646 (2004).
45. K. Li, S. Li, N. Li, D. A. Dixon, and T. M. Klein, *J. Phys. Chem. C* **114**, 14061 (2010).
46. NIST Standard Reference Database, <http://webbook.nist.gov/chemistry>, accessed December 2010.
47. M. Siodmiak, G. Frenking, and A. Korkin, *J. Phys. Chem. A* **104**, 1186 (2000).
48. Y. S. Won, S. S. Park, Y. S. Kim, T. J. Anderson, and L. McElwee-White, *J. Cryst. Growth* **311**, 3587 (2009).
49. A. D. Mah and N. L. Gellert, *J. Am. Chem. Soc.* **78**, 3261 (1956).
50. C. Stampfl and A. J. Freeman, *Phys. Rev. B* **71**, 024111 (2005).
51. Y. Travaly, J. Schuhmacher, A. M. Hoyas, M. Van Hove, K. Maex, T. Abell, V. Sutcliffe, and A. M. Jonas, *J. Appl. Phys.* **97**, 084316 (2005).
52. L.-Q. Xia, M. E. Jones, N. Maity, and J. R. Engstrom, *J. Vac. Sci. Technol. A* **13**, 2651 (1995).
53. M. G. Evans and M. Polanyi, *Trans. Faraday Soc.* **32**, 1333 (1936).
54. M. G. Evans and M. Polanyi, *Trans. Faraday Soc.* **34**, 11 (1938).

- 55. N. N. Semenov, *Some Problems in Chemical Kinetics and Reactivity* (Princeton University Press, Princeton, NJ, 1958).
- 56. Z. G. Szabó, Chem. Soc. (London), Spec. Publ. **16**, 113 (1962).
- 57. Z. G. Szabó and T. Bérces, Z. Phys. Chem. **57**, 113 (1968).
- 58. J. C. Spagnola, B. Gong, S. A. Arvidson, J. S. Jur, S. A. Khan, and G. N. Parsons, J. Mater. Chem. **20**, 4213 (2010).
- 59. G. Dercher, Science **277**, 1232-1237 (1997)
- 60. P. Bertrand, A. Jonas, A. Laschewsky and R. Legras, Macromol. Rapid. Commun. **21**, 319-348 (2000):

## 5. Atomic layer deposition of titanium and tantalum nitrides on substrates modified by branched polymer layers\*

### 5.1 Overview

In this chapter, a series of experiments are described which were undertaken to study the ALD of  $\text{TaN}_x$  and  $\text{TiN}_x$  on  $\text{SiO}_2$  and porous low- $\kappa$  substrates modified using thin organic films. Two organic films were used: polyglycidol, a branched molecule with hydroxyl and ether functionality, and poly(ethylene imine), a branched molecule with amine functionality. *In situ* XPS analysis using a molecular beam based ALD technique showed that the chemical structure of the adlayer which chemisorbs in the first half cycle of ALD is strongly influenced by the chemistry of the substrate ( $\text{SiO}_2$  vs. low- $\kappa$ , and unmodified substrates vs. substrates modified with thin organic films). It was found that both polyglycidol and poly(ethylene imine) films decrease the uptake of the  $\text{TaN}_x$  precursor  $\text{Ta}[\text{N}(\text{CH}_3)_2]_5$  in the first half cycle on a  $\text{SiO}_2$  substrate. However, on a low- $\kappa$  substrate, poly(ethylene imine) enhances uptake of  $\text{Ta}[\text{N}(\text{CH}_3)_2]_5$ , and also increases the subsequent rate of  $\text{TaN}_x$  deposition. In addition to the rate of growth, XPS shows that the chemistry of the substrate influences both the oxidation state of the growing film, and the incorporation of nitrogen, over the first 10 ALD cycles ( $\sim 6\text{-}10$  Å). When conventional ALD techniques are used, angle resolved XPS demonstrates that a thin film of poly(ethylene imine) has the effect of decreasing infiltration of  $\text{Ta}[\text{N}(\text{CH}_3)_2]_5$  into the interconnected pore structure of a low- $\kappa$  material,

---

\* K. J. Hughes, A. Dube, M. Sharma, and J. R. Engstrom, *under review at the time of dissertation submission*.

while enhancing uptake of the precursor at the vacuum|low- $\kappa$  interface. Regarding  $\text{TiN}_x$  ALD, the presence of poly-G inhibits growth, and causes the formation of a rough, islanded film on low- $\kappa$ . This is similar to results obtained on  $\text{SiO}_2$  substrates, and is believed to be due to the ability of the highly 3-d network of the poly-G film to strongly bind to the  $\text{Ti}[\text{N}(\text{CH}_3)_2]_4$  molecule, stripping  $-\text{N}(\text{CH}_3)_2$  ligands in the process, and making it unreactive in the second half cycle of ALD.

## 5.2. Introduction

Atomic layer deposition (ALD) [1,2] provides the ability to form extremely thin, conformal films with precise thickness control. These characteristics make it an attractive technique for a number of applications, notably in semiconductor device manufacturing [3]. In addition, precursors and recipes now exist for the ALD of a wide variety of materials, including oxides, nitrides, pure metals, and other compounds containing a wide variety of elements. Because ALD relies on the chemisorption of gas-phase precursors and other chemical reactions localized to the gas/solid interface, one may expect that the chemistry (active site density and type) and microstructure (roughness and porosity) of the starting substrate will play an important role in determining the early stages of film growth, and could potentially affect interface quality. Indeed, a number of studies have demonstrated that the initial stages of ALD can involve a transition or “incubation” period in which the growth rate is not constant, and that the duration and growth per cycle during this period is sensitive to the identity of the initial substrate [2-9]. Further, recent studies utilizing *in*



*situ* analysis techniques have demonstrated that, during the initial stages of ALD, chemical properties of the growing film including oxidation state and chemical composition can be quite different from the properties of the steady-state growing film [10-13]. For some applications, it is possible that the entirety of film growth will take place within an early transition regime. Therefore, research is ongoing to more fully understand processes taking place in the initial stages of the ALD for a number of industrially important films, with the goal of improving interface properties or initial film growth for given applications.

An application for which ALD is particularly well suited, and where control over interface chemistry and morphology is critical, is the formation of diffusion barrier films between metallic lines and the surrounding insulating material in the interconnect structures of integrated circuits [14]. The purpose of this barrier film is to prevent diffusion of metals, primarily copper, into the dielectric, and its integrity is essential in device reliability [15]. Refractory metal nitrides, TaN and WCN for example, are commonly used as barrier materials [3,16], and are deposited on the insulating material after the formation of high aspect ratio trenches and other features. The low dielectric constant, or “low- $\kappa$ ” insulating materials used in current and future generations of integrated circuits present challenges for the growth of barrier materials by ALD. Low- $\kappa$  is a somewhat general term, because there are several types of materials which may be used for this application [17], however, two major issues with low- $\kappa$  materials are frequently encountered. First, low- $\kappa$  materials tend to have a low density of chemically reactive surface sites from which to nucleate thin film growth, particularly when compared to other commonly used dielectrics such as SiO<sub>2</sub>. This is

partly because many of the reactive Si-OH terminations which are present on pure SiO<sub>2</sub> are replaced by more inert Si-CH<sub>3</sub> or other Si-alkyl terminations in low- $\kappa$ . This low density of active surface sites can lead to non-ideal ALD growth behavior in the initial stages of growth, including low initial thickness deposited per cycle, as well the formation of islands, leading to rough and possibly discontinuous films [4,6,18-21]. Furthermore, it has been shown that the density of reactive sites on a substrate can influence the density of thin ( $\sim 5$  nm) ALD TaN films [22,23]. A second issue with ALD growth on low- $\kappa$  dielectrics is that many of these materials contain a network of connected meso- and micropores, intentionally added to decrease the dielectric constant. Any near-surface void spaces, by definition, have no heterogeneous nucleation sites for ALD. In addition, because the ALD process leads to extremely conformal film deposition, it is possible that film material may infiltrate and fill porous low- $\kappa$  materials [24-26]. Infiltration of barrier material into the low- $\kappa$  is undesirable obviously, because it could cause degradation of the electrical properties of the low- $\kappa$ .

Two general methods exist to alter the properties of low- $\kappa$  materials to make them more suitable for ALD film growth. The first involves exposing the low- $\kappa$  to a highly reactive plasma, which can create active sites on the surface, enhancing nucleation, and/or it can densify the surface, decreasing infiltration of gas-phase species [19,20,25,27-32]. The main drawback to plasma-based modifications is that they can potentially modify the low- $\kappa$ , degrading its electrical or physical properties [17,33-35]. A second method that may be used to alter the surface chemistry of low- $\kappa$  is the deposition of a thin film overlayer, for example SiO<sub>2</sub> [21,36], Al<sub>2</sub>O<sub>3</sub> [37], SiC:H

[38,39] or parylene [40-42]. Similarly, an important concern with these “additive” strategies is to achieve the desired interfacial properties without altering the internal structure of the low- $\kappa$ .

The subject of the work presented here is to investigate ALD of the diffusion barrier materials  $\text{TiN}_x$  and  $\text{TaN}_x$  on two dielectric substrates, nonporous  $\text{SiO}_2$  and a porous low- $\kappa$  material, modified using branched organic layers. The use of thin organic films, notably self-assembled monolayers (SAMs) [43,44], is a well-established method to alter the chemical functionality of a surface prior to inorganic film growth [7-9,45-50]. Straight chain SAMs, while versatile, are intrinsically limited by their structure in that they only have one active functional group per anchoring site on the underlying substrate. On the other hand, a branched molecule with a distribution of functional groups available to interact with either the substrate or with gas-phase ALD precursors has the potential to “multiply” nucleation sites present on the substrate [9,48]. Branched oligomers or polymer molecules are also more effective at filling space, an important property if the molecule is to be used to seal porous materials.

The experiments described here involve two branched organic films. One film, polyglycidol, contains hydroxyl and ether groups, while the other, poly(ethylene imine), contains amine functionality (primary, secondary, and tertiary). They also differ in the method of formation: the former grown/grafted from a surface; the latter deposited intact from solution. First discussed are the effects of these branched organic layers on the initial chemisorption of the metalorganic ALD precursor  $\text{Ta}[\text{N}(\text{CH}_3)_2]_5$ , with a focus on the density and chemical state of the chemisorbed species, similar to

previous results presented for other branched and straight chain organic layers on nonporous SiO<sub>2</sub> [47,48]. A second set of experiments will examine the effect of the branched organic layer on the initial stages of ALD, specifically the effect on the amount of material deposited per cycle and the chemical composition of the deposited film. For ALD on the porous low-κ material, a key measurement will be the degree of infiltration of the ALD film into the pore network of the low-κ. Experimental techniques will include the use of ellipsometry to quantify the kinetics of growth, *in situ* x-ray photoelectron spectroscopy to quantify chemical state and density of near-surface species, and AFM evaluate the evolution of thin film morphology.

### 5.3. Experimental Procedures

The experiments described here were conducted in the following sequence. First the polyglycidol and poly(ethylene imine) films were prepared on either SiO<sub>2</sub> or low-κ substrates. Second, the organic layers were characterized using XPS, ellipsometry, and contact angle measurements. Next, in one set of experiments, bare SiO<sub>2</sub>, bare low-κ, and both substrates modified with layers of polyglycidol or poly(ethylene imine) were exposed to Ta[N(CH<sub>3</sub>)<sub>2</sub>]<sub>5</sub> under UHV conditions. The resulting chemisorbed layers were analyzed *in situ* using XPS. In a second set of experiments, ALD was conducted in UHV on unmodified substrates and substrates modified with polyglycidol or poly(ethylene imine), with *in situ* XPS conducted between ALD cycle intervals in some cases. Finally, thin films were also deposited using a conventional viscous flow ALD reactor. Selected thin films in these cases

were characterized *ex situ* using ellipsometry, AFM, and XPS (including angle-resolved XPS).

### 5.3.1. Substrate preparation and formation of thin organic films

For experiments involving nonporous SiO<sub>2</sub>, substrates were cleaved from single-side polished, 100 mm Si(100) wafers (B doped, resistivity 38-63  $\Omega$  cm). The procedure used for preparation of thin SiO<sub>2</sub> films on these substrates, described in detail in Sec. 2.3 and elsewhere [46], produces a flat,  $\sim 15$ -20 Å thick layer of nonporous SiO<sub>2</sub> with a surface Si-OH density of  $\sim 5 \times 10^{14}$  cm<sup>-2</sup> [46,51,52]. There are two low- $\kappa$  substrates used here, referred to as low- $\kappa$  I and low- $\kappa$  II. Most experiments were performed using low- $\kappa$  I, a carbon doped SiO<sub>2</sub>-based thin film ( $\sim 1500$ -4500 Å) formed on 300 mm Si wafers, which is described in Sec. 2.2. From XPS, the low- $\kappa$  I material consists of approximately, by atomic fraction, 34% Si, 52% O, and 14% C. Heating to the temperature used for TaN<sub>x</sub> ALD (230 °C for  $\sim 20$  min.) results in a decrease in the molar content of C to approximately 10% (with increases in the molar content of Si and O to  $\sim 37\%$  and  $54\%$ ), due presumably to decomposition and desorption of carbon containing groups at elevated temperature in vacuum. As received, the void fraction of low- $\kappa$  I is  $\sim 18.4\%$  measured using ellipsometric porosimetry, with a dielectric constant ( $\kappa$ ) of 2.5. The internal structure of the material has been elucidated in detail by TEM tomography and ellipsometric porosimetry (EP) [53]. It contains a network of interconnected micro- and mesopores, with 90 % of the pores having a diameter of less than 5 nm. From EP, the pore size distribution is

bimodal with modes at approximately 0.9 and 1.6 nm. Taken together, the complementary EP and TEM results suggest that the structure of this low- $\kappa$  includes large ellipsoidal pores connected through smaller necks or micropores in the skeleton material. The contact angle of water on the unmodified low- $\kappa$  I is  $\sim 90^\circ$ . Low- $\kappa$  II is a similar material consisting by atomic fraction of  $\sim 36\%$  Si,  $45\%$  O, and  $19\%$  C. Low- $\kappa$  II has a network of interconnected pores, with total void fraction of  $\sim 21\%$  by EP, a bimodal pore size distribution with similar modes, and  $\sim 86\%$  of pores having diameter less than 5 nm. The dielectric constant of low- $\kappa$  II is 2.47.

The formation and structure of thin films of polyglycidol (poly-G) on nonporous  $\text{SiO}_2$  using the glycidol monomer has been described in detail previously [47,54]. Prior to deposition of poly-G, low- $\kappa$  substrates were exposed to one of two pretreatments: exposure to a 7.16 W air plasma for 2 seconds (Harrick Plasma, Ithaca, NY), or exposure to UV light in the presence of ozone (SAMCO UV-1 UV/Ozone cleaner, SAMCO, Inc., Kyoto, Japan). These pretreatments are used to enhance the density of hydrophilic oxygen-containing groups on the outer surface of the low- $\kappa$ . With the exception of these pretreatments, poly-G was deposited on  $\text{SiO}_2$  and the low- $\kappa$  substrates using identical methods. The thickness (and degree of branching) of the poly-G layer can be controlled by varying the amount of time the substrate is submerged in neat glycidol. On  $\text{SiO}_2$ , the growth rate of poly-G was measured to be  $\sim 1.1 \text{ \AA min}^{-1}$ .

Thin films of PEI were deposited by submerging substrates in a 0.1 wt% solution of PEI in deionized water for 15 minutes. The pH of the deposition solution is  $\sim 11$ . At this pH, PEI molecules are not highly charged [55], which minimizes

electrostatic repulsion between molecules. Substrates were then rinsed with deionized water and dried using a stream of nitrogen. The thin films of PEI formed on chemical oxide are characterized elsewhere [56]. PEI was deposited on SiO<sub>2</sub> and low-κ substrates using identical methods.

### 5.3.2. ALD of TiN<sub>x</sub> and TaN<sub>x</sub> films

TiN<sub>x</sub> and TaN<sub>x</sub> films were deposited in the custom-designed UHV chamber described in Sec. 2.5 [57-59] in an ALD mode using Ti[N(CH<sub>3</sub>)<sub>2</sub>]<sub>4</sub> or Ta[N(CH<sub>3</sub>)<sub>2</sub>]<sub>5</sub> in combination with NH<sub>3</sub>. These reactants have been shown previously to produce TiN<sub>x</sub> [60,61] and TaN<sub>x</sub> [62,63] films in conventional ALD reactors. Conducting ALD under UHV conditions involved a number of modifications from a typical ALD process. First, in this system the substrate is exposed to the transition metal precursors via a seeded supersonic molecular beam. This beam is generated by passing H<sub>2</sub> through a stainless steel vessel containing the transition metal precursor. The vessel is heated to generate the desired vapor pressure of the precursor (~ 100 mTorr). This requires a temperature of ~ 25 °C for Ti[N(CH<sub>3</sub>)<sub>2</sub>]<sub>4</sub> and ~ 60 °C for Ta[N(CH<sub>3</sub>)<sub>2</sub>]<sub>5</sub>. The resulting gas mixture is expanded through a heated 150 μm aperture, or nozzle, into the UHV chamber. Collisions in the nozzle region accelerate the heavier transition metal coordination complexes in the beam to an average kinetic energy of 2.07 eV, as measured using time-of-flight techniques [64]. The beam passes through a conical skimmer, then into an antechamber containing a shutter, which allows the passage of the beam into the deposition chamber to be modulated. Finally, an aperture defines the

beam into an approximately  $12 \times 12 \text{ mm}^2$  square area on the substrate surface at normal incidence. The approximate impingement rate for precursor molecules on the substrate surface is  $\sim 2.2 \times 10^{15} \text{ molecules cm}^{-2} \text{ s}^{-1}$  for  $\text{Ti}[\text{N}(\text{CH}_3)_2]_4$ , and  $\sim 1.3 \times 10^{15} \text{ molecules cm}^{-2} \text{ s}^{-1}$  for  $\text{Ta}[\text{N}(\text{CH}_3)_2]_5$ , at normal incidence for  $\text{Ti}[\text{N}(\text{CH}_3)_2]_4$  and  $30^\circ$  off normal for  $\text{Ta}[\text{N}(\text{CH}_3)_2]_5$ . Note that this  $30^\circ$  angle between the molecular beam and surface normal stretches the projected beam on the sample by  $\sim 15\%$ . The impingement rates given here would be equivalent to partial pressures of  $\sim 0.016 \text{ mTorr}$  and  $\sim 0.013 \text{ mTorr}$  in a conventional reactor, in which precursor molecules would possess a thermal energy distribution.  $\text{NH}_3$  was delivered via a doser utilizing a glass microcapillary array (Burle Technologies, Lancaster, PA), producing a flux of  $\text{NH}_3$  at the surface of  $\sim 1.3 \times 10^{17} \text{ molecules cm}^{-2} \text{ s}^{-1}$  for  $\text{TiN}_x$  ALD (*cf.*  $0.263 \text{ mTorr}$ ) [65,66]. For  $\text{TaN}_x$  ALD, the use of *in situ* XPS required a modification of the position of the  $\text{NH}_3$  doser, resulting in a  $\text{NH}_3$  flux of  $\sim 0.54 \times 10^{17} \text{ molecules cm}^{-2} \text{ s}^{-1}$  (*cf.*  $0.109 \text{ mTorr}$ ). Modulation of the  $\text{NH}_3$  exposure was achieved using a pneumatic valve on the delivery line.

In these experiments, the first step in the ALD cycle was the exposure of the surface to the beam containing the transition metal complex by opening the shutter for a specified time period, followed by a pump-out period to clear the chamber of residual species. Because of the low pressure of the deposition chamber during ALD (typically  $< 10^{-5} \text{ Torr}$ ), it operates in the molecular flow regime, so a purge gas is not used. The surface was then exposed to  $\text{NH}_3$ , followed by a second pump-out period. The ALD cycle was then repeated. This technique has been shown to deposit  $\text{TiN}_x$  films in a self-limiting, ALD mode at substrate temperatures from  $167$  to  $207^\circ\text{C}$  for



TiN<sub>x</sub> [7,8], and at approximately 230 °C for TaN<sub>x</sub>. For TiN<sub>x</sub> deposition, cycle times were: 10 s Ti[N(CH<sub>3</sub>)<sub>2</sub>]<sub>4</sub>|15 s (pump)|30 s NH<sub>3</sub>|100 s (pump). For TaN<sub>x</sub> deposition, a similar sequence was: 40|30|120|120 s. For TaN<sub>x</sub> ALD, XPS spectra were collected *in situ* for each substrate prior to initiating growth, then again at certain cycle intervals during ALD, typically after 5, 10, 15, and 20 ALD cycles. Additional experiments were conducted with no pauses for XPS during growth, with XP spectra collected only after 15 or 20 cycles, to determine what effect, if any, the pauses have on the film growth process. In all cases, during XPS analysis the substrate temperature was maintained at 230 °C. XPS was conducted in the same chamber as film growth.

A second set of *in situ* UHV experiments were undertaken to study the chemisorption of Ta[N(CH<sub>3</sub>)<sub>2</sub>]<sub>5</sub> on the initial substrate, i.e. the first half cycle of ALD. For experiments involving poly-G, surfaces were exposed at room temperature to pure Ta[N(CH<sub>3</sub>)<sub>2</sub>]<sub>5</sub> via a glass capillary array doser, at a flux of approximately  $1.2 \times 10^{12}$  molecules cm<sup>-2</sup> s<sup>-1</sup>, for ~ 3 hours. After dosing, XPS spectra were collected. For experiments involving PEI, substrates were exposed to a molecular beam of Ta[N(CH<sub>3</sub>)<sub>2</sub>]<sub>5</sub> seeded in H<sub>2</sub> at normal incidence ( $\sim 1.5 \times 10^{15}$  molecules cm<sup>-2</sup> s<sup>-1</sup>) for a period of 100 s, at a substrate temperature of 230 °C. XPS spectra were then collected as quickly as possible, maintaining the surface temperature of 230 °C. It was found that the chemisorbed species underwent slight changes over time at this temperature, evidenced by changes in the N(1s)/Ta(4p<sub>3/2</sub>) spectra over time scales of ~ 10 to 100 min. Therefore, all data shown here was collected for the same time interval, 18 min 30 s, from the end of the Ta[N(CH<sub>3</sub>)<sub>2</sub>]<sub>5</sub> exposure period to the start of XPS.

In addition to the UHV process described above, TaN<sub>x</sub> thin films were also deposited using conventional ALD in an Oxford FlexAL reactor (Oxford Instruments, Oxfordshire, UK). In this reactor, substrates were pre-heated to a temperature of 230 °C in 200 mTorr Ar, then exposed to repeated cycles of Ta[N(CH<sub>3</sub>)<sub>2</sub>]<sub>5</sub>|Ar purge|NH<sub>3</sub>|Ar purge at 230 °C, with individual cycle times of 2s|3s|5s|5s. These reaction conditions have been optimized to ensure saturation of the surface with precursor in each half-cycle at steady-state growth conditions, and adequate purging between cycles. During the Ta[N(CH<sub>3</sub>)<sub>2</sub>]<sub>5</sub> exposure step, the total chamber pressure was 80 mTorr, and the Ta[N(CH<sub>3</sub>)<sub>2</sub>]<sub>5</sub> was delivered to the chamber using an Ar flowrate of 150 standard cm<sup>3</sup> min<sup>-1</sup>. The Ta[N(CH<sub>3</sub>)<sub>2</sub>]<sub>5</sub> vessel or “bubbler” was heated to a temperature of 85 °C. During the NH<sub>3</sub> exposure step, the total chamber pressure was 80 mTorr.

### 5.3.3. Characterization techniques

For experiments involving chemisorption of Ta[N(CH<sub>3</sub>)<sub>2</sub>]<sub>5</sub> on poly-G utilizing an effusive capillary array doser, XPS was conducted *in situ* using a VSW CLASS 100 concentric hemispherical energy analyzer operated at constant pass energy of 90 eV, and a VSW twin anode x-ray source (VSW Worldwide, Cheshire, U.K.), with a photoelectron takeoff angle of 38.5°. *In situ* XPS analysis of the chemisorption of Ta[N(CH<sub>3</sub>)<sub>2</sub>]<sub>5</sub> delivered via a molecular beam was conducted using an Omicron Sphera U5 concentric hemispherical electron energy analyzer operated at a constant pass energy of 50 eV, and an Omicron DAR 400 twin anode source (Omicron

Nanotechnology USA, Eden Prairie, MN), described in Chapter 9. This XPS system was also used to collect spectra during ALD of  $\text{TaN}_x$ . Collecting XP spectra involved turning the substrate  $\sim 90^\circ$  from the deposition position, then translating the XPS hardware into the position used for analysis. A photoelectron takeoff angle of  $15^\circ$  was used for chemisorption experiments, and  $0^\circ$  (normal takeoff) for spectra collected during ALD. In all cases, non-monochromated Mg K $\alpha$  x-rays (1253.6 eV excitation energy) were used. For angle-resolved XPS (ARXPS) measurements, the takeoff angle was varied between  $0^\circ$  and  $60^\circ$  by rotating the substrate with respect to the analyzer axis.

For calculation of absolute atomic density using XPS, a reference standard consisting of 1000 Å polycrystalline Au (e-beam evaporated)/100 Å Cr/native  $\text{SiO}_2/\text{Si}(100)$  was used (full procedure discussed below). Correct alignment of the ARXPS position was confirmed using the Au reference standard, which exhibited constant Au(4f $_{7/2}$ ) intensity with takeoff angle.

The binding energy scale was corrected for substrate charging effects using the position of the dominant feature of the Si(2p) peak. In the case of  $\text{SiO}_2/\text{Si}(100)$ , the thickness of the  $\text{SiO}_2$  layer is small enough such that the dominant feature is from  $\text{Si}^0$  from the underlying Si substrate, and the binding energy was set to  $99.5 \pm 0.2$  eV. Because the precise chemical environment of the Si atoms in the low- $\kappa$  material is not known, published values were not available to set the correct Si(2p) binding energy in this case, and an alternate method was used. This method involved a measurement of the binding energy of the C(1s) core level of carbon in unreacted  $-\text{N}(\text{CH}_3)_2$  ligands, which are present in chemisorbed  $\text{Ta}[\text{N}(\text{CH}_3)_2]_5$  adlayers, and in thin  $\text{TaN}_x$  films

deposited on SiO<sub>2</sub> and low-κ. For SiO<sub>2</sub> substrates, the corrected binding energy of this peak was found to be  $286.2 \pm 0.22$  eV. The binding energy of this peak, as well as the dominant Si(2p) peak, was then measured for Ta[N(CH<sub>3</sub>)<sub>2</sub>]<sub>5</sub> adlayers and thin TaN<sub>x</sub> films on low-κ. Using the value of  $286.2 \pm 0.22$  as a reference for the C(1s) position, the corrected Si(2p) binding energy for the Si in low-κ I was found to be  $103.37 \pm 0.24$  eV. This value agrees well with the range of values reported for the Si(2p) binding energies reported for SiO<sub>2</sub> [67,68]. As a check, using this binding energy calibration method results in a corrected C(1s) binding energy of  $284.7 \pm 0.26$  eV for the main carbon component in the unmodified, bare low-κ, which is close to reported values of 284.38 eV and 284.8 eV for methyl carbons bound to silicon in poly(dimethyl siloxane) [69,70]. For thicker films of TaN<sub>x</sub> deposited on low-κ (~ 4 nm), the uncorrected Si(2p) binding energy decreases significantly, indicating that the static charge is dissipated through the TaN<sub>x</sub> film. Here the measured (uncorrected) Si(2p) binding energy is 103.48 eV, which is a likely upper bound for the true binding energy. Again using measurements of the C(1s) binding energy for -N(CH<sub>3</sub>)<sub>2</sub>, a value of  $103.35 \pm 0.23$  eV was determined for the binding energy of the dominant Si(2p) feature in low-κ II.

Concerning *ex situ* analysis, film thicknesses were measured using either a Rudolph AutoEL-II single-wavelength ellipsometer or Woollam VASE spectroscopic ellipsometer. Atomic force microscopy (AFM) was carried out using a Digital Instruments Dimension 3100 atomic force microscope. XPS was conducted *ex situ* on TaN<sub>x</sub> films deposited in the conventional ALD reactor using the Omicron Sphera U5 electron energy analyzer described above.

## 5.4 Results and discussion

### 5.4.1. Initial chemisorption of Ta[N(CH<sub>3</sub>)<sub>2</sub>]<sub>5</sub> on unmodified substrates

To characterize the first half cycle of TaN<sub>x</sub> ALD, a variety of surfaces were exposed to a constant dose of Ta[N(CH<sub>3</sub>)<sub>2</sub>]<sub>5</sub>, as described above, via a molecular beam. XP spectra of the chemisorbed layer were then collected *in situ*. The dose used ( $\sim 1.5 \times 10^{17}$  molecules cm<sup>-2</sup>) was sufficient to achieve saturation in the thickness deposited per cycle for ALD on SiO<sub>2</sub>, and is similar to exposures used for similar experiments involving Ti[N(CH<sub>3</sub>)<sub>2</sub>]<sub>4</sub> [7,8,46,50] and Ta[N(CH<sub>3</sub>)<sub>2</sub>]<sub>5</sub> [47,48]. Six substrates were investigated here: one SiO<sub>2</sub> (chemical oxide) substrate held at room temperature, two different types of low-κ held at 230 °C, and three chemical oxide substrates held at 230 °C. Two of the chemical oxide substrates were annealed in UHV for 1 hour prior to exposure to Ta[N(CH<sub>3</sub>)<sub>2</sub>]<sub>5</sub>, one substrate at 400 °C and the other at 550 °C. Annealing in vacuum reduces the concentration of Si-OH groups on the SiO<sub>2</sub> surface [71], and has been used previously to study the effect of the Si-OH site density on the early stages of TiN<sub>x</sub> ALD [4,5]. Although a direct measurement of the Si-OH density was not possible here, we estimate that the Si-OH surface concentration has been reduced by  $40 \pm 15$  % (annealed to 400 °C) and  $60 \pm 15$  % (550 °C) after the two annealing treatments [71-73].

The results of the chemisorption experiments are summarized in Fig. 5-1, which shows the position of the Ta(4p<sub>3/2</sub>) peak versus the atomic N:Ta ratio of the

chemisorbed species. This representation provides information on the chemical structure of the Ta[N(CH<sub>3</sub>)<sub>2</sub>]<sub>5</sub> layer [as the number of N(CH<sub>3</sub>)<sub>2</sub> ligands lost upon chemisorption is reflected in the N:Ta ratio], and the chemical binding environment of the Ta center {as the binding energy of the Ta(4p<sub>3/2</sub>) core level correlates with the oxidation state of Ta in the layer [74]}. The combined Ta(4p<sub>3/2</sub>) and N(1s) region (~ 395 - 410 eV binding energy) was a focus here, as with subsequent analysis, over other Ta core levels because of the ability to quickly collect data related to both Ta and N, and because the similar kinetic energy of the Ta(4p<sub>3/2</sub>) and N(1s) photoelectrons simplifies quantification, as discussed below. XP spectra from the Ta(4p<sub>3/2</sub>)/N(1s) region for SiO<sub>2</sub> and low-κ, examples of the spectra used to calculate the values shown in Fig. 5-1, are given later in Figs 5-4(a) and 5-4(c).

The atomic N:Ta ratio was calculated using the following formula:

$$\frac{I_{N(1s)}}{I_{Ta(4p_{3/2})}} = \frac{n_N \sigma_{N(1s)} T(E_{N(1s)}) \lambda_{N(1s)}}{n_{Ta} \sigma_{Ta(4p_{3/2})} T(E_{Ta(4p_{3/2})}) \lambda_{Ta(4p_{3/2})}} \quad (5-1)$$

Where  $I$  is the integrated area of the N(1s) or Ta(4p<sub>3/2</sub>) peak,  $n$  is the atomic density,  $\sigma$  is the photoionization cross-section,  $T(E)$  is the electron energy analyzer transmission function, and  $\lambda$  is the mean free path of the photoelectron. Because of the similarity of the kinetic energies of N(1s) and Ta(4p<sub>3/2</sub>) photoelectrons, the transmission function and mean free path terms can be ignored, so ultimately the intensities are corrected using the ratio of photoionization cross sections,  $\sigma_{Ta(4p_{3/2})} / \sigma_{N(1s)} = 3.93/1.77 = 2.22$  [75].

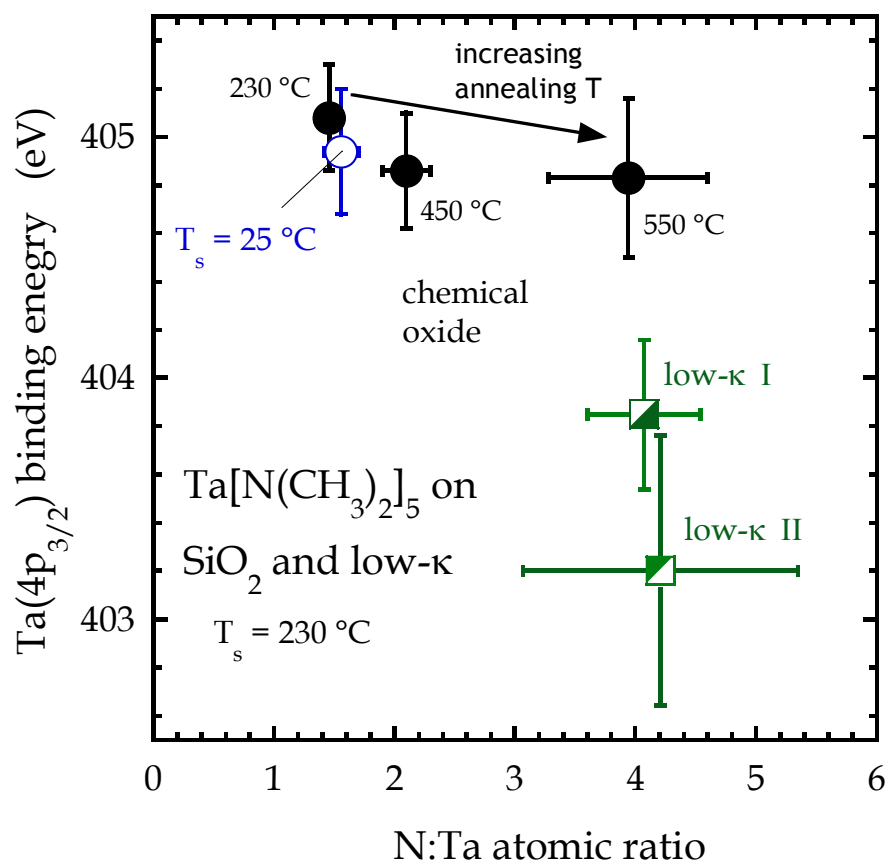


**Figure 5-1:** Peak binding energy of the Ta(4p<sub>3/2</sub>) XPS feature versus N:Ta atomic ratio for a number of substrates after a constant exposure to Ta[N(CH<sub>3</sub>)<sub>2</sub>]<sub>5</sub>. The substrate temperature was 230 °C, with one data point collected at room temperature, as noted. The substrates include two low-κ materials, and SiO<sub>2</sub> subjected to either no pre-anneal, or pre-annealing at 450 °C or 550 °C.

The Ta(4p<sub>3/2</sub>) peak positions were obtained through the use of a binding energy calibration based on the position of the Si(2p) peak from the underlying substrate. As discussed above, binding energies were shifted to obtain a Si(2p) position of 99.5 eV for the underlying Si(100) substrate in the case of SiO<sub>2</sub>, and 103.37 and 103.35 for the two low-κ materials.

The measured N:Ta ratios shown in Fig. 5-1 range from ~ 1.5 to 4. Given the N:Ta ratio of 5 for gas-phase Ta[N(CH<sub>3</sub>)<sub>2</sub>]<sub>5</sub>, a measured ratio of less than 5 would indicate partial loss of dimethylamido ligands upon chemisorption. The primary route for ligand loss involves a reaction between Ta[N(CH<sub>3</sub>)<sub>2</sub>]<sub>5</sub> and surface Si-OH groups, leading to the formation of (Si-O)<sub>x</sub>Ta[N(CH<sub>3</sub>)<sub>2</sub>]<sub>5-x</sub> species and gaseous HN(CH<sub>3</sub>)<sub>2</sub>. This process has been observed during the chemisorption of Ti[N(CH<sub>3</sub>)<sub>2</sub>]<sub>4</sub> and Ti[N(C<sub>2</sub>H<sub>5</sub>)<sub>2</sub>]<sub>4</sub> on SiO<sub>2</sub> [76,77], including the loss of multiple HNR<sub>2</sub> groups and formation of multiple SiO-Ti bonds for substrates with high Si-OH concentration. Other routes to ligand loss could involve reactions within or between adsorbed species. One possibility, observed by others as part of the thermal decomposition pathways for dialkylamido complexes of both Ta and Ti [77-81], involves intramolecular β-H abstraction by a remaining dimethylamido ligand, creating HN(CH<sub>3</sub>)<sub>2</sub> and leading to the formation of a Ta-N-C metallacycle complex. However, a clear signature of the formation of such a structure is the presence of a ‘carbide-type’ C(1s) peak at ~283 eV [81], which was not observed here. A related possibility, which cannot be ruled out here, is another intramolecular H abstraction to lead to the formation of an imine ligand [i.e. N(CH<sub>3</sub>)(=CH<sub>2</sub>)] [82].



A detailed peak fitting of the combined N(1s) / Ta(4p<sub>3/2</sub>) feature for the surfaces examined here indicates the presence of nitrogen in two binding states, with N(1s) binding energy  $399.0 \pm 0.2$  eV and  $397.4 \pm 0.2$  eV. The first type accounts for >90% all N present on the three SiO<sub>2</sub> surfaces at 230 °C, and 70-80% of the N on the two low- $\kappa$  surfaces. This peak can be assigned to retained -N(CH<sub>3</sub>)<sub>2</sub> ligands based on the previously reported N(1s) binding energy of 398.2 eV for N in Ta[N(C<sub>2</sub>H<sub>5</sub>)<sub>2</sub>]<sub>5</sub> [83], where the marginally higher binding energy measured in this case could be attributed to the likely more oxidized state of the Ta center when it is chemisorbed on an oxygen containing surface. The second, lower binding energy peak is ambiguous in that it could represent N either strongly bound to Ta, in a Ta=N or similar bond [83], or bound to a Si atom in the underlying substrate [85]. Considering the former, the spontaneous formation of Ta=N bonds in tantalum dialkylamido compounds has been observed [78,84], though notably not for Ta[N(CH<sub>3</sub>)<sub>2</sub>]<sub>5</sub>. The route to Ta=N bond formation is believed to involve first the formation of a metallacycle species involving Ta, -N(CH<sub>2</sub>R), and -CHR. This intermediate species can then release HC=R, leading to the formation of -Ta=N(CH<sub>2</sub>R). One possibility, then, is the participation of nearby alkyl groups on the low- $\kappa$  substrate in a similar mechanism. The lack of -CH<sub>x</sub> groups on SiO<sub>2</sub> then would explain the higher contribution from this type of nitrogen on the low- $\kappa$  surface. Alternately, the N(1s) peak at  $\sim 397.4$  eV could indicate that the N from a dissociated dimethylamido ligand is strongly bound to Si in the underlying substrate, as has been observed during the initial stages of HfO<sub>2</sub> ALD using Hf[N(CH<sub>3</sub>)<sub>2</sub>]<sub>4</sub> on hydrogen terminated Si [85]. A higher amount of N-Si bonding on the low- $\kappa$  substrates as compared to SiO<sub>2</sub> could be explained by the desorption of -

CH<sub>x</sub> groups at elevated temperatures, leaving residual Si atoms on the surface in a potentially more reactive state than the Si atoms in SiO<sub>2</sub>.

The position of the Ta(4p<sub>3/2</sub>) peak is related to the chemical binding environment of the Ta center, where generally a higher core level binding energy indicates a higher oxidation state [74]. From the data shown in Fig. 5-1, we observe a significant correlation between the Ta(4p<sub>3/2</sub>) peak position and the N:Ta ratio, where the layers with a lower Ta(4p<sub>3/2</sub>) peak position tend to have a higher N:Ta ratio. This is consistent with the process of Ta[N(CH<sub>3</sub>)<sub>2</sub>]<sub>5</sub> chemisorption taking place via the formation of Ta-O bonds [increasing the Ta(4p<sub>3/2</sub>) binding energy], with concomitant loss of HN(CH<sub>3</sub>)<sub>2</sub>. As expected, surfaces with a high concentration of Si-OH sites (i.e., SiO<sub>2</sub> which was not pre-annealed) lead to a more oxidized Ta center and lower N:Ta ratio as compared to surfaces with lower concentration of Si-OH groups (i.e., SiO<sub>2</sub> pre-annealed to 550 °C and low-κ). That a correlation between Ta oxidation state and N:Ta ratio is observed also supports the conclusion that most nitrogen remaining on the surface is bound to Ta as Ta-N(CH<sub>3</sub>)<sub>2</sub>, rather than bound directly to the substrate.

The N:Ta ratio of close to 4 measured for Ta[N(CH<sub>3</sub>)<sub>2</sub>]<sub>5</sub> on 550 °C annealed SiO<sub>2</sub> suggests reaction between Ta[N(CH<sub>3</sub>)<sub>2</sub>]<sub>5</sub> and isolated Si-OH groups, leading to a single ligand exchange and a Si-O-Ta[N(CH<sub>3</sub>)<sub>2</sub>]<sub>4</sub> species. This is consistent with the thermal annealing step leaving behind mostly isolated Si-OH [as well as geminal Si-(OH)<sub>2</sub>] groups, as compared to the closely spaced (< 3.3 Å) hydrogen bonded vicinal Si-OH groups which are present at 230 °C [71,73]. This, combined with the more extensive ligand loss for the Ta[N(CH<sub>3</sub>)<sub>2</sub>]<sub>5</sub> layer on non-annealed SiO<sub>2</sub> at 230 °C suggests extensive reactions between Ta[N(CH<sub>3</sub>)<sub>2</sub>]<sub>5</sub> and adjacent hydrogen bonded Si-

OH groups, when present. What is not entirely clear at this point is that there is little shift in the binding energy for Ta species bound to SiO<sub>2</sub> annealed at 550 °C, and non-annealed SiO<sub>2</sub>, even as the N:Ta ratio of the adlayer changes from ~ 4:1 to ~ 1.5:1.

#### **5.4.2 PEI and poly-G film characterization**

Before discussing the effect of PEI and poly-G on the chemisorption of Ta[N(CH<sub>3</sub>)<sub>2</sub>]<sub>5</sub> (Sec. 5.4.3), we will first discuss the PEI and poly-G organic layers themselves. The formation of thin films of poly-G and PEI on (nonporous) SiO<sub>2</sub> has been characterized using ellipsometry and XPS, in Refs. **47**, **54**, and **56**, and in Sec. 4.4.1, however their formation on the low- $\kappa$  materials used in this work has not been studied. XPS will be the primary method to characterize both organic films on low- $\kappa$ , and here, and for all results reported below, these results are for low- $\kappa$  I. The use of ellipsometry is problematic in this case, because the organic films are thinner than the low- $\kappa$  thin film by ~ 2-3 orders of magnitude. Slight changes in the optical properties of the porous low- $\kappa$  material (due to uptake of water, for example), or variations in the thickness of the low- $\kappa$  across the wafer can introduce significant error in the measured thickness of the organic layer.

For PEI|low- $\kappa$ , the N(1s) feature can be used to derive the density, chemical binding environment, and spatial extent of the near-surface amine groups. These measurements are displayed in Fig. 5-2. The method used to calculate absolute density from XPS intensity, which has been described previously [**9,46**], relies on the use of an Au calibration standard, as well as correction factors based on the atomic density of

Au,  $N_{\text{Au}} = 5.90 \times 10^{22} \text{ cm}^{-3}$  [86], attenuation length of the Au(4f<sub>7/2</sub>) photoelectrons in Au,  $\lambda_{\text{Au}} = 15.5 \text{ \AA}$  [87], photoelectron cross-sections,  $\sigma_{\text{Au}}/\sigma_{\text{N}} = 5.53$  [75], and analyzer transmission functions of the photoelectrons of interest,  $T(E_{\text{Au}})/T(E_{\text{N}}) = (1170 \text{ eV}/853 \text{ eV})^{-1}$ . In Fig. 5-2(a) we summarize the density and N(1s) binding energy for: (i) PEI thin films as deposited; (ii) PEI thin films after annealing at 230 °C in a 200 mTorr Ar for 3 min. (in the conventional ALD reactor); and (iii) PEI thin films annealed at 230 °C in UHV for ~ 20 min. Here we have considered PEI thin films formed on SiO<sub>2</sub> (chemical oxide) and low-κ. For cases (i) and (ii) the XP spectra were collected *ex situ* after transfer from ambient, with the substrate at room temperature. For case (iii) the spectra were collected *in situ*, with the substrate held at 230 °C. The latter two cases represent a good approximation of the state of the PEI film at the point at which ALD is initiated in (ii) the conventional, and (iii) the UHV ALD reactor. In Fig. 5-2(b) we present an example of the N(1s) XP spectra used to determine the densities and binding energies shown in Fig. 5-2(a). We note that most densities plotted in Fig. 5-2(a) represent values that have not been corrected for photoelectron attenuation effects. In three cases, we also plot values that have been corrected using angle-resolved XPS (*vide infra*). The attenuation correction leads to an increase in the calculated density of ~ 23-32%, and the magnitude of the correction is approximately equivalent for PEI|SiO<sub>2</sub> and PEI|low-κ.

The N(1s) binding energies for PEI|SiO<sub>2</sub> and PEI|low-κ fall between values reported for neutral amines, 398.6-399.1 eV [70,88-90] and for quaternary amines in which the N atom carries a positive charge, 401.3-402.5 eV [91-94]. An intermediate value indicates a mixture of these two groups in the PEI layer, and/or species in which

the N atom carries a partial positive charge. For example, partially charged amines might bind with the surfaces via Si-OH groups. If the implied charge state of the N in the layer is associated with bonding to the surface, then the slightly lower N(1s) binding energies measured for PEI|low- $\kappa$  would then indicate weaker bonding between PEI and the low- $\kappa$  substrates. Regarding the measured densities, as deposited PEI|low- $\kappa$  and PEI|SiO<sub>2</sub> surfaces have an (uncorrected) amine density of  $\sim 4.5 \times 10^{14}$  cm<sup>-2</sup>. Both surfaces degrade upon heating, with 15% and 28% of the total N density lost by SiO<sub>2</sub> and low- $\kappa$  after annealing for 3 min at 230 °C in Ar. For extended periods of heating (20 min. in UHV), N loss is much more significant for PEI|low- $\kappa$ . A reason for this could again be weaker bonding between the PEI and low- $\kappa$ , leading to a more significant loss of PEI and/or PEI fragments to the gas phase on heating.

In addition to the density and chemical state of amine groups, an important characteristic of the PEI films is their spatial extent normal to the surface. Using angle-resolved XPS (ARXPS), the spatial extent of the film can be quantified, representing a combination of the thickness of the film above the substrate, and the depth of infiltration of the PEI into the substrate in the case of porous low- $\kappa$ . In Fig. 5-2(c) we plot the integrated N(1s) intensity as a function of photoelectron takeoff angle ( $\theta$ ) for PEI|SiO<sub>2</sub> and PEI|low- $\kappa$ , both after annealing at 230 °C in 200 mTorr Ar for 3 min. If we assume that the N present in the PEI exists in a uniform, flat film of finite thickness, the integrated N(1s) intensity,  $I_N$ , is described by

$$I_N = I_{N,0} \left[ 1 - \exp\left(\frac{-d_{PEI}}{\lambda_N \cos \theta}\right) \right] \quad (5-2)$$

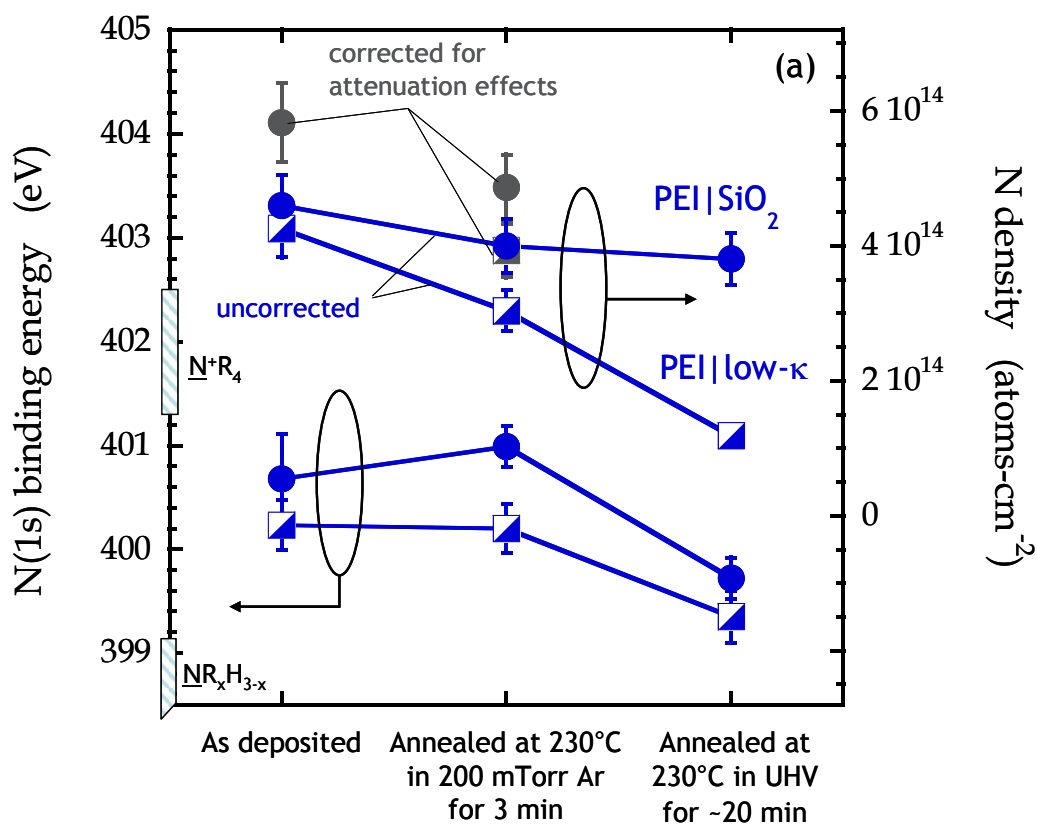


**Figure 5-2: (a)** Summary of N(1s) peak binding energy and surface atomic N concentration for PEI films deposited on SiO<sub>2</sub> and low-κ and subjected to various treatments. Expected ranges for neutral amines, NR<sub>x</sub>H<sub>2-x</sub>, and quaternary amines are shown on the binding energy axis.

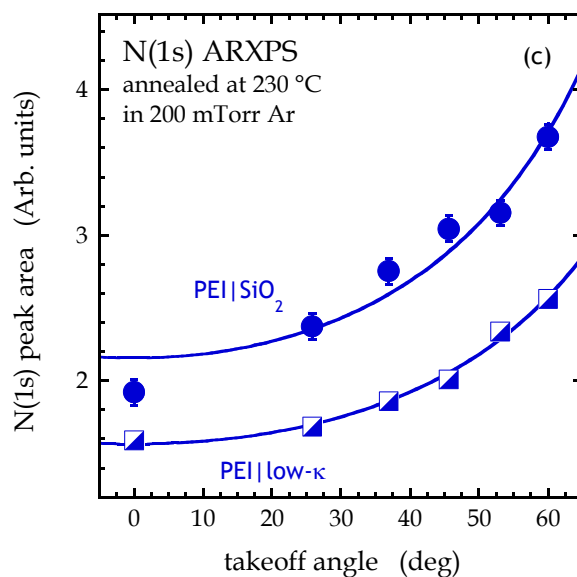
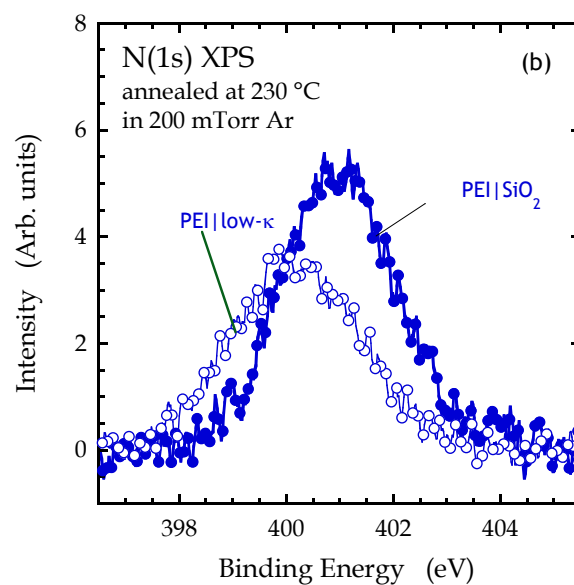


**Figure 5-2, continued: (b)** Detailed XP spectra in the N(1s) region and **(c)** integrated area under the N(1s) peak as a function of photoelectron takeoff angle for PEI films on SiO<sub>2</sub> and low-κ. Films were annealed at 230 °C in 200 mTorr Ar.

where  $d_{PEI}$  is the thickness of the PEI film in the direction normal to the substrate,  $\lambda_N$  is the attenuation length of N(1s) photoelectrons in the region of the PEI film, and  $I_{N0}$  is the N(1s) intensity from a theoretical PEI film of infinite thickness. A fit to the data [solid line in Fig. 5-2(c)] results in  $d_{PEI}/\lambda_N$  values of  $0.33 \pm 0.17$  for PEI/SiO<sub>2</sub> and  $0.44 \pm 0.06$  for PEI/low- $\kappa$ . Because infiltration of PEI is not possible in the case of the nonporous SiO<sub>2</sub>, the similarity of these two values rules out significant infiltration of the low- $\kappa$  by PEI. This is not unexpected, as the large size of the PEI molecule relative to the average pore diameter in the low- $\kappa$ , as well as the high contact angle of the deposition solvent on the inner surface of the pores would work in combination to block infiltration of PEI. Using a previously derived value of  $\lambda_N \sim 19.7 \text{ \AA}$  [56] we estimate thicknesses of  $6.5 \pm 3.3 \text{ \AA}$  for PEI on SiO<sub>2</sub> and  $8.7 \pm 1.2 \text{ \AA}$  for PEI on low- $\kappa$ . The thickness of PEI on SiO<sub>2</sub> measured using spectroscopic ellipsometry is  $4.3 \pm 0.7 \text{ \AA}$  [56], in reasonable agreement with these values. Note that this analysis assumes a constant value for  $\lambda_N$  across the thickness of the PEI film, ignoring the possible formation of a mixed interfacial layer between PEI and low- $\kappa$ . This assumption, if incorrect, may result in an underestimate of up to 40% in the calculated spatial extent of the PEI on low- $\kappa$ . However, even if this is the case the, ARXPS analysis confirms that the PEI is confined to the top  $\sim 1 \text{ nm}$  of the low- $\kappa$  layer.

The same issues with ellipsometry exist with the measurement of poly-G film thickness on low- $\kappa$ . Further compounding the issue, all elements present in poly-G (C, O, and H), are also present in high concentration in the low- $\kappa$  material. Therefore, the thickness of the poly-G film on low- $\kappa$  will be estimated using the Si(2p) signal from the underlying low- $\kappa$ , as shown in Fig. 5-3.



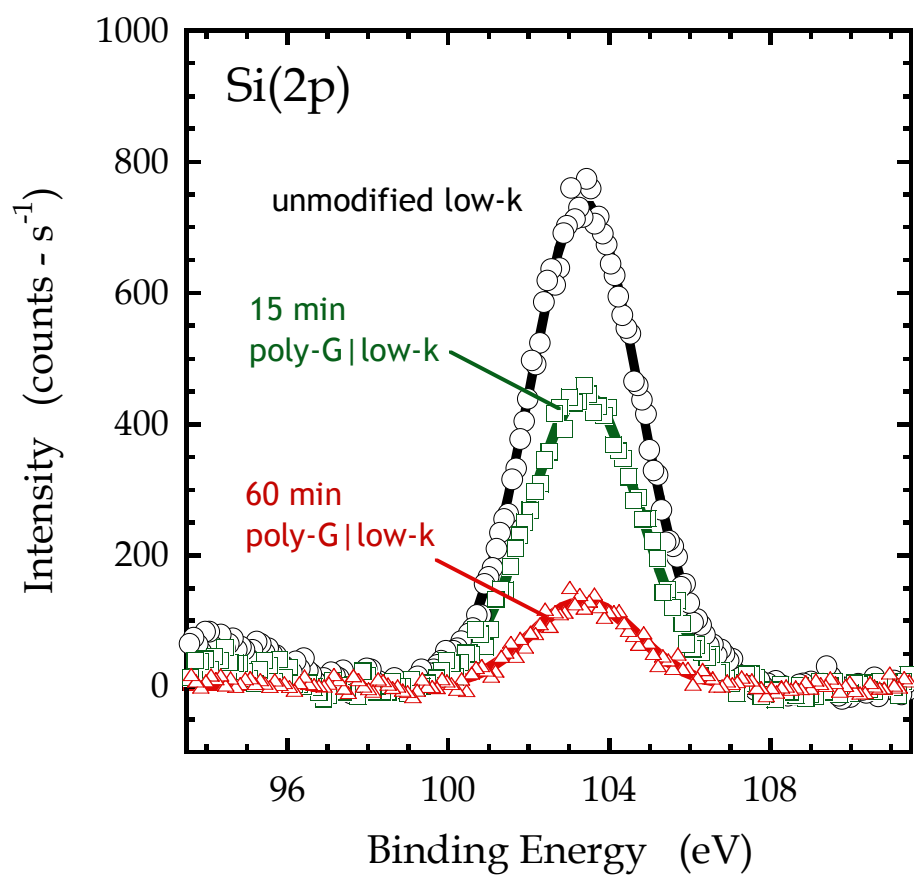


**Figure 5-3:** X-ray photoelectron spectra of the Si(2p) region for polyglycidol films deposited on low- $\kappa$  substrates.

Assuming that the poly-G layer is well approximated as a uniform, flat film on the low- $\kappa$  substrate, the integrated intensity of the Si(2p) signal,  $I_{Si}$ , will be attenuated as a function of the poly-G film thickness  $d_{poly-G}$  as described by the function

$$I_{Si} = I_{0,Si} \exp\left(\frac{-d_{poly-G}}{\lambda_{Si(2p)} \cos \theta}\right) \quad (5-3)$$

Where  $I_{0,Si}$  is the unattenuated Si(2p) intensity from the low- $\kappa$  substrate and  $\lambda_{Si(2p)}$  is the attenuation length of Si(2p) photoelectrons in the poly-G. Using a value of 48.3 Å for  $\lambda_{Si(2p)}$ , measured previously for poly-G films grown on SiO<sub>2</sub> [47] the calculated physical thicknesses of poly-G films after 15 and 60 minute exposures to the glycidol monomer are 20 Å and 67 Å, respectively. These figures represent a decrease of 33% and 21% from the thickness that would be obtained at the same growth time on SiO<sub>2</sub> [47]. This is not unexpected, as the density of surface Si–OH groups, which serve as nucleation sites for polyglycidol growth, are expected to be lower on the low- $\kappa$  substrate. In addition to XPS measurements, the contact angle of water has been measured on poly-G films on low- $\kappa$ . The contact angle on the bare low- $\kappa$  treated with UV/O<sub>3</sub> is ~60°, while after either 15 or 60 minutes of exposure to the glycidol monomer, the contact angle has decreased to <10°. This indicates an increase in the density of hydrophilic groups, presumably in the form of R–OH, are on the surface. Contact angles between 6-18° have been measured for poly-G films on SiO<sub>2</sub>, with a weak increasing dependence on poly-G thickness [47].

### 5.4.3. Effect of PEI and poly-G on initial chemisorption of Ta[N(CH<sub>3</sub>)<sub>2</sub>]<sub>5</sub>

In Fig. 5-4(a-d) XP spectra are displayed for the N(1s) and Ta(4p<sub>3/2</sub>) region for adlayers of Ta[N(CH<sub>3</sub>)<sub>2</sub>]<sub>5</sub> resulting from a dose of  $1.5 \times 10^{17}$  Ta[N(CH<sub>3</sub>)<sub>2</sub>]<sub>5</sub> molecules cm<sup>-2</sup> on SiO<sub>2</sub> (chemical oxide), low-κ, and both surfaces modified with thin layers of PEI (PEI/SiO<sub>2</sub> and PEI/low-κ). These spectra represent those used to calculate Ta(4p<sub>3/2</sub>) peak positions and N:Ta ratios shown in Fig. 5-1. A detailed fitting of the N(1s) feature to two peaks, as shown in Figs. 5-4(a) and 5-4(c), and discussed above in Sec. 5.4.1, is not shown in cases where PEI was present, because the high concentration of N atoms in this layer rendered the fitting to two peaks unreliable.

PEI affects the chemisorption of Ta[N(CH<sub>3</sub>)<sub>2</sub>]<sub>5</sub> on SiO<sub>2</sub> in two ways. First, the adsorbed density of Ta[N(CH<sub>3</sub>)<sub>2</sub>]<sub>5</sub> is significantly reduced. From the Ta(4d<sub>5/2</sub>) peak area (not shown here), we calculate Ta surface densities of  $(2.32 \pm 0.70) \times 10^{14}$  cm<sup>-2</sup> and  $(0.86 \pm 0.26) \times 10^{14}$  cm<sup>-2</sup> on unmodified SiO<sub>2</sub> (no pre-anneal) and PEI/SiO<sub>2</sub>, respectively, a reduction of 63%. Second, the presence of PEI reduces the oxidation of the Ta center, as evidenced by the shift to lower binding energy observed for both the Ta(4p<sub>3/2</sub>) and Ta(4d<sub>5/2</sub>) peaks. The shift for the former is from  $405.1 \pm 0.2$  eV (SiO<sub>2</sub>) to  $403.5 \pm 0.8$  eV (PEI/SiO<sub>2</sub>). These two effects are also shown in Fig. 5-5, where we plot the Ta(4p<sub>3/2</sub>) peak position vs. the Ta density [deduced from analysis of the Ta(4d<sub>5/2</sub>) peak]. A plot of the Ta(4d<sub>5/2</sub>) peak position vs. Ta density gives a similar result. Thus, both the density and nature of the species formed on SiO<sub>2</sub> appear to be modified by PEI. PEI could modify the chemisorptive properties of SiO<sub>2</sub> in two ways: (i) via its amine groups, it could simply bind to surface –OH species, rendering them

inaccessible to  $\text{Ta}[\text{N}(\text{CH}_3)_2]_5$ , and/or (ii) amine groups in PEI could react with  $\text{Ta}[\text{N}(\text{CH}_3)_2]_5$ , displacing  $-\text{N}(\text{CH}_3)_2$  ligands and forming  $(\text{RR}'\text{N})_x\text{-Ta}[\text{N}(\text{CH}_3)_2]_{5-x}$  species. The observed reduction in Ta density clearly indicates that chemisorption is affected by process (i). The decreased  $\text{Ta}(4p_{3/2})$  binding energy for  $\text{PEI}|\text{SiO}_2$  compared to unmodified  $\text{SiO}_2$  is consistent with both (i) and (ii). A decrease in the oxidation state of Ta indicates a decrease in the degree of  $(\text{Si-O})_x\text{-Ta}$  bonding. This could mean that, on  $\text{PEI}|\text{SiO}_2$ , more  $-\text{N}(\text{CH}_3)_2$  ligands are retained, or that  $-\text{N}(\text{CH}_3)_2$  ligands are being displaced by amine groups on PEI. It has been shown previously that amines are chemically reactive towards  $\text{Ta}[\text{N}(\text{CH}_3)_2]_5$  [48], and chemisorption of  $\text{Ta}[\text{N}(\text{CH}_3)_2]_5$  via amine groups would lead to a lower degree of oxidation of the Ta center compared to ligand exchange with the  $\text{Si-OH}$  groups on unmodified  $\text{SiO}_2$ . Unfortunately, deduction of the N:Ta ratio of the chemisorbed fragment, allowing a calculation of the number of ligands lost, is not feasible in the presence of PEI.

We can compare the effects of PEI on  $\text{SiO}_2$  to those due to annealing of unmodified  $\text{SiO}_2$ . In the latter case, as shown in Fig. 5-5, we find that high temperature annealing ( $550^\circ\text{C}$ ) decreased the amount of Ta uptake by  $\sim 66\%$  from the case where there was no pre-anneal, similar to the decrease in Ta density due to PEI. There was also a decrease in the apparent ligand loss for chemisorption on the annealed surface, but interestingly, a much smaller change in the oxidation state of the Ta. In view of these results, it seems that PEI is suppressing Ta uptake on  $\text{SiO}_2$  to an extent similar to the high temperature anneal, but is different concerning the nature of the species that is formed upon chemisorption. The latter suggests that amine groups on  $\text{PEI}|\text{SiO}_2$  may be

involved in ligand exchange reactions with the Ta complex and binding it to the surface [case (ii) *vide supra*].

We next consider the effect of PEI on the chemisorption of  $\text{Ta}[\text{N}(\text{CH}_3)_2]_5$  on low- $\kappa$ . In contrast to  $\text{SiO}_2$ , we observe an *increase* of  $\sim 17\%$  in the Ta density on PEI|low- $\kappa$  over bare low- $\kappa$ , while the oxidation state of the Ta center is essentially unchanged, as may be seen in Fig. 5-5. If we compare this result to that found for  $\text{Ta}[\text{N}(\text{CH}_3)_2]_5$  on PEI| $\text{SiO}_2$  we see that this result for PEI|low- $\kappa$  and, in fact, unmodified low- $\kappa$ , are similar in terms of both Ta uptake and Ta oxidation state. Above it was argued that PEI may attach to  $\text{SiO}_2$  through binding between some fraction of the amine groups on PEI and surface  $-\text{OH}$ , rendering both inactive with respect to the Ta complex. Remaining free amine groups may then react with  $\text{Ta}[\text{N}(\text{CH}_3)_2]_5$  in ligand exchange reactions to bind the complex. If this mechanism is correct, then the PEI bound to low- $\kappa$  retains a higher density of free amine to react with the Ta complex when compared to  $\text{SiO}_2$ —from Fig. 5-5 PEI|low- $\kappa$  binds  $\sim 48\%$  more Ta than PEI| $\text{SiO}_2$ . Note that this is apparently true even though the total density of N from PEI is higher for PEI| $\text{SiO}_2$  (*cf.* Fig. 5-2). This suggests either weaker binding between low- $\kappa$  and the PEI molecule, where a  $\text{Ta}[\text{N}(\text{CH}_3)_2]_5$  molecule could potentially disrupt a bond between PEI and low- $\kappa$ , or a higher fraction of unbound amine groups in PEI|low- $\kappa$ . Both of these situations are supported by the lower binding energy of N(1s) measured for PEI|low- $\kappa$  compared to PEI| $\text{SiO}_2$  (*cf.* Fig. 5-2), indicating weaker binding between PEI and the low- $\kappa$  substrate.

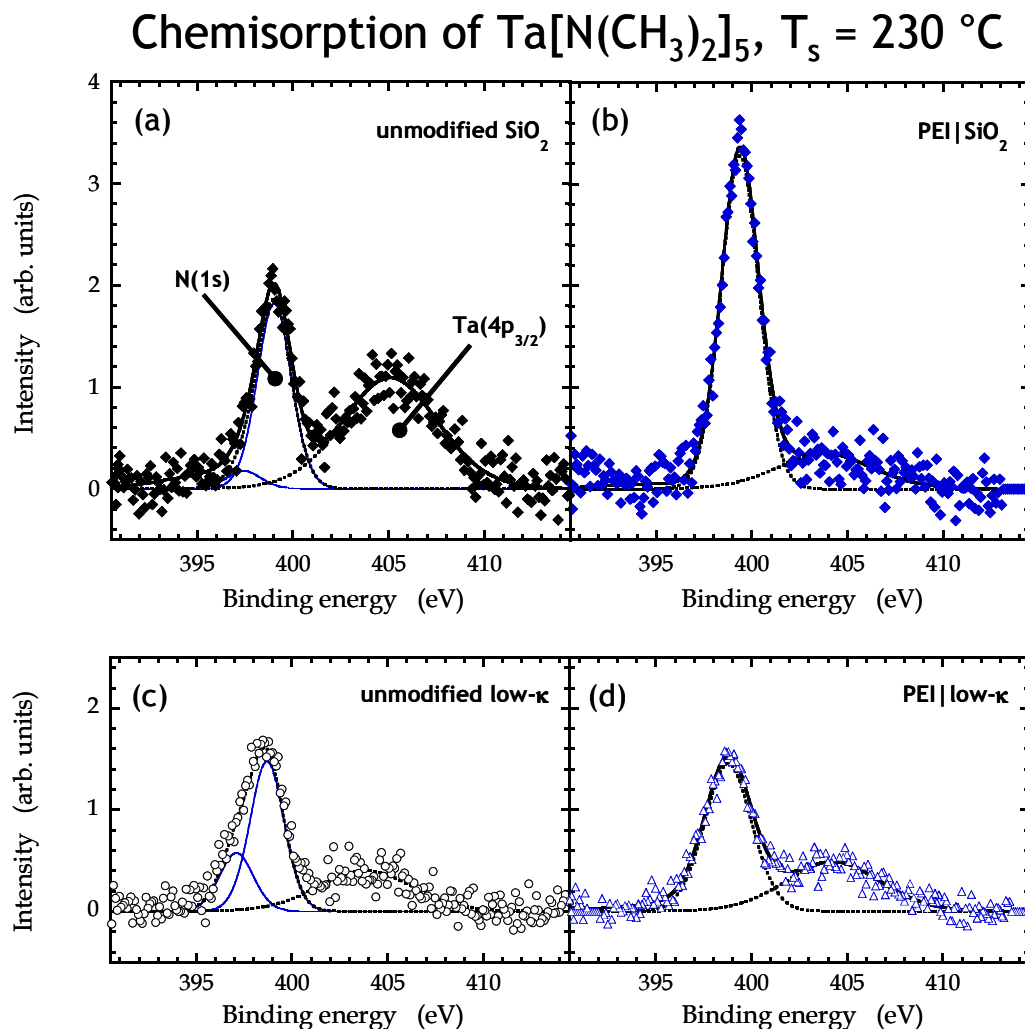


**Figure 5-4:** X-ray photoelectron spectra of the combined Ta(4p<sub>3/2</sub>) and N(1s) regions for adlayers of Ta[N(CH<sub>3</sub>)<sub>2</sub>]<sub>5</sub> on (a) SiO<sub>2</sub>, (b) a thin film of PEI on SiO<sub>2</sub>, (c) low-κ, and (d) a thin film of PEI on low-κ. Solid lines correspond to a fit described in the text.

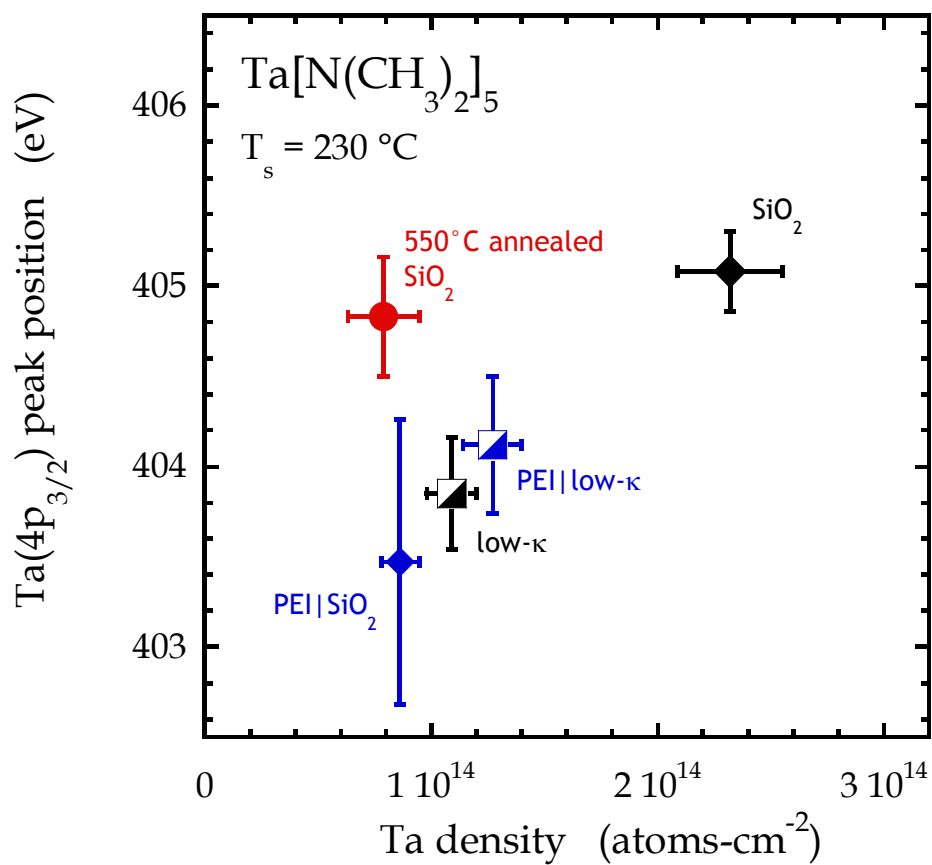


**Figure 5-5:** Binding energy of the Ta(4p<sub>3/2</sub>) XPS feature vs. the density of Ta for adlayers formed on a variety of surfaces, each after a constant dose of Ta[N(CH<sub>3</sub>)<sub>2</sub>]<sub>5</sub> delivered in UHV via a molecular beam.

ARXPS has also been performed in order to quantify the spatial extent of the Ta atoms in the chemisorbed layers on both low- $\kappa$  and PEI|low- $\kappa$ . Fig. 5-6(a) displays the area of the Ta(4d<sub>5/2</sub>) peak as a function of photoelectron takeoff angle for layers of unmodified low- $\kappa$  and PEI|low- $\kappa$ , where both have been exposed to a molecular beam of Ta[N(CH<sub>3</sub>)<sub>2</sub>]<sub>5</sub> at  $T_s = 230$  °C ( $\sim 1.5 \times 10^{17}$  molec-cm<sup>-2</sup>), equivalent to the surfaces examined in Fig. 5-4(c) and 5-4(d). The behavior of the Ta(4d<sub>5/2</sub>) intensity with takeoff angle is nearly indistinguishable for the two cases, indicating a similar spatial distribution of Ta for bare low- $\kappa$  and PEI|low- $\kappa$ . A fit of this data to Eq. 5-2, which assumes that the Ta is distributed in a uniform, flat film of finite thickness, gives parameters of  $d_{Ta}/\lambda = 0.43 \pm 0.13$  for bare low- $\kappa$  and  $0.45 \pm 0.10$  for PEI|low- $\kappa$ . These can be compared to the values found for a fit to the N(1s) feature for the unreacted layer of PEI| low- $\kappa$  [*cf.* Fig. 5-2(c)]:  $d_{PEI}/\lambda_N = 0.44 \pm 0.06$ . Thus, a fit of the N(1s) data for the unreacted layer, and the Ta(4d<sub>5/2</sub>) data for the reacted layer, gives essentially identical parameters. This result indicates a close connection between the spatial distribution of Ta in the chemisorbed layer and N in the PEI.

A more rigorous test of the effect of PEI on low- $\kappa$ , particularly concerning the infiltration of Ta, is to examine the behavior of the layer when Ta[N(CH<sub>3</sub>)<sub>2</sub>]<sub>5</sub> is delivered to the surface using a conventional ALD reactor. The driving force for diffusion into the porous low- $\kappa$  is proportional to the partial pressure gradient, which for UHV molecular beam delivery is minimal, whereas it can be sizeable for the conventional ALD reactor (< 80 mTorr here). Also, in the case of conventional ALD the incident Ta[N(CH<sub>3</sub>)<sub>2</sub>]<sub>5</sub> molecules will possess a wide range of incident trajectories. For experiments involving exposure in a conventional ALD system, ARXPS was



conducted *ex situ* with an air break between deposition of the Ta[N(CH<sub>3</sub>)<sub>2</sub>]<sub>5</sub> layer and analysis. Air exposure likely leads to loss of ligands such as -N(CH<sub>3</sub>)<sub>2</sub> in the layer, while we expect that Ta will remain by and large where it was originally deposited. In Fig. 7(b) we display the results from ARXPS for exposure of low-κ and PEI|low-κ to Ta[N(CH<sub>3</sub>)<sub>2</sub>]<sub>5</sub> in the conventional ALD reactor. As may be seen here, unlike the results from molecular beam UHV exposure, a *significant* difference is observed due to the presence of PEI. Namely, we observe both a higher intensity of the Ta feature at fixed takeoff angle, as well as a more significant increase in intensity with takeoff angle for PEI|low-κ as compared to unmodified low-κ. This more dramatic increase in Ta(4d<sub>5/2</sub>) intensity at high takeoff angle indicates that more of the Ta is localized near the vacuum|substrate interface for PEI|low-κ.

In order to fit the ARXPS data shown in Fig. 5-6(b) it will be useful to develop alternative models to the ones associated with Eq. 5-2, where Ta is assumed to be distributed uniformly over a finite thickness. If diffusion is playing a role, we expect a gradient in the Ta concentration in the direction normal to the surface. Two simple functions we can make use of for this concentration gradient are: an exponential decay,  $C = C_0 \exp(-z/d)$ ; and the complementary error function,  $C = C_0 \operatorname{erfc}(z/d)$ , where  $C_0$  is the concentration of Ta at the vacuum|substrate interface,  $z$  is the depth, and  $d$  is a characteristic infiltration depth. Using the former, the predicted functionality for the intensity from ARXPS is:

$$I(\theta) = \frac{I_0}{[(\lambda \cos \theta)/d] + 1} \quad (5-4)$$

While the functionality for the erfc concentration profile is:

$$I(\theta) = I_0 \left\{ 1 - \exp \left[ \left( \frac{d}{2\lambda \cos \theta} \right)^2 \right] \operatorname{erfc} \left( \frac{d}{2\lambda \cos \theta} \right) \right\} \quad (5-5)$$

A fit to the exponential decay model, shown as a solid line in Fig. 5-6(b), gives  $d/\lambda = 0.10 \pm 0.03$  and  $3.7 \pm 2.8$  for Ta on PEI|low- $\kappa$  and unmodified low- $\kappa$ , respectively. As expected from the raw data, the Ta is much more localized to the top surface of the substrate in the case of PEI| low- $\kappa$ . We have also fit the data in Fig. 5-6(b) to the model assuming the concentration follows an erfc functionality and found similar results, with values of  $d/\lambda = 0.22 \pm .06$  for PEI|low- $\kappa$  and  $5.2 \pm 3.4$  for low- $\kappa$ . In Fig. 5-7 we plot the concentration profiles predicted by a fit of the data in Fig. 5-6 to Eq. 5-4. Similar profiles are generated by fits to the erfc functionality. We present the data in terms of absolute densities, making appropriate corrections for photoelectron sensitivity factors, etc. This plot underscores the large effect of PEI concerning penetration of the low- $\kappa$  using conventional, higher pressure exposures to the Ta precursor.

These results also can be used to obtain an equivalent absolute uptake of Ta per exposed (planar) surface area. For beam delivery we find similar values, namely,  $(1.40 \pm 0.43) \times 10^{14}$  atoms-cm<sup>-2</sup> for unmodified low- $\kappa$  and  $(1.65 \pm 0.50) \times 10^{14}$  atoms-cm<sup>-2</sup> for PEI|low- $\kappa$ . These values change little if we use the results from either the uniform thin film model, or the erfc functionality. Concerning conventional delivery, we find  $(1.71 \pm 1.18) \times 10^{14}$  atoms-cm<sup>-2</sup> for unmodified low- $\kappa$  and  $(0.76 \pm 0.23) \times 10^{14}$  atoms-cm<sup>-2</sup> for PEI|low- $\kappa$ .

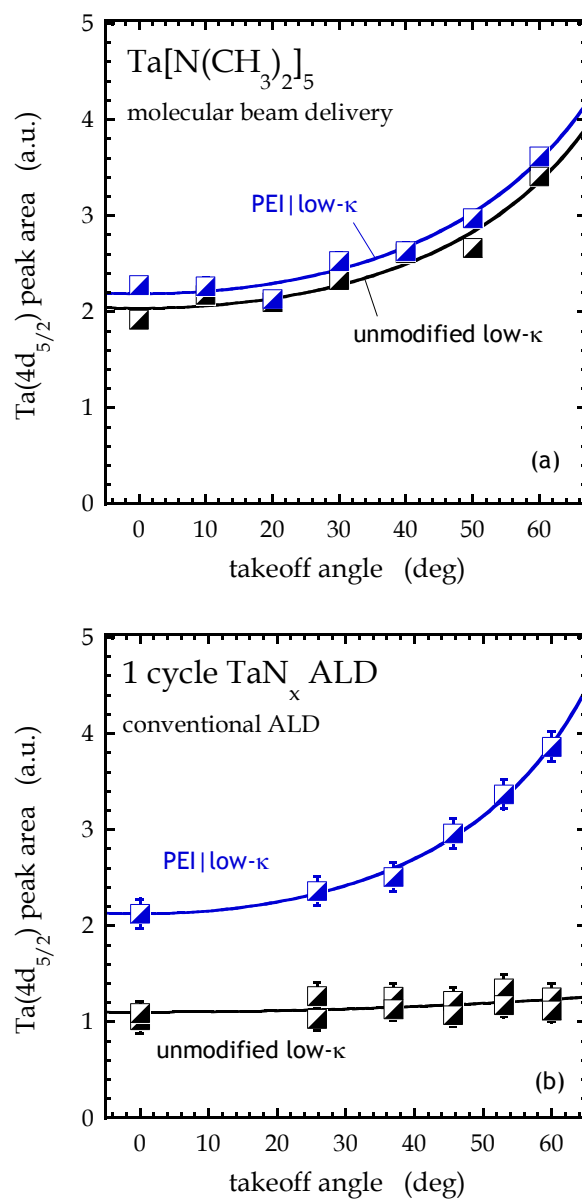


**Figure 5-6:** Area of the Ta(4d<sub>5/2</sub>) peak as a function of photoelectron takeoff angle for unmodified low-κ and PEI|low-κ substrates after exposure to Ta[N(CH<sub>3</sub>)<sub>2</sub>]<sub>5</sub>. Ta[N(CH<sub>3</sub>)<sub>2</sub>]<sub>5</sub> was delivered using **(a)** a supersonic molecular beam under UHV conditions and **(b)** using a conventional ALD reactor. Smooth lines represent fits to the data in which the concentration of Ta falls off exponentially with depth, Eq. 5-4.

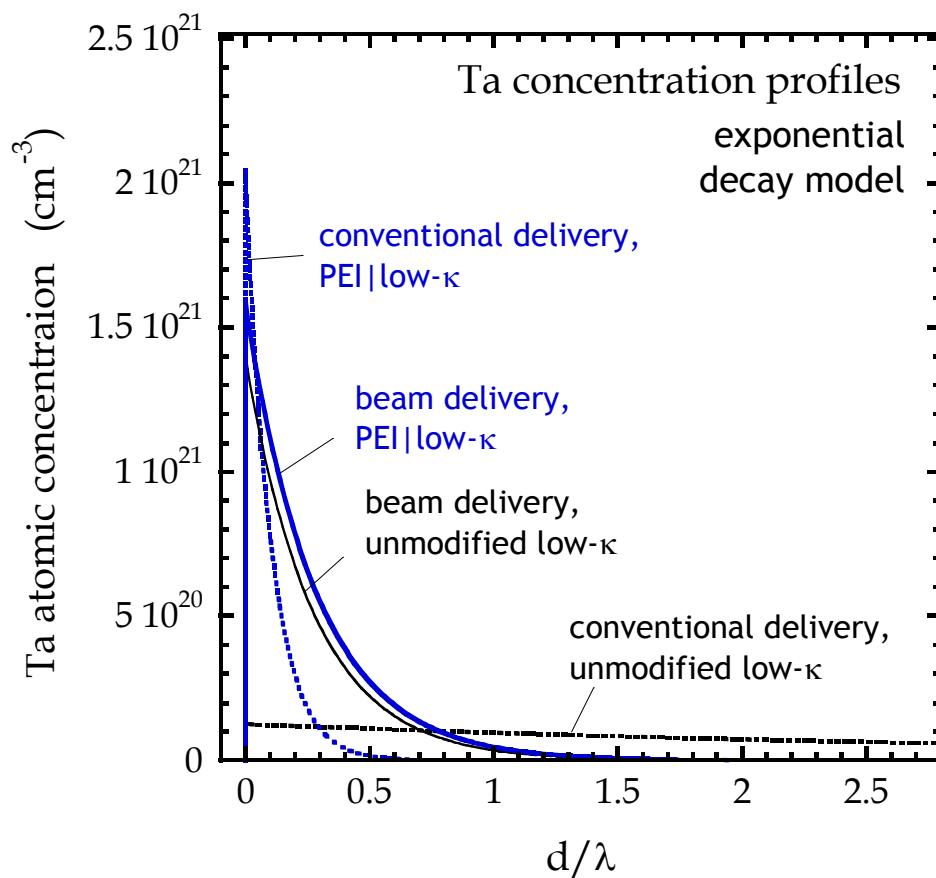


**Figure 5-7:** The concentration of Ta vs. depth below the substrate|vacuum interface for unmodified low- $\kappa$  and PEI|low- $\kappa$  exposed to  $\text{Ta}[\text{N}(\text{CH}_3)_2]_5$  via a molecular beam, or via conventional ALD methods. These profiles were obtained by fitting the data shown in Fig. 5-6 to the model given by Eq. 5-4.

The smaller uptake of Ta on PEI|low- $\kappa$  for conventional ALD could reflect differences in the PEI layers present before exposure to Ta[N(CH<sub>3</sub>)<sub>2</sub>]<sub>5</sub> in the two cases, as discussed above in connection with Fig. 5-2. For example, reduced degradation of the PEI in the case of conventional exposure might provide a better barrier to infiltration.

Turning now to the surfaces modified by thin layers of poly-G, first recall that there are two significant differences between these experiments and those presented in Figs. 5-1, 5-4, and 5-6(a). First, the set of experiments involving on surfaces modified by poly-G (and corresponding unmodified surfaces) were performed with the substrate at room temperature, as opposed to 230 °C. Second, the Ta[N(CH<sub>3</sub>)<sub>2</sub>]<sub>5</sub> was delivered via an effusive doser, which imparts a thermal energy distribution to the incident Ta[N(CH<sub>3</sub>)<sub>2</sub>]<sub>5</sub>. Fig. 5-8(a) shows the XP spectrum of a chemisorbed layer of Ta[N(CH<sub>3</sub>)<sub>2</sub>]<sub>5</sub> on unmodified SiO<sub>2</sub>. In this case, a Ta density of  $(2.18 \pm 0.66) \times 10^{14}$  cm<sup>-2</sup> is calculated, with a Ta(4p<sub>3/2</sub>) binding energy  $405.0 \pm 0.26$  eV, very similar to the values measured for a the chemisorbed Ta[N(CH<sub>3</sub>)<sub>2</sub>]<sub>5</sub> layer on SiO<sub>2</sub> at 230 °C where molecular beam delivery was used [density of  $(2.32 \pm 0.70) \times 10^{14}$  cm<sup>-2</sup>, Ta(4p<sub>3/2</sub>) binding energy  $405.1 \pm 0.22$  eV]. A similar phenomenon was observed for the chemisorption of Ti[N(CH<sub>3</sub>)<sub>2</sub>]<sub>4</sub> on SiO<sub>2</sub>, where the Ti(2p<sub>3/2</sub>) binding energy and Ti saturation density did not vary significantly at substrate temperatures of -50, 30, and 110 °C [46]. One major difference between Ta[N(CH<sub>3</sub>)<sub>2</sub>]<sub>5</sub> chemisorbed on SiO<sub>2</sub> at 230 °C [Fig. 5-4(a)] and at room temperature [Fig. 5-8(a)] is a significant broadening of the N(1s) feature at room temperature. This broadening is attributed to the presence of N in two chemical binding environments for the room temperature case.

## Chemisorption of $\text{Ta}[\text{N}(\text{CH}_3)_2]_5$ , $T_s = \text{RT}$

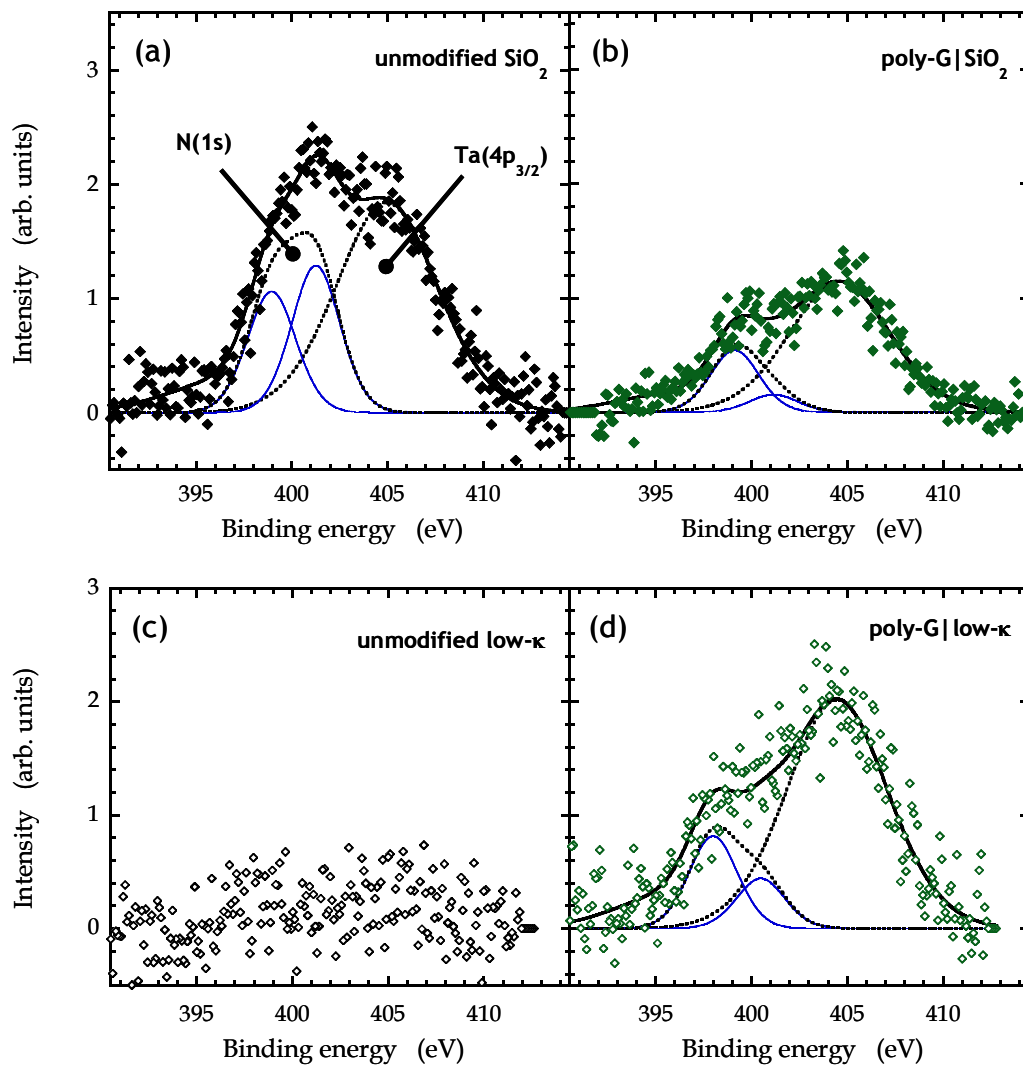


**Figure 5-8:** X-ray photoelectron spectra of the combined Ta(4p<sub>3/2</sub>) and N(1s) regions for adlayers of  $\text{Ta}[\text{N}(\text{CH}_3)_2]_5$  on (a) SiO<sub>2</sub>, (b) a thin film of polyglycidol on SiO<sub>2</sub>, (c) low-κ, and (d) a thin film of polyglycidol on low-κ. Solid lines correspond to a fit described in the text.

Fitting the N(1s) feature assuming two types of N are present results in peak binding energies of  $\sim 399$  eV and  $\sim 401.3$  eV. The former can be assigned to residual  $-\text{N}(\text{CH}_3)_2$  ligands attached to Ta, as observed above in Fig. 5-4. The higher binding energy of the latter N(1s) peak suggests hydrogen bonding involving loss of electron density by the N atom, likely in the form of bonds between  $\text{HN}(\text{CH}_3)_2$  and surface Si-OH groups, or residual water molecules that are present on the  $\text{SiO}_2$  surface at room temperature. This type of nitrogen is also observed for chemisorbed  $\text{Ta}[\text{N}(\text{CH}_3)_2]_5$  on  $\text{SiO}_2$  at room temperature when the  $\text{Ta}[\text{N}(\text{CH}_3)_2]_5$  is delivered via a molecular beam, as can be seen in Fig. 5-9. Therefore, the presence of this type of nitrogen in the chemisorbed layer is due to the lower substrate temperature, rather than the lower kinetic energy of the incident  $\text{Ta}[\text{N}(\text{CH}_3)_2]_5$  molecules.

As shown in Fig. 5-8(b), the presence of a  $\sim 30$  Å layer of poly-G on  $\text{SiO}_2$  decreases the saturation density of Ta, and reduces the N:Ta ratio, indicating that more  $-\text{N}(\text{CH}_3)_2$  ligands are lost on poly-G/ $\text{SiO}_2$  as compared to unmodified  $\text{SiO}_2$ . The mechanism for this increased ligand loss has been discussed in detail previously [47]. Briefly, it is believed that a high number of reactions take place between the Ta center and R-OH groups in poly-G due to the distributed 3-d nature of the -OH groups and the flexibility of the organic backbone of poly-G. On unmodified low- $\kappa$ , Fig. 5-8(c), the amount of  $\text{Ta}[\text{N}(\text{CH}_3)_2]_5$  on the surface is below the detection limit for Ta(4p<sub>3/2</sub>) and N(1s). This is in contrast to the result shown above in Fig. 5-4(c) where significant Ta was measured on unmodified low- $\kappa$  at 230 °C. This is most likely due to chemical changes in the substrate induced by the higher temperature in the latter case.

### Adsorbed $\text{Ta}[\text{N}(\text{CH}_3)_2]_5$ layers on $\text{SiO}_2$ , $T_s = \text{RT}$

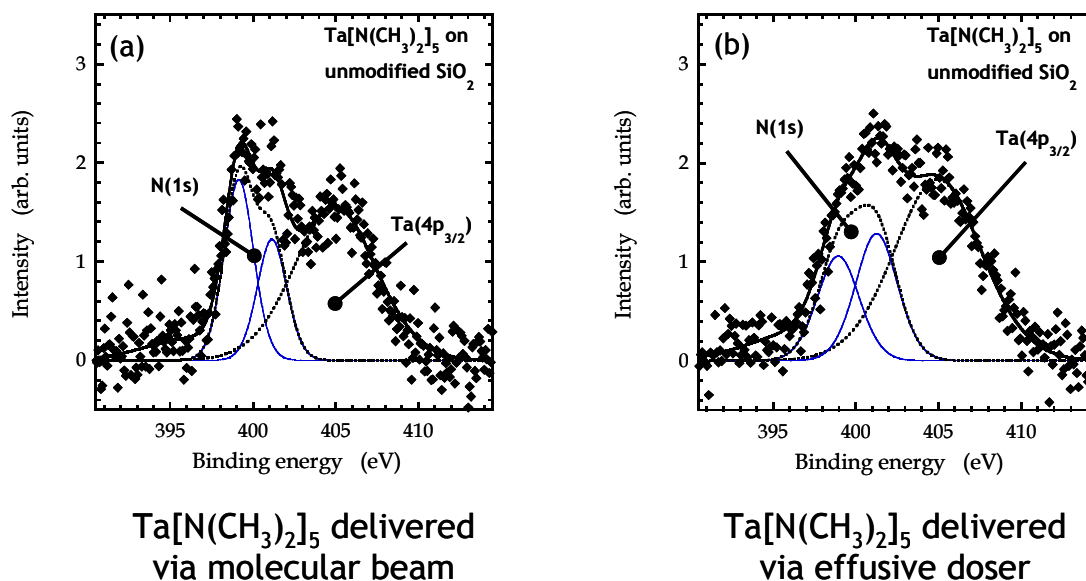


**Figure 5-9:** X-ray photoelectron spectra in the  $\text{Ta}(4p_{3/2})$  and  $\text{N}(1s)$  region for  $\text{Ta}[\text{N}(\text{CH}_3)_2]_5$  adlayers on unmodified  $\text{SiO}_2$ . **(a)**  $\text{Ta}[\text{N}(\text{CH}_3)_2]_5$  was delivered via a hyperthermal molecular beam (Olin hall 312 system), and **(b)**  $\text{Ta}[\text{N}(\text{CH}_3)_2]_5$  was delivered via an effusive doser (Olin hall B1 system). Note that the smaller peak width in **(a)** is due different XPS equipment used for the two experiments.



As discussed above, heating the low- $\kappa$  material in vacuum causes a decrease in the carbon concentration, indicating a potential loss of terminating  $-\text{C}_x\text{H}_y$  groups. Loss of these groups, which are not expected to have significant reactivity towards  $\text{Ta}[\text{N}(\text{CH}_3)_2]_5$ , could produce Si dangling bonds or other reactive sites. As shown in Fig. 5-8(d), the addition of a 20 Å layer of poly-G to the low- $\kappa$  material enhances the uptake of  $\text{Ta}[\text{N}(\text{CH}_3)_2]_5$ . Moreover, the N:Ta atomic ratios measured for  $\text{Ta}[\text{N}(\text{CH}_3)_2]_5$  on poly-G|SiO<sub>2</sub> and poly-G|low- $\kappa$  are similar and  $\sim 0.66$  in both cases, indicating the formation of similar chemisorbed species for both substrates, and that this species is different from that formed on unmodified SiO<sub>2</sub> (atomic N:Ta  $\sim 1.36$ ).

As with PEI, ARXPS was performed to determine the spatial extent of  $\text{Ta}[\text{N}(\text{CH}_3)_2]_5$  chemisorption on poly-G|SiO<sub>2</sub> and poly-G|low- $\kappa$ . The results of this measurement are shown in Fig. 5-10. Here, because of the larger thickness of the poly-G layer as compared to PEI, and the high density of active sites available for reaction across the thickness of poly-G, this set of ARXPS data was fit assuming that Ta exists at a uniform concentration to a depth of  $d$ . From a fit to the data in Fig. 5-10 we find  $d/\lambda = 0.68 \pm 0.17$  for poly-G|low- $\kappa$  and  $0.74 \pm 0.25$  for poly-G|SiO<sub>2</sub>. Employing the  $\lambda$  value measured previously for poly-G [47], we can calculate  $d$  values of  $33.9 \pm 8.5$  Å for poly-G|low- $\kappa$  and  $36.9 \pm 12.5$  Å for poly-G|SiO<sub>2</sub>. This result indicates reaction of the  $\text{Ta}[\text{N}(\text{CH}_3)_2]_5$  throughout the poly-G layer, with possible infiltration into the pore structure limited to the top  $\sim 1$ -2 nm.

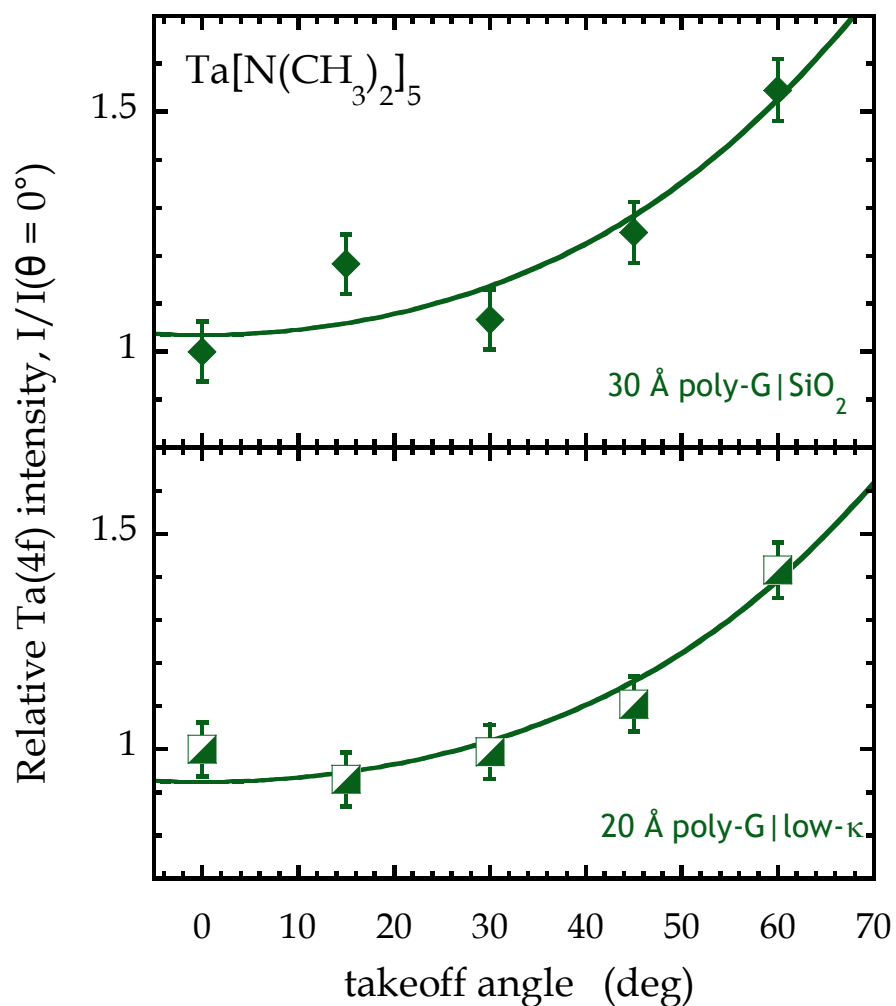


**Figure 5-10:** Integrated area of the Ta(4f<sub>7/2</sub>) peak for poly-G|SiO<sub>2</sub> and poly-G|low-κ after exposure to Ta[N(CH<sub>3</sub>)<sub>2</sub>]<sub>5</sub>, delivered via a glass capillary array doser under UHV conditions. Exposures were conducted at room temperature. The solid line represents a fit to a model which assumes that Ta exists at a uniform concentration to a depth of  $d/\lambda$ .

#### 5.4.4. Effect of PEI on TaN<sub>x</sub> ALD conducted in UHV

We next consider the effects of PEI and poly-G on the initial stages of ALD on the substrates considered in the previous sections. Fig. 5-11 presents calculated 2-d densities of Ta as a function of ALD cycles for SiO<sub>2</sub>, low-κ, PEI|SiO<sub>2</sub> and PEI|low-κ substrates. These densities are calculated based on the intensity of the Ta(4d<sub>5/2</sub>) peak, using the Au calibration method described above. In this case the absolute density calculation also involved a correction based on the finite thickness of the TaN<sub>x</sub> thin films based on  $d/\lambda$  values derived from the attenuation of the Si(2p) signal from the substrate. Here ALD was performed under UHV conditions (see experimental section above), and XP spectra were collected *in situ*. Physical thicknesses for the films considered in Fig. 5-11 can also be calculated by using the attenuation of the Si signal from the underlying substrate. These thicknesses follow the same trends as the 2-d densities, and are considered below in Fig. 5-18. The smooth curves in Fig. 5-11 are fits to the density vs. cycles data using the equation

$$D = D'_{\infty} \{n + m(1 - \alpha)[\exp(-n/m) - 1]\} \quad (5-6)$$

where  $D$  is the calculated 2-d density,  $n$  is the number of ALD cycles,  $D'_{\infty}$  is the deposited density per cycle as  $n \rightarrow \infty$ , and  $\alpha$  and  $m$  are parameters [7,8,95]. This model has the following characteristics:  $D|_{n=0} = 0$ ;  $dD/dn|_{n=0} = \alpha D'_{\infty}$ , and  $dD/dn|_{n \rightarrow \infty} = D'_{\infty}$ , i.e., the initial deposited density per cycle is attenuated by a factor of  $\alpha$ , and approaches its asymptotic value ( $D'_{\infty}$ ) with an exponential decay constant of  $m$  cycles.

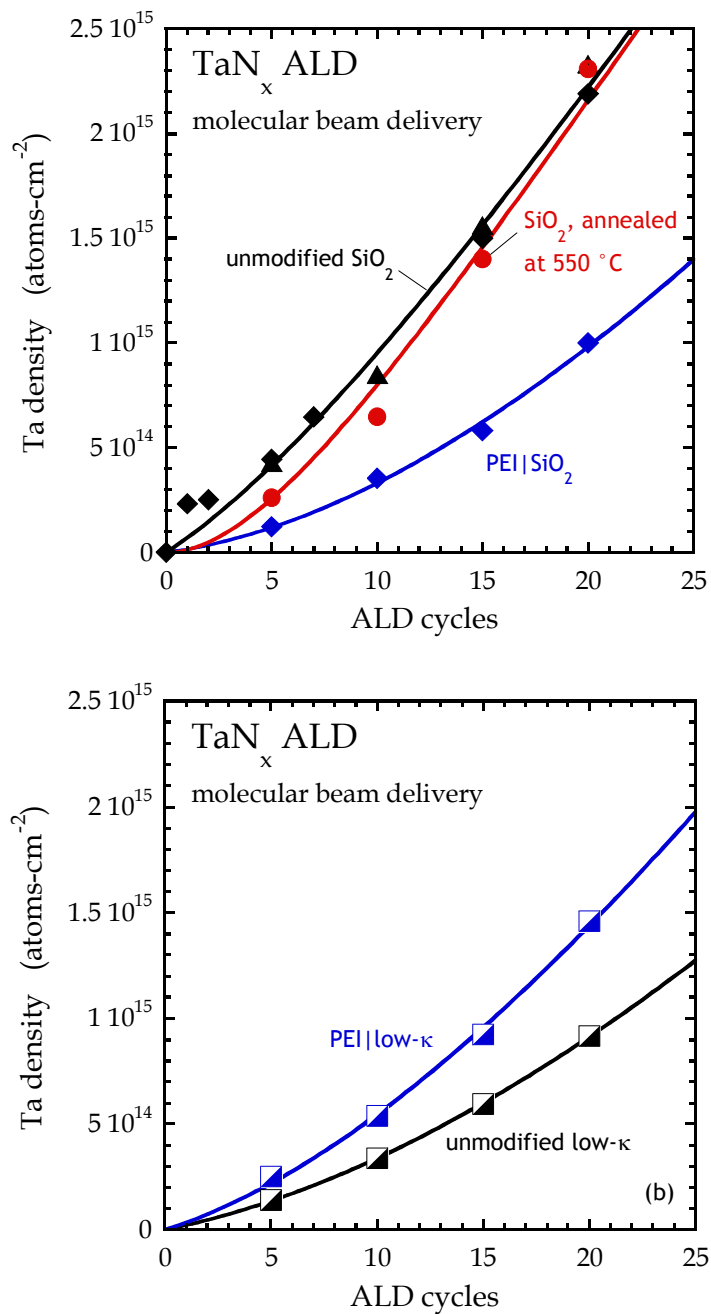


**Figure 5-11:** Calculated atomic density of Ta, deduced from in situ XPS, as a function of number of ALD cycles for TaN<sub>x</sub> ALD conducted in UHV at a substrate temperature of 230 °C. **(a)** includes SiO<sub>2</sub> substrates, unmodified, pre-annealed at 550 °C, or modified with a thin layer of PEI, and **(b)** includes low-κ substrates, unmodified or modified with a thin layer of PEI. Solid lines represent a fit to Eq. 5-6 in the text.

Here,  $D'_\infty$  was determined by calculating the deposited density per cycle for the 5 cycle interval for thickest films deposited, 15 to 20 cycles on SiO<sub>2</sub>. This reason for selecting this 5 cycle interval is that, because it is the thickest film, it will be the closest to the eventual ultimate growth rate. Using this method, a value of  $D'_\infty \sim 1.46 \times 10^{14} \text{ cm}^{-2} \text{ cycle}^{-1}$  was determined. This can be compared to the expected rate of  $2.1 \times 10^{14} \text{ cm}^{-2} \text{ cycle}^{-1}$  for stoichiometric TaN,  $1.4 \times 10^{14} \text{ cm}^{-2} \text{ cycle}^{-1}$  for Ta<sub>3</sub>N<sub>5</sub>, and  $1.5\text{-}1.9 \times 10^{14} \text{ cm}^{-2} \text{ cycle}^{-1}$  for Ta<sub>2</sub>O<sub>5</sub>, using the previously reported values of 0.5 Å-cycle<sup>-1</sup> for TaN<sub>x</sub> ALD [63], 0.65-0.85 Å-cycle<sup>-1</sup> for Ta<sub>2</sub>O<sub>5</sub> ALD [96,97], and the published bulk densities of these materials [86,98]. Ta<sub>2</sub>O<sub>5</sub> is included here due to the high O impurity level of the films deposited in UHV, the reasons for which are discussed below.

From the data shown in Fig. 5-11, a PEI film has the effect of suppressing growth on SiO<sub>2</sub>, and enhancing growth on low-κ. Recall that this is the same trend as observed for the effect of PEI on the density of Ta adsorbed in the first half cycle of ALD on SiO<sub>2</sub> and low-κ. In order to determine if the correlation between the Ta density after the first half cycle and the initial growth rate can be generalized, films were deposited on SiO<sub>2</sub> which had been pre-annealed to 550 °C. The density of Ta[N(CH<sub>3</sub>)<sub>2</sub>]<sub>5</sub> after the first ALD half cycle on this substrate is approximately equal to that of Ta[N(CH<sub>3</sub>)<sub>2</sub>]<sub>5</sub> on PEI/SiO<sub>2</sub>. From the result shown in Fig. 5-11(a), TaN<sub>x</sub> ALD proceeds much differently on PEI/SiO<sub>2</sub> and 550 °C annealed SiO<sub>2</sub>, indicating that there is not a general correlation between Ta density after the first half cycle and the amount of material deposited per cycle. Instead, it would seem that there is a difference in the ability of the Ta[N(CH<sub>3</sub>)<sub>2</sub>]<sub>5</sub> layers on 550 °C annealed SiO<sub>2</sub> and PEI/SiO<sub>2</sub> to

effectively regenerate active sites for subsequent Ta[N(CH<sub>3</sub>)<sub>2</sub>]<sub>5</sub> adsorption. On 550 °C annealed SiO<sub>2</sub>, the chemisorbed Ta[N(CH<sub>3</sub>)<sub>2</sub>]<sub>5</sub> layer possesses adequate reactivity to obtain the ideal growth rate after ~ 10 cycles, while the Ta[N(CH<sub>3</sub>)<sub>2</sub>]<sub>5</sub> layer on PEI|SiO<sub>2</sub> with approximately the same Ta density does not. The tendency for thin films of PEI to suppress the second half cycle of ALD has been observed for conventional ALD of HfO<sub>2</sub> and TaN<sub>x</sub> [56], as described in Chapter 4.

Beyond measuring the density of Ta on the surface during ALD, the use of *in situ* XPS also allows the chemical state and composition of the growing films to be characterized. First, the characterization of the oxidation state of the Ta in the film will be addressed, then the chemical binding environment of nitrogen. As we will see, the two are strongly correlated, and depend on the identity of the initial substrate. As shown in Figs. 5-1 and 5-5, the starting substrate can significantly affect the oxidation state of the Ta center and the atomic N:Ta ratio of the chemisorbed Ta[N(CH<sub>3</sub>)<sub>2</sub>]<sub>5</sub> precursor. Therefore, one may expect the initial substrate to also affect the initial stages of film growth in a similar way. Fig. 5-12, the binding energies of the (a) Ta(4d<sub>5/2</sub>) and (b) Ta(4p<sub>3/2</sub>) peaks are plotted as a function of Ta density for films deposited after 0.5-20 ALD cycles (identical to the films considered in Fig. 5-11). We observe that the Ta(4d<sub>5/2</sub>) binding energy decreases with the amount of Ta deposited for all substrates. Furthermore, for three substrates (PEI|SiO<sub>2</sub>, low-κ, and PEI|low-κ), the Ta(4d<sub>5/2</sub>) binding energy as a function of Ta density is similar, while in the initial stages the Ta(4d<sub>5/2</sub>) binding energy for the fourth substrate, unmodified SiO<sub>2</sub>, is higher. After approximately  $1.0 \times 10^{15}$  Ta atoms-cm<sup>-2</sup> have been deposited (~10 cycles on SiO<sub>2</sub>), the binding energies begin to converge.

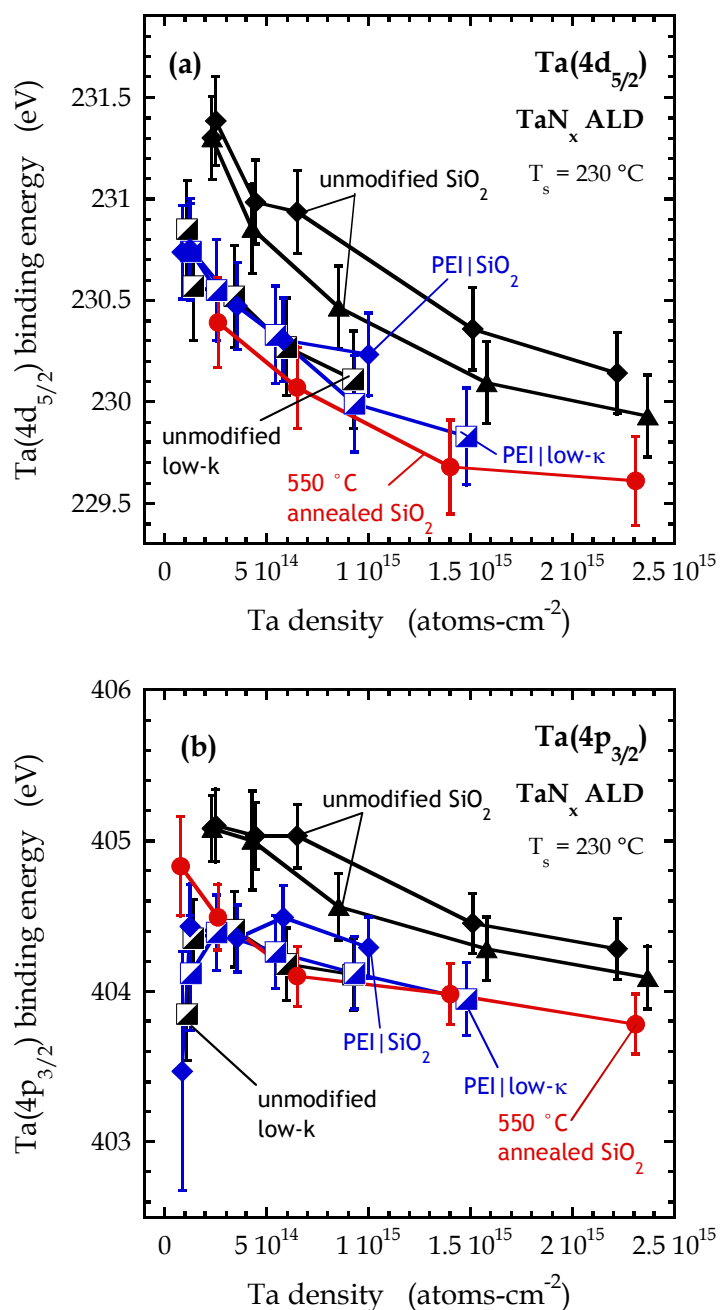


**Figure 5-12:** The binding energies of the (a) Ta(4d<sub>5/2</sub>) and (b) Ta(4p<sub>3/2</sub>) core levels as a function of the density of Ta for TaN<sub>x</sub> ALD conducted in UHV on several substrates. These XPS measurements were conducted *in situ*. The binding energy scales were corrected for charging effects using the Si(2p) signal from the underlying substrates.

This trend in Ta oxidation state follows the trend observed for Ta[N(CH<sub>3</sub>)<sub>2</sub>]<sub>5</sub> chemisorbed in the first half cycle of ALD (the first point displayed for all substrates in Fig. 5-12), suggesting that the additional Ta-O bonds formed in the chemisorbed layer of Ta[N(CH<sub>3</sub>)<sub>2</sub>]<sub>5</sub> on unmodified SiO<sub>2</sub> lead to the formation of a more oxidized TaN<sub>x</sub> layer in the initial stages of growth. The presence of PEI apparently suppresses oxidation during these initial stages, and has the effect of ‘normalizing’ the oxidation state of Ta in TaN<sub>x</sub> deposited in cases where the underlying substrates, low-κ and SiO<sub>2</sub>, lead to very different levels of oxidation in the absence of PEI.

The decrease in Ta(4d<sub>5/2</sub>) binding energy with increasing film thickness is similar to behavior observed for TiO<sub>2</sub> ALD on SiO<sub>2</sub> [13], where the Ti(2p<sub>3/2</sub>) binding energy decreased by ~ 0.4 eV over the first 5 ALD cycles (TiCl<sub>4</sub> / H<sub>2</sub>O ALD at 100 °C). Of note here is that the Ti(2p<sub>3/2</sub>) binding energy was higher in the initial stages of ALD as compared to the TiO<sub>2</sub> film deposited at steady state, which the authors also attribute to the formation of Si-O-Ti bonds at the SiO<sub>2</sub>/TiO<sub>2</sub> interface, in contrast to the Ti-O-Ti bonds formed in the bulk TiO<sub>2</sub> film.

Because the elements of interest exist in an extended thin film, other methods to calibrate the binding energy scale were explored which would eliminate any effects of differential charging between the substrate and the film. The binding energy of the Ta and N core levels vary depending on substrate type and film thickness, and are therefore unsuitable for use as reference elements. “Adventitious” C, commonly used for this purpose, would be unreliable due to its overlap with the carbon component in the low-κ substrate. Therefore, we have chosen the amine-type carbon present in the -N(CH<sub>3</sub>)<sub>2</sub> ligand as the reference component, and have made alternate plots referencing



the Ta(4d<sub>5/2</sub>) and Ta(4p<sub>3/2</sub>) peak positions to this component, which is assumed to lie at  $286.2 \pm 0.22$  eV. This result is presented in Fig. 5-13 for unmodified SiO<sub>2</sub>, annealed SiO<sub>2</sub>, and low-κ. The presence of a large amine carbon peak in PEI precludes this analysis in the case of PEI/SiO<sub>2</sub> and PEI/low-κ. As one can see, the results presented in Fig. 5-13 follow the same trends as those shown in Fig. 5-12. Since these substrates have very different types of Si, and surface charging characteristics, this gives credibility to the method of using the underlying Si shown in Fig. 5-12.

The next aspect to be considered is the chemical state of the nitrogen atoms in the growing film. The most significant chemical change observed in nitrogen in the initial stages is a shift from the most abundant chemical binding environment being the amine N found in the dimethylamido ligand [N(1s) binding energy  $\sim 399$  eV], to nitride N found in TaN<sub>x</sub> [N(1s) binding energy  $\sim 397.5$  eV]. This is demonstrated in Fig. 5-14, where a shift to significantly lower N(1s) binding energy from 0.5 to 15 cycles is clearly observed. It is likely that the amount of amine N in the near surface region does not vary significantly during growth, since it represents residual ligands which have not yet been removed through reaction with NH<sub>3</sub>. Therefore the apparent shift seen in Fig. 5-14 is an indication of the buildup of nitride N as the TaN<sub>x</sub> film grows. Because of the significant separation in N(1s) binding energy between the amine and nitride type N, the N feature can be reliably fit to two peaks, allowing an independent calculation of the N:Ta atomic ratio for both types of N. As stated above, the concentration of amine N does not vary significantly during growth, and after the early stages is small compared to the concentrations of other components in the film.

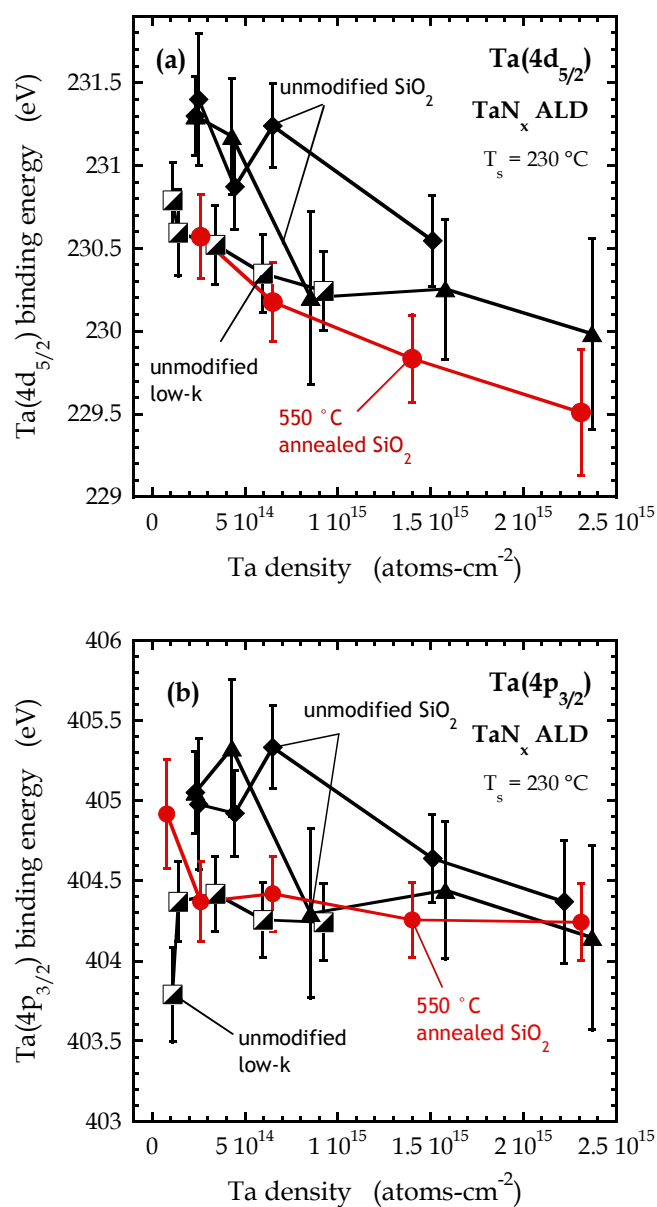


**Figure 5-13:** The binding energies of the **(a)** Ta(4d<sub>5/2</sub>) and **(b)** Ta(4p<sub>3/2</sub>) XPS features as a function of the density of Ta for TaN<sub>x</sub> ALD conducted in UHV on several substrates. The construction of this plot utilized the same data as Fig. 5-12, but in this case the C(1s) peak from amine type carbon was used to correct the binding energy scale for sample charging effects (see text for details).

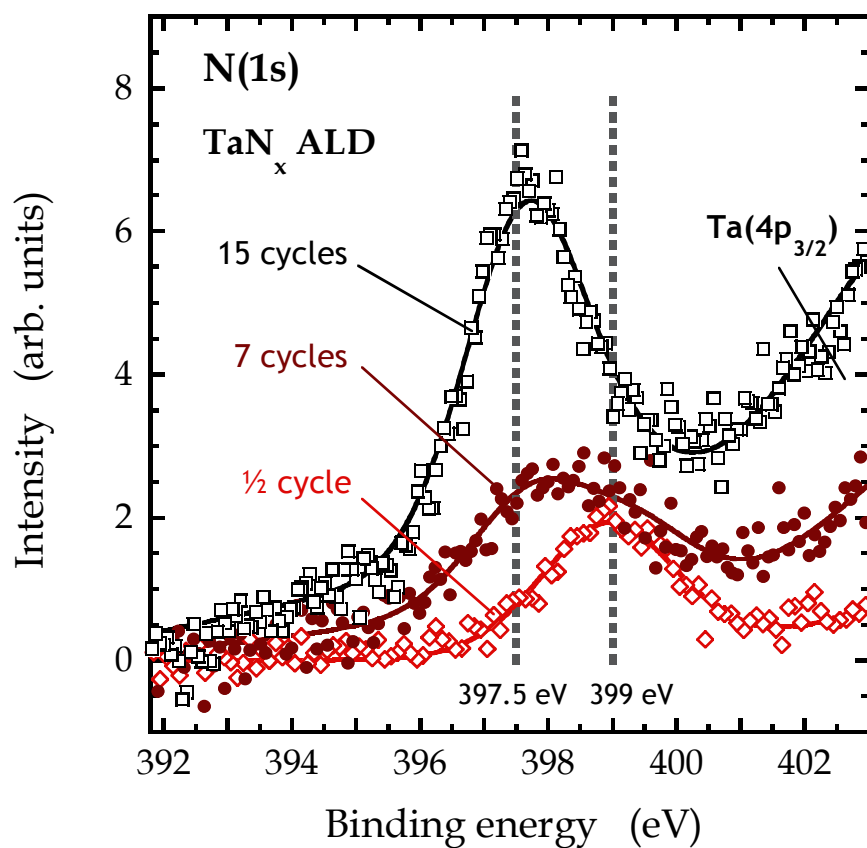


**Figure 5-14:** X-ray photoelectron spectra in the N(1s) region for 0.5, 7, and 15 cycles of TaN<sub>x</sub> ALD on unmodified SiO<sub>2</sub>. Vertical marks indicate the binding energies measured for the dominant types of nitrogen observed after 1/2 cycle (an amine-type nitrogen at ~ 399 eV) and 20 cycles of ALD (a nitride-type nitrogen at ~ 397.5 eV).

As shown Fig. 5-15, the behavior of the nitride type N:Ta atomic ratio for unmodified SiO<sub>2</sub> is different than the other three substrates examined. Specifically, films deposited on unmodified SiO<sub>2</sub> tend to have a lower nitride N:Ta ratio, with convergence to an equivalent value for all films around  $1.5 - 2.0 \times 10^{15}$  Ta atoms-cm<sup>-2</sup>. This indicates a correlation between Ta oxidation state (Fig. 5-12) and nitride N:Ta ratio, which can be explained in the following way: the Ta-O oxide bond is thermodynamically more stable than the Ta-N nitride bond, as evidenced by the higher bond dissociation energy of Ta-O as compared to Ta-N [86], and also by the fact that TaN<sub>x</sub> forms a native oxide upon exposure to air [99]. Therefore, in the presence of suitable oxygen containing groups (such as Si-OH), the more likely bond to be formed is Ta-O. If oxygen containing groups are less abundant (low-κ), or are blocked by the presence of a second surface film (PEI/SiO<sub>2</sub>), then a Ta-N bond can be formed. In other words, the growing film can more easily incorporate N as nitride in the absence of oxidizing groups. Again, here it is shown that the presence of an interfacial layer of PEI changes the early stages of growth of TaN<sub>x</sub> on SiO<sub>2</sub>, leading to behavior more like ALD on low-κ and PEI|low-κ.

A second aspect to note in Fig. 5-15 is that the nitride N:Ta ratio that is reached at ~ 20 cycles on all substrates (0.6-0.8) is not the value expected for either stoichiometric TaN or Ta<sub>3</sub>N<sub>5</sub>. This is likely due to oxygen incorporation in the film. Due to the low pressure (and therefore low incident reactant flux) used for deposition, the presence of contaminants in the reaction chamber, even at levels of ~ 10<sup>-9</sup> torr, may have a significant effect on film composition due to competition between adsorption of the contaminants and adsorption of reactants.

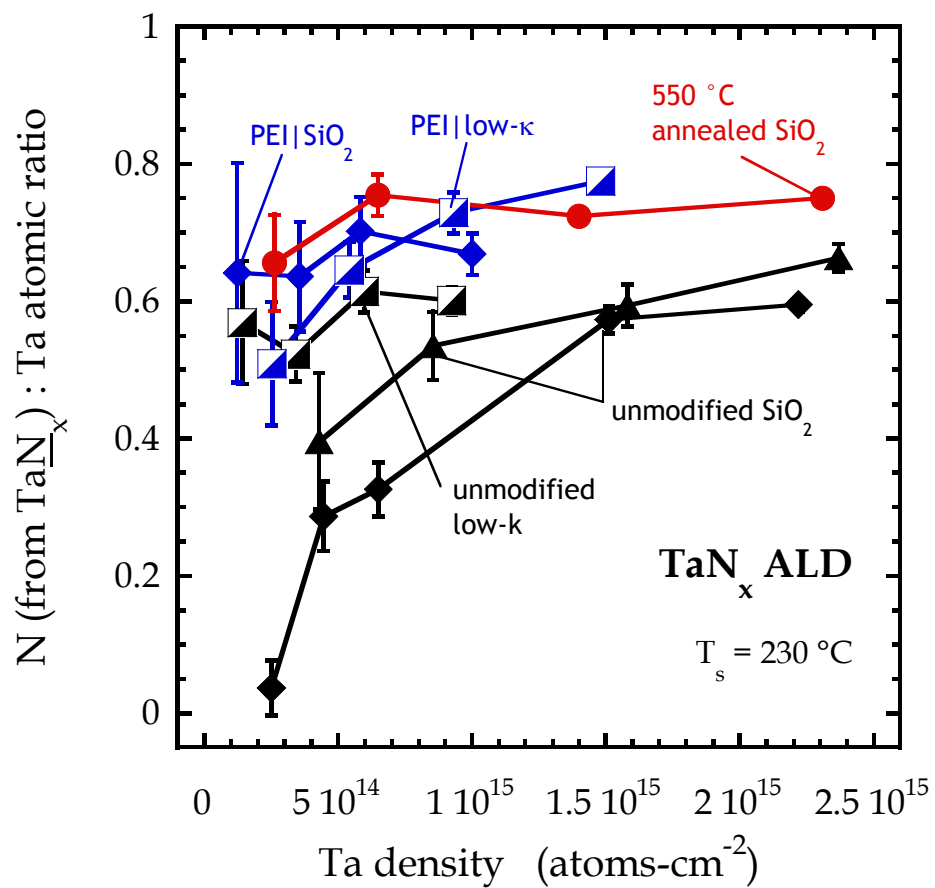


**Figure 5-15:** The atomic ratio of N (nitride, or TaN<sub>x</sub> type only) to Ta as a function of the density of Ta. These atomic ratios were calculated based on XPS data collected *in situ*.

First, the presence of relatively high pressures of reactant, purge, or carrier gases in the chamber in a conventional ALD reactor limit the mean free path of contaminant molecules, meaning that the substrate surface is partially ‘protected’ by the higher pressure of gas against contaminant flux from, for example, the chamber walls. Furthermore, the relatively low pressure of  $\text{NH}_3$  used in the coreactant step may also increase the incorporation of O and C {where the presence of C could be attributed to the  $\text{Ta}[\text{N}(\text{CH}_3)_2]_5$  molecule} as compared to films deposited in a conventional ALD reactor utilizing a higher pressure  $\text{NH}_3$  dose.

Before moving on, some mention should be made of the N(1s) peak observed at  $\sim 397.5$  eV for  $\text{Ta}[\text{N}(\text{CH}_3)_2]_5$  adlayers formed after the first cycle of ALD (*cf.* Fig 5-4). As discussed above, this may be due to the binding of dimethylamido ligands to Si dangling bond sites, forming, say  $(\text{CH}_3)_2\text{N-Si(R)}_2\text{-O-}$  species. If this is in fact the species being formed, and these species are retained during the subsequent stages of thin film growth, then this type of nitrogen would be incorrectly assigned as ‘nitride-type N’ in the analysis presented here. Due to the somewhat ambiguous nature of the chemical binding environment this type of N in the chemisorbed  $\text{Ta}[\text{N}(\text{CH}_3)_2]_5$  adlayers, we have not attempted to make any correction to the data shown in Fig. 5-15. However, an appropriate method to analyze data from 5-20 ALD cycles may be to subtract the contribution of this type of N from the measured nitride-like N intensity. The expected contribution to the measured nitride-like N component from the initially adsorbed  $\text{Ta}[\text{N}(\text{CH}_3)_2]_5$  was determined by first measuring the intensity of this component for  $\text{Ta}[\text{N}(\text{CH}_3)_2]_5$  adlayers on each substrate (using the spectra shown in Fig. 5-4). This intensity was then subtracted from the measured nitride-like N intensity

measured for each point in Fig. 5-15, after making suitable corrections based on XPS analyzer sensitivity, and assuming that the intensity of the signal from the initial adlayer was attenuated by a factor of  $\exp(-d/\lambda)$ .  $d/\lambda$  is the normalized thickness of the of the deposited  $\text{TaN}_x$  film determined using the  $\text{Si}(2p)$  intensity from the substrate. The nitride-like N to Ta atomic ratio was then recalculated using the “corrected” value, and the resulting alternate version of Fig. 5-15 is shown in Fig. 5-16. If the correction resulted in a negative value for the nitride-like N to Ta ratio, the result is plotted as zero in Fig. 5-16. Using this method, the nitride N:Ta ratio for low- $\kappa$  is close to that for unmodified  $\text{SiO}_2$  for all  $\text{TaN}_x$  thin film thicknesses, while the nitride N:Ta ratio for and  $\text{PEI}||\text{low-}\kappa$  is close to unmodified  $\text{SiO}_2$  in the early stages ( $< 5 \times 10^{14}$  Ta atoms  $\text{cm}^{-2}$ ), with no significant change to the other data series.

As stated above, a number of experiments were conducted to gauge the effect of the  $\sim 30$  minute pauses in growth required to collect XPS data. For these experiments,  $\text{TaN}_x$  films were deposited on unmodified  $\text{SiO}_2$ ,  $\text{PEI}|\text{SiO}_2$ , and unmodified low- $\kappa$  under UHV conditions using identical methods to those used to form the films analyzed above. However, in this case ALD was not stopped for XPS until after 15 cycles ( $\text{SiO}_2$ ) or 20 cycles ( $\text{PEI}|\text{SiO}_2$  and low- $\kappa$ ). In other words, for these experiments, measurements were taken only at 0 and 15 or 20 cycles, instead of at 0, 5, 10, 15, and 20 cycles. The results of these experiments, in the form of Ta density as a function of cycle (similar to Fig. 5-11) and  $\text{Ta}(4d_{5/2})$  binding energy as a function of Ta density (similar to Fig. 5-12), are shown in Fig. 5-17. Relevant results from the previous figures are also shown for comparison.

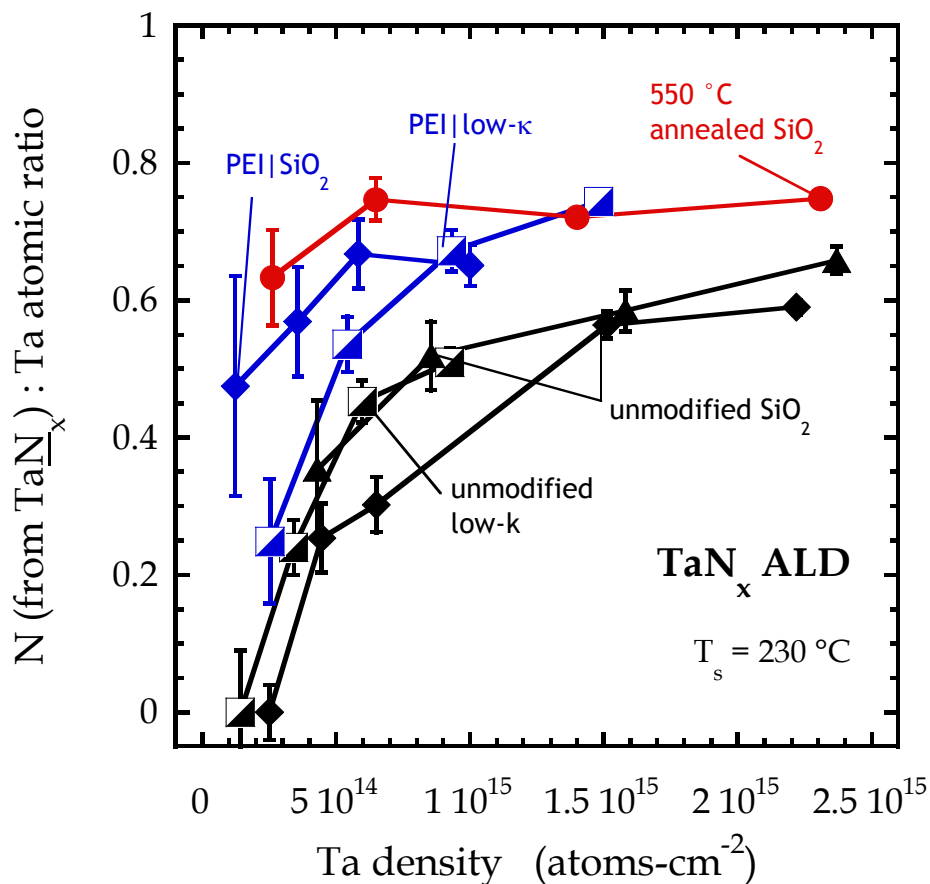


**Figure 5-16:** Calculated atomic ratio of N (of nitride, or  $\text{TaN}_x$  type only) to Ta as a function of deposited Ta density. This plot was constructed using the same data used to construct Fig. 5-15, but in this case the N intensity was corrected by removing the low binding energy N contribution measured after 0.5 cycles of ALD (described further in text), which may be due to N binding to Si in the substrate.



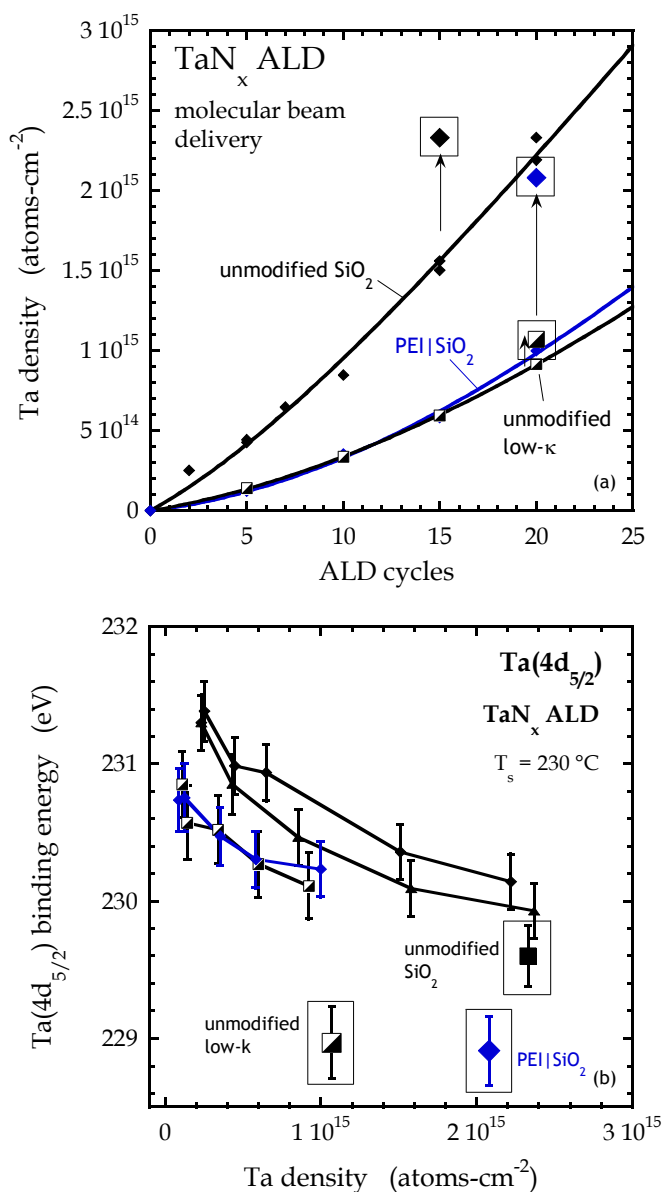


**Figure 5-17:** Results highlighting the effect of the pause in ALD to collect XPS data on TaN<sub>x</sub> film properties. Conditions are the same as given in Figs. 5-11 and 5-12, and relevant data from those figures are repeated here. Data points collected with no pauses for XPS until 15 or 20 cycles indicated by boxes. **(a)** Calculated atomic density of Ta, from *in situ* XPS, as a function of number of ALD cycles, and **(b)** binding energy of the Ta(4d<sub>5/2</sub>) core level as a function of atomic density of Ta.

From Fig. 5-17(a), we can conclude that the pauses in growth have the effect of generally decreasing the growth per cycle, though the effect is much more pronounced in the case of SiO<sub>2</sub> substrates. This may indicate reactions taking place between adsorbed precursors, between background contaminants in the chamber and surface species, or between the adsorbed precursors and the substrate, all which could lead to a decreased reactivity of the surface with the subsequent precursor pulse. Since the effect is substrate dependent, it would seem that the final possibility is most likely, i.e. that adsorbed species react with the SiO<sub>2</sub> substrate during the pause in growth during XPS analysis to an extent that is not possible with the low- $\kappa$  substrate. In Fig. 5-17(b), we observe that the pauses in growth also have the effect of increasing the oxidation state of Ta in the film, evidenced by a higher Ta(4d<sub>5/2</sub>) binding energy. This result can clearly be interpreted as an effect of the reaction with the film surface with background H<sub>2</sub>O in the UHV chamber, which could be present at a level of  $\sim 10^{-9}$  Torr. It may also be possible that reactions between adsorbed precursors and the surface could have this effect, though the change in oxidation state does not appear to be substrate dependent, making this possibility less likely.

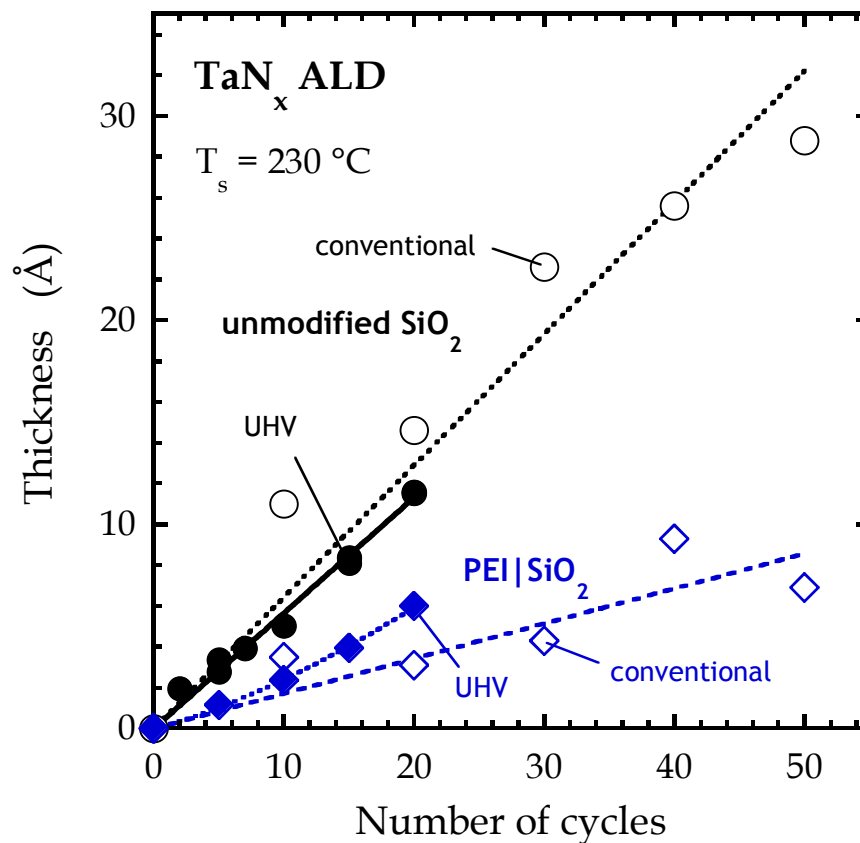
Note that for both measurements, ALD deposition rate and Ta oxidation state, the *relative* effect of the substrate is the same if growth is interrupted for XPS analysis. For the case when measurements are taken only at 15-20 cycles of growth, the rate of TaN<sub>x</sub> growth is lower on PEI/SiO<sub>2</sub> and low- $\kappa$  relative to unmodified SiO<sub>2</sub>, and the oxidation state of the Ta is lower on PEI/SiO<sub>2</sub> and low- $\kappa$  as compared to SiO<sub>2</sub>, i.e. trends that were observed in Figs. 5-11 and 5-12. The results shown in Fig. 5-17(b), in particular, suggest that the effect of the substrate may be stronger and longer

lasting than that which would be indicated when XPS is collected after every 5 cycles. In other words, the effect of the substrate would be partially damped by the interaction of adsorbed precursors with residual H<sub>2</sub>O in the UHV chamber.

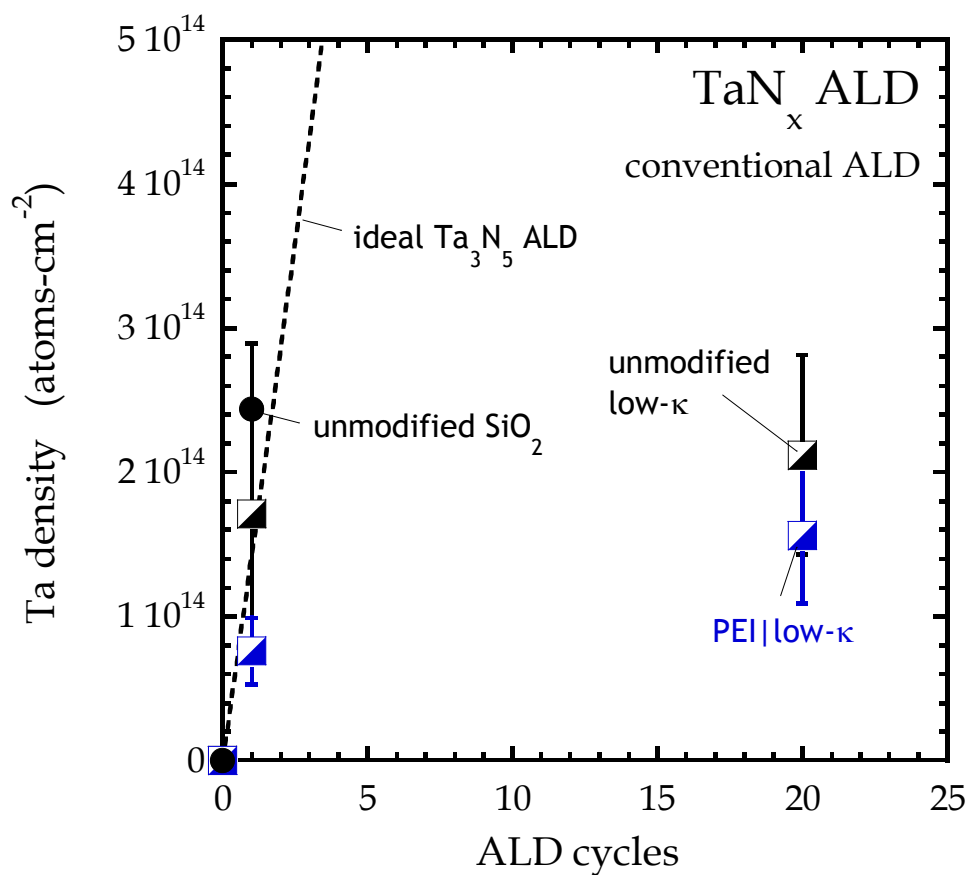
#### 5.4.5. Effect of PEI on TaN<sub>x</sub> ALD conducted in a conventional ALD reactor

Fig. 5-18 presents results involving TaN<sub>x</sub> ALD using a commercial ALD reactor (Oxford FlexAL). Here substrates were preheated to 230 °C in 200 mTorr Ar, then exposed to repeated cycles of Ta[N(CH<sub>3</sub>)<sub>2</sub>]<sub>5</sub>/Ar purge/NH<sub>3</sub>/Ar purge. *Ex situ* ellipsometry was used to measure the thickness of the TaN<sub>x</sub> layers. Substrates were not reintroduced to the ALD chamber after ellipsometry, so each point for conventional ALD in Fig. 5-18 represents a separate film. For comparison, the thickness of films deposited in UHV are also displayed, calculated from the attenuation of the Si(2p) signal from the underlying substrate (i.e., Eq. 5-3), with an empirical correlation used to determine a value of 20.8 Å for TaN<sub>x</sub> [100]. First note that the deposited thickness as a function of cycles on SiO<sub>2</sub> is similar for the two deposition methods (0.57 Å-cycle<sup>-1</sup> for UHV vs. 0.64 Å-cycle<sup>-1</sup> for conventional). Also, the presence of PEI on the SiO<sub>2</sub> surface has the effect of attenuating growth to approximately the same degree for both ALD methods.

This is in contrast to the case of ALD on low-κ and PEI|low-κ, which proceeds very differently in UHV and in a conventional reactor. The deposited 2-d density of Ta on low-κ and PEI|low-κ as a function of ALD cycles in conventional reactor is shown in Fig. 5-19.



**Figure 5-18:** Film thickness as a function of ALD cycles for TaN<sub>x</sub> films deposited on unmodified SiO<sub>2</sub> and PEI|SiO<sub>2</sub> using either UHV techniques (filled symbols) or a conventional ALD reactor (Oxford FlexAL, empty symbols). For the films deposited in UHV, attenuation of the underlying Si(2p) signal intensity in XPS was used to calculate the film thickness, while *ex situ* spectroscopic ellipsometry was used to measure film thickness for films deposited using the conventional reactor.



**Figure 5-19:** Deposited Ta density, calculated from ex situ XPS, as a function of ALD cycles for TaN<sub>x</sub> films on unmodified low-κ and PEI|low-κ. Shown for reference are the calculated Ta density after 1 ALD cycle on unmodified SiO<sub>2</sub>, and the expected Ta density versus ALD cycles that would be expected for ideal Ta<sub>3</sub>N<sub>5</sub> ALD.

*Ex situ* XPS was used in this case, instead of ellipsometry, again due to the issues with ellipsometry for films deposited on porous low- $\kappa$  discussed above in Sec. 5.4.2. As observed for similar types of low- $\kappa$  material [18-21], the 2-d density of Ta on low- $\kappa$  is much lower than the ‘ideal’ density for the equivalent number of ALD cycles on SiO<sub>2</sub>. Also, XPS indicates a significantly higher density of Ta taken up in the first cycle compared to each of the subsequent 19 cycles. In the case of ALD on porous substrates, XPS density results should be considered in combination with measurements of the degree of infiltration of the film into the substrate. Similar to the result shown in Fig. 5-6(b), an ARXPS measurement at 20 ALD cycles is shown in Fig. 5-20. Note that an equivalent analysis of the data is justified for both 1 and 20 cycles, because, from the result shown in Fig. 5-19, the total amount of Ta deposited on both substrates at 20 cycles has only increased by a factor of  $\sim 2$ , and is still less than the total amount deposited after 1 cycle on unmodified SiO<sub>2</sub>. As with 1 cycle of ALD, we observe significantly different behavior on unmodified low- $\kappa$  and PEI|low- $\kappa$ . If the data in Fig. 5-20 is fit to a model which assumes that the concentration profile follows  $c = c_0 \exp(z/d)$  (Eq. 5-4),  $d/\lambda$  values of  $0.64 \pm 0.18$  for unmodified low- $\kappa$  and  $0.14 \pm 0.02$  for PEI|low- $\kappa$  are obtained. Comparing these results to results from the equivalent fits for ARXPS of 1 cycle on low- $\kappa$  and PEI|low- $\kappa$ , the characteristic infiltration length for unmodified low- $\kappa$  has decreased significantly from  $3.7 \pm 2.8$ , while the value for PEI|low- $\kappa$  has increased slightly, from  $0.10 \pm 0.03$ . These changes are not unexpected, as they indicate the initial stages of thin film growth at the vacuum|substrate interface. For PEI|low- $\kappa$ , this increases the measured  $d/\lambda$  due to the slight increase in film thickness compared to the chemisorbed Ta[N(CH<sub>3</sub>)<sub>2</sub>]<sub>5</sub> layer.

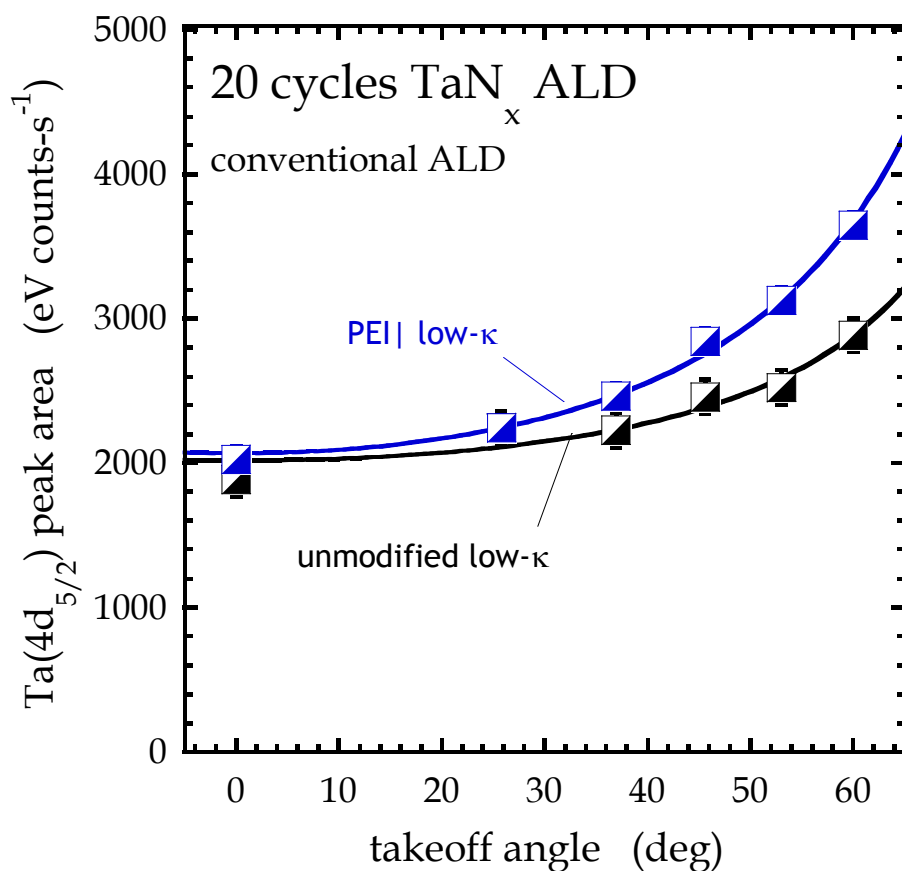


**Figure 5-20:** Integrated area under the Ta(4d<sub>5/2</sub>) peak for unmodified low-κ and PEI|low-κ substrates after 20 cycles of TaN<sub>x</sub> ALD using a conventional ALD reactor. (Oxford FlexAL). Smooth lines represent fits to the data in which the Ta concentration decreases exponentially from a maximum concentration at the vacuum|substrate interface (Eq. 5-4).

In the case of unmodified low- $\kappa$ , the increase in Ta concentration at the vacuum|substrate interface reduces the average depth of Ta, which leads to the decrease in the calculated  $d/\lambda$  value.

#### 5.4.6. Effect of poly-G on TiN<sub>x</sub> ALD conducted in UHV

Turning to TiN<sub>x</sub> films deposited on poly-G, Fig. 5-21 shows the thickness of TiN<sub>x</sub> films grown on unmodified SiO<sub>2</sub>, low- $\kappa$ , poly-G|SiO<sub>2</sub> and poly-G|low- $\kappa$  as a function of ALD cycles. TiN<sub>x</sub> films were deposited under UHV conditions, and thicknesses were measured using single wavelength ellipsometry *ex situ*. Here, the much higher thickness of the TiN<sub>x</sub> film mitigates the large errors associated with using ellipsometry to measure film thickness on porous low- $\kappa$  (error bars are shown to estimate the effect of these issues). For both SiO<sub>2</sub> and low- $\kappa$ , significant attenuation of growth is observed with poly-G present. As has been discussed previously, the initial growth rate on poly-G|SiO<sub>2</sub> decreases with increasing poly-G thickness [9]. Neglecting the effect of the underlying substrate, the higher growth rate on poly-G|low- $\kappa$  compared to poly-G|SiO<sub>2</sub> is consistent with this trend, as the thickness of the poly-G film on low- $\kappa$  is ~33% lower. Fitting the thickness vs. ALD cycles data to Eq. 5-6, the values of  $\alpha$  calculated for growth on low- $\kappa$  and on poly-G|low- $\kappa$  are equivalent within the uncertainty, and fall in the range of 0-0.4. The calculated  $m$  parameters, however, are significantly different, with the bare low- $\kappa$  having an  $m$  value of  $74 \pm 37$  cycles and the poly-G|low- $\kappa$  with a value of  $295 \pm 66$  cycles.



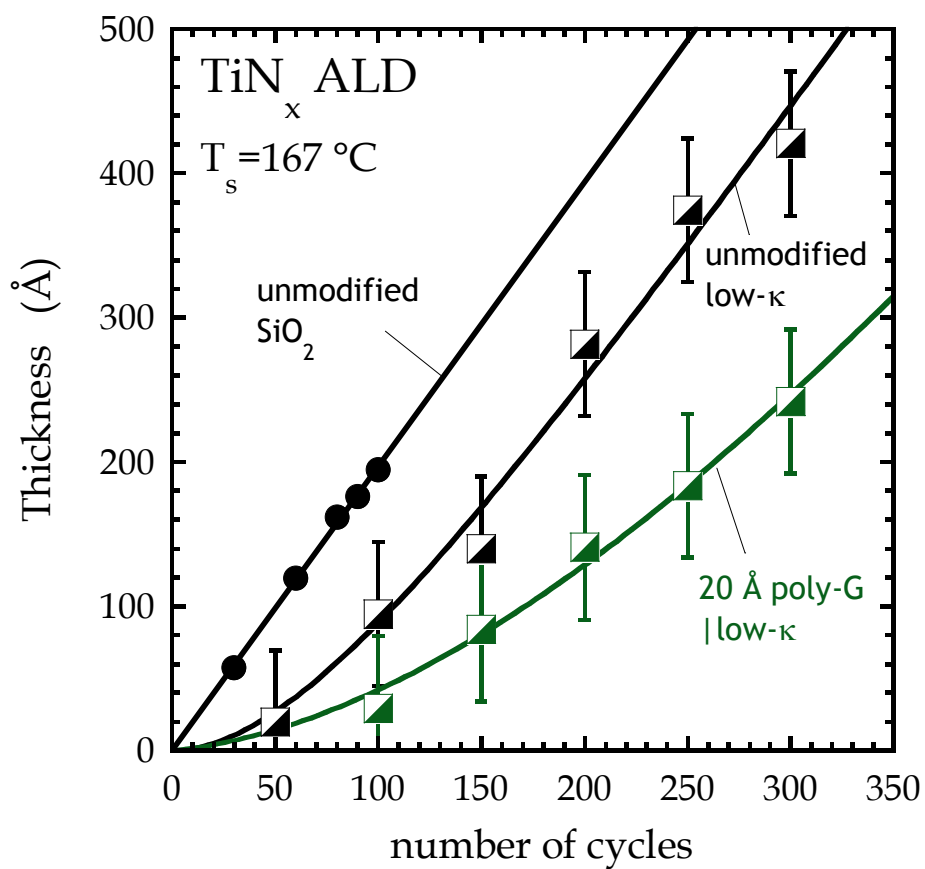


**Figure 5-21:**  $\text{TiN}_x$  film thickness as a function of ALD cycles for deposition on unmodified  $\text{SiO}_2$ , unmodified low- $\kappa$ , and low- $\kappa$  modified with a film of polyglycidol. ALD was carried out in UHV, and thickness was measured using ex situ ellipsometry.

This result is consistent with a visual inspection of the two data sets in Fig. 5-21, which clearly shows that the slope of the thickness vs. cycles curve for  $\text{TiN}_x$  grown on low- $\kappa$  approaches the ideal value measured on  $\text{SiO}_2$  much earlier than for poly-G|low- $\kappa$ . This shows that there are fundamental differences in the mechanism by which growth is attenuated on low- $\kappa$  and poly-G|low- $\kappa$  from the ‘ideal’ rate of growth on  $\text{SiO}_2$ . The reduction in growth per cycle on unmodified low- $\kappa$  is short-lived, and the ideal growth rate is obtained rather quickly, while the effect of poly-G is apparent in the growing film at much longer cycle intervals. The lack of reliable data below 150 cycles introduces significant uncertainty in fitting  $\alpha$  and  $m$  values for growth on poly-G| $\text{SiO}_2$  films, however given that the deposited thickness vs. cycles from 250 to 300 cycles is much lower than the ideal rate of growth, it can be estimated that  $m > 300$  cycles, which indicates that the effect of poly-G is also relatively long lived for  $\text{TiN}_x$  ALD on poly-G| $\text{SiO}_2$  as well.

To summarize the effects of the two branched organic layers on the kinetics of growth in the early stages of  $\text{TiN}_x$  and  $\text{TaN}_x$  ALD, it is first observed that both suppress the rate of deposition per cycle on  $\text{SiO}_2$ . This is most likely due to a combination of effects caused by the organic layers, including a reduction in the number of active sites on the starting substrate, and a decrease in the chemical reactivity of the chemisorbed species towards the coreactant,  $\text{NH}_3$  in this case. On the other hand, both organic layers enhance the uptake of  $\text{Ta}[\text{N}(\text{CH}_3)_2]_5$  in the first cycle of ALD. For PEI, this leads to an increase in the  $\text{TaN}_x$  deposition rate over the first 20 cycles. However, the presence of poly-G on the low- $\kappa$  surface attenuates  $\text{TiN}_x$  growth in this case also, again attributed to the tendency of the poly-G layer to strongly

suppress the chemical reactivity of the adsorbed transition metal coordination complex.

#### **5.4.7. Effect of poly-G and PEI on TaN<sub>x</sub> and TiN<sub>x</sub> thin film morphology**

The effect of thin films of PEI and poly-G on the morphology of TiN<sub>x</sub> and TaN<sub>x</sub> films deposited by ALD has been discussed previously [9,56]. In summary, the presence of poly-G on SiO<sub>2</sub> induces the growth of much rougher films as compared to unmodified SiO<sub>2</sub>, and in fact there is a strong positive correlation between deposited film roughness and poly-G film thickness. Combined with the decrease in deposited TiN<sub>x</sub> thickness per cycle with increasing poly-G thickness, it is concluded that the higher roughness of TiN<sub>x</sub> films deposited on poly-G/SiO<sub>2</sub> is due to the formation of islands in the initial stages of growth because of the low density of active nucleation sites on the surface. For PEI/SiO<sub>2</sub>, only a marginal increase in roughness is observed for ALD TaN<sub>x</sub> films (grown by conventional ALD) as compared to films deposited on SiO<sub>2</sub>, consistent with TiN<sub>x</sub> ALD films deposited in UHV on other R<sub>x</sub>-NH<sub>3-x</sub> functional organic thin films [8].

AFM images for 0 and 5 cycles of TaN<sub>x</sub> ALD on low-κ and PEI/low-κ are shown in Fig. 5-22. The initial morphology is comparable for both substrates, consistent with the formation of a thin, smooth film of PEI on low-κ. Noted on the AFM images are the correlation lengths (ξ) determined using the 1-d power spectral densities, which are shown in Fig. 5-23 [8]. At zero cycles, the two the substrates are similar, as expected, with correlation lengths of 107 nm and 126 nm for low-κ and

PEI|low- $\kappa$ .. In the case of low- $\kappa$ , we see little change from the initial substrate to the substrate after 5 ALD cycles ( $\xi \sim 111$  nm). The morphology of the PEI|low- $\kappa$  surface changes significantly, and at 5 cycles has a correlation length of  $\sim 53$  nm. The formation of small features ( $< 100$  nm lateral correlation length) is observed for both  $\text{TiN}_x$  and  $\text{TaN}_x$  ALD films [8,56], so the transition to a surface morphology with lower correlation length is consistent with the nucleation of a  $\text{TaN}_x$  film. However, from XPS the density of Ta at 5 cycles on PEI|low- $\kappa$  is still  $< 50\%$  of the density of Ta after 1 cycle of  $\text{TaN}_x$  ALD on  $\text{SiO}_2$ . An alternate possibility, then, is that the higher concentration of  $\text{Ta}[\text{N}(\text{CH}_3)_2]_5$  at the vacuum substrate interface leads to a morphological change in either the low- $\kappa$  surface, or the PEI layer. In either case, the AF micrographs shown in Fig. 5-22 demonstrate that PEI|low- $\kappa$  and unmodified low- $\kappa$  possess two distinct surface morphologies after 5 cycles of  $\text{TaN}_x$  ALD.

Turning to the surface morphology of  $\text{TiN}_x$  films deposited on low- $\kappa$  and poly-G|low- $\kappa$ , Fig. 5-24 shows four AF micrographs, representing the bare low- $\kappa$  and poly-G|low- $\kappa$  surfaces, and both after 100 cycles of  $\text{TiN}_x$  ALD, conducted in UHV. As with PEI, the presence of poly-G on the low- $\kappa$  surface does not induce significant changes in morphology. However, after 100 cycles of  $\text{TiN}_x$  ALD, these two surfaces are quite different, with a much higher roughness and correlation length observed for the  $\text{TiN}_x$  film deposited on poly-G|low- $\kappa$ . Fig. 5-25 displays the rms roughness of  $\text{TiN}_x$  thin films from AFM as a function of thickness for ALD on a number of substrates. First, note that films grown on unmodified low- $\kappa$  are not significantly rougher than those grown on  $\text{SiO}_2$ . On both poly-G| $\text{SiO}_2$  and poly-G|low- $\kappa$ , however, roughness increases sharply from 0 cycles.

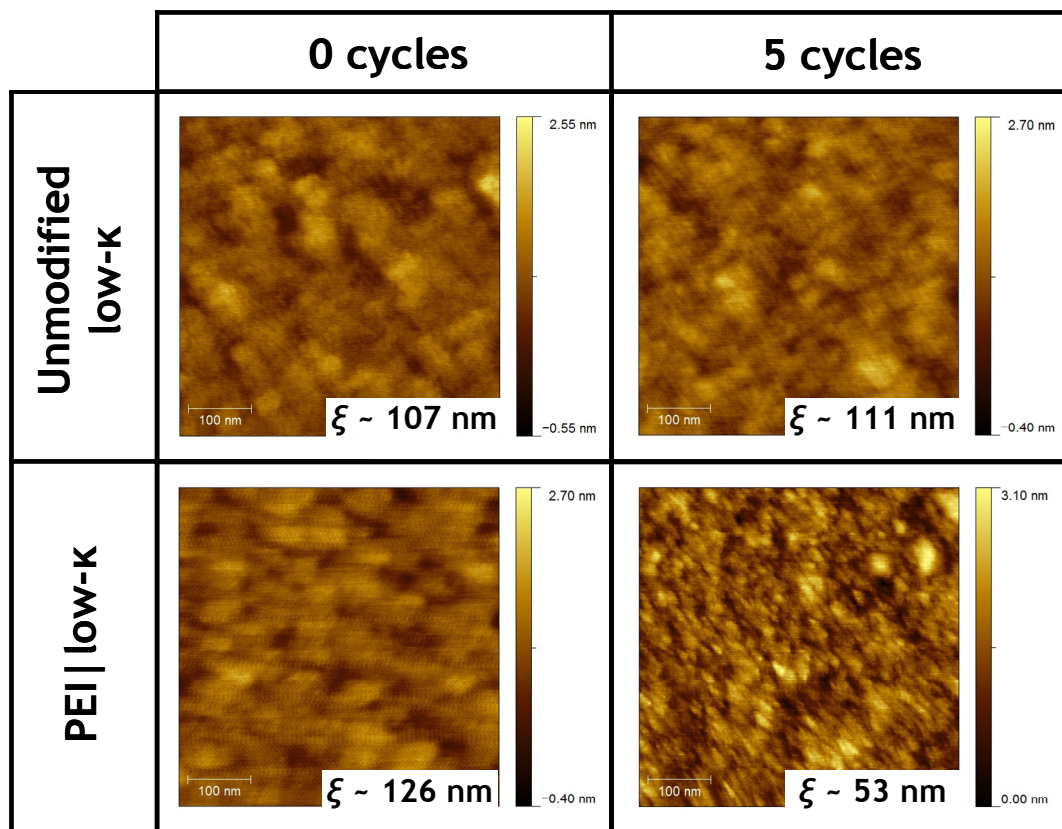


**Figure 5-22:** Atomic force micrographs of unmodified low-κ, low-κ modified with a thin film of PEI, after 0 cycles and after 5 cycles of TaN<sub>x</sub> ALD, conducted in a conventional ALD reactor. Values in the lower right represent in-plane correlation lengths calculated from the image (see text and Fig. 5-23 for details).

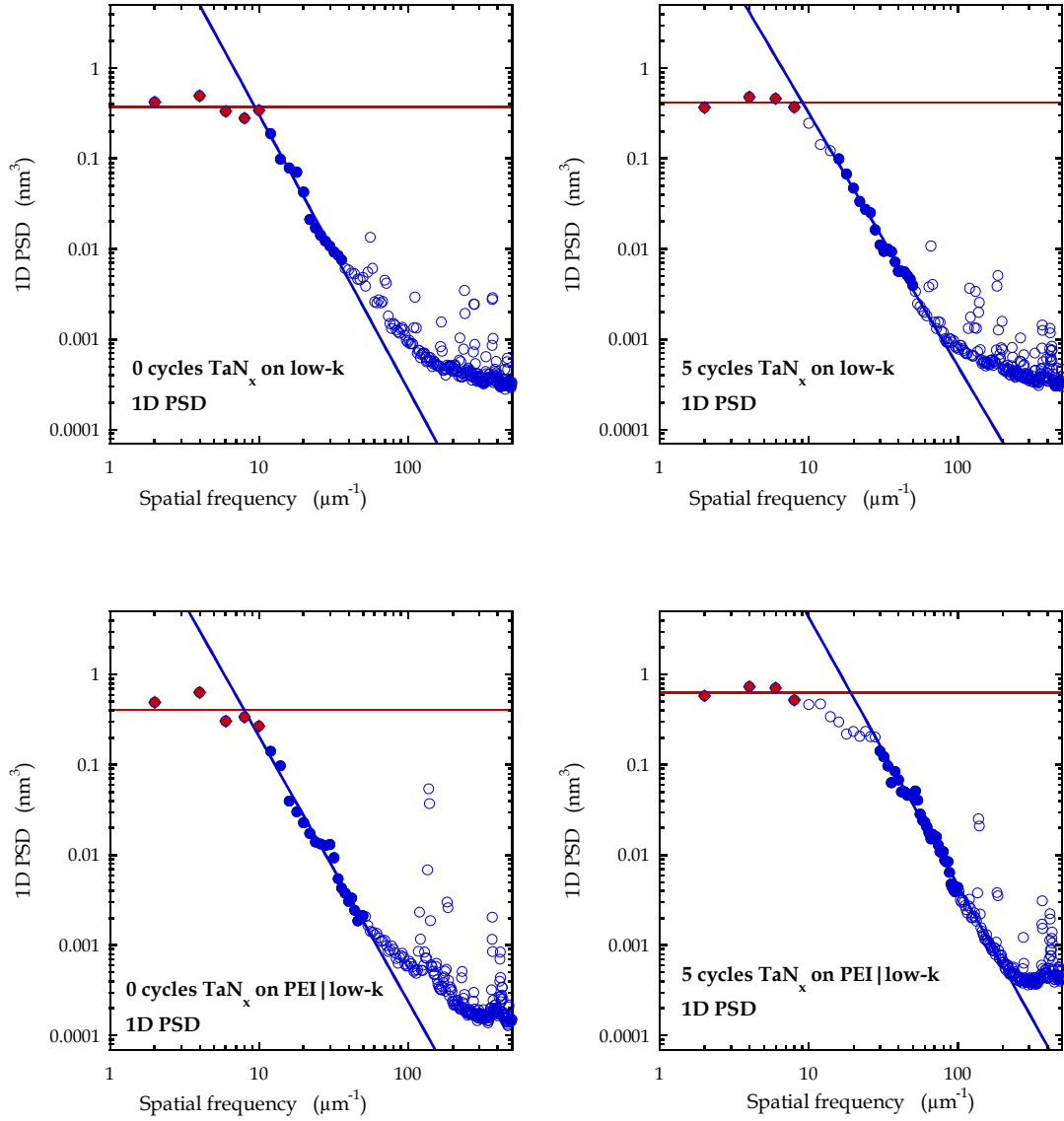


**Figure 5-23:** Power spectral density (PSD) plots extracted from the AFM images shown in Fig. 5-22. These are used to determine the in-plane correlation length  $\xi$  (the intersection of the plateau and fall-off regions in the PSD plot).

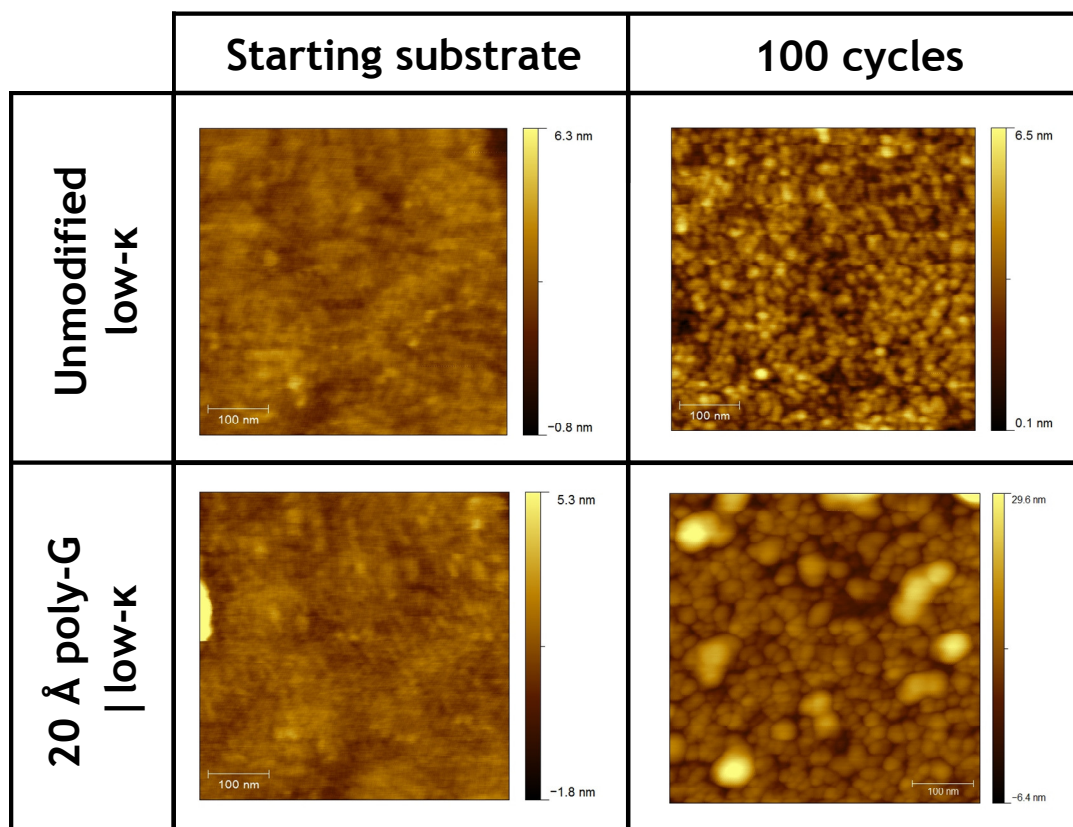


**Figure 5-24:** Atomic force micrographs of unmodified low-κ, low-κ modified with a thin film of polyglycidol (as deposited), and both substrates after 100 cycles of TiN<sub>x</sub> ALD conducted under UHV conditions.

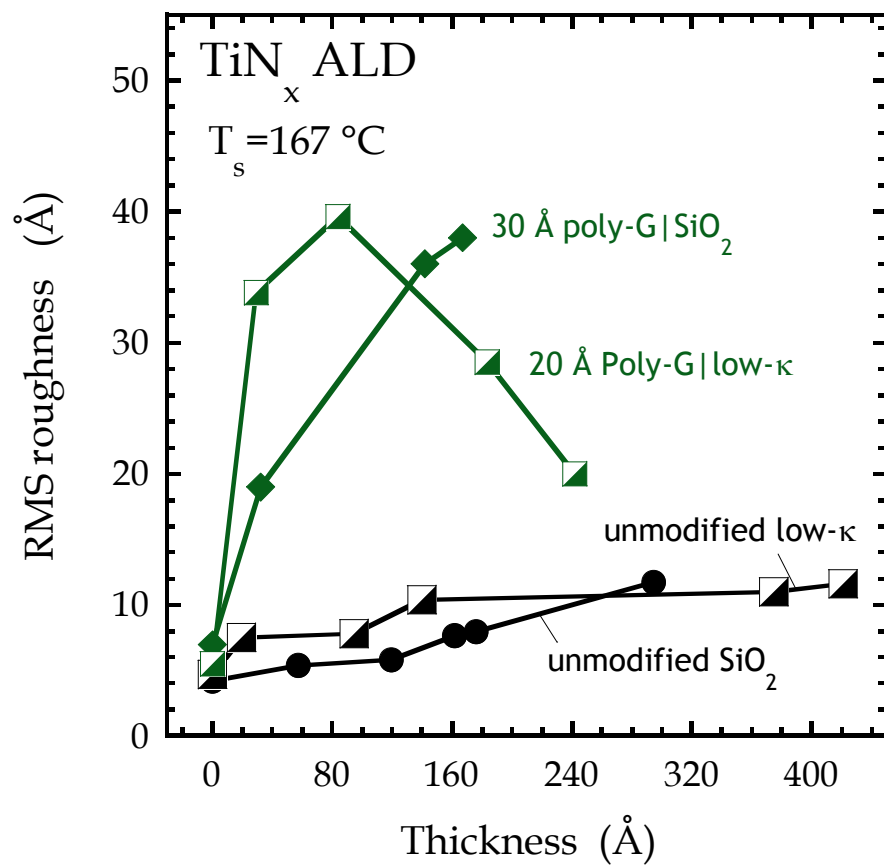


**Figure 5-25:** Root mean squared (RMS) roughness as a function of film thickness for TiN<sub>x</sub> ALD films deposited in UHV on unmodified SiO<sub>2</sub>, unmodified low-κ, and both substrates modified with a thin layer of polyglycidol.



This is consistent with the previously discussed correlation between initial growth attenuation and roughness in the early stages of ALD, due to a scarcity of nucleation sites. At higher thicknesses, the roughness of the  $\text{TiN}_x$  film grown on poly-G|low- $\kappa$  begins to decrease, which may be ascribed to the eventual coalescence of islands formed during the nucleation period [9].

## 5.5. Conclusions and future directions

The initial stages of atomic layer deposition of  $\text{TaN}_x$  and, to a lesser extent,  $\text{TiN}_x$ , have been investigated on substrates including  $\text{SiO}_2$ , a low- $\kappa$  material, and both of these modified by branched organic layers. These organic layers included poly(ethylene imine) (PEI), which contains amine functionality, and polyglycidol (poly-G), which contains ether and hydroxyl functionality. On a flat, nonporous  $\text{SiO}_2$  substrate, both PEI and poly-G have the effect of suppressing the initial chemisorption of the gas phase transition metal coordination complex  $\text{Ta}[\text{N}(\text{CH}_3)_2]_5$  (i.e., the first half cycle of  $\text{TaN}_x$  ALD). For a porous low- $\kappa$  substrate, however, the presence of a PEI film enhances chemisorption. The difference observed between the effect of PEI on chemisorption on  $\text{SiO}_2$  and low- $\kappa$  can be attributed to the presence of a higher density of amine groups free to react with  $\text{Ta}[\text{N}(\text{CH}_3)_2]_5$  in the case of PEI|low- $\kappa$ . For substrates modified with PEI, there appears to be a positive correlation between the density of  $\text{Ta}[\text{N}(\text{CH}_3)_2]_5$  adsorbed in the first half cycle and the subsequent ALD growth rate. However, this trend does not hold for poly-G, where, as seen previously [9], there seems to be a negative correlation between ALD growth rate of  $\text{TiN}_x$  and the

density of adsorbed  $\text{Ta}[\text{N}(\text{CH}_3)_2]_5$  after the first half cycle. The presence of poly-G on the substrate also leads to the formation of rough, islanded  $\text{TiN}_x$  films, indicative of suppressed nucleation, which is not observed for PEI. On an  $\text{SiO}_2$  surface which has been pre-annealed to decrease the density of Si-OH groups, we see a similar Ta density after the first half cycle as in the case of  $\text{PEI}|\text{SiO}_2$ , but with much less attenuation in the subsequent ALD growth. Taken together, these results show that both the *chemical state*, as well as the *density* of the chemisorbed species after the first half cycle have a strong effect on nucleation and the early stages of film growth. It can be concluded that ALD growth rate in the early cycles is maximized if the chemisorbed layer after the first half cycle contains a high metal density, is not sterically blocked (by a polymer layer, for example), and incorporates limited chemical bonding between the metal and the substrate. Regarding the last point, we can consider chemical bonding limited if the number of bonds is small (i.e. the Si-O-Ta bonds formed on annealed  $\text{SiO}_2$ ), or if the bonds are chemically weak (i.e. between Ta and an amine group vs. an oxygen containing group).

In addition to the initial growth rate, the effect of a thin layer of PEI on the infiltration of porous low- $\kappa$  by  $\text{Ta}[\text{N}(\text{CH}_3)_2]_5$  was investigated using angle-resolved XPS. Here it was shown that, using conventional ALD techniques, PEI significantly reduced infiltration compared to an unmodified low- $\kappa$  substrate, after both 1 and 20 ALD cycles. Furthermore, the presence of PEI on a low- $\kappa$  substrate shortens the transition to the film morphology observed for  $\text{TaN}_x$  films deposited on nonporous  $\text{SiO}_2$ . This which is consistent with PEI enhancing adsorption and film growth at the vacuum|low- $\kappa$  interface.

Using *in situ* XPS, it was shown that the oxidation state of Ta atoms in the film is influenced by the substrate, up to  $\sim 10$  ALD cycles ( $\sim 6\text{-}10$  Å). The oxidation state of Ta is generally lower on films deposited on PEI/SiO<sub>2</sub>, unmodified low- $\kappa$ , and PEI/low- $\kappa$  as compared to films deposited on unmodified SiO<sub>2</sub>. The oxidation state of the film also correlates with the relative amount of nitride type (TaN<sub>x</sub>) N in the film. Films which are less oxidized tend to more efficiently incorporate nitrogen as nitride, which can be viewed as a result of the more favorable chemical bonding between O and Ta, as compared to N and Ta. Overall, these results show that for the ALD of TaN<sub>x</sub> films, through the use of branched organic surface layers it is possible to affect the initial chemisorption of metal coordination complexes, as well as the rate of film growth, aspects of the chemical composition of the deposited film, and the infiltration of film material into porous substrates.

One set of results which may warrant future study involves the ALD of TaN<sub>x</sub> on porous low- $\kappa$  substrates. First is the presence of the N(1s) peak at  $\sim 397.5$  eV for adlayers of Ta[N(CH<sub>3</sub>)<sub>2</sub>]<sub>5</sub> on low- $\kappa$ . This was tentatively assigned to N bound strongly to Ta, or to Si in the low- $\kappa$  substrate. Future studies may resolve this, perhaps by exposing low- $\kappa$  substrates to dimethylamine or similar gas-phase species at elevated temperatures, to determine if a strongly bound layer is formed. These studies may also address the possible formation of reactive surface Si atoms on low- $\kappa$  at elevated temperatures, due to degradation of the low- $\kappa$  leading to the loss of alkyl groups. A related set of results involves discrepancies for ALD of TaN<sub>x</sub> under different conditions. For example, in Figs. 5-11(b) and 5-19 we observe that the growth rate is significantly higher for ALD on low- $\kappa$  conducted in UHV as compared to when ALD

is conducted in a conventional reactor, a phenomenon which was not fully explored here. A future set of studies, then, may involve an *in situ* study of ALD on low- $\kappa$  and low- $\kappa$  modified with thin organic films, with one goal to find the reasons for this discrepancy.

With regard to possible applications of this work, in the future a number of variations may be attempted which could improve upon the results described here. First, one may combine what has been learned in Chapter 4 with the conclusions made here. For example, while it has been shown that the presence of a thin film of PEI dramatically reduces the infiltration of  $\text{TaN}_x$  into a porous low- $\kappa$ , the rate of ALD growth remains well below the measured ‘ideal’ rate on  $\text{SiO}_2$ . As stated in Chapter 4, one route to achieve a higher growth rate may be to use an alternate coreactant, such as hydrazine or N plasma, to increase the thermodynamic driving force of the second half of the ALD reaction. Alternately, one could use a thin interfacial layer of a film which grows rapidly on PEI,  $\text{Ta}_2\text{O}_5$  or  $\text{Al}_2\text{O}_3$  for example, provided that additional measurements confirm that PEI also limits the infiltration of these materials as well. In the case of a diffusion barrier, the presence of an additional insulating film may also be undesirable. A more promising solution may be to use an organic layer, also consisting of a multifunctional polymer which can be deposited from aqueous solution. The results presented here clearly demonstrate that such layers can be reliably formed on low- $\kappa$ , while other work (presented in Chapter 6) demonstrates that this route to the organic layer formation does not alter the bulk pore structure of the low- $\kappa$ .

Finally, further investigation is required to determine the ability of PEI (or another alternate organic layer) to prevent infiltration and/or enhance ALD growth on other low- $\kappa$  materials. It seems likely that the density and chemical identity of active sites on the low- $\kappa$  surface, as well as properties involving the pore structure of the low- $\kappa$  may affect the effectiveness of PEI in this regard. A future study may involve, for example, the use of similar SiO<sub>2</sub>-based materials with variable porosity and pore size, as well as low- $\kappa$  materials of different composition, including polymer based materials.

## 5.6 References

1. M. Ritala and M. Leskelä, in *Handbook of Thin Film Materials, Vol. 1*, edited by H. S. Nalwa (Academic, San Diego, CA, 2001).
2. R.L. Puurunen, J. Appl. Phys. **97**, 121301-1-52 (2005), and references therein.
3. International Technology Roadmap for Semiconductors, <http://www.itrs.net>, 2009.
4. E. Langereis, S. B. S. Heil, M. C. M. van de Sanden, and W. M. M. Kessels, Phys. Status Solidi C **2**, 3958 (2005).
5. E. Langereis, S. B. S. Heil, M. C. M. van de Sanden, and W. M. M. Kessels, J. Appl. Phys. **100**, 023534 (2006).
6. A. Martin Hoyas, C. M. Whelan, J. Schuhmacher, J. P. Celis, and K. Maex, Electrochem. Solid-State Lett. **9**, F64-F68 (2006).
7. A. Dube, M. Sharma, P. F. Ma, and J. R. Engstrom, Appl. Phys. Lett. **89**, 164108 (2006).
8. A. Dube, M. Sharma, P. F. Ma, P. A. Ercius, D. A. Muller, and J. R. Engstrom, J. Phys. Chem. C **111**, 11045 (2007).
9. K. J. Hughes and J. R. Engstrom, J. Vac. Sci. Technol. A **28**, 1033 (2010).
10. A. M. Lemonds, T. Bolom, W. J. Ahearn, D. C. Gay, J. M. White, and J. G. Ekerdt, Thin Solid Films **488**, 9 (2005).
11. M. Tallarida, K. Karavaev, and D. Schmeisser, J. Appl. Phys. **104**, 064116 (2008).
12. M. Tallarida, K. Karavaev, and D. Schmeisser, J. Vac. Sci. Technol. B **27**, 300, (2009).
13. R. Methaapanon, and S. F. Bent, J. Phys Chem. C **114**, 10498 (2010).
14. G. Beyer, A. Satta, J. Schuhmacher, K. Maex, W. Besling, O. Kilpela, H. Sprey, G. Tempel, Microelectron. Eng. **64**, 233 (2002).
15. Zs. Tőkei, M. Patz, M. Schmidt, F. Iacopi, S. Demuynck, and K. Maex, Microelectron. Eng. **76**, 70 (2004).
16. Kaloyeros, A. E.; Eisenbraun, E. *Annu. Rev. Mater. Sci.* **2000**, *30*, 363.

17. K. Maex, M. R. Baklanov, D. Shamiryan, F. Iacopi, S. H. Brongersma, and Z. S. Yanovitskaya, *J. Appl. Phys.* **93**, 8793 (2003).
18. O. Van der Straten, Y. Zhu, J. Rullan, K. Topol, K. Dunn, A. Kaloyeros, *Mater. Res. Soc. Symp. Proc.* **812**, F3.13.1 (2004).
19. A. Satta, M. Baklanov, O. Richard, A. Vantomme, H. Bender, T. Conard, K. Maex, W. M. Li, K.-E. Elers, S. Haukka, *Microelectron. Eng.* **60**, 59 (2002).
20. J. Liu, J. Bao, M. Scharnberg, W. C. Kim, P. S. Ho, and R. Laxman, *J. Vac. Sci. Technol. A* **23**, 1107 (2005).
21. F. Volpi, L. Cadix, G. Berthomé, E. Blanquet, N. Jourdan, J. Torres, *Microelectron. Eng.* **85**, 2068 (2008).
22. Y. Travaly, J. Schuhmacher, A. Martin Hoyas, T. Abell, V. Sutcliffe, A. M. Jonas, M. Van Hove, and K. Maex, *Microelectron. Eng.* **82**, 639 (2005).
23. Y. Travaly, J. Schuhmacher, A. M. Hoyas, M. Van Hove, K. Maex, T. Abell, V. Sutcliffe, A. M. Jonas, *J. Appl. Phys.* **97**, 084316 (2005).
24. A. Furuya, N. Ohtsuka, K. Misawa, M. Shimada, S. Ogawa, *J. Appl. Phys.* **98**, 094902 (2005).
25. W. Besling, A. Satta, J. Schuhmacher, T. Abell, V. Sutcliffe, A.-M. Hoyas, G. Beyer, D. Gravesteijn, and K. Maex, *International Interconnect Technology Conference June 6–8 2002, IEEE 2002*, pp. 288–291.
26. Y. Travaly, J. Schuhmacher, M. R. Baklanov, S. Giangrandi, O. Richard, B. Brijs, M. Van Hove, K. Maex, T. Abell, K. R. F. Somers, M. F. A. Hendrickx, L. G. Vanquickenborne, A. Ceulemans, and A. M. Jonas, *J. Appl. Phys.* **98**, 083515 (2005).
27. J.-N. Sun, D. W. Gidley, Y. Hu, W. E. Frieze, and E. T. Ryan, *Appl. Phys. Lett.* **81**, 1447 (2002).
28. T. Abell and K. Maex, *Microelectron. Eng.* **76**, 16 (2004).
29. N. Possémé, T. David, T. Chevolleau, and O. Joubert, *Electrochem. Sol. St. Lett.* **8**, G112 (2005).
30. H.-G. Peng, D.-Z. Chi, W.-D. Wang, J.-H. Li, K.-Y. Zeng, R. S. Vallery, W. E. Frieze, M. A. Skalsey, D. W. Gidley, and A. F. Yee, *J. Electrochem. Soc.* **154**, G85 (2007).

31. A. M. Urbanowicz, M. R. Baklanov, J. Heijlen, Y. Travalay, and A. Cockburn, *Electrochem. Solid-State Lett.* **10**, G76-G79 (2007).
32. N. Poss  m  , T. Chevolleau, T. David, M. Darnon, J. P. Barnes, O. Louveau, C. Licitra, D. Jalabert, H. Feldis, M. Fayolle, and O. Joubert, *Microelectron. Eng.* **85**, 1842 (2008).
33. E. Kondoh, T. Asano, A. Nakashima, and M. Komatu, *J. Vac. Sci. Technol. B* **18**, 1276 (2000).
34. D. Shamiryan, M. R. Baklanov, S. Vanhaelemeersch, and K. Maex, *J. Vac. Sci. Technol. B* **20**, 1923 (2002).
35. K. Yonekura, S. Sakamori, K. Goto, M. Matsuura, N. Fujiwara, and M. Yoneda, *J. Vac. Sci. Technol. B* **22**, 548 (2004).
36. P. de Rouffignac, Z. Li, and R. G. Gordon, *Electrochem. Solid-State Lett.* **G306** (2004).
37. J. W. Elam, C. A. Wilson, M. Schuisky, Z. A. Sechrist, and S. M. George, *J. Vac. Sci. Technol. B* **21**, 1099 (2003).
38. V. Jousseau, M. Fayolle, C. Guedj, P. H. Haumesser, C. Huguet, F. Pierre, R. Pantel, H. Feldis, and G. Passemard, *J. Electrochem. Soc.* **152**, F156-F161 (2005).
39. A. Furuya, K. Yoneda, E. Soda, T. Yoshie, H. Okamura, M. Shimada, N. Ohtsuka, and S. Ogawa, *J. Vac. Sci. Technol. B* **23**, 2522 (2005).
40. C. Jezewski, C. J. Wiegand, D. Ye, A. Mallikarjunan, D. Liu, C. Jin, W. A. Lanford, G.-C. Wang, J. J. Senkevich, and T.-M. Lu, *J. Electrochem. Soc.* **151**, F157 (2004).
41. J. S. Juneja, G. A. Ten Eyck, H. Bakhru, and T.-M. Lu, *J. Vac. Sci. Technol. B* **23**, 2232 (2005).
42. J. S. Juneja, P.-I Wang, T. Karabacak, and T.-M. Lu, *Thin Solid Films* **504**, 239-242 (2006).
43. A. Ulman, *An Introduction to Ultrathin Organic Films, From Langmuir-Blodgett to Self-Assembly* (Academic Press, Boston, MA 1991).
44. F. Schreiber, *Prog. Surf. Sci.* **65**, 151 (2000).
45. X. Jiang and S. F. Bent, *J. Phys. Chem. C* **113**, 17613 (2009).



46. A. S. Killampalli, P. F. Ma, and J. R. Engstrom, *J. Am. Chem Soc.* **127**, 6300 (2005).
47. M. Sharma, A. Dube, K. J. Hughes, and J. R. Engstrom, *Langmuir* **24**, 8610 (2008).
48. M. Sharma, A. Dube, and J. R. Engstrom, *J. Am. Chem. Soc.* **129**, 15022 (2007).
49. A. Dube, A. R. Chadeayne, M. Sharma, P. T. Wolczanski, and J. R. Engstrom, *J. Am. Chem. Soc.* **127**, 14299 (2005).
50. P. F. Ma, A. Dube, A. S. Killampalli, and J. R. Engstrom, *J. Chem. Phys.* **125**, 034706 (2006).
51. L. T. Zhuravlev, *Langmuir* **3**, 316 (1987).
52. S. R. Wasserman, Y. T. Tao, and G. M. Whitesides, *Langmuir* **5**, 1074 (1989).
53. H. L. Xin, P. Ercius, K. J. Hughes, J. R. Engstrom, and D. A. Muller, *Appl. Phys. Lett.* **96**, 223108 (2010).
54. M. Khan and W. T. S. Huck, *Macromolecules* **36**, 5088 (2003).
55. H. Wang, Y. Wang, H. Yan, J. Zhang, and R. K. Thomas, *Langmuir* **22**, 1526 (2006).
56. K. J. Hughes and J. R. Engstrom, *under review*.
57. N. Maity, PhD dissertation, Cornell University, 1996.
58. S. E. Roadman, N. Maity, J. N. Carter, and J. R. Engstrom, *J. Vac. Sci. Technol. A* **16**, 3423 (1998).
59. A. Dube, PhD dissertation, Cornell University, 2007.
60. J.-W. Lim, H.-S. Park, and S.-W. Kang, *J. Electrochem. Soc.* **148**, C403 (2001).
61. J. W. Elam, M. Schuisky, J. D. Ferguson, and S. M. George, *Thin Solid Films* **436**, 145 (2003).
62. Y. Y. Wu, A. Kohn, and M. Eizenberg, *J. Appl. Phys.* **95**, 6167 (2004).
63. A. Furuya, N. Ohtsuka, N. Ohashi, S. Kondo, and S. Ogawa, *J. Vac. Sci. Technol. A* **24**, 103 (2006).
64. T. W. Schroeder, PhD dissertation, Cornell University, 2004.

65. C. T. Campbell and S. M. Valone, *J. Vac. Sci. Technol. A* **3**, 408 (1985).
66. J. T. Yates, *Experimental Innovations in Surface Science* (Springer-Verlag, New York, 1998), pp. 604-607, and references therein.
67. *Practical Surface Analysis: Volume I, Auger and X-ray Photoelectron Spectroscopy, 2nd ed.*, M. P. Seah, and D. Briggs, Eds. (John Wiley and Sons, Chichester, England, 1990).
68. National Institute of Standards and Technology X-ray Photoelectron Spectroscopy Database, <http://srdata.nist.gov/xps/>
69. N. M. Patel, D. W. Dwight, J. L. Hedrick, D. C. Webster, and J. E. McGrath, *Macromolecules* **21**, 2689 (1988).
70. *High Resolution XPS of Organic Polymers: the Scienta ESCA300 Database*, G. Beamson and D. Briggs, Eds. (Wiley, New York, 1992).
71. *Sol-gel Science: The Physics and Chemistry of Sol-gel Processing*, J. C. Brinker and G. W. Scherer (Academic Press, San Diego, CA, 1990).
72. V. Ya. Davydov, A. V. Kiselev, and L. T. Zhuravlev, *Trans. Faraday. Soc.* **60**, 2254 (1964).
73. L. T. Zhuravlev, *Colloids Surf. A* **173**, 1 (2000).
74. G. E. McGuire, G. K. Schweitzer, and T. A. Carlson, *Inorg. Chem.* **12**, 2450 (1973).
75. J. H. Scofield, *J. Electron. Spectrosc. Rel. Phen.* **8**, 129 (1976).
76. A. O. Bouh, G. L. Rice, and S. L. Scott, *J. Am. Chem. Soc.* **121**, 7201 (1999).
77. M. Beaudoin and S. L. Scott, *Organometallics* **20**, 237 (2000).
78. Y. Takahashi, N. Onoyama, Y. Ishikawa, S. Motojima, and K. Sugiyama, *Chem. Lett.* **7**, 525 (1978).
79. J. M. Mayer, C. J. Curtis, and J. E. Bercaw, *J. Am. Chem. Soc.* **105**, 2651 (1983).
80. L. H. Dubois, B. R. Zegarski, and G. S. Girolami, *J. Electrochem. Soc.* **139**, 3603 (1992).
81. G. Ruhl, R. Rehmet, M. Knižová, R. Merica, and S. Vepřek, *Chem. Mater.* **8**, 2712 (1996).

82. C. M. Truong, P. J. Chen, J. S. Corneille, W. S. Oh, and D. W. Goodman, *J. Phys. Chem.* **99**, 8831 (1995).
83. J.-B. Wu, Y.-F. Lin, J. Wang, P.-J. Chang, C.-P. Tasi, C.-C. Lu, H.-T. Chiu, and Y.-W. Yang, *Inorg. Chem.* **42**, 4516 (2003).
84. D. C. Bradley and I. M. Thomas, *Can. J. Chem.* **40**, 1355 (1962).
85. J. C. Kim, Y. S. Cho, and S. H. Moon, *Jpn. J. Appl. Phys.* **48**, 066515 (2009).
86. *CRC handbook of Chemistry and Physics*, 91st Ed., D. R. Lide, Ed. (CRC Press, Boca Raton, 2011).
87. C. J. Powell and A. Jablonski, *J. Vac. Sci. Technol. A* **17**, 1122 (1999).
88. M. Barber, J. A. Connor, M. F. Guest, I. H. Hiller, M. Schwarz, and M. Stacey, *J. Chem. Soc. Faraday Trans. 2* **69**, 551 (1973).
89. B. J. Lindberg and J. Hedman, *Chem. Scr.* **7**, 155 (1975).
90. B. Lindberg, R. Maripuu, K. Siegbahn, R. Larsson, C.-G. Gölander, and J. C. Eriksson, *J. Colloid Interface Sci.* **95**, 308 (1983).
91. J. T. Sampanthar, K. G. Neoh, S. W. Ng, E. T. Kang, and K. L. Tan, *Adv. Mater.* **12**, 1536 (2000).
92. Z. J. Yu, E. T. Kang, and K. G. Neoh, *Polymer* **43**, 4137 (2002).
93. J. Thome, A. Holländer, W. Jaeger, I. Trick, and C. Oehr, *Surf. Coat. Technol.* **174-175**, 584 (2003).
94. E. H. Jeong, J. Yang, and J. H. Youk, *Mater. Lett.* **61**, 3991 (2007).
95. M. A. Alam and M. L. Green, *J. Appl. Phys.* **94**, 3403 (2003).
96. D. M. Hausmann, P. de Rouffignac, A. Smith, R. Gordon, and D. Monsma, *Thin Solid Films* **443**, 1 (2003).
97. W. J. Maeng and H. Kim, *Electrochem. Sol. St. Lett.* **9**, G191 (2006).
98. G. Brauer and J. R. Weidlein, *Angew. Chem., Int. Ed.* **4**, 241 (1965).
99. A. O. Ibidunni, *Oxid. Met.* **40**, 5 (1993).
100. S. Tanuma, C. J. Powell, and D. R. Penn, *Surf. Interface Anal.* **21**, 165 (1993).

## 6. Infiltration of organic film precursors into porous low- $\kappa$ material

### 6.1. Overview

A significant issue in the integration of porous low- $\kappa$  materials into semiconductor manufacturing is the infiltration of precursors into the pore structure, leading to the formation of unwanted thin films on the pore walls. Given the very small dimensions of these pores, this could significantly degrade the electrical properties of the low- $\kappa$ , or produce short circuits. This issue, as it relates to the ALD of TaN<sub>x</sub>, was addressed in Chapter 5. This issue must also be considered when modifying the outer surface of low- $\kappa$  materials with organic molecules, which is the focus of this chapter. The infiltration of a small fluorinated molecule (8 carbon backbone), FOTS, is characterized using spectroscopic ellipsometry, ellipsometric porosimetry, and XPS. The diffusion of the FOTS molecule across the entire thickness of the low- $\kappa$  is fast compared to the time required to achieve full surface coverage, so that the inner pore surfaces, and the outer surface of the material, are covered with FOTS at similar rates. The infiltration behavior as a function of molecule size, type, and low- $\kappa$  pretreatment is also examined. Pre-baking the low- $\kappa$  to remove residual water, and using liquid vs. gas-phase deposition techniques are found to have little effect on infiltration. Pre-treating the material with an air plasma appears to decrease infiltration for larger organic molecules ( $\sim 11$  carbon backbone), but this may also irreversibly damage the low- $\kappa$ . The main factors in determining infiltration appear to

involve molecular size effects, with the most extreme examples of this being PEI, which does not infiltrate the pores of the model low- $\kappa$  used here.

## 6.2. Introduction

The semiconductor industry faces a number of challenges related to the integration of porous low dielectric constant or “low- $\kappa$ ” materials in the interconnect structures of integrated circuits [1-3]. One set of challenges involves the deposition of thin conformal films, diffusion barriers for example, on low- $\kappa$  material. A combination of design requirements make atomic layer deposition (ALD) [4] an ideal technique for the deposition of these films. However depositing films by ALD on low- $\kappa$  materials is not straightforward. First, because ALD relies on the exposure of the substrate to small reactant molecules, one danger is that the barrier material will deposit inside the pore structure of the low- $\kappa$  [5-9], causing an increase in the dielectric constant and failures related to short circuits. Furthermore, because the nucleation of ALD films requires chemical reactions between gas-phase species and reactive sites on the substrate, the characteristically low density of active sites on low- $\kappa$  can lead to slow nucleation [10-12], or the formation of a rough, islanded film, causing increased line resistance [13] or, of greater concern, pinholes in the barrier layer [11]. It has also been shown that a low nucleation site density can lead to a reduced bulk density of the barrier [14]. One potential solution to these issues is the deposition of thin organic [15-17] or inorganic [18,19] layers to both seal the low- $\kappa$  against ALD precursor infiltration and enhance growth by multiplying the active site density. The use of organic molecules to alter the

surface properties is of particular interest, due to the high degree of customization available through the use of organic molecules.

A second challenge involves minimizing damage to fragile low- $\kappa$  materials resulting from the etching and ashing steps of patterning, which often utilize extremely reactive plasmas [2,3]. It has been shown that porous low- $\kappa$  materials are particularly susceptible to plasma induced damage due to infiltration of reactive species into the pore network [20]. Reactive plasmas degrade the electrical properties of a porous low- $\kappa$  by removing hydrophobic  $-\text{CH}_3$  groups from the pore walls, leading to uptake of water [20-23]. Therefore, a potential solution for fixing plasma damage in low- $\kappa$  is to deposit organic molecules which, by binding to polar surface groups, will restore the hydrophobic character to the inner pore walls and prevent increases in the dielectric constant [24-29].

When using small molecules to treat a porous low- $\kappa$ , one should consider the infiltration and deposition of the molecules within the pores. If the sole purpose of the treatment is to increase the surface density of active sites or seal the low- $\kappa$  for subsequent ALD, then infiltration would be undesirable as it would have the effect of increasing the dielectric constant. On the other hand, for treatments intended to restore the hydrophobic nature of the inner pore walls, controlled infiltration may be required. The use of surface modifiers to treat porous materials is by no means unique to the semiconductor field, and in fact is commonly encountered in several other applications, notably in the preparation of liquid chromatography columns. A unique difficulty with the analysis of organic infiltration in the case of low- $\kappa$  and other porous thin films, however, is that traditional techniques used to measure porosity and pore

size are normally not practical, because these methods require a relatively large amount of porous material, which may not be available in the case of thin films, or may require destructive techniques such as scraping large areas of thin films from the substrate.

The work described here involves a set of experiments undertaken to characterize infiltration of porous low- $\kappa$  by organic thin film precursors, using mainly two nondestructive ellipsometry-based techniques which are well suited for application to thin film samples. The deposition of  $\text{Cl}_3\text{Si}(\text{CH}_2)_2(\text{CF}_2)_5\text{CF}_3$ , or FOTS, on low- $\kappa$  will be discussed first. Two methods will be utilized to characterize infiltration, spectroscopic ellipsometry (SE) [30] and ellipsometric porosimetry (EP) [31,32]. There are a number of advantages to using FOTS as a model surface modifier. First, it has a structure typical of the molecules normally used to form self-assembled monolayers on surfaces possessing Si-OH terminations, including a  $-\text{SiCl}_3$  endgroup used to bind the molecule to the surface, and a flexible carbon based tail group  $[-(\text{CH}_2)_2-(\text{CF}_2)_5-\text{CF}_3]$ . Second, the fluorine atoms present in FOTS allow it to be distinguished in XPS measurements from the low- $\kappa$  material, which contains only C, O, and Si. Furthermore, it has sufficient vapor pressure that it can be deposited at reasonable temperatures from the vapor phase. Beyond FOTS, we will examine the infiltration of a variety of other organic molecules into the same low- $\kappa$  using SE, to determine the effect of molecule size and other factors on the degree of infiltration. These other molecules can be divided into two classes. The first includes small molecules which, like FOTS, are known to form covalently bound monolayers on  $\text{SiO}_2$  and are deposited from either nonaqueous solutions or the vapor phase. This class

includes  $(\text{CH}_3)_2(\text{CH}_3\text{CH}_2\text{O})\text{Si}(\text{CH}_2)_3\text{NH}_2$  (APDMES),  $(\text{CH}_3\text{O})_3\text{Si}(\text{CH}_2)_3\text{NH}_2$  (APTMS),  $(\text{CH}_3\text{CH}_2\text{O})_3\text{Si}(\text{CH}_2)_{11}\text{NH}_2$  (AUTES),  $\text{Cl}_3\text{Si}(\text{CH}_2)_{17}\text{CH}_3$  (ODTS), and  $\text{Cl}_3\text{Si}(\text{CH}_2)_{29}\text{CH}_3$  (TTS). Structures of these molecules are given in Fig. 2-1. The deposition of poly(ethylene imine) or PEI on low- $\kappa$  was also investigated. PEI represents a second class of organic surface modifiers: it is a much larger molecule ( $\text{MW} \sim 60,000 \text{ g}\cdot\text{mol}^{-1}$  versus 161 to 556  $\text{g}\cdot\text{mol}^{-1}$  for the molecules in the first class), is deposited from an aqueous solution, and attaches to the surface through electrostatic or hydrogen bonding interactions, rather than covalent bonds.

### 6.3. Experimental methods

#### 6.3.1. Materials, substrate preparation, and formation of organic films

A full accounting of the materials and methods used to deposit organic thin films is given in Sections 2.2-2.4. The low- $\kappa$  material is the same as that used in Chapter 5, and is described in detail in Sec. 2.2. To summarize, the material contains a network of interconnected pores, with 90% of the pores (by volume) having a diameter of less than 5 nm (full pore size distribution is given in Fig. 6-9). EP and TEM results suggest that the structure of this low- $\kappa$  includes larger ( $\sim 2 \text{ nm}$ ) ellipsoidal pores connected through necks or micropores in the skeleton material [33]. The low- $\kappa$  was either used as-received (water contact angle of  $93^\circ/71^\circ$  advancing/receding), or exposed to one of two pre-treatments: a 2 second exposure to an air plasma (Harrick Plasma PDC-001, plasma power of 7.16 W), which reduced the



water contact angle to 30°/19°, or a simultaneous exposure to ozone and UV irradiation for 2 minutes (Samco model UV-1, 5 L/min O<sub>2</sub> flowrate into O<sub>3</sub> generator), reducing the contact angle to 67°/46°. Both pre-treatments enhance the reactivity of the low- $\kappa$ , and the air plasma exposure in particular can be used as a simulation for plasma damage due to processing steps used to pattern low- $\kappa$  in practice.

### 6.3.2. Characterization techniques

Two methods were used to evaluate the degree of infiltration of organic material into the low- $\kappa$ . Spectroscopic ellipsometry was carried out using a Woollam VASE ellipsometer (J. A. Woollam Co, Inc., Lincoln, NE) using a photon energy range of 1.5 to 3 eV (wavelength range 413 nm to 827 nm), at an incident angle of 75°. This range was chosen because it corresponds to a region in which the low- $\kappa$  is optically transparent (extinction coefficient  $k = 0$ ), which greatly simplifies data analysis. The raw output from the ellipsometric measurement was used to obtain film thickness and optical properties using WVASE32 software (J. A. Woollam Co.). Changes in the optical properties were then used to calculate the amount of organic material in the bulk of the low- $\kappa$  (calculation details are provided below). In a second set of measurements, ellipsometric porosimetry [31,32] was carried out in a SOPRA EP-12 instrument (SOPRALAB, Courbevoie, France) to measure the overall porosity and pore size distribution of the low- $\kappa$ . In this tool, the sample is placed in a vacuum chamber and exposed to increasing steps in partial pressure of an adsorbate vapor, in this case 2-propanol. After each step change in partial pressure, the thickness and

refractive index of the porous film are measured *in situ*. When the partial pressure of the adsorbate reaches its vapor pressure, the process is reversed and the film is exposed to decreasing steps in the partial pressure of the adsorbate. The amount of adsorbate condensed within the film can be calculated during adsorption and desorption using measured changes in refractive index. Through the use of an appropriate model (discussed below), the pore size distribution and total porosity of the low- $\kappa$  film can be derived from this measurement. One aspect of EP that should be noted is that it is only sensitive to *open* pores, or pores which are accessible to solvent molecules. Blind pores, those which are not connected to the outer surface, are not detected in EP. This technique is well suited to measure the porosity and pore size distribution of porous low- $\kappa$  materials, and its use for the characterization of low- $\kappa$  materials, including SiOCH deposited by CVD, has been demonstrated previously [32, 34-41]. EP has also been shown to give results consistent with other common methods for analyzing porous films [34,38].

The elemental composition of the near surface region of the low- $\kappa$  was characterized using XPS. Measurements were taken using a VSW CLASS 100 concentric hemispherical energy analyzer (VSW Worldwide, Cheshire, U.K.) operated at constant pass energy of 90 eV, with a photoelectron takeoff angle of 38.5°. Unmonochromated Mg K $\alpha$  x-rays (1253.6 eV) were generated by a VSW twin anode x-ray source using a 20 mA emission current and 12 kV anode potential. The effect of sample charging due to photoelectron emission was corrected for by shifting all spectra such that the binding energy of the Si(2p) peak was equal to 103.46 eV, as described in Sec. 5.3.3.

## 6.4 Results and Discussion

As discussed above, the results will be divided into two sections. The first will focus on the details of the infiltration of FOTS into porous low- $\kappa$  using SE, EP, and XPS. In the second, we will discuss experiments using a range of organic surface modifiers and deposition parameters.

### 6.4.1. Deposition of FOTS on low- $\kappa$

In the first set of experiments, a series of identical low- $\kappa$  substrates were exposed to FOTS vapor for varying amounts of time, from 20 s to 1200 s, and analyzed *ex situ* using SE after exposure. In a typical SE measurement, the change in polarization state of light as a result of interacting with a thin film sample is measured, and expressed in the two parameters  $\Psi$  and  $\Delta$  at each photon energy [30]. In principle,  $\Psi$  and  $\Delta$  can be used to simultaneously determine the thickness of a film, as well as its optical properties  $n$  (refractive index) and  $k$  (extinction coefficient) over the measurement range. Concerning the latter, it is useful to constrain  $n$  and  $k$  to follow one of a number of established optical models. Here, the Sellmeier approximation, which is applicable to transparent, dielectric materials ( $k = 0$ ) [42] was used. The choice of a model which assumes  $k = 0$  is based on the assumption that the low- $\kappa$  is mainly a mixture of a SiO<sub>2</sub>-based skeleton and air, both of which have  $k = 0$  in the range of 1.5 to 3 eV.

This assumption will be tested below using a direct calculation of  $k$ . The Sellmeier approximation is:

$$n(\Lambda) = \sqrt{1 + \sum_j \frac{A_j \Lambda^2}{\Lambda^2 - \Lambda_{0,j}^2}} \quad (6-1)$$

Where  $\Lambda$  is the wavelength of the incident light, and  $A_1, A_{0,1}, A_2, A_{0,2}$ , etc., are fit parameters. For the level of precision typically required for SE data analysis, a single term (i.e.,  $j = 1$ ) is sufficient [42]. In a fitting procedure conducted using Woollam WVASE32 software, we begin with initial guesses for the film thickness and the Sellmeier approximation parameters. An optimization routine then varies these initial guesses to achieve the best fit of the measured  $\Psi$  and  $\Delta$  values, based on a minimization of the mean squared error weighted by the uncertainty of the measured values at each photon energy [43]. In Fig. 6-1 the results of this optimization procedure are demonstrated for two cases, the UV/Ozone pretreated low- $\kappa$  film with no FOTS, and the same film after 1200 s of exposure to FOTS vapor. The measured  $\Psi$  and  $\Delta$  are shown as discrete points, while results of the fitting procedure (i.e., the  $\Psi$  and  $\Delta$  values that would be obtained using the optimized thickness and Sellmeier constants) are shown as a solid line. An excellent fit to the data is obtained in both cases. Similar quality of fit was obtained for intermediate FOTS exposures, as well as low- $\kappa$  films without UV/Ozone pretreatment before and after FOTS exposure. For all fits, one term in the Sellmeier approximation was utilized, so that only three parameters,  $A_1$  and  $A_{0,1}$ , and the low- $\kappa$  film thickness were active.

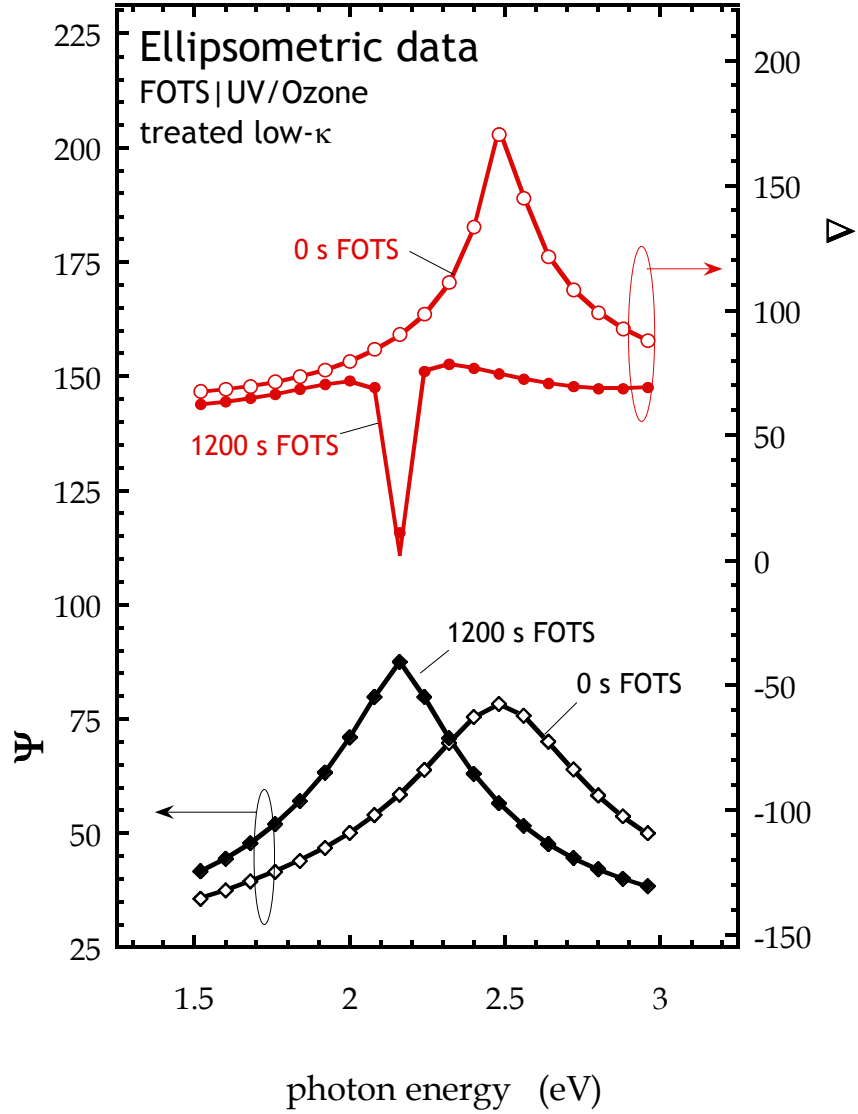


**Figure 6-1:** Measured  $\Psi$  and  $\Delta$  values as a function of photon energy for low- $\kappa$  exposed to 0 s and 1200 s exposure to FOTS vapor. Solid lines represent a fit to the data, described in the text. Fit parameters included the low- $\kappa$  film thickness, and two parameters from the Sellmeier approximation (Eq. 6-1,  $j = 1$ ).

The maximum element in the cross-correlation matrix for the three parameters was  $\leq 0.86$  for all films analyzed, indicating that all three terms could be fit independently (a cross correlation matrix element of  $\geq 0.97$  indicates that fit parameters are too correlated to obtain a reliable fit of all simultaneously [44]). A repeat of the fit routine using two terms in the Sellmeier approximation (total of 5 fit parameters) was also attempted, with no significant improvement in the quality of fit.

In a second check of the quality of fit, the thickness of the film was fixed to be the thickness obtained from the previously described method, then  $n$  and  $k$  values were directly calculated at each photon energy without using the Sellmeier approximation. Direct calculation of  $n$  and  $k$  is possible because  $\Psi$  and  $\Delta$  represent two independent parameters measured at each photon energy. Fig. 6-2, shows the results obtained from direct calculation (points), as well as through use of the Sellmeier approximation with  $k = 0$  (solid lines). The optical properties obtained from fitting do not vary significantly from those obtained by direct calculation, with good fitting of  $n$  over the entire wavelength range. The direct calculation indicates that  $k < 0.002$  for all wavelengths between 1.5 and 3 eV, validating the assumption that  $k = 0$  required for use of the Sellmeier approximation. Fitting over the entire range available in the instrument (0.8 to 6 eV) indicated significantly nonzero values of  $k$  below 1.5 eV, likely due to an artifact related to reflections of the light beam from the backside of the Si substrate at wavelengths at which Si is appreciably transparent.  $k$  also became significant at photon energies above 3 eV, due to optical absorption by the low- $k$  material in the UV region.

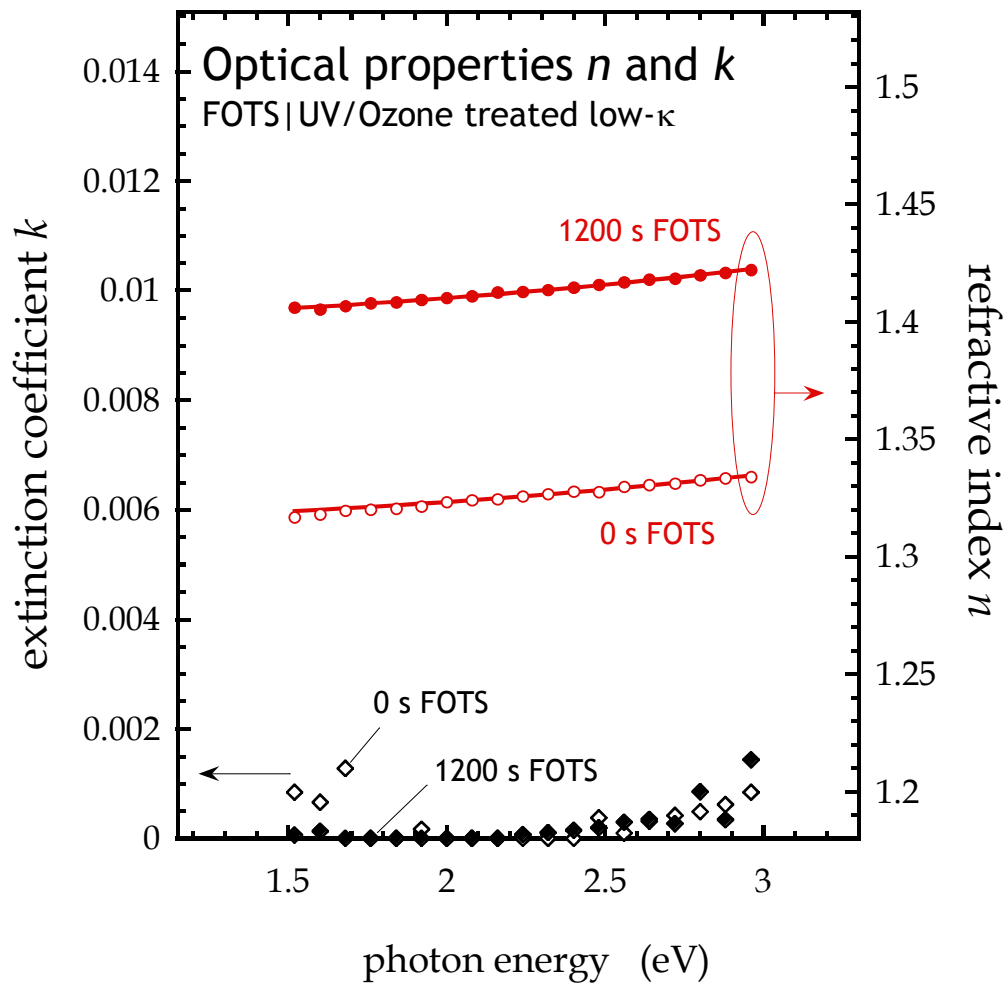


**Figure 6-2:** Direct calculation of  $n$  and  $k$  for as a function of photon energy for low- $\kappa$  after 0 s and 1200 s exposure to FOTS vapor. The thickness was fixed to be that obtained from the fit of the data in Fig. 6-1. Solid lines represent  $n$  values obtained from a fit described in the text, which used two parameters from the Sellmeier approximation (Eq. 6-1,  $j = 1$ ).

In Fig. 6-3(a), the thickness derived from SE of the low- $\kappa$  layer is shown as a function of exposure time to FOTS vapor. The thickness has no clear dependence on exposure time. Therefore, we can conclude that the low- $\kappa$  is not considerably swelling due to FOTS adsorption, and that the formation of an FOTS multilayer on the top surface of the low- $\kappa$  is unlikely. Fig. 6-3(b) shows the refractive index  $n$  at 589 nm as a function of exposure time, as calculated from the Sellmeier constants obtained from the fit of the ellipsometric data. 589 nm, equivalent to the emission wavelength of the sodium D line, is a common wavelength to express refractive index. It is used here because the refractive index of several materials relevant to this study have been published at 589 nm. Also note that 589 nm ( $\sim 2.11$  eV) is within the range where  $k = 0$  for the low- $\kappa$  material and for FOTS/low- $\kappa$  (Fig. 6-2). A correlation between  $n$  and FOTS exposure time is clearly seen, indicating a filling of the inner pore volume by FOTS. The overall volume fraction of FOTS within the pores can be calculated through the use of an effective medium approximation (EMA) which describes the overall refractive index of a mixture of several materials. The EMAs used here have the following general form:

$$\frac{\tilde{\epsilon} - \tilde{\epsilon}_{host}}{\tilde{\epsilon} + 2\tilde{\epsilon}_{host}} = \sum_{components} f_i \frac{\tilde{\epsilon}_i - \tilde{\epsilon}_{host}}{\tilde{\epsilon}_i + 2\tilde{\epsilon}_{host}} \quad (6-2)$$

Where  $\tilde{\epsilon}$ ,  $\tilde{\epsilon}_i$ , and  $\tilde{\epsilon}_{host}$  are the complex dielectric function of the film after FOTS exposure, and the complex dielectric functions of each individual component  $i$  and of the ‘host’ material.  $f_i$  represents the volume fraction of each component.



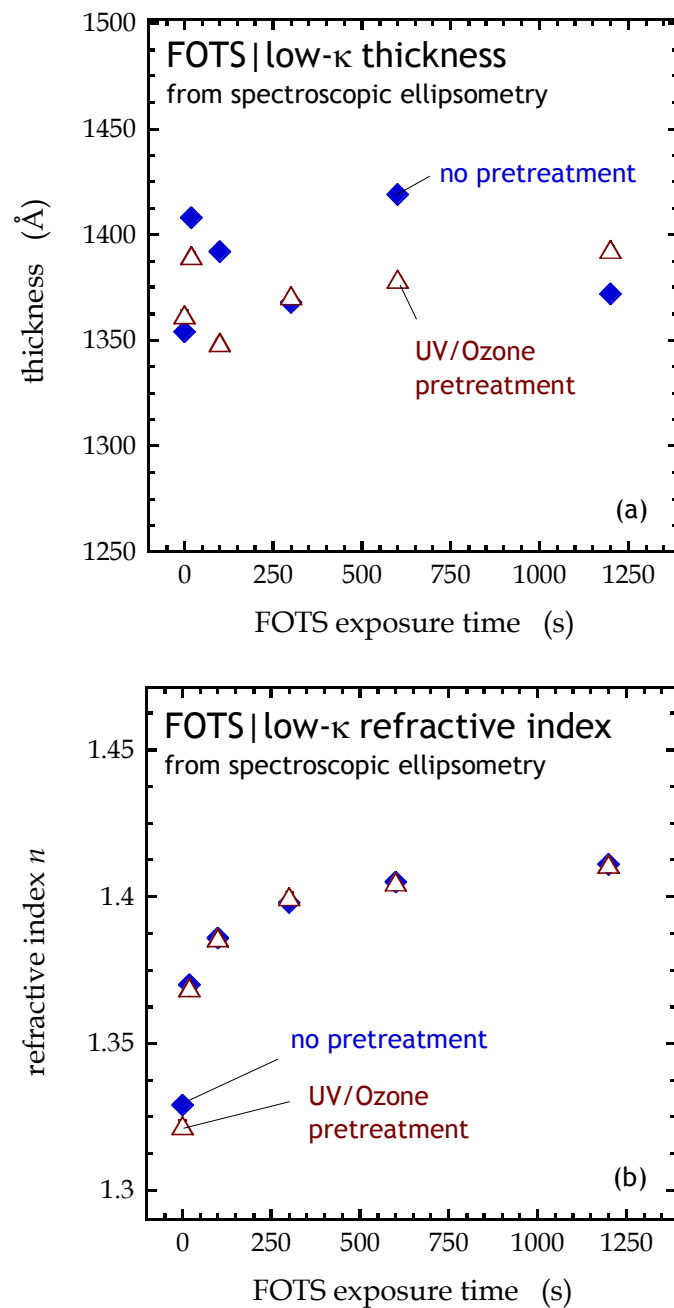


**Figure 6-3: (a) Thickness and (b) refractive index  $n$  at 589 nm ( $\sim 2.1$  eV photon energy) of FOTS|low- $\kappa$  as a function of FOTS vapor exposure time. Both values were obtained from a fit of SE data which included film thickness and one term in the Sellmeier approximation (Eq. 6-1,  $j = 1$ ) as parameters.**

The complex dielectric function can be written as  $\tilde{\epsilon} = (n - ik)^2$  [30], and because  $k = 0$  at the wavelength used for this analysis Eq. 6-2 can be rewritten

$$\frac{n^2 - n_{host}^2}{n^2 + 2n_{host}^2} = \sum_{components} f_i \frac{n_i^2 - n_{host}^2}{n_i^2 + 2n_{host}^2} \quad (6-3)$$

We will apply one of two EMAs, which differ only on the choice of the ‘host’ material. In the Maxwell Garnett form [45], the host material is assumed to be the component with the highest volume fraction, which in this case would be the solid skeleton material of the low- $\kappa$ , i.e.  $n_{host} = n_{skeleton}$ . In the Bruggeman form [42], the dielectric function of the host material is assumed to be the measured overall dielectric function, i.e.  $n_{host} = n$ . As would be expected, it has been shown that the Maxwell Garnett EMA is a better representation of isolated particles embedded in a host material, while the Bruggeman EMA is a better representation of a random aggregation of materials, where no single material is clearly the host [46,47]. TEM and EP analysis indicates that the actual arrangement of void spaces in the low- $\kappa$  is somewhere between these two extremes [33], therefore we will use both approximations and determine if they result in significantly different results. It should be noted that the use of both EMA equations requires the assumption that the FOTS, skeleton material, and void spaces are mixed at a length scale much smaller than the wavelength of the light used for ellipsometry. This is reasonable, given the pore size of  $< 5$  nm and the ellipsometry wavelengths of 413 to 827 nm.

Before FOTS exposure, Eq. 6-3 can be written:

$$\frac{n^2 - n_{host}^2}{n^2 + 2n_{host}^2} = (1 - f_{void}) \frac{n_{skeleton}^2 - n_{host}^2}{n_{skeleton}^2 + 2n_{host}^2} + f_{void} \frac{n_{void}^2 - n_{host}^2}{n_{void}^2 + 2n_{host}^2} \quad (6-4)$$

and after FOTS exposure:

$$\frac{n^2 - n_{host}^2}{n^2 + 2n_{host}^2} = (1 - f_{void}) \frac{n_{skeleton}^2 - n_{host}^2}{n_{skeleton}^2 + 2n_{host}^2} + (f_{void} - f_{FOTS}) \frac{n_{void}^2 - n_{host}^2}{n_{void}^2 + 2n_{host}^2} + f_{FOTS} \frac{n_{FOTS}^2 - n_{host}^2}{n_{FOTS}^2 + 2n_{host}^2} \quad (6-5)$$

By definition,  $n_{void} = 1$  at all wavelengths. For  $n_{FOTS}$ , the chemical supplier provides a refractive index of 1.352 at 589 nm for bulk liquid FOTS (Sigma-Aldrich Corp.). This may differ from the refractive index of the FOTS layer after deposition, due to chemical and structural changes related to the adsorption process (losing Cl atoms, for example). However, because the refractive index of the adsorbed FOTS layer is not available, the value for bulk FOTS will be used. The lack of a precise figure for  $n_{FOTS}$  is a significant source of uncertainty in the calculations. Published  $n$  values of chemically similar materials fall in the range of 1.25 to 1.37 at 589 nm [48-51], which provides some indication of the possible range of values for  $n_{FOTS}$ . Having established values for  $n_{void}$  and  $n_{FOTS}$ , we are left with three unknowns,  $f_{FOTS}$ ,  $f_{void}$  and  $n_{skeleton}$ . However, in practice, if a value of  $f_{void}$  is assumed anywhere within reasonable limits (0 to 0.5), calculated values of  $f_{FOTS}$  are obtained that do not vary by more than  $\pm 3\%$ . Therefore, the desired quantity  $f_{FOTS}$  can be calculated without knowing  $f_{void}$  and  $n_{skeleton}$  to a high degree of certainty. From the possible sources of error described here,

we can estimate an uncertainty in the calculated absolute value of  $f_{FOTS}$  to be  $\pm 25\%$ , while the relative error, arising from uncertainty in the fitting of the ellipsometry data, is  $\pm 10\%$  or less.

Fig. 6-4 displays a plot of the calculated value of  $f_{FOTS}$ , the volume fraction of FOTS in the low- $\kappa$  layer, for the same series of samples considered in Fig. 6-3. Comparing the two EMA forms, we find that the Maxwell Garnett form results in a  $\sim 5\%$  higher value of  $f_{FOTS}$  compared to the Bruggeman form in all cases. The values shown in Fig. 6-4 are the average of the values obtained using the two methods. Error bars here represent the estimated relative uncertainty. Significant infiltration takes place over time scales of 10-100 s, with approximately 50% of the total change in  $f_{FOTS}$  taking place in the first 20 s. After 1200 s exposure to FOTS vapor, from ellipsometry we estimate that the UV/Ozone treated low- $\kappa$  contains  $0.242 \pm 0.005$  volume fraction FOTS, while the low  $\kappa$  which was not pretreated contains  $0.223 \pm 0.007$  volume fraction FOTS. EP measurements indicated that the UV/Ozone pretreatment increases the open porosity of the low- $\kappa$  by  $\sim 23\%$ , which would likely explain the higher amount of FOTS infiltration in the pretreated film with UV/Ozone.

In addition to the SE based technique, EP has been used to determine the degree of FOTS infiltration for the UV/Ozone pretreated low- $\kappa$  film exposed to 600 s FOTS. As described above, this method involves exposing the porous film to varying partial pressures of an adsorbate gas. Forces which become relevant within small pores cause the condensation of the adsorbate at pressures below the vapor pressure ( $P_0$ ) (see Sec. 6.5 for more detail).

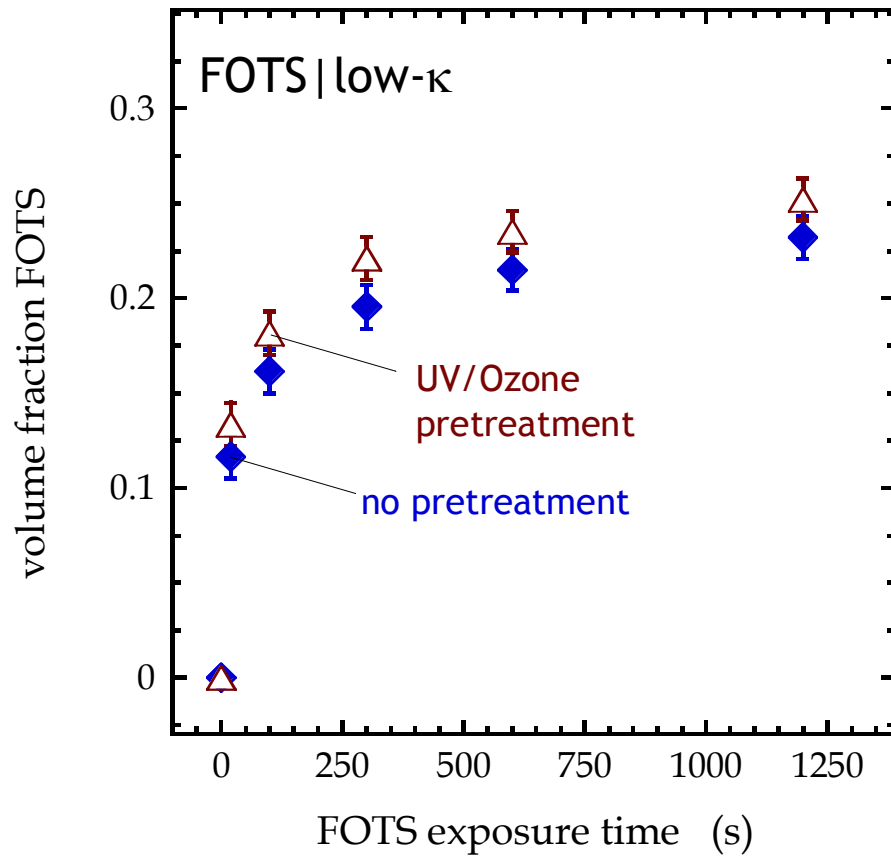


**Figure 6-4:** Volume fraction of FOTS in low- $\kappa$  as a function of FOTS vapor exposure time. Values were obtained using the refractive index values presented in Fig. 6-3, in combination with Eqs. 6-4 and 6-5.

The isotherms shown in Fig. 6-5 represent the total amount of 2-propanol condensed in the pores of the low- $\kappa$  as a function of partial pressure of 2-propanol. Compared here are UV/Ozone treated low- $\kappa$  with no FOTS, and the same film after 600 s exposure to FOTS. Note that the range  $P > 0.9P_0$  is not considered due to possible condensation of 2-propanol on the top surface of the low- $\kappa$  [31]. Initial examination of these isotherms indicates that the total open pore volume, approximated by the volume fraction of condensed 2-propanol at the highest  $P/P_0$  considered, decreases significantly as a result of FOTS adsorption. Roughly, the open pore volume has decreased from 0.227 to 0.086, indicating an FOTS volume fraction of 0.141. This value can be compared to the value obtained from spectroscopic ellipsometry of  $0.225 \pm 0.056$ . One possible source of discrepancy between these two figures is the uncertainty in the refractive index of adsorbed FOTS, which was assumed to be equal to the refractive index of liquid FOTS. However, it is possible that the density, and therefore refractive index, of the FOTS film is significantly different than the liquid state [52,53]. Comparing the total open pore fraction measured by EP (0.227) to the volume fraction of FOTS adsorbed at 1200 s exposure time from SE (0.242) suggests that the SE values contain a systematic error which leads to an overestimation of  $f_{FOTS}$ , with the most likely source of this error being the assumed value of  $n_{FOTS}$ . One possible scenario is that the confined space and curvature of the low- $\kappa$  pores lead to enhanced packing in the FOTS layer, which could cause a significant increase the density and refractive index compared to bulk FOTS liquid.

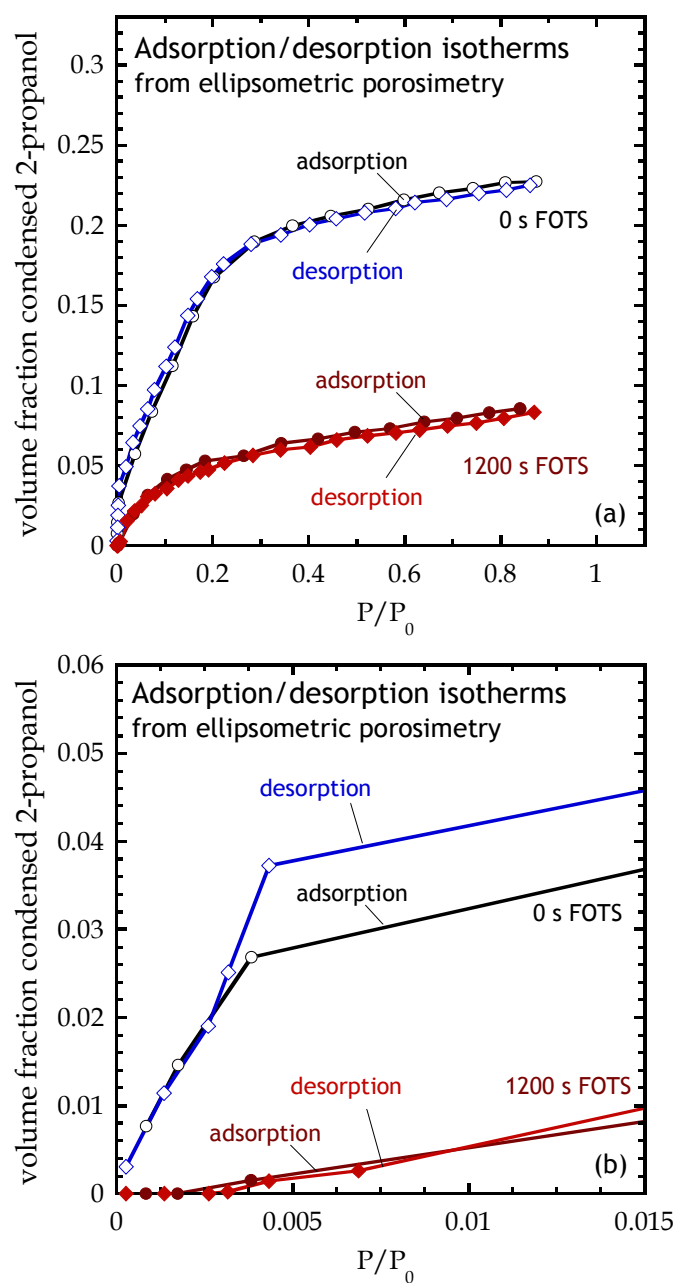


**Figure 6-5:** Volume fraction of 2-propanol condensed within low- $\kappa$  or FOTS|low- $\kappa$  as a function of the pressure of 2-propanol relative to its vapor pressure, shown for adsorption (increasing 2-propanol pressure) and desorption (decreasing 2-propanol pressure), obtained from EP. These are commonly called the adsorption and desorption isotherms. **(a)** shows the entire range of the measurement, while **(b)** highlights the behavior at low pressure.

In addition to the total void fraction of the low- $\kappa$ , the isotherms shown in Fig. 6-5 may be used to calculate the pore size distribution [31,32]. Details of this calculation for the low- $\kappa$  prior to FOTS exposure are given below in Sec. 6.5. As stated above, calculations of the pore size distributions for Si based low- $\kappa$  materials has been demonstrated previously, however the technique has not been studied in the case of porous materials altered with a fluorinated surface layer. The presence of FOTS may cause changes in the interaction of the adsorbate with the low- $\kappa$ , which could in turn influence the adsorption processes necessary for determination of pore size, particularly in the case of micropores at low values of  $P/P_0$ . One measure for the adsorbate/low- $\kappa$  interaction is the macroscopic contact angle of liquid 2-propanol on the low- $\kappa$  surface, which is measured to be  $< 10^\circ$ . This would suggest that the changes in adsorbate/low- $\kappa$  interaction are not major, but nevertheless it will not be possible to decouple the changes in low- $\kappa$  surface chemistry with changes in pore size. While the pore size distribution cannot be reliably calculated for the FOTS/low- $\kappa$  film, a close examination of the isotherms may still reveal certain aspects of FOTS infiltration. In the low pressure region of the isotherms, shown in Fig. 6-5(b), we see that below  $P/P_0 = 0.005$  much more adsorption takes place in the low- $\kappa$  film with no FOTS. This indicates a significant change in the smallest pores in the film, in which adsorption takes place at very low  $P/P_0$ . There are three specific possibilities which would explain this: FOTS could (i) fill the smallest micropores in the film, (ii) block the entrances to micropores, or (iii) change the surface chemistry within the micropores such that condensation is delayed. Logically, process (iii) would happen in combination with process (i). Given the overall length of the FOTS molecules ( $\sim 1$  nm) and the size of



the smallest pores in the film ( $< 2$  nm), change in the pore wall surface chemistry in the case of micropores would also involve almost complete pore filling.

The two measurement techniques described up to this point are sensitive to changes over the entire thickness of the low- $\kappa$  film. XPS, on the other hand, is sensitive to changes only in the top  $\sim 10$  nm region of the low- $\kappa$ , or  $< 1\%$  of the total thickness of the low- $\kappa$  layer. Therefore, inspection of XPS data, particularly focusing on the Si and F features, will provide insight to the adsorption process close to the vacuum|low- $\kappa$  interface. Fig. 6-6 contains XP spectra of the Si(2p)/Si(2s) and F(1s) regions for the UV/Ozone pretreated low- $\kappa$  exposed to FOTS vapor for 20 s and 1200 s. First, significant intensity from the two silicon core levels is observed after both 20 s and 1200 s of exposure [Fig. 6-6(a)]. This indicates that the thickness of the FOTS at the vacuum|low- $\kappa$  interface is low, on the order of nm, providing confirmation that significant multilayer formation is not taking place. The F(1s) signal [Fig. 6-6(b)], which is directly proportional to the density of fluorine atoms in this region (neglecting attenuation effects), increases by a factor of  $\sim 2.6$  between 20 s and 1200 s. From SE, the volume fraction of FOTS in the bulk of the low- $\kappa$  increases by a factor of  $\sim 1.9$  over the same range. This comparison shows that FOTS does not fill the low- $\kappa$  by first depositing at the surfaces closest to the vacuum interface. Rather, the coverage of low- $\kappa$  at the vacuum interface follows approximately the coverage within the bulk of the low- $\kappa$ , and given these figures the FOTS may deposit at a slightly higher rate within the bulk of the low- $\kappa$ . In other words, it appears that the diffusion of gas phase FOTS molecules within the low- $\kappa$  is fast, and that the deposition of FOTS on the low- $\kappa$  surface is reaction rate limited.

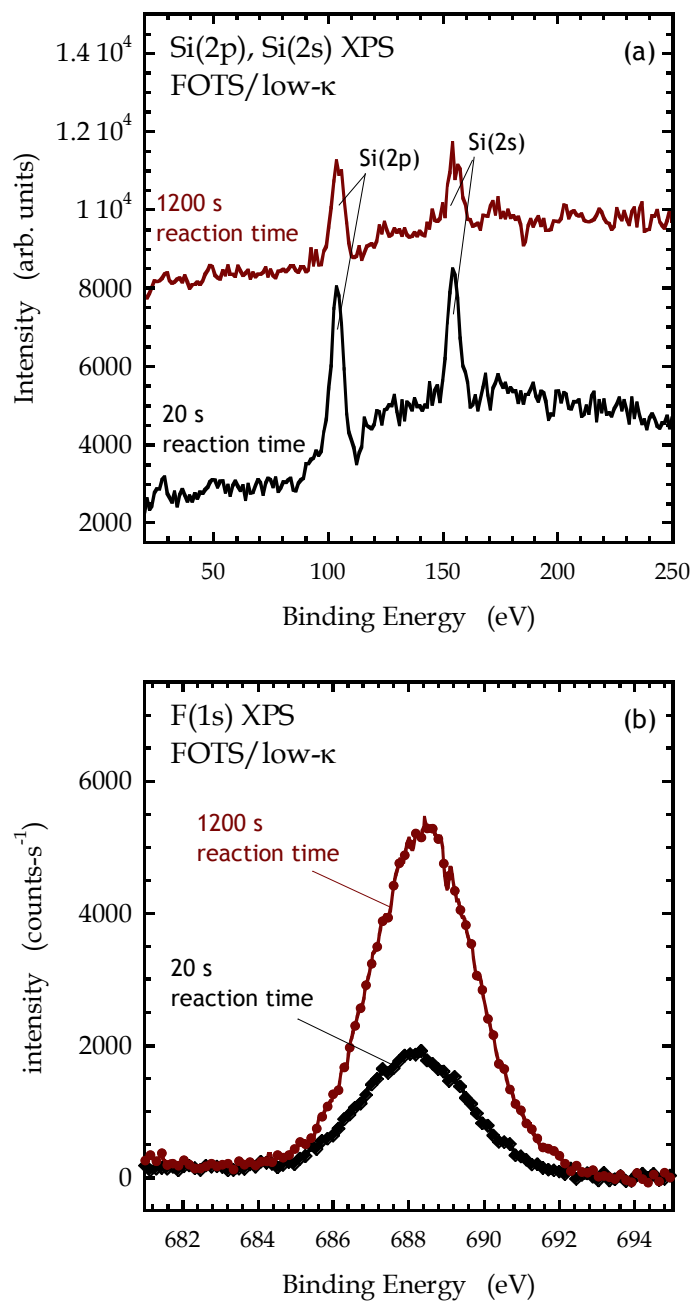


**Figure 6-6:** X-ray photoelectron spectra of the (a) Si(2p) / Si(2s) and (b) F(1s) regions for low-κ substrates exposed to FOTS vapor for 20 s and 1200 s.

If this were not the case, and the deposition process was mainly diffusion limited, then one would expect to see deposition of FOTS much more quickly at the vacuum interface (in XPS) as compared to deposition within the bulk pore structure (ellipsometry).

The diffusion of molecules through a porous material is a relatively well studied area. Given the range of pore size in this low- $\kappa$ , and the size of the FOTS molecule, the two relevant types of diffusion are Knudsen and configurational [54,55]. Using the diffusion of hydrocarbons through zeolites as an analogous system, Knudsen diffusion ( $D \sim 10^{-5}$  to  $10^{-9}$  m<sup>2</sup>/s) dominates when the kinetic diameter of the diffusing molecule ( $d_m$ ) is  $> 1.7$  times the diameter of the pore ( $d_p$ ). Configurational diffusion, an activated process controlled by the interactions between the diffusing molecule and the pore wall ( $D < 10^{-9}$  m<sup>2</sup>/s), takes over as the diameter of the molecule approaches the pore diameter. It is likely that both types of diffusion take place in the system under investigation here. In order for the deposition process to be reaction rate limited, the FOTS molecule must be able to diffuse across the entire thickness of the low- $\kappa$  film over time scales much shorter than the FOTS exposure time. To diffuse a length of 10  $\mu$ m, which is long compared to the low- $\kappa$  thickness, over 20 s, the shortest exposure time examined, would require a diffusion coefficient of  $\sim 8 \times 10^{-14}$  m<sup>2</sup>/s. This is well within the range of  $D$  measured for hydrocarbons diffusing through zeolite [54], even for configurational diffusion taking place when  $d_m/d_p \sim 1$ , which would be the case for FOTS diffusing through the smallest pore size measured by EP. It is not unexpected then that after 20 s, an FOTS molecule would be able to diffuse across the

entire thickness of the low- $\kappa$  several times, and it is therefore plausible that the infiltration deposition process is reaction rate limited.

#### **6.4.2. Effect of surface modifier structure and deposition parameters on infiltration**

In this section, the same SE based method described above will be used to investigate the effect of a number of parameters, including organic molecule size, pretreatment, and low- $\kappa$  type on infiltration.

First, because the diameter of the pores in the low- $\kappa$  is comparable to the size of typical molecules used to form organic monolayers, one may expect that the size of the molecule will play a role in limiting infiltration by simple size exclusion effects. In order to confirm this, molecules of varying size have been deposited on the low- $\kappa$  material. For this study the low- $\kappa$  was exposed to either UV/Ozone pretreatment, or plasma pretreatment, as described above in Sec. 6.3.1. The molecules deposited were  $(\text{CH}_3)_2(\text{CH}_3\text{CH}_2\text{O})\text{Si}(\text{CH}_2)_3\text{NH}_2$  (APDMES),  $(\text{CH}_3\text{CH}_2\text{O})_3\text{Si}(\text{CH}_2)_{11}\text{NH}_2$  (AUTES),  $\text{Cl}_3\text{Si}(\text{CH}_2)_{17}\text{CH}_3$  (ODTS),  $\text{Cl}_3\text{Si}(\text{CH}_2)_{29}\text{CH}_3$  (TTS), and  $(\text{CH}_3\text{O})_3\text{Si}(\text{CH}_2)_3\text{NH}_2$  (APTMS). Chemical structures of these molecules are given in Fig. 2-1. For APDMES, AUTES, ODTS, and TTS, the substrate was exposed to a solution of the organic molecule in toluene for 48 hours. For APTMS, the substrate was exposed to pure APTMS vapor for 900 s. The results of these experiments, expressed as volume fraction of the organic as a function of molecular volume are shown in Fig. 6-7 (solid points).

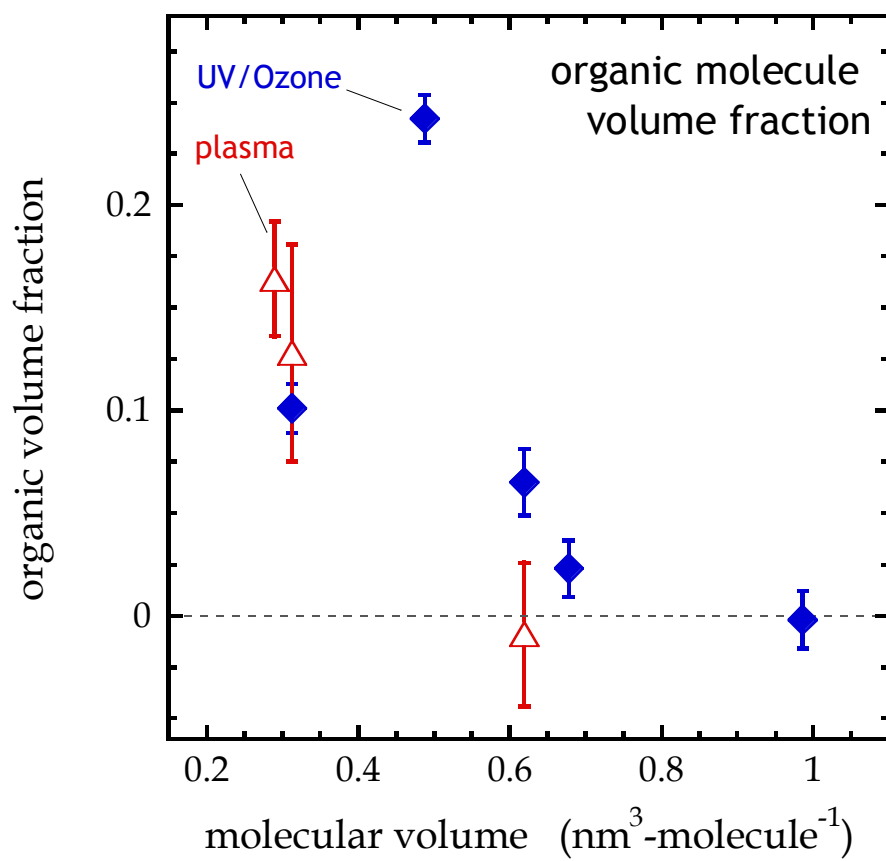


**Figure 6-7:** Volume fraction of infiltrated organic material as a function of molecular volume of the organic, for two low- $\kappa$  pretreatments. Values were obtained using  $n$  values from SE, and Eqs. 6-4 and 6-5. The organic molecules include APTMS, APDMES, AUTES, FOTS, ODTs, and TTS. See Fig. 2-1 for molecular structures.

In applying Eq. 6-5 for all molecules except FOTS, the  $n_{FOTS}$  term has been replaced with the refractive index of bulk  $\text{Cl}_3\text{Si}(\text{CH}_2)_{17}\text{CH}_3$  (1.432) [53]. The molecular volume was determined from bulk liquid density figures supplied by the manufacturer or, in the case of TTS, using the molecular modeling software ChemDraw Ultra (version 8.0, CambridgeSoft Corp.). Included in this plot is the calculated volume fraction of FOTS in the low- $\kappa$  after 1200 s exposure to FOTS vapor. From the data in Fig. 6-7, it is apparent that there is a correlation between molecular volume and the degree of infiltration. This may be due to a number of factors. First, the larger molecules may be excluded from the smallest pores in the low- $\kappa$ . However, while the volumes of the four molecules are very different, the smallest cross-sections of the molecules, which would presumably control size exclusion, are similar. A more likely possibility is that the large molecular volume, combined with the size and shape constraints within the pore structure simply leads to less efficient packing of the larger molecules. Another possibility is that the larger molecules diffuse much more slowly through the low- $\kappa$  compared to the small molecules. As the deposition times for all four were the same, this could lead to incomplete coverage of the large molecules. As these depositions were conducted in the presence of a liquid solvent, viscosity effects may play a larger role compared to deposition using FOTS.

A second comparison shown in Fig. 6-7 is the infiltration of a small molecule,  $(\text{CH}_3)_2(\text{CH}_3\text{CH}_2\text{O})\text{Si}(\text{CH}_2)_3\text{NH}_2$ , and a larger molecule,  $(\text{CH}_3\text{CH}_2\text{O})_3\text{Si}(\text{CH}_2)_{11}\text{NH}_2$ , on UV/Ozone versus plasma pretreated low- $\kappa$ . Here we see that the infiltration of the smaller molecule is similar with the two pretreatments, while for the larger molecule significant infiltration into the UV/Ozone treated low- $\kappa$  is observed, with no

infiltration into the plasma treated low- $\kappa$ . This may be explained by structural changes in the low- $\kappa$  due to the plasma exposure. As stated above, plasmas can be used to seal low- $\kappa$  materials against the infiltration of ALD processes into low- $\kappa$  and so it would not be unexpected that a plasma treatment could also seal the surface against an organic molecule. In this case, however, the sealing provided by the plasma exposure is not perfect, as the smaller molecule is easily able to penetrate any sealing layer and deposit within the bulk of the low- $\kappa$ .

As stated above, a clear result from the analysis of Fig. 6-7 is that molecule size plays a large role in determining the degree of infiltration. Therefore, one strategy which may be employed to modify the surface of porous low- $\kappa$  with a minimum amount of infiltration is the use of a polymer such as PEI. PEI was deposited on the low- $\kappa$  used here, and found no infiltration was observed (no measurable change in refractive index of the low- $\kappa$  after deposition). However, we know that PEI does form a film on the outer surface of the low- $\kappa$  with N atomic density of  $\sim 4 \times 10^{14} \text{ cm}^{-2}$ , as discussed in Sec. 5.4.2 and shown in Fig. 5-2. Therefore, given the results presented here a promising method to modify low- $\kappa$  without appreciable infiltration of the modifying material into the pore structure is the use of oligomers or polymers. A further advantage to the use of water-soluble polymers such as PEI is that, given the high contact angle of water on most low- $\kappa$  materials, it is likely that capillary effects limit infiltration of small pores.

A further aspect investigated here is the effect of water within the low- $\kappa$  structure. Despite the high contact angle of water on the low- $\kappa$  surface, it is well known that it can infiltrate the pore network from ambient air, particularly if the low- $\kappa$

has been exposed to an oxygen containing plasma [2,20-24]. To remove any water that may be in the low- $\kappa$  film, samples were held at 150 °C for 1 hour in an air oven before deposition of APTMS from the vapor phase. APTMS was chosen because no water is used in the deposition process. After the baking step, samples were cooled then transferred as quickly as possible to the deposition chamber. The amount of infiltration of the organic molecule into a pre-baked sample was then compared to infiltration into a sample which had not been baked prior to exposure to APTMS vapor. To maximize the potential effect of adsorbed water, both samples were exposed to the air plasma described above prior to baking. The pre-baking had no significant effect on the amount of infiltration, with  $18.5 \pm 3.5$  volume % APTMS in the pre-baked sample and  $16.4 \pm 2.8$  volume % APTMS in the sample which was not pre-baked. This result suggests that trapping of the organic molecules within the pore structure is not mediated by water absorbed water, but by intrinsic reactive sites, or sites added during the plasma exposure step. We note that measurements of the refractive index before and after the 150 °C bake indicate that the volume fraction of water in the plasma treated low- $\kappa$  was  $\sim 0.02$  after extended exposure to ambient air ( $> 12$  hours).

Beyond the single low- $\kappa$  discussed up to this point, the infiltration of APTMS into four additional low- $\kappa$  samples provided by an industrial collaborator was investigated. The low- $\kappa$  materials represent a range of dielectric constant, porosity, and pore connectivity, as summarized in Table 6-1. For this series of experiments, the low- $\kappa$  samples were treated using UV/Ozone prior to exposure to APTMS vapor.

Ellipsometric  $\Psi$  and  $\Delta$  values measured before and after APTMS exposure are shown in Fig. 6-8.



Sample #	Dielectric Constant	Polar Liquid Diffusivity	void fraction	APTMS vol % (from SE)
B1	2.75	Very Low		-0.6% $\pm$ 1.6%
B2	2.55	Moderate		-0.33% $\pm$ 2.8%
B3	3	Nonexistent	6-8 %	-0.13% $\pm$ 1.7%
B4	2.47	Very High	25-30%	9.58% $\pm$ 3.6%

**Table 6-1:** Properties of alternate low- $\kappa$  materials used in organic infiltration studies.

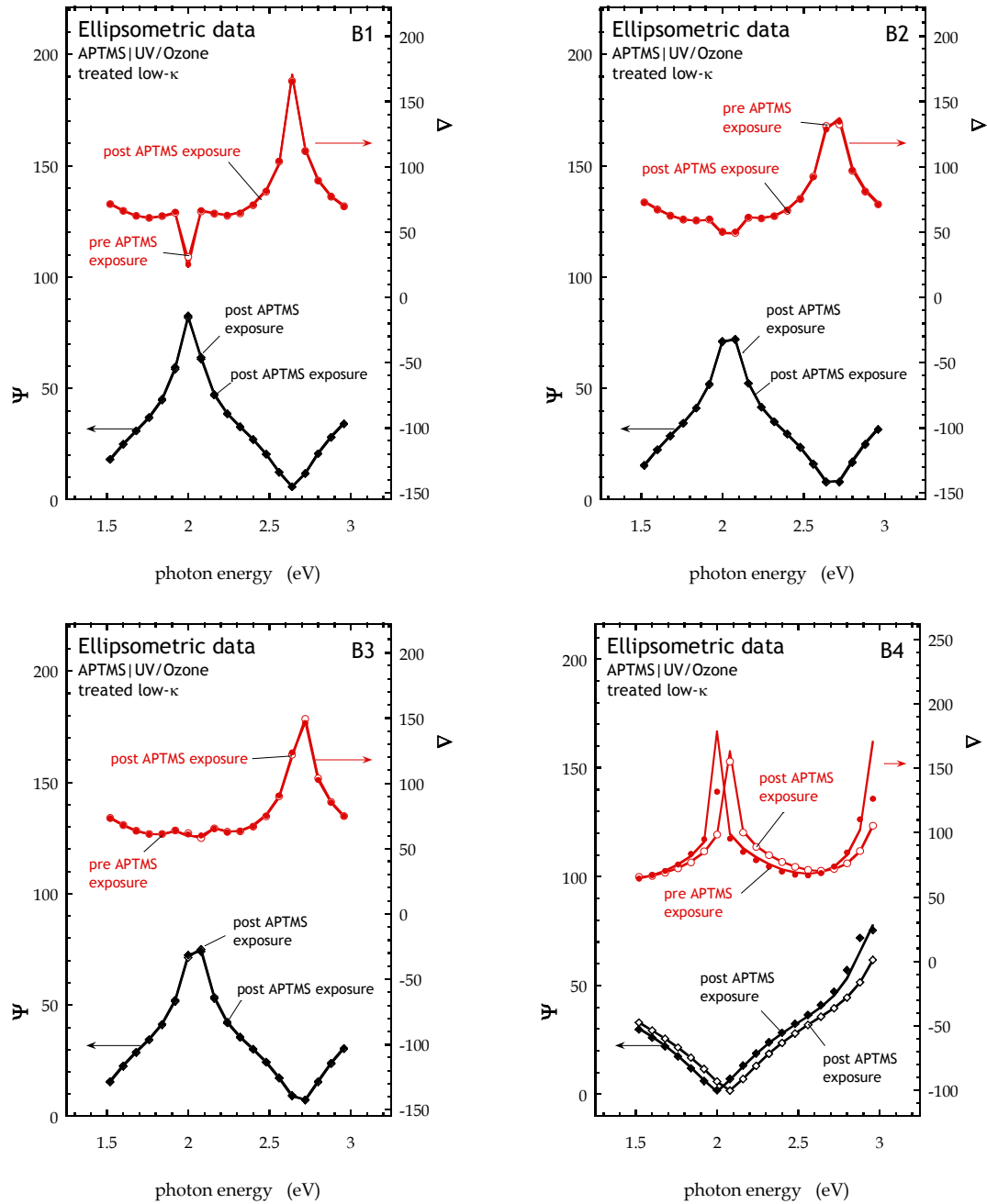


**Figure 6-8:** Measured  $\Psi$  and  $\Delta$  values as a function of photon energy for 4 low- $\kappa$  samples before and after exposure to APTMS vapor. Solid lines represent a fit to the data, described in the text. Fit parameters included the low- $\kappa$  film thickness, and two parameters from the Sellmeier approximation (Eq. 6-1,  $j = 1$ ).

Clearly, the only sample which exhibited any change was B4, which was reported to have a void fraction of 25-30% and the highest polar liquid diffusivity of the four. This change is reflected in the calculated volume fraction of APTMS after deposition, which is  $(9.58 \pm 3.6) \%$  for sample B4, and  $\sim 0 \%$  for the other three. N(1s) XPS (not shown) indicated significant APTMS deposition at the vacuum|low- $\kappa$  interface for samples B1, B2, and B3.

### 6.5. Determination of pore size distribution from EP isotherms

Pore size distributions can be extracted from EP isotherms using two complementary methods. The first is based on the Kelvin equation, which relates the vapor pressure of an adsorbate to the radius of its liquid meniscus within the pore [56], and is generally valid for mesopores (2 to 50 nm [57]). Assuming a cylindrical pore shape, the Kelvin equation can be written as:

$$\ln\left(\frac{P}{P_0}\right) = -\frac{2\gamma V_L \cos \varphi}{r_K RT} \quad (6-6)$$

Where  $P$  is the vapor pressure for a given radius of curvature  $r_K$ ,  $\gamma$  is the surface tension,  $V_L$  is the molar volume of the liquid adsorbate, and  $\varphi$  is the adsorbate/substrate contact angle. To obtain a physical pore radius  $r_p$  from  $r_K$ , a correction factor must be added due to the thickness of adsorbate on the pore walls which forms independently of capillary condensation, i.e.  $r_p = r_K + t$ . The thickness of

adsorbate on the pore wall  $t$ , which is due to monolayer/multilayer adsorption, is also function of the adsorbate pressure, and can be described by the Brunauer-Emmett-Teller (BET) equation [58]. To obtain a pore size distribution, it can be assumed that at a given pressure  $P$  all pores with radius  $r_K + t$  are filled, with an additional correction factor for the adsorbed layer of thickness  $t$  which exists within pores with radius greater than  $r_K + t$  [59].

For pores with a diameter  $< 2$  nm (classified as ‘micropores’ by IUPAC [57]), the pore size is on the order of several adsorbate molecular diameters. Here the continuum approximations of the Kelvin equation begin to break down, and a second description of pore filling is required. For this we will rely on theory concerning changes in the characteristic energy of condensation due to intermolecular interactions in the confined region of a micropore [60,61]. A simple expression of this theory is the Dubinin-Radushkevich equation (a specific case of the Dubinin-Astakhov equation):

$$V = V_0 \exp \left\{ - \left[ \frac{RT \ln(P_0 / P)}{\beta E_0} \right]^2 \right\} \quad (6-7)$$

Where  $E_0$  is a characteristic energy of adsorption,  $\beta$  is an affinity coefficient [62],  $V_0$  is the total volume of micropores, and  $V$  is the volume of these pores filled at a pressure  $P$ . A number of researchers have proposed relationships between  $E_0$  and the pore width  $w$  [63]. One of the simplest relations, which has been used in several cases to analyze Si-based porous low- $\kappa$  materials, is  $w = K/E_0$ , where  $K \approx 12\text{-}14$  nm-mol-kJ<sup>-1</sup> [32,34,64,65]. Although the DR equation was originally derived to describe adsorption

behavior in microporous carbons, which contain mainly slit-shaped pores, it was later shown that the pore sizes derived from DR agree well with a more complex theory developed by Dultsev to describe cylindrical pores [64,66]. The pore size distribution can be obtained by modeling pore filling is a sum of terms given by Eq. 6-7, where each term represents a population of pores with width  $w$ , contributing a volume of  $V_0$  to the total pore volume [56,67].

Calculation of the pore size distribution for the low- $\kappa$  (no FOTS) was carried out using the built-in software of the SOPRA EP-12 instrument. In the analysis, both the Kelvin equation (Eq. 6-6) and the Dubinin-Radushkevich equation (Eq. 6-7) were implemented, with the instrument automatically determining which to use based on the shape of the isotherm. In regions where the isotherm indicated filling of micropores (steep region in at low  $P/P_0$ ), the Dubinin-Radushkevich equation was used, and where the isotherm indicated mesopore filling (higher pressures up to  $P/P_0 = 0.9$ ), the Kelvin equation was used. The pore size distribution obtained through this method is shown in Fig. 6-9 (solid line). As this is somewhat of a ‘black box’ calculation, checks were performed by analyzing the isotherms manually to extract the pore size distribution using either the Kelvin or Dubinin-Radushkevich equations only, shown in Fig. 6-9 as dashed lines. Both the automated SOPRA analysis and the Dubinin-Radushkevich equations result in a bimodal pore size distribution, centered at  $\sim 0.8$  nm and  $\sim 2$  nm, while the Kelvin equation predicts only one pore size mode at  $\sim 1.7$  nm. The population of pores at 1.7 - 2 nm is at the borderline where both the Kelvin and Dubinin-Radushkevich equations are applicable, so agreement in that size range would be expected.

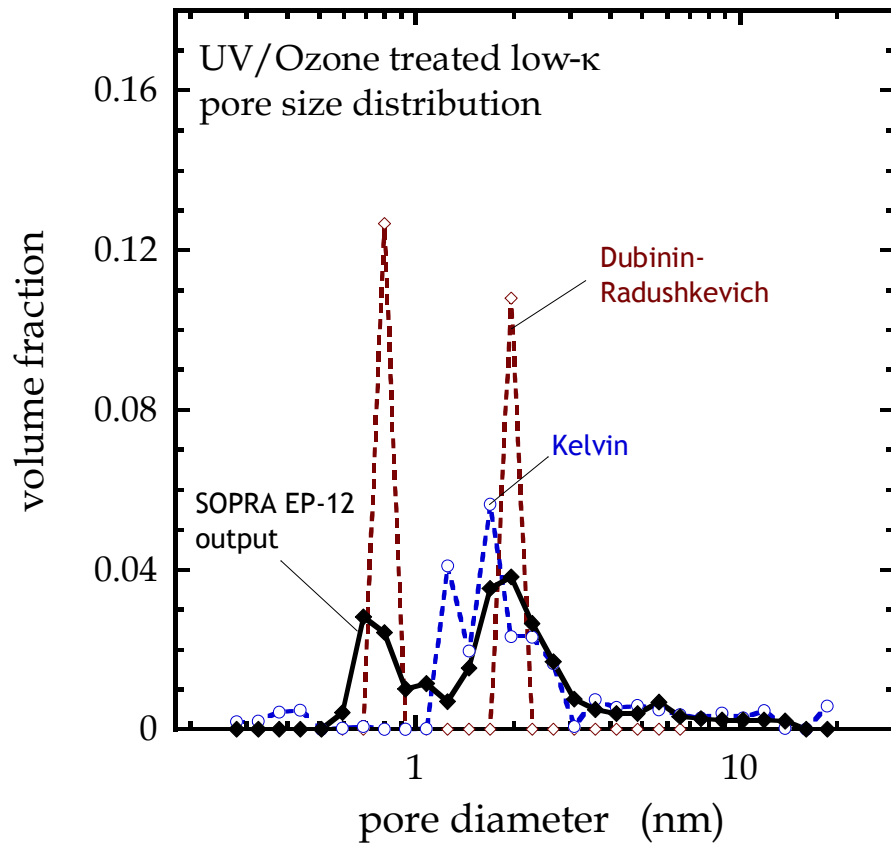


**Figure 6-9:** Pore size distribution for UV/Ozone treated low- $\kappa$ , obtained three ways: from the SOPRA EP-12 automatic calculation routine, manual calculations using the Kelvin equation (Eq. 6-6), and manual calculations using the Dubinin-Radushkevich equation (Eq. 6-7).

Likewise, the region in which no pores are detected in the Kelvin analysis ( $< 1$  nm) is well below the limit of applicability for that method. However, as expected, quantitative agreement between the Kelvin and SOPRA derived pore size distributions is observed for pores  $>2$  nm.

## 6.6. Conclusions

The infiltration of organic film precursors into a porous low- $\kappa$  material was investigated, focusing first on a study of the infiltration the fluorinated molecule FOTS as a model system, using SE, EP, and XPS, and second on comparisons between different types of organic molecules, using mainly SE. In the first section, it was shown that SE is a viable method to measure infiltration, though there may be a systematic underestimation of the FOTS volume fraction in low- $\kappa$ , most likely due to error in the assumed refractive index of FOTS. EP confirmed the infiltration of FOTS, providing a more direct measurement of the FOTS volume fraction after infiltration. EP indicated significant changes in the pore structure upon FOTS infiltration, including changes in the smallest ( $\sim 8$  Å diameter) pores. Combining these with XPS analysis of the fluorine concentration in the near surface region, it can be concluded that the process of FOTS film formation on the inner pore walls is a reaction-rate limited process, and that diffusion of FOTS through the low- $\kappa$  film is much faster than the reaction which causes FOTS molecules to attach to the pore walls.

Investigation using other molecules showed that the size of the organic molecule was the primary factor in determining the degree of infiltration. Pre-

treatment with an air plasma also reduces infiltration of larger molecules, but pre-baking to remove water, or use of a liquid phase deposition process (vs. vapor phase) does not. For modifying the inner pore surfaces, organic molecules with characteristic sizes of  $< 1$  nm are desirable. On the other hand, if the goal is to modify only the outer surface of the low- $\kappa$ , water-soluble polymers are a viable option.



## 6.7. References

1. International Technology Roadmap for Semiconductors, <http://www.itrs.net>, 2009.
2. K. Maex, M. R. Baklanov, D. Shamiryan, F. Iacopi, S. H. Brongersma, and Z. S. Yanovitskaya, *J. Appl. Phys.* **93**, 8793 (2003).
3. R. J. O. M. Hoofman, G. J. A. M. Verheijden, J. Michelon, F. Iacopi, Y. Travaly, M. R. Baklanov, Zs. Tőkei, and G. P. Beyer, *Microelectron. Eng.* **80**, 337 (2005).
4. R.L. Puurunen, *J. Appl. Phys.* **97**, 121301-1-52 (2005), and references therein.
5. W. Besling, A. Satta, J. Schuhmacher, T. Abell, V. Sutcliffe, A.-M. Hoyas, G. Beyer, D. Gravesteijn, and K. Maex, International Interconnect Technology Conference June 6–8 2002, IEEE 2002, pp. 288–291.
6. G. Beyer, A. Satta, J. Schuhmacher, K. Maex, W. Besling, O. Kilpela, H. Sprey, G. Tempel, *Microelectron. Eng.* **64**, 233 (2002).
7. A. Furuya, N. Ohtsuka, K. Misawa, M. Shimada, S. Ogawa, *J. Appl. Phys.* **98**, 094902-1-6 (2005).
8. Y. Travaly, J. Schuhmacher, M. R. Baklanov, S. Giangrandi, O. Richard, B. Brijs, M. Van Hove, K. Maex, T. Abell, K. R. F. Somers, M. F. A. Hendrickx, L. G. Vanquickenborne, A. Ceulemans, and A. M. Jonas, *J. Appl. Phys.* **98**, 083515 (2005).
9. N. Possémé, T. Chevolleau, T. David, M. Darnon, J. P. Barnes, O. Louveau, C. Licitra, D. Jalabert, H. Feldis, M. Fayolle, O. Joubert, *Microelectron. Eng.* **85**, 1842 (2008).
10. A. Martin Hoyas, J. Schuhmacher, D. Shamiryan, J. Waeterloos, W. Besling, J. P. Celis, and K. Maex, *J. Appl. Phys.* **94**, 381 (2004).
11. O. Van der Straten, Y. Zhu, J. Rullan, K. Topol, K. Dunn, A. Kaloyeros, *Mater. Res. Soc. Symp. Proc.* **812**, F3.13.1 (2004).
12. J. Liu, J. Bao, M. Scharnberg, W. C. Kim, P. S. Ho, and R. Laxman, *J. Vac. Sci. Technol. A* **23**, 1107 (2005).
13. S. M. Rossnagel and T. S. Kuan, *J. Vac. Sci. Technol. B* **22**, 240 (2004).
14. Y. Travaly, J. Schuhmacher, A. M. Hoyas, M. Van Hove, K. Maex, T. Abell, V. Sutcliffe, and A. M. Jonas, *J. Appl. Phys.* **97**, 084316 (2005).

15. C. Jezewski, C. J. Wiegand, D. Ye, A. Mallikarjunan, D. Liu, C. Jin, W. A. Lanford, G.-C. Wang, J. J. Senkevich, and T.-M. Lu, *J. Electrochem. Soc.* **151**, F157 (2004).
16. S. Juneja, G. A. Ten Eyck, H. Bakhru, and T.-M. Lu, *J. Vac. Sci. Technol. B* **23**, 2232-2235 (2005).
17. J. S. Juneja, P.-I Wang, T. Karabacak, and T.-M. Lu, *Thin Solid Films* **504**, 239 (2006).
18. P. de Rouffignac, Z. Li, and R. G. Gordon, *Electrochem. Solid-State Lett.* **7**, G306 (2004).
19. J. W. Elam, C. A. Wilson, M. Schuisky, Z. A. Sechrist, and S. M. George, *J. Vac. Sci. Technol. B* **21**, 1099 (2003).
20. K. Yonekura, S. Sakamori, K. Goto, M. Matsuura, N. Fujiwara, M. Yoneda, *J. Vac. Sci. Technol. B* **22**, 548 (2004).
21. E. Kondoh, T. Asano, A. Nakashima, M. Komatu, *J. Vac. Sci. Technol. B* **18**, 1276 (2000).
22. Y. Li, Z. Tökei, J. Van Aelst, L. Carbonell, M. R. Baklanov, O. Richard, H. Bender, G. Groeseneken, and K. Maex, *Semicond. Sci. Technol.* **22**, 320 (2007).
23. T. Tatsumi, *App. Surf. Sci.* **253**, 6716 (2007).
24. T. C. Chang, P. T. Liu, Y. S. Mor, T. M. Tsai, C. W. Chen, Y. J. Mei, F. M. Pan, W. F. Wu, and S. M. Sze, *J. Vac. Sci. Technol. B* **20**, 1561 (2002).
25. Y. S. Mor, T. C. Chang, P. T. Liu, T. M. Tsai, C. W. Chen, S. T. Yan, C. J. Chu, W. F. Wu, F. M. Pan, W. Lur, and S. M. Sze, *J. Vac. Sci. Technol. B* **20**, 1334 (2002).
26. S. Rogojevic, A. Jain, W. N. Gill, and J. Plawsky, *Electrochem. Sol. St. Lett.* **5**, F22 (2002).
27. B. P. Gorman, R. A. Orozco-Teran, Z. Zhang, P. D. Matz, D. W. Mueller, and R. F. Reidy, *J. Vac. Sci. Technol B* **22**, 1210 (2004).
28. B. Xie and A. J. Muscat, *Microelectron. Eng.* **76**, 52 (2004).
29. J. Liu, W. Kim, J. Bao, H. Shi, W. Baek, and P. S. Ho, *J. Vac. Sci. Technol. B* **25**, 906 (2007).

30. H. G. Tompkins and W. A. McGahan, *Spectroscopic Ellipsometry and Reflectometry: A User's Guide* (John Wiley & Sons, New York, 1999).
31. M. R. Baklanov, K. P. Mogilnikov, V. G. Polovinkin, and F. N. Dultsev, J. Vac. Sci. Technol. B **18**, 1385 (2000).
32. M. R. Baklanov and K. P. Mogilnikov, Microelectron. Eng. **64**, 335 (2002)
33. H. L. Xin, P. Ercius, K. J. Hughes, J. R. Engstrom, and D. A. Muller, Appl. Phys. Lett. **96**, 223108 (2010).
34. A. Grill, V. Patel, K. P. Robdell, E. Huang, M. R. Baklanov, K. P. Mogilnikov, M. Toney, and H.-C. Kim, J. Appl. Phys. **94**, 3427 (2003).
35. C. M. Whelan, Q. T. Le, F. Cecchet, A. Satta, J.-J. Pireaux, P. Rudolf, and K. Maex, Electrochem. Sol. St. Lett. **7**, F8 (2004).
36. P. Revol, D. Perret, F. Bertin, F. Fusalba, V. Rouessac, A. Chabli, G. Passemard, A. Ayral, J. Porous Mater. **12**, 113 (2005).
37. K. H. Lee, J.-H. Yim, and M. R. Baklanov, Microporous Mesoporous Mater. **94**, 113 (2006).
38. M. R. Baklanov, M. Green, and K. Maex, *Dielectric Films for Advanced Microelectronics* (John Wiley and Sons Ltd., Chichester, England, 2007).
39. C. Guedj, G. Imbert, E. Martinez, C. Licitra, N. Rochat, and V. Arnal, Microelectron. Reliab. **47**, 764 (2007).
40. V. Jousseau, G. Rolland, D. Babonneau, and J.-P. Simon, Appl. Surf. Sci. **254**, 473 (2007).
41. P. Marsik, P. Verdonck, D. Schneider, D. De Roest, S. Kaneko, and M. R. Baklanov, Phys. Stat. Sol. C **5**, 1253 (2008).
42. H. G. Tompkins and E. A. Irene, *Handbook of Ellipsometry* (William Andrew Publishing, Norwich, NY, 2005).
43. G. E. Jellison, Thin Solid Films **313-314**, 33 (1998).
44. J. A. Woollam Co., Inc. Standard short course on data analysis for spectroscopic ellipsometry, Cornell University, July 30 - August 2, 2007.
45. J. C. Maxwell Garnett, Phil. Trans. R. Soc. Lond. A **203**, 385 (1904).
46. D. E. Aspnes, Am. J. Phys. **50**, 704 (1982).

47. G. A. Niklasson, C. G. Granqvist, O. Hunderi, Appl. Opt. **20**, 26 (1981).
48. A. R. Hawkins and H. Schmidt, *Handbook of Optofluidics*, (CRC Press, Taylor and Francis Group, Boca Raton, FL, 2010).
49. M. K. Yang, R. H. French, and E. W. Tokarsky, J. Micro/Nanolithogr., MEMS, MOEMS **7**, 033010 (2008).
50. D. R. Defibaugh, E. Carillo-Nava, J. J. Hurly, M. R. Moldover, J. W. Schmidt, and L. A. Weber, J. Chem. Eng. Data **42**, 488 (1997).
51. *CRC handbook of Chemistry and Physics, 91st Ed.*, D. R. Lide, Ed. (CRC Press, Boca Raton, 2011).
52. M. Fujii, S. Sugisawa, K. Fukada, T. Kato, T. Shirakawa, and T. Seimiya, Langmuir **10**, 984 (1994).
53. D. A. Styrkas, J. L. Keddie, J. R. Lu, T. J. Su, and P. A. Zhdan, J. Appl. Phys. **85**, 868 (1999).
54. J. Xiao and J. Wei, Chem. Eng. Sci. **47**, 1123 (1992).
55. S. Sommer, T. Melin, J. L. Falconer, and R. D. Noble, J. Membrane Sci. **224**, 51 (2003).
56. S. J. Gregg and K. S. W. Sing, *Adsorption, Surface Area and Porosity, 2nd Ed.* (Academic Press, New York, 1982).
57. K. S. W. Sing, D. H. Everett, R. A. W. Haul, L. Moscou, R. W. Pierotti, J. Rouquérol, and T. Siemieniewska, Pure Appl. Chem. **57**, 603 (1985).
58. S. Brunauer, P. H. Emmett, and E. Teller, J. Am. Chem. Soc. **60**, 309 (1938).
59. E. P. Barrett, L. G. Joyner, and P. P. Halenda, J. Am. Chem. Soc. **73**, 373 (1951).
60. M. M. Dubinin, J. Colloid Interface Sci. **23**, 487 (1967).
61. H. F. Stoeckli, Carbon **28**, 1 (1990).
62. G. O. Wood, Carbon **39**, 343 (2001).
63. P. A. Gauden, A. P. Terzyk, G. Rychlicki, P. Kowalczyk, M. S. Cwiernia, J. K. Garbacz, J. Colloid Interface Sci. **273**, 39 (2004).
64. F. N. Dultsev, Thin Solid Films **458**, 137 (2004).

65. R. Saxena, O. Rodriguez, W. Cho, W. N. Gill, J. L. Plawsky, M. R. Baklanov, K. P. Mogilnikov, *J. Non-cryst. Solids* **349**, 189 (2004).
66. F. N. Dultsev, *J. Struct. Chem.* **47**, 674 (2006).
67. H. F. Stoeckli, *J. Colloid Interf. Sci.* **59**, 184 (1977), and references therein.

## **7. *In situ* XPS study of the initial stages of cobalt CVD on tantalum using dicobalt hexacarbonyl tert-butylacetylene (CCTBA)**

### **7.1 Overview**

Chemical vapor deposition (CVD) of cobalt films using CCTBA on a tantalum substrate was studied using primarily *in situ* XPS. Deposition was conducted under UHV conditions using a collimated molecular beam. Angle resolved XPS measurements indicate that the early stages of Co CVD involve the formation of a mixed Co/Ta interfacial region. Carbon was found to be incorporated in this region in a carbide-type binding environment. After the formation of the intermixed layer, a second phase of growth initiated which is characterized by the formation of a mixed Co/C film with very high carbon content (~ 77 atomic %). Although this film was oxygen free as grown, it was found to be susceptible to oxidation upon exposure to air. These results represent the initial part of an ongoing study.

### **7.2. Introduction**

In this chapter, a series of experiments are described which were conducted to better understand the initial stages of cobalt film deposition via CVD on tantalum. As discussed in Sec. 1.3, after the deposition of a Ta/TaN<sub>x</sub> barrier layer on a dielectric material (low- $\kappa$ , for example), an additional thin film is often deposited to facilitate the subsequent plating of copper. Cobalt, deposited via CVD (chemical vapor deposition),

is a material that can be used for this application [1]. As with the diffusion barrier layer, the initial stages of film growth can have a large effect on the structure and properties of the deposited film, in part because it is extremely thin. In addition, as we will see, there are additional complications involved in the Co/Ta system due to the existence of stable mixed phases formed by the two elements. The cobalt precursor used here is dicobalt hexacarbonyl tert-butylacetylene (CCTBA). Although CCTBA is commercially available, there have been a limited number of publications regarding its use [2-5], with most of these examples addressing the CVD on Co films on Si to form cobalt silicides.

### 7.3 Experimental procedures

Substrates were generated by depositing 500 Å-800 Å Ta via sputtering on cleaned SiO<sub>2</sub>/Si(100). In air transfer between sputter deposition and introduction into the UHV chamber, a native oxide formed on the Ta surface. Prior to deposition, substrates were annealed at ~ 350°C *in situ* for 1 hour, which reduced the near surface oxygen concentration (see results shown in Fig. 7-2).

Deposition was carried out in the Olin Hall 312 UHV system described in Sec. 2.5. A hyperthermal CCTBA/He molecular beam was generated by passing ultra high purity He (35 standard cm<sup>3</sup> min<sup>-1</sup>) through a stainless steel vessel containing liquid CCTBA held at 40 °C, and expanding the resulting mixture through a heated 150 µm aperture, or nozzle, into UHV. A conical skimmer and aperture downstream from the nozzle defined the beam into a 12 x 12 mm<sup>2</sup> cross section on the sample surface.

Further details concerning the formation of the molecular beam are given in Sec. 2.5. The direct CCTBA beam, as well as the background components present during growth, were analyzed using a quadrupole mass spectrometer (QMS) mounted perpendicular to the molecular beam (Hiden 3F/EPIC QMS, Hiden Analytical, Warrington, UK). The ionization region of the QMS was aligned with the molecular beam axis, allowing the direct beam to be analyzed. During deposition, the sample surface was perpendicular to the beam axis, and turned towards the XPS hardware for post deposition analysis (deposition and analysis setup shown in Fig. 7-1). During deposition, the sample was held at 160 °C, and was then cooled to room temperature prior to in situ XPS analysis. Post deposition XPS and ARXPS focused on four regions: Ta(4d), Co(2p), O(1s), and C(1s). Detailed XPS spectra were collected at a fixed photoelectron takeoff angle of 38.5°, with angular acceptance of  $\pm 7^\circ$ , and a spot size on the sample of  $\sim 600 \mu\text{m}$ . ARXPS was conducted by collecting XP spectra at 6 takeoff angles from 0°-60°, at even intervals of  $\cos \theta$ . Here lens settings were used which produced a spot size of  $\sim 2.5 \text{ mm}$ , with angular acceptance of  $\pm 2^\circ$ . Where appropriate, atomic ratios were calculated based on previously published empirical sensitivity factors [6].

In the antechamber, the beam passes through an annulus, which can be cooled using liquid nitrogen ( $\text{LN}_2$ ). This annulus acts as a pump for the effusive components of the beam. When it is used, the amount of background CCTBA in the main chamber, and therefore the deposition of Co outside of the molecular beam spot, is reduced. The effect of cooling the annulus with  $\text{LN}_2$  is demonstrated in Fig. 7-4.



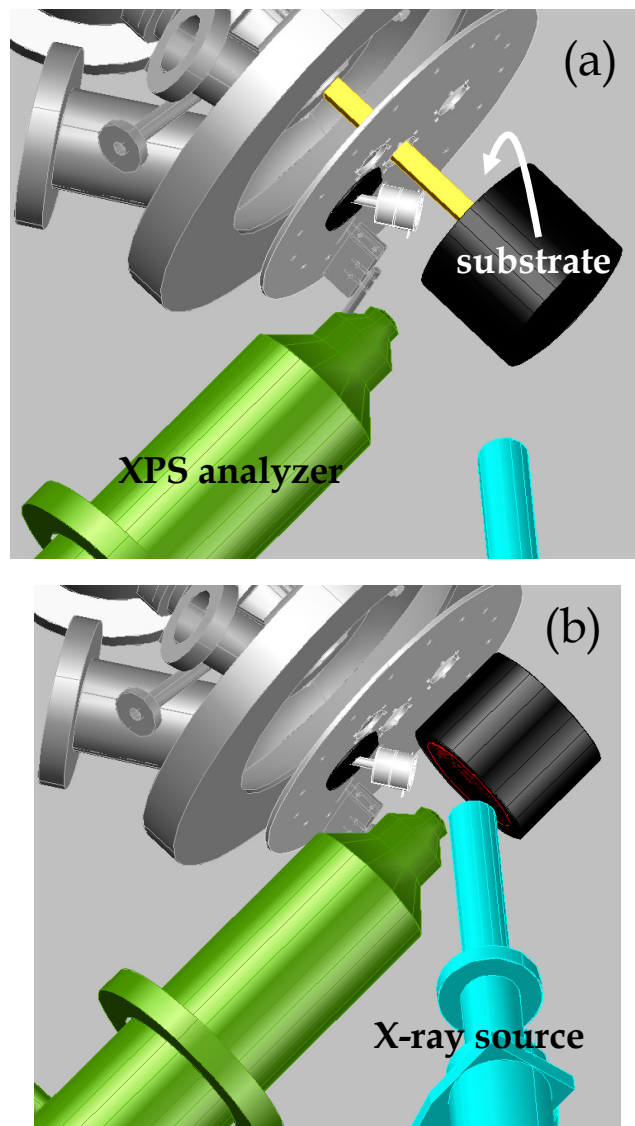


**Figure 7-1:** Schematic of the setup within the UHV chamber used for experiments. Sample in **(a)** deposition position and **(b)** XPS analysis position (shown at  $0^\circ$  photoelectron takeoff angle).

The results presented subsequently include analysis of several beam exposure times. Here each exposure time represents a distinct film. To increase experimental throughput and reduce sample to sample variations, terraces were formed, allowing the analysis of generally three different exposure times in a single deposition “run”. This was achieved by translating the sample perpendicular to the beam axis at set intervals during beam exposure. A schematic of this, along with XPS analysis of the terrace structure, is shown in Fig. 7-6. Exposure times of 5 s, 15 s, 30 s, 1 min, 2 min, 4 min, 8 min, 15 min, 30 min and 3 hours were studied. For most films (5 s, 15 s, 30 s, 8 min, 15 min, and 30 min exposures), the annulus in the antechamber was cooled using liquid nitrogen (LN<sub>2</sub>).

## **7.4 Results and discussion**

### **7.4.1 Characterization of the tantalum substrate**

The XP spectrum of the pre-annealed Ta substrate sample, shown in Fig. 7-2(a), reveals the presence of two Ta(4f) doublets. The doublet with higher binding energy can be attributed to oxidized Ta [7]. This oxide layer consists of 79 atomic % O, suggesting it is primarily Ta<sub>2</sub>O<sub>5</sub> (71 atomic % O). Ta metal signal was also observed, consistent with a thin oxide film on at the top surface of the Ta metal [7].

After annealing for 1 hour at ~ 350 °C, the peaks corresponding to Ta<sub>2</sub>O<sub>5</sub> in the Ta(4f) spectrum are not detectable. A significant amount of O still present, however as shown in Fig. 7-2(b) it has been reduced by a factor of ~4.

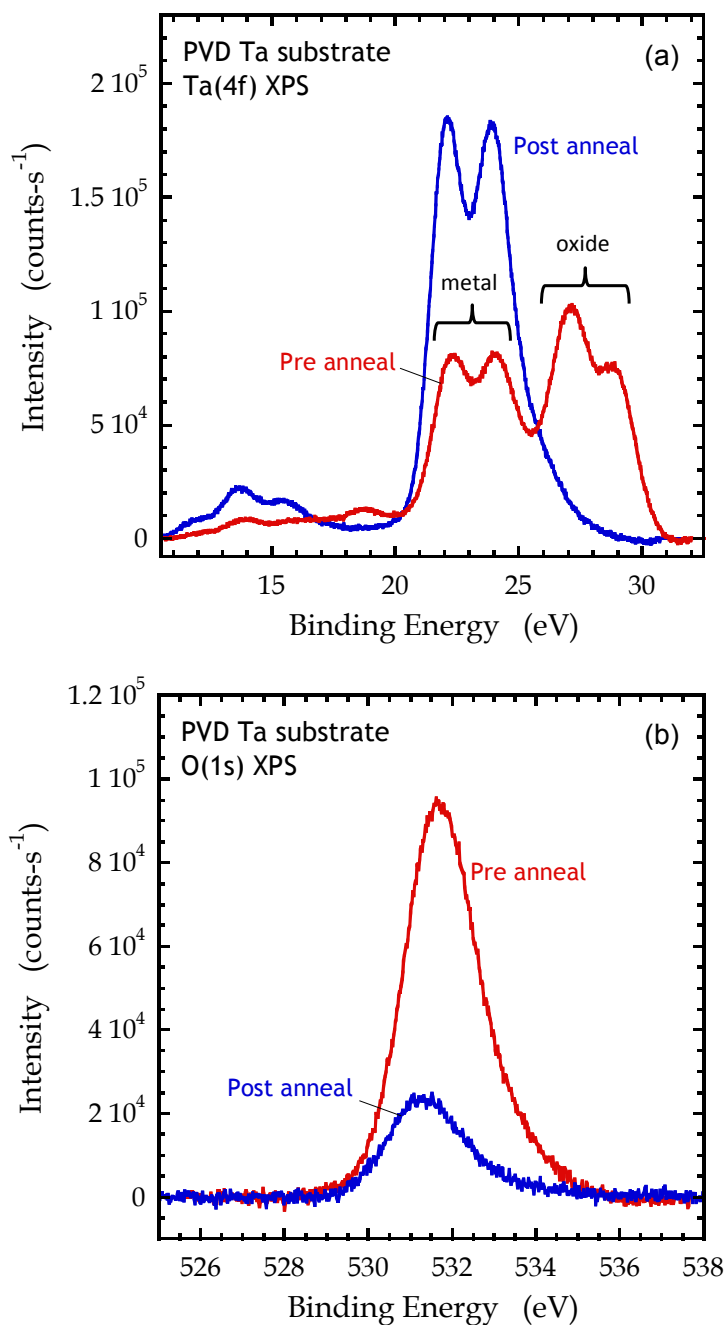


**Figure 7-2:** XP Spectra of sputtered Ta surface before and after anneal treatment, in the (a) Ta(4f) and (b) O(1s) regions. In (a), the contributions of Ta(4f) doublets from the native tantalum oxide surface layer and underlying Ta metal are labeled.

The post-anneal substrate can be termed TaO<sub>x</sub>, with  $x \sim 0.35$  to  $0.40$ ). We hypothesize that the reduction in the near surface oxygen concentration is due to the diffusion of O from the starting Ta<sub>2</sub>O<sub>5</sub> film deeper into the Ta metal layer during the anneal step, leading to the formation of a thicker TaO<sub>x</sub> layer, with consequently lower O content. Oxygen can be an interstitial solute in tantalum and, based on measured activation energies for diffusion of O in Ta [8,9], diffusivity in Ta is significant in the length scales relevant here at 350 °C (O atoms can move, on average, several microns per hr), therefore this hypothesis seems to be a reasonable explanation for the reduction in the near surface oxygen content.

#### **7.4.2 Characterization of the CCTBA beam and formation of terraces**

Mass spectrometry experiments were performed to confirm formation of a CCTBA beam, and to characterize the effect of the LN<sub>2</sub> cooled annulus. In Fig. 7-3, a mass spectrum of the direct CCTBA beam is shown, in a range of low ( $m/z = 0$  to  $70$ ) and high ( $m/z = 70$  to  $300$ ) mass. Note that the  $m/z$  of the CCTBA parent ( $368$ ) is not accessible with the QMS used here, which has a range of  $0$  to  $300$ . However, earlier results have shown that the parent peak has a low intensity relative to the primary decomposition products [10]. As can be seen in Fig. 7-3(b), one set decomposition products include a series of  $m/z = 368 - 28x$ , where  $x = 3-6$ . These peaks represent CCTBA ( $m/z = 368$ ) with an increasing degree of CO ligand loss ( $m/z = 28$ ). As expected, a large CO peak at  $m/z = 28$  is also observed. An additional decomposition product has  $m/z = 118$ , which can be assigned to Co<sub>2</sub>.

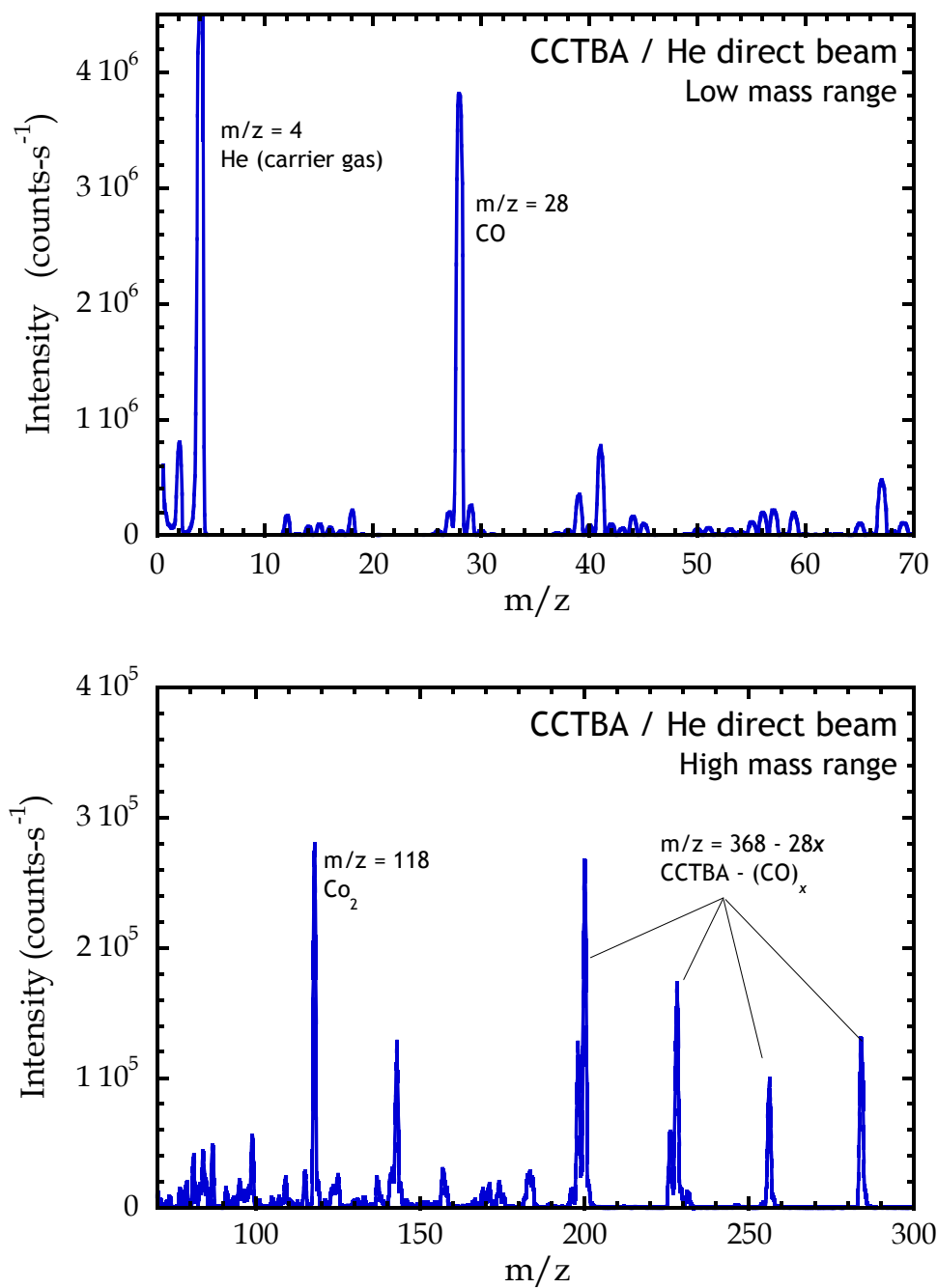


**Figure 7-3:** Mass spectra of the direct beam of CCTBA in He. Note that the CCTBA parent (m/z) was outside the mass limit of the QMS used.

It has not been determined whether these decomposition products exist in the beam, or if they are created in the ionization region of the mass spectrometer.

The modulation of the CCTBA beam by the shutter in the antechamber was confirmed by tracking the intensity of a the CCTBA fragment at 118 amu while opening, then closing the shutter (Fig. 7-4). Here the shutter was opened at  $\sim 20$  s after the start of data collection, and closed  $\sim 30$  s later. This can clearly be seen in the sharp increase, plateau, and decrease in the  $m/z = 118$  signal. Two conclusions can be made based on this experiment. First, the molecular beam is effectively modulated with the shutter. Second, the use of the  $\text{LN}_2$  cooled annulus has the effect of decreasing the background of CCTBA, both with the beam shutter open and closed.

In order to roughly align the position of the beam spot with respect to the sample, and to confirm that the CCTBA beam is well collimated, an annealed Ta substrate was exposed to the CCTBA beam for 3 hours, which produced a visible deposition spot, as shown in Fig. 7-5(a). Finer alignment was conducted using XPS measurements (see below). XPS survey scans taken before and after 3 hours of CCTBA exposure, shown in Fig. 7-5(b), show a full transition of the surface; only Ta, C, and O are detected in the annealed substrate, and only Co and C are detected after exposure.

As described above, terraced films were produced by translating the sample holder perpendicular to the beam axis during CCTBA exposure. A schematic of the resulting terrace structure is shown in Fig. 7-6 (right). The exact positions of the terraces, required to accurately analyze each individually, were determined by collecting XP spectra in the Co(2p) region as a function of  $z$  (vertical) position.

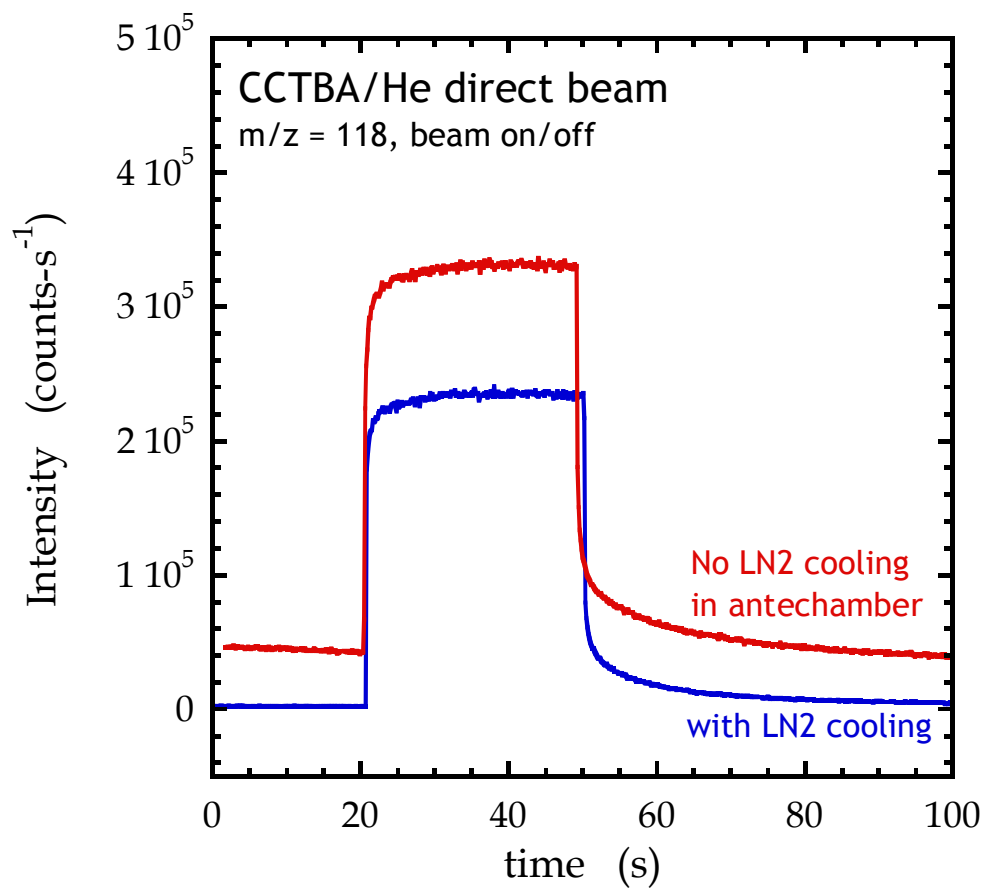


**Figure 7-4:** QMS intensity at  $m/z = 118$  (a prominent fragment of CCTBA) as a function of time, for a case where the a LN2 cooled pump was used in the antechamber, and a case where it was not. In this experiment the beam shutter was opened from  $\sim 20$  s to 50 s.

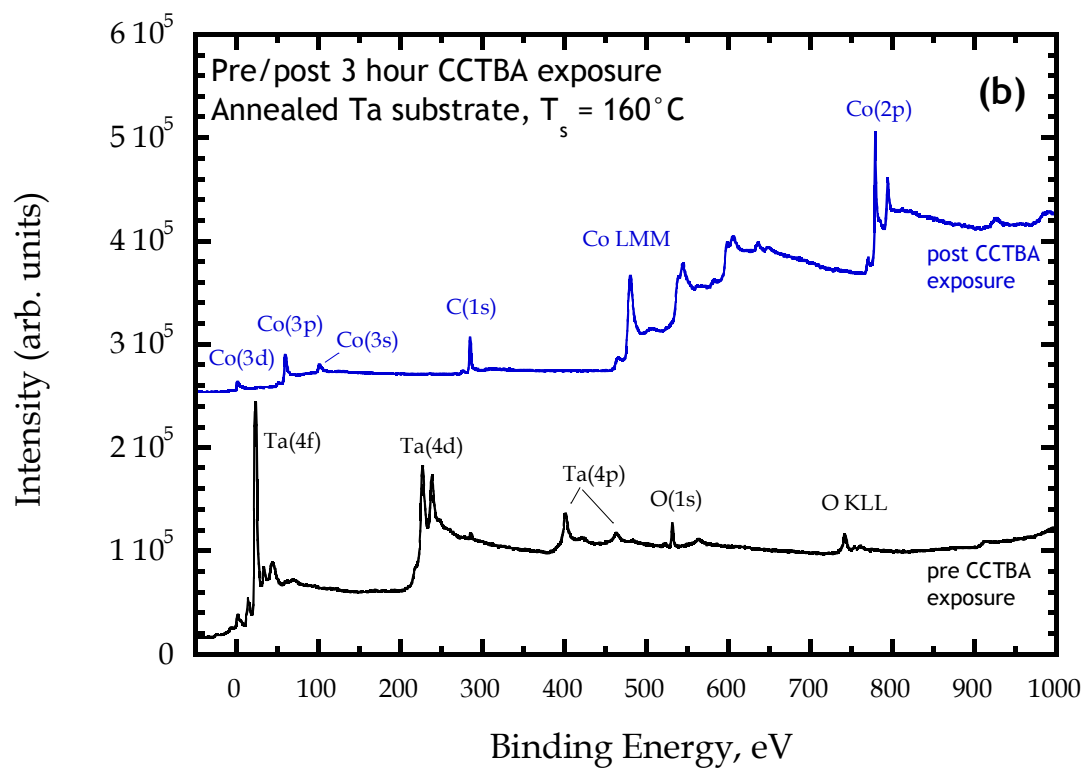
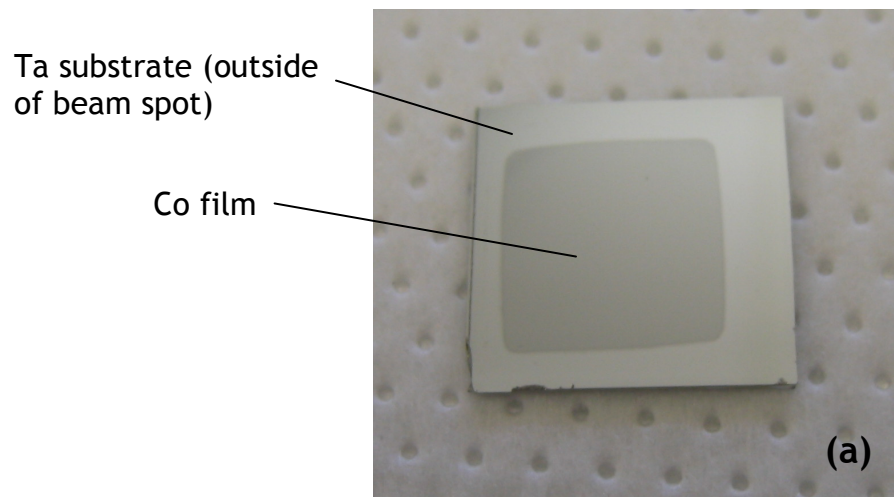


**Figure 7-5:** (a) Photograph of the visible beam spot observed on Ta substrate after 3 hour exposure to CCTBA molecular beam. (b) XPS survey scans taken before (bottom) and after (top) 3 hours of CCTBA exposure.



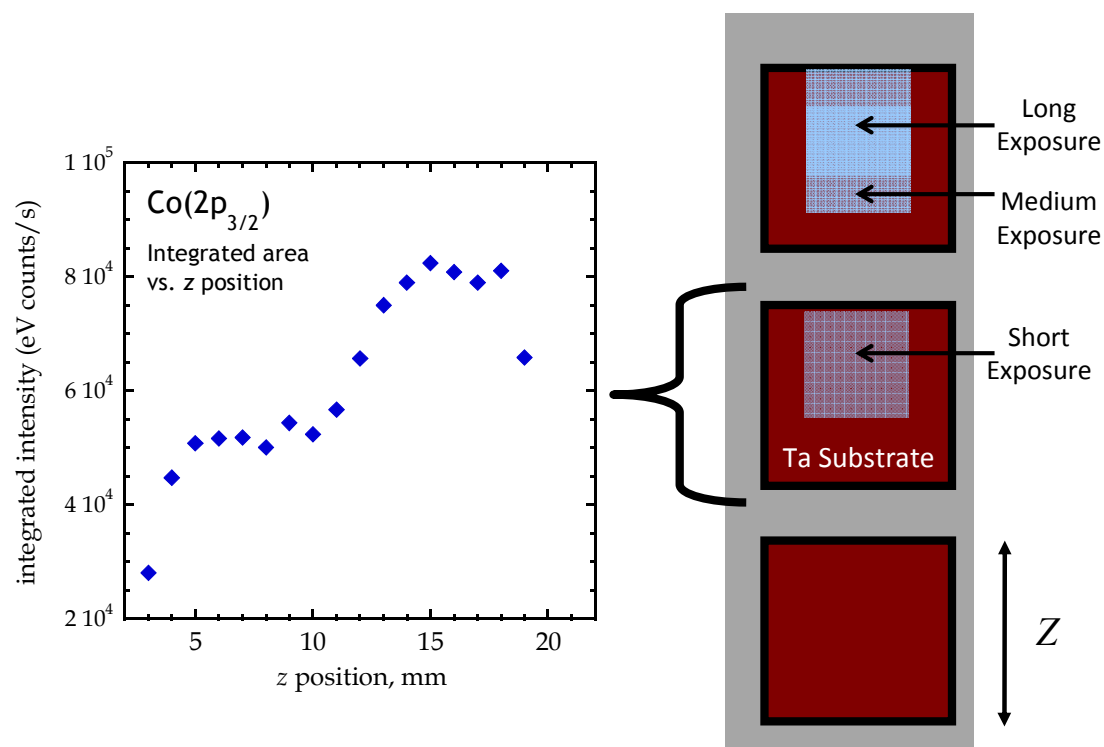


**Figure 7-6:** (Right) Schematic of beam spot terraces on substrates. (Left) XPS Co(2p<sub>3/2</sub>) integrated intensity as a function of vertical position on middle sample. Edges of the beam spot are indicated by plateaus in the Co(2p<sub>3/2</sub>) intensity.

Fig. 7-6 (left) presents the result from this experiment. Here, plateaus in the integrated Co(2p<sub>3/2</sub>) intensity plot correspond to terraces. In the particular experiment shown in Fig. 7-6, the LN<sub>2</sub> cooled annulus was not used, and as such a relatively high background deposition of Co was observed, evidenced by the high Co(2p<sub>3/2</sub>) intensity measured outside the beam spot. When LN<sub>2</sub> cooling was used, background deposition was still observed, though it was significantly reduced. The ratio of beam to background deposition when LN<sub>2</sub> was used was calculated to be ~28.5 using XPS.

#### **7.4.4. Evolution of Co and Ta**

Fig. 7-7 displays typical XP spectra from the Co(2p) and Ta(4d) regions for the bare substrate and after CCTBA exposure. For all CCTBA beam exposure times, spectra indicated the presence of only a single chemical state for both elements. Furthermore, from 5 s to 900 s of CCTBA beam exposure, a finite signal intensity was measured for both elements. In Fig. 7-8, we display the integrated area of the Co(2p<sub>3/2</sub>) and Ta(4d<sub>5/2</sub>) peaks as a function of CCTBA beam exposure. As expected, the Co signal increases, then saturates at high exposure time. Likewise, the Ta signal decreases, eventually reaching at 1800 s CCTBA beam exposure. These integrated intensities demonstrate that Co is being deposited on the Ta substrate, and that for high exposure times (> 900 s) a Co film is formed which is thick enough to completely obscure the signal from the underlying Ta.

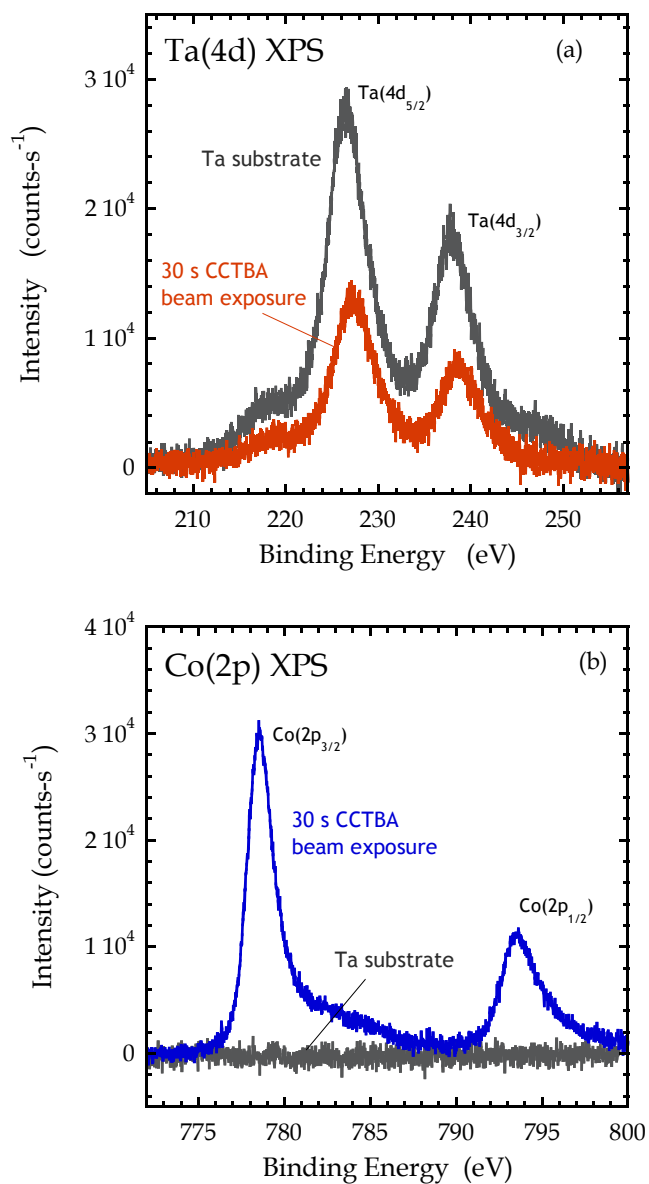


**Figure 7-7:** X-ray photoelectron spectra taken in the **(a)** Ta(4d) and **(b)** Co(2p) regions for the bare Ta substrate and after 30s of exposure to the CCTBA beam.

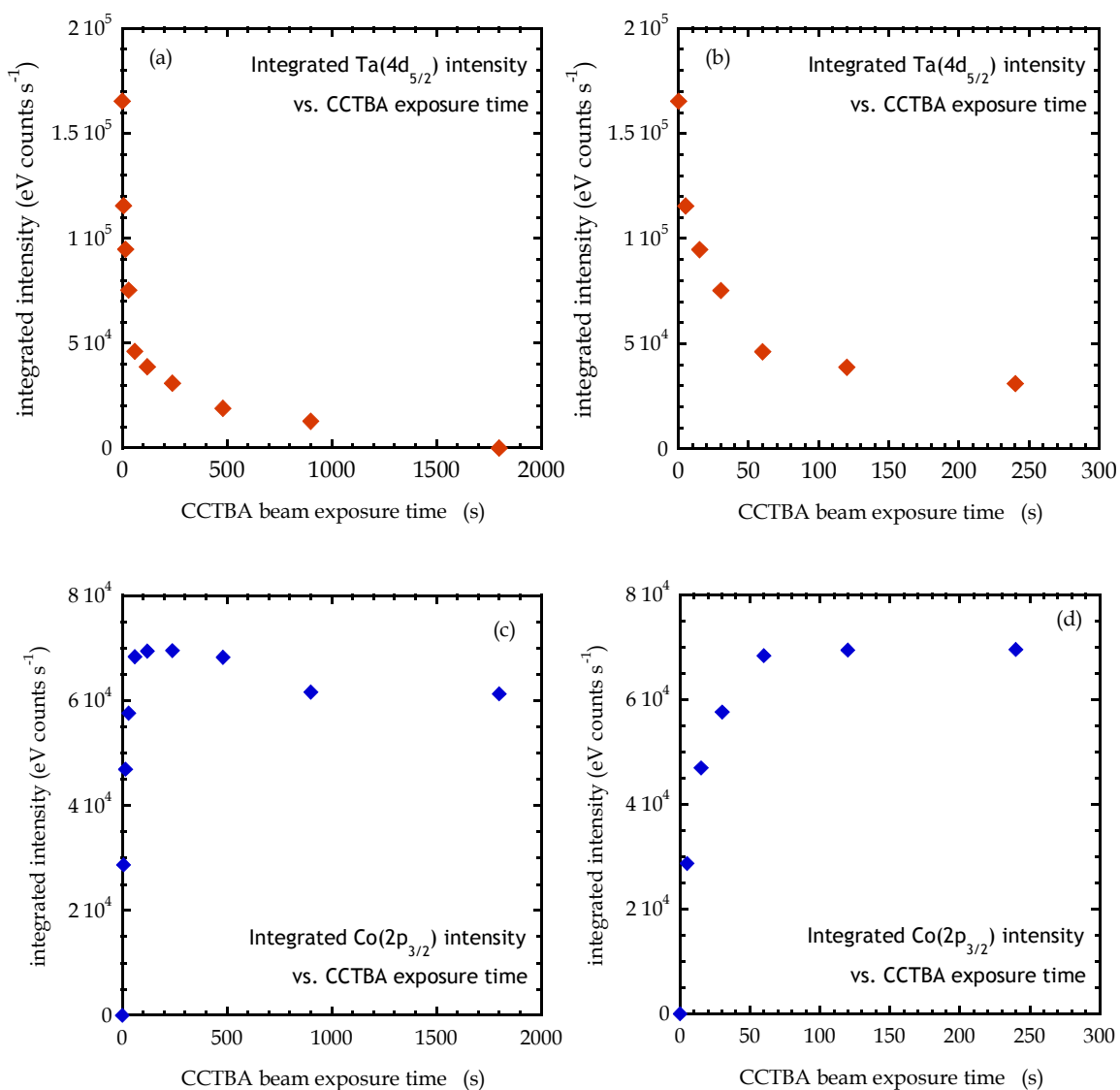


**Figure 7-8:** Integrated intensities of the **(a,b)** Ta(4d<sub>5/2</sub>) and **(c,d)** Co(2p<sub>3/2</sub>) peaks as a function of beam exposure time. Parts **(a)** and **(c)** show results from all beam exposure times, while **(b)** and **(d)** highlight the low exposure time regime.

Regarding the structure of the Co/Ta interface formed, one can consider three limiting cases: (i) a flat, essentially 2-d Co film on Ta, (ii) Co islands on Ta, (iii) an intermixed layer of Co and Ta. Angle-resolved XPS (ARXPS) can be used to determine if one of these cases is dominant. Due to geometric effects, cases (i) and (iii) are nearly indistinguishable in ARXPS in the case of thick ( $> \sim 5$  nm) Co islands; the use of a complementary method, AFM, to rule out the formation of thick islands is discussed below. The results of ARXPS measurements for three representative CCTBA exposures are shown in Fig. 7-9. The first CCTBA exposure is for the deposition which takes place outside of the beam spot during the 30 s CCTBA beam exposure. The reason for showing this data set is twofold: first, it represents the lowest CCTBA exposure for which we have data, and second it rules out the possibility that the finite size of the beam spot effects the ARXPS measurement. In addition to the measured data, two dotted lines are shown, representing the expected behavior for the formation of a thin film of Co on Ta, and another for the formation of an intermixed layer. In all cases, the ARXPS data indicate intermixing of Ta and Co. The bulk diffusion rate in metals is expected to be very low at the growth temperature ( $\sim 13\%$  of the absolute melting temperature of Ta); however grain boundary diffusion leading to an intermixed layer is possible, particularly if the grain boundaries are vertical. Furthermore, unlike the Cu-Ta system, a number of stable Co-Ta phases are stable at room temperature [11], which lends more credence to the formation of a mixed layer. After 900 s of deposition, the intermixed layer is covered and Ta is no longer observed.

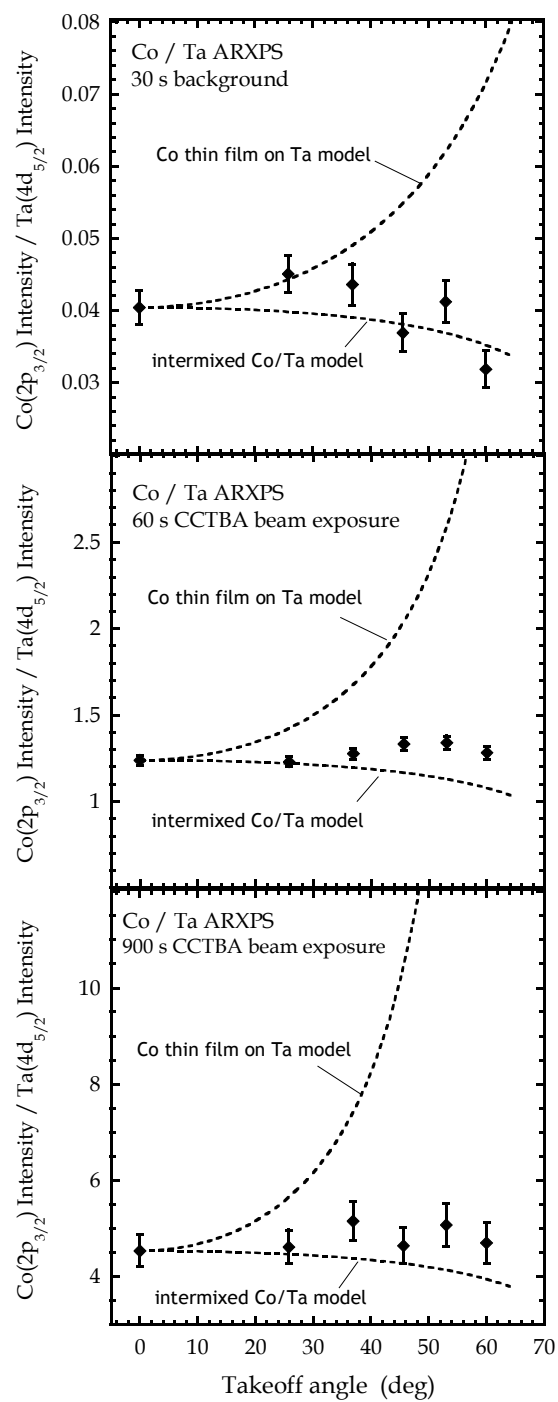


**Figure 7-9:** Angle-resolved XPS measurements (ratio of Co to Ta intensity) for three representative CCTBA exposures. Dotted lines represent the trends which would be observed in the case of a thin Co overlayer, and an intermixed layer of Co and Ta.

The measured binding energies of the Ta(4d<sub>5/2</sub>) and Co(2p<sub>3/2</sub>) core levels are shown in Fig. 7-10, both corrected and uncorrected for substrate charging effects using adventitious carbon present at 284.6 eV (corrections were in all cases <0.5 eV). The binding energy of the Co peak is relatively constant, and falls in the range reported for metallic Co (777.8-778.5 eV). The position of the Ta peak, however, increases with CCTBA beam exposure time, from a metallic-like binding energy for the bare substrate (measured 226.2 eV, reported metallic range 226.3-226.7 eV) to a range closer to an oxide at 900 s exposure (measured 228.8 eV, reported Ta<sub>2</sub>O<sub>5</sub> range 229.6-230.6 eV). Although the reason for this is not definitively known, it may be due to increases in the O:Ta ratio (shown in the Fig. 7-10 inset).

#### **7.4.5. Film Morphology**

In Fig. 7-11 we display atomic force micrographs of the bare substrate (after annealing in UHV) and after exposure to CCTBA beam for 60 s. Both surfaces are smooth, with rms roughness < 0.8 nm. No major 3-d features are observed in the post-CCTBA AFM. If thick Co islands were being formed, the surface would be ~62% covered with these islands based on Ta XPS (assuming total attenuation of the Ta signal in areas covered by Co). This result indicates that the best interpretation of the ARXPS data shown in Fig. 7-9 is intermixing at the Co/Ta interface.

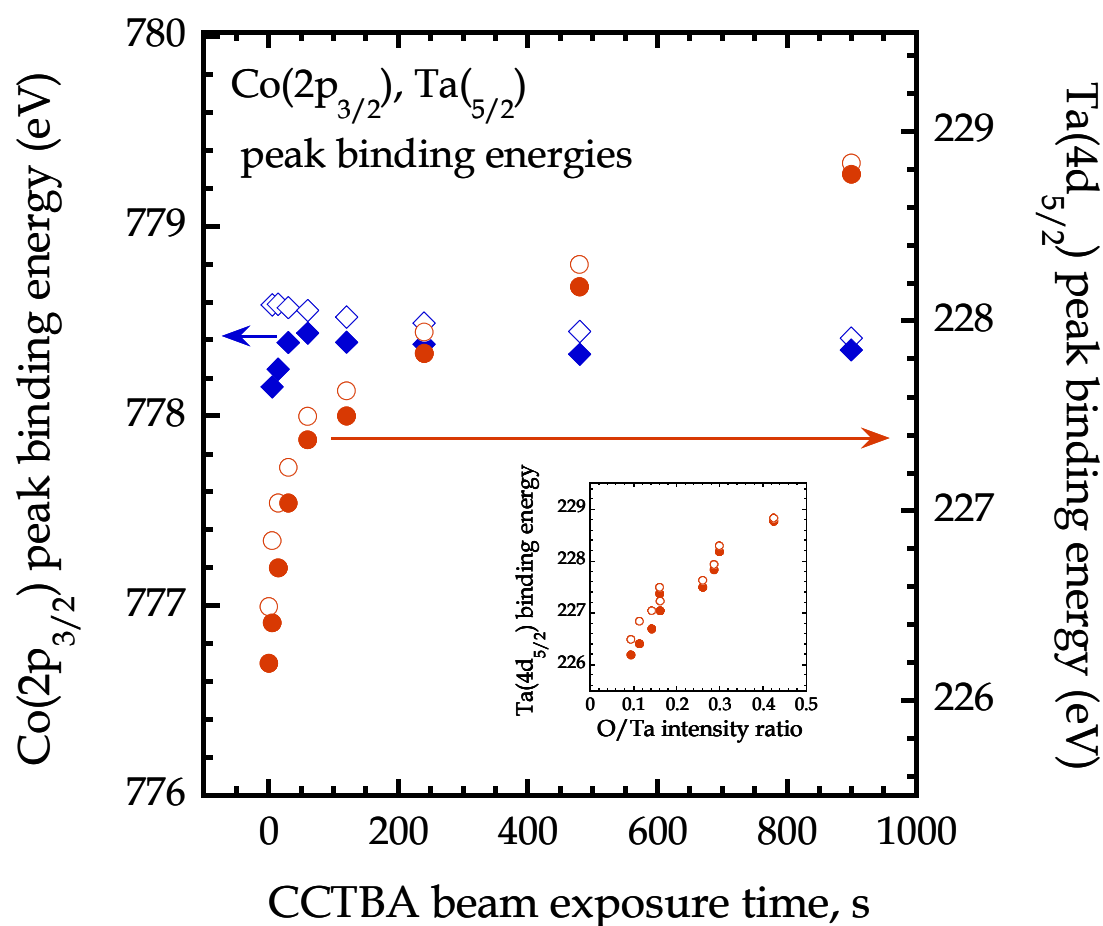


**Figure 7-10:** Co(2p<sub>3/2</sub>) and Ta(4d<sub>5/2</sub>) peak binding energies as a function of CCTBA beam exposure time. Results are shown for uncorrected binding energies (open symbols), and binding energies corrected for charging effects using the C(1s) signal of adventitious carbon (filled symbols). Inset shows the Ta(4d<sub>5/2</sub>) binding energy as a function of the O/Ta signal intensity.



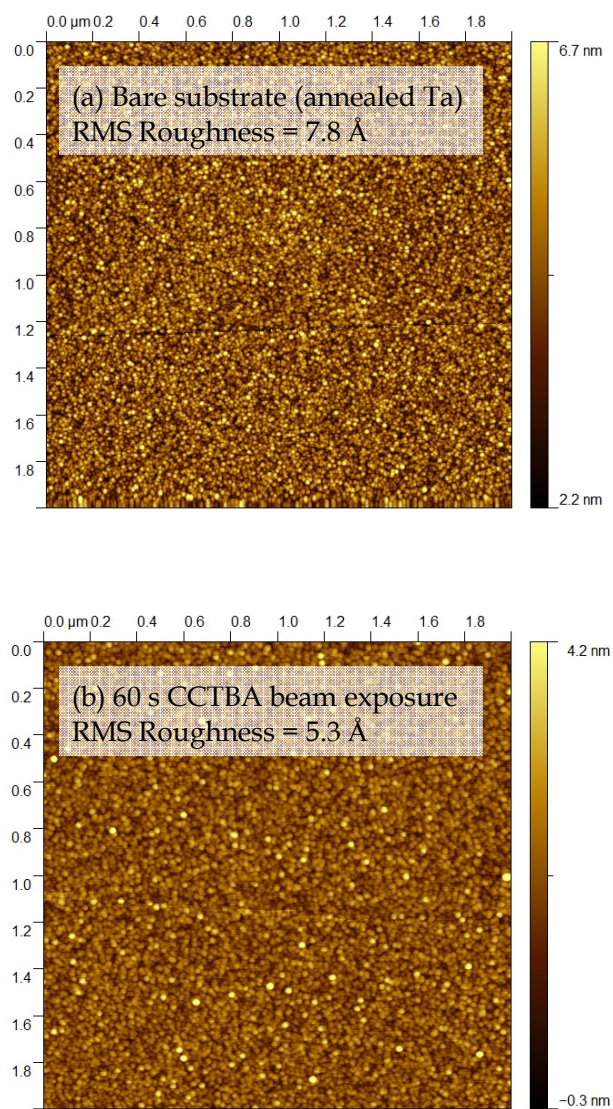


**Figure 7-11:** Atomic force micrographs of **(a)** the bare Ta substrate, post annealing, and **(b)** the film formed after 60 s exposure to the CCTBA beam. In both cases, the field of view is 2  $\mu\text{m}$  x 2  $\mu\text{m}$ , with a vertical range of 4.5 nm.

#### 7.4.6. Evolution of carbon

The C(1s) XPS feature measured for the Co/Ta films can be deconvoluted into three components. An example (60 s CCTBA beam exposure) is shown in Fig. 7-12(a). The components can be assigned to the following binding environments for the carbon atom: an aliphatic (C-C) type (binding energy  $\sim 284.6$  eV), a higher binding energy component resulting from C-O bonds ( $\sim 286.5$  eV), and carbide type binding environment ( $\sim 283.4$  eV). Angle-resolved XPS was performed to determine the depth of each type of carbon species. Due to the low intensity of the C-O species, and because the C-O type is found to be present on the bare substrate, while the carbide type is not, we will divide the C(1s) contributions into ‘carbide’ and ‘non-carbide’. As can be seen in Fig. 7-12(b), after 60 s of exposure to the CCTBA beam the non-carbide type and carbide type integrated signals behave differently. The signal from the non-carbide component increases with takeoff angle, a clear sign that it represents a thin surface film. Such thin carbon films are not unusual for on metal substrates held at room temperature in a UHV system. In contrast, the carbide signal is nearly constant with takeoff angle, similar to the signal from Co and Ta. This indicates that the carbide-type C is intermixed with Co.

If we examine ARXPS signals for all CCTBA beam exposures, we find that the division of carbide and non-carbide types into intermixed and surface species is consistent up to 480 s exposure. Because the C and Co atoms are present at the same depth, we can calculate the ratio of carbide C atoms to total Co atoms. The ratio decreases from  $\sim 1.1$  to 0.27 from 5 s to 480 s exposure.

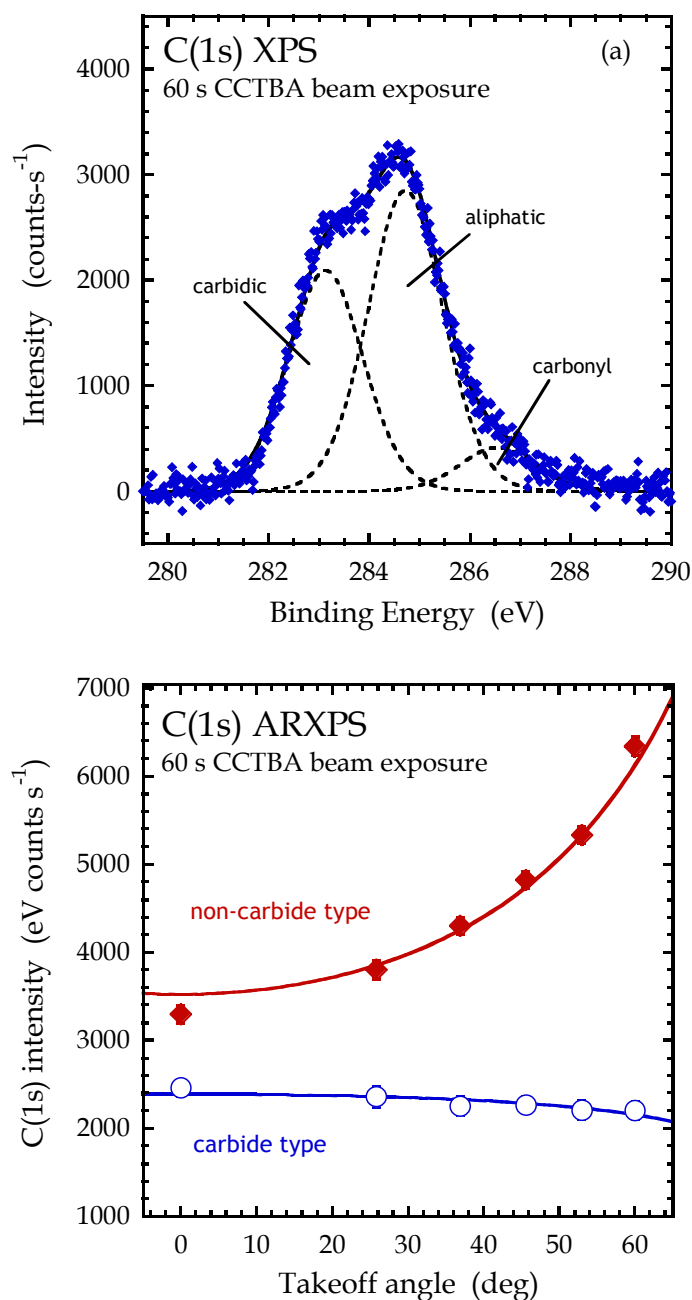


**Figure 7-12:** (a) XP spectrum in the C(1s) region for a 60 s exposure to the CCTBA beam. The feature has been fit to three peaks, representing a carbide type (~283.4 eV), an aliphatic type (~284.6 eV), and a R-C-OR' (carbonyl) type (~286.5 eV) binding environment. (b) Angle-resolved XPS of the feature shown in (a). Here the non-carbide type represents the sum of the latter two.

Considering both Co and Ta, the ratio of carbide C atoms to total metal atoms varies from 0.14 to 0.28, with no clear trend with CCTBA exposure.

However, the incorporation of C is very different after the Ta signal has disappeared (1800 s CCTBA exposure). First, as shown in Fig. 7-13, the carbide C signal decreases, while the non-carbide signal increases after 240 s CCTBA exposure, indicating that more carbide C, or possibly all of the carbide C, is formed at the Ta/Co interface. ARXPS measurements, shown in Fig. 7-14, indicate that for a CCTBA beam exposure of 1800 s the aliphatic type C is no longer present as a surface film, but rather mixed with the Co layer. This behavior was also observed for 3 hr (10800 s) CCTBA beam exposure. The atomic ratio of C to Co was measured to be 3.1 and 3.3 for the 1800 s and 3 hr beam exposures. The C:Co ratio in CCTBA, not including the CO ligands, is 3, suggesting that a likely source of C in the film after the Ta substrate is covered is incorporation of the tert-butyl acetylene group.

#### **7.4.7. Evolution of oxygen**

The binding energies measured for O(1s) after exposure to the CCTBA beam were in the range 530.7-530.9 eV, which lies on the upper end of the range reported for oxides of Ta (529.8-530.9 eV) and Co (529.2-531.35 eV). The integrated intensity of the O(1s) feature as a function of CCTBA beam exposure time is shown in Fig. 7-15. Generally the intensity of the oxygen signal follows the intensity of Ta, decreasing progressively before falling to a nearly undetectable level after 1800 s and 3 hrs of exposure to the CCTBA beam.

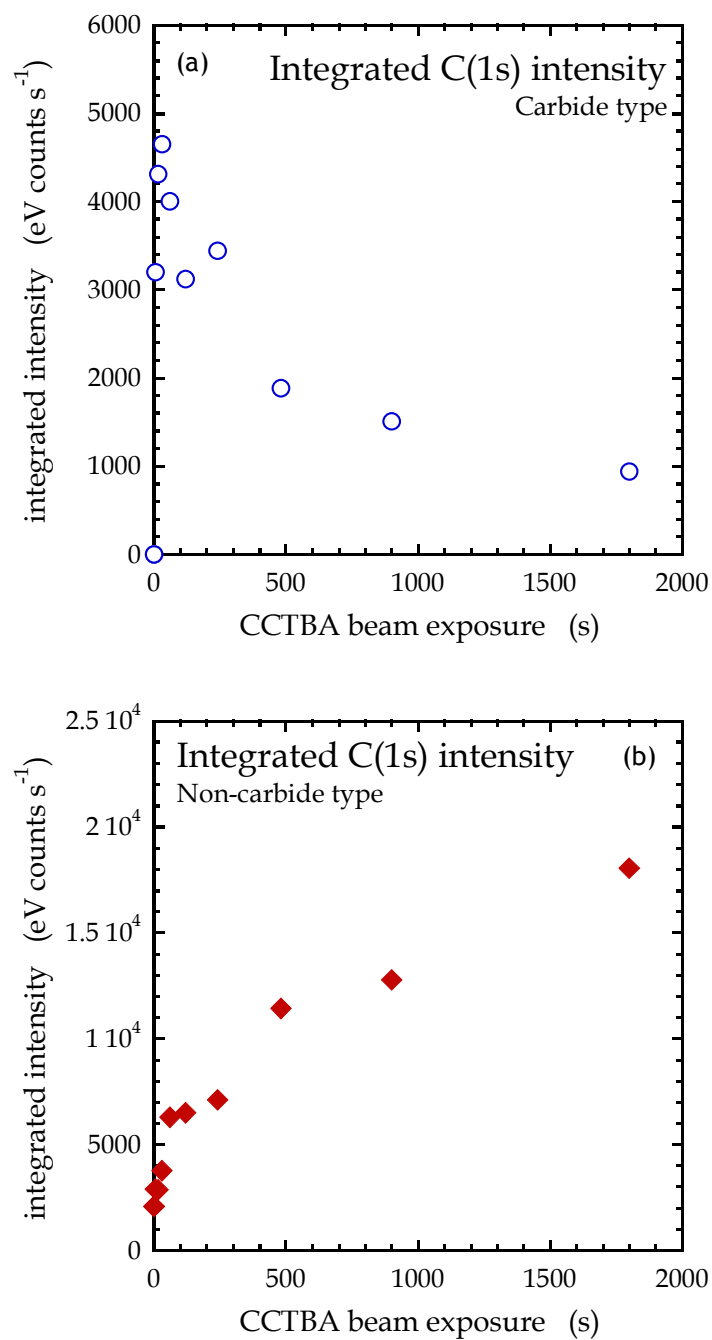


**Figure 7-13:** Integrated intensity of the (a) carbide-type and (b) non-carbide type C peaks as a function of CCTBA beam exposure time.

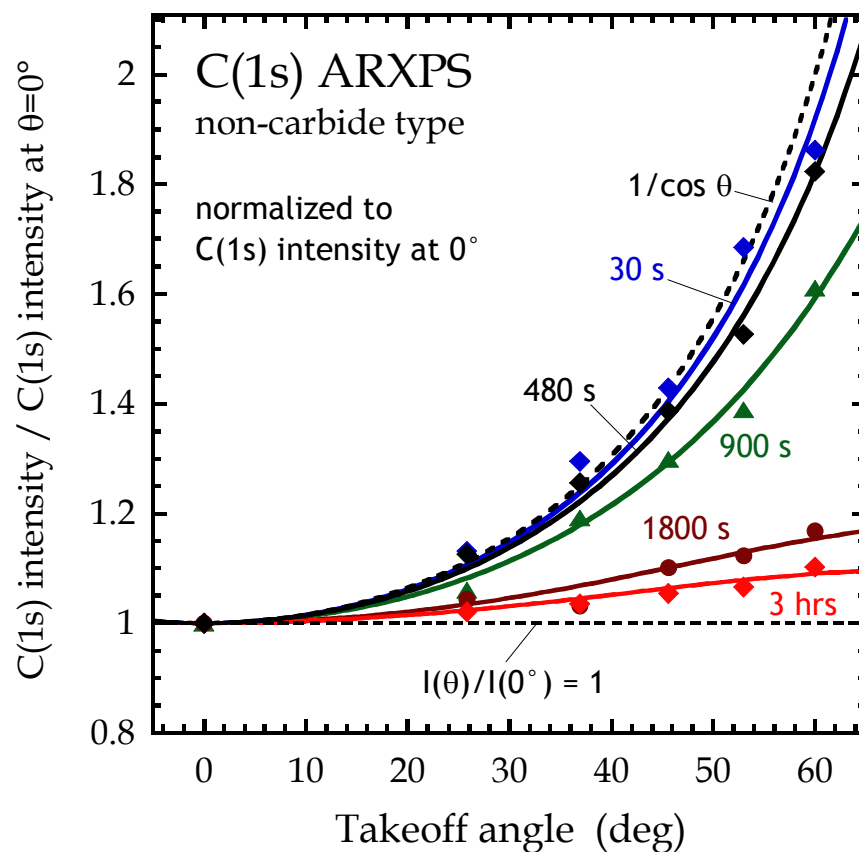


**Figure 7-14:** Angle-resolved XPS measurement of the non-carbide type C signal for a number of representative CCTBA beam exposure times. Dotted lines represent the behavior expected for cases where the C is present in a surface film ( $1/\cos \theta$ ) and where it is mixed with the substrate (constant at 1).

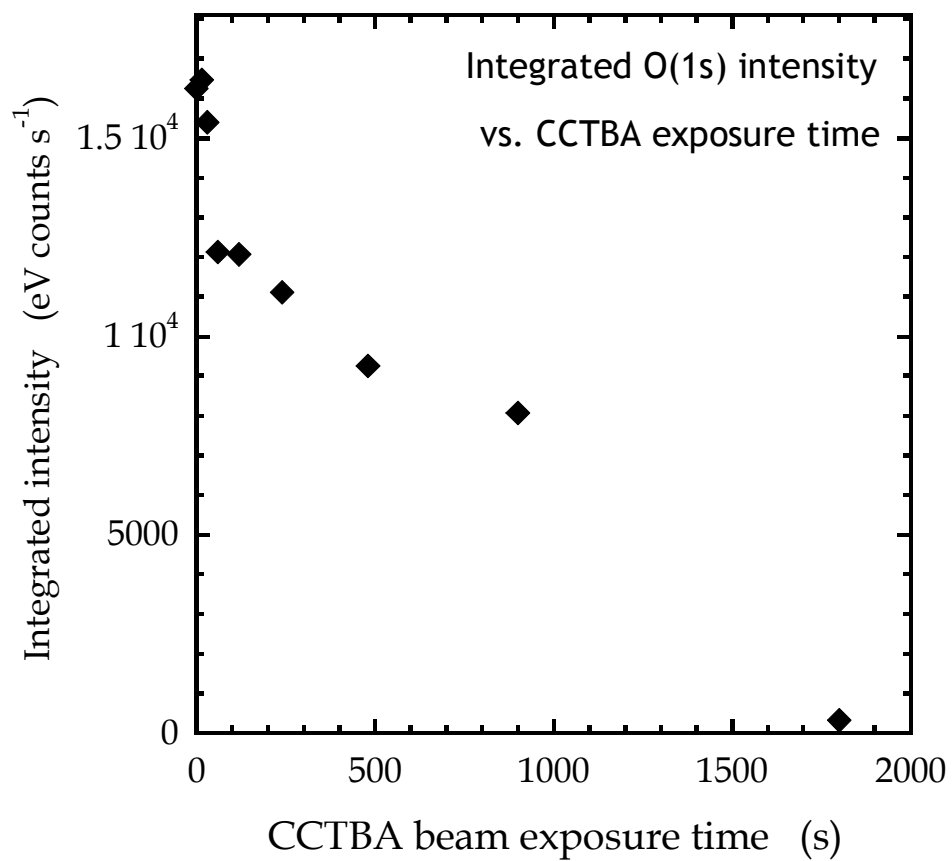


**Figure 7-15:** Integrated O(1s) intensity as a function of CCTBA beam exposure time.

We conclude that the films formed after Ta has been completely covered are oxygen free. ARXPS results are shown for O(1s) for 0 s to 900\_s in Fig. 7-16. The signal is approximately constant with takeoff angle up to 900 s exposure, indicating that the oxygen is incorporated into the substrate.

Having developed information on the evolution of Co, Ta, C, and O, as well as the depth distribution of these elements, it can now be summarized that Co film growth on Ta takes place in two stages. The first stage, at  $\leq 480$  s exposure, involves the formation of a mixed Co/Ta layer with O and C (as carbide) contamination. A second stage of growth is initiated after the intermixed layer is covered; the film formed in this layer contains only C and Co. Schematics of the proposed film structures during these two growth phases are shown in Fig. 7-17.

In order to determine the susceptibility of the deposited film to oxidation in air, the film formed after 3 hours of CCTBA exposure was taken out of the vacuum chamber and allowed to remain in ambient lab air for a period of 20 min. XP spectra in the Co(2p) and O(1s) regions before and after air exposure are shown in Fig. 7-18. Note that in this case the O(1s) signal overlaps with an Auger peak from Co; this issue was avoided in all other O(1s) scans by using Al K $\alpha$  x-ray excitation. The emergence of an O(1s) peak, as well as a high binding energy shoulder on the peaks of the Co(2p) doublet, indicate significant oxidation upon 20 min exposure to air.



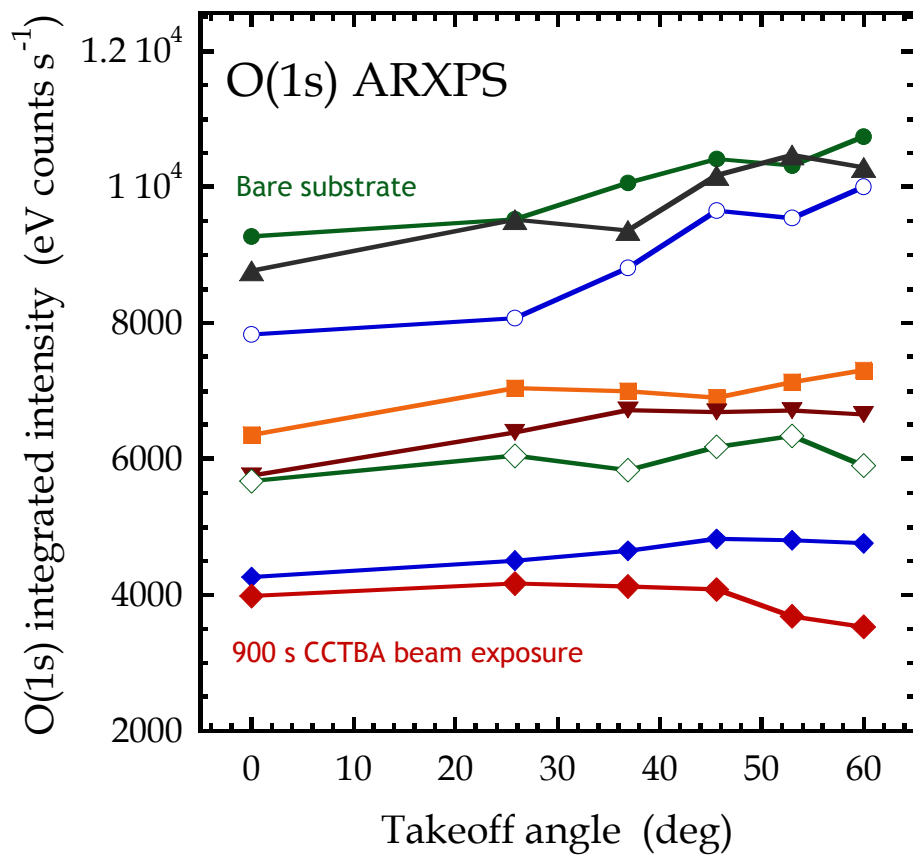
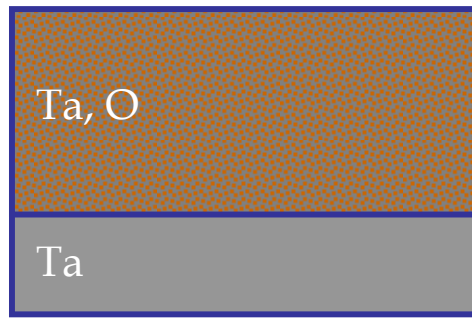
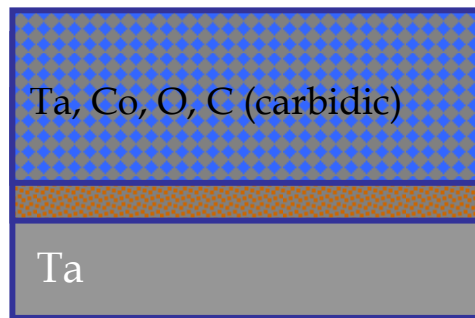


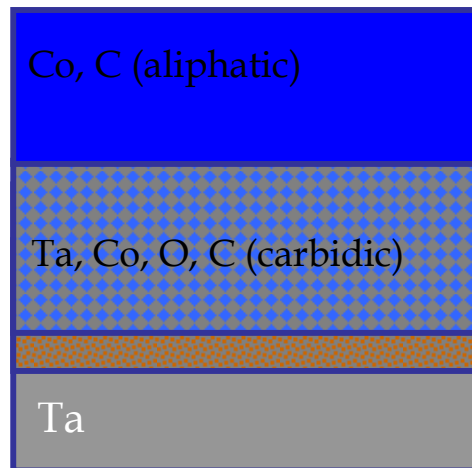
**Figure 7-16:** Angle-resolved XPS of the O(1s) feature for CCTBA beam exposures from 0 s to 1800 s. Beam exposure increases from top to bottom.



Bare substrate



Growth stage 1  
 $\leq 480$  s CCTBA beam exposure



Growth stage 2  
 $\geq 1800$  s CCTBA beam exposure

**Figure 7-17:** Proposed film structures during the main stages of film growth.

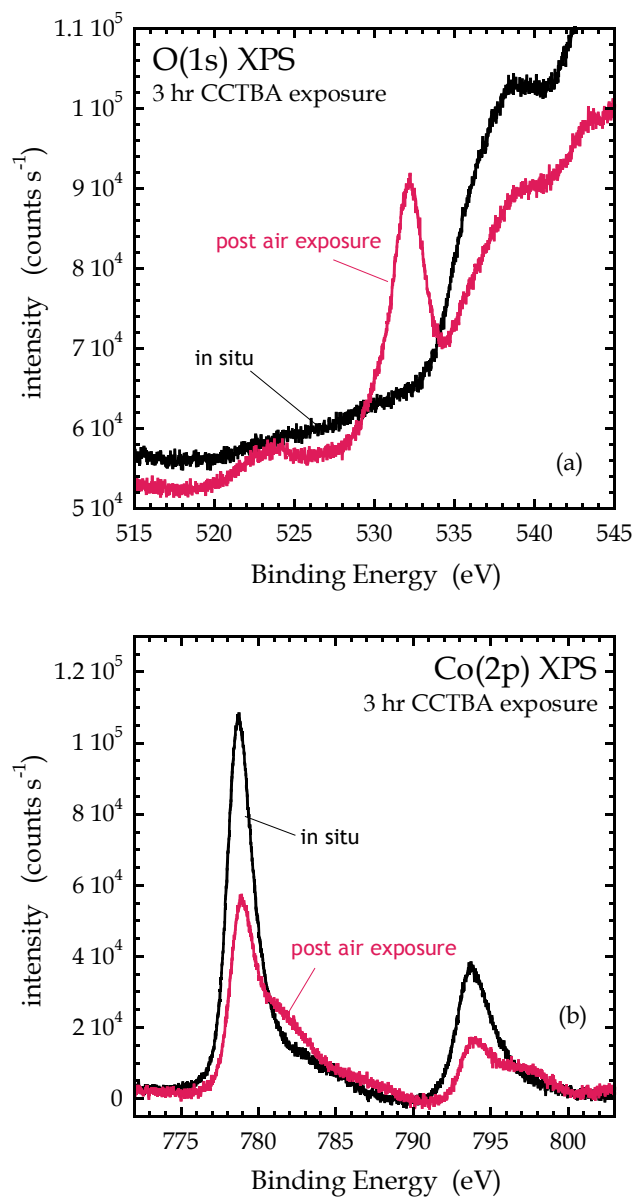


**Figure 7-18:** XP spectra in the **(a)** O(1s) and **(b)** Co(2p) regions of the film resulting from 3 hours of exposure to the CCTBA beam before and after 20 minutes exposure to ambient air.

## 7.5. Future experiments

As stated above, these experiments represent the initial stage of an ongoing project. As such, the results discussed above suggest a need for a number of changes to the experimental protocol, or for additional experiments. First is the replacement of the 350 °C annealing step, which is not well understood, with *in situ* pre-cleaning of the substrate with ion beam sputtering. Second is the co-dosing of the surface with atomic hydrogen during deposition. The addition of H<sub>2</sub> in the reaction chamber during Co CVD using CCTBA at relatively high pressure has been shown to greatly reduce the carbon content of the resulting Co films and improve their electrical properties [2]. The pressure of H<sub>2</sub> needed to affect growth is probably not achievable in this UHV system, however a viable alternative for UHV may be the use of atomic H. Therefore, a possible set of future experiments would involve co-dosing the surface with CCTBA and atomic H to determine the effect on growth rate and chemical composition of the resulting Co film. Finally, because these results showed significant interaction between the substrate and the growing film, a final aspect which warrants future consideration is the use of alternate substrate materials, TaN<sub>x</sub> and other candidate barrier materials in particular.

## 7.6. Conclusions

XPS was used to observe the formation of a film of Co on an annealed Ta substrate. The substrate was initially a layer of Ta<sub>2</sub>O<sub>5</sub> native oxide on sputtered Ta; *in*

*situ* annealing was used to clean the substrate and reduce the near-surface O concentration. Angle-resolved XPS, in combination with AFM, revealed that the formation of the Co film involved the intermixing of Co and Ta. At long exposure times, a Co film was formed which completely obscured the Ta signal in XPS. It was found that, in the early intermixing phase of growth, that carbon was incorporated in the film as a carbide-like species, with a C:Co ratio between 0.2 and 1. After the Ta substrate was covered, however, aliphatic carbon was also incorporated in the film, forming a very high C content layer (~ 75-80 atomic % C). Oxygen was present at the Co/Ta interface, but the Co/C film formed after the substrate was covered did not contain O. These results are summarized graphically in Fig. 19. The thickest Co/C film grown (10800 s CCTBA beam exposure) was found to be susceptible to oxidation by 20 minutes of exposure to ambient air.

## 7.7. References

1. L. Carbonell, H. Volders, N. Heylen, K. Kellens, R. Caluwaerts, K. Devriendt, E. A. Sanchez, J. Wouters, V. Gravey, K. Shah, Q. Luo, A. Sundarajan, L. Jiang, J. Aubuchon, P. Ma, N. Narasimhan, A. Cockburn, Z. Tökei, G. P. Beyer, IEEE International Interconnect Technology Conference 2009, pp 200-202.
2. S. B. Kang, H. S. Kim, K. J. Moon, W. H. Sohn, G. H. Choi, S. H. Kim, N. J. Bae, U. I. Chung, J. T. Moon, IEEE International Electron Devices Meeting Technical Digest, 20.6.1, (2003).
3. S.-B. Kang, G.-H. Choi, K.-J. Moon, H.-S. Kim, S.-G. Yang, U.S. Patent No. 7,285,483 B2 (2007).
4. K. Lee, T. Park, J. Lee, J. Kim, J. Kim, N. Kwak, S. Yeom, and H. Jeon, Jpn. J. Appl. Phys. **47**, 5396 (2008).
5. T. Nogami *et al*, IEEE Interconnect Technology Conference Proc., 1, (2010).
6. C. D. Wagner, L. E. Davis, M. V. Zeller, J. A. Taylor, R. H. Raymond, L. H. Gale, Surf. Interface Anal. **3**, 211-225 (1981).
7. G. E. McGuire, G. K. Schweitzer, and T. A. Carlson, Inorg. Chem. **12**, 2450 (1973).
8. J. S. Lee and C. J. Alstetter, Acta Metall. **34**, 131-138 (1986).
9. R. W. Powers and M. V. Doyle, J. Appl. Phys. **30**, 514-524 (1959).
10. E. R. Kish, unpublished result.
11. H. Okamoto, J. Phase Equilib. Diff. **25**, 571-572 (2004).

## 8. Summary

The need to deposit extremely thin, conformal films for a number of applications has led to a significant amount of research into atomic layer deposition (ALD), particularly in the field of semiconductor device fabrication. Because ALD relies on chemical reactions which are localized at the interface, one route to controlling ALD growth is through the use of surface bound organic molecules, which alter the chemical identity and distribution of active sites on the substrate. Here we have examined the first stages of ALD, including the initial interactions of gas-phase ALD precursors with the substrate, and the period in which the growing surface transitions from the starting substrate to the steady-state growing film. ALD has been examined on both unmodified substrates, and substrates which have been modified through the addition of a thin organic film.

This began with a review of relevant prior work in the area, focusing mainly on the ALD of  $\text{TiN}_x$  on a variety organic films, including self-assembled monolayers with an essentially 2-d arrangement of chemically reactive groups, and more complex branched molecules with a 3-d distribution of such groups. Connections were found between the effect of the organic layers on the first half cycle of ALD (i.e. the initial chemisorption of the transition metal coordination complex) and the effect of the organic layer on subsequent growth. In some cases, the relationship simply involves a correlation between the saturation density of the complex after the first half cycle and the rate of subsequent growth. Substantial attenuation was observed, for example, in cases where the organic layer blocked active sites on the surface ( $-\text{CH}_3$  terminated SAMs); a lower degree of attenuation was observed for ALD on organic layers possessing reactive endgroups ( $-\text{OH}$  and  $-\text{NH}_2$ ). In other cases, notably for branched,  $-\text{OH}$  terminated organic layers, the chemical structure of the adsorbed precursor, not

its density, was the critical factor in determining subsequent growth rate. Layers which formed a high number of oxygen containing bonds to the metal center of the complex were found to strongly attenuate growth (poly-G). Examining ALD on a range of organic films, we also found that the initial rate of ALD could be connected with the resulting film morphology. Lower initial ALD growth rate due to a low density of nucleation sites led generally to rougher, more islanded films. Ultimately, these results suggest that, if the purpose of the organic layer is to block or attenuate growth, then a dense, thick organic layer should be used, in order to effectively block the diffusion of precursors to the organic film/substrate interface. If the purpose of the organic layer is to enhance growth, however, organic materials should be used which lead to the adsorption of transition metal coordination complexes at the vacuum interface, with minimal loss of the surrounding ligands.

Next, the deposition of several film materials ( $\text{Al}_2\text{O}_3$ ,  $\text{HfO}_2$ ,  $\text{Ta}_2\text{O}_5$ , and  $\text{TaN}_x$ ), on a single organic film, poly(ethylene imine) (PEI) was examined. Here we observed a range of effects due to PEI, from no measurable attenuation ( $\text{Al}_2\text{O}_3$ ), to strong attenuation even after 50 ALD cycles were completed ( $\text{TaN}_x$ ). Analysis of the ALD reactions revealed a strong correlation between the net energy change associated with the ALD reaction and the degree of attenuation, suggesting that ALD processes in which there is a strong thermodynamic driving force, or low activation barrier, for the formation of the final products can more easily overcome the obstacles presented by the organic layer. Along this line of research, future investigation was suggested using coreactants which would lead to an increase in the thermodynamic driving force, such as ozone (for oxide processes), hydrazine (for  $\text{TaN}_x$ ), or plasma-generated radicals.

The ALD of one material,  $\text{TaN}_x$ , was examined in more detail using *in situ* XPS. This required the installation of new XPS hardware on the UHV chamber used



to conduct ALD. Substrates in this case included nonporous SiO<sub>2</sub>, a porous low dielectric constant or ‘low-κ’ material, and both substrates modified by PEI films. Through the use of spectroscopic ellipsometry, it was shown that the deposition of thin organic films using small molecules was problematic, due to the infiltration of these molecules into the pore network of the low-κ. PEI was used here in part because of its relatively large size, which prevented infiltration. The use of *in situ* XPS required the addition of new XPS hardware in the UHV chamber used for ALD. *In situ* XPS after the first half cycle of TaN<sub>x</sub> ALD {chemisorption of the transition metal coordination complex Ta[N(CH<sub>3</sub>)<sub>2</sub>]<sub>5</sub>} showed that the chemical structure of the adsorbed complex was strongly related to the substrate type, and, to some degree, to the substrate temperature. Furthermore, the oxidation state and chemical composition of the TaN<sub>x</sub> film in the first 10 ALD cycles (~ 6-10 Å) was strongly affected by the starting substrate. Substrates with a high density of oxygen containing groups led to a more oxidized TaN<sub>x</sub> film, and less efficient incorporation of N in a nitride binding state. Of interest in the application of barrier film deposition for the interconnect structures of integrated circuits, the presence of a PEI film enhanced the uptake of Ta[N(CH<sub>3</sub>)<sub>2</sub>]<sub>5</sub> at the topmost surface of the porous low-κ, and limited its infiltration into the pore network of the low-κ. However, ALD on PEI-treated low-κ, particularly when ALD is conducted using conventional techniques, did not proceed at the same rate as the ‘ideal’ ALD observed on SiO<sub>2</sub>. Therefore, additional improvements could be made, where possible routes to improvement are suggested by this work (Chapter 5), as well as that presented in Chapters 3 and 4. One route to higher ALD growth rates could involve the use of an alternate organic film material which does not bind as strongly to the Ta[N(CH<sub>3</sub>)<sub>2</sub>]<sub>5</sub> precursor. There are many examples of water-soluble, multifunctional polymers which could be employed. Here again, a key aspect to the organic film seems to be the ability to increase Ta[N(CH<sub>3</sub>)<sub>2</sub>]<sub>5</sub> uptake close to the

vacuum interface, while leaving the chemisorbed species sufficiently reactive towards the second half cycle of ALD. Considering the results discussed in the previous paragraph (Chapter 4), another route to overcoming the initial attenuation of ALD in the presence of PEI may be the deposition of a second inorganic layer, such as  $\text{Ta}_2\text{O}_5$ , prior to  $\text{TaN}_x$  ALD.

A final set of experiments involved the early stages of cobalt film formation on tantalum substrates using chemical vapor deposition with the metalorganic precursor dicobalt hexacarbonyl tert-butylacetylene (CCTBA). Here it was found that growth proceeded in two phases. The first of these involved the formation of an intermixed cobalt/tantalum layer, while the second took place after the intermixed layer was covered and was characterized by the formation of a mixed carbon/cobalt film. In this area, further investigation is ongoing to characterize the process of Co film formation on Ta and  $\text{TaN}_x$  films sputter cleaned *in situ*, as well as the addition of  $\text{H}_2$  or atomic H during growth.

## **9. Appendix: Addition of x-ray photoelectron spectroscopy components to the Olin Hall 312 ultra-high vacuum system**

The capability to perform x-ray photoelectron spectroscopy (XPS) was added to the UHV system in Olin Hall 312 (system described fully in Sec. 2.5) in September 2008 through the installation of an Omicron Sphera U5 concentric hemispherical electron energy analyzer (serial no. 154/1250/U5/34/08, Omicron Nanotechnology USA, Eden Prairie, MN) and an Omicron DAR 400 Mg/Al twin anode x-ray source (serial no. 173, Omicron Nanotechnology USA). Full details of the operation, features, and capabilities of both components are provided in the user manuals, so discussion here will be limited to the aspects of the components which are unique to this system. The analyzer and x-ray source were mounted to 6" and 2.75" CF flanges on the west side of the chamber, as shown in Fig. 9-1. Space restrictions within the main chamber of the system required mounting both components on translation stages. The x-ray source was mounted on a bellows-sealed linear translation stage (LSM39-100-H, UHV Design, East Sussex, England) which allows 100 mm of travel. The electron energy analyzer was also mounted on a bellows-sealed linear translator (BLT66-04-SP, McAllister Technical Services, Coeur d'Alene, ID). A stage was required to support the weight of the analyzer. Schematics of this stage, designed and fabricated by McAllister Technical Services, are shown in Fig. 9-2.

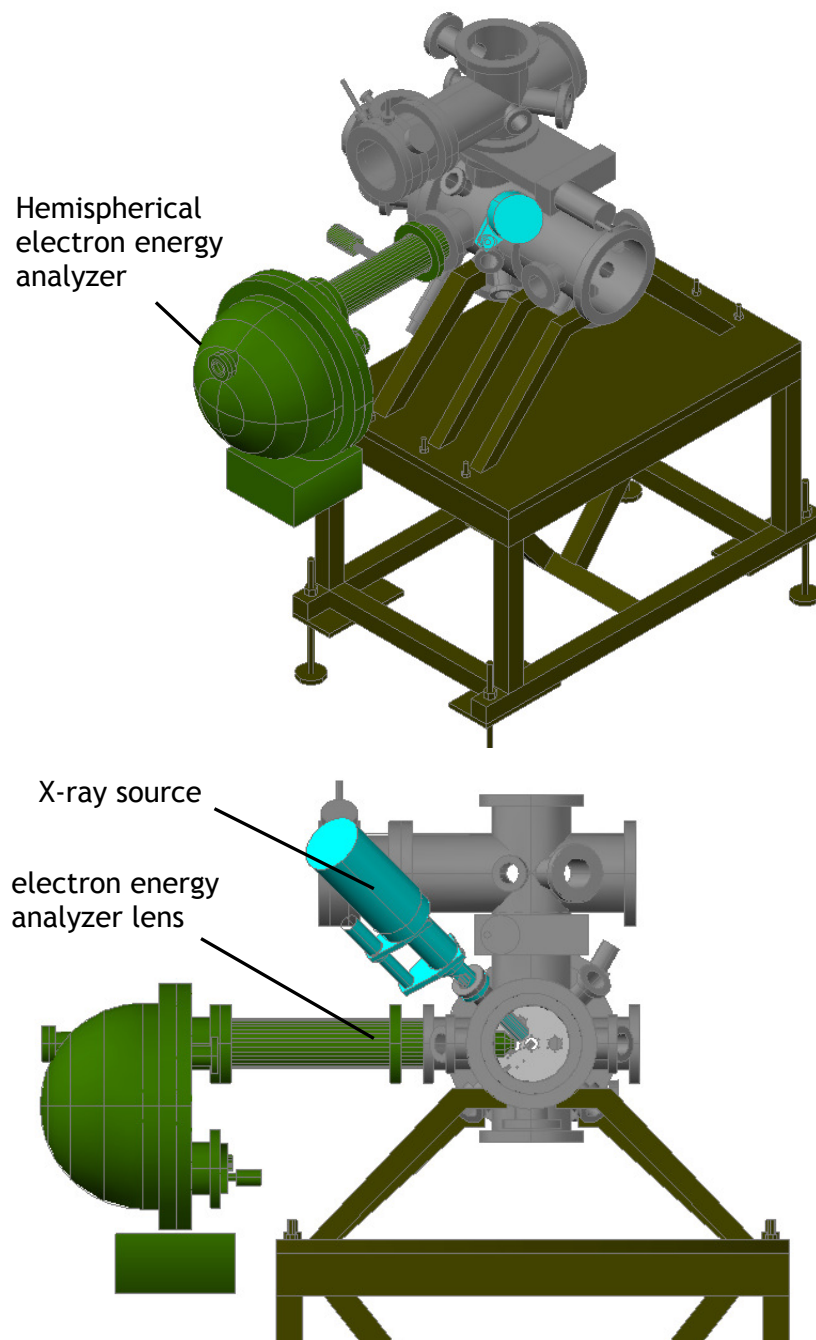


**Figure 9-1:** AutoCAD drawing of the Olin Hall 312 system with installed XPS components.

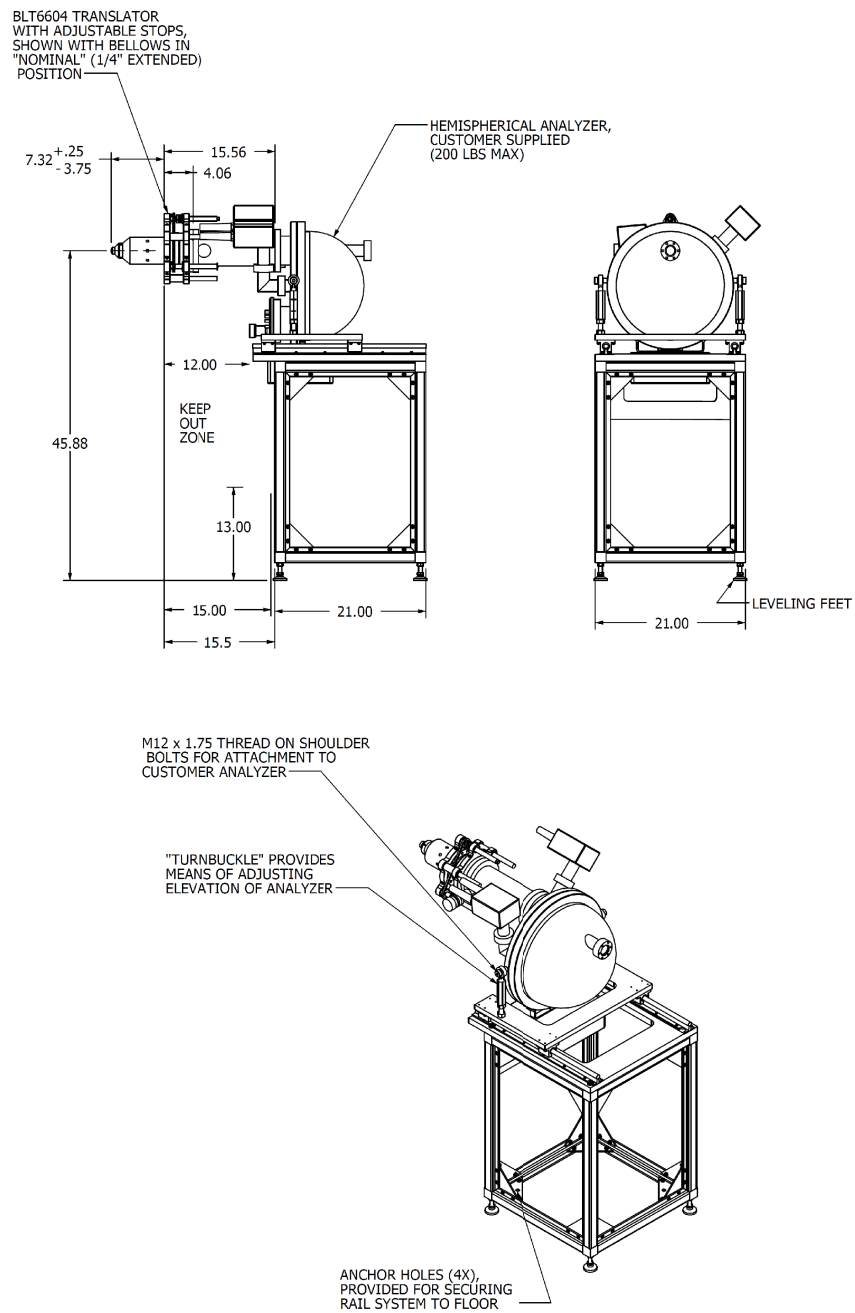


**Figure 9-2:** Schematics of the translation stage built for the Sphera U5 electron energy analyzer (courtesy McAllister Technical Services).

The use of angle-resolved XPS (ARXPS) required the fabrication of a new molybdenum sample platen in which the samples are positioned along the axis of rotation of the sample manipulator (Thermionics Northwest, Port Townsend, WA). Schematic drawings of this new platen are given in Fig. 9-3. This platen was designed to be compatible with the existing sample manipulator (Thermionics SMR-3) and sample transfer system (Thermionics STLC Series II) [1]. As with the sample platens used previously in this system, 17 x 17 mm<sup>2</sup> samples are held in shallow wells by a cover plate secured by clips. The backs of the sample wells are open, allowing efficient heating of the sample by radiation from the pyrolytic boron nitride sample heater. Two threaded holes were tapped on either side of the center sample well, which allowed the use of clips to directly hold irregularly shaped samples to a back plate of standard size. Correct alignment of the axis of rotation of the sample and the analyzer lens axis is critical in ARXPS, and will be discussed in further detail below.

The angle between the x-ray source and electron energy analyzer centerline axes is fixed at 52.6°. For unpolarized photons, the differential cross-section for photoemission as a function of the angle between photoelectron emission and the photon source,  $\phi$ , for a given electron core level is given by [2]:

$$\frac{d\sigma}{d\Omega} = \frac{\sigma_{total}}{4\pi} \left[ 1 - \frac{\beta}{4} (3 \cos^2 \phi - 1) \right] \quad (9-1)$$

Where  $\sigma_{total}$  is the overall photoionization cross-section for the core level, and  $\beta$  is an asymmetry parameter.

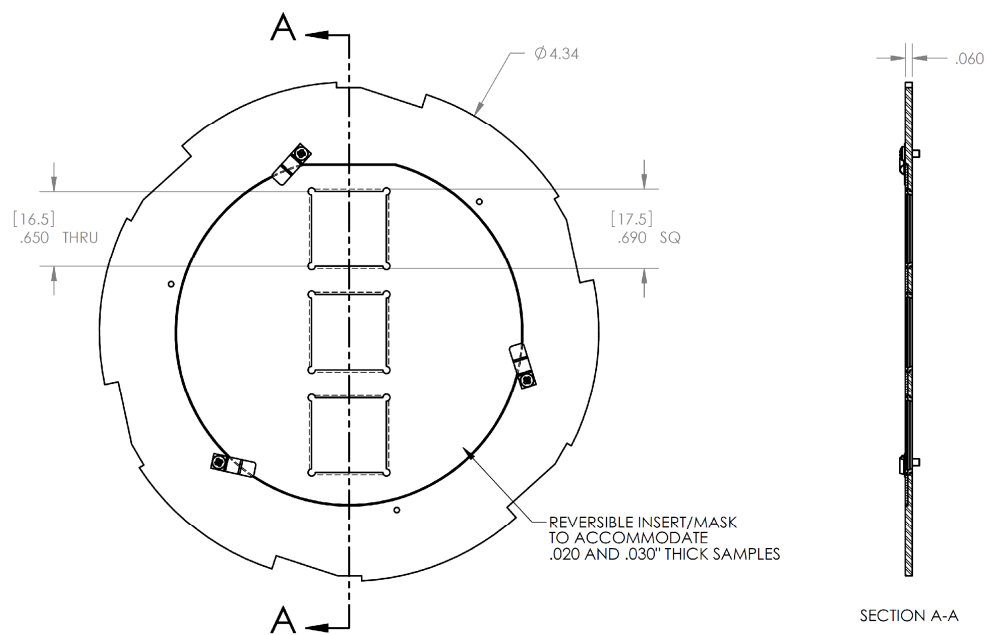


**Figure 9-3:** Drawing of the Mo sample platen used for angle-resolved XPS (courtesy Thermionics Northwest, Inc.).

This parameter depends on the angular momentum and kinetic energy of the electron. Note that the ‘magic angle’ of  $54.7^\circ$ , where  $d\sigma/d\Omega$  does not vary with  $\beta$ , is very close to the fixed value in this system. Values of  $\beta$  have been tabulated for kinetic energies of interest in XPS for a range of elements from atomic number 1 to 100 [3]. Given the fixed  $\phi$  used here, the value of the relevant factor which must be used to correct  $\sigma_{total}$  used for quantitative elemental analyses,  $(d\sigma/d\Omega)/(\sigma_{total}/4\pi)$ , does not vary from the range of 0.95 to 0.97 for the elements and core levels considered here.

After installation, the initial setup of the XPS components included electrical testing of the vacuum hardware and optimization of the electron multiplier supply voltages as instructed in the user manual. Next, a series of tests was conducted to (i) confirm correct operation of the components as a set, (ii) characterize the resolution of the instrument with settings commonly used for analysis, and (iii) to determine the correct position of the sample during XPS analysis. Concerning point (i), three materials of known composition were analyzed. The materials included a film of 1000 Å polycrystalline Au (e-beam evaporated) / 100 Å Cr / native SiO<sub>2</sub> / Si(100), a film of ~ 20 Å SiO<sub>2</sub> film on Si(100), and a foil consisting of pure Ta (99.95%). Survey scans of the three materials are shown in Fig. 9-4. As can be seen, all peaks can be assigned to the materials analyzed, with no missing peaks. This, along with the absence of unexplained ghost or satellite peaks, confirms the correct operation and cleanliness of the X-ray source and analyzer electronics. Similar testing using Al K $\alpha$  excitation later confirmed proper operation and cleanliness of the Al anode.



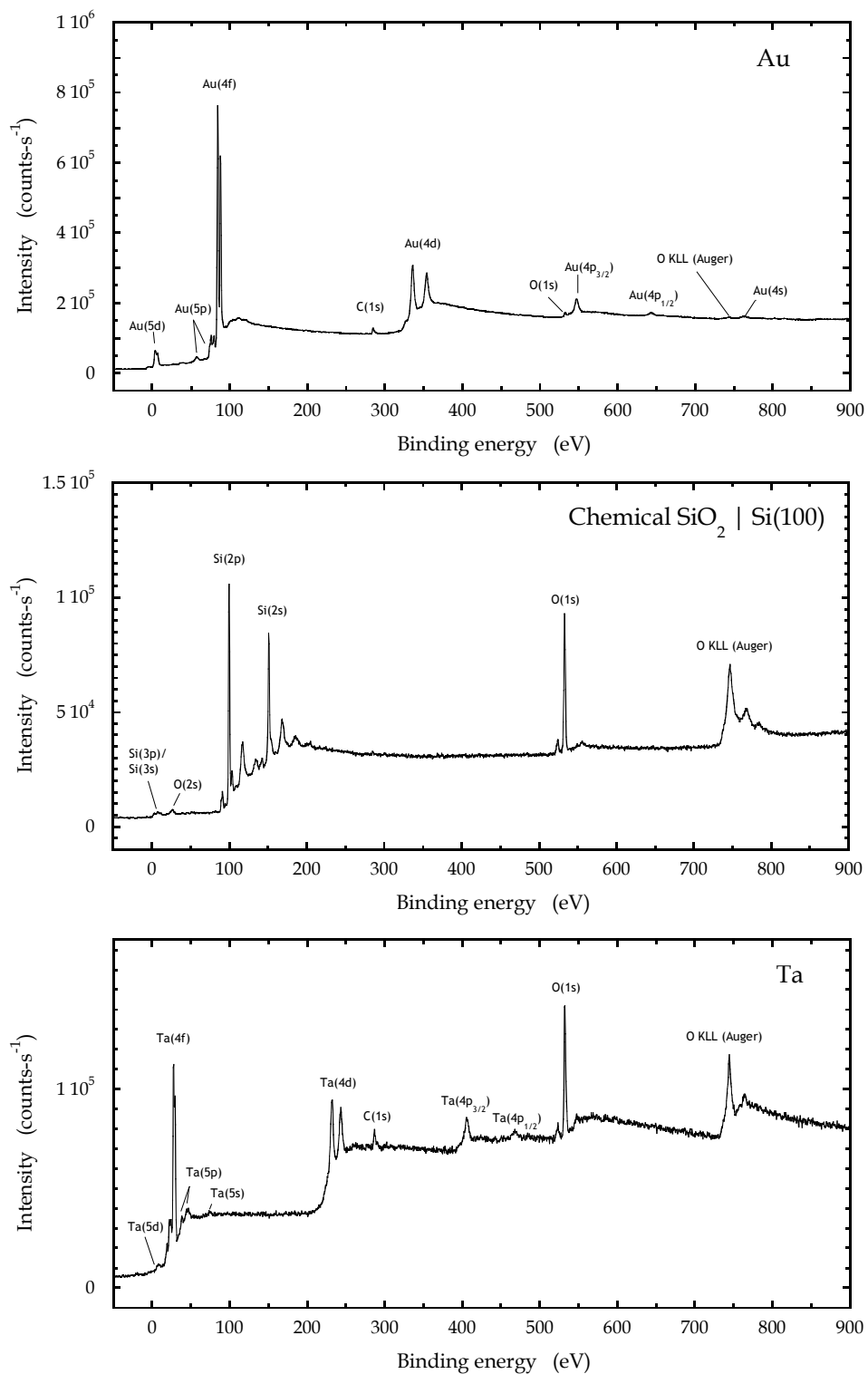


**Figure 9-4:** XPS survey scans of three films of known composition, taken using the new XPS equipment after installation.

Concerning (ii), the resolution of the spectrometer, the full width at half maximum (FWHM) of the Au(4f<sub>7/2</sub>) peak was measured using two different entrance apertures, at 50 eV pass energy and with a 5 mm x 11 mm exit slit. The Au(4f<sub>7/2</sub>) FWHM was 1.70 ± 0.03 eV with a circular entrance aperture of 6.3 mm diameter, and 1.55 ± 0.02 eV with a circular entrance aperture of 3.1 mm diameter. In XPS, the width of a peak from an individual core level, in a single chemical state, can be described by [4]:

$$\Delta E = (\Delta E_x^2 + \Delta E_i^2 + \Delta E_a^2)^{1/2} \quad (9-2)$$

Where  $\Delta E$  is the measured FWHM,  $\Delta E_x$  is the characteristic spread of the x-ray excitation energy,  $\Delta E_i$  is the intrinsic width of the core level, and  $\Delta E_a$  is the contribution of the analyzer, where all parameters are given as FWHM values. In this experiment,  $\Delta E_x$ , the characteristic spread of unmonochromated Mg K $\alpha$  x-ray line, is known to be 0.7 eV [4], while  $\Delta E_i$ , the intrinsic width of the Au(4f<sub>7/2</sub>) core level due to core hole lifetime effects is 0.317 eV [5]. Using Eq. 9-2, we obtain  $\Delta E_a$  values of 1.52 eV and 1.35 eV for the 6.3 mm and 3.1 mm entrance apertures respectively. This can be compared to a  $\Delta E_a$  value of 2.62 eV for the other set of XPS components used in the Engstrom group, a VSW Class 100 hemispherical electron energy analyzer with unmonochromated Mg K $\alpha$  source, operated at 90 eV pass energy with 5 mm circular entrance and exit apertures. The better resolution obtained using the Omicron U5 spectrometer is expected, due to its higher radius of curvature (125 mm vs. 100 mm), and the lower pass energy used for this test (50 eV vs. 90 eV).

To address point (iii), determining the correct sample position during XPS, we must consider alignment along 3 axes, as shown in Fig. 9-5. For the vertical axis,  $z$ , alignment simply involves positioning the XPS analysis spot over the desired location on the sample. The sample position along the other two axes, however, affects the distance between the sample and both the electron energy analyzer and the x-ray source. Therefore, the position of the sample in the  $x$  and  $y$  directions must be precisely aligned, and should be fixed during XPS for quantitative analysis. Considering the  $x$  axis first, the specified working distance between the end of the analyzer lens and the sample is 30 mm. The correct  $x$  axis setting, as well as the distance between fixed and traveling flanges on the analyzer translation stage, was set by using a ‘pointer’ extension provided by the manufacturer. When mounted on the end of the lens, the pointer indicates the correct sample position.

Optimal focusing of the XPS analysis spot on the sample provides confirmation that the working distance, and therefore the  $x$  axis position, has been set correctly. Focus of the analysis spot was confirmed by rotating the sample to  $0^\circ$  photoelectron takeoff angle, then taking XPS measurements close to the edge between the sample and sample platen, using the smallest analysis spot available (200  $\mu\text{m}$  circular aperture at high magnification, giving an analysis spot on the sample of  $\sim 60$   $\mu\text{m}$ ). The sharpness of the edge measured using this technique can then be compared to the factory test data provided by the manufacturer. Here, a sample consisting of  $\text{SiO}_2/\text{Si}$  was used, which provided good material contrast to the Mo sample platen. As can be seen in Fig. 9-6, at an  $x$  position of 9.75 mm, the edge of the XPS analysis spot compares well with the factory provided data.

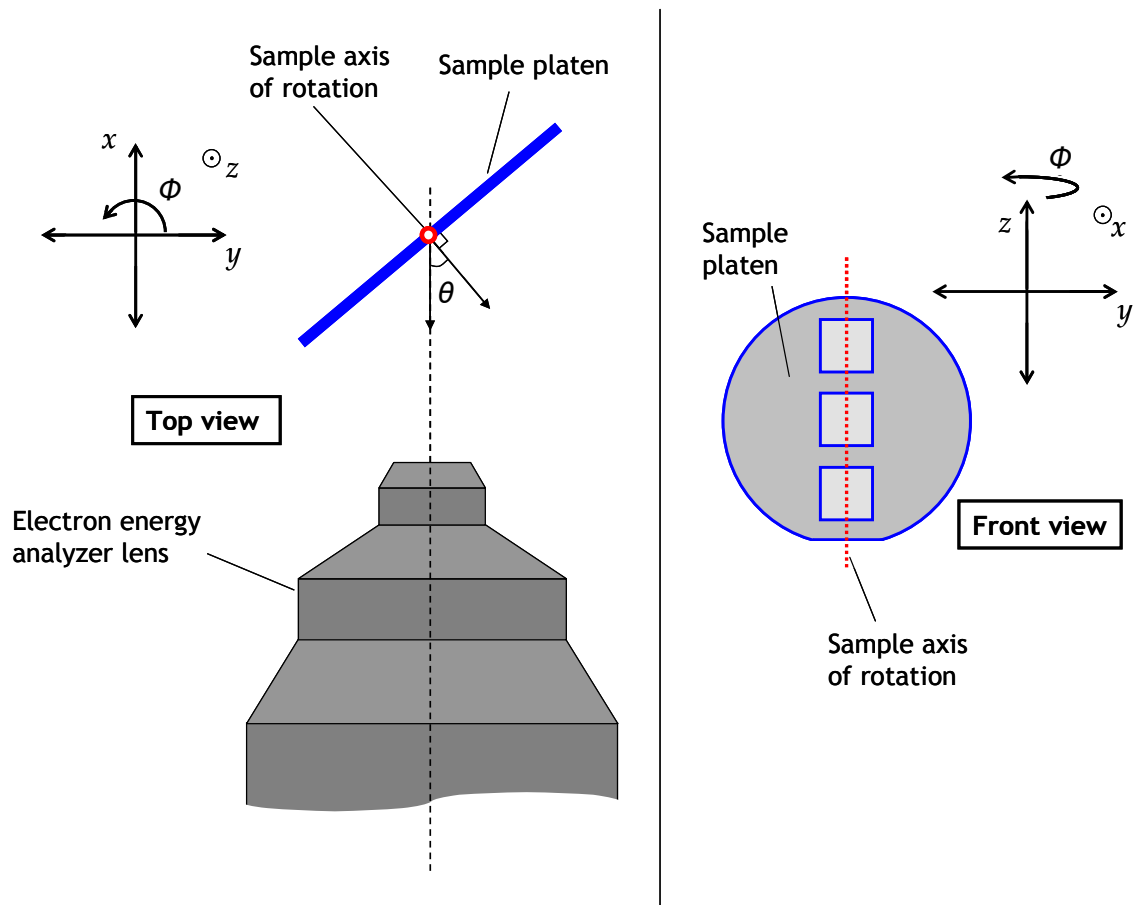


**Figure 9-5:** Schematic of the sample position during XPS analysis.

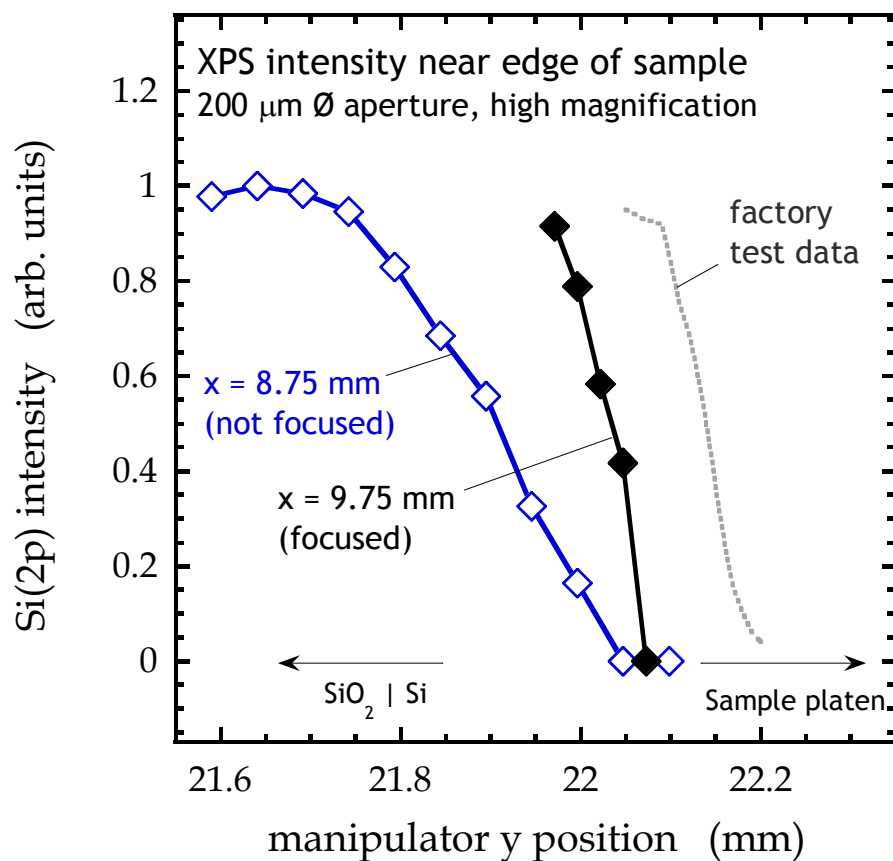


**Figure 9-6:** XPS intensity as a function of y axis position (see Fig. 9-5), for positions close to the sample/sample platen edge. Factory test data, provided by Omicron Nanotechnology USA, is shown for comparison.

Moving the  $x$  position 1 mm away from the lens, to 8.75 mm, causes defocusing of the analysis spot, evidenced by the widening of the transition between the sample and sample platen.

In ARXPS, the axis of rotation of the sample must intersect the analyzer lens axis (shown in Fig. 9-5). Deviation from this condition will lead to variation in the lens to sample and/or x-ray source to sample distance with takeoff angle, causing systematic errors in the measured intensity in ARXPS. Correct alignment of the sample axis of rotation was achieved by adjusting the position along the  $y$  axis. Initially, the sample was aligned along this axis by moving to a  $y$  position such that the analysis spot was centered of the sample, for the middle of the three sample wells shown in Fig. 9-3. Proper alignment was confirmed by measuring XPS intensity as a function of photoelectron takeoff angle ( $\theta$  in Fig. 9-5) for a semi-infinite film with no overlayers or long-range crystal structure. For this type of sample, XPS intensity should be constant with takeoff angle, provided the sample is correctly aligned [4]. For this test, a  $\sim 200$  nm film of Ta deposited using sputtering was used. Annealing the sample at 375 °C for 1 hour removed the native Ta<sub>2</sub>O<sub>5</sub> and contamination carbon overlayers from the Ta surface. As shown in Fig. 9-7, no systematic intensity variation is measured as a function of takeoff angle, with all random variation confined to a window of  $\pm 4\%$ . This confirms accurate alignment in the  $y$  axis. ARXPS was also performed on an Au reference standard, with no attempt made to clean the sample surface. Here the intensities of both the Au(4f<sub>7/2</sub>) and C(1s) peaks were measured, due to the expected presence of a carbon containing contamination layer.

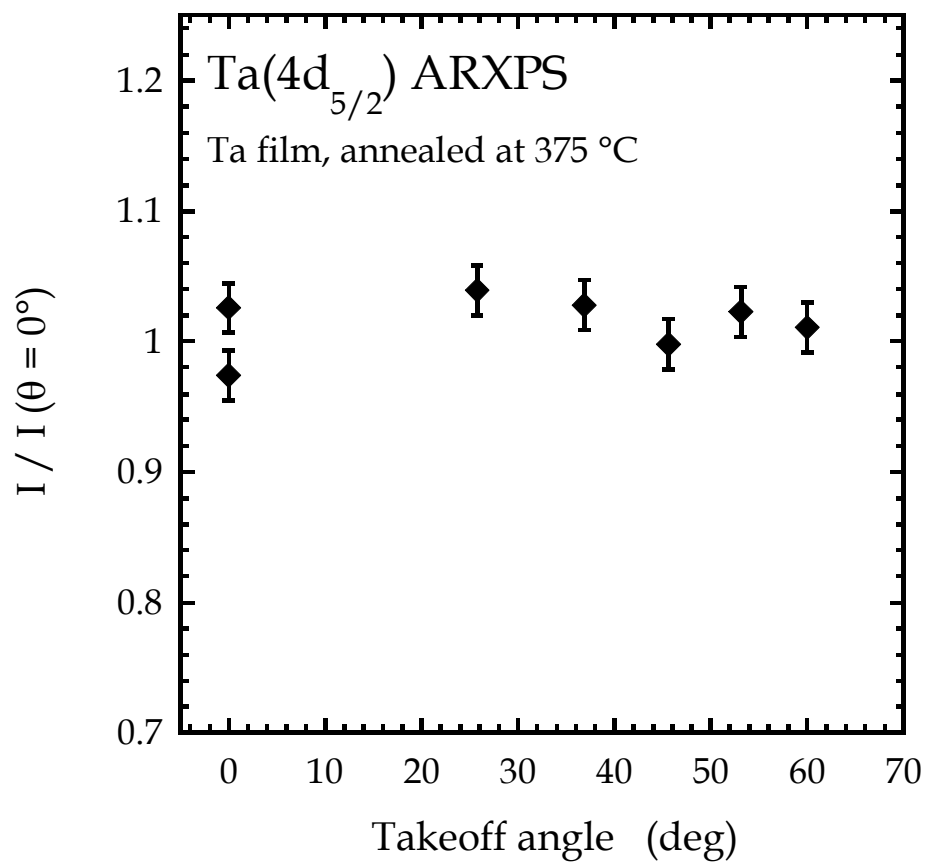


**Figure 9-7:** Ta(4d<sub>5/2</sub>) intensity as a function of photoelectron takeoff angle, normalized by the intensity at 0° takeoff, for a thick Ta film after annealing at 375 °C for 1 hour.

In Fig. 9-8, we see that the Au(4f<sub>7/2</sub>) intensity decreases with takeoff angle, while the C(1s) intensity increases, as would be expected for a thin layer of carbon-containing material on a semi-infinite Au substrate. This ARXPS data can be fit to simple models by approximating the carbon-containing layer as a uniform thin film. The Au(4f<sub>7/2</sub>) intensity,  $I_{Au}$ , as a function of photoelectron takeoff angle,  $\theta$ , can be described by:

$$I_{Au} = I_{Au,0} \exp\left(\frac{-d_{Au}}{\lambda_{Au4f} \cos \theta}\right) \quad (9-3)$$

Where  $I_{Au,0}$  is the unattenuated intensity of the Au(4f<sub>7/2</sub>) signal,  $d_{Au}$  is the thickness of the carbon overlayer, and  $\lambda_{Au4f}$  is the attenuation length of the Au(4f<sub>7/2</sub>) photoelectrons through the carbon layer. Likewise, the C(1s) intensity can be described by:

$$I_C = I_{C,0} \left[ 1 - \exp\left(\frac{-d_C}{\lambda_{C1s} \cos \theta}\right) \right] \quad (9-4)$$

Where  $I_{C,0}$  is the unattenuated intensity of a theoretical semi-infinite film of the carbon containing layer,  $d_C$  is the thickness of the layer, and  $\lambda_{C1s}$  is the attenuation length of the C(1s) photoelectrons through the layer. If the assumptions used here are valid, then we would expect that independent fits using the Au(4f<sub>7/2</sub>) and C(1s) features would give equivalent values for  $d_{Au}/\lambda_{Au4f}$  and  $d_C/\lambda_{C1s}$ .



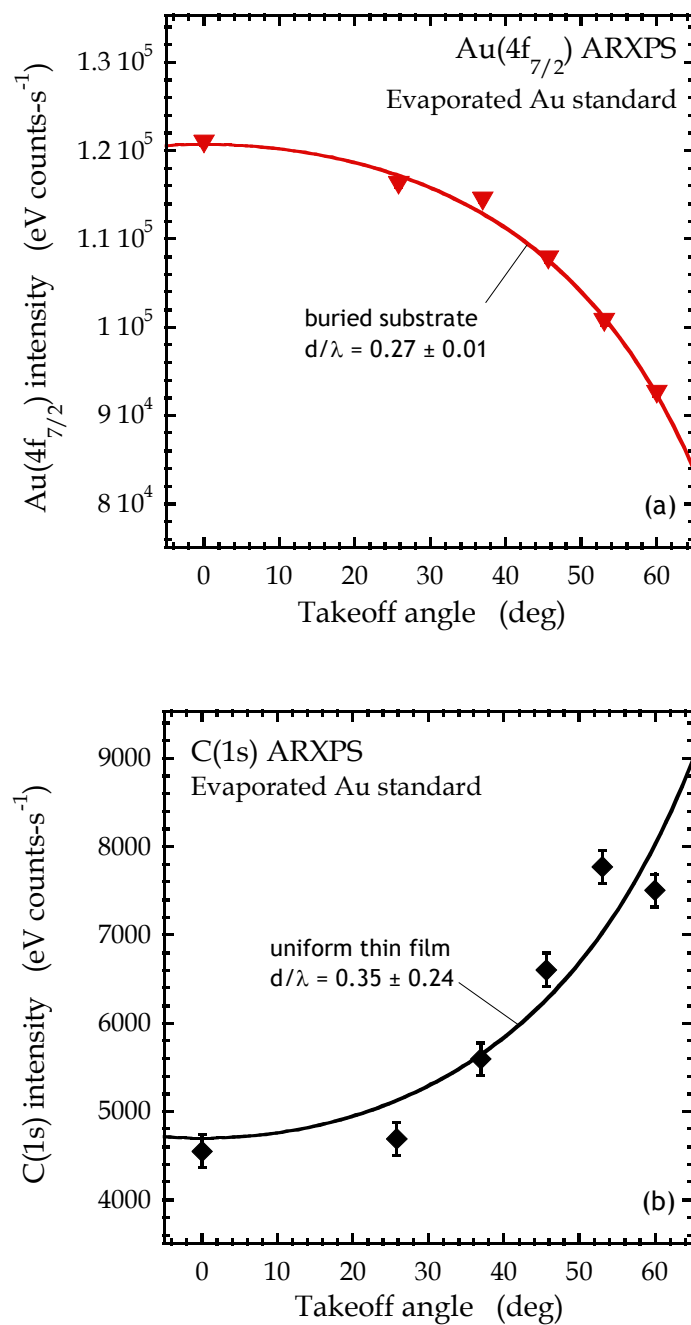


**Figure 9-8: (a) Au(4f<sub>7/2</sub>) and (b) C(1s) peak intensity as a function of photoelectron takeoff angle for a thick Au film with no sputter cleaning.**

Fits to the two sets of data, shown as solid lines in Fig. 9-8, we obtain values of  $d_{Au}/\lambda_{Au4f} = 0.27 \pm 0.01$  and  $d_C/\lambda_{C1s} = 0.35 \pm 0.24$ . To compare these values accurately, we use the correlation  $\lambda_{C1s}/\lambda_{Au4f} = \{E[C(1s)]/E[Au(4f_{7/2})]\}^{1/2}$  [6] to obtain  $d_C/\lambda_{Au4f} = 0.32 \pm 0.22$ . The close agreement between the calculated  $d_{Au}/\lambda_{Au4f}$  and  $d_C/\lambda_{Au4f}$  values again indicates proper alignment along the y axis. Finally, the Au film can be cleaned by sputtering with a beam of 3 keV Ar<sup>+</sup> (Ion Source IQE 12/38, SPECS Surface Nano Analysis GmbH, Berlin, Germany). As shown in Fig. 9-9(a), the sputter cleaning effectively removes the carbon contamination from the sample surface. As a result of the decrease in attenuation from the carbon layer, an increase in the Au(4f) intensity is also observed [Fig. 9-9(b)]. Results of Au(4f<sub>7/2</sub>) ARXPS for the sputter cleaned Au surface are shown in Fig. 9-9(c). The equivalent result for the non sputter cleaned Au sample is also shown in Fig. 9-9(c) for comparison. As expected, the photoelectron intensity is nearly constant with takeoff angle after sputter cleaning. The effect of the analysis spot size was also examined for the sputter cleaned Au surface. It was found that equivalent results were obtained using circular apertures of 3.16 and 0.63 mm, as indicated in Fig. 9-6(c). Because both apertures lead to the expected behavior in ARXPS, and because the 3.16 mm aperture provides a better signal to noise ratio, we have chosen to use the 3.16 mm aperture for most experiments. The angular acceptance used for ARXPS was the smallest available on the instrument,  $\pm 2^\circ$  (angular acceptance of up to  $\pm 7^\circ$  is available). At this angular acceptance ('low magnification mode') the size of the analyzed spot on the sample surface is  $\sim 2.5$  mm in diameter at normal photoelectron takeoff when using the 3.16 mm circular entrance aperture.

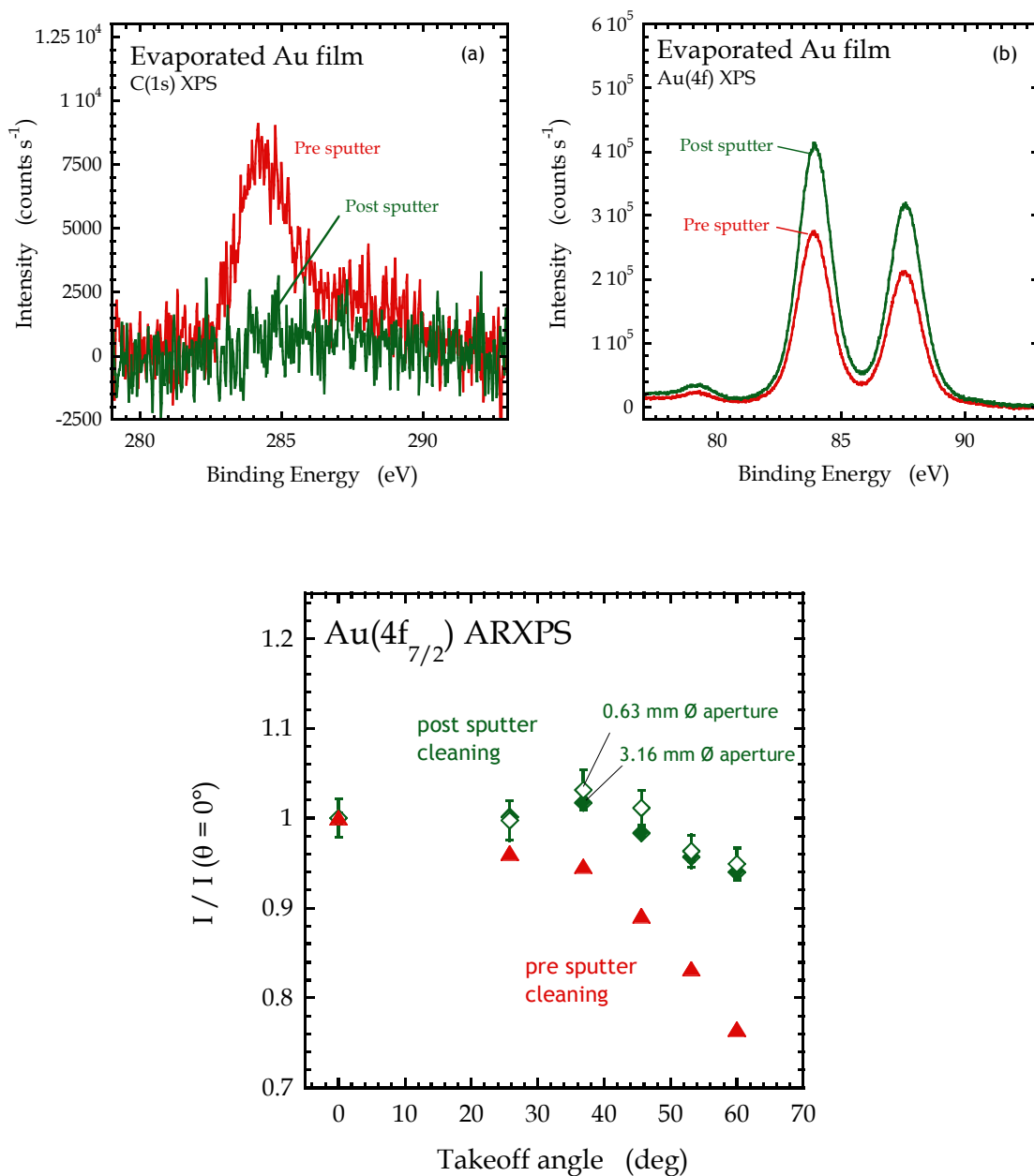


**Figure 9-9:** (a) C(1s) and (b) Au(4f<sub>7/2</sub>) XP spectra taken before and after sputter cleaning with 3 keV Ar<sup>+</sup>. (c) Au(4f<sub>7/2</sub>) intensity as a function of photoelectron takeoff angle, before and after sputter cleaning with 3 keV Ar<sup>+</sup>.

## 9.1 References

1. N. Maity, Ph.D. thesis, Cornell University, 1996.
2. J. Cooper and R. N. Zare, J. Chem. Phys. **48**, 942 (1968).
3. I. M. Band, Yu. I. Kharitonov, and M. B. Trzhaskovskaya, At. Data Nucl. Data Tables **23**, 443 (1979).
4. *Practical Surface Analysis: Volume I, Auger and X-ray Photoelectron Spectroscopy, 2nd ed.*, M. P. Seah and D. Briggs, Eds. (John Wiley and Sons, Chichester, England, 1990).
5. P. H. Citrin, G. K. Wertheim, and Y. Baer, Phys. Rev. Lett. **41**, 1425 (1978).
6. M. P. Seah and W. A. Dench, Surf. Interface Anal. **1**, 2 (1979).